



**HAL**  
open science

# Structural Control of Mineral Deposits. Theory and reality

Alain Chauvet

► **To cite this version:**

Alain Chauvet. Structural Control of Mineral Deposits. Theory and reality. MDPI, 2019, 978-3-03897-785-8. hal-02127353

**HAL Id: hal-02127353**

**<https://hal.umontpellier.fr/hal-02127353>**

Submitted on 13 May 2019

**HAL** is a multi-disciplinary open access archive for the deposit and dissemination of scientific research documents, whether they are published or not. The documents may come from teaching and research institutions in France or abroad, or from public or private research centers.

L'archive ouverte pluridisciplinaire **HAL**, est destinée au dépôt et à la diffusion de documents scientifiques de niveau recherche, publiés ou non, émanant des établissements d'enseignement et de recherche français ou étrangers, des laboratoires publics ou privés.



Distributed under a Creative Commons Attribution - NoDerivatives 4.0 International License



*minerals*

# Structural Control of Mineral Deposits

## Theory and Reality

---

Edited by  
Alain Chauvet

Printed Edition of the Special Issue Published in *Minerals*

# **Structural Control of Mineral Deposits**



# Structural Control of Mineral Deposits

## Theory and Reality

Special Issue Editor

**Alain Chauvet**

MDPI • Basel • Beijing • Wuhan • Barcelona • Belgrade



*Special Issue Editor*

Alain Chauvet

University of Montpellier

France

*Editorial Office*

MDPI

St. Alban-Anlage 66

4052 Basel, Switzerland

This is a reprint of articles from the Special Issue published online in the open access journal *Minerals* (ISSN 2075-163X) from 2018 to 2019 (available at: <https://www.mdpi.com/journal/minerals/special.issues/structural.control.deposits>).

For citation purposes, cite each article independently as indicated on the article page online and as indicated below:

LastName, A.A.; LastName, B.B.; LastName, C.C. Article Title. <i>Journal Name</i> <b>Year</b> , Article Number, Page Range.
---

**ISBN 978-3-03897-784-1 (Pbk)**

**ISBN 978-3-03897-785-8 (PDF)**

Cover image courtesy of Alain Chauvet.

© 2019 by the authors. Articles in this book are Open Access and distributed under the Creative Commons Attribution (CC BY) license, which allows users to download, copy and build upon published articles, as long as the author and publisher are properly credited, which ensures maximum dissemination and a wider impact of our publications.

The book as a whole is distributed by MDPI under the terms and conditions of the Creative Commons license CC BY-NC-ND.

# Contents

<b>About the Special Issue Editor</b> . . . . .	<b>vii</b>
<b>Preface to “Structural Control of Mineral Deposits”</b> . . . . .	<b>ix</b>
<b>Alain Chauvet</b> Editorial for Special Issue “Structural Control of Mineral Deposits: Theory and Reality” Reprinted from: <i>Minerals</i> <b>2019</b> , <i>9</i> , 171, doi:10.3390/min9030171 . . . . .	<b>1</b>
<b>Alain CHAUVET</b> Structural Control of Ore Deposits: The Role of Pre-Existing Structures on the Formation of Mineralised Vein Systems Reprinted from: <i>Minerals</i> <b>2019</b> , <i>9</i> , 56, doi:10.3390/min9010056 . . . . .	<b>5</b>
<b>Alexandre Cugerone, Emilien Oliot, Alain Chauvet, Jordi Gavalda Bordes, Angèle Laurent, Elisabeth Le Goff and Bénédicte Cenko-Tok</b> Structural Control on the Formation of Pb-Zn Deposits: An Example from the Pyrenean Axial Zone Reprinted from: <i>Minerals</i> <b>2018</b> , <i>8</i> , 489, doi:10.3390/min8110489 . . . . .	<b>27</b>
<b>Antonio Funedda, Stefano Naitza, Cristina Butta, Fabrizio Cocco and Andrea Dini</b> Structural Controls of Ore Mineralization in a Polydeformed Basement: Field Examples from the Variscan Baccu Locci Shear Zone (SE Sardinia, Italy) Reprinted from: <i>Minerals</i> <b>2018</b> , <i>8</i> , 456, doi:10.3390/min8100456 . . . . .	<b>47</b>
<b>Valery Y. Fridovsky, Maxim V. Kudrin and Lena I. Polufuntikova</b> Multi-Stage Deformation of the Khangalas Ore Cluster (Verkhoyansk-Kolyma Folded Region, Northeast Russia): Ore-Controlling Reverse Thrust Faults and Post-Mineral Strike-Slip Faults Reprinted from: <i>Minerals</i> <b>2018</b> , <i>8</i> , 270, doi:10.3390/min8070270 . . . . .	<b>70</b>
<b>Yang Song, Chao Yang, Shaogang Wei, Huanhuan Yang, Xiang Fang and Hongtao Lu</b> Tectonic Control, Reconstruction and Preservation of the Tiegelongnan Porphyry and Epithermal Overprinting Cu (Au) Deposit, Central Tibet, China Reprinted from: <i>Minerals</i> <b>2018</b> , <i>8</i> , 398, doi:10.3390/min8090398 . . . . .	<b>88</b>
<b>Johann Tuduri, Alain Chauvet, Luc Barbanson, Jean-Louis Bourdier, Mohamed Labriki, Aomar Ennaciri, Lakhlifi Badra, Michel Dubois, Christelle Ennaciri-Leloix, Stanislas Sizaret and Lhou Maacha</b> The Jbel Saghro Au(-Ag, Cu) and Ag-Hg Metallogenic Province: Product of a Long-Lived Ediacaran Tectono-Magmatic Evolution in the Moroccan Anti-Atlas Reprinted from: <i>Minerals</i> <b>2018</b> , <i>8</i> , 592, doi:10.3390/min8120592 . . . . .	<b>105</b>
<b>Alexis Grare, Olivier Lacombe, Julien Mercadier, Antonio Benedicto, Marie Guilcher, Anna Trave, Patrick Ledru and John Robbins</b> Fault Zone Evolution and Development of a Structural and Hydrological Barrier: The Quartz Breccia in the Kiggavik Area (Nunavut, Canada) and Its Control on Uranium Mineralization Reprinted from: <i>Minerals</i> <b>2018</b> , <i>8</i> , 319, doi:10.3390/min8080319 . . . . .	<b>153</b>

<b>Ingrid B. Maciel, Angela Dettori, Fabrizio Balsamo, Francisco H.R. Bezerra, Marcela M. Vieira, Francisco C.C. Nogueira, Emma Salvioli-Mariani and Jorge André B Sousa</b>	
Structural Control on Clay Mineral Authigenesis in Faulted Arkosic Sandstone of the Rio do Peixe Basin, Brazil	
Reprinted from: <i>Minerals</i> <b>2018</b> , <i>8</i> , 408, doi:10.3390/min8090408 . . . . .	<b>181</b>
<b>Tao Sun, Ying Xu, Xuhui Yu, Weiming Liu, Ruixue Li, Zijuan Hu and Yun Wang</b>	
Structural Controls on Copper Mineralization in the Tongling Ore District, Eastern China: Evidence from Spatial Analysis	
Reprinted from: <i>Minerals</i> <b>2018</b> , <i>8</i> , 254, doi:10.3390/min8060254 . . . . .	<b>198</b>
<b>Safouane Admou, Yannick Branquet, Lakhlifi Badra, Luc Barbanson, Mohamed Outhounjite, Abdelali Khalifa, Mohamed Zouhair and Lhou Maacha</b>	
The Hajjar Regional Transpressive Shear Zone (Guemassa Massif, Morocco): Consequences on the Deformation of the Base-Metal Massive Sulfide Ore	
Reprinted from: <i>Minerals</i> <b>2018</b> , <i>8</i> , 435, doi:10.3390/min8100435 . . . . .	<b>224</b>



## About the Special Issue Editor

**Alain Chauvet** (Dr. HDR) is a senior CNRS Researcher at the Géosciences Montpellier laboratory, France. After a Ph.D. in Structural Geology devoted to the late-orogenic extension in Norway, he specialized in Tectonic Control of Ore Deposits with a focus on the perigranitic mineralizations of South America, China, Europe, . . . , and the characterization of the relationships between Large Igneous Provinces and Mineralizations in North Africa. He is involved in several collaborative projects and expertises with industrial mining companies.



# Preface to “Structural Control of Mineral Deposits”

This compilation of publication results from more than 20 years of questioning and of applying structural geology in mining geology by the guest editor. If it is common to place the various deposits of the earth into large classes that allow recognizing and identifying some characters useful to detect, explore, and find other similar deposits, experience demonstrates that each deposit is unique and cannot answer perfectly to a generic model. This is why we suspect that there exists a gap between theory (i.e., the classical model) and reality that needs to be estimated and taken into account in any type expertise or study of an unknown mineral deposit. The following publications try to be concerned by this way of working.

My knowledge and interest in the structural control of mineral deposits benefited from several discussions, suggestions, and field trip shared with a lot of persons that are greatly acknowledged here. An exhaustive list is impossible, but I want to particularly acknowledge the CVRD (Vale), Buenaventura, Cedimin, Managem, Kasbah Resource, CMS, SMI, and CTT mining companies and all geologists that took the time to discuss with me of structural problems in mining geology, with a special mention of A.S. André, L. Badra, L. Bailly, L. Barbanson, Y. Branquet, X. Charonnat, A. Ennaciri, C. Ennaciri, M. Faure, L. Fontboté, A. Gaouzi, S. Gialli, E. Gloaguen, M. Iseppi, K. Kouzmanov, J. Onezime, P. Piantone, S. Sizaret, E. Tourneur, J. Tuduri, N. Volland. All the reviewers that significantly improved the quality of this book are also warmly acknowledged.

**Alain Chauvet**  
*Special Issue Editor*



Editorial

## Editorial for Special Issue “Structural Control of Mineral Deposits: Theory and Reality”

Alain Chauvet

UMR 5243, Géosciences Montpellier, University of Montpellier, cc 60, CEDEX 5, 34095 Montpellier, France; chauvet@gm.univ-montp2.fr; Tel.: +33-(0)4-67-14-48-57

Received: 7 March 2019; Accepted: 8 March 2019; Published: 11 March 2019

“Structural Control” remains a crucial point that is frequently absent in scientific and/or economic analyses of ore deposits, whatever their type and class, although a selection of references illustrates its importance [1–5]. The case of lode deposits is particularly adapted, but other types, like breccia pipes, stockwork, massive sulphides, skarn, etc., also concern Structural Control. Works on the Structural Control of ore deposits are not abundant in the recent literature, and, as frequently suggested, structural geology often is not sufficiently developed in the exploration programs of many mining camp’s strategies. A few compilations have been devoted to this theme in the last two decades, such as (i) the special publication of the Geological Society of London, concerned with the link between fracturing, flow, and mineralization [6], (ii) the review of the Society of Economic Geology, devoted to Structural Control [7], (iii) a special publication of the Geological Society of London, looking to study the genetic link that can exist between mineralization and orogenic domains [8], and finally, (iv) a special issue of the Journal of Structural Geology, devoted to the application of Structural Geology in mineral exploration and mining [9]. In addition to these four compilations, only a few publications have been concerned with this theme, and most of them are dated before the year 2000. These publications mostly concerned vein internal infilling textures [10,11], the vein formation model, with the contribution and controversy of the crack seal, dissolution-precipitation, diffusion, and seismic-valves mechanisms (e.g., [12–16]). In his review, Chauvet [17] discussed some of these concepts, in order to highlight the role and the significance of pre-existing structures in the formation of vein-style deposits.

Three publications of this volume explore the development of mineralization in the specific context of orogenic domains. Cugerone et al. [18] offer a detailed study of a rather complex Pb–Zn mineralisation developed within the orogenic Hercynian Pyrenees during two mineralization stages, each of them linked with a deformational event. The syntectonic primary mineralization is remobilized and helps the formation of the second one. The same approach is used within the two following contributions on the same theme [19,20]. Funedda et al. [19] and Fridovsky et al. [20] also used a detailed description of the relationships between mineralization and deformation in deformed domains, such as the Variscan domain of Sardinia and the Verkhovansk-Kolyma folded region of NE Russia. Funedda et al. [19] pay close attention to the opening process of structures that will serve as traps for mineralised fluid catching, a fact that is fundamental in any tectonic understanding of a mineralised vein system [17]. Fridovsky et al. [20] also proposed a pluri-deformational model associated with multiple stages of mineralisation formation.

The relationship between magmatism, regional tectonic context, and mineralization remain a question that has still been debated in several recent publications [21,22], thus demonstrating that this question is still relevant and may help in the distinction between intrusion-related, orogenic deposits and the Cu–Au-rich porphyry types. Two contributions explore new methods of investigation that provide an innovative vision of the relationship between magmatism and mineralization. Song et al. [23] examine the consequences of the telescoping of two mineralized systems (a subsequent epithermal system affects a primary porphyritic one within the Tiegelongnan Porphyry and the epithermal overprinting Cu (Au) deposit, Central Tibet, China) with a focus on the role of the

dislocation effects on ore reserve calculations and future deposits discoveries. Tuduri et al. [24] suggest an original way to demonstrate the genetic link between mineralization and magmatism by establishing that both are developed in the same regional tectonic context, in the highly mineralised Moroccan Anti-Atlas. This contribution represents an indirect but efficient way to relatively date the emplacement of magmatism and mineralization formations, and their relationships.

In the past, the concept of a gold-bearing shear zone has not given satisfying results in terms of our understanding of gold deposits, and has been more or less totally abandoned, except within few specific sectors of the Canadian shield in which the role of major crustal faults is still at the centre of the accepted models [25]. In the domain of economic geology, faults are fundamental structures that can have two contrasting behaviours: (i) Hydrogeological barriers that help the concentration of ore, as demonstrated by the contribution of Grare et al. [26] in the case of the Kiggavik uranium example (Canada), and (ii) a zone of permeability that can favour fluid circulation and can serve as a guide for the mineralisation trapping. The work of Maciel et al. [27] proposes a surprising example in which fault occurrences have a negative role for clay authigenesis efficiency; this work also discusses the consequence on reservoir characteristics. Sun et al. [28] end the section on relations with brittle tectonics by presenting an innovative GIS-based spatial analysis of mineral deposit patterns in correlation with detailed structural features, in order to propose some implications on Structural Control. The chosen example was provided from the Copper deposit of the Tongling Ore district of Eastern China.

Concerning other orebodies than vein-type ones, volcanic-hosted massive sulphide deposits (VHMS) have been recently the subject of much debate, specifically with the suggestion of a significant contribution of “replacement processes” in their modes of formation [29,30]. In addition, it has been demonstrated that stockwork within VHMS environments can result in subsequent syntectonic veining instead of earlier veins related to feeder zones [31]. Indeed, the observation of stockwork within a VHMS context needs to be considered with particular attention because of the possible coexistence of the two types of stockwork: the one related to the feeder zone and the other the result of subsequent deformation [17]. It has been suggested that the second event and associated metal may contribute significantly to a relative enrichment in VHMS environment. Without any reference to some replacement process, the contribution of Admou et al. [32] ends the special issue with a very attractive formation model of the Moroccan Guemassa VHMS deposit, strongly involving the active role of normal faults and Structural Control, since the beginning of the volcanic activity. In fact, it appears that most of the VHMS deposits certainly do not present the classical geometrical model exhibited within all teaching books, but instead form by wall-rock replacement (metasomatism) strongly helped by the re-using of pre-existing structures, such as folds, unconformities, and/or fault and deformation features. Such a contribution is frequently underestimated.

**Conflicts of Interest:** The author declares no conflicts of interest.

## References

1. Forde, A.; Bell, T.H. Late structural control of mesothermal vein-hosted gold deposits in Central Victoria, Australia: Mineralization and exploration potential. *Ore Geol. Rev.* **1994**, *9*, 33–59. [[CrossRef](#)]
2. Davis, B.K.; Hippertt, J.F.M. Relationships between gold concentration and structure in quartz veins from the Hodgkinson Province, northeastern Australia. *Mineral. Depos.* **1998**, *33*, 391–405. [[CrossRef](#)]
3. Chauvet, A.; Piantone, P.; Barbanson, L.; Nehlig, P.; Pedroletti, I. Gold deposit formation during collapse tectonics: Structural, mineralogical, geochronological, and fluid inclusion constraints in the Ouro Preto gold mines, Quadrilátero Ferrífero, Brazil. *Econ. Geol.* **2001**, *96*, 25–48. [[CrossRef](#)]
4. Chauvet, A.; Bailly, L.; André, A.S.; Monié, P.; Cassard, D.; Llosa Tajada, F.; Vargas, J.R.; Tuduri, J. Internal vein texture and vein evolution of the epithermal Shila-Paula district, southern Peru. *Mineral. Dep.* **2006**, *41*, 387–410. [[CrossRef](#)]
5. Tunks, A.J.; Cooke, D.R. Geological and structural controls on gold mineralization in the Tanami District, Northern Territory. *Mineral. Dep.* **2007**, *42*, 107–126. [[CrossRef](#)]

6. McCaffrey, K.; Lonergan, L.; Wilkinson, J. *Fractures, Fluid Flow and Mineralization*; Geological Society of London Special Publication: London, UK, 1999; Volume 155, 328p.
7. Richards, J.P.; Tosdal, R.M. Structural Controls on Ore Genesis. In *Reviews in Economic Geology*; Society of Economic Geologists, Inc.: Littleton, CO, USA, 2001; 181p.
8. Blundell, D.J.; Neubauer, F.; Von Quadt, A. *The Timing and Location of Major Ore Deposits in an Evolving Orogen*; Geological Society of London Special Publication: London, UK, 2002; Volume 204, 358p.
9. Vearncombe, J.R.; Blenkinsop, T.G.; Reddy, S.M. Applied Structural Geology for Mineral Exploration and Mining. *J. Struct. Geol.* **2004**, *26*, 989–994. [[CrossRef](#)]
10. Dowling, K.; Morrison, G. Application of quartz textures to the classification of gold deposits using North Queensland examples. *Econ. Geol. Mon.* **1990**, *6*, 342–355.
11. Dong, G.; Morrison, G.; Jaireth, S. Quartz textures in epithermal veins, Queensland - classification, origin, and implication. *Econ. Geol.* **1995**, *90*, 1841–1856. [[CrossRef](#)]
12. Ramsay, J.G. The crack-seal mechanism of rock deformation. *Nature* **1980**, *284*, 135–139. [[CrossRef](#)]
13. Cox, S.F.; Etheridge, M.A. Crack-seal fibre growth mechanism and their significance in the development of oriented layer silicate microstructures. *J. Struct. Geol.* **1983**, *92*, 147–170. [[CrossRef](#)]
14. Bons, P.D.; Jessell, M.W. Experimental simulation of the formation of fibrous veins by localised dissolution-precipitation creep. *Mineral. Mag.* **1997**, *61*, 53–63. [[CrossRef](#)]
15. Boullier, A.M.; Robert, F. Paleoseismic events recorded in Archean gold quartz vein networks, Val-Dor, Abitibi, Quebec, Canada. *J. Struct. Geol.* **1992**, *14*, 161–177. [[CrossRef](#)]
16. Bons, P.D.; Elburg, M.A.; Gomez-Rivas, E. A review of the formation of tectonic veins and their microstructures. *J. Struct. Geol.* **2012**, *43*, 33–62. [[CrossRef](#)]
17. Chauvet, A. Structural Control of Ore Deposits: The Role of Pre-existing Structures on the Formation of Mineralised Vein Systems. *Minerals* **2019**, *9*, 56. [[CrossRef](#)]
18. Cugerone, A.; Oliot, E.; Chauvet, A.; Gavalda Bordes, J.; Laurent, A.; Le Goff, E.; Cenki-Tok, B. Structural Control on the Formation of Pb-Zn Deposits: An Example from the Pyrenean Axial Zone. *Minerals* **2018**, *8*, 489. [[CrossRef](#)]
19. Funedda, A.; Naitza, S.; Buttau, C.; Cocco, F.; Dini, A. Structural Controls of Ore Mineralization in a Polydeformed Basement: Field Examples from the Variscan Baccu Locci Shear Zone (SE Sardinia, Italy). *Minerals* **2018**, *8*, 456. [[CrossRef](#)]
20. Fridovsky, V.Y.; Kudrin, M.V.; Polufuntikova, L.I. Multi-Stage Deformation of the Khangalas Ore Cluster (Verkhoyansk-Kolyma Folded Region, Northeast Russia): Ore-Controlling Reverse Thrust Faults and Post-Mineral Strike-Slip Faults. *Minerals* **2018**, *8*, 270. [[CrossRef](#)]
21. Dressel, B.C.; Chauvet, A.; Trzaskos, B.; Biondi, J.C.; Bruguier, O.; Monié, P.; Villanova, S.N.; Newton, J.B. The Passa Tres lode gold deposit (Parana State, Brazil): An example of structurally-controlled mineralisation formed during magmatic-hydrothermal transition and hosted within granite. *Ore Geol. Rev.* **2018**, *102*, 701–727. [[CrossRef](#)]
22. Tuduri, J.; Chauvet, A.; Barbanson, L.; Labriki, M.; Dubois, M.; Trapy, P.H.; Lahfid, A.; Poujol, M.; Melleton, J.; Badra, L.; et al. Structural control, magmatic-hydrothermal evolution and formation of hornfels-hosted, intrusion-related gold deposits: Insight from the Thaghassa deposit in Eastern Anti-Atlas, Morocco. *Ore Geol. Rev.* **2018**, *97*, 171–198. [[CrossRef](#)]
23. Song, Y.; Yang, C.; Wei, S.; Yang, H.; Fang, X.; Lu, H. Tectonic Control, Reconstruction and Preservation of the Tiegelongnan Porphyry and Epithermal Overprinting Cu (Au) Deposit, Central Tibet, China. *Minerals* **2018**, *8*, 398. [[CrossRef](#)]
24. Tuduri, J.; Chauvet, A.; Barbanson, L.; Bourdier, J.L.; Labriki, M.; Ennaciri, A.; Badra, L.; Dubois, M.; Ennaciri-Leloix, C.; Sizaret, S.; Maacha, L. The Jbel Saghro Au(-Ag, Cu) and Ag-Hg Metallogenetic Province: Product of a Long-Lived Ediacaran Tectono-Magmatic Evolution in the Moroccan Anti-Atlas. *Minerals* **2018**, *8*, 592. [[CrossRef](#)]
25. Poulsen, K.H.; Robert, F. Shear zones and gold: Practical examples from the southern Canadian Shield. *Geol. Assoc. Can. Short Course Notes* **1989**, *6*, 239–266.
26. Grare, A.; Lacombe, O.; Mercadier, J.; Benedicto, A.; Guilcher, M.; Trave, A.; Ledru, P.; Robbins, J. Fault Zone Evolution and Development of a Structural and Hydrological Barrier: The Quartz Breccia in the Kiggavik Area (Nunavut, Canada) and Its Control on Uranium Mineralization. *Minerals* **2018**, *8*, 319. [[CrossRef](#)]

27. Maciel, I.B.; Dettori, A.; Balsamo, F.; Bezerra, F.H.R.; Vieira, M.M.; Nogueira, F.C.C.; Salvioli-Mariani, E.; Sousa, J.A.B. Structural Control on Clay Mineral Authigenesis in Faulted Arkosic Sandstone of the Rio do Peixe Basin, Brazil. *Minerals* **2018**, *8*, 408. [[CrossRef](#)]
28. Sun, T.; Xu, Y.; Yu, X.; Liu, W.; Li, R.; Hu, Z.; Wang, Y. Structural Controls on Copper Mineralization in the Tongling Ore District, Eastern China: Evidence from Spatial Analysis. *Minerals* **2018**, *8*, 254. [[CrossRef](#)]
29. Aerden, D.G.A.M. Formation of Massive Sulfide Lenses by Replacement of folds: The Hercules Pb–Zn Mine, Tasmania. *Econ. Geol.* **1993**, *88*, 377–396. [[CrossRef](#)]
30. Perkins, W.G. Mount Isa lead-zinc orebodies: Replacement lodes in a zoned syndeformational copper–lead–zinc system? *Ore Geol. Rev.* **1997**, *12*, 61–110. [[CrossRef](#)]
31. Chauvet, A.; Onézime, J.; Charvet, J.; Barbanson, L.; Faure, M. Syn- to late-tectonic stockwork emplacement within the Spanish section of the Iberian Pyrite Belt: Structural, textural and mineralogical constraints in the Tharsis-La Zarza areas. *Econ. Geol.* **2004**, *99*, 1781–1792. [[CrossRef](#)]
32. Admou, S.; Branquet, Y.; Badra, L.; Barbanson, L.; Outhounjite, M.; Khalifa, A.; Zouhair, M.; Maacha, L. The Hajar Regional Transpressive Shear Zone (Guemassa Massif, Morocco): Consequences on the Deformation of the Base-Metal Massive Sulfide Ore. *Minerals* **2018**, *8*, 435. [[CrossRef](#)]



© 2019 by the author. Licensee MDPI, Basel, Switzerland. This article is an open access article distributed under the terms and conditions of the Creative Commons Attribution (CC BY) license (<http://creativecommons.org/licenses/by/4.0/>).



Review

# Structural Control of Ore Deposits: The Role of Pre-Existing Structures on the Formation of Mineralised Vein Systems

Alain CHAUVET 

CNRS-UMR 5243, Géosciences Montpellier, University of Montpellier, cc 60,  
34095 Montpellier CEDEX 5, France; alain.chauvet@univ-montp2.fr; Tel.: +3-34-6714-4857

Received: 29 October 2018; Accepted: 15 January 2019; Published: 17 January 2019

**Abstract:** The major role played by pre-existing structures in the formation of vein-style mineral deposits is demonstrated with several examples. The control of a pre-existing decollement level on the formation of a crustal extension-related (collapse) gold deposit is first illustrated in the Quadrilátero Ferrífero from Brazil. Shear zone and decollement structures were also examined and shown to control veins formation by three distinct processes: (i) re-aperture and re-using of wrench shear zones in the case of Shila gold mines (south Peru); (ii) remobilisation of metal in volcanic-hosted massive sulphide (VHMS) deposit by subsequent tectonic events and formation of a secondary stockwork controlled by structures created during this event (Iberian Pyrite Belt, Spain); (iii) formation of economic stockwork by contrasting deformation behaviours between ductile black schist versus brittle more competent dolomite (Cu-Ifri deposit, Morocco). Two examples involve changing of rheological competence within zones affected by deformation and/or alteration in order to receive the mineralisation (case studies of Achmmach, Morocco, and Mina Soriana, Spain). The last case underscores the significance of the magmatic–hydrothermal transition in the formation of mesothermal gold deposits (Bruès mine, Spain). All these examples clearly demonstrate the crucial role played by previously formed structures and/or texture in the development and formation of ore deposits.

**Keywords:** vein; structure; textures; infilling; breccia; comb quartz; pull-apart; exploration; pre-existing structures; decollement

---

## 1. Introduction

Numerous studies have been devoted to the process of vein formation mainly because of their significance in term of tectonics and deformation (stress and strain determination), e.g., [1–5], but also because of their significant economic interest in the case of metal-bearing veins, e.g., [6–8]. Several works have concentrated on the external geometry of veins and their relationships with the mode of opening and, consequently, the local or regional stress field during vein formation [9–11]. Complementary studies have also integrated information that can be deduced from vein infilling textures, such as the classical tripartite division in syntaxial (inward growth), antitaxial (outward growth) and stretching veins (complex pattern with no consistent growth direction) [12–14]. In economic geology, and particularly in vein-type deposits, the study of the nature and texture of vein infilling is particularly important because it lies at the base of the ore-forming process itself. No recent works have been concerned by this kind of analysis. The latest contributions [15–17] only deal with the internal texture of ore deposits without considering the (external) geometry of the veins themselves.

This paper, as an introduction to the Minerals Special Issue “Structural Control of Ore Deposits, Theory and Reality” focuses on the relationships between the shape and internal texture of ore-bearing veins with the objectives to better understanding vein formation processes and, consequently, to improve mining exploration strategies. I will present and discuss seven case studies of metal-bearing

veins with different modes of formation that highlight the role of pre-existing features on their development. This aspect seems to be frequently underestimated, at least in the case of vein deposits, and this work aims to demonstrate its significance in the development of exploration and exploitation programs. The re-using of some previously formed structures has, in that case, a significant but passive role with respect to the formation of the economic feature. This concept is already exemplified in another contribution of this volume [18]. Each of the seven cases presented herein include a brief overview of the regional geology and deformation history, followed by a detailed geometrical and textural analysis of ore-bearing veins and a regional-scale genetic model that integrates these data. The relationships between neo-formed structures versus pre-existing ones will be highlighted in each case as well as its implications for regional vein distribution and, consequently, exploration programs.

## 2. Methodology: Structural Analysis Applied to Metallogeny

The literature on structurally controlled vein-style mineral deposits, e.g., [7,8], has provided a number of theoretical concepts that link vein orientation and geometry with respect to the tectonic stresses. However, only a few studies have integrated regional tectonic context, vein shape and internal vein texture [19–21].

The present work emphasises the importance of multidisciplinary work on vein-style mineralisation combining (micro) structural, textural, and mineralogical analyses, in order to answer to the following questions:

- What tectonic context is responsible for trap formation? (the geometrical analysis)
- What is the mode and condition of filling? (the internal analysis)

### 2.1. Trap Formation

Figure 1 illustrates three classic tectonic traps found frequently in the literature [22] and described in this work. We can distinguish (i) vein opening during flexural folding of multilayers with contrasted lithology with a void being created within competent levels by (re-)opening of the coeval axial plane cleavage (Figure 1a); (ii) gaps formed by differential shearing due to fracturing and boudinage of more competent layers leading to stockwork development (Figure 1b); (iii) aperture controlled by extensional relay (pull-apart) associated with either fibrous/comb veins or breccia veins (Figure 1c). The factors determining these alternative types will be treated further. These three mechanisms are the ones most commonly invoked to explain vein formation in economic interest with probably more cases resembling Figure 1c. Figure 2 illustrates the mechanism of re-using a previously formed structure left lateral shear zone showing a main shearing vein with breccia and secondary cleavage parallel veins that opened during a subsequent tectonic event with different stress directions as when the shear zone originally formed. Internal filling for each stage is drastically different: brecciation without infilling in the case of the main shearing plane and comb or fibrous crystallisation in the secondary cleavage parallel veins (Figure 2).

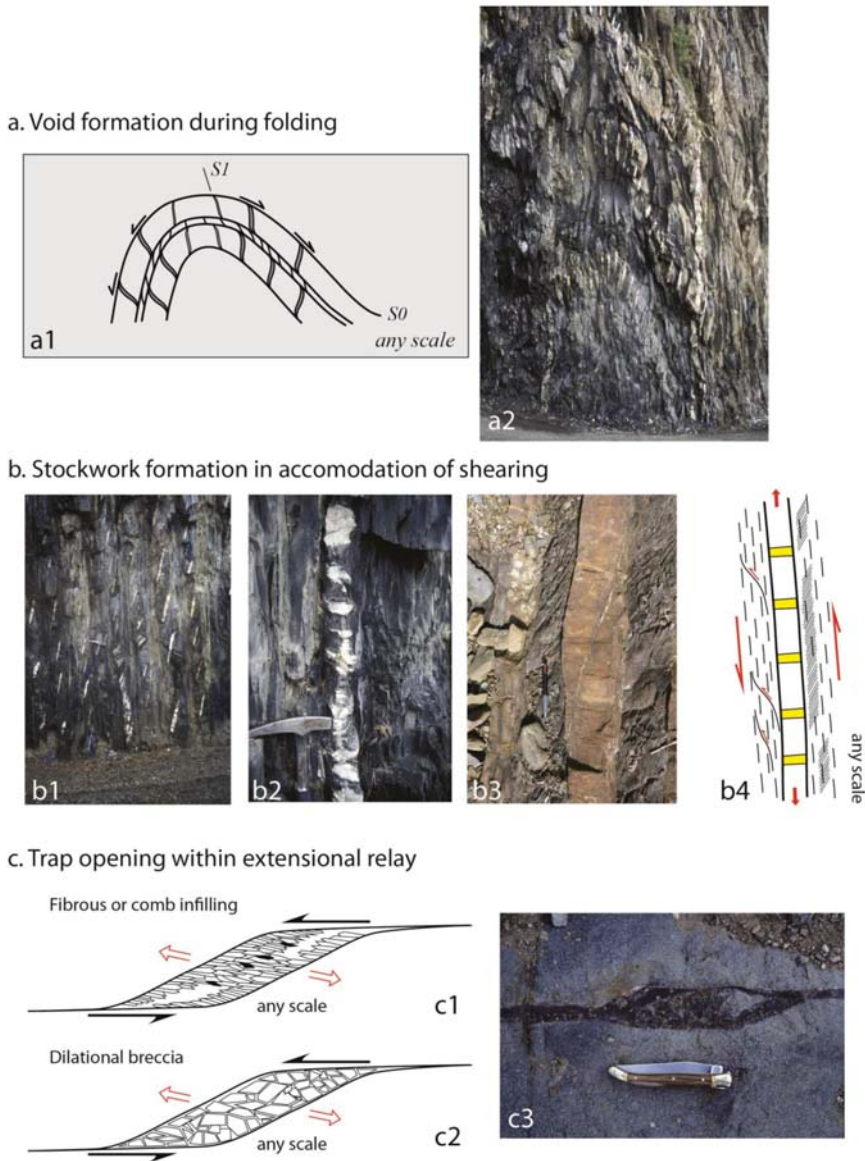


**Figure 1.** Three examples of traps and voids mode of formation. (a) Model of formation of sigmoidal veins by antithetic bedding-controlled gliding during fold development (a1). Example from the Bourg-d’Oisans area (a2). (b) Stockwork formation in accomodation of shearing affecting some multi-layers rocks with contrast of competence (b1, b2 and b3). Conceptual sketch (b4) in which yellow veins represent the stockwork formed in more competent layers. (c) Trap opening within left lateral pull-apart (c3). The two sketches c1 and c2 illustrate the process and show the two types of filling encountered within these structures. See text for explanation.

It may be surprising to see that Figures 1a and 2, propose that a cleavage plane, reputed to be a plane of maximum flattening, is used as a syntectonic trap for mineralisation during its formation.

However, this solution has been adopted and demonstrated within two works on this topic [23,24]. We will see, in the following examples, what are our arguments to defend this unconventional concept. The case of Figure 2 should not raise the same concern because, here, cleavage serves as a receptacle for ore concentration in a late deformation event that causes dilation parallel to a pre-existing cleavage.

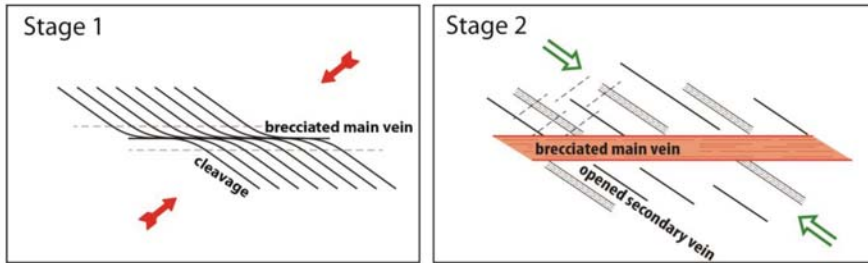


**Figure 2.** Example of re-using and re-opening of a previously formed left-lateral shear zone during two different states of stress. Red and green arrows correspond to the shortening direction of each stage. Note that main infilling is realised during stage 2.

## 2.2. Internal Texture

The following internal texture of ore-bearing veins can be distinguished.

- **Massive or buck texture:** rare examples of this texture have been interpreted to result where voids are filled after, not during their formation. This texture is frequently characterised by euhedral or anhedral grain of variable size throughout the vein [15] due to uniform growth rates. Grain orientation can also be highly variable. In fact, such a texture provides limited information about the tectonic conditions prevailing during vein formation.
- A **fibrous or comb crystal shape** corresponds to crystallisation coeval with vein opening and represents the more interesting texture for the topics of this study (Figure 3). Whether comb or fibrous textures develop depends on the rate of trap opening versus crystal growth (see below).

Comb quartz is commonly related to (Figure 3a) (i) a supersaturated fluid invading an open space (the initial fracture) with competitive crystal growth normal to the walls [16,25,26]; and (ii) a slow opening rate of the fracture keeping pace with the rate of crystal growth [15,27]. Veins formed by this process only differ from crack-seal veins [28–30] by the lack of fibrous crystallisation and evidence for incremental cracking, such as successive and parallel inclusion trails. Indeed, fibrous textures result from the same process as comb infilling, except that crystal growth is incremental instead of continuous. In this case, the crack is caused by fluid overpressure and crystallisation occurs immediately after the aperture with a unique free direction for crystal growth—the vein centre. The succession of cracking event and, consequently, of immediate filling, explains the continuous crystallisation and, therefore, the fibres (Figure 3b) [31]. By contrast, comb texture is supposed to form where the rate of crystallisation is lower than the opening rate. In this case, the crystallisation only covers the vein wall, and crystals are larger as in the case of fibrous veins and can develop during multiple growth stages (Figure 3a), sometimes associated with a change of fluid composition and chemistry [15]. It is still uncertain, though, if all fibrous veins form by the crack-seal mechanism, or whether they can also form by continuous fibre growth, where diffusion keeps pace with the rate of dilation [26,32].

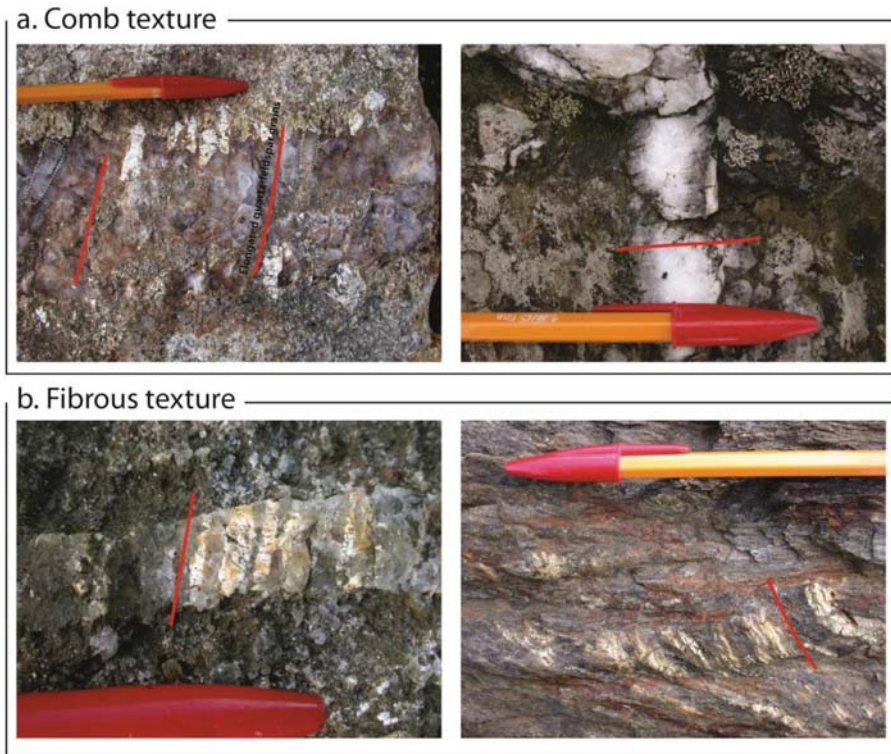


**Figure 3.** Examples of comb and fibrous textures from the Hercynian mining district of Tras-os-Montes, Galicia, Spain. Red lines illustrate the elongated quartz and feldspar grains indicate the opening direction. Note the difference between fibres that cross-cut the veins and comb grains that do not traverse the vein.

- **Breccia textures** are witnesses of complex processes for which we have to take into account three parameters based on the recognition between fragments and matrix in order to understand their process of formation:
  - The nature of the matrix or cement (rock flour, sediment, volcanic, magmatic, hydrothermal, . . . );
  - The nature and shape of the fragments (circularity, size, distribution, fabrics, monogenic or polygenic, lithological nature);
  - The relationships between fragments and matrix/cement (matrix-supported or grain-supported).

As a function of these three parameters, a genetic classification of breccia has been proposed by [33], which is frequently used as an indicator of the conditions of vein formation [34–39]. The most used in lode-related economic geology are the tectonic, hydrothermal, magmatic, collapse-related, crackle, hydraulic and dilational breccia. Their recognition is based on the following features (Figure 4):

- **Tectonic breccia** is easily recognisable because of grain reduction and oriented fragments (Figure 4a). Depending of its maturity (function of the strain intensity), fragments can be in contact (grain-supported breccia, beginning of fragmentation and subsequent comminution) or finally flooded in a largely developed matrix (matrix-supported breccia). Tectonic breccia is more

frequently monogenic. With respect to the intensity of the deformation and the presence or lack of clay minerals, they can be called cataclasite, ultracataclasite or gouge.

- *Hydrothermal breccia* is characterised by more-or-less rounded fragments of the same nature (not always) in place within a hydrothermal matrix. Frequently, the final voids are filled by cement that can frequently contain some metals in economic contexts (Figure 4b).
- *Magmatic breccia* is more or less similar to the hydrothermal ones, except that the matrix is only magmatic and there is no cement (Figure 4c). In this case, the fragments are rounded and never in contact (matrix supported breccia). Due to the explosive processes, magmatic breccias are frequently polygenic. The differentiation between matrix and fragments, both magmatic, is sometimes difficult, especially in thin sections.
- *Collapse breccia* is easy to recognise because they show a large variation of fragment size, the presence of cement, and grain-supported texture (Figure 4d). Their geometry is clearly consistent with their mode of formation: (i) collapse of the fragments in response to an underlying explosion or void formation by dissolution and (ii) posterior cementation.
- *Crackle breccia* is an early stage of what is going becoming a hydrothermal, tectonic or hydraulic breccia. Due to their mode of formation, they are monogenic, with a low matrix and they can be assimilated to early fragmentation in response to either tectonic stress or fluid-related fracturing. Some parts frequently exhibit the host rocks being not totally disrupted whether other parts can be more mature with well-expressed breccia texture (Figure 4e).
- *Hydraulic breccia* is the result of hydraulic fracturing. It exhibits typical jigsaw geometry with a monogenic character and a very regular pattern (Figure 4f). The matrix is well represented, and fragments are never in contact. The mode of formation is only due to cracking due to fluid overpressure. *Dilational breccia* forms within extensional relay or pull-apart (Figures 1c, 2 and 5). In this case, breccia formation is explained by the fact that void creation causes the fragmentation of the hosted rock affected by the pull-apart formation. Fragments are weakly transported and sometimes rotated and the occurrence of cement is common. Why some pull-aparts are filled by fibrous/comb crystals or dilational breccia remains an open question (Figure 2c). The outcrop in Figure 5 can help because the two types of infilling have been observed within the same structure. Since dilational breccia has been observed on the wall of the secondary formed comb infilling (Figure 5b), we suspect that both types of texture can be developed in the same structural context. Field relationships demonstrate that dilational breccia texture can form at the beginning of the process, when rates of aperture are weak and late and rapid opening can explain the superposition of fibrous/comb infilling. Indeed, the alternative formation of dilational breccia or comb texture in the core of pull-apart can appear as a function of opening velocity, crystal growth rate, and fluid saturation. We guess that dilational breccia in the core of pull-apart can be created during all main tectonic contexts (i.e., compression, extension, transtension, etc.) and not restricted to the only case of wrench tectonics, as this has been established for the large-scale pull-apart-related basin formation along crustal-scale faults [40].

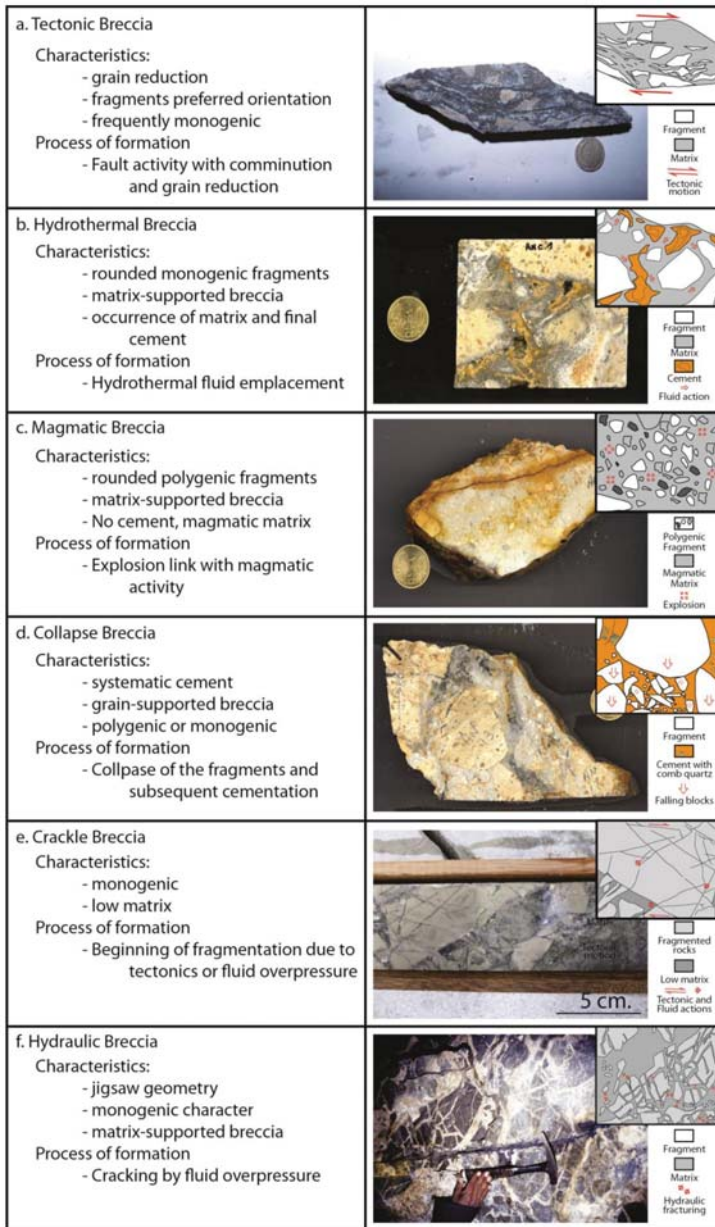


**Figure 4.** Breccia texture classification frequently used in ore geology. Each case is described in detail in the text. A conceptual sketch is indicated for each photograph in order to correctly interpret the image. The scale of these sketches is the same as the corresponding photograph. In red, some indications about the process responsible for breccia formation are provided.

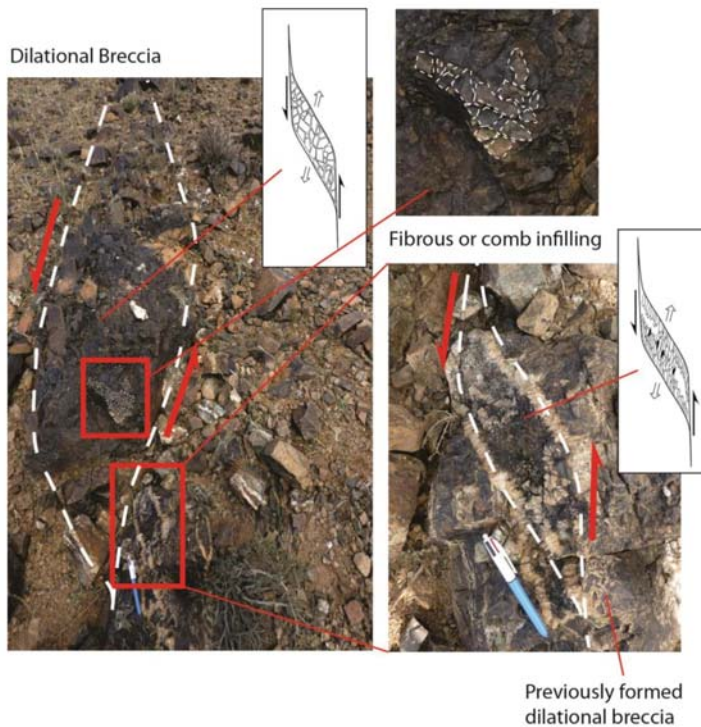


**Figure 5.** Superposition of dilational breccia texture and fibre/comb ones within similar left-lateral pull-apart structures (see text for explanation of the cause of occurrence of fibrous or breccia texture).

### 3. Vein Formation Process and Tectonics: Examples from Ore Deposit Study

#### 3.1. Gold Concentration during Collapse Tectonics

A pluridisciplinary approach has been undertaken with the study of gold-bearing quartz veins of the Quadrilátero Ferrífero (Minas Gerais, Brazil) [41]. This deposit has been classically interpreted as a strongly deformed pre-tectonic one on the basis of the sigmoid shape (Figure 6) exhibited by ore-bearing veins and, also, as a typical Archean orogenic gold deposit [42]. The internal vein texture study combined with regional tectonic constraints suggests an alternative model in which veins are formed in response to the late collapse tectonics, later with respect to the nappes emplacement [41]. During these movements, sigmoid voids were created and filled by elongate quartz grains associated with sulphides, tourmaline and carbonates (Figure 6a). Such a normal motion has been facilitated by the existence of mica-rich levels (Figure 6b) that underline the foliation of the hosted meta-sediments. This result has been obtained essentially because the internal texture has revealed that quartz grains are un-deformed and that their formation was the result of only one opening episode, within free tectonic stress context. The superposition of sigmoidal pull-apart formation on earlier shearing deformational event has been clearly observed (Figure 6c). The process of formation is similar to the conceptual sketch of the Figure 2 with re-using and re-opening of pre-existing shear zone. Here, the sigmoidal shape of the mica-rich level due to the earlier thrust event is re-used. Inferred hydrothermal effects were responsible for the formation of illite, sulphides, carbonate, garnet and green biotite within the matrix.



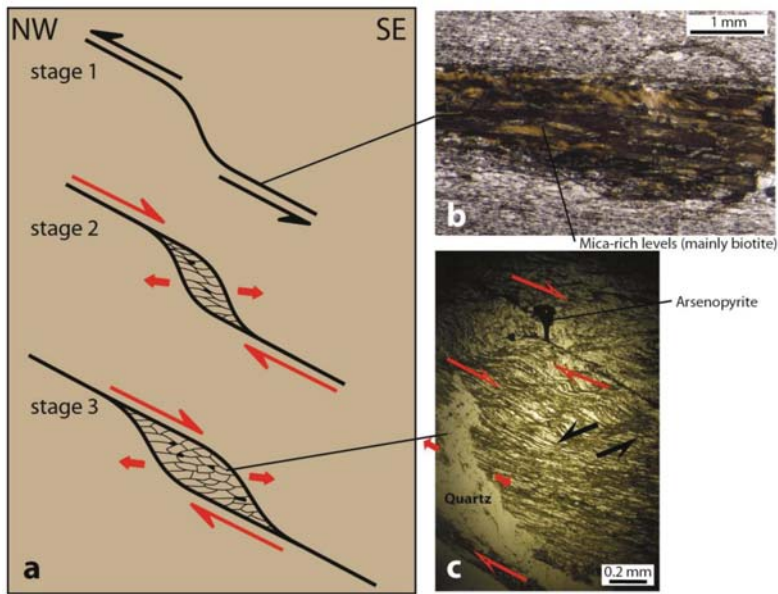


**Figure 6.** (a) Formation of sigmoid vein during late-orogenic collapse tectonics (red arrows) within the Quadrilátero Ferrífero (Minas Gerais, Brazil). Note that vein re-used an early level formed by mica alignment related to the nappe emplacement (b). The sigmoidal shape reflects thrust-related emplacement (black arrows). Extensional pull-apart post-dated thrust-related structures and controlled gold-bearing quartz-sulphide veins (c).

This study demonstrates that the Ouro Preto mesothermal gold deposit was formed in context of late-orogenic collapse, drastically different from the conventional auriferous shear-zone model, model that has been intensively used during the 1990s [43,44]. A recent study confirms this hypothesis by the demonstration of resetting of older zircons by ca. 496 Ma old hot fluid rock interactions in the area of Passagem [45].

This example clearly illustrates the importance of the systematic observation of the internal vein texture before concluding on the mechanism of vein formation based only on the geometrical analysis.

### 3.2. Vein Opening and Filling Controlled by Regional-Scale Structures within Volcanic Domains

The Shila-Paula district is one of the numerous Au/Ag low sulfidation epithermal one of Southern Peru. It is characterised by numerous veins hosted by the tertiary subaerial volcanics of the Western Cordillera. Field studies shown that most of the mineralised bodies consist of the systematic association of main E–W veins and secondary N120–135°E veins (Figure 7) [46]. Two main stages of ore deposition are identified [47]. Stage 1 consists of a quartz–adularia–pyrite–galena–sphalerite–chalcopyrite–electrum–Mn silicates and carbonates assemblage that fills the main E–W veins (Figure 7a,b,e). Stage 2, also called the bonanza stage, carries most of the precious mineralisation and consists of quartz, Fe-poor sphalerite, chalcopyrite, pyrite, adularia, galena, tennantite–tetrahedrite, polybasite–pearceite, and electrum. This stage is mainly observed within secondary veins, in final geodic filling (Figure 7c,f) and in veinlets that cut stage 1 assemblage (Figure 7d,g). In main veins, the ore is systematically brecciated, whereas tectonic-free environment characterised the filling of secondary veins. The age of veins was estimated to be around 10.8 Ma using  $^{40}\text{Ar}/^{39}\text{Ar}$  ages on adularia crystals from different veins [47].

A two-stage model is proposed to explain vein formation. The first stage was assumed to correspond to the development of E–W sinistral shear zones and associated N120°E cleavages under

the effects of a NE–SW trending shortening direction, which has been previously recognised at the Andean scale (Quechua II phase) (Figure 7a). These structures serve as a receptacle for the emplacement of stage 1 ore assemblage that was brecciated during ongoing deformation (Figure 7b). The second event operates a re-opening of the previously formed structures under a NW–SE trending shortening direction that allowed the re-opening of pre-existing cleavage and the formation of scarce N50°E trending S2 cleavages (Figure 7c), such as in the model in Figure 2. This stage was followed by the bonanza ore emplacement both within geodes in core of the main E–W veins and in secondary N120–135°E veins (Figure 7d). The two directions of shortening, NE–SW for the first event and NW–SE for the second one, are also recorded by the orientation of fluid inclusion planes within quartz crystals from the host rocks.

This study represents a unique example, constrained by combined tectonic, textural, mineralogical, geochronological, and fluid inclusion data, of the establishment of a complete model of deposit formation in which the re-using of previously formed tectonic features as a factor of gold concentration in epithermal environment is evidenced.

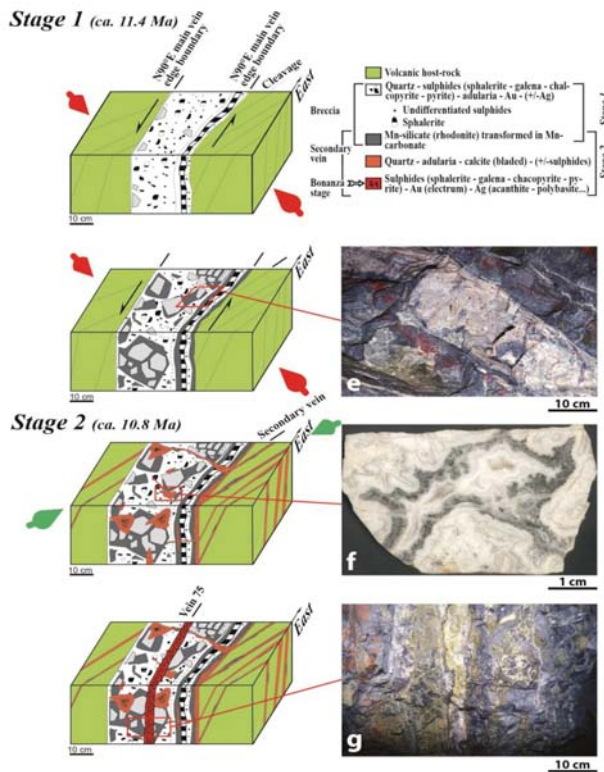


**Figure 7.** Example of vein formation by the re-using of pre-existing structures within the Volcanic domain of South Peru (see text for explanation). (a) Formation and filling of sinistral shear zone and creation of associated cleavage under the effect of NE–SW shortening direction (red arrows). (b) Formation of Mn-rich breccia under the same shortening direction. (c) Formation of secondary veins by re-opening of the cleavage by N120°E trending shortening direction (green arrows). Formation of geodic structures filled by stage 2-related paragenesis and subsequent “bonanza” stage and richer veins (Veta 75) (d).

### 3.3. Tectonic Stockwork Development in Fold and Thrust Belt Environment

#### 3.3.1. The Iberian Pyrite Belt Example

The Variscan Iberian Pyrite Belt is affected by a continuous and progressive deformation that integrates the formation of south-directed folds and thrust vs. north-verging features [48]. In the light of this structural model, a microtectonic, textural, and mineralogical study of the stockworks associated with the volcanic-hosted massive sulphide (VHMS) deposits has been performed [24].

In addition to the first and primary stockwork assimilated to represent the feeder veins of the VHMS, a second stockwork occurs under the form of undeformed veins frequently emplaced within cleavage and shear planes characteristic of the south-verging deformation (Figure 8a). The characteristic mineral of both stages is pyrite. Within the primary stockwork, sulphides have Co–As-rich rims that are interpreted as overgrowths formed during the second event. Instead of that, the base metal assemblage that characterised the second stockwork is similar to the one seen within the primary stockwork, especially when developed at its contact. Conversely, second stockwork is observed far away from the primary one and VHMS is only filled by quartz and pyrite. The internal texture indicates that pyrite is systematically fractured by ongoing deformation and quartz fibres develop within asymmetric pressure consistent with the south-verging tectonics. Geochemical analysis of pyrites emphasises the discrimination between both stockworks and pyrites from early stockwork are S-depleted/Fe-enriched with respect to those of the second stockwork. Since sulphides are located within the cleavage and shearing plane (Figure 8b,c) and quartz fibres systematically develop around pyrite grains, the second stockwork is interpreted as developing during the south-directed tectonics [24]. Moreover, the second stockwork has been encountered within axial plane cleavage related to the south-directed tectonics (Figure 8d), similar to the conceptual trap formation within cleavage of Figure 1a. This is strongly confirmed by sulphide textural analysis that demonstrates the co-existence of deformational effects (pyrite subgrain boundary, blow-up pull-apart, Figure 8e) and post-tectonic pyrite overgrowth (Figure 8f). If the mineralised fluids responsible for this second stockwork result from the VHMS and early stockwork remobilisation or from external metamorphic source remain uncertain.

#### 3.3.2. The Moroccan Palaeozoic High-Atlas Example

The mineralised district of the High Seksaoua (Western High Atlas, Morocco) is characterised by a lithological succession marked by an alternation of schists and limestones attributed to the Cambrian and affected by the Hercynian orogeny. The existence of stratiform masses of pyrite first suggests that this deposit can be a VHMS (Figure 9a) [49]. However, copper mineralisation, the first economic goal, is absent from the stratiform pyrite levels but systematically localised close to the dolomite/black schist contact in which a top-to-the-N–NW décollement-type tectonics [50,51] has been identified (Figure 9b). The economic mineralisation is a syntectonic stockwork (Figure 9c,d) formed in response to this top-to-the-N–NW shearing event that only affects the black schist layers (Figure 9). We suggest that vein formation is a brittle response, within competent dolomite levels, of the ductile deformation that affects the black schist (Figure 9a) [51], as described in the conceptual model of the Figure 1b.

This tectonic has been correlated to the late-Hercynian tectonics on the base of the Permo-Triassic age (ca. 270 Ma) given by  $^{40}\text{Ar}/^{39}\text{Ar}$  dating realised on white micas related to the stockwork [51]. This important result questions the syngenetic interpretation accepted until now for this mineralisation, and allows us to propose a new model of formation in which the “décollement”-type tectonics represent the main factor of ore concentration.

The Iberian and Moroccan examples illustrated the role of decollement structures in the emplacement of stockworks associated with metal-rich minerals. If no economic concentration can be deduced from the remobilisation process during Hercynian orogeny in the case of the South Iberian Pyrite Belt and, moreover, compared to the huge metal mass represented by the VHMS, a similar process applied to the Ifri deposit led to the formation of the Cu-rich economic orebodies.

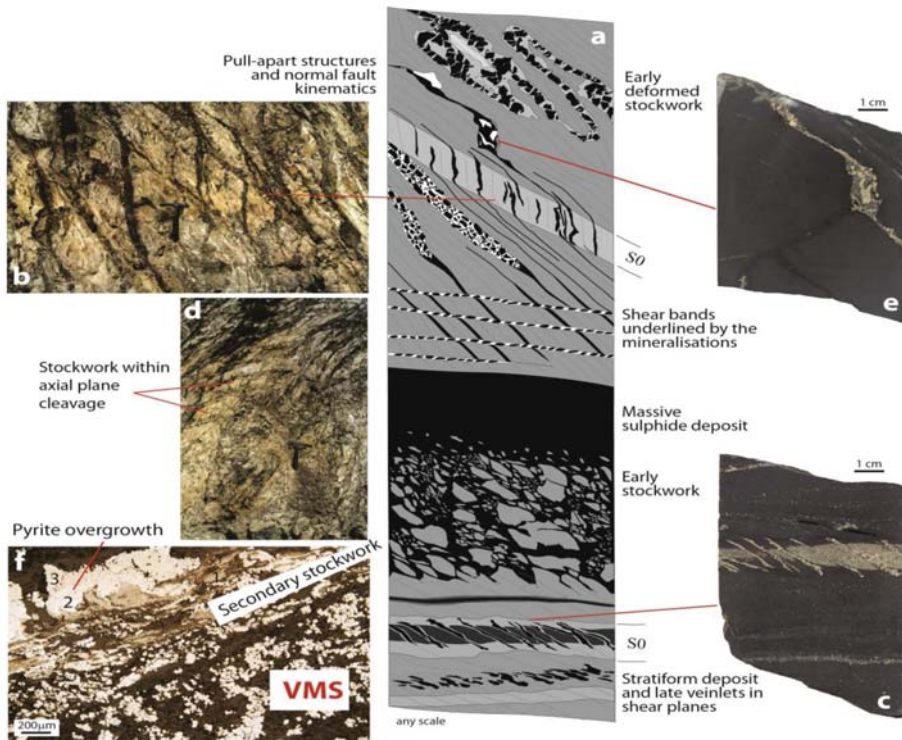


**Figure 8.** Schematic illustration showing the relationships between first stockwork and secondary one around the VHMS of the Iberian Pyrite Belt (south Spain). (a) Schematic distribution of the different stockwork and mineralised features close to a VHMS body. Occurrence of second stockwork within meter-scale shear bands (b) and within axial planar cleavage (d). (c) Stratiform pyrite-rich level cut by secondary pyrite-rich veins. (e) Small pull-apart filled by syntectonic quartz and pyrite. (f) Pyrite metablasts and overgrowths (2 and 3) formed close to a synkinematic second stockwork.

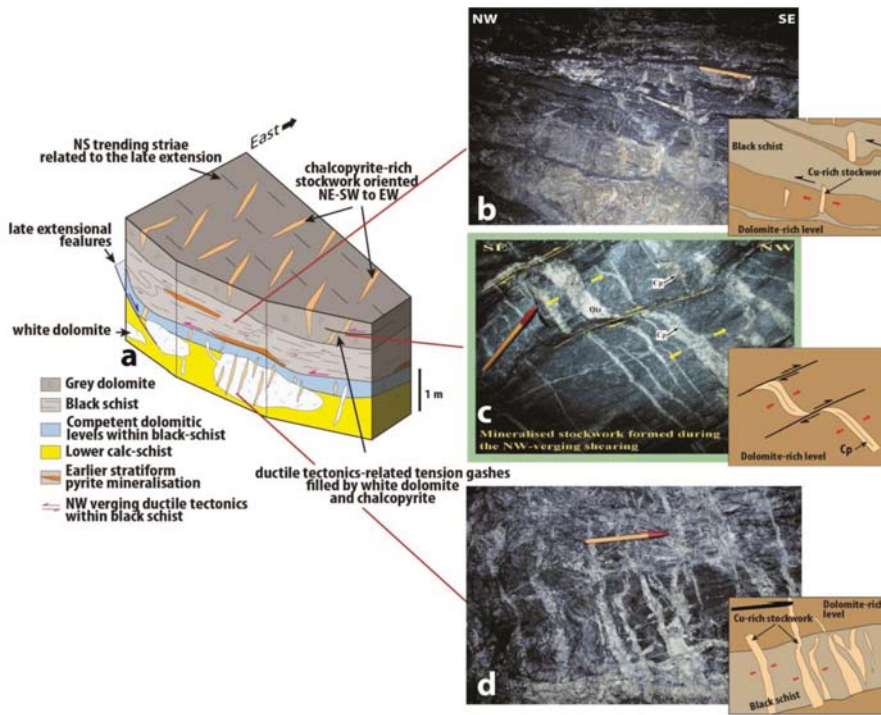


**Figure 9.** (a) Illustrations of the Ifri Cu mine model showing some images of the Cu-rich stockwork formed in response of ductile decollement within black schist. Each photograph is associated to a schematic cartoon in order to explain the geological process. (b) Example of vein formation within competent dolomite rich level in response of the ductilely deformed black schist. (c) Opening of chalcopryite/quartz-rich veins due to NW-directed shearing. (d) Stockwork formation by contrasted behaviour of dolomite and black schist.

### 3.4. Rheological Control on Ore Concentration

In this chapter, we illustrate the significant role of rheological conditions on the development of ore deposits. Here, we will highlight two cases in which changing rheological conditions due to intensive tourmaline-rich alteration process favoured the formation of lode-related deposits.

#### 3.4.1. Sn-rich Breccia Formation of the Achmmach Prospect (Moroccan Central Massif)

The Achmmach tin mineralisation occurs within the NE part of the Massif Central domain of Morocco, hosted by Ordovician, Silurian, and Devonian low-grade meta-sediments affected by the Hercynian deformational events, weakly represented in this area. The region concerned by the deposit exhibits a regular, N030–045°E trending cleavage mainly within the Silurian calc-schists. The mineralisation is the result of a long-lived process that includes four events that occurred in a transensional tectonic regime associated with the late magmatic-hydrothermal evolution of the Hercynian orogeny (see details in [52]).

- The first event is the formation of tourmaline-rich halos in core of the calc-schist. These halos have ellipsoidal shape resembling tension gashes and are supposed to have formed during E–W trending shortening. Since they follow the N070°E trend of the cleavage, most halos are “en echelon” and indicators of a right-lateral potential shearing. Conjugate left-lateral “en echelon”

tourmaline halos also exist but are less common. The rock shown in Figure 10 was collected in the core of one of the alteration halos and is entirely affected by the tourmalinisation.

- The second event is link to the development of right-lateral shearing only in levels affected by the tourmalinisation (Figure 10a,c). It is noteworthy that this deformation is consistent with the same tectonic context and therefore probably result from ongoing transtension controlled by E–W shortening. Main shear bands are oriented N070°E.
- Third, we have evidence of transformation of the previously formed shear band in tourmaline-rich breccia levels (Figure 10a,c). Such levels can reach thickness of 2 or 3 meters. The breccia is matrix-supported with a well-developed tourmaline-rich matrix, and can exhibit some domains with fragment-preferred orientation thus translating to tectonic- and hydrothermal-type breccia.
- The fourth texture is the most important because it is associated with cassiterite and thus representative of the economic stage. Transtension is transformed in extension and normal faults developed with the formation of a clast-supported breccia with numerous voids formation and cassiterite crystallisation (Figure 10b). These mineralised structures are systematically formed at the core of the first breccia levels and always in association with the tourmaline halos.

To conclude, mineralisation in the case of Achmmach prospect is clearly the result of polyphase deformation during the late orogenic evolution of this Hercynian domain and certainly associated with some granite emplacement. Granite remains hidden except for the occurrence of some rare outcrops. Magmatic affinity is demonstrated by the ubiquitous presence of tourmaline at each stage of the process. It is suggested in this case that ore concentration benefitted from the change of rheology due to tourmaline invasion (tourmaline-rich halos). The process was achieved by ongoing successive structures until the final formation of mineralised orebodies (shearing, brecciation and cassiterite crystallisation).

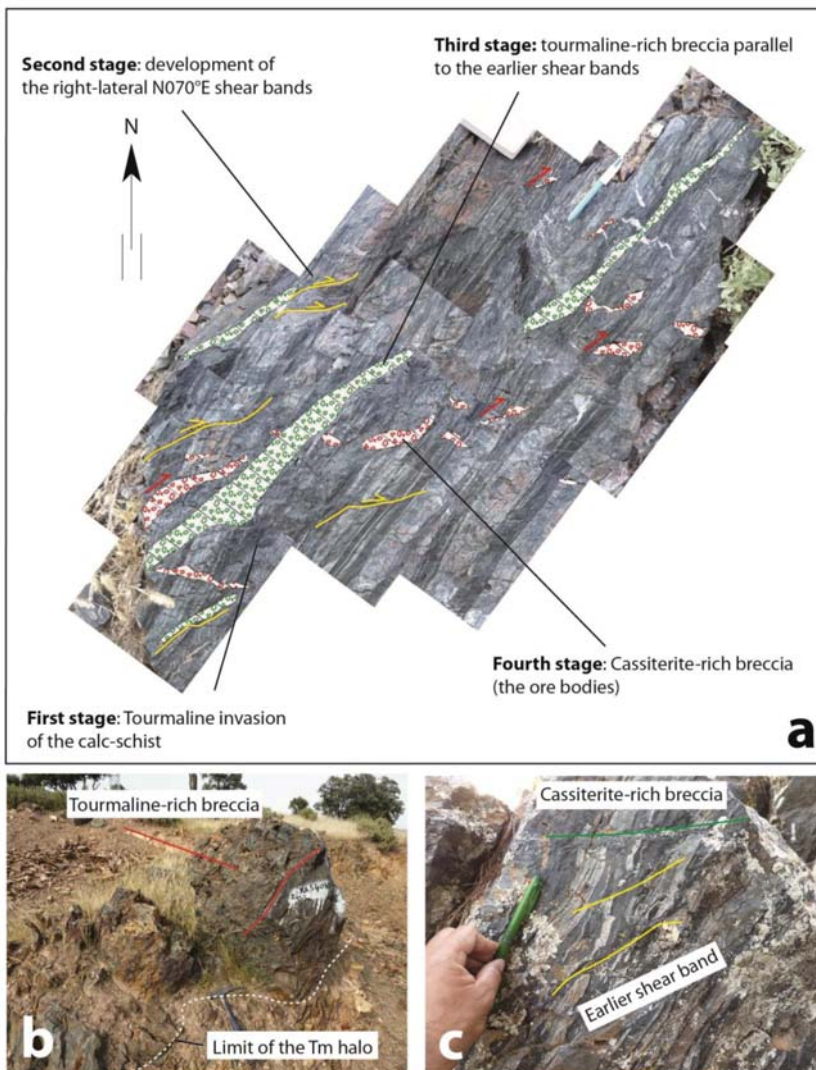


**Figure 10.** Deposit history and evolution of the four stages that explain the formation of the Achmmach tin deposit (Morocco) recognised in a unique block (a). (b) Image of the “North Zone” area in which the succession of structure can be observed. Note the limit of the tourmaline alteration halo that delimitate the zone where mineralisation developed. (c) Parallelism between ductile shear bands and mineralised breccia showing that breccia re-used the earlier plane of deformation to develop.

### 3.4.2. The Sn–W-rich Perigranitic Mineralisations of Beariz (Galicia, Spain)

The Hercynian orogenic cycle is reputed for abundant calc-alkaline granites that were emplaced during late orogenic Carboniferous extension (collapse of the thickened crust) [53]. This event also related to an intensive ore formation frequently starting with Sn–W mineralisation close to the granitic bodies grading to As–Au towards more distal parts [54]. This event has been called “Or 300” by the French school, and recognised throughout the European Hercynides from the Bohemia Massif to Maghreb [55,56]. In Galicia (NW Spain), the Tras-os-Montes area is a segment of the Hercynian orogen

and characterised by voluminous magmatic complexes emplaced between 325 and 300 Ma (from G1 to G4 granitic events, [57]). The area is the site of abundant ore deposits (Au, W, Sn, REE). The example shown herein concerns the Sn–W deposit of the Mina Soriana in which mineralised veins were formed during a tectonic context dominated by NS extension linked to EW shortening [58]. The veins formed with E–W strike normal to a NS stretching lineation. This phenomenon is clearly exposed within the Mina Soriana outcrop. The Mina Soriana outcrop (Figure 11a) exposes a horizontal sill of leucogranite that was injected into mica schist during the N–S lineation-related tectonic event. Tourmaline halos (50 cm of thickness) are developed along the upper and lower host rocks (Figure 11b). Steeply dipping veins mainly filled by quartz and tourmaline occur normal to the magmatic sill and only within the tourmaline-rich halo (Figure 11c). This indicates that micaschist affected by the alteration had changed its competence and reacted differently than the surrounding unaltered micaschist. Veins are limited to the alteration halo although some of them cross cut the magmatic sill, as in boudinage-related structures (Figure 11a). Since tourmaline grains are aligned N–S within the alteration halo but also at the margin of quartz vein (Figure 11d), all features, i.e., magmatic sill emplacement, tourmaline-rich halo, and quartz vein development, are coeval and controlled by the same tectonic event.

In this case, the different behaviour, as explained in Figure 1b, lies at the origin of vein formation and, hence, of the formation of the Mina Soriana main vein, which outcrops further north, with the same orientation as the small-scale quartz veins and is mined as the main orebody. The difference with Figure 1b is that, in this case, the variation of rheology is not a pre-existing lithological feature, but was created during the same process that produced the ore concentration.

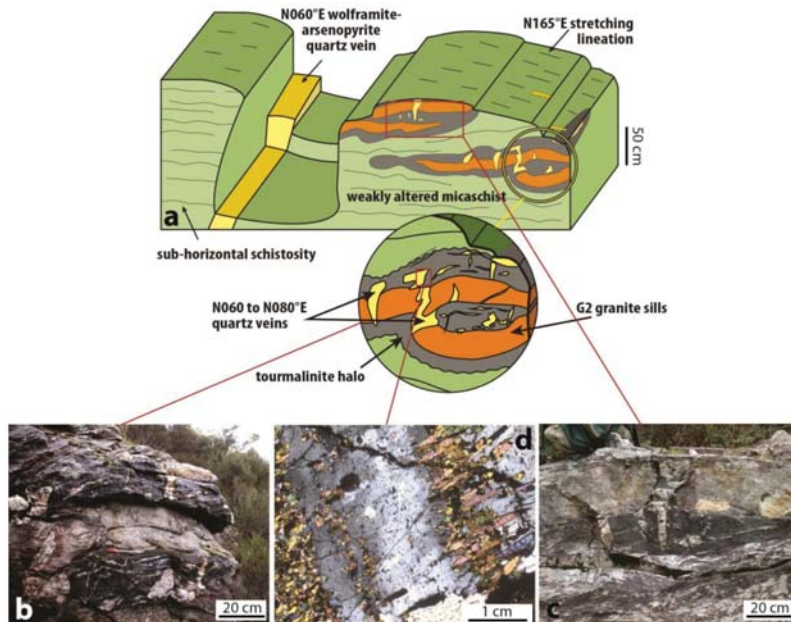


**Figure 11.** (a) Mina Soriana outcrop, Galicia (Spain), showing the development of mineralised quartz veins thanks to tourmaline-rich alteration halos developed in response to granitic sill emplacement (modified from [59]). (b) Close view of the granitic sill, tourmaline halo and vertical quartz veins. (c) Microscopic view of quartz vein rim showing tourmaline syntectonic growing. (d) Development of vertical quartz mineralised veins limited to the tourmaline-rich alteration halo.



### 3.5. Re-Use of Magmatic Structures: The Magmatic-Hydrothermal Transition

In the same geological context as the Mina Soriana outcrop, gold mineralisation exists, but close to the G3 granites (the Bruès one, in this case). Gold is associated with quartz-bearing veins that form a regular network emplaced at the Northern cupola of the Bruès G3 granite [58]. This network is also E–W oriented, and veins dip steeply to the north. A link with the G3 granite emplacement has been demonstrated by field and microstructure analysis [57,58]. Few direct arguments have been advanced, but the fact that mineralised quartz veins are systematically emplaced at the contact with the aplite–pegmatite dikes (Figure 12a), which are both controlled by the same structural context, is probably the strongest evidence. In thin sections, the transition from the magmatic stage to the hydrothermal is illustrated (Figure 12b) by an intermediate stage (magmatic-hydrothermal) marked by the crystallisation of K-feldspars that are larger than the ones in the surrounding granite (Figure 12b). In addition, comb shapes confirm that feldspars are syntectonic, neo-formed, and indicate the vein opening direction. Internal fractures show that opening continued after feldspar crystallisation, as evidence for a continuous process. In the centre of the vein and after comb quartz crystallisation (the hydrothermal stage), we find a thin fracture in which small white micas, recrystallised quartz, and sulphides (essentially arsenopyrite and pyrite) occur. White micas and oblique fabrics of recrystallised quartz (Figure 12c) also indicate a normal shearing consistent with the direction of vein opening. This demonstrates that a similar tectonic control prevailed from the late magmatic stages (border of the vein) until the final ore formation (sulphide and white mica at the centre of the vein).

This example confirms the indisputable spatial relationship between early magmatism, late magmatism and hydrothermalism. We highlight, here, the fact that we can follow, mineralogically and texturally, the continuity between late magmatic features (the border of the vein with K-feldspar formation), hydrothermal quartz and late sulphide growth. Once more, the role of the pre-existing network (the magmatic dike on top of the Bruès granite) seems essential for the development of the mineralised system.

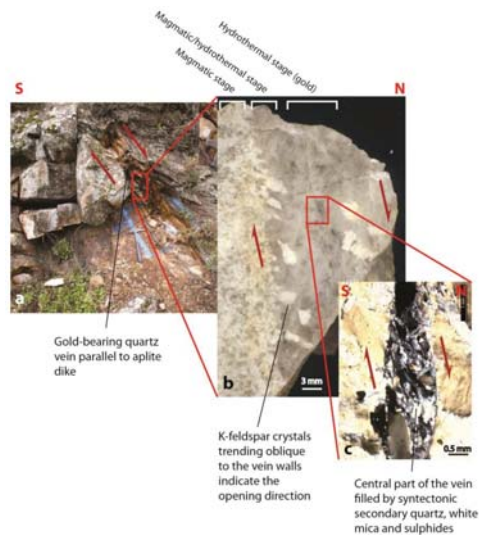


**Figure 12.** Relationships between gold-bearing quartz vein and granitic dike within the Bruès granite cupola, Galicia. (a) Outcrop view showing the close relationship between quartz vein and granitic dike. (b) Sample view showing the transitional contact between granite and quartz hydrothermal vein. (c) Thin section of the central part of the hydrothermal vein representative of the mineralised stage. Note the occurrence of dynamic recrystallised quartz and white mica indicating a normal sense of shearing. Red arrows indicate the sense of motion.

#### 4. Discussion and Conclusions

- (i) Detailed study of geometry and composition of vein associated with ore deposits, combined with mineralogical and textural constraints, is indispensable in order to understand the mode of formation of mineralised systems. In the case of the epithermal veins of the Shila deposit, the model of formation suggests that the formation of the economic deposit is strongly dependent on the pre-existing structuring of the area.
- (ii) Without studying internal textures, the interpretation of (external) vein shape can be ambiguous and is not enough to constrain the vein formation process. The example shown of epithermal veins in southern Peru is highly illustrative in this sense. Vein geometry (main vein and associated cleavage) indicates left-lateral shearing, but the opposite conclusion is deduced when taking into account the fact that the veins and, particularly, the secondary ones, are characterised by aperture and stress-free textures that are not consistent with the classical status of what we call a cleavage. This highlights the importance of examining internal vein texture in addition to tectonic and geometrical analyses of any type of ore deposit. A similar conclusion can be drawn from the Passagem gold-bearing veins that were originally interpreted as pre-tectonic but later recognised to have formed during late-orogenic collapse affecting the area. This has significant implications for exploration and exploitation strategies because of the different age and predicted local geometries (angle, elongation) of the potential orebodies.
- (iii) Two examples demonstrate the existence of syntectonic stockwork, i.e., metal remobilisation within the huge VHMS of the Iberian Pyrite Belt and the copper mineralisation of the Moroccan High Atlas. Few studies have really demonstrated this hypothesis, but our results provide strong evidence for the synchronism between stockwork formation/emplacement and deformation. Even if secondary stockwork formation does not represent an economic goal within the Iberian Pyrite Belt, such a process led to the formation of the economic orebodies of Ifri (Moroccan High Atlas). This highlights the importance of detailed study of any type of mineralised veins, even if at first inspection they do not seem to be of direct economic interest.
- (iv) Although the term “magmatic-hydrothermal transition” may sound old fashioned [60], we demonstrate with the example of Bruès (the last one) that, even though we cannot prove that the mineralising fluid were magmatic, ore formation is intimately associated with the late evolution of magmatic systems in many orogenic and/or mesothermal gold deposits [61]. The Bruès outcrop is a wonderful demonstration of continuity between late magmatic process and hydrothermal mineralisation. It is remarkable that, although detailed absolute geochronology is lacking, the evidence for the same tectonic control from the earliest magmatic stages to the latest hydrothermal stage strongly favours a continuous process. This cannot be enough for affirming the link between mineralisation and granite activity but strongly argued for this and re-addressed the discussion concerning the characteristics of orogenic and intrusion-related gold deposit (IRGD) [62,63].
- (v) Competency contrasts in a volume of rock also appear to be a favourable factor for ore concentration and vein formation [64], as shown herein for the Achmmach tin deposit and Mina Soriana W. In these cases, rheological variation was not due to original lithological differences, but induced during early stages of the mineralisation event itself, by heterogeneous alteration. It has been argued that tin mineralisation could not have formed in the Achmmach domain without earlier development of a tourmaline halo within the monotonous calc-schist. These alteration halos, formed during an early stage of transtension tectonics, create a drastic contrast in competency contrast, which controlled the partitioning of ongoing deformation and, eventually, the mineralisation. The case of Mina Soriana is similar, but the link with magmatism is, here, highlighted by the occurrence of a granitic sill responsible for the tourmaline-rich alteration. Nonetheless, in both cases, a link with late magmatic activity can be inferred in view of the above discussion about the role of the magmatic-hydrothermal transition.

In the light of these results, the importance of tectonic and microtectonic analysis at different scales in modern metallogenic studies is underlined. This work should be realised at the regional scale down to the scale of internal vein textures. The complementarity nature of pluridisciplinary works, even though already adopted in many previous studies, has been again demonstrated by the examples proposed and discussed in this paper. Change of scale and integration within the regional, geological and tectonic context are two additional conditions for a comprehensive analysis. The benefits of such an approach are both fundamental, leading to a better understanding of the mechanism of vein formation process, and economics, leading to better knowledge of specific orebody geometry and distribution and hence highly recommended in any type of exploration program.

**Funding:** This research was partly funded by Projects CAPES-COFECUB and CNRS GDR Transmet.

**Acknowledgments:** The mining companies SEIMSA (Iberian Pyrite Belt, Spain), CVRD (Vale group, Brazil), CEDIMIN and BUENAVENTURA (Peru), MANAGEM (Morocco), SMS (Seksoua, Morocco) and KASBAH RESSOURCES (Achmmach, Morocco) are gratefully acknowledged for their constant help, support and fruitful discussions. L. Badra, L. Bailly, L. Barbanson, Y. Branquet, P. Chaponnière, P. Couderc, M. Dardennes, A. Gaouzi, J.M. Georgel, E. Gloaguen, M. Majhoubi, M. Menezes, J. Onezime, J. Rosas, and J. Tuduri, are thanked for their contribution. Two anonymous reviewers and D. Aerden are kindly acknowledged for their fruitful and constructive review.

**Conflicts of Interest:** The authors declare no conflict of interest. The funders had no role in the design of the study; in the collection, analyses, or interpretation of data; in the writing of the manuscript, or in the decision to publish the results.

## References

1. Durney, D.W.; Ramsay, J.G. Incremental strains measured by syntectonic crystal growths. In *Gravity and Tectonics*; De Jong, K.A., Scholten, K., Eds.; Wiley: New York, NY, USA, 1973; pp. 67–96.
2. Durney, D.W. Pressure solution and crystallization deformation. *Philos. Trans. R. Soc. Lond.* **1976**, *A283*, 229–240. [[CrossRef](#)]
3. Beach, A. The geometry of en-echelon vein arrays. *Tectonophysics* **1975**, *28*, 245–263. [[CrossRef](#)]
4. Bons, P.D. The formation of large quartz veins by rapid ascent of fluids in mobile hydrofractures. *Tectonophysics* **2001**, *336*, 1–17. [[CrossRef](#)]
5. Bons, P.D.; Elburg, M.A.; Gomez-Rivas, E. A review of the formation of tectonic veins and their microstructures. *J. Struct. Geol.* **2012**, *43*, 33–62. [[CrossRef](#)]
6. Fisher, D.; Byrne, T. The character and distribution of mineralized fractures in the Kodiak Formation, Alaska: Implications for fluid flow in an underthrust sequence. *J. Geophys. Res.* **1990**, *95*, 9069–9080. [[CrossRef](#)]
7. McCaffrey, K.; Lonergan, L.; Wilkinson, J. *Fractures, Fluid Flow and Mineralization*; Geological Society of London Special Publication: London, UK, 1999; 155p.
8. Richards, J.P.; Tosdal, R.M. Structural controls on ore genesis. *Rev. Econ. Geol.* **2001**, *14*, 181.
9. Smith, J.V. En echelon sigmoidal vein arrays hosted by faults. *J. Struct. Geol.* **1996**, *18*, 1173–1179. [[CrossRef](#)]
10. Smith, J.V. Geometry and kinematics of convergent conjugate vein array systems. *J. Struct. Geol.* **1996**, *18*, 1291–1300. [[CrossRef](#)]
11. Cox, S.F. Deformational controls on the dynamics of fluid flow in mesothermal gold systems. In *Fractures, Fluid Flow and Mineralization*; McCaffrey, K., Lonergan, L., Wilkinson, J., Eds.; Geological Society of London Special Publication: London, UK, 1999; Volume 155, pp. 123–140.
12. Spencer, S. The use of syntectonic fibres to determine strain estimates and deformation paths: An appraisal. *Tectonophysics* **1991**, *194*, 13–34. [[CrossRef](#)]
13. Hilgers, C.; Urai, J.L. Microstructural observations on natural syntectonic fibrous veins: Implications for the growth process. *Tectonophysics* **2002**, *352*, 257–274. [[CrossRef](#)]
14. Barker, S.L.L.; Cox, S.F.; Eggins, S.M.; Gagan, M.K. Microchemical evidence for episodic growth of antitaxial veins during fracture-controlled fluid flow. *Earth Planet. Sci. Lett.* **2006**, *250*, 331–344. [[CrossRef](#)]
15. Dowling, K.; Morrison, G. Application of quartz textures to the classification of gold deposits using North Queensland examples. *Econ. Geol. Monogr.* **1990**, *6*, 342–255.
16. Dong, G.; Morrison, G.; Jaireth, S. Quartz textures in epithermal veins, Queensland—Classification, origin, and implication. *Econ. Geol.* **1995**, *90*, 1841–1856. [[CrossRef](#)]

17. Taylor, R. *Ores Textures, Recognition and Interpretation*; Economic Geology Research Unit and Springer: Berlin, Germany, 2009; 288p.
18. Funedda, A.; Naitza, S.; Buttau, C.; Cocco, F.; Dini, A. Structural Controls of Ore Mineralization in a Polydeformed Basement: Field Examples from the Variscan Baccu Locci Shear Zone (SE Sardinia, Italy). *Minerals* **2018**, *8*, 456. [[CrossRef](#)]
19. De Roo, J.A. Mass transfer and preferred orientation development during extensional microcracking in slate-belt folds, Elura Mine, Australia. *J. Metamorph. Geol.* **1989**, *7*, 311–322. [[CrossRef](#)]
20. Davis, B.K.; Hippertt, J.F.M. Relationships between gold concentration and structure in quartz veins from the Hodgkinson Province, northeastern Australia. *Miner. Depos.* **1998**, *33*, 391–405. [[CrossRef](#)]
21. Forde, A. The late orogenic timing of mineralisation in some slate belt gold deposits, Victoria, Australia. *Miner. Depos.* **1991**, *26*, 257–266. [[CrossRef](#)]
22. Cox, S.F.; Knackstedt, M.A.; Braun, J. Principles of structural control on permeability and fluid flow in hydrothermal systems. In *Structural Controls on Ore Genesis*; Richards, J.P., Tosdal, R.M., Eds.; Reviews in Economic Geology; Society of Economic Geologists: Littleton, CO, USA, 2001; Volume 14, pp. 1–24.
23. Gratier, J.P.; Vialon, P. Deformation pattern in a heterogeneous material: Folded and cleaved sedimentary cover immediately overlying a crystalline basement (Oisans, French Alps). *Tectonophysics* **1980**, *65*, 151–180. [[CrossRef](#)]
24. Chauvet, A.; Onézime, J.; Charvet, J.; Barbanson, L.; Faure, M. Syn- to late-tectonic stockwork emplacement within the Spanish section of the Iberian Pyrite Belt: Structural, textural and mineralogical constraints in the Tharsis—La Zarza areas. *Econ. Geol.* **2004**, *99*, 1781–1792. [[CrossRef](#)]
25. Cox, S.F.; Etheridge, M.A. Crack-seal fibre growth mechanism and their significance in the development of oriented layer silicate microstructures. *J. Struct. Geol.* **1983**, *92*, 147–170. [[CrossRef](#)]
26. Fisher, D.M.; Brantley, S.L. Models of quartz overgrowth and vein formation: Deformation and episodic fluid flow in an ancient subduction zone. *J. Geoph. Res.* **1992**, *97*, 20043–20061. [[CrossRef](#)]
27. Hilgers, C.; Köhn, D.; Bons, P.D.; Urai, J.L. Development of crystal morphology during uniaxial growth in a progressively widening vein: II. Numerical simulations of the evolution of antitaxial fibrous veins. *J. Struct. Geol.* **2001**, *23*, 873–885. [[CrossRef](#)]
28. Ramsay, J.G. The crack-seal mechanism of rock deformation. *Nature* **1980**, *284*, 135–139. [[CrossRef](#)]
29. Cox, S.F. Antitaxial crack-seal vein microstructures and their relationship to displacement paths. *J. Struct. Geol.* **1987**, *9*, 779–787. [[CrossRef](#)]
30. Hilgers, C.; Urai, J.L. On the arrangement of solid inclusions in fibrous veins and the role of the crack-seal mechanism. *J. Struct. Geol.* **2005**, *27*, 481–494. [[CrossRef](#)]
31. Boullier, A.M.; Robert, F. Paleoseismic events recorded in Archean gold quartz vein networks, Val-Dor, Abitibi, Quebec, Canada. *J. Struct. Geol.* **1992**, *14*, 161–177. [[CrossRef](#)]
32. Bons, P.D.; Jessell, M.W. Experimental simulation of the formation of fibrous veins by localised dissolution-precipitation creep. *Mineral. Mag.* **1997**, *61*, 53–63. [[CrossRef](#)]
33. Jébrak, M. Hydrothermal breccias in vein-type ore deposits: A review of mechanisms, morphology and size distribution. *Ore Geol. Rev.* **1997**, *12*, 111–134. [[CrossRef](#)]
34. Sibson, R.H. Brecciation Processes in Fault Zones: Inferences from Earthquake Rupturing. *Pure Appl. Geophys.* **1986**, *124*, 159–175. [[CrossRef](#)]
35. Taylor, R.G.; Pollard, P.J. *Mineralized Breccia Systems—Methods of Recognition and Interpretation*, Economic Geology Research Unit Contribution 46; James Cook University of North Queensland: Douglas, Australia, 1993; 36p.
36. Clark, C.; James, P. Hydrothermal brecciation due to fluid pressure fluctuations: Examples from the Olary Domain, South Australia. *Tectonophysics* **2003**, *366*, 187–206. [[CrossRef](#)]
37. Tarasewicz, J.P.T.; Woodcock, N.H.; Diskson, J.A.D. Carbonate dilation breccias: Examples from the damage zone to the Dent Fault, northwest England. *Geol. Soc. Am. Bull.* **2005**, *117*, 736–745. [[CrossRef](#)]
38. Davies, A.G.S.; Cooke, D.R.; Gemmill, J.B.; Van Leeuwen, T.; Cesare, P.; Hartshorn, G. Hydrothermal Breccias and Veins at the Kelian Gold Mine, Kalimantan, Indonesia: Genesis of a Large Epithermal Gold Deposit. *Econ. Geol.* **2008**, *103*, 717–757. [[CrossRef](#)]
39. Woodcock, N.H.; Mort, K. Classification of fault breccias and related fault rocks. *Geol. Mag.* **2008**, *145*, 435–440. [[CrossRef](#)]

40. Burchfiel, B.C.; Stewart, J.H. “Pull-apart” origin of the central segment of Death Valley, California. *Geol. Soc. Am. Bull.* **1966**, *77*, 439–442. [[CrossRef](#)]
41. Chauvet, A.; Piantone, P.; Barbanson, L.; Nehlig, P.; Pedroletti, I. Gold deposit formation during collapse tectonics: Structural, mineralogical, geochronological, and fluid inclusion constraints in the Ouro Preto gold mines, Quadrilátero Ferrífero, Brazil. *Econ. Geol.* **2001**, *96*, 25–48. [[CrossRef](#)]
42. Souza Martins, B.; Lobato, L.M.; Rosière, C.A.; Hagemann, S.G.; Schneider Santos, J.O.; dos Santos Peixoto Villanova, F.L.; Figueiredo e Silva, R.C.; de Ávila Lemos, L.H. The Archean BIF-hosted Lamego gold deposit, Rio das Velhas greenstone belt, Quadrilátero Ferrífero: Evidence for Cambrian structural modification of an Archean orogenic gold deposit. *Ore Geol. Rev.* **2016**, *72*, 963–988. [[CrossRef](#)]
43. Kerrich, R. Geodynamic setting and hydraulic regimes: Shear zone hosted mesothermal gold deposits. In *Mineralisation and Shear Zones*; Bursnell, J.T., Ed.; Geological Association of Canada Short Course Notes; Mineralogical Association of Canada: Quebec City, QC, Canada, 1989; Volume 6, pp. 89–128.
44. Poulsen, K.H.; Robert, F. Shear Zones and Gold: Practical Examples from the Southern Canadian Shield. In *Mineralisation and Shear Zones*; Bursnell, J.T., Ed.; Geological Association of Canada Short Course Notes; Mineralogical Association of Canada: Quebec City, QC, Canada, 1989; Volume 6, pp. 239–266.
45. Cabral, A.R.; Zeh, A. Detrital zircon without detritus: A result of 496-Ma-old fluid–rock interaction during the gold-lode formation of Passagem, Minas Gerais, Brazil. *Lithos* **2015**, *212–215*, 415–427. [[CrossRef](#)]
46. Cassard, D.; Chauvet, A.; Bailly, L.; Llosa, F.; Rosas, J.; Marcoux, E.; Lerouge, C. Structural control and K/Ar dating of the Au–Ag epithermal veins in the Shila Cordillera, southern Peru. *C. R. Acad. Sci. Paris* **2000**, *330*, 23–30. [[CrossRef](#)]
47. Chauvet, A.; Bailly, L.; André, A.S.; Monié, P.; Cassard, D.; Llosa Tajada, F.; Rosas Vargas, J.; Tuduri, J. Internal vein texture and vein evolution of the epithermal Shila-Paula district, southern Peru. *Miner. Depos.* **2006**, *41*, 387–410. [[CrossRef](#)]
48. Onézime, J.; Charvet, J.; Faure, M.; Bourdier, J.L.; Chauvet, A. A new geodynamic interpretation for the South Portuguese Zone (SW Iberia) and the Iberian Pyrite Belt genesis. *Tectonics* **2003**, *22*, 1027. [[CrossRef](#)]
49. Barbanson, L.; Chauvet, A.; Gaouzi, A.; Badra, L.; Mechiche, M.; Touray, J.C.; Oukarou, S. Les minéralisations Cu–(Ni–Bi–U–Au–Ag) d’Ifri (district du Haut Seksaoua, Maroc): Apport de l’étude texturale au débat syngénèse versus épigénèse. *C. R. Géosci.* **2003**, *335*, 1021–1029. [[CrossRef](#)]
50. Gaouzi, A.; Chauvet, A.; Barbanson, L.; Badra, L.; Touray, J.C.; Oukarou, S.; El Wartiti, M. Mise en place syntectonique des minéralisations cuprifères du gîte d’Ifri (District du Haut Seksaoua, Haut-Atlas occidental, Maroc). *C. R. Acad. Sci. Paris* **2001**, *333*, 277–284.
51. Chauvet, A.; Barbanson, L.; Gaouzi, A.; Badra, L.; Touray, J.C.; Oukarou, S. Example of a structurally controlled copper deposit from the Hercynian Western High-Atlas (Morocco): The High Seksaoua mining district. In *The Timing and Location of Major Ore Deposits in an Evolving Orogen*; Blundell, D.J., Neuber, F., Von Quadt, A., Eds.; Geological Society of London Special Publication: London, UK, 2002; Volume 204, pp. 247–271.
52. Mahjoubi, E.M.; Chauvet, A.; Badra, L.; Sizaret, S.; Barbanson, L.; El Maz, A.; Chen, Y.; Amman, M. Structural, mineralogical, and paleoflow velocity constraints on Hercynian tin mineralization: The Achmmach prospect of the Moroccan Central Massif. *Miner. Depos.* **2015**, *51*, 431–451. [[CrossRef](#)]
53. Chauvet, A.; Volland-Tuduri, N.; Lerouge, C.; Bouchot, V.; Monié, P.; Charonnat, X.; Faure, M. Geochronological and geochemical characterization of magmatic-hydrothermal events within the southern Variscan external domain. *Intern. J. Earth Sci.* **2012**, *101*, 69–86. [[CrossRef](#)]
54. Poulsen, K.H.; Robert, F.; Dubé, B. *Geological Classification of Canadian Gold Deposits*; Geological Survey of Canada, Bulletin: Ottawa, ON, Canada, 2000; Volume 540, 113p.
55. Bouchot, V.; Milési, J.P.; Lescuyer, J.L.; Ledru, P. Les minéralisations aurifères de la France dans leur cadre géologique autour de 300 Ma. *Chron. Rech. Min.* **1997**, *528*, 13–62.
56. Bouchot, V.; Ledru, P.; Lerouge, C.; Lescuyer, J.L.; Milési, J.P. Late Variscan mineralizing systems related to orogenic processes: The French Massif. *Ore Geol. Rev.* **2005**, *27*, 169–197. [[CrossRef](#)]
57. Gloaguen, E. Apport D’une Étude Intégrée sur les Relations Entre Granites et Minéralisations Filoniennes (Au et Sn–W) en Contexte Tardi Orogénique (Chaîne Hercynienne, Galice Centrale, Espagne). Ph.D. Thesis, University of Orléans, Orléans, France, 2006.

58. Gloaguen, E.; Branquet, Y.; Chauvet, A.; Bouchot, V.; Barbanson, L.; Vignerresse, J.L. Tracing the magmatic/hydrothermal transition in regional low-strain zones: The role of magma dynamics in strain localization at pluton roof, implications for intrusion-related gold deposits. *J. Struct. Geol.* **2014**, *58*, 108–121. [[CrossRef](#)]
59. Sizaret, S.; Branquet, Y.; Gloaguen, E.; Chauvet, A.; Barbanson, L.; Arbaret, L.; Chen, Y. Estimating the local paleo-fluid flow velocity: New textural method and application to metasomatism. *Earth Planet. Sci. Lett.* **2009**, *280*, 71–82. [[CrossRef](#)]
60. Audétat, A.; Günther, D.; Heinrich, C.A. Formation of magmatic-hydrothermal ore deposits: Insights from LA-ICP-MS analysis of fluid inclusions. *Science* **2008**, *279*, 2091–2094.
61. Pe-Piper, G.; Piper, D.J.W.; McFarlane, C.R.M.; Sangster, C.; Zhang, Y.; Boucher, B. Petrology, chronology and sequence of vein systems: Systematic magmatic and hydrothermal history of a major intracontinental shear zone, Canadian Appalachians. *Lithos* **2018**, *304–307*, 299–310. [[CrossRef](#)]
62. Groves, D.I.; Goldfarb, R.J.; Gebre-Mariam, M.; Hagemann, S.; Robert, F. Orogenic gold deposits: A proposed classification in the context of their crustal distribution and relationship to other gold deposit types. *Ore Geol. Rev.* **1998**, *13*, 7–27. [[CrossRef](#)]
63. Lang, J.R.; Baker, T. Intrusion-related gold systems: The present level of understanding. *Miner. Depos.* **2001**, *36*, 477–489. [[CrossRef](#)]
64. Everall, T.J.; Sanislav, I.V. The Influence of Pre-Existing Deformation and Alteration Textures on Rock Strength, Failure Modes and Shear Strength Parameters. *Geosciences* **2018**, *8*, 124. [[CrossRef](#)]



© 2019 by the author. Licensee MDPI, Basel, Switzerland. This article is an open access article distributed under the terms and conditions of the Creative Commons Attribution (CC BY) license (<http://creativecommons.org/licenses/by/4.0/>).

Article

# Structural Control on the Formation of Pb-Zn Deposits: An Example from the Pyrenean Axial Zone

Alexandre Cugerone <sup>1,\*</sup>, Emilien Oliot <sup>1</sup>, Alain Chauvet <sup>1</sup>, Jordi Gavalda Bordes <sup>2</sup>, Angèle Laurent <sup>1</sup>, Elisabeth Le Goff <sup>3</sup> and Bénédicte Cenki-Tok <sup>1</sup>

<sup>1</sup> Géosciences Montpellier, UMR CNRS 5243, Université de Montpellier, Place E. Bataillon, CC 60, 34095 Montpellier, France; emilien.oliot@umontpellier.fr (E.O.); alain.chauvet@umontpellier.fr (A.C.); angele.laurent@etu.umontpellier.fr (A.L.); benedicte.cenki-tok@umontpellier.fr (B.C.-T.)

<sup>2</sup> Conselh Generau d’Aran, Vielha, 25530 Lleida, Spain; j.gavalda@aran.org

<sup>3</sup> Bureau de Recherches Géologiques et Minières (BRGM), Territorial Direction Languedoc-Roussillon, 1039 Rue de Pinville, 34000 Montpellier, France; e.legoff@brgm.fr

\* Correspondence: alexandre.cugerone@umontpellier.fr; Tel.: +33-643-983-585

Received: 21 September 2018; Accepted: 23 October 2018; Published: 26 October 2018

**Abstract:** Pb-Zn deposits and specifically Sedimentary-Exhalative (SEDEX) deposits are frequently found in deformed and/or metamorphosed geological terranes. Ore bodies structure is generally difficult to observe and its relationships to the regional structural framework is often lacking. In the Pyrenean Axial Zone (PAZ), the main Pb-Zn mineralizations are commonly considered as Ordovician SEDEX deposits in the literature. New structural field analyzes focusing on the relations between mineralization and regional structures allowed us to classify these Pb-Zn mineralizations into three types: (I) Type 1 corresponds to minor disseminated mineralization, probably syngenetic and from an exhalative source. (II) Type 2a is a stratabound mineralization, epigenetic and synchronous to the Variscan D<sub>1</sub> regional deformation event and (III) Type 2b is a vein mineralization, epigenetic and synchronous to the late Variscan D<sub>2</sub> regional deformation event. Structural control appears to be a key parameter in concentrating Pb-Zn in the PAZ, as mineralizations occur associated to fold hinges, cleavage, and/or faults. Here we show that the main exploited type 2a and type 2b Pb-Zn mineralizations are intimately controlled by Variscan tectonics. This study demonstrates the predominant role of structural study for unraveling the formation of Pb-Zn deposits especially in deformed/metamorphosed terranes.

**Keywords:** Pb-Zn deposits; Pyrenean Axial Zone; SEDEX; remobilization; structural control; sphalerite

## 1. Introduction

The world’s most important Pb-Zn resources consist in Sedimentary-Exhalative (SEDEX) mineralizations [1]. These types of ore deposits are syngenetic sedimentary to diagenetic. Occurrence of laminated sulfides parallel to bedding associated to sedimentary features (graded beds, etc.) are the key geological argument [2]. These important deposits occur often in ancient metamorphosed and highly deformed terranes for example in Red Dog, Alaska [3,4]; Rampura, India [5]; or Broken Hill, Australia [6]. In these cases, the processes of ore formation are still largely debated. In consequence, unraveling the relationships between mineralization and orogenic remobilization(s) is essential in order to understand the genesis of Pb-Zn deposits in deformed and metamorphosed environments. For example, in Broken Hill [6–8] and Cannington [9] deposits in Australia some authors argued for a metamorphogenic and epigenetic mineralization as large metasomatic zones may have refined pre-existing Pb-Zn rich rocks. Other authors consider a pre-metamorphic and syngenetic origin with only limited remobilization linked to tectonic events [10–12]. In the world-class Jinding Pb-Zn deposit, the host rock has undergone a complex tectonic deformation [13]. Some authors proposed a syngenetic

origin of the deposit [14,15] whereas others argued for an epigenetic genesis of the deposit based on field study, textural evidences [16–19], fluid inclusion [19,20], and paleomagnetic age [13]. Nowadays, these high-tonnage Pb-Zn deposits are the preferential target of numerous academic and industrial studies also for the presence of rare metals like Ge, Ga, In, or Cd associated with sulfides.

The Pb-Zn deposits hosted in the Pyrenean Axial Zone (PAZ) area that has suffered Variscan tectonics [21–23] are usually considered to be SEDEX. As an example, due to their geometry and the presence of distal volcanic rocks, Bois et al. [24] and Pouit et al. [25] considered as SEDEX the Pb-Zn mineralizations located in the Pierrefitte anticlinorium. In Bentaillou area, Fert [26] and Pouit [27,28] demonstrated that the stratigraphic and sedimentary controls were dominant processes during the genesis of these mineralizations. In the Aran Valley, deposits (Liat, Victoria-Solitaria, and Margalida) have been studied by Pujals [29] and Cardellach et al. [30,31]. These authors concluded on a stratiform and possibly exhalative formation of Pb-Zn mineralizations associated with a poor remobilization during Variscan deformation. Only few authors have documented the impact of Variscan tectonics on the genesis of these mineralizations. These are Alonso [32] in Liat, Urets, and Horcalh deposits or Nicol [33] for Pierrefitte anticlinorium deposits. In the Benasque Pass area, south of the Bossòst anticlinorium, Garcia Sansegundo et al. [34] indicated probable Ordovician stratiform or stratabound Pb-Zn mineralizations intensely reworked during Variscan tectonics. The Pb isotopes study realized by Marcoux [35] showed a unique major event of Pb-Zn mineralization interpreted as sedimentary-controlled and Ordovician or Devonian in age. Remobilization processes of Pb isotopes seem however poorly constrained and a complete structural study related to these analyzes is lacking.

Pyrenean sulfide mineralizations are an excellent target for investigating the links between orogenic deformation(s) and the genesis of associated mineralization(s), as well as finding key arguments to make the distinction between strictly syngenetic or rather epigenetic mineralizations and structurally remobilized mineralizations. In this work we will demonstrate that Pb-Zn deposits from five districts in the PAZ, previously largely considered SEDEX, were actually formed through processes involving a strong structural control.

## 2. Geological Setting

The Pyrenean Axial Zone (PAZ, Figure 1) is the result of the collision between the Iberian and Eurasian plates since the Lower Cretaceous. Deep parts of the crust were exhumed during this orogeny. The PAZ is composed of Paleozoic metasedimentary rocks locally intruded by Ordovician granites deformed and metamorphosed during the Variscan orogeny, like the Aston or Canigou gneiss domes [23,36].

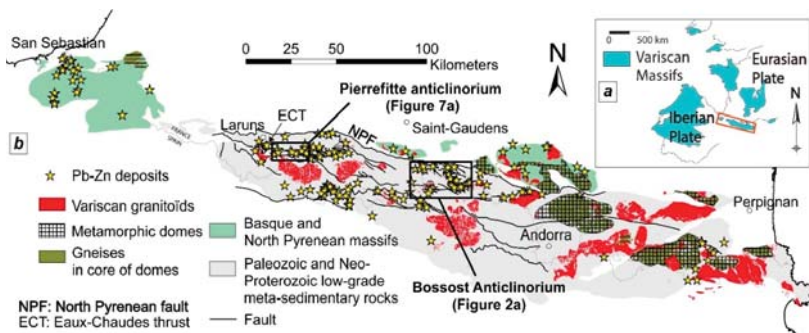


**Figure 1.** (a) Location of the Pyrenean Axial Zone (PAZ) within the Variscan belt of Western Europe. (b) Schematic map of the Pyrenean Axial Zone (PAZ) and location of all recognized Pb-Zn deposits (based on BRGM (French geological survey) and IGME (Spanish geological survey) databases). Note the abundance of these deposits especially in the central and western domains of the PAZ.



The PAZ is generally divided in two domains [21,36–39]: (i) a deep-seated domain called Infrastructure, which contains medium to high-grade metamorphic rocks and (ii) a shallow-seated domain called the Superstructure, which is composed of low-grade metamorphic rocks. The Infrastructure presents flat-lying foliations but highly deformed domains appear locally with steep and penetrative crenulation foliations. Alternatively, the Superstructure presents moderate deformation associated to a slaty cleavage [40,41] These two domains are intruded by Late-Carboniferous granites, like the Bossòst and the Lys-Caillaouas granites [37,42,43].

In the PAZ several deformation phases essentially Variscan in age (325–290 Ma) are recognized. The first deformation event ( $D_1$ ) is marked by a cleavage ( $S_1$ ) that is often parallel to the stratification ( $S_0$ ). Regional  $M_1$  metamorphism is of Medium-Pressure and Low-Temperature (MP/LT) and synchronous of this first  $D_1$  deformation [22]. The second deformation event ( $D_2$ ) is expressed by a moderate to steep axial planar ( $S_2$ ) cleavage.  $M_2$  is a Low-Pressure and High-Temperature (LP/HT) metamorphism linked to the Late-Variscan granitic intrusions, and it is superposed to the  $M_1$  metamorphism [44,45]. Late-Variscan and/or Pyrenean-Alpine  $D_3$  deformations are locally expressed as fold and shear zones like the Merens and/or probably the Bossòst faults [41,46,47].

The Pyrenean Pb-Zn regional district is the second largest in France with ~400,000 t Zn and ~180,000 t Pb extracted [48,49]. These sulfides deposits are localized in the PAZ in the Pierrefitte and Bossòst anticlinoriums (Figure 1b). Sphalerite (ZnS) and galena (PbS) are essentially present in Ordovician and Devonian metasediments. Few Pb-Zn deposits are hosted in granitic rocks [50].

This study focuses on Pb-Zn deposits located in the Bossòst anticlinorium (Figure 1) [42,44,51] and includes a comparison with Pb-Zn deposits occurring in the Pierrefitte anticlinorium. The southern part of the Bossòst anticlinorium forms the Aran Valley synclinorium. The northern part is limited by the North Pyrenean fault (Figure 2a). It is mostly composed of Cambrian to Devonian rocks and an intruding Late-Variscan leucocratic granite named the Bossòst granite.

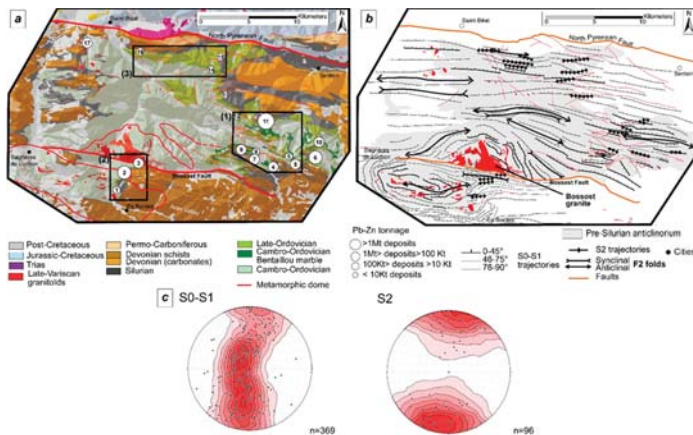


**Figure 2.** The Bossòst Anticlinorium. (a) Geological map with positions of the three districts: (1) Bentaillou-Liat-Urets district, see Figures 3 and 4; (2) Margalida-Victoria-Solitaria district, see Figure 5; and (3) Pale Bidau-Argut-Pale de Rase district, see Figure 6. Pb-Zn deposits are numbered as follows: 1: Solitaria; 2: Victoria; 3: Margalida; 4: Plan del Tor; 5: Urets; 6: Horcall; 7: Mauricio-Reparadora; 8: Estrella; 9: Liat; 10: Malh de Bolard; 11: Bentaillou; 12: Crabere; 13: Uls; 14: Pale Bidau; 15: Pale de Rase; 16: Argut. Lithologies are based on geological map of BRGM (France [52–54]) and IGME (Spain, Aran Valley; Garcia-Sansegundo et al. [55]). Metamorphic dome boundaries are related to andalusite isograd presented by Zwart; (b) Structural map with foliation trajectories of  $S_0$ - $S_1$ , subvertical  $S_2$ , and related  $F_2$  folds. Note preferential apparition of Pb-Zn deposits when  $S_2$  cleavage is well-expressed. (c) Schmidt stereographic projections (lower hemisphere) of poles to  $S_0$ - $S_1$  and  $S_2$  subvertical foliation planes.

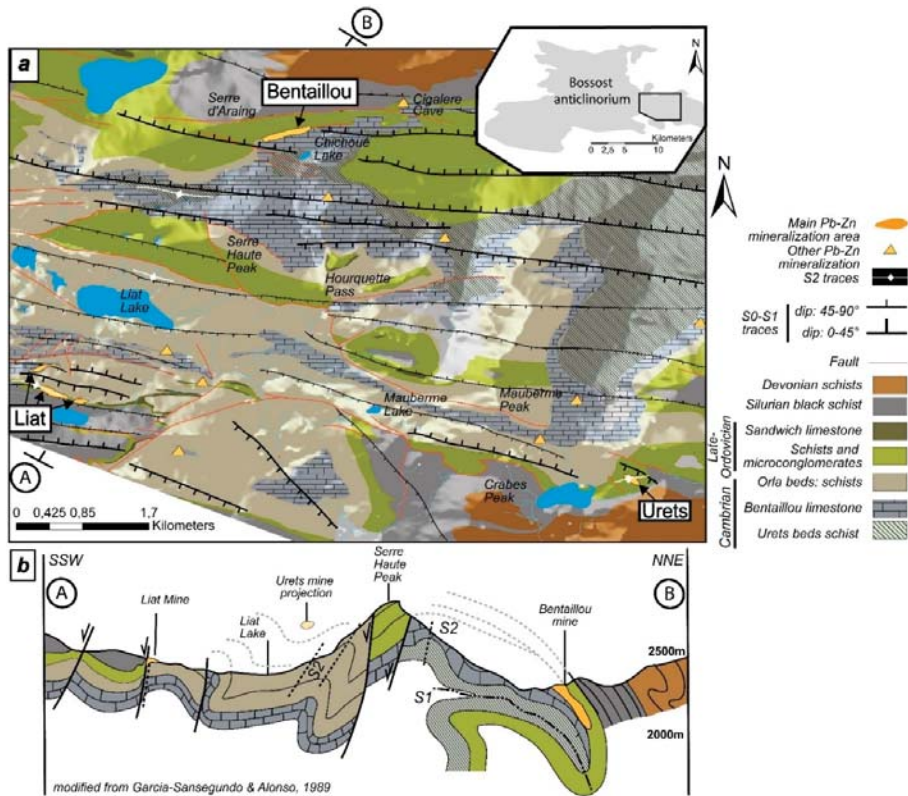


**Figure 3.** (a) Structural map of the Bentailou-Liat-Urets district based on field study and BRGM/IGME geological maps. Location in Bossost anticlinorium is indicated in the small sketch map (see also location on Figure 2a); (b) Structural NNE-SSW cross-section of the Liat-Bentailou area. Location of the cross-section is indicated in the Figure 3a (modified from Garcia-Sansegundo and Alonso [56]). Note presence of Pb-Zn mineralization at rock competence interface and close to F1 fold hinge in Bentailou mine.

Three main Pb-Zn districts are recognized in the Bossost anticlinorium (Figure 2): (I) The Bentailou-Liat-Urets district is located in the eastern part of the anticlinorium and was the most productive in the Bossost anticlinorium, ~1.4 Mt at 9% of Zn and 2% of Pb metals [32,33]. (II) The Margalida-Victoria-Solitaria district is located in the southern part of the anticlinorium, close to the Bossost granite. Production reached ~555,000 t with 11% Zn and 0.1% Pb [49]. (III) The Pale Bidau-Argut-Pale de Rase district is located in the northern part of the anticlinorium. Pb-Zn production did not exceed ~7000 t of Zn and ~3000 t of Pb [57].

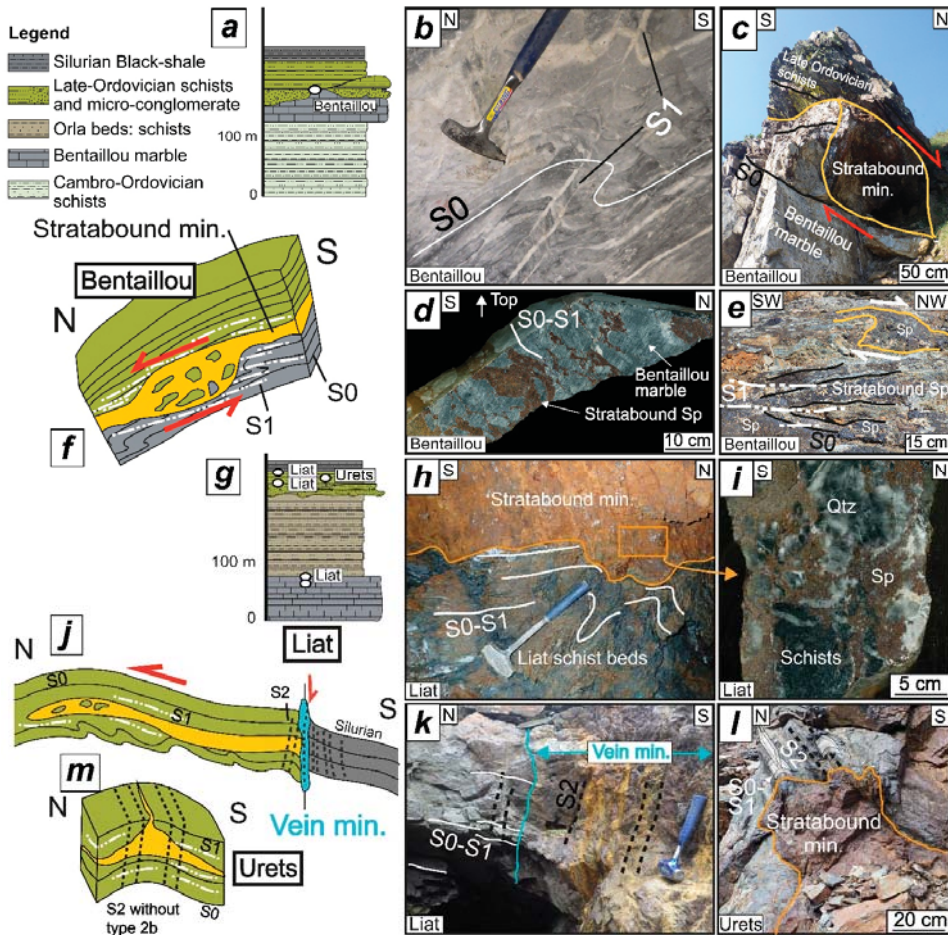


**Figure 4.** Field observation and structural models in the Bentaillou-Liat-Urets deposits (see location in Figure 3a). (a) Stratigraphic log of Bentaillou areas with position of the Pb-Zn deposits; (b)  $F_1$  fold in Bentaillou marble with  $S_1$  cleavage marked by calcite recrystallization; (c) pull-apart geometry of Pb-Zn mineralization in Bentaillou area; (d) oriented sample of typical mineralization in Bentaillou marble; and (e) relationship between sphalerite mineralization and host rock structure. Note that sphalerite is not folded by  $F_1$  folds and intersect  $S_0$  stratification; (f) 3D structural model of Bentaillou deposits with Pb-Zn mineralization in cm to pluri-m pull apart geometry; (g) stratigraphic log of Liat-Urets area with position of the Pb-Zn deposits; (h) stratabound mineralization in top of folded schist beds in Liat area; (i) brecciated Pb-Zn mineralization in Liat area with clast of schist and quartz in sphalerite matrix; (j) 3D structural model of Liat deposit with dm to m stratabound and vein mineralizations; (k) vein Pb-Zn mineralization in Liat deposit; (l) stratabound mineralization in  $F_2$  fold hinge in Urets deposit; (m) 3D structural model of Urets deposit with pluri-dm to m Pb-Zn mineralization in  $F_2$  fold hinge. Mineral abbreviations: Qtz-quartz; Sp-sphalerite.

Pierrefitte anticlinorium is located north of the Cauteret granite and intersected by the Eaux-Chaudes thrust (ECT; Figure 1). It is essentially composed of Ordovician rocks in the West and Devonian terranes in the East. Two districts are studied: (I) Pierrefitte mines is the largest district in the PAZ which produced ~180,000 t of Zn, ~100,000 t of Pb and ~150 t of Ag [48]. (II) Arre and Anglas mines are located west to Pierrefitte mines. Pb-Zn production did not exceed ~6500 t of Zn [48].

### 3. Structural Analysis of Three Pb-Zn Districts in the Bossòst Anticlinorium

The Bossòst anticlinorium is a  $30 \times 20$  km E-W-trending asymmetric antiform hosting a metamorphic dome (Figure 2a). Pre-Silurian lithologies are dominated by Cambro-Ordovician schists. Locally, other lithologies are present like the Cambro-Ordovician Bentaillou marble or the late-Ordovician microconglomerate and limestone (Figure 2b).

Two distinct cleavages can be observed in the Bossòst anticlinorium.  $S_1$  transposes the  $S_0$  stratification and is roughly oriented N090–N120°E with varied dip angles both to the north and to the south (Figure 2b,c).  $S_0$ - $S_1$  dip angles are low in the metamorphic dome (Figure 2b) but this pattern is not restricted to the core of the anticlinorium. In the eastern part of the anticlinorium, foliation is generally low to moderately dipping (0–45° N or S, Figure 2b) and Garcia-Sansegundo and Alonso [54] supposed the presence of large recumbent  $F_1$  folds in the Bentaillou and Horcalh-Malh de Bolard areas. The presence of a Late Ordovician microconglomerate at the base of Bentaillou limestone is described by Garcia-Sansegundo and Alonso [56] and confirms this hypothesis. Furthermore, the presence of these folds is inferred by the observation of dm- to pluri-m north-verging recumbent  $F_1$  folds in Bentaillou marble in the underground levels of the mine and also by their presence in the Devonian schists.

Close to the southern boundary of the Bossòst granite,  $S_0$ - $S_1$  foliation in high-grade schists is steeply dipping (Figure 2b). The  $S_2$  cleavage trends N080–120°E and is generally sub-vertical (Figure 2c) as axial plane of  $F_2$  south-verging folds.  $S_2$  cleavage and related  $F_2$  folds are particularly well developed in the southern part of the Bossòst anticlinorium (Figure 2b).

In the PAZ districts, three Pb-Zn mineralization types are commonly observed and two of these will be described below: Stratabound mineralization is subparallel to  $S_0$ - $S_1$  and Vein mineralization is parallel to  $S_2$ . Disseminated mineralization is not a key mineralization type and is spread in the host rocks.

#### 3.1. District of Bentaillou-Liat-Urets

This district is located in the southeastern part of the Bossòst anticlinorium. Three main extraction areas are present in this district: (i) Bentaillou mine is located in the north of the district (Figure 3a). Exploitation finished in 1953 and produced ~110,000 t of Zn and ~40,000 t of Pb. At that time, it was the second largest mine in the Pyrenees [58], (ii) the Liat mine lays southwest of the district and (iii) Urets is located southeast of the district (Figure 3a). Both produced ~60,000 t of Zn [49]. Mineralization occurrences will be described in the following parts.

##### 3.1.1. Bentaillou Area

Mineralization lays close to the hinge of a N090–110°E kilometer-size  $F_1$  recumbent fold (Figure 3b) and is essentially located at the top of the Cambro-Ordovician marble, below the Late-Ordovician schists (Figure 4a). Mineralized stratabound bodies are broadly parallel to  $S_0$ - $S_1$  which is sub horizontal with a progressive increase of the dip from 45°N to 80°N to the lowest underground mine levels in the north (Figure 3b). Relicts axial planar  $S_1$  of  $F_1$  recumbent isoclinal folds are locally underlined by recrystallized calcite in N090–100°E axial planes (Figure 4b).

Pb-Zn stratabound mineralizations are present in cm- to pluri-m N-S open-filling structures which can be assimilated to pull-apart features (Figure 4c) that were formed in association with a dextral top to the north kinematic. These mineralized bodies show typical impregnation textures (Figure 4d) and sphalerite presents mm to cm grain sizes. Pb-Zn mineralization is absent in weakly  $D_1$  deformed areas whereas it occurs in highly deformed domains associated to the appearance of  $S_1$  cleavage in  $F_1$  fold hinges (Figure 4e,f).

##### 3.1.2. Liat Area

Pb-Zn mineralization is located at the rock interface (Figure 4g) and can be hosted in Bentaillou marble, especially on top of the marble, between the microconglomerate and Liat beds or between

Liat beds and the Silurian black-shale. The large hm-size open  $F_2$  fold is bordered to the south by a Silurian synclinorium (Figure 3a,b).  $S_1$  cleavage is strictly parallel to  $S_0$  in the area.  $D_2$  deformation is well expressed in the south at the contact between Silurian black-shale and Late Ordovician schists.

Mineralized stratabound bodies with pluri-dm to m-thickness appear parallel to the shallow dipping  $S_0$ - $S_1$ . Folds in Liat schists are present locally at the base of the mineralization (Figure 4h). It presents a brecciated texture (Figure 4i) with clasts of quartz and schists. Sphalerite presents cm grain sizes. At the contact with the Silurian black-shale the dip of Late Ordovician schist increases and a normal fault is inferred. Vertical Pb-Zn vein mineralization parallel to  $S_2$  is present in this fault. It intersects  $S_0$  stratification,  $S_1$  cleavage as well as stratabound mineralizations (Figure 4j,k). Vein mineralization also presents a brecciated texture and sulfide grains are oriented parallel to  $S_2$ . Sphalerite presents an infra-mm grain size.

### 3.1.3. Urets Area

This Pb-Zn mineralization is hosted in Liat schist.  $D_2$  deformation is intensively present in this area, with numerous  $N100$ – $130^\circ E$   $F_2$  open to isoclinal folds associated to a subvertical  $N90$ – $120^\circ E$   $S_2$  cleavage. Stratabound pluri-dm to m Pb-Zn mineralization is mainly located in  $F_2$  fold hinges (Figure 4l) and can locally intersect  $S_0$  stratification (Figure 4m). Pb-Zn mineralization has a brecciated texture with mm sphalerite grains and mm to cm quartz clasts.

### 3.2. District of Margalida-Victoria-Solitaria

This district is located south of the Bossòst anticlinorium (Figure 2a). Three main extraction areas are present in this district from north to the south (Figure 5a): (i) Margalida mine is located close to the Bossòst granite next to the Bossòst fault, (ii) Victoria mine, and (iii) Solitaria mine lays south of the granite and north and west to Arres village. Margalida and Solitaria mine produced less than 50,000 t of ore with ~10% of Zn and 1% of Pb [49]. Victoria produced ~504,000 t with 11% of Zn and 1% of Pb [49].

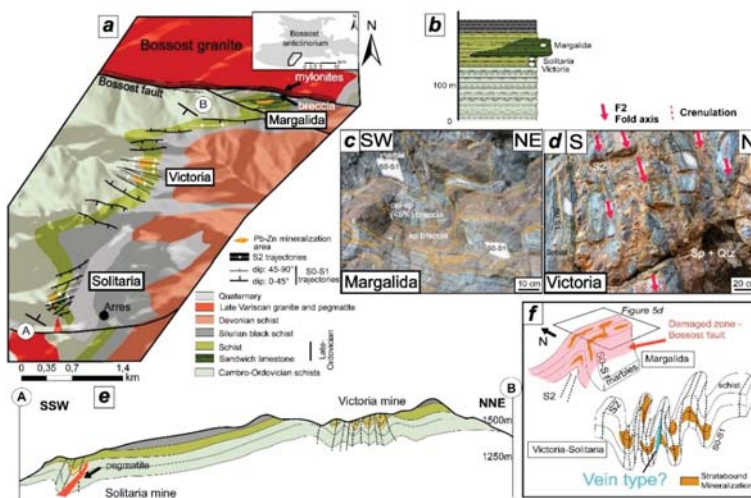


**Figure 5.** Margalida-Victoria-Solitaria district (see location on Figure 2a). (a) Structural map (lithologies are based on IGME geological map (Spain, Aran Valley; Garcia-Sanseguendo et al. [1]) and location on the Bossòst anticlinorium (pre-Silurian rocks); (b) stratigraphic log; (c) stratabound Pb-Zn mineralization in Margalida mine hosted in Sandwich limestone level; (d) typical stratabound folded mineralization ( $F_2$  isoclinal folds) in Victoria; (e) structural NNE-SSW cross-section of Victoria-Solitaria area; and (f) structural model of Margalida and Victoria-Solitaria mines. Mineral abbreviations: Cal—Calcite; Qtz—Quartz; Sp—Sphalerite.

### 3.2.1. Margalida Area

Pb-Zn mineralization is located in Late-Ordovician sandwich limestone (Figure 5a,b) which forms the core of an anticlinorium presenting a vertical N100°E-trending axial plane (supposed  $F_2$  fold). Mineralization is located in the damaged zone of the Bossòst N090°E-trending fault. Mineralization appears as pluri-dm lenses generally parallel to  $S_0$ - $S_1$ . Still mineralization is not always concordant to  $S_0$ - $S_1$  (Figure 5c). The texture of sulfide mineralization in Margalida area is different to this in Victoria-Solitaria area as sulfide grain size is infra-mm.

### 3.2.2. Victoria-Solitaria Areas

Pb-Zn mineralization is hosted by Late Ordovician schists (Figure 5a,b,d) and generally parallel to  $S_0$ - $S_1$ . Locally  $S_0$ - $S_1$  is intensively folded by  $F_2$  asymmetrical isoclinal N090–N120°E folds and a vertical  $S_2$  N070–110°E axial planar cleavage can be observed. Stratabound mineralization appears only in domains where  $F_2$  folds imprint is intense (Figure 5e). Furthermore, in Victoria and Solitaria mines exploitation was preferentially undertaken in  $F_2$  fold hinges. Pb-Zn mineralization is thicker in fold hinge (dm to m in thickness) and probably reworked during this  $D_2$  deformation phase (Figure 5e,f). Sphalerite grains are often sub-millimetric. The presence of vein mineralization cannot be completely excluded as vertical galleries are present.

### 3.3. District of Pale Bidau-Argut-Pale de Rase

The general structural description of the district is given in [53]. In this section more details are given on the structural features of the Pale Bidau area (see location on Figure 2a).

Two different Pb-Zn mineralization geometries appear: a first stratabound mineralization is hosted only in  $F_2$  fold pelitic level and concordant to  $S_0$ - $S_1$ , marked by cm to pluri-m box-work texture. The second mineralization consists of veins oriented N090–120°E and consists of dm to m veins largely developed when  $D_2$  deformation is important. Various dips are present for this mineralization but is mainly subvertical. Geometry of this mineralization can be interpreted as a pull-apart (Figure 6a) opened in a dextral top to the north movement and controlled by  $S_2$  cleavage. Where  $S_2$  cleavage is less pronounced, mineralization is thinner and seems to present in the sub-horizontal to 45°N  $S_0$ - $S_1$  cleavage (Figure 6b,c). Sphalerite crystals did not reach mm grain size.

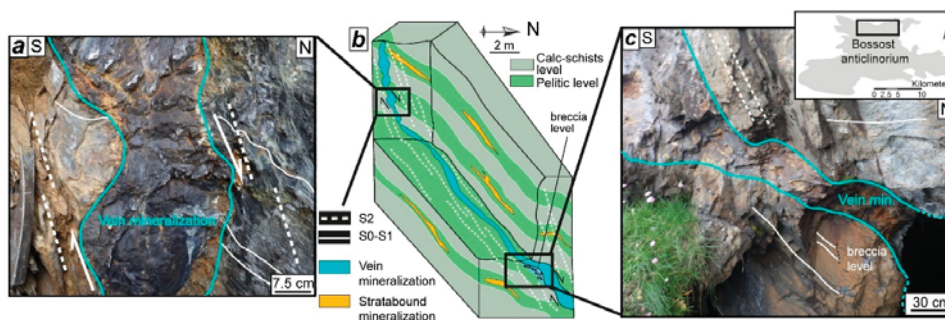


**Figure 6.** Field observations and 3D structural model of Pale Bidau deposit (see location in Figure 2a). (a) Vein Pb-Zn mineralization that occurs in pull-apart geometry; (b) 3D model presenting the relations between stratabound and vein Pb-Zn mineralizations; and (c) vein mineralization with presence of breccia at the base of a pull-apart mineralized structure.

## 4. Comparison with the Pierrefitte Anticlinorium: Pierrefitte and Arre-Anglas-Uziou Districts

The Pierrefitte anticlinorium is a 25 × 10 km NNW-SSE anticlinorium located in the western part of the PAZ (Figures 1b and 7a). Its core is composed of Ordovician schists and Late-Ordovician carbonated breccias. Upper stratigraphic levels are made of Silurian black-shales and Devonian rocks.

In western parts km-scale Valentin NNW-SSE anticlinal is included in the Pierrefitte anticlinorium. Compared to the Bossost anticlinorium, the volume of late-Variscan granite or pegmatitic rocks outcropping is smaller and there is no metamorphic dome in the core (Figure 7a).

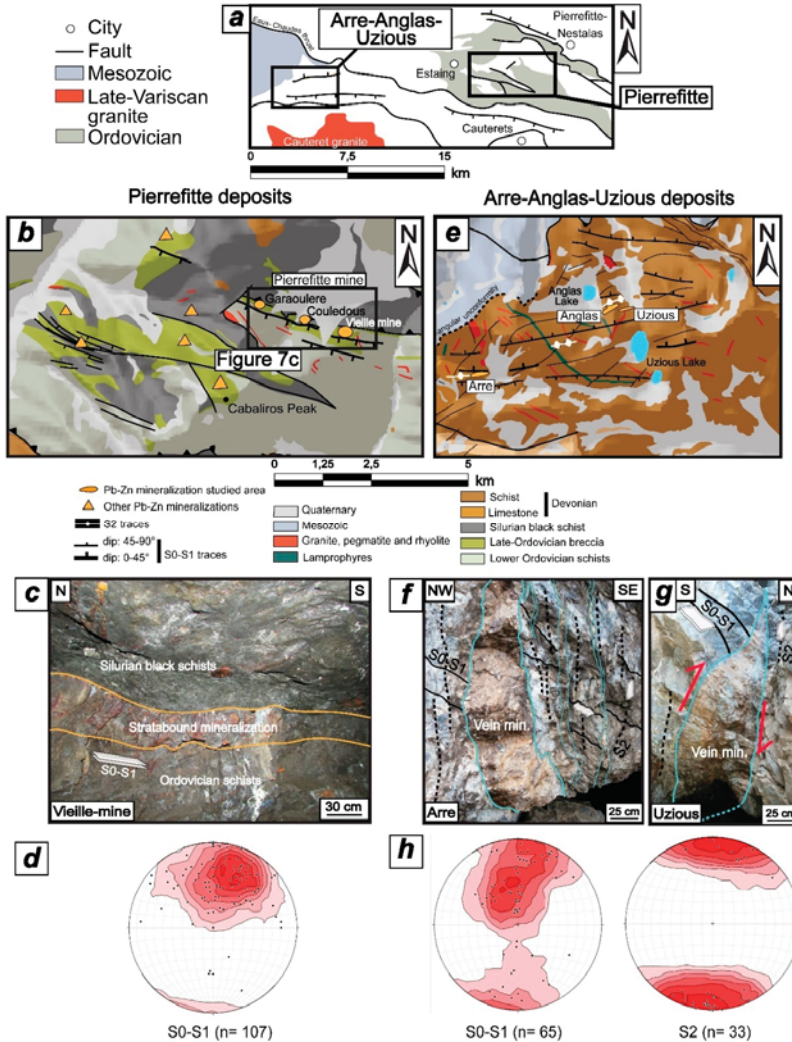


**Figure 7.** The Pierrefitte anticlinorium. (a) Simplified structural map showing the location of (b,e); (b) structural map zoomed on Pierrefitte mine (Lithologies are based on BRGM geological maps [59]); (c) photograph of typical stratabound Pb-Zn mineralization in Pierrefitte mine; (d) Schmidt stereographic projections (lower hemisphere) of poles to S<sub>0</sub>-S<sub>1</sub> foliations measured in the Pierrefitte anticlinorium; (e) structural map of the Pierrefitte-Valentin anticlinorium zoomed on Anglas-Uzious and Arre mines (Lithologies are based on BRGM geological maps); (f) photograph of Arre vein mineralization parallel to S<sub>2</sub> cleavage; (g) photograph of Anglas-Uzious vein mineralization; and (h) Schmidt stereographic projections (lower hemisphere) of poles to S<sub>0</sub>-S<sub>1</sub> and S<sub>2</sub> foliations measured in Anglas-Uzious and Arre areas.

The Pierrefitte anticlinorium is structured by several thrusts within Silurian levels (Figure 7b,c) associated to D<sub>1</sub> deformation. S<sub>2</sub> vertical N090–100°E cleavage is well expressed in Devonian levels at the rim of the anticlinorium but is less visible in the Ordovician core.

Numerous Pb-Zn mines are present in Late-Ordovician and Devonian terranes. These have produced ~3 Mt (average 9% of Zn and 5% of Pb).

#### 4.1. Pierrefitte District

The Pierrefitte mines (Garaoulere, Couledous, Vieille-Mine) are located at the contact with Late Ordovician rocks mainly carbonate breccia. N100–110°E S<sub>0</sub>-S<sub>1</sub> foliation moderately dips (20° to 60°) to the south (Figure 7d).

Stratabound mineralization lays at the top of the Late Ordovician series at the contact or within the Silurian black-shales (Figure 7c), which follows a regional thrust parallel to S<sub>0</sub>-S<sub>1</sub>. The presence of a thrust in Pierrefitte area is reported in [21,60,61] and this observation is supported in galleries by the occurrence of dm-scale dextral shear bands with a top-to-the-north-east kinematic. The mine galleries and the main exploited ore follow this regional thrust zone. S<sub>1</sub> cleavage often transposed S<sub>0</sub> stratification and corresponds to axial planes of isoclinal recumbent F<sub>1</sub> N090–120°E folds.

#### 4.2. Arre-Anglas-Uzious District

Arre and Anglas-Uzious mines are hosted by Devonian schists and Lower Devonian limestone respectively (Figure 7e). S<sub>2</sub> cleavage is well-expressed even in Devonian limestone in the area and subvertical with a N090–100°E trend.

Arre mine is located in the western hinge of the Pierrefitte anticlinorium close to the contact of limestone and schistose rocks. The mineralization is composed of two ore bodies showing a trend of N040–090°E and a dip of 70°N to 90°N. Mineralization appears parallel to S<sub>2</sub> cleavage and discordant to S<sub>0</sub>-S<sub>1</sub> (Figure 7f) which is typical of a vein mineralization. Anglas and Uzious mines are located in the northern part of the Pierrefitte anticlinorium. Mineralization consists in multiple pluri-centimeters to m vein orebodies, with several orientations from N060° to N100°E and subvertical dips. Uzious veins intersect magmatic aplite with a N050°E trend and have a pull-apart geometry (Figure 7g) linked to the presence of N090–100°E S<sub>2</sub> weak structures (Figure 7h). Many conjugate fractures N030–50°E with various dips are filled with mineralization close to the veins but their extension is limited to few dm.

### 5. Ore Petrology and Microstructures

A synthetic paragenetic sequence of the three Pb-Zn mineralization geometries investigated in this study is presented in the Figure 8. Disseminated mineralization represents the primary layered ore that is essentially composed of sparsely disseminated pluri- $\mu$ m to mm grains of sphalerite, pyrite, magnetite, and galena. In all the studied deposits this mineralization is minor and does not constitute the exploited ore. Sulfides may appear in graded-beds or have a typical framboidal appearance (Figure 9a).

Stratabound and vein mineralizations constitute the main sulfides mineralizations. Sphalerite is the more widespread sulfide in these two mineralizations. Pyrite, galena pyrrhotite, chalcopyrite, and arsenopyrite are present in minor amounts. Metamorphic muscovite, chlorite, or biotite are intimately associated to sulfide mineralization. In Victoria-Solitaria, metamorphic Zn-spinel or gahnite is present in the host rocks and in breccia clasts in stratabound sulfide mineralization. The presence of gahnite in Victoria was previously reported [62]. In the host rock gahnite is elongated parallel to S<sub>1</sub> and is intersected by stratabound mineralization (Figure 9b).



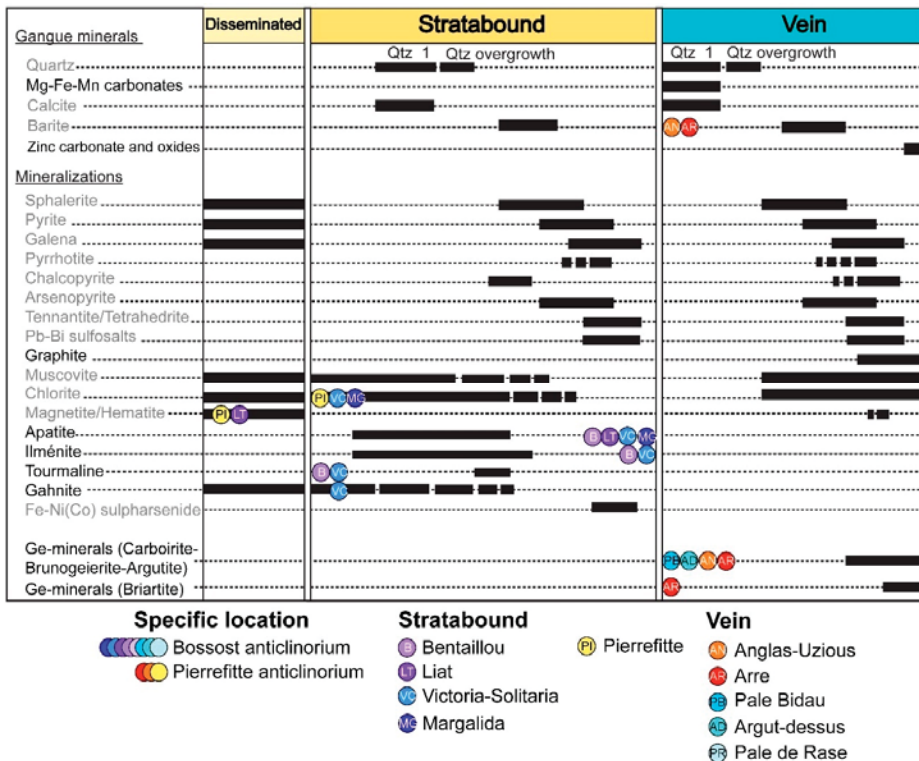


**Figure 8.** Paragenetic succession of ore and gangue minerals for all the eleven Pyrenean-studied Pb-Zn deposits. Minerals in grey are common to both stratabound and vein mineralizations and minerals in black are only present in stratabound or vein. Minerals only reported in a deposit are noted with the deposit circle. Several minerals like apatite, ilmenite, or tourmaline are only present in stratabound mineralization. Ge-minerals, graphite zinc carbonates or oxides, and Mg-Fe-Mn carbonates are only observed in vein mineralization ( $n = 110$ ).

Stratabound Pb-Zn mineralization is a post-disseminated mineralization. SEM images show a primary framboidal galena intersected by a secondary stratabound pull-apart mineralization in the Bentaillou mine (Figure 9a).

In the Pierrefitte anticlinorium stratabound magnetite is abundant, especially in the Pierrefitte mine. It has crystallized prior to sphalerite. In the Pierrefitte mine syn-cinematic sphalerite crystallizes in asymmetric pressure shadows around a clast of magnetite (Figure 9c). Sphalerite appears parallel to  $S_1$  cleavage and intersects  $S_0$  stratification in an isoclinal  $F_1$  fold hinge (Figure 9d). In the Bossòst anticlinorium and especially in Liat mine, sphalerite and quartz mineralization intersect  $F_2$  folded pelitic rocks (Figure 9e). The same quartz associated to sphalerite is present in crack and seal veins (Figure 9e). In Margalida a typical *durchbewegung* texture with quartz spheroids in a sphalerite matrix shows a deformational imprint on this mineralization.

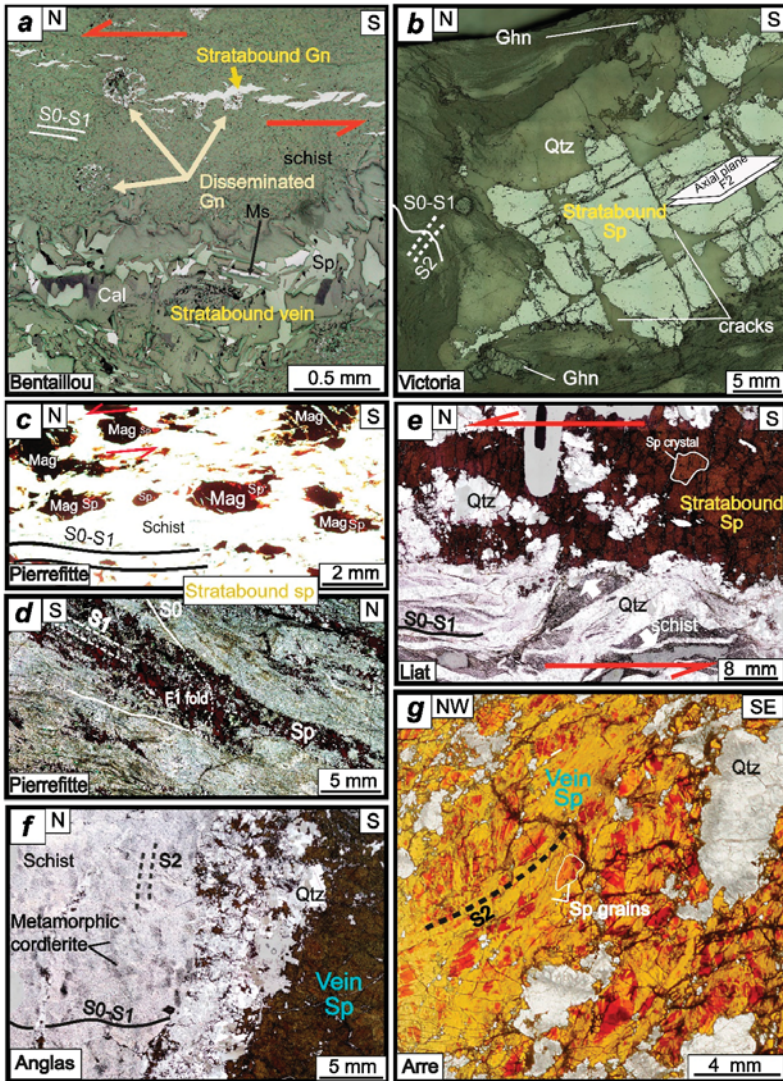


**Figure 9.** Microphotographs showing characteristics textures in the three mineralization types. (a) Bentaillou disseminated mineralization truncated by stratabound mineralizations (reflected light); (b) stratabound Victoria folded mineralization which intersects gahnite D<sub>1</sub> metamorphic mineral (reflected light); (c) syn-kinematic sphalerite which crystallizes in asymmetric pressure shadows around clasts of magnetite in Pierrefitte mine (transmitted light); (d) sphalerite mineralization from Pierrefitte mine parallel to S<sub>1</sub> and in F<sub>1</sub> isoclinal fold hinge. Mineralization intersects S<sub>0</sub> stratification (transmitted light); and (e) stratabound sphalerite and quartz mineralizations which intersect pelitic host rock in Liat mine. Sphalerite is interpreted syn-kinematic D<sub>1</sub> (transmitted light); (f) vein mineralization in Anglas mine which intersect S<sub>0</sub>-S<sub>1</sub> and parallel to S<sub>2</sub> cleavage marked by metamorphic cordierite (transmitted light); and (g) deformed and recrystallized vein sphalerite in Arre deposit. The two textures are identified with white line Recrystallization area in yellow marked S<sub>2</sub> cleavage (transmitted light). Mineral abbreviations: Cal—Calcite; Ghn—Gahnite; Gn—Galena; Mag—Magnetite; Ms—Muscovite; Qz—Quartz; Sp—Sphalerite.

Stratabound mineralization contain apatite, ilmenite, and tourmaline minerals that are only observed in this mineralization. In the Pierrefitte mineralization, the abundance of chlorite and muscovite associated to the mineralization is remarkable compared to other Pyrenean deposits.

Vein mineralization intersects  $S_0$  at the micron scale (Figure 9f). In the Anglas deposit, vein mineralization is essentially composed of sphalerite, galena, quartz and calcite. The hanging wall of the vein is parallel to  $S_2$  foliation and is marked by cordierite crystallization. Sphalerite in vein mineralization appears highly deformed and recrystallized with mm relictual grains and recrystallized  $\mu\text{m}$ -size crystals (like in Arre deposit, see Figure 9g). In Pale Bidau deposit, vein mineralization is only present in domains where the  $S_2$  cleavage is well-marked. Note that Ge-minerals are exclusively present in the vein mineralization (Figure 8).

## 6. Discussion

### 6.1. Types of Pb-Zn Mineralizations in the PAZ

The presence of three major types of Pb-Zn mineralizations is demonstrated in this study: Disseminated but layered mineralization, which is now defined as Type 1, appears with graded-beds and framboidal appearance (Figure 9a). Stratabound mineralization (now defined as Type 2a) is a syn- $D_1$  mineralization concordant to the  $S_1$  foliation. Vein mineralization (now defined as Type 2b) is a syn- to post- $D_2$  vein-type mineralization, parallel to the subvertical  $S_2$  foliation. Type 2a and Type 2b are undoubtedly epigenetic and were formed as a consequence of Variscan tectonics.

The first and earlier Type 1 mineralization (Figure 10) is recognized in all the studied deposits in the Bossòst and Pierrefitte anticlinoriums, but it is not the main exploited resources. Its formation may be linked to the early volcanic Ordovician or Devonian events as proposed by Pouit [27] and Reyx [63]. In Pierrefitte anticlinorium, Nicol [55] proposed a unique Devonian source for the Pb-Zn mineralizations. Syngenetic formation is preferred for the Type 1 mineralization as sulfides appear layered and with sedimentary affinities. Nevertheless, framboidal texture may as well form in a post-sedimentation environment like in hydrothermal veins [64].

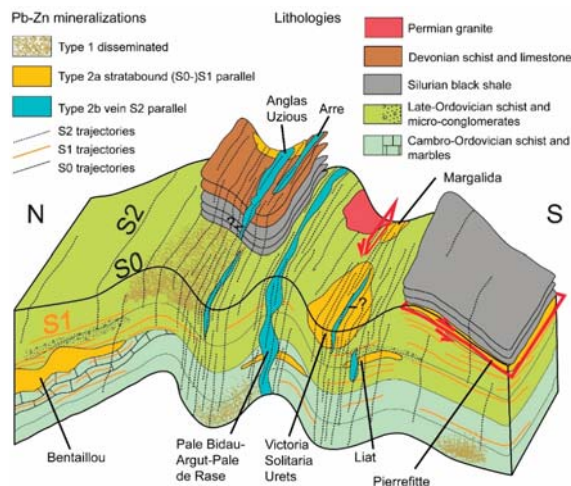


**Figure 10.** Schematic 3D sketch displaying the three main mineralization types which are typically observed in the studied area and related to each studied deposit. Note cm to pluri-m pull apart geometries in Bentaillou Type 2a mineralizations and in Type 2b mineralizations. Type 2b vein mineralizations are located in intensely  $S_2$  deformed domains. Other structural traps like saddle-reef formation in fold hinge or rock competence interfaces are represented for Victoria-Solitaria, Urets, Pierrefitte, and Liat deposits respectively.

The second stratabound Type 2a mineralization (Figure 10) is deposited parallel to  $S_0$ - $S_1$ . It corresponds to the main Pb-Zn mineralization episode in the PAZ (~95% of the total exploited ore volume). In the Bentaillou area, Type 2a mineralization intersects  $S_0$  stratification and is hosted by  $S_1$  cleavage (Figure 4e), which is axial planar to isoclinal  $F_1$  folds. Fert [26] and Pouit [27,28] proposed a syngenetic model for the Bentaillou deposit and described a normal stratigraphic succession that has been later folded by  $F_2$  folds.  $F_1$  isoclinal recumbent N090°E folds are absent in their model. Here we observe that Bentaillou Pb-Zn mineralization is localized essentially close to  $F_1$  fold hinges at the interface between marble and schist or microconglomerate (Figure 4c). The source for Type 2a sulfides may be related to layered and supposed syngenetic Type 1 sulfides that are disseminated in the Ordovician and Devonian neighboring metasediments, or to Late-Variscan granitic intrusions, probably at least temporally close to the Type 2a mineralizations. Opening of top to the north cm to pluri-m pull-apart-type structures (Figure 4c) enables the formation of the large amount of mineralizations in Bentaillou. Pb-Zn ore is not observed at the base of Bentaillou marbles due to important karstification (Cigalere cave, Figure 3a), however it is deposited at Bularic [65] both above and below this marble level. In the Liat area, Pujals [29] described a syngenetic or diagenetic mineralization with apparent limited reworking. Our model shows that Type 2a stratabound mineralization is linked to the Variscan  $D_1$  deformation. In the Victoria-Solitaria area, Type 2a stratabound mineralization occurs where  $D_2$ -related structures are present and can be locally remobilized in fold hinges. These thicker mineralizations in fold hinge may be linked to the saddle-reef process [66–68] associated with formation of the dilatation zone during folding. These deposits have been studied by Pujals [29], Cardellach et al. [30,69], Alvarez-Perez et al. [70], and Ovejero-Zappino [49,71]. These authors argued for a SEDEX origin based on syngenetic mineralization associated to the presence of syn-sedimentary faults. These models differ from our hypothesis: here we report that  $S_1$  cleavage is parallel to axial plane of recumbent km-size isoclinal folds and transposes the  $S_0$  stratification.  $F_2$  folded Type 2a stratabound mineralization is thicker in fold hinge and intersects metamorphic minerals as gahnite. Presence of this Zn-spinel may be linked to a primary minor sulfide mineralization (Type 1, Figure 10) or to a  $D_1$  metamorphic fluid rich in Zn. Chemistry of gahnite was analyzed by Pujals [29] and its composition is typical to metamorphosed zinc deposits. This testifies that Type 2a Pb-Zn mineralization is syn- to post- $M_1$  metamorphism. Alonso [32] demonstrated a predominant role of mechanical remobilization associated to deformation in the Bossòst anticlinorium and, especially,  $F_2$  folds in Horcalh and fault in Liat. Our model is similar as we consider that the Variscan  $D_2$  deformation locally remobilized Type 2a mineralization. The Margalida deposit records an additional deformational event compared to Victoria and Solitaria. Hosted in a ductile deformed marble and close to the Bossòst ductile fault, the Type 2a mineralization appears largely deformed with a typical *durchbewegung* texture. No sedimentary structure is recognized in the marble [70]. This attests for a Late Hercynian and/or Pyrenean deformation associated to the fault on the mineralization. Comparison with the Pierrefitte anticlinorium shows the same syn- $D_1$  Type 2a mineralization associated to regional thrust tectonics. The main exploited Pb-Zn mineralization in Pierrefitte mine was pluri-m scale levels parallel to  $S_0$ - $S_1$  and the regional thrust (Figure 10). Our work comforts the study of Nicol [60] which has shown an important remobilization of the mineralization in Ordovician and Devonian metasediments linked to  $D_1$  deformation. On the contrary, Bois et al. [24] proposed a syngenetic deposition related to the activity of Late-Ordovician syn-sedimentary faults and volcanism that may have induced these mineralizations. In this case, remobilization is weak and sulfides crystallize prior to Variscan metamorphism [24]. But the presence of sphalerite parallel to  $S_1$  cleavage and in pressure shadows around magnetite clast concordant to  $S_1$  rather attests for a syn- $D_1$  mineralization event.

The third Type 2b vein mineralization (Figure 10) is parallel to  $S_2$  cleavage. It intersects  $S_0$ - $S_1$  cleavage and former Type 2a stratabound mineralization. It has been recognized in the Pale Bidau-Argut-Pale de Rase districts [57] and Arre-Uziou-Anglas districts. It appears in a limited number of deposits in the PAZ. Type 2b mineralization is present in pluri-dm veins with restricted extension and highly differs structurally and mineralogically. The presence of Ge-minerals and absence of apatite, tourmaline, or

ilmeneite are remarkable here. Nonetheless, possible Type 2a remobilization with external contribution is not excluded in the Type 2b vein formation. In the Uzious mine mineralization intersects magmatic aplite. Therefore it has probably emplaced syn- or post-Cauteret granite and is certainly late-Variscan in age (aplite from late-Variscan Cauteret granite) as supposed by Reyx [63]. Deformation of sphalerite, which is supposed to be syn-D<sub>2</sub> and/or syn-D<sub>3</sub>, and the unusual sulfide paragenesis are inconsistent with a Mesozoic age as described in Aulus-Les Argentieres undeformed sphalerite [72]. Other Pb-Zn deposits, like the La Gela deposit [73] or Carboire deposit, could be attached to this third type as they are characterized by vertical Pb-Zn veins and presence of Ge-minerals. These late-Variscan Pb-Zn deposits have been recognized in Saint-Salvy (cf. M<sub>2</sub> mineralization) even if the main Pb-Zn mineralization event is Mesozoic [74].

6.2. Genetic Model of PAZ Pb-Zn Deposits Formation Linked to Regional Geology

The genetic model comprises four stages (Figure 11) based on the regional tectonic event model of Mezger and Passchier [22] and Garcia-Sansegunido and Alonso [56].

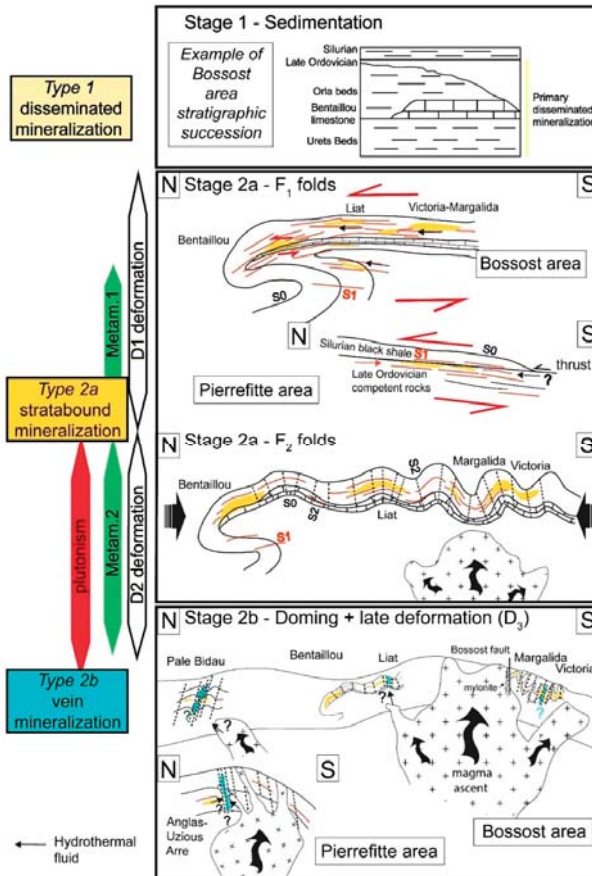


**Figure 11.** Genetic model for the formation of the three main Pb-Zn mineralization types. **Stage 1** is the disseminated Type 1 mineralization that is supposed to be syn-sedimentary. **Stage 2a** is the syn-D<sub>1</sub> Type 2a stratabound mineralization which is followed by the formation of F<sub>2</sub> folds and local remobilization of Pb-Zn mineralizations (saddle reef). **Stage 2b** represents the Type 2b late-Variscan vein mineralizations.

Stage 1 represents the syn-sedimentary layered mineralization (SEDEX deposit, Pb-Zn Type 1 disseminated mineralization). Primary sulfides were recognized in all pre-Silurian stratigraphic succession in the Bossòst area (Figure 11) and in Devonian rocks in Anglas-Uzious-Arre district. In the Pierrefitte area primary sphalerite is absent, which is probably linked to important hydrothermal low-grade alteration and D<sub>1</sub> overprint.

Stage 2a starts during the D<sub>1</sub> Variscan deformation and induces Type 2a stratabound mineralization. This mineralization occurs preferentially where a rheological contrast exists between two lithologies (e.g., marble-schist; schist-microconglomerates) and in highly D<sub>1</sub> deformed area (Figure 11). Stage 2a continues with D<sub>2</sub> Variscan deformation and the formation of N090–110°E F<sub>2</sub> upright folds. Granitic intrusions occur at that stage (Figure 11). This D<sub>2</sub> deformation locally reworked mineralization like in Victoria mines where the mineralization is remobilized in fold hinges. Horcalh mineralized fault [32] is interpreted as synchronous to D<sub>2</sub> deformation.

Stage 2b occurs during the doming phase and the late-Variscan Type 2b vein mineralizations (Figure 11). This mineralization type preferentially occurs parallel to the vertical S<sub>2</sub> cleavage and is mostly observed in the Pierrefitte and Bossòst anticlinoriums. Pull-apart-type structures are observed in Pale Bidau and Uzious mines. A late deformation D<sub>3</sub> corresponds to faults like the Bossòst mylonitic fault close to Margalida district.

We have shown that the Pb-Zn deposits in the PAZ were polyphased and closely linked to Variscan tectonics. There are at least three Pb-Zn mineralization-forming events, and two of them are evidently structurally controlled. Type 1 may be syngenetic, but little ore is present. The main exploited ores are Type 2a and Type 2b which have emplaced under a marked structural control, either associated to S<sub>1</sub> and trapped in F<sub>1</sub> fold hinge, at lithology interface or in highly D<sub>1</sub> or D<sub>2</sub> deformed areas.

### 6.3. Is Pb-Zn Deposits Emplacement Sedimentary- or Structurally-Controlled?

SEDEX deposits are sedimentary controlled and syn- to diagenetic, and sulfides in them are laminated and included into the bedding [2]. In our study area, Pyrenean Pb-Zn mineralizations have been previously described as SEDEX by many authors [24,28–30,75,76]. The origin of several world-class Pb-Zn deposits is debated as well. For example, the geneses of Broken Hill-type deposit [6–12] or Jinding deposit [14–20] are still not understood and the authors have not yet decided between syngenetic or epigenetic models. In the Pyrenees, authors interpreted stratiform and lenses ore body shapes. The stratiform argument is not relevant because frequently S<sub>0</sub> stratification is parallel to the S<sub>1</sub> axial plane of isoclinal recumbent folds, typical of intensively deformed areas. Crystallization of sphalerite secant to isoclinal recumbent fold hinges attests that the main mineralization is parallel to S<sub>1</sub> and not to S<sub>0</sub>. Structural observations are supported by the mineralogical study. The three PAZ Pb-Zn mineralization types contain the same constitutive minerals, like sphalerite, galena, and pyrite, but various trace minerals are present according to the type. These mineralogical differences are key parameters to distinguish between different Pb-Zn mineralization events in a single deposit.

In intensely deformed and metamorphosed terranes, the simple geometric link between mineralization and stratification is not relevant enough to distinguish between sedimentary or structural control. Structures are often parallelized due to pervasive tectonic events which makes the structural analysis difficult. Reworking of the ore-body during deformation can have obliterated geochemical tracers like isotopic data, especially Pb isotopes [77–79]. Consequently, a detailed structural study from regional to micro-scale focusing on the relationships between mineralization and cleavages is crucial. Pinpointing locations where structures like cleavage are secant (fold hinge), as well as deciphering textural relations between metamorphic minerals and mineralization, will lead to a better understanding of the ore-body genesis.

## 7. Conclusions

Three main types of Pb-Zn mineralizations have been distinguished in the Pyrenean Axial Zone. A minor type (Type 1) is a stratiform disseminated mineralization that presents syngenetic

characteristics. The two other mineralization types, previously described as SEDEX, are in reality post-sedimentation and formed as a result of Variscan polyphased tectonics: Type 2a is a syn-D<sub>1</sub> stratabound mineralization that is parallel to S<sub>1</sub> foliation. Type 2b is a syn to post-D<sub>2</sub> vein-type mineralization that is parallel to subvertical S<sub>2</sub> cleavage. Structural control is thus a key parameter for the remobilization of Pb-Zn mineralizations in this area like in (D<sub>1</sub> and D<sub>2</sub>) fold hinges (saddle reef), high (D<sub>1</sub>) deformed zones, rock contrast interfaces, and S<sub>2</sub> cleavages. A multiscale detailed structural study is essential for unraveling the formation of Pb-Zn deposits, especially in deformed and/or metamorphosed terranes.

**Author Contributions:** A.C. (Alexandre Cugerone) and B.C.-T. conceived the research within the framework of the A.C. (Alexandre Cugerone)'s PhD project; A.C. (Alexandre Cugerone), E.O., A.C. (Alain Chauvet), B.C.-T., J.G.B., and A.L. participated in field work; A.C. (Alexandre Cugerone) acquired the samples and performed all the analytical work under the guidance of A.C. (Alain Chauvet) and B.C.-T.; A.C. (Alexandre Cugerone) wrote the paper with contributions from E.O., B.C.-T., E.L.G., and J.G.B.

**Funding:** This research was funded by the French Geological Survey (Bureau de Recherches Géologiques et Minières; BRGM) through the national program "Référentiel Géologique de France" (RGF-Pyrénées).

**Acknowledgments:** The authors gratefully acknowledge Kalin Kouzmanov and Stefano Salvi for their involvement in the project. We thank the ARSHAL association for Bentaillou mine access and Jean-Marc Poudevigne, Louis de Pazzis, and Bernard Lafage for their precious knowledge of the Pyrenean Pb-Zn mines. We acknowledge Christophe Nevado and Doriane Delmas for thin section preparation. The authors are thankful for the editorial handling of Jax Jiang and for the constructive comments of the three anonymous reviewers.

**Conflicts of Interest:** The authors declare no conflicts of interest.

## References

1. Wilkinson, J.J. Sediment-Hosted Zinc-Lead Mineralization: Processes and perspectives. *Treatise Geochem.* **2013**, *13*, 219–249.
2. Leach, D.L. Sediment-hosted lead-zinc deposits: A global perspective. *Econ. Geol.* **2005**, *100*, 561–607.
3. Moore, D.W.; Young, L.E.; Modene, J.S.; Plahuta, J.T. Geologic setting and genesis of the Red Dog zinc-lead-silver deposit, western Brooks Range, Alaska. *Econ. Geol.* **1986**, *81*, 1696–1727. [[CrossRef](#)]
4. Kelley, K.D.; Jennings, S. A special issue devoted to barite and Zn-Pb-Ag deposits in the Red Dog district, Western Brooks Range, northern Alaska. *Econ. Geol.* **2004**, *99*, 1267–1280. [[CrossRef](#)]
5. Hazarika, P.; Upadhyay, D.; Mishra, B. Contrasting geochronological evolution of the Rajpura-Dariba and Rampura-Agucha metamorphosed Zn-Pb deposit, Aravalli-Delhi Belt, India. *J. Asian Earth Sci.* **2013**, *73*, 429–439. [[CrossRef](#)]
6. Lawrence, L.J. Polymetamorphism of the sulphide ores of Broken Hill, NSW, Australia. *Miner. Depos.* **1973**, *8*, 211–236. [[CrossRef](#)]
7. Gibson, G.M.; Nutman, A.P. Detachment faulting and bimodal magmatism in the Palaeoproterozoic Willyama Supergroup, south-central Australia; keys to recognition of a multiply deformed Precambrian metamorphic core complex. *J. Geol. Soc.* **2004**, *161*, 55–66. [[CrossRef](#)]
8. Hobbs, B.E.; Walshe, J.L.; Ord, A.; Zhang, Y.; Carr, G.C. The Broken Hill orebody: A high temperature, high pressure scenario. *AGSO Rec.* **1998**, *2*, 98–103.
9. Walters, S.; Bailey, A. Geology and mineralization of the Cannington Ag-Pb-Zn deposit: An example of Broken Hill-Type mineralization in the eastern succession, Mount Isa Inlier, Australia. *Econ. Geol.* **1998**, *93*, 1307–1329. [[CrossRef](#)]
10. Webster, A.E. The Structural Evolution of the Broken Hill Pb-Zn-Ag Deposit, New South Wales, Australia. Ph.D. Thesis, University of Tasmania, Hobart, Australia, 2004.
11. Bodon, S.B. Paragenetic relationships and their implications for ore genesis at the Cannington Ag-Pb-Zn deposit, Mount Isa inlier, Queensland, Australia. *Econ. Geol.* **1998**, *93*, 1463–1488. [[CrossRef](#)]
12. Haydon, R.C.; McConachy, G.W. The stratigraphic setting of Pb-Zn-Ag mineralization at Broken Hill. *Econ. Geol.* **1987**, *82*, 826–856. [[CrossRef](#)]
13. Yalikun, Y.; Xue, C.; Symons, D.T.A. Paleomagnetic age and tectonic constraints on the genesis of the giant Jinding Zn-Pb deposit, Yunnan, China. *Miner. Depos.* **2018**, *53*, 245–259. [[CrossRef](#)]

14. Shi, J.X.; Yi, F.H.; Wen, Q.D. The rock-ore characteristics and mineralisation of Jinding lead-zinc deposit, Lanping. *J. Yunnan Geol.* **1983**, *2*, 179–195.
15. Wang, J.B.; Li, C.Y.; Chen, X. A new genetic model for the Jinding lead-zinc deposit. *Geol. Explor. Non Ferr. Met.* **1992**, *1*, 200–206. (In Chinese)
16. Leach, D.L.; Song, Y.C.; Hou, Z.Q. The world-class Jinding Zn–Pb deposit: Ore formation in an evaporite dome, Lanping Basin, Yunnan, China. *Miner. Depos.* **2017**, *52*, 281–296. [[CrossRef](#)]
17. Kyle, J.R.; Li, N. Jinding: A giant tertiary sandstone-hosted Zn–Pb deposit, Yunnan, China. *SEG Newsl.* **2002**, *50*, 1–9.
18. Chi, G.; Xue, C.; Qing, H.; Xue, W.; Zhang, J.; Sun, Y. Hydrodynamic analysis of clastic injection and hydraulic fracturing structures in the Jinding Zn–Pb deposit, Yunnan, China. *Geosci. Front.* **2012**, *3*, 73–84. [[CrossRef](#)]
19. Xue, C.; Zeng, R.; Liu, S.; Chi, G.; Qing, H.; Chen, Y.; Yang, J.; Wang, D. Geologic, fluid inclusion and isotopic characteristics of the Jinding Zn–Pb deposit, western Yunnan, South China: A review. *Ore Geol. Rev.* **2007**, *31*, 337–359. [[CrossRef](#)]
20. Chi, G.; Qing, H.; Xue, C. An overpressured fluid system associated with the giant sandstone-hosted Jinding Zn–Pb deposit, western Yunnan, China Chapter. In *Mineral Deposit Research: Meeting the Global Challenge*; Mao, J., Bierlein, F.P., Eds.; Springer: Berlin, German, 2005; pp. 93–96.
21. Zwart, H.J. The Geology of the Central Pyrenees. *Leidse Geol. Meded.* **1979**, *50*, 1–74.
22. Mezger, J.E.; Passchier, C.W. Polymetamorphism and ductile deformation of staurolite-cordierite schist of the Bossòst dome: Indication for Variscan extension in the Axial Zone of the central Pyrenees. *Geol. Mag.* **2003**, *140*, 595–612. [[CrossRef](#)]
23. Denèle, Y.; Laumonier, B.; Paquette, J.-L.; Olivier, P.; Gleizes, G.; Barbey, P. Timing of granite emplacement, crustal flow and gneiss dome formation in the Variscan segment of the Pyrenees. *Geol. Soc. Lond. Spec. Publ.* **2014**, *405*, 265–287. [[CrossRef](#)]
24. Bois, J.P.; Pouit, G. Les minéralisations de Zn (Pb) de l’anticlinorium de Pierrefitte: Un exemple de gisements hydrothermaux et sédimentaires associés au volcanisme dans le Paléozoïque des Pyrénées centrales. *Bureau Rech. Geol. Min.* **1976**, *6*, 543–567. (In French)
25. Pouit, G.; Fortuné, J.-P. Métallogénie comparée des Pyrénées et du Sud du Massif-central. In Proceedings of the 26ème Congrès Géologique International, Paris, France, 7–17 July 1980; p. 61. (In French)
26. Fert, D. Un Aspect de la Métallogénie du Zinc et du Plomb Dans l’Ordovicien des Pyrénées Centrales: Le District de Sentein (Ariège, Haute-Garonne). Ph.D. Thesis, University Pierre Marie Curie, Paris, France, 1976.
27. Pouit, G. Différents Modèles de Mineralisations «Hydrothermale Sédimentaire», à Zn (Pb) du Paléozoïque des Pyrénées Centrales. *Miner. Depos.* **1978**, *13*, 411–421. (In French) [[CrossRef](#)]
28. Pouit, G. Les minéralisations Zn–Pb exhalatives sédimentaires de Bentaillou et de l’anticlinorium paléozoïque de Bosost (Pyrénées ariégeoises, France). *Chron. Rech. Min.* **1986**, *485*, 3–16. (In French)
29. Pujals, I. Las Mineralizaciones de Sulfuros en el Cambro-Ordovícico de la Val d’Aran (Pirineo Central, Lérida). Ph.D. Thesis, University Autònoma Barcelona, Barcelona, Spain, 1992.
30. Cardellach, E.; Phillips, R.; Ayora, C. Metamorphosed stratiform sulphides of the Liat area, Central Pyrenees, Spain. *Inst. Min. Metall. Trans.* **1982**, *91*, 90–95. (In Spanish)
31. Cardellach, E. Estudio microscópico de las mineralizaciones de Pb–Zn de Liat, Baguerque y Montoliu. *Acta Geol. Hisp.* **1977**, *12*, 120–122. (In Spanish)
32. Alonso, J.L. Deformaciones Sucesivas en el Area Comprendida Entre Liat y el Puerto de Orla—Control Estructural de los Depositos de Sulfuros (Valle de Aran, Pirineos Centrales). Master’s Thesis, University Oviedo, Oviedo, Spain, 1979. (In Spanish)
33. Nicol, N. Etude Structurale des Minéralisations Zn–Pb du Paléozoïque du Dôme de Pierrefitte (Hautes-Pyrénées). Goniométrie de Texture Appliquée aux Minéraux Transparents et Opaques. Ph.D. Thesis, University Orléans, Orléans, France, 1997. (In French)
34. García-Sansegundo, J.; Martín-Izard, A.; Gavalda, J. Structural control and geological significance of the Zn–Pb ores formed in the Benasque Pass area (Central Pyrenees) during the post-late Ordovician extensional event of the Gondwana margin. *Ore Geol. Rev.* **2014**, *56*, 516–527. [[CrossRef](#)]
35. Marcoux, E. Isotope du plomb et paragenèses métalliques, traceurs de l’histoire des gîtes minéraux. *Bur. Rech. Geol. Min.* **1986**, *117*, 1–289. (In French)
36. Zwart, H.J. Metamorphic history of the Central Pyrenees, Part II, Valle de Aran. *Leidse Geol. Meded.* **1963**, *28*, 321–376.






37. Kleinsmiede, W.F.J. Geology of the Valle de Aran (Central Pyrenees). *Leidse Geol. Meded.* **1960**, *25*, 129–245.
38. Cochelin, B.; Lemirre, B.; Denèle, Y.; De Saint Blanquat, M.; Lahfid, A.; Duchêne, S. Structural inheritance in the Central Pyrenees: The Variscan to Alpine tectonometamorphic evolution of the Axial Zone. *J. Geol. Soc. Lond.* **2017**, *175*, 16. [[CrossRef](#)]
39. De Sitter, L.U.; Zwart, H.J. Tectonic development in supra and infra-structures of a mountain chain. In *Structure of the Earth's Crust and Deformation of Rocks*; Det Berlingske Bogtrykkeri: Copenhagen, Denmark, 1960; Volume 18, pp. 248–256.
40. Carreras, J.; Capellà, I. Tectonic levels in the Palaeozoic basement of the Pyrenees: A review and a new interpretation. *J. Struct. Geol.* **1994**, *16*, 1509–1524. [[CrossRef](#)]
41. Carreras, J.; Druguet, E. Framing the tectonic regime of the NE Iberian Variscan segment. *Geol. Soc. Lond. Spec. Publ.* **2014**, *405*, 249–264. [[CrossRef](#)]
42. Cochelin, B. Champ de déformation du socle Paléozoïque des Pyrénées. Ph.D. Thesis, Université Toulouse 3 Paul Sabatier, Toulouse, France, 2016. (In French)
43. Mezger, J.E.; Gerdes, A. Early Variscan (Visean) granites in the core of central Pyrenean gneiss domes: Implications from laser ablation U-Pb and Th-Pb studies. *Gondwana Res.* **2016**, *29*, 181–198. [[CrossRef](#)]
44. Pouget, P. Hercynian tectonometamorphic evolution of the Bosost dome (French Spanish Central Pyrenees). *J. Geol. Soc. Lond.* **1991**, *148*, 299–314. [[CrossRef](#)]
45. Mezger, J.E. Comparison of the western Aston-Hospitalet and the Bossost domes: Evidence for polymetamorphism and its implications for the Variscan tectonic evolution of the Axial Zone of the Pyrenees. *J. Virtual Explor.* **2005**, *19*, 1–19. [[CrossRef](#)]
46. Mezger, J.E.; Schnapperelle, S.; Rölke, C. Evolution of the Central Pyrenean Mérens fault controlled by near collision of two gneiss domes. *Hallesches Jahrb.* **2012**, *34*, 11–29.
47. Carreras, J. Zooming on Northern Cap de Creus shear zones. *J. Struct. Geol.* **2001**, *23*, 1457–1486. [[CrossRef](#)]
48. BRGM International Report: *Les Gisements de Pb-Zn Français (Situation en 1977)*; BRGM: Orléans, France, 1984; pp. 1–278. (In French)
49. Ovejero Zappino, G. Mineralizaciones Zn-Pb ordovícicas del anticlinorio de Bossost. Yacimientos de Liat y Victoria. Valle de Arán. Pirineo (España). *Bol. Geol. Min.* **1991**, *102*, 356–377. (In Spanish)
50. Castroviejo Bolibar, R.; Serrano, F.M. Estructura y metalogenia del campo filoniano de Cierco (Pb-Zn-Ag), en el Pirineo de Lérida. *Bol. Geol. Min.* **1983**, *1983*, 291–320. (In Spanish)
51. Aerden, D.G.A. Kinematics of orogenic collapse in the Variscan Pyrenees deduced from microstructures in porphyroblastic rocks from the Lys-Caillaouas massif. *Tectonophysics* **1994**, *238*, 139–160. [[CrossRef](#)]
52. Barrère, P.; Bouquet, C.; Debroas, E.J.; Pelissonnier, H.; Peybernes, B.; Soulé, J.C.; Souquet, P.; Ternet, Y. Arreau. In *BRGM Geological Map 1/50,000 with Note*; BRGM: Orléans, France, 1984; p. 60. (In French)
53. Clin, M.; Taillefer, F.; Pouchan, P.; Muller, A. Bagnères de Luchon. In *BRGM Geological Map 1/50,000 with Note*; BRGM: Orléans, France, 1989; p. 78. (In French)
54. Lavigne, J. Pic de Mauberme. In *BRGM Geological Map 1/50,000 with Note*; BRGM: Orléans, France, 1972; p. 24. (In French)
55. García-Sansegunado, J.; Merino, J.R.; Santisteban, R.R.; Leyva, F. Canejan-Vielha Mapa geológico 1:50,000. *Inst. Geol. Min. Espana* **2013**, *1*, 66. (In French)
56. Garcia-Sansegunado, J.; Alonso, J.L. Stratigraphy and structure of the southeastern Garona Dome. *Geodin. Acta* **1989**, *3*, 127–134. [[CrossRef](#)]
57. Cugerone, A.; Cenki-Tok, B.; Chauvet, A.; Le Goff, E.; Bailly, L.; Alard, O.; Allard, M. Relationships between the occurrence of accessory Ge-minerals and sphalerite in Variscan Pb-Zn deposits of the Bossost anticlinorium, French Pyrenean Axial Zone: Chemistry, microstructures and ore-deposit setting. *Ore Geol. Rev.* **2018**, *95*, 1–19. [[CrossRef](#)]
58. Dubois, C. *Manguses d'homme: L'épopée des Mines de Bentaillou et de Bulard en Ariège*; Privat Edition: Toulouse, France, 2015; p. 320. (In French)
59. Barrère, P.; Bois, J.-P.; Soulé, J.-C.; Ternet, Y. Argelès-Gazost. In *BRGM Geological Map 1/50,000 with Note*; BRGM: Orléans, France, 1980; pp. 1–48. (In French)
60. Nicol, N.; Legendre, O.; Charvet, J. Les minéralisations Zn-Pb de la série paléozoïque de Pierrefitte (Hautes-Pyrénées) dans la succession des événements tectoniques hercyniens. *C. R. Acad. Sci.* **1997**, *324*, 453–460. (In French)

61. Calvet, P. Etude Structurale et Métallogénique de L'anticlinorium de Pierrefitte: Influence de la Déformation sur les Minéralisations Stratiformes. Ph.D. Thesis, University d'Orléans, Orléans, France, 1988; p. 283. (In French)
62. Alvarez-Perez, A.; Campa-Vineta, J.A.; Montoriol-Pous, J. Sobre la presencia de gahnita ferrífera en Bossost (Vall D'Aran, Lérida). *Acta Geol. Hisp.* **1974**, *9*, 111–113. (In Spanish)
63. Reyx, J. Relations entre Tectonique, Métamorphisme de Contact et Concentrations Metalliques dans le Secteur des Anciennes Mines d'Arre et Anglas (Hautes-Pyrénées-Pyrénées atlantiques). Ph.D. Thesis, University Paris VI, Paris, France, 1973; p. 83. (In French)
64. Scott, R.J.; Meffre, S.; Woodhead, J.; Gilbert, S.E.; Berry, R.F.; Emsbo, P. Development of framboidal pyrite during diagenesis, low-grade regional metamorphism, and hydrothermal alteration. *Econ. Geol.* **2009**, *104*, 1143–1168. [[CrossRef](#)]
65. Vernhet, Y. Les Minéralisations Zincifères de l'Ordovicien et du Dévonien du Val d'Orle (District de Sentein, Ariège) et de la région de Fourcaye (Val d'Aran, Espagne). Ph.D. Thesis, University Pierre Marie Curie, Paris, France, 1981; p. 279. (In French)
66. Windh, J. Saddle Reef and Related Gold Mineralization, Hill End Gold Field, Australia: Evolution of an Auriferous Vein System during Progressive Deformation. *Econ. Geol.* **1995**, *90*, 1764–1775. [[CrossRef](#)]
67. Bull, S.W.; Large, R.R. Setting the stage for the genesis of the giant Bendigo ore system. *Geol. Soc. Lond. Spec. Publ.* **2015**, *393*, 161–187. [[CrossRef](#)]
68. Zeng, M.; Zhang, D.; Zhang, Z.; Li, T.; Li, C.; Wei, C. Structural controls on the Lala iron-copper deposit of the Kangdian metallogenic province, southwestern China: Tectonic and metallogenic implications. *Ore Geol. Rev.* **2018**, *97*, 35–54. [[CrossRef](#)]
69. Cardellach, E.; Alvarez-Perez, A. Interpretación genética de las mineralizaciones de Pb-Zn del Ordovícico Sup. de la Vall de Aran. *Acta Geol. Hisp.* **1979**, *14*, 117–120. (In Spanish)
70. Alvarez-Perez, A.; Campa-Vineta, J.A.; Montoriol-Pous, J. Mineralogénesis de los yacimientos del área de Bossost (Vall d'Aran, Lérida). *Acta Geol. Hisp.* **1977**, *4–6*, 123–126. (In Spanish)
71. Ovejero Zappino, G. Mineralizaciones Zn-Pb del Ordovícico Superior del Valle de Aran (Anticlinorio de Bossost). Pireneo de Lerida (España). *Bol. Soc. Esp. Mineral.* **1987**, *10*, 35–37.
72. Munoz, M.; Baron, S.; Boucher, A.; Béziat, D.; Salvi, S. Mesozoic vein-type Pb-Zn mineralization in the Pyrenees: Lead isotopic and fluid inclusion evidence from the Les Argentières and Lacore deposits. *C. R. Geosci.* **2015**, *348*, 322–332. [[CrossRef](#)]
73. Militon, C. Métallogénie polyphasée à Zn, Pb, Ba, F et Mg, Fe de ma région de Gèdre-Gavarnie-Barroude (Hautes-Pyrénées). Ph.D. Thesis, University d'Orléans, Orléans, France, 1987. (In French)
74. Munoz, M.; Boyce, A.J.; Courjault-Rade, P.; Fallick, A.E.; Tollon, F. Multi-stage fluid incursion in the Palaeozoic basement-hosted Saint-Salvy ore deposit (NW Montagne Noire, southern France). *Appl. Geochem.* **1994**, *9*, 609–626. [[CrossRef](#)]
75. Pouit, G. Les minéralisations Zn-Pb dans l'Ordovicien des Pyrénées centrales-Etude préliminaire. *Rapp. BRGM* **1974**, *74*, 50. (In French)
76. Pouit, G.; Bois, J.P. Arrens Zn (Pb), Ba Devonian deposit, Pyrénées, France: An exhalative-sedimentary-type deposit similar to Meggen. *Miner. Depos.* **1986**, *21*, 181–189. [[CrossRef](#)]
77. Wagner, T.; Schneider, J. Lead isotope systematics of vein-type antimony mineralization, Rheinisches Schiefergebirge, Germany: A case history of complex reaction and remobilization processes. *Miner. Depos.* **2002**, *37*, 185–197. [[CrossRef](#)]
78. Marcoux, E.; Moelo, Y. Lead isotope geochemistry and paragenetic study of inheritance phenomena in metallogenesis: Examples from base metal sulfide deposits in France. *Econ. Geol.* **1991**, *86*, 106–120. [[CrossRef](#)]
79. Kamona, A.F.; Lévêque, J.; Friedrich, G.; Haack, U. Lead isotopes of the carbonate-hosted Kabwe, Tsumeb, and Kipushi Pb-Zn-Cu sulphide deposits in relation to Pan African orogenesis in the Damaran-Lufilian Fold Belt of Central Africa. *Miner. Depos.* **1999**, *34*, 273–283. [[CrossRef](#)]



Article

# Structural Controls of Ore Mineralization in a Polydeformed Basement: Field Examples from the Variscan Baccu Locci Shear Zone (SE Sardinia, Italy)

Antonio Funedda <sup>1,\*</sup>, Stefano Naitza <sup>1</sup>, Cristina Buttau <sup>1</sup>, Fabrizio Cocco <sup>1</sup> and Andrea Dini <sup>2</sup>

<sup>1</sup> Dipartimento di Scienze Chimiche e Geologiche, Università degli Studi di Cagliari, Cittadella Universitaria (Blocco A), S.S. 554 bivio per Sestu, 09042 Monserrato (CA), Italy; snaitza@unica.it (S.N.); cbuttau@gmail.com (C.B.); fabrccoco@gmail.com (F.C.)

<sup>2</sup> Consiglio Nazionale delle Ricerche (CNR)-Istituto di Geoscienze e Georisorse, 56100 Pisa, Italy; andrea.dini@igg.cnr.it

\* Correspondence: afunedda@unica.it

Received: 2 July 2018; Accepted: 11 October 2018; Published: 16 October 2018

**Abstract:** The Baccu Locci mine area is located in a sector of the Variscan Nappe zone of Sardinia (the Baccu Locci shear zone) that hosts several type of ore deposits mined until the first half of the last century. The orebodies consist of lenses of Zn–Cu sulphides, once interpreted as stratabound, and Qtz–As–Pb sulphide ± gold veins; the implication of structural controls in their origin were previously misinterpreted or not considered. Detailed field mapping, structural analyses, and ore mineralogy allowed for unraveling how different ore parageneses are superimposed each other and to recognize different relationships with the Variscan structures. The sulphide lenses are parallel to the mylonitic foliation, hosted in the hinges of minor order upright antiforms that acted as traps for hydrothermal fluids. The Qtz–As–Pb sulphide veins crosscut the sulphide lenses and are hosted in large dilatational jogs developed in the hanging wall of dextral-reverse faults, whose geometry is influenced by the attitude of reverse limbs of late Variscan folds. The ores in the Baccu Locci shear zone are best interpreted as Variscan orogenic gold-type; veins display mutual crosscutting relationships with mafic dikes dated in the same district at  $302 \pm 0.2$  Ma, a reliable age for the mineralizing events in the area.

**Keywords:** sulphide lenses; hinge trap; dilatational jogs; orogenic gold; mafic dikes; mineralization chronology; arsenopyrite; late Variscan strike-slip faults

---

## 1. Introduction

Structural controls of ore deposits hosted in poly-deformed low-grade metamorphic basements are often not easy to recognize, even more so when there are multiple generations of mineralization, mostly because the relationships between structures and ore bodies are often not clear. The correct understanding of the structural controls is, in fact, relevant for defining the characteristics of the deposit, its emplacement style, its age, and therefore, its origin. In some cases, the difficulties in unravelling the tectonic structures prevent the understanding of the ore bodies' geometry, leading to mistakes in mineral exploration, evaluation of ore deposits, mine planning, and even mineral exploitation. Recognizing whether the structural controls on ore deposits are “passive”, and therefore attributable to tectonic structures developed before mineralization, or, conversely, “active,” i.e., related to tectonic structures progressively evolving with mineralization, can provide valuable indications in this sense. Indeed, passive structural controls imply that there are no direct correlations between tectonic and mineralizing events; the physical parameters that characterized the deformational

events, e.g., thermo-baric conditions, presence of fluids, state of stress, etc., were independent from mineralization processes and they had no influence on ore formation. Conversely, in the case of active controls, these features were critical for mineralization and shaped both the deformational context and the genesis of the ores.

In the nappe zone of the Variscan basement of SE Sardinia, several Sb–W, As–Au, and As–Pb–(Cu, Zn, Ag, Au) ore deposits are located along a lower green-schist facies mylonitic belt, folded by a plurikilometric antiform (the Flumendosa Antiform) during the Variscan collisional phases and then affected by extensional tectonics. During the postcollisional extension, early phases were characterized by ductile-type structures that, with progressive exhumation of deeper tectonic units, further evolved in brittle–ductile to brittle regimes [1], supporting large-scale hydrothermal fluid circulation in the crust. In this frame, mineralization processes and ore deposition were structurally controlled, both passively and actively, at all scales.

In this work, we present a case study of the mineralized systems occurring in the Bacchu Locci mine area, located in the core of the Flumendosa Antiform. In this area, several stacked tectonic units are separated by thick mylonitic zones and folded together [2]. Exhumation of the antiformal core is evidenced by the superposition of brittle–ductile and brittle structures over ductile ones; accordingly, different kinds of structurally controlled mineral deposits exposed in the area allow a distinction between passive and active emplacement styles, also leading to a relative chronology of tectonic and mineralizing events. Recent studies in the Bacchu Locci mine area [1,3–5] highlighted that: (1) ore formation was structurally controlled and related to the tectonic evolution, during late Variscan extensional phases, of the Bacchu Locci regional shear zone, and (2) the relationships between different ores materialize a superposition of tectonic events, further complicated by mafic magmatism and diking. Apart from this general picture, however, several unsolved issues still persist: (1) type and timing of different mineralization, (2) their relationships with tectonic structures and structural controls, (3) ore mineral associations and mafic dikes, and (4) relationships with regional and local stress fields.

In this paper, we intend to contribute to the first two issues and provide some new data for the third one.

## **2. Geological and Ore Deposits Outline of Bacchu Locci Mine District**

### *2.1. Regional Geology*

The section of Variscan chain exposed in Sardinia consists of three tectono-metamorphic zones: (1) an inner zone in the north, with medium- to high-grade regional metamorphism, thrust on (2) a nappe zone in central-south, with low-grade regional metamorphism, in turn thrust on (3) a foreland zone in the southwest, non-metamorphosed or with very low-grade regional metamorphism (Figure 1a,b). The emplacement of the tectonic units is generally from the top to the south, with some exceptions [6]. At the map scale, in the nappe zone a distinction can be made between external nappes in the south, displaying a well recognizable lithostratigraphic succession, and internal nappes in the central-north, where it is not easy to recognize the litho-stratigraphic succession. The study area is part of the external nappe zone (Figure 2) and it consists of three tectonic units (from the bottom: Riu Gruppa, Gerrei, and Meana Sardo units) stacked one above the other during the Variscan shortening phases and then affected by late orogenic extension (Figure 3).

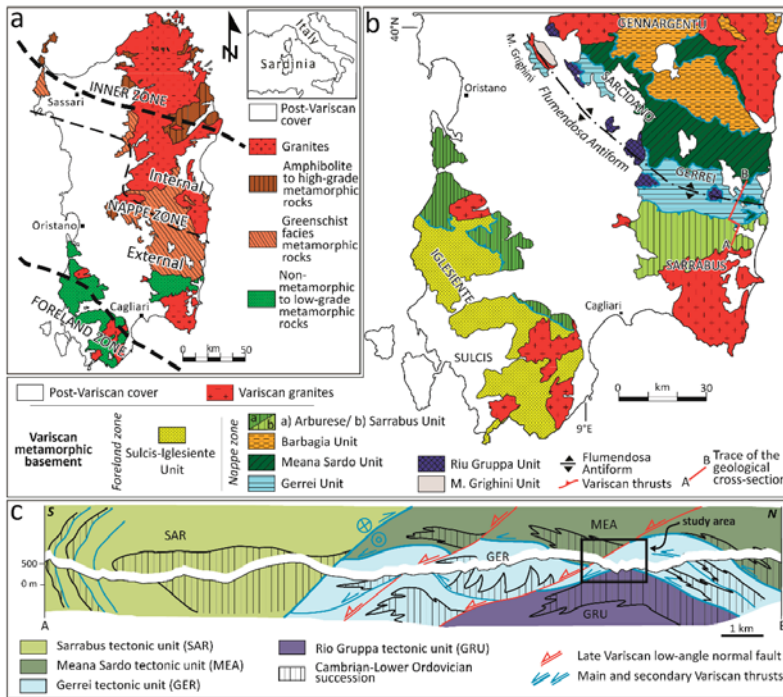


Figure 1. (a) Geological sketch map of the Variscan basement of Sardinia. (b) Tectonic sketch of the SE Sardinia Variscan basement. (c) Geological cross-section of the Gerrei-Sarrabus region in SE Sardinia; modified after [7], reprinted with permission.

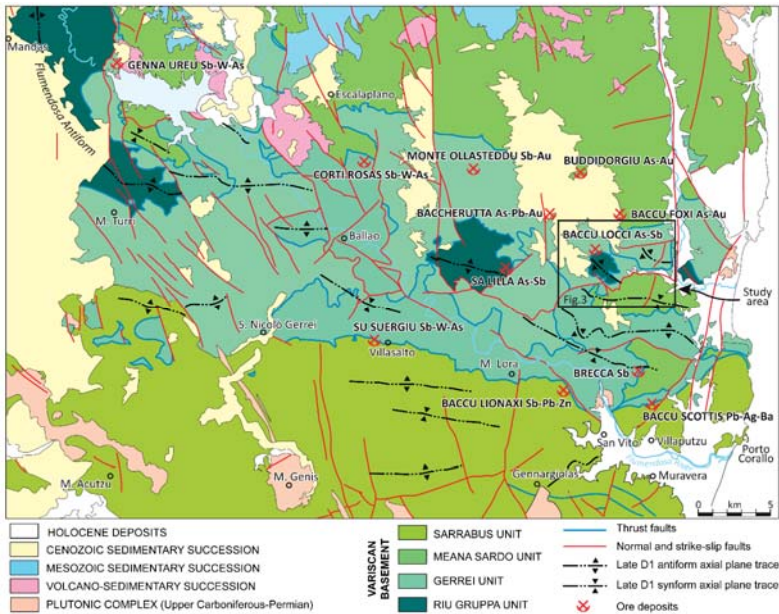


Figure 2. Tectonic sketch map and mineral deposits of the Gerrei district.



### 2.1.1. Stratigraphic Outline

The tectonic units share a similar lithostratigraphic outline (with some differences, especially in the Middle Ordovician volcanic sequences), which consists of four middle Cambrian to lower Carboniferous successions, separated by three large regional unconformities [8]. They are:

- a mainly siliciclastic succession, with rare interlayered volcanic rocks, of middle Cambrian to Early Ordovician age (*Arenarie di San Vito* Fm.);
- a Middle Ordovician volcano-sedimentary succession with tuffites, metavolcanoclastites, and interlayered epiclastites, andesitic in the lower part (M. S. Vittoria Fm.) and rhyolitic in the upper part ("*Porfiroidi*" Auct. Fm.); the basal contact of this succession is marked by some discontinuous conglomerates (*Metaconglomerato di Muravera* Fm.);
- a siliciclastic to carbonatic succession of Late Ordovician to early Carboniferous age, with lithic sandstones and arkosic arenites (*Metarose di Genna Mesa* Fm., Late Ordovician), siltstones and marls (*Scisti di Rio Canoni* Fm., Late Ordovician.), black shales and limestones ("*Scisti neri a graptoliti*" Auct. Fm., Silurian to Early Devonian; "*Calcari di Villasalto*" Auct. Fm., Early Devonian to early Carboniferous);
- a lower Carboniferous siliciclastic sequence with conglomerates, sandstones, and olistoliths of the older formations that unconformably rests on the Devonian formations, which does not crop out in the study area (*Pala Manna* Fm., early Carboniferous); it is the youngest formation involved by the Variscan orogeny in Sardinia.

The metamorphic basement of SE Sardinia is then intruded by an upper Palaeozoic (upper Carboniferous to lower Permian) intrusive complex. Lower Permian leucogranitic rocks outcrop close to the study area in the Quirra sector [9]; they belong to a calc-alkaline, ferroan, F-bearing, ilmenite-series intrusion, part of a magmatic suite dated at  $286 \pm 2$  Ma [10]. The entire period of granitoid magmatism is associated with calc-alkaline volcanism [11] and with widespread mafic and felsic diking [12]. Early diking phases are represented by swarms of calc-alkaline (spessartitic) mafic dikes; one of them, crosscutting the same tectonic unit in a nearby area, is dated at 302 Ma [13].

The early Eocene *Monte Cardiga* Fm., made up of conglomerates, sandstones, and marls that are deposited in littoral environments lies unconformably on the metamorphic basement and the intrusive complex. In the surrounding areas, the oldest deposits that unconformably cover the Variscan basement are Middle Pennsylvanian continental deposits [14].

### 2.1.2. Structural Outline

The oldest tectonic features that are recognizable in the Baccu Locci mine district involve the lower Carboniferous rocks and are related to the Variscan orogeny. Indeed, there is no evidence of the pre-Middle Ordovician tectonic structures recognized in adjacent areas [7], as they were probably obliterated by Variscan deformation. The overlap of several early to late Carboniferous deformation events is evidence that a D1 collisional phase with crustal thickening and subhorizontal shortening occurred under ductile conditions and a D2 postcollisional extension with the reactivation of some of D1 structures occurred in the ductile–brittle transition (Figure 4) [6,8,15]. The D1 phase is characterized by a general SSW-directed nappe emplacement, regional folding and thrusting, and syntectonic regional lower green-schist facies metamorphism. An exception is represented by the Sarrabus unit, the shallowest nappe of the stack, which crops out south of the study area and it is emplaced from the top to the west [16]. The D1 early shortening structures are large kilometer-scale recumbent isoclinal folds facing southward, with well-developed penetrative axial plane foliation—generally a slaty cleavage produced in lower green-schist facies metamorphism—followed by almost contemporary south-southwest thrusts that produced thick mylonitic belts. Development of such shear zones between the different tectonic units, thick up to several hundred meters, is common in the Variscan basement of Sardinia [17–24]. Among them, the Baccu Locci shear zone is one of the most noteworthy [3]. It can be followed in the field for more than 30 km; the study area is located on its eastern side. The Baccu

Locci shear zone is characterized by widespread and penetrative mylonitic foliation with a mineral assemblage typical of lower green-schist facies metamorphism that is parallel to the large thrust and generally cuts at a low angle the early D1 axial plane foliation [3]. The deformation is highly partitioned; in the core of the shear zone, it is not possible to recognize the mylonite protolith, although several slices of less deformed rocks have been recognized and mapped [2,3,19]. (Note that, following the choice by [2,3], in Figures 3 and 5 we distinguished the mylonite whose protolith is not recognizable from the mylonite whose protolith is still recognizable). At a later stage during the collisional phase, a late-D1 (LD1) N-S shortening event led to development at a regional scale of large, weakly east-plunging upright folds, with axes up to 50 km long that refolded both isoclinal folds and ductile shear zones. Of these late folds, the main fold is the Flumendosa Antiform [1] (Figures 1 and 2), which runs roughly from WNW to ESE for more than 50 km, folding the D1 nappe stack. In detail, the Flumendosa Antiform consists of some minor order antiforms and synforms with km-size wavelength. One such northern minor order folds crops out in the study area. The LD1 axis is generally east-plunging, and at the hinge zone, a subvertical spaced crenulation cleavage discontinuously developed. Then, the LD1 folds were in turn deformed during the D2 postcollisional extensional phase. The limbs of the LD1 antiforms are deformed by several asymmetric recumbent folds with subhorizontal axial planes and axes parallel to the LD1 limb attitude [1] (Figure 4). The D2 folds are overturned away from the antiformal hinge zone [1]. They are often associated with low-angle normal shear zones that allowed for the exhumation of deeper units and enhanced the antiformal structure. They have opposite structural-facing direction in the fold flanks: north-facing in the northern limb and south-facing in the southern limb. Their major order wavelength exposed in the field is about 30 to 40 m. Folds with “outer” structural facing and low-angle normal faults are interpreted as produced by vertical shortening of steeply inclined bedding and earlier foliations. During exhumation, rocks were progressively carried to shallower structural levels, where brittle behavior became prevalent. Thus, the deformation style changed, and the final stage of postcollisional extension was accommodated by high-angle normal faults [6]. A D3 folding event, with vertical axial planes and axis trend changing from N-S to N 40°, is also recognized, but it is still not clear whether it could be related to a final stage of postcollisional extension or to the following D4 strike slip faulting [8]. Finally, D4 strike-slip faults affected the exhumed basement but did not involve the Permian to Eocene successions that crop out in the study area. At the Variscan Realm scale, a late strike-slip tectonics is from far recognized. Moreover, is clearly observable in the field that the lower Permian granitoids postdate the D1, D2, and D3 structures, whereas there is less evidence about their relationship with strike-slip tectonics. As we will describe below, LD1 and D2 folds, as well as late faults, played a significant role in controlling the geometry of orebodies.

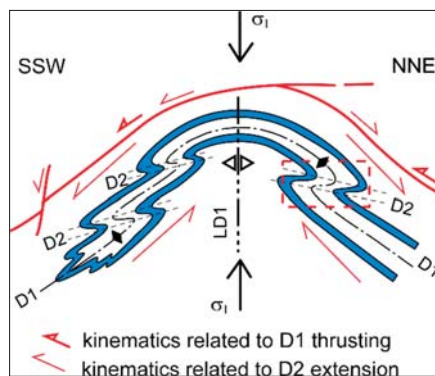


**Figure 4.** Schematic relationships between D1, LD1, and D2 structure. Note the development of recumbent D2 folds in the limb of upright LD1 antiform (modified after [1]). The red dashed box indicates the location of the scheme in Figure 15.



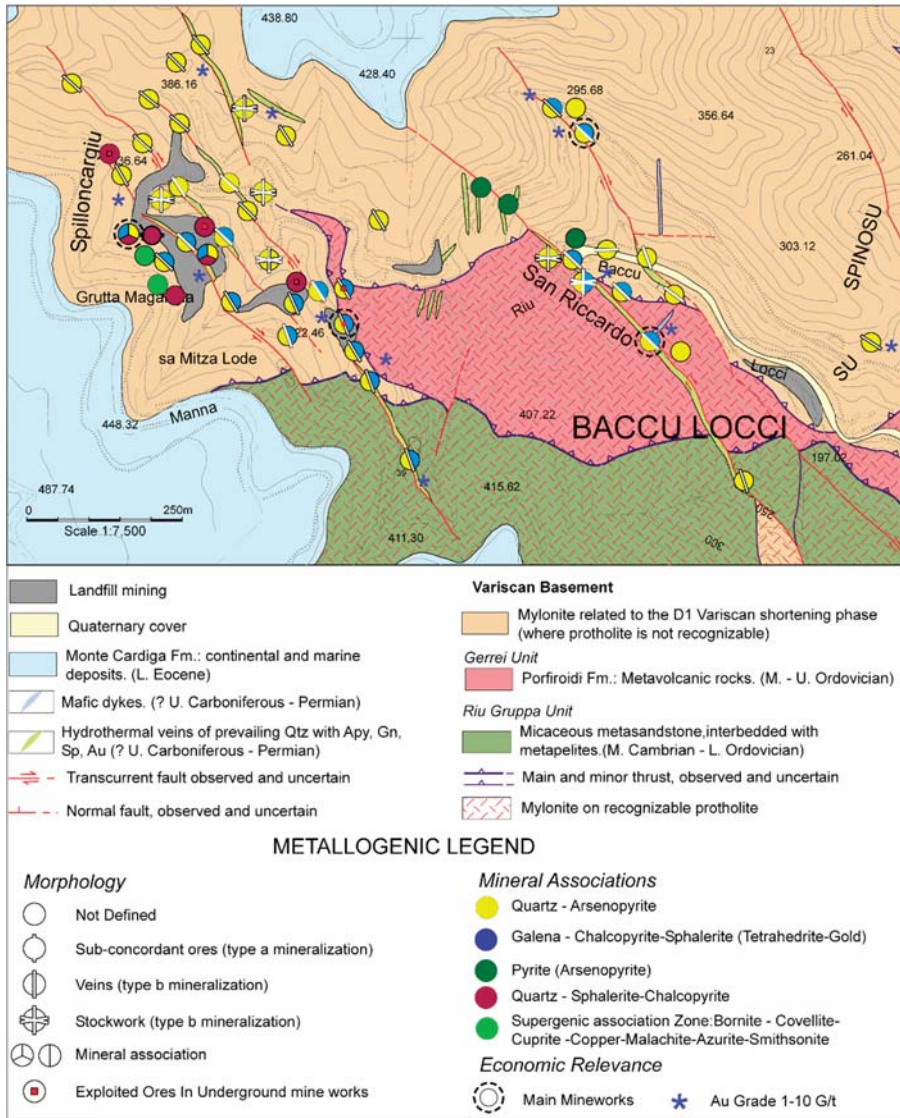


Figure 5. Mineralized outcrops in the Bacchu Locci mine area, after [2].

### 2.2. The Gerrei-Sarrabus Metallogenic District

The Gerrei-Sarrabus region has been historically the second most important mining area in Sardinia and the most important antimony district in Italy (Villasalto–Ballao district). Several reviews of the district’s mineral deposits have been done in the past [25–27], including a recent attempt to interpret some of the main mineral associations in the Variscan metallogenic epoch of Sardinia [28]. The main mineral deposits of the region include the following (Figure 2):

- (a) Zn–Cu–Pb sulphide lenses, disseminations, and ores;
- (b) Sb–W, As–Au, and As–Pb–(Cu, Zn, Ag, Au) mesothermal systems with quartz–sulphide veins, stockwork, and disseminated ores;

- (c) Mo–W–F greisen and vein-type ores;
- (d) F–Ba ± Pb–Ag–Cu–Zn vein systems.

Ores of (a) and (b)-types are hosted in the Palaeozoic metamorphic basement, and mostly occur in the northern part of the district (Gerrei); (c) type ores are hosted in and/or related to the suite of F-bearing Permian granites of San Vito and Quirra intrusions [9,29]; and, (d) type ores occur prevalently in the southern part of the district (Sarrabus), are broadly typified by the “Sarrabus Silver Lode” [30] and Silius [31] deposits, and they are possibly related to another suite of F-rich Permian granites (Sette Fratelli and Monte Genis intrusions [9]). Although still very lacking and non-systematic, some isotope and fluid inclusion data on different Gerrei-Sarrabus ore deposits are available from several recent studies [10,25,30–32].

Only (a) and (b) type ores are present in the study area, and thus will be considered in detail in this work. Both types are structurally controlled and are located at different structural levels.

### 3. Materials and Methods

To reconstruct the orebodies and their relationships with the tectonic structures, detailed field work was performed, mapping at 1:5000 and 1:10,000 scale both mineral deposits and tectonic features (foliations, folds, faults, kinematic indicators). The surface data have been integrated with the subsurface data, in rare cases directly sampled in the mine when still accessible, but generally taken from 1:500 scale exploitation maps related to the last period of mining activities in 1961. The grade of detail reported in those maps allows us, in some cases, to recognize not only the mine works, but also the geometries of the ores. Importing and processing these data in the three-dimensional (3D) workspace of Rhinoceros© and Move (©Midland Valley, Edinburgh, Scotland, UK), allow minimization of the unbalanced area and validation of the geological-structural map (see description in [2]).

The kinematic analysis of fault slip data was performed using FaultKin 5.2 by Allmendinger [33]. The slip direction and the sense of slip were inferred from several types of kinematic indicators—slickenlines, tension gashes, drag folds, and S-C structures—all collected along the D4 transpressive faults and related orebodies. They all indicate similar kinematics, suggesting that the paleostress remained the same during vein formation. The occurrence of different types of kinematics indicators during the same tectonic event (i.e., D4 faulting), sometimes exactly along the same fault, can depend on the mechanic behavior of the involved rocks. In general, when the damage zone is large enough and there is a relevant grain-size reduction in cataclased rocks, S-C-like fabric easily developed, although physical condition and deformation mechanisms are those typical of shallow structural levels [34,35]. The orientation of the principal strain axes that was achieved from fault slip data analysis gives an idea about the paleostress field accounting for the fault kinematics.

In this study, ore mineralogy and microtextural studies were performed on polished sections by optical microscopy in reflected light. Several transmitted light studies on thin sections of ores and their host rocks have been performed in past works [3,5,7,19].

## 4. Results

### 4.1. Structures and Mineralization in the Baccu Locci Mine Area

The mineralized deposits of the Baccu Locci mine area (NE Gerrei, Figures 2 and 5) occur in a key area for studying the structural and metallogenic evolution of the region. In Baccu Locci, the ores are exposed at different structural levels along the hinge zone of the Flumendosa Antiform, hosted by the strongly mylonitized siliciclastic metasediments and felsic metavolcanics of the Gerrei tectonic unit [3]. Both Zn–Cu–Pb sulphide lenses (*type a* mineralization) and Qtz–As–Pb sulphide hydrothermal vein deposits (*type b* mineralization) are represented in the area, where it is also possible to recognize spatial relationships of ore deposits with coeval mafic dikes [4].

#### 4.1.1. The Zn–Cu–Pb Sulphide Lenses (*Type a* Mineralization)

Zn–Cu–Pb sulphide lenses occur in the Su Spilloncargiu mine sector (Figure 5), hosted in phyllitic quartz–mylonite rocks (Figure 6a–e), whose protolith was made mainly by siliciclastic sediments, with a high occurrence of recrystallized quartz and muscovite, metamorphosed in lower green-schist facies during the Variscan Orogeny. Due to supergene alteration (Figure 7b), the Spilloncargiu primary ore is not well exposed on the surface; access to underground works is not easy, but some samples can be found in the dumps of the lowermost mineworks.

#### Ore Mineralogy and Textures

At the outcrop scale, the mineralization shows a laminated texture, with the sulphides being disposed along the mylonitic foliation. At the microscopic scale, it is possible to recognize that the deposition of ore minerals is polyphasic. The first event is characterized by dark ferroan sphalerite with abundant and finely dispersed chalcopyrite and pyrrhotite inclusions (*chalcopyrite disease* [36]). This early sphalerite is the prevailing sulphide in the ore (Figure 7a) and it displays an evident cataclastic texture. Voids and fractures in cataclased sphalerite aggregates are filled by abundant galena, chalcopyrite, and pyrite, while arsenopyrite and tetrahedrite-group minerals are usually subordinate (Figure 7b). Galena crystals show only slight evidence of deformation and have not suffered the cataclastic deformation that involved the sphalerite. Gangue minerals are subordinate to sulphides and consist of two recognized generations of gray quartz: early quartz, macrocrystalline, and cataclased, is related to the sphalerite stage of mineralization; late quartz is microcrystalline, fills the microfractures, and is associated with galena and other sulphides (Figure 7c). Wall rock hydrothermal alteration is difficult to recognize, due to late superposed supergene phenomena, but it certainly included silicification and pervasive dispersion of carbonaceous matter, possibly precipitated during mineralization, which gave the sulphide-bearing mylonite a distinctive black color. No free gold was ever identified in this ore, whose Au geochemical contents are very low [2,26,37].

#### Structures

The old mine exploited several lenticular sulphide orebodies that were located in the hinge zone of a km-size open, upright antiform (a minor order structure of the largest Flumendosa Antiform) related to the LD1 collisional phase (see cross-section in Figure 3 and the scheme in Figure 4). The antiform axis weakly plunges toward N120 (Figures 3 and 8); the structure deformed the foliated isoclinal folds related to the early stage of shortening (D1 Variscan phase) and the mylonitic shear zone that separates the Riu Gruppa and Gerrei tectonic units. The exploited sulphide lens-shaped orebodies developed parallel to the D1 mylonitic foliation, which in this area is at a low angle with the D1 axial plane foliation (Figure 9). There is no evidence of the primary bedding, completely transposed during the D1 tectonic phase. The lenses attain a maximum thickness of 6–7 m for maximum extension in a strike of 80–100 m. Although located in the hinge zone of an antiform, they cannot simply be classified as typical saddle reefs, as they do not display the classical triangular shape related to hinge collapse. The main dip of the mineralized lenses is up to 20° toward N 140°, so more or less in the axis plunge direction. The shape of the orebodies is well detectable by studying the old room-and-pillar mineworks, still being partially accessible.

In detail, it is possible to recognize crosscut relationships between different events of mineralization. The large lens-shaped orebodies are mainly characterized by abundant Zn–Cu sulphides forming veinlets 1 to 10 cm in size hosted in the mylonite (Figure 6a), being generally parallel to the mylonitic foliation of the hinge zone (Figure 9). Galena, chalcopyrite, pyrite, and other sulphides are arranged in cm-sized veinlets that involve the hosting rocks for about 1 m of thickness; they cut at low angle the Zn–Cu lenses (Figure 6e), thus postdating them. In the field, these veins became progressively steeper and more arsenopyrite-rich (Figure 7c).

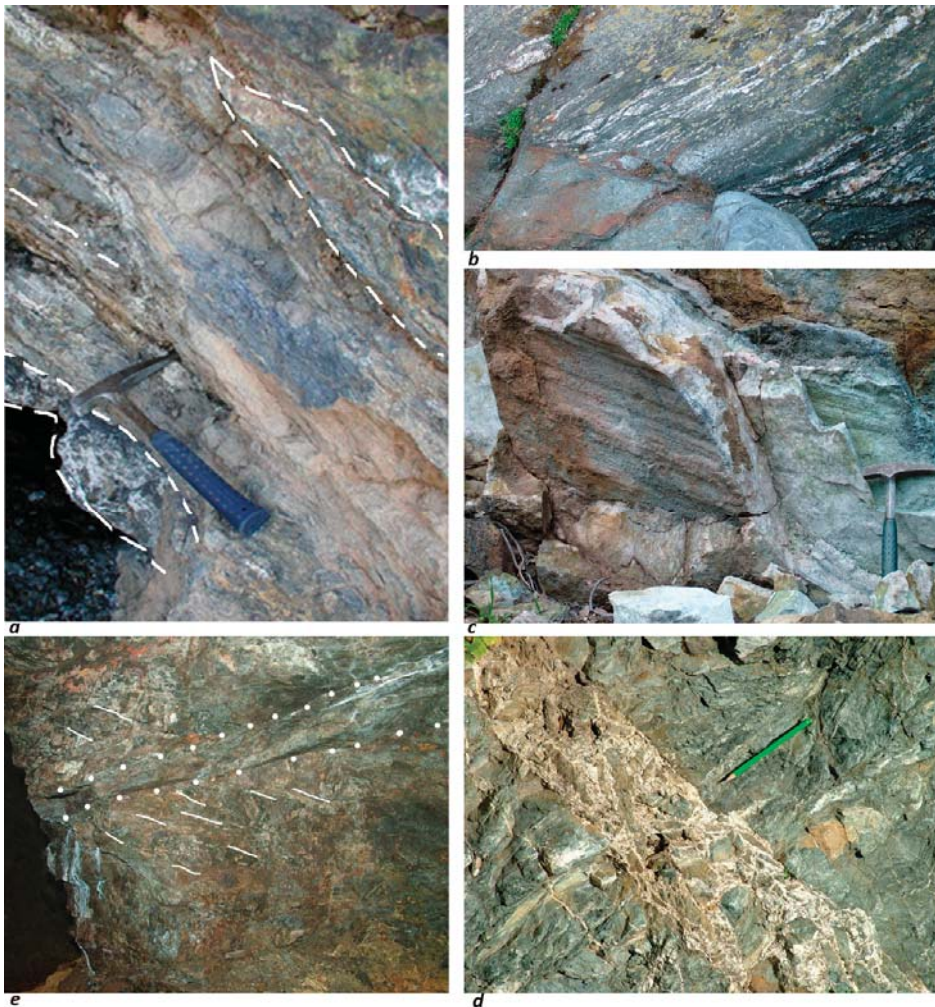


**Figure 6.** Outcrop pictures of the Baccu Locci mineral deposits: (a) Su Spilloncargiu mineworks: Zn–Cu–Pb sulphide lens ore (*type a* mineralization). The thin sulphide “beds” (dashed line) are parallel to the Variscan mylonitic foliation (solid line). (b) Baccu Trebini outcrop (*type b* mineralization): Qtz–As–Pb sulphide sheeted veins along a SW-dipping brittle shear zone. (c) Along Rio Baccu Locci, close to San Riccardo mineworks (*type b* mineralization): Qtz–As–Pb dm-size vein with subhorizontal slickenlines. (d) Baccu Trebini outcrop (*type b* mineralization): Fault breccia with Qtz–As–Pb sulphides wrapping wall rock clasts along SW-dipping fault. (e) Su Spilloncargiu mineworks (*type a* mineralization): in a pillar of the exploited mine a *type b* Qtz–As–Pb sulphide vein (white dotted line) crosscuts a sulphide lens that is parallel to Variscan foliation (white lines).

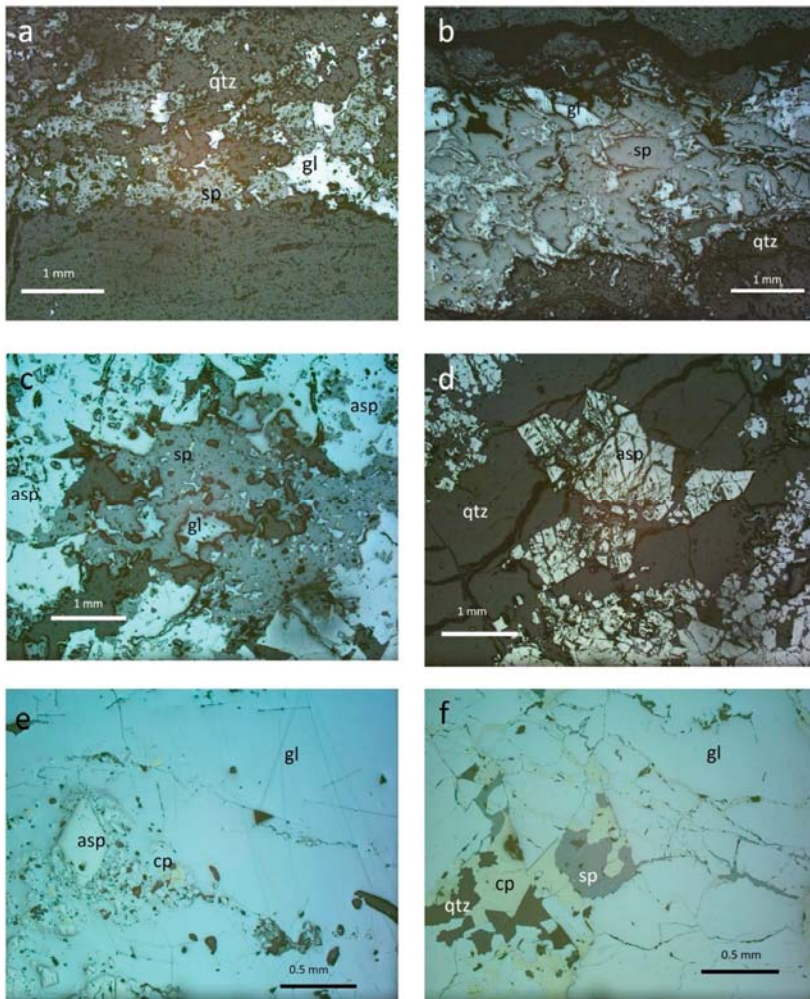


**Figure 7.** Microtextural features of ores in the study area (polished sections, reflected light): (a) Su Spilloncargiu mineworks, early mixed sulphide ore (*type a* mineralization): Brecciated quartz–sphalerite layer infilled by late galena; the mineralized layer follows the  $S_m$  foliation and exhibits sharp contact with a phyllosilicate layer in the mylonitic matrix; high-Fe sphalerite shows a distinct *chalcopyrite disease* with large chalcopyrite and pyrrhotite exsolutions. (b) Su Spilloncargiu mineworks, early mixed sulphide ore (*type a* mineralization cementation zone): Brecciation of sphalerite, infilled by primary galena, is particularly highlighted by cementing fine veinlets of secondary galena. (c) Su Spilloncargiu mineworks, quartz–arsenopyrite veins (*type b* mineralization crosscutting *type a* mineralization): Arsenopyrite aggregates enveloping early sphalerite aggregates (with some galena) from mixed sulphide ore. (d) Su Spilloncargiu mineworks, quartz–arsenopyrite veins (*type b* mineralization): Typical brecciated arsenopyrite texture, with large aggregates of fractured sub-idiomorphic crystals. (e) San Riccardo mineworks (*type b* mineralization): large galena (chalcopyrite) enveloping arsenopyrite crystals. (f) San Riccardo mineworks (*type b* mineralization): Detail of the late ore, with abundant fractured galena infilled by late chalcopyrite and inclusion poor sphalerite; sphalerite only displays very fine chalcopyrite exsolutions along crystallographic planes. Qtz, quartz, gl, galena, sp, sphalerite, asp, arsenopyrite.

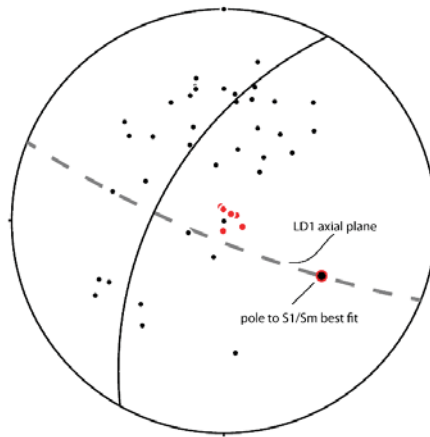


**Figure 8.** Stereographic projection (equal area, lower hemisphere) of D1 tectonic foliation (black dot), LD1 axial surface (dashed line), and calculated axis (red circle), attitude of sulphide orebodies (red dot).

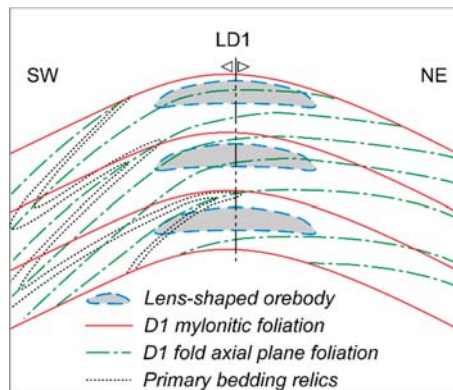


**Figure 9.** Schematic relationships between lens-shaped sulphide orebodies, D1 fold axial plane foliation, and D1 mylonitic foliation in the hinge zone of LD1 antiform at Spilloncargiu mine works (not to scale).

#### 4.1.2. Qtz–As–Pb Sulphide Vein Systems (*Type b* Mineralization)

Swarms of quartz–As–Pb (Zn, Cu, Ag, Au) sulphide hydrothermal veins occur frequently in the Baccu Locci mine area and in several nearby localities along the highly mineralized Baccu Locci shear zone. The best exposition occurs in the San Riccardo/Su Spinosu mine (Figure 5), where the veins reach the maximum mapped thickness.

#### Ore Mineralogy and Textures

Textural and mineralogical observations of the Qtz–As–Pb sulphide vein ores are the basis for a general paragenetic sequence that includes: (1) a *pre-ore stage*, with large precipitation of coarse-grained white quartz and rare scheelite [37]; (2) an *As–Fe sulphide stage*, following the diffuse cataclasis of white quartz, with abundant arsenopyrite (I) and pyrite in quartz macro- and microfractures, after an initial arsenopyrite–pyrite dissemination in the wall rock; (3) a *sulphide/sulfosalts stage*, after new cataclasis (Figure 7), with infilling of gray microcrystalline quartz, Pb–Zn–Cu–Ag sulphides (galena, sphalerite, chalcopyrite, argentite), euhedral arsenopyrite (II), phyrrothite, Cu–Ag–Sb–As sulfosalts (tetrahedrite–freibergite, bournonite, stephanite), rare stibnite, and gold/electrum [37,38];

and, (4) a late stage, with cryptocrystalline quartz and pyrite. In the sulphide/sulfosalts stage, textural evidence indicates an initial deposition of galena, which is the most abundant mineral (Figure 7); sphalerite, chalcopyrite, and other sulphides followed. Fine disseminations of euhedral (sometimes needle-shaped) arsenopyrite (II) in cataclased wall rocks are probably related to this stage. Sphalerite in *type b* ores is distinctly different from that in *type a* sulphide lenses, being much less abundant, less deformed, less dark (it shows more evident internal reflections), and much less affected by *chalcopyrite disease*. Wall rock alteration occurred from the earliest stages, but it is substantially limited to narrow zones close to the veins, commonly marked by intense sericitization, sulphidation (fine pyrite dispersion), and silicification; in many outcrops, the footwall of the veins is strongly cataclastic and displays a characteristic black color (*black cataclasite*), further indication of diffuse precipitation of carbonaceous matter during some of the mineralizing phases. A system of E-W quartz–feldspar cm-thick veinlets has been locally observed; it distinctly crosscuts the quartz–sulphide veins and may be related to a different (and very late) phase of fluid circulation in the area. Gold grades in sulphide veins are 1–12 g/t [27,38], with good persistence in the whole mineralized vein system; silver grades are 1000–1200 g/t [27]. The Au/Ag ratio in gold grains is <1, in opposition to regional trends [37]. According to Bakos et al. [37], 10 µm sized gold grains are particularly associated with chalcopyrite and galena/bourbonite myrmekitic intergrowths that infill microfractures in cataclased arsenopyrite aggregates.

### Structures

Qtz–As–Pb sulphide veins are generally hosted in narrow brittle shear zones, usually not thicker than 10 m, of high-angle faults dipping about 70° toward N 230°, confirming the structural trend recognizable at the scale of the entire district for *type b* mineralization [26,27]. The faults generally involve both the quartz mylonite, whose protolith is not possible to ascribe to one of the mapped formations, and the Ordovician rhyolitic volcanites with augen-textures (“Porfiroidi” Fm.) that constitute some hectometer-sized tectonic slices inside the shear zone (Figure 3).

The faults clearly cut all the ductile D1, LD1, D2, and D3 structures (shear zone, folds, and foliations) and are sealed by the lower Eocene sediments. From the structural map (Figure 3), it is evident that the mineralized faults are parallel to the LD1 antiform axis and are mainly located in the hinge zone. We can interpret this occurrence considering two likely types of reactivation of previous structures, both occurring at a shallower structural level than the LD1 phase. They could be hinge-parallel fractures developed in the fold outer arc, parallel to the *bc* plane according to the fold-related joints classification by Hancock [39]; or, more probably, the faults reactivated the noncontinuous, spaced crenulation cleavage that discontinuously developed just in the hinge zone of LD1 antiforms.

The mineralized bodies are lenticular, elongated to laminated veins that are typical of a fault-fill vein system. They can vary from isolated veinlets no more than 1 cm thick to sheeted veinlets and laminated veins in which the hydrothermal mineral component prevails over the host rock component (Figure 6b). Along the fault zones hosting the veins, several kinematic indicators are found, frequently at the contact between veins and wall rocks. In some damage zones there are fault breccia with wall rock clasts wrapped by dominant hydrothermal quartz (Figure 6d); furthermore, some shear zone is characterized by a foliated black cataclasite showing S-C type fabric. Slickensides and striated surfaces occur also on the contact between the fault-fill veins (Figure 6c). Slickenlines, tension gashes and S-C type complex foliations collected along the SW-dipping faults hosting the main quartz–sulphide veins all indicate a dextral strike-slip kinematic with a small reverse component (a tectonic transport direction from the top to the NW, some data are plotted in Figure 10b). A kinematic analysis was performed also considering faults hosting Qtz–As–Pb sulphide veins but with a different orientation allow for us to reconstruct a strain ellipsoid with a subvertical intermediate axis ( $\lambda_2$ , and subhorizontal shortest ( $\lambda_3$ ) and longest ( $\lambda_1$ ) axes, respectively, oriented roughly N-S and E-W (Figure 10). Although parallelism between strain and stress ellipsoid cannot be demonstrated and we did not perform a

paleostress inversion, the kinematics suggests a paleostress field with a subhorizontal  $\sigma_1$  in agreement with strike-slip tectonics.

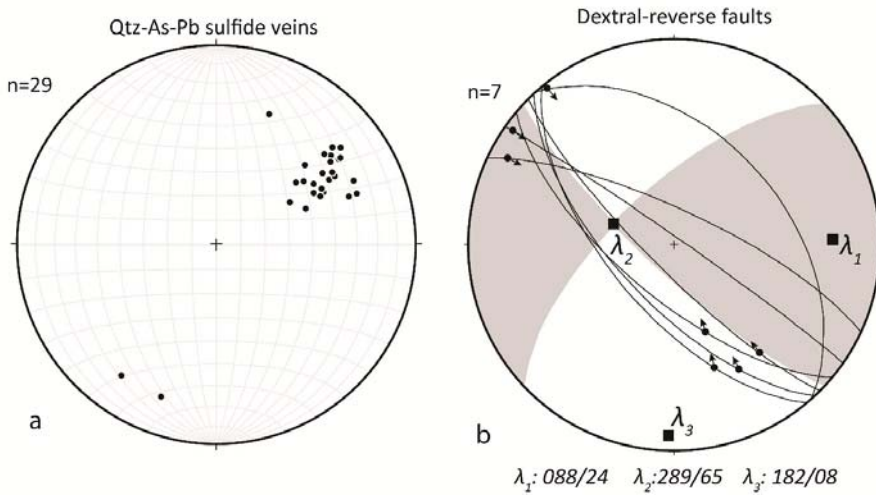


**Figure 10.** (a) Stereographic projection (equal area, lower hemisphere) of poles to Qtz–As–sulphide main orebodies in the Bacchu Locci zone; (b) Kinematic analysis of the SW dipping faults hosting quartz Qtz–As–sulphide veins.  $\lambda_1$ ,  $\lambda_2$ , and  $\lambda_3$  are the directions of maximum, intermediate, and minimum strain ellipsoid axes, respectively.

Typical economic orebodies exploited in the past mine were sulphide-rich ore shoots up to 8–9 m thick, extending along the SW-dipping faults 100–300 m along strike, and over 100 m down dip. By using the available detailed maps of mineworks, it is possible to construct a 3D model of these orebodies, particularly for the San Riccardo/Su Spinosu mine (Figure 11b). Along the stretched mineralized zones, the orebody thickness increases where the fault surface is less inclined, almost subhorizontal, and decreases where the fault is steeper, generally becoming no thicker than 2 m. At the underground level 214.68 in the San Riccardo mineworks, which is unfortunately hardly accessible today, this geometry has been observed exactly along section C–C' in Figure 11a, where the fault plane and the sulphide veins are subhorizontal (Figure 12). Although no longer accessible, from the 3D model and from the old mine reports, the room-and-pillar exploitation between levels 201.68 and 179.68 can be considered as a less inclined sector of the fault, marked by an increase in thickness of the orebody (section A–A' in Figure 11a). From these observations, the more relevant economic orebodies of *type b* mineralization may be associated with very large dilational jogs developed on the hanging wall of the transpressive faults (Figure 11a), where the occurrence of less inclined segments connecting the subvertical ones (Figure 11c) produced room for the emplacement of the orebodies during the fault activity.



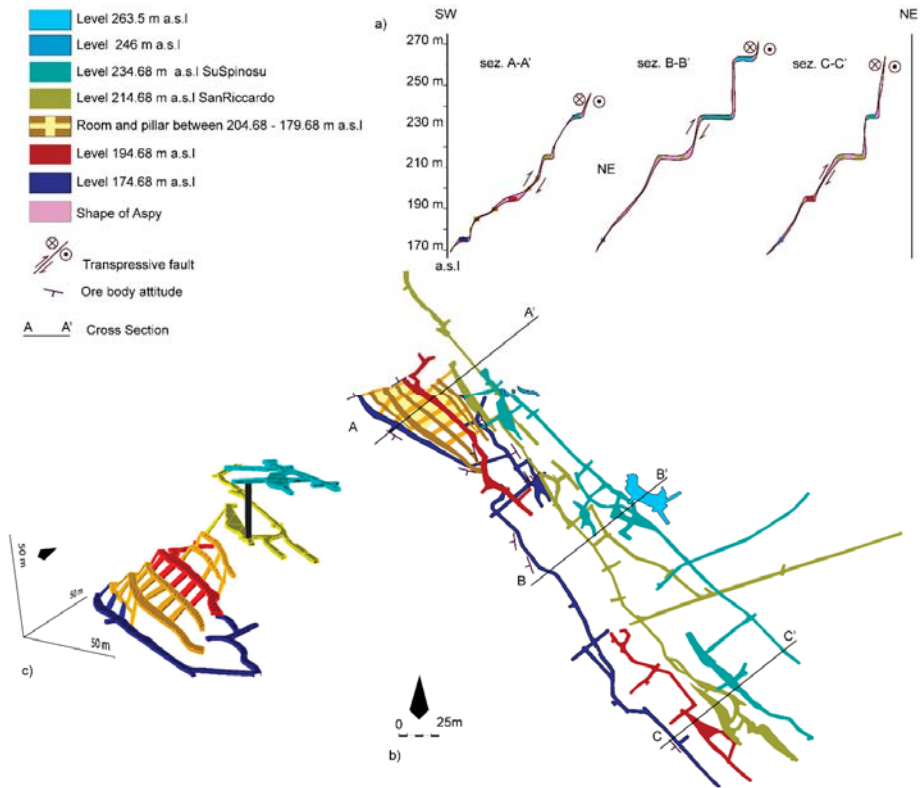


**Figure 11.** The Bacchu Locci/San Riccardo mine, *type b* mineralization (numbers are elevation above sea level, a.s.l.): (a) schematic vertical sections that point out the sigmoid shape of the sulphide veins of the San Riccardo orebodies (see trace in b), interpreted as large dilational jogs; (b) minework plans based on the original mine maps (different levels are identified by colors; and, (c) three-dimensional (3D) model of the northern part of mineworks in b, in the area of section A-A'; note that the orientation is different from the map in b.

#### 4.1.3. Mafic Dikes

Detailed mapping of the Bacchu Locci mine area [2] revealed a wide occurrence of mafic dikes, verifying complex mutual geometrical relationships among them and the ores (see also [26,38]). Dikes are variable in size (0.1–10 m thick) and orientation (from subvertical to subhorizontal), with a prevalence of N-S direction. They distinctly crosscut the foliation of the hosting mylonites, extending along for tens of meters. In different outcrops there is clear evidence that the dikes cut across and partly follow the structural pattern of the quartz–sulphide veins. Moreover, they are also locally crosscut by *type b* quartz–sulphide veins. Of particular interest is the relationships along the large dilational jogs that were observed at the San Riccardo mineworks; there, a mafic dike abruptly changes its attitude from subvertical to subhorizontal, following the tectonic foliation in the reverse limb of a D2 recumbent fold, and becoming parallel to the fault plane hosting the *type b* veins (Figure 12a).

Zucchetti [38] first classified the mafic rocks as spessartitic lamprophyres: under the microscope they show an aphanitic to porphyritic (doleritic) texture, with small labradoritic–bytownitic plagioclase, idiomorphic hornblende phenocrysts, and corroded quartz xenocrysts in a strongly altered groundmass; accessory phases are apatite, titanite, magnetite, ilmenite. These features allow for us to frame them among the calc-alkaline mafic dikes widely intruded in the SE Sardinia basement

during the late Variscan extension [12] and recently dated, in the Gerrei district, at  $302 \pm 0.2$  Ma (U–Pb dating on zircon [13]).

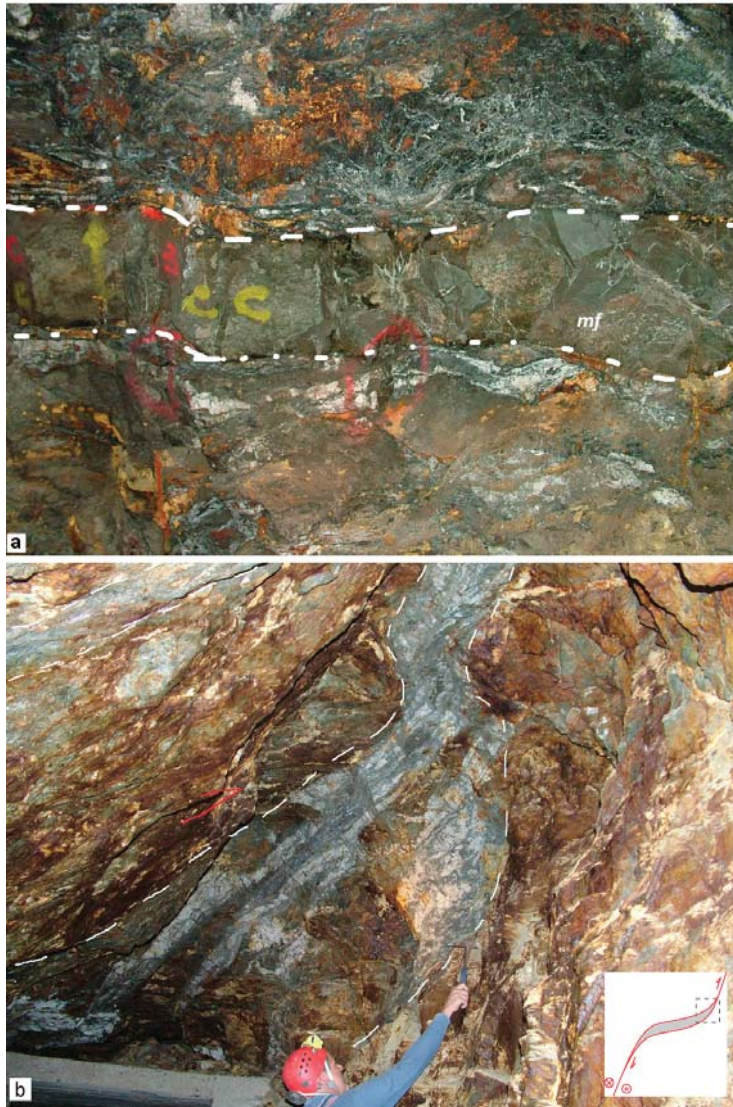


**Figure 12.** Outcrop relationships between Late Variscan mafic dikes and *type b* ores in the southern branch of San Riccardo underground mineworks: (a) sub-horizontal Qtz–As–Pb sulphides veins parallel to a mafic dike (mf) about 1.0 m thick (contact is highlighted by dashed white line); and, (b) Qtz–As–Pb sulphide ore (underlined by dashed white line) that progressively became less steep toward the left (ESE). The dashed box in the small picture indicates the location of the outcrop respect to the whole lens-shaped orebody. Photo in a is about 2 m to the left (i.e., west) of photo in b.

## 5. Discussion

As previously discussed, the basic approach of this study was mainly focused on finding field and ore microscopy elements that are able to: (1) unravel the reciprocal relationships between ore deposit types and (2) provide indications on the controls operated by the Variscan tectonic structures during mineralization events in the Baccu Locci mine area.

Previous works have usually considered the occurrence of *type a* sulphide lenses in the Baccu Locci mine area as a single ore. This was interpreted in different ways, essentially trying to establish genetic links with different phases of mineralization and with the *type b* ores. Thus, according to a proposed “synsedimentary” model, the Zn–Cu–Pb sulphides would represent an initial (predeformation) concentration of metals (*proto-ore*) that, remobilized during Variscan deformation, provided the sulphide component to *type b* veins [37,40]. An interesting issue was first raised by the study of Zucchetti [38], which evidenced a partial superposition of mineral assemblages in both ores. This was considered as indicative of an origin of Zn–Cu–Pb sulphides by lateral infilling from Qtz–As–Pb sulphide veins, but without clearly distinguishing the two mineralization in space and time.

Structural data and ore mineralogy observations that were carried out with this study document a complex mineralization history, including two distinct kinds of polyphasic ores (here, *type a* and *type b* ores in this text) that show different minerals assemblage and different spatial relationships with tectonic structures (Figure 13).

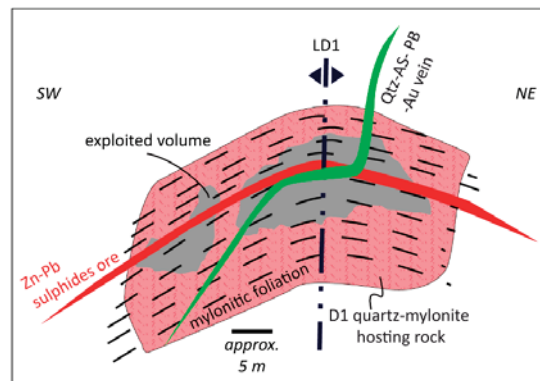
	1	2			3
<b>STRUCTURAL REGIME</b>	Passive infilling of sulphides in D1 mylonite foliation occurred after D2 Variscan phase	<ul style="list-style-type: none"> <li>D4 strike-slip tectonics. Development of large dilational jogs in NW-SE dextral strike-slip (reverse movement) faults.</li> <li>Reopening of foliation in hinge zone of antiforms.</li> <li>Mafic diking.</li> <li>Repeated cataclasis of ores, including <i>type-a</i> and early <i>type-b</i></li> </ul>			Late cataclasis of ores
<b>MINERALIZING EVENT</b>	Zn-Cu ORE STAGE: Lenticular sulphide orebodies (TYPE-A ORE)	Pre-ORE STAGE: Swarms of NW-SE high-angle Qtz veins also crosscutting <i>type-a</i> ores	As-Fe ORE STAGE: infilling of quartz and arsenopyrite in cataclased pre-ore quartz veins (TYPE-B ORE) and in cataclased <i>type-a</i> ore	Pb-Zn-Cu-(Sb, Au) ORE STAGE: diffuse infilling of sulphides in cataclased TYPE-A and TYPE-B ores and in mafic dikes.	Post-ORE STAGE: swarms of barren veinlets crosscutting all previous orebodies
Quartz	—————	—————	—————	—————	—————
Scheelite		----- ?	----- ?		
Arsenopyrite			—————	—————	
Pyrite			—————	—————	—————
Galena				—————	
Chalcopyrite	—————			—————	
Sphalerite	—————			—————	
Pyrrhotite	—————				
Tetrahedrite				—————	
Gold-Electrum			----- ?	----- ?	

Figure 13. Evolution of mineralizing events in the Baccu Locci mine area and their relationships with tectonic events.

### 5.1. Relationships between Ore Type Deposits

The *type a* ore crops out in the Spilloncargiu mine, where the Zn–Cu sulphide lenses are cut by a swarm of *type b* veins (Figure 14). Ore microscopy evidence corroborates the relationships at the outcrop scale; in fact, *type a* minerals (mainly sphalerite, chalcopyrite, and pyrrhotite) are strongly cataclased and *type b* minerals (mainly galena and chalcopyrite with subordinate arsenopyrite and tetrahedrite) infill the voids that were created by cataclasis. These textures confirm that *type b* postdates *type a* mineralization and that a brittle tectonic event occurred in between. In turn, the *type b* minerals

show mutual crosscutting relationships that demonstrate the progressive and polyphased deposition of white quartz (pre-ore stage in Figure 13), arsenopyrite (As–Fe stage), and galena (Pb–Zn–Cu–Sb–Au stage) as the most abundant mineral phases. This *type b* mineral assemblage is well represented in the San Riccardo/Su Spinosu ore, where the ore paragenesis is not associated with a *type a* ore and linkage between the ore and transpressive dextral faults is manifest. Furthermore, ore microscopy shows that between the several *type b* mineralizing stages, there are progressive mutual relationships of cataclasis and successive mineral infilling, showing that *type b* was synkinematic with a brittle deformation. The post-ore stage of mineralization (cryptocrystalline quartz, pyrite) is widespread and crosscuts all of the previous mineral assemblages, so it postdates the main mineralizing events. Only in *type b* veins does gold occurrence assume economic relevance. On the contrary, a lack of significant gold grades in *type a* mineralization is noteworthy; it could be related to lower content in arsenopyrite, which has been recorded in other areas of the Gerrei–Sarrabus district as a probable first carrier for gold (Brecca mine: [5,41]).



**Figure 14.** Sketch of the mutual relationships between *type a* and *type b* ores located at the top of LD1 antiform hinge zone.

## 5.2. Orebody/Tectonic Structure Relationships and Structural Control

The *type a* ore is hosted in the mylonites that characterize the Bacchu Locci shear zone and it is located at the top of the hinge of a large LD1 antiform that folded together bedding, D1 folding axial-plane foliation, and mylonitic foliation. Interpreting the mylonite as Silurian black shales, some previous studies considered the tectonic foliation as primary bedding and classified the ores as stratiform and synsedimentary of probable volcano-exhalative origin [37,40]. From the definition of the Bacchu Locci mylonitic shear zone [3], it is well established that the Zn–Cu sulphide lenses developed parallel to D1 Variscan foliations, in both the axial plane and mylonitic (Figure 6a). Furthermore, *type a* Zn–Cu sulphides show no physical relationship with the Ordovician metavolcanics (“Porfiroidi” Fm., Figures 3 and 5) that crop out as less deformed tectonic slices in the Bacchu Locci shear zone. On the whole, these geometric relationships clearly rule out the possible syngenetic (“stratiform” or “stratabound”) options for mineralization, excluding any connection between the primary bedding (now completely obliterated by the Variscan tectonic imprint) and orebodies. Similarly, field relationships and ore textures exclude possible syn-D1 (“syn-metamorphic”) deposition; in fact, the sulphides infill the D1 foliations but they are not in turn affected by them. In this way, the LD1 hinge zone operated as a typical structural trap, but it essentially exerted “passive” structural control, because there is no evidence of synkinematic formation of mineral deposits. At the Gerrei–Sarrabus district scale, *type a* ores have not been recognized in places other than hinge zones of LD1 folds, also by the extensive surveys that were made during mine exploitation. Further confirmation may be found in an adjacent LD1 antiform, a few kilometers west of the study area (Riu Gruppa

antiform, Sa Lilla mine; Figure 2), where previously reputed “stratoid” orebodies of sulphides, similar by mineral association and texture [42] to those of Baccu Locci/Spilloncargiu, are located at the top of a comparable hinge zone, in which development of sulphide “beds” was once again parallel to the D1 tectonic foliations.

Some speculation can be made about the modality that allowed the brittle reactivation of horizontal tectonic foliations to create space for *type a* mineral deposition. Structural data point out that *type a* ores postdate D1 and LD1 structures. Further, the creation of horizontal lens-shaped voids now filled with mineral deposits during the D2 extensional phase sounds unrealistic, because the vertical stress  $\sigma_1$  (that we can image roughly higher than the lithostatic stress) operating during the rocks’ exhumation would have prevented the opening of subhorizontal discontinuities. So, we can argue that *type a* ores could have been developed after the Gerrei and Rio Grappa tectonic units got to shallower crustal levels, where the fluid pressure could overcome the lithostatic stress, possibly when the vertical stress  $\sigma_1$  related to the extensional dynamics ceased. The role of decreased lithostatic stress in allowing for the development of open spaces that are suitable for mineralization should be confirmed by the absence of similar orebodies in deeper parts of the hinge zone. Anyway, this interpretation can be demonstrated when data about the baric environment are available. Up to now, the only available data from fluid inclusions [10] highlight that a metamorphic environment can be excluded, thus mineralization might postdate D2 deformation.

The *type b* Qtz–As–Pb veins are hosted in narrow brittle–ductile shear zones, generally developed inside the quartz–mylonitic rocks. We described their occurrence in the Spilloncargiu mine at the top of an LD1 antiform, where they cut at low angle *type a* ore, but they reach their main thickness in the San Riccardo/Su Spinosu mine. There, the availability of detailed mineworks plans permitted the recognition of the tectonic relationship and highlighted the occurrence of large dilational jogs (Figure 13). Interestingly, there are close relationships between jog geometry and older D1–LD1–D2 structures, although jogs clearly postdate them. In fact, the San Riccardo main fault is a generally WSW–steepening dipping transpressive fault that mostly cuts at high angle the NE-dipping D1 foliation in the northeast limb of LD1 antiform (Figure 15). The fault abruptly changes the dip direction to WSW, gently dipping just where it crosses gently SW-dipping D1 foliation in the reverse limb of a D2 recumbent fold (Figure 15). So, dilational jogs developed when the D4 fault reactivated preexisting anisotropies (in this case, D1 tectonic foliations) if they had the right attitude. Ore mineralogy shows repeated cataclasis and mineral infilling during the several mineralizing stages of *type b* veins, suggesting a progressive brittle deformation that in some cases produced large dilational jogs that were suitable to host orebodies with economic relevance [43,44]. Actually, the most important mineral assemblage—the galena- (and gold-) rich ore related to the Pb–Zn–Cu–Sb–Au stage of mineralization (Figure 13)—is associated with the largest jogs. The jog structures are not perfectly cylindrical, so their geometries can change slightly along strikes (Figure 11). This is probably due to a change in the D1 foliation attitude in the reverse limbs of D2 recumbent folds or to a change of the local stress field.

The recognition of such large dilational jogs is not very common [44] and it has been possible by the availability of observations at different scales. Moreover, the case of Baccu Locci/San Riccardo reveals that the occurrence of previous reactivable foliation, possibly with different attitude due to a polyphase deformation, can be one of the situations suitable for the development of large jogs. In the study area, the understanding of such active structural control would allow a different way to find new, possibly more fruitful, orebodies. In the case study, the change in dip direction of D1 tectonic foliation on the limbs of LD1 folds could be ignored, because it is not directly linkable with the mineralized veins, but it could be a clue to identify the occurrence of large dilational jogs.

Finally, some considerations might be given to the relationships between mafic dikes and the Qtz–As–Pb sulphide vein system, which is problematic. The definition of possible genetic links between the mafic magmatism and the mineralization processes falls well outside the scope of this work, requiring a wider geochemical study at the district scale. However, field mapping and explorations into the old mineworks showed several mutual relationships between dikes and ore veins (Figure 12).

These spatial relationships suggest a coeval emplacement. Mafic dikes may have intruded in an interval between the main mineralizing events of *type b* ore, in particular, between the first and second mineralization stages (pre-ore/As-Fe sulphide stages) and the third stage (sulphide/sulfosalts stage) of the paragenetic sequence, producing apparently contrasting timing relationships in the field. Under this hypothesis, considering the age available for these rocks in the neighboring areas [13], mafic dikes assume a chronological constraint, suggesting an age of mineralizing events around 302 Ma; that is, an age in which the Variscan basement of southern Europe suffered a widespread tectonic extension. This age is, in fact, consistent with: (a)  $^{40}\text{Ar}$ - $^{39}\text{Ar}$  dating of hydrothermal white mica in quartz-arsenopyrite-gold veins in the nearby Monte Ollastedu area ( $307 \pm 3$  Ma) [10], and (b) several geological constraints occurring in the whole Gerrei district [26], indicating that the quartz-arsenopyrite-gold vein systems clearly predate the previously described mineralized vein systems related to F-bearing granites, dated at 286 Ma [9,12], and they are unconformably covered by lower Permian sediments dated at 295 Ma [13]. However, it cannot be excluded that the latest stages of mineralization in Baccu Locci (including the *type b* Pb-Zn-Cu-Sb-Au sulphide/sulfosalts stage that affects the mafic dikes) could be related to events referable to the younger part of the outlined chronological interval. Overall, these constraints allow for us to consider the ore deposits of the Baccu Locci mine area as part of a much wider metallogenic event that affected various massifs of the Variscan orogen between 310 and 300 Ma [45,46]. From their geological, mineralogical, and geochemical characteristics, they can be best classified as Variscan orogenic gold type [47]. As in other massifs of European Variscides, in Sardinia this metallogenic event involved a crustal-scale flow of fluids during the late Variscan extension, resulting in widespread mineralizing processes in major regional structures, such as the Flumendosa Antiform. Large shear zones, such as the Baccu Locci shear zone, are part of the main plumbing system through which deep fluids were focused toward the shallower parts of the crust.

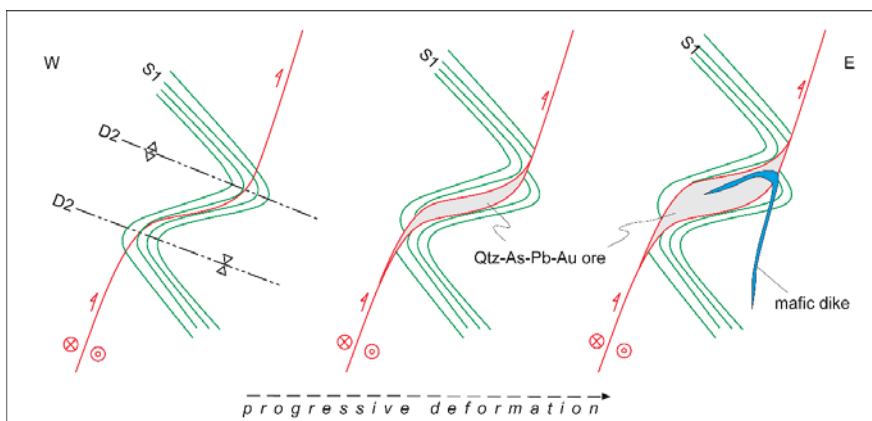


**Figure 15.** Baccu Locci/San Riccardo mine: scheme of the geometric relationships between foliation, faults, mafic dikes, and Qtz-As-Pb sulphide veins. See the location of this structure in the larger LD1 antiform in the cross-section in Figures 3 and 4.

## 6. Conclusions

The ores in Baccu Locci are a good example of structurally controlled mineralization in a basement characterized by the overprinting of several tectonic phases, from ductile to brittle, during both compressive and extensional regimes. The control exerted was either a passive reactivation of older foliations to create space for mineral deposition, or an active syn-kinematic deposition of minerals during the progressive evolution of the hosting structure. In particular, the emplacement of the older types of ores exposed in Baccu Locci emerges as the result of the opening of previous discontinuities

(foliations) in the hinge zone of large antiforms, where they are subhorizontal, after their exhumation to shallow structural levels when postcollisional extension ceased. Afterward, a different stress field produced transpressive faults that reactivated anisotropic surfaces parallel to the axial plane in the hinge zone. Along the transpressive dextral faults, large dilational jogs developed, whose geometry was influenced by sudden changes of the attitude of Variscan foliation in the reverse limbs of recumbent folds. The jogs formed together with mineral deposits, exerting in this way an “active” control of mineralization and hosting the more economically relevant ores. As a general statement, the occurrence of older tectonic foliations and folds might be taken into account not only because they can be directly presumed to be hosting mineralized veins, a common concept in the study of structure–orebody relationships, but also when considering the influence that they could have in modifying hosting structures and favoring the formation of more significant orebodies, being in this way a good tool for prospecting new relevant ores.

Although the overprinting relationships between the different ores and the mafic dikes are now clearer, more data are needed to better constrain the thermobaric environment in which the minerals were deposited, the time interval between them, the source of the ore fluids, and finally the role of mafic dikes in the large frame of the Late Variscan metallogenic epoch in Sardinia.

**Author Contributions:** A.F., A.D., and S.N. conceptualized the study. A.F. performed the geological mapping. A.F., C.B., and F.C. performed the structural analysis and 3D structural modelling. A.D. and S.N. performed the orebodies’ survey. S.N. performed the macro to micro-scale ore mineralogy. A.F. and S.N. wrote the original draft and with C.B. and F.C. reviewed and edited the draft. Funding acquisition and project administration were performed by A.F. and S.N.

**Funding:** This research was funded by FdS-RAS Fondazione di Sardegna and Regione Autonoma della Sardegna grant number F72F16003080002 and by Italian Government, project PRIN-2005 grant number 2005047008.

**Acknowledgments:** The authors are grateful to two anonymous reviewers for their comments that improved the quality of the paper and thank the editors for the careful editorial management.

**Conflicts of Interest:** The authors declare no conflict of interest.

## References

- Conti, P.; Carmignani, L.; Oggiano, G.; Funedda, A.; Eltrudis, A. From thickening to extension in the Variscan belt—Kinematic evidence from Sardinia (Italy). *Terra Nova* **1999**, *11*, 93–99. [CrossRef]
- Funedda, A.; Naitza, S.; Conti, P.; Dini, A.; Buttau, C.; Tocco, S.; Carmignani, L. The geological and metallogenic map of the Bacchu Locci mine area (Sardinia, Italy). *J. Maps* **2011**, *2011*, 103–114. [CrossRef]
- Conti, P.; Funedda, A.; Cerbai, N. Mylonite development in the Hercynian basement of Sardinia (Italy). *J. Struct. Geol.* **1998**, *20*, 121–133. [CrossRef]
- Funedda, A.; Naitza, S.; Conti, P.; Dini, A.; Buttau, C.; Tocco, S.; Carmignani, L. Structural control of ore deposits: The Bacchu Locci shear zone (SE Sardinia). *Rend. Online SGI* **2011**, *15*, 66–68.
- Lerouge, C.; Bouchot, V.; Douguet, M.; Naitza, S.; Tocco, S.; Funedda, A. *Variscan Gold Mineralisation of Bacchu Locci and Brecca, Southeastern Sardinia: Petrographic and Geochemical Studies*; BRGM Report N RP-54431-FR; BRGM: Orleans, France, 2007; p. 47. Available online: <http://infoterre.brgm.fr/rappports/RP-54431-FR.pdf> (accessed on 13 October 2018).
- Conti, P.; Carmignani, L.; Funedda, A. Change of nappe transport direction during the Variscan collisional evolution of central-southern Sardinia (Italy). *Tectonophysics* **2001**, *332*, 255–273. [CrossRef]
- Cocco, F.; Funedda, A. The Sardinic Phase: Field evidence of Ordovician tectonics in SE Sardinia, Italy. *Geol. Mag.* **2017**, *1–14*. [CrossRef]
- Carmignani, L.; Conti, P.; Barca, S.; Cerbai, N.; Eltrudis, A.; Funedda, A.; Oggiano, G.; Patta, E.D.; Ulzega, A.; Orrù, P.; et al. *Foglio 549-Muravera. Note Illustrative*; Servizio Geologico d’Italia: Roma, Italy, 2001; p. 140.
- Conte, A.M.; Cuccuru, S.; D’Antonio, M.; Naitza, S.; Oggiano, G.; Secchi, F.; Casini, L.; Cifelli, F. The post-collisional late Variscan ferroan granites of southern Sardinia (Italy): Inferences for inhomogeneity of lower crust. *Lithos* **2017**, *294–295*, 263–282. [CrossRef]

10. Dini, A.; Di Vincenzo, G.; Ruggieri, G.; Rayner, J.; Lattanzi, P. Monte Ollasteddu, a new late orogenic gold discovery in the Variscan basement of Sardinia (Italy)—Preliminary isotopic ( $^{40}\text{Ar}$ - $^{39}\text{Ar}$ , Pb) and fluid inclusion data. *Miner. Depos.* **2005**, *40*, 337–346. [[CrossRef](#)]
11. Cortesogno, L.; Cassinis, G.; Dallagiovanna, G.; Gaggero, L.; Oggiano, G.; Ronchi, A.; Seno, S.; Vanossi, M. The Variscan post-collisional volcanism in Late Carboniferous-Permian sequences of Ligurian Alps, Southern Alps and Sardinia (Italy): A synthesis. *Lithos* **1998**, *45*, 305–328. [[CrossRef](#)]
12. Ronca, S.; Del Moro, A.; Traversa, G. Geochronology, Sr-Nd isotope geochemistry and petrology of Late Hercynian dike magmatism from Sarrabus (SE Sardinia). *Period. Mineral.* **1999**, *68*, 231–260.
13. Dack, A. Internal Structure And geochronology of the Gerrei Unit in the Flumendosa Area, Variscan External Nappe Zone, Sardinia, Italy. Master's Thesis, Boise State University, Boise, ID, USA, 2009.
14. Cassinis, G.; Ronchi, A. Upper Carboniferous to Lower Permian continental deposits in Sardinia (Italy). *Geodiversitas* **1997**, *19*, 217–220.
15. Carmignani, L.; Carosi, R.; Di Pisa, A.; Gattiglio, M.; Musumeci, G.; Oggiano, G.; Pertusati, P.C. The Hercynian chain in Sardinia (Italy). *Geodin. Acta* **1994**, *7*, 31–47. [[CrossRef](#)]
16. Conti, P.; Patta, E.D. Large scale W-directed tectonics in southeastern Sardinia. *Geodin. Acta* **1998**, *11*, 217–231. [[CrossRef](#)]
17. Carosi, R.; Musumeci, G.; Pertusati, P.C. Senso di trasporto delle unità tettoniche erciniche della Sardegna dedotto dagli indicatori cinematici nei livelli cataclastico-milonitici. *Rend. Soc. Geol. Ital.* **1990**, *13*, 103–106.
18. Casini, L.; Funedda, A. Potential of pressure solution for strain localization in the Baccu Locci Shear Zone (Sardinia, Italy). *J. Struct. Geol.* **2014**, *66*, 188–204. [[CrossRef](#)]
19. Casini, L.; Funedda, A.; Oggiano, G. A balanced foreland–hinterland deformation model for the Southern Variscan belt of Sardinia, Italy. *Geol. J.* **2010**, *45*, 634–649. [[CrossRef](#)]
20. Funedda, A. Foreland- and hinterland-verging structures in fold-and-thrust belt: An example from the Variscan foreland of Sardinia. *Int. J. Earth Sci.* **2009**, *98*, 1625–1642. [[CrossRef](#)]
21. Funedda, A.; Meloni, M.A.; Loi, A. Geology of the Variscan basement of the Laconi-Asuni area (central Sardinia, Italy): The core of a regional antiformal refolding of a tectonic nappe stack. *J. Maps* **2015**, *11*, 146–156. [[CrossRef](#)]
22. Montomoli, C.; Iaccarino, S.; Simonetti, M.; Lezzerini, M.; Carosi, R. Structural setting, kinematics and metamorphism in a km-scale shear zone in the Inner Nappes of Sardinia (Italy). *Ital. J. Geosci.* **2018**, *137*, 294–310. [[CrossRef](#)]
23. Carmignani, L.; Pertusati, P.C. Analisi strutturale di un segmento della catena ercinica: Il Gerrei (Sardegna sud-orientale). *Boll. Soc. Geol. Ital.* **1977**, *96*, 339–364.
24. Carmignani, L.; Oggiano, G.; Barca, S.; Conti, P.; Salvadori, I.; Eltrudis, A.; Funedda, A.; Pasci, S. *Geologia della Sardegna. Note Illustrative della Carta Geologica in Scala 1:200.000*; Servizio Geologico d'Italia: Roma, Italy, 2001.
25. Carmignani, L.; Cortecchi, G.; Dessau, G.; Duchi, G.; Oggiano, G.; Pertusati, P.; Saitta, M. The antimony and tungsten deposit of Villasalto in South-Eastern Sardinia and its relationship with Hercynian tectonics. *Schweiz. Mineral. Petrogr. Mitt.* **1978**, *58*, 163–188.
26. Funedda, A.; Naitza, S.; Tocco, S. Caratteri giacimentologici e controlli strutturali nelle mineralizzazioni idrotermali tardo-erciniche ad As-Sb-W-Au del basamento metamorfico paleozoico della Sardegna Sud-orientale. *Resoconti dell'Associazione Mineraria Sarda* **2005**, *110*, 25–46.
27. Garbarino, C.; Naitza, S.; Tocco, S.; Farci, A.; Rayner, J. Orogenic Gold in the Paleozoic Basement of SE Sardinia. In *Mineral Exploration and Sustainable Development*; Eliopoulos, D.G., Ed.; Mill Press: Rotterdam, The Netherlands, 2003; pp. 767–770.
28. Naitza, S.; Oggiano, G.; Cuccuru, S.; Casini, L.; Puccini, A.; Secchi, F.; Funedda, A.; Tocco, S. Structural and magmatic controls on Late Variscan Metallogensis: Evidences from Southern Sardinia (Italy). In *Mineral Resources in a Sustainable World, Proceedings of the 13th Biennial SGA Meeting, Nancy, France, 24–27 August 2015*; André-Mayer, A.S., Cathelineau, M., Muchez, P.H., Pirard, E., Sindern, S., Eds.; The Society for Geology Applied to Mineral Deposits (SGA): Nancy, France, 2015; pp. 161–164.
29. Naitza, S.; Conte, A.M.; Cuccuru, S.; Oggiano, G.; Secchi, F.; Tecce, F. A Late Variscan tin province associated to the ilmenite-series granites of the Sardinian Batholith (Italy): The Sn and Mo mineralisation around the Monte Linas ferroan granite. *Ore Geol. Rev.* **2017**, *80*, 1259–1278. [[CrossRef](#)]



30. Belkin, H.E.; De Vivo, B.; Valera, R. Fluid inclusion study of some Sarrabus fluorite deposits, Sardinia, Italy. *Econ. Geol.* **1984**, *79*, 409–414. [[CrossRef](#)]
31. Boni, M.; Balassone, G.; Fedele, L.; Mondillo, N. Post-Variscan hydrothermal activity and ore deposits in southern Sardinia (Italy): Selected examples from Gerrei (Silius Vein System) and the Iglesias district. *Period. Mineral.* **2009**, *78*, 19–35.
32. Giamello, M.; Protano, G.; Riccobono, F.; Sabatini, G. The W-Mo deposit of Perda Majori (SE Sardinia, Italy): A fluid inclusion study of ore and gangue minerals. *Eur. J. Mineral.* **1992**, *4*, 1079–1084. [[CrossRef](#)]
33. Allmendinger, R.W.; Cardozo, N.; Fisher, D. *Structural Geology Algorithms: Vectors and Tensors*; Cambridge University Press: Cambridge, UK, 2012; p. 302.
34. Lena, G.; Barchi, M.R.; Alvarez, W.; Felici, F.; Minelli, G. Mesostructural analysis of S-C fabrics in a shallow shear zone of the Umbria–Marche Apennines (Central Italy). *Geol. Soc. Lond. Spec. Publ.* **2018**, *409*, 149–166. [[CrossRef](#)]
35. Rutter, E.H.; Maddock, R.H.; Hall, S.H.; White, S.H. Comparative microstructures of natural and experimentally produced clay-bearing fault gouges. *Pure Appl. Geophys.* **1986**, *124*, 3–30. [[CrossRef](#)]
36. Barton, P.B.; Bethke, P.M. Chalcopyrite disease in sphalerite: Pathology and epidemiology. *Am. Mineral.* **1987**, *72*, 451–467.
37. Bakos, F.; Carcangiu, G.; Fadda, S.; Mazzella, A.; Valera, R. The gold mineralization of Baccu Locci (Sardinia, Italy): Origin, evolution and concentration processes. *Terra Nova* **1990**, *2*, 232–237. [[CrossRef](#)]
38. Zucchetti, S. The lead-arsenic-sulfide ore deposit of Bacu Locci (Sardinia-Italy). *Econ. Geol.* **1958**, *53*, 867–876. [[CrossRef](#)]
39. Hancock, P.L. Brittle microtectonics: Principles and practice. *J. Struct. Geol.* **1985**, *7*, 437–457. [[CrossRef](#)]
40. Schneider, H.-J. Schichtgebundene NE-Metall- und F-Ba-Lagerstätten im Sarrabus-Gerrei-Gebiet, SE-Sardinien. I. Bericht: Zur Lagerstättenkunde und Geologie. *Neues Jahrb. Mineral. Monatshefte* **1972**, *1972*, 529–541.
41. Lerouge, C.; Naitza, S.; Bouchot, V.; Funedda, A.; Tocco, S. Invisible gold in arsenopyrite of the Variscan Au-Sb Brecca mineralization (Gerrei district, Southeastern Sardinia). *Geol. Fr.* **2007**, *2*, 124.
42. Violo, M. Contributo alla conoscenza dei giacimenti stratoidi polimetallici, in area metamorfica. Il giacimento di Sa Lilla (San Vito, Cagliari-Sardegna). *Resoconti dell'Associazione Mineraria Sarda* **1966**, *71*, 5–110.
43. Cox, S.F.; Braun, J.; Knackstedt, M.A. Principles of structural control on permeability and fluid flow in hydrothermal systems. *Rev. Econ. Geol.* **2001**, *14*, 1–24.
44. Robert, F.; Poulsen, K.H. Vein formation and deformation in greenstone gold deposits. *Rev. Econ. Geol.* **2001**, *14*, 111–155.
45. Bouchot, V.; Ledru, P.; Lerouge, C.; Lescuyer, J.L.; Milesi, J.P. Late Variscan mineralizing systems related to orogenic processes: The French Massif Central. *Ore Geol. Rev.* **2005**, *27*, 169–197. [[CrossRef](#)]
46. De Boorder, H. Spatial and temporal distribution of the orogenic gold deposits in the Late Palaeozoic Variscides and Southern Tianshan: How orogenic are they? *Ore Geol. Rev.* **2012**, *46*, 1–31. [[CrossRef](#)]
47. Bouchot, V.; Milesi, J.P.; Ledru, P. Crustal Scale Hydrothermal Palaeofield and Related Au, Sb, W Orogenic Deposits at 310–305 Ma (French Massif Central, Variscan Belt). *SGA News* **2000**, *10*, 6–12.



© 2018 by the authors. Licensee MDPI, Basel, Switzerland. This article is an open access article distributed under the terms and conditions of the Creative Commons Attribution (CC BY) license (<http://creativecommons.org/licenses/by/4.0/>).

Article

# Multi-Stage Deformation of the Khangalas Ore Cluster (Verkhoyansk-Kolyma Folded Region, Northeast Russia): Ore-Controlling Reverse Thrust Faults and Post-Mineral Strike-Slip Faults

Valery Y. Fridovsky<sup>1,\*</sup>, Maxim V. Kudrin<sup>1</sup> and Lena I. Polufuntikova<sup>2</sup>

<sup>1</sup> Diamond and Precious Metal Geology Institute, SB RAS, Yakutsk 677000, Russia; kudrinmv@mail.ru

<sup>2</sup> M.K. Ammosov North-Eastern Federal University, Yakutsk 677000, Russia; pli07@list.ru

\* Correspondence: 710933@list.ru; Tel.: +7-4112-33-58-72

Received: 4 May 2018; Accepted: 22 June 2018; Published: 26 June 2018

**Abstract:** This study reports the results of the analysis of multi-stage deformation structures of the Khangalas gold ore cluster, northeast Russia. Four Late Mesozoic-Early Eocene deformation stages were identified. The first deformation event (D1) was characterized by the development of NW-striking tight to isoclinal folds of the first generation (F1) and interstratal detachment thrusts. Major folds, extensive thrusts, boudinage, cleavage, auriferous mineralized fault zones and quartz-vein gold mineralization were formed in the reverse and thrust fault stress field during the progressive deformation stage (D1), with NE-SW-oriented  $\sigma_1$ . Post-ore deformation is widely manifested in the region. Structures D2 and D3 are coaxial. Sinistral strike-slip motions (D2 and D3) occurred along NW-trending faults under prevailing W-E compression. They were accompanied by the formation of NS- and NE-striking F2–3 folds with steep hinges and by bending of the earlier formed structures, among them ore-controlling ones. The last deformation event (D4) was represented by normal-dextral strike-slip faulting, refolding of rocks, pre-existing structures and ore bodies and by the development of folds with steep hinges. Key structural elements of varying age are described, the chronology of deformation events and mineralization reconstructed and their relation to geodynamic events in northeast Asia established.

**Keywords:** Verkhoyansk-Kolyma folded region; Khangalas ore cluster; orogenic gold mineralization; deformation structure; thrust fault; strike-slip fault

---

## 1. Introduction

The Khangalas ore cluster (KOC) is located in the southeastern part of the Kular-Nera slate belt of the Verkhoyansk-Kolyma folded region in northeast Russia. It was discovered in the 1940s. Rich placer deposits with large gold nuggets are known there. Commercial exploitation of the KOC commenced in the latter half of the 20th Century and continues to present day. At an early stage of geologic investigation (1940–1980), considerable attention was given to concordant ore bodies confined to the limbs of brachyantoclinal folds [1]. Then, in the late 1980s to the early 2000s, mineralized fault zones of complex structure with diverse mineralization were identified and investigated, which considerably enlarged the mineral resource potential of the KOC [2,3]. Southeasterly, in the Upper Kolyma gold district with a similar geological-structural setting, several small- and medium-sized gold deposits are found, such as Vetrenskoye, Chay-Yuruye, Svetloye, etc. [4,5]. Gold mineralization of the KOC is of the orogenic type, which is characterized by a close relationship with Late Jurassic-Neocomian tectonomagmatic events in the Verkhoyansk-Kolyma folded region [6–10]. The paper presents new data on the KOC geology obtained by the authors in the last few years, which provide a better understanding of the relations between folds, faults and mineralization in the region.

## 2. Materials and Methods

Structural-tectonic factors are among the most important in controlling localization of orogenic Au-quartz deposits [11,12]. Structural-kinematic studies in the Khangalas ore cluster were conducted using up-to-date methods [13–17]. The morphology of ore veins in natural exposures and mine workings was studied and their relations to geological structures established. Interactions between the veins and faults were studied using the belt method [18]. This is based on the regular position of vein poles relative to faults in stereographic projection. The method enables determination of the sense of displacement during vein formation [18]. Measurements of planar and linear structures (bedding, cleavage, vein-veinlet bodies, faults, ore zones, jointing, fold hinges, boudinage, slickenlines, etc.) were made. The kinematics of main deformation stages and the paleo-orientation of stress were reconstructed relative to major deformation structures of NW strike. Structural data were statistically analyzed and plotted on the upper hemisphere of the Wulff stereographic net.

In 2005, detailed field studies and structural mapping were conducted at the Nagornoye deposit and the Dvoynoye, Ampir and Klich-Kontrolnoye occurrences, at Mudeken and other localities and in 2014 and 2017 at the Khangalas deposit and Ozhidaniye occurrence. The nomenclature of structural elements is taken from [19]. Planar structures (S) are given as dip azimuth/dip angle (e.g., 90/60 denotes eastward dip at 60°). For linear deformation elements (l), denotation plunge azimuth/plunge angle is used (e.g., 215/45 means plunge azimuth of 215° and plunge angle of 45°). Signs S1 and l1 denote the relation of a structural element to a particular deformation stage (D1) event. The studies enabled refining the general architecture of the region, revealing the particularities of the ore-controlling structures, identifying key structural elements, reconstructing the chronology of deformational events and mineralization and establishing their relationship with regional geodynamic events in northeast Asia.

## 3. Geology of the Southeastern Part of the Kular-Nera Slate Belt and the Khangalas Ore Cluster

The Kular-Nera slate belt (KNSB) is situated in the central part of the Verkhoyansk-Kolyma folded region [6]. It is mainly composed of Upper Permian, Triassic and Lower Jurassic terrigenous rocks. Extensive faults separate the belt from adjacent tectonic structures. In the northeast, it is separated from the In'yali-Debin synclinorium by the Charky-Indigirka and Chai-Yureye faults, and in the southwest, the Adycha-Taryn fault separates it from structures of the passive margin of the North Asian craton. The structural pattern of KNSB is defined by linear folds and faults of NW strike that developed over several deformation stages. Within the KOC, NW-striking faults represent branches of the Nera Fault, which manifests itself as 4 km-wide zones of intensive deformations and subvertical foliation of the rocks. Dextral strike-slip motions have been reported along the Nera Fault [20].

Magmatism is poorly manifested in KNSB. It is mainly represented by granitoid massifs, subvolcanic magma of dacite composition and dikes belonging to the NNW-striking Tas-Kystabyt magmatic belt. They were formed in Late Jurassic-Albian times [21]. Various tectonomagmatic events characteristic of the Late Jurassic-Late Cretaceous history of the eastern margin of the North Asian craton are manifested within KNSB [6,22,23]. The Late Jurassic-Early Cretaceous was marked by accretion and collision of the Kolyma-Omolon microcontinent against the craton margin and by subduction processes in the Uda-Murgal island arc. These events produced different-age fold and thrust structures, S- and I-type granitoids and orogenic gold deposits. In the Late Neocomian, the direction of the Kolyma-Omolon microcontinent motion and of subduction in the Uda-Murgal arc changed [6]. At that time, left-lateral strike slip motions first occurred in KNSB along NW-trending faults. Post-accretionary tectonic events and Au-Sb and Ag mineralization events were related to Late Cretaceous subduction within the Okhotsk-Chukotka arc [24].

The Khangalas ore cluster is located in the arch of the Nera anticlinorium that is represented in the study area by the NW-striking Dvoynaya anticline composed of dislocated Upper Permian and Lower-Middle Triassic terrigenous rocks (Figure 1). The Upper Permian (P<sub>2</sub>) deposits make up the core of the Dvoynaya anticline. The lower part of the section consists of massive brownish-grey

and grey greywacke sandstones with thin siltstone interbeds. The upper part is dominated by an 800 m thick sequence of dark-grey and black siltstones with inclusions of pebbles of sedimentary, magmatic and metamorphic rocks. The limbs of the Dvoynaya anticline are made of 680–750 m thick Lower-Middle Triassic deposits ( $T_1$ ), mainly dark-grey shales, mudstones and siltstones with rare interbeds of light-grey sandstones. The Middle Triassic deposits of the Anisian stage ( $T_2a$ ) are represented by a 700–800 m thick sequence of alternating sandy siltstones and siltstones with rare fine-grained sandstone interbeds. The Ladinian strata ( $T_2l$ ) are chiefly made of interbedded siltstones and sandstones with a total thickness of 850–950 m.

The main ore-controlling rupture dislocations are the Khangalas, Dvoynoy and Granitny faults represented by zones of breccia and fracture, low sulfidation of rocks and quartz-carbonate vein mineralization (Figure 1). The Khangalas Fault crosscuts the Khangalas ore cluster in a northwest direction. It controls localization of the Khangalas deposit and Ampir and Klich-Kontrolnoye occurrences. Within the study area, the exposed fault changes its strike from NW-SE to E-W and has a dip direction to S-W and S. The bedding of rocks exposed in the S-W wall strikes N-W, and rocks of the N-E wall strike NE-SW and E-W. The Dvoynoy Fault strikes E-W, and its fault plane is subvertical. In the central part of the KOC, northward of the Klich-Kontrolnoye occurrence, the Dvoynoy Fault adjoins the Khangalas Fault. The northeastern branch of the Dvoynoy Fault controls mineralization at the Nagornoye deposit. The rocks of the S wall of the fault have a N-E strike, while those of the N one strike E-W. The Granitny Fault is located in the southwestern part of the KOC. Outside the Khangalas ore cluster, the Ala-Chubuk massif of biotite granites is confined to it.

Magmatic activity is manifested by rare mafic and intermediate dikes of the normal and subalkaline series of Late Jurassic (Nera Complex ( $J_3n$ )) and Late Cretaceous (Khulamrinsk Complex ( $K_2ch$ )) age (Figure 1). The Nera magmatic complex includes basalt, gabbro and diorite porphyry dikes that extend for a distance from a few tens of meters to 2 km and have NE strike and a thickness of 1–20 m. The dikes underwent alteration. They contain quartz-carbonate veinlets. The Khulamrinsk magmatic complex consists of rare trachybasalt dikes extending for 200–500 m. They have a NW strike and are 1–10 m thick.

At 7 km to the northwest of the Khangalas ore cluster is the exposed Ala-Chubuk massif of biotite granites. The K-Ar age of the massif determined on orthoclase from porphyry phenocrysts is  $145.0 \pm 3.0$  Ma and on biotite from the groundmass  $149.0 \pm 3.0$  Ma [25]. The available geophysical data imply the presence of unexposed intrusions of similar composition at the Nagornoye and Khangalas deposits [25]. The Khangalas, Dvoynoy and Duk ore fields are identified within the KOC. The first field occurs in the southeast of the ore cluster and includes the Khangalas deposit and the Ozhidaniye occurrence. To the northwest of them are the Klich-Kontrolnoye, Dvoynoye and Ampir occurrences belonging to the Dvoynoye ore field. The Duk ore field includes the Nagornoye deposit. The ore bodies consist of extensive mineralized fault zones and concordant and cross-cutting gold-quartz veins and veinlets with simple mineral composition. The amount of ore minerals does not exceed 1–3%. These are arsenopyrite, pyrite, galena, sphalerite, chalcopyrite and native gold with 820–830‰ fineness and rare antimonite and Pb-sulfosalts. Quartz is the main gangue mineral, with less abundant carbonates (calcite and siderite) and chlorite. A series of successive mineral assemblages are identified in the ores of the deposits. These are pyrite-arsenopyrite-quartz metasomatic, quartz-pyrite-arsenopyrite vein, chalcopyrite-sphalerite-galena and sulfosalt-carbonate assemblages. The early pyrite-arsenopyrite-quartz mineralization is developed in wall-rock metasomatites. It is represented by irregular disseminations of pyrite and arsenopyrite metacrysts and by thin quartz streaks. Pyrite prevails over arsenopyrite. Minerals of the metasomatic assemblage are characterized by euhedral and subhedral crystals and a streaky-disseminated structure. Pyrite and arsenopyrite grains show evidence of deformation and corrosion. Pyrite and arsenopyrite of the early vein assemblage occur as disseminated euhedral grains and intergrowths. Pyrites of the vein assemblage contain Co, Sb, As, Ni, Cu and Zn trace contaminants. Minerals of the productive chalcopyrite-sphalerite-galena assemblage sporadically occur as disseminations and small aggregates in milk-white quartz and

as microinclusions in early sulfides. The principal mineral of the sulfosalts-carbonate assemblage is siderite. Sulfosalts are represented by boulangierite, tetrahedrite and bournonite.

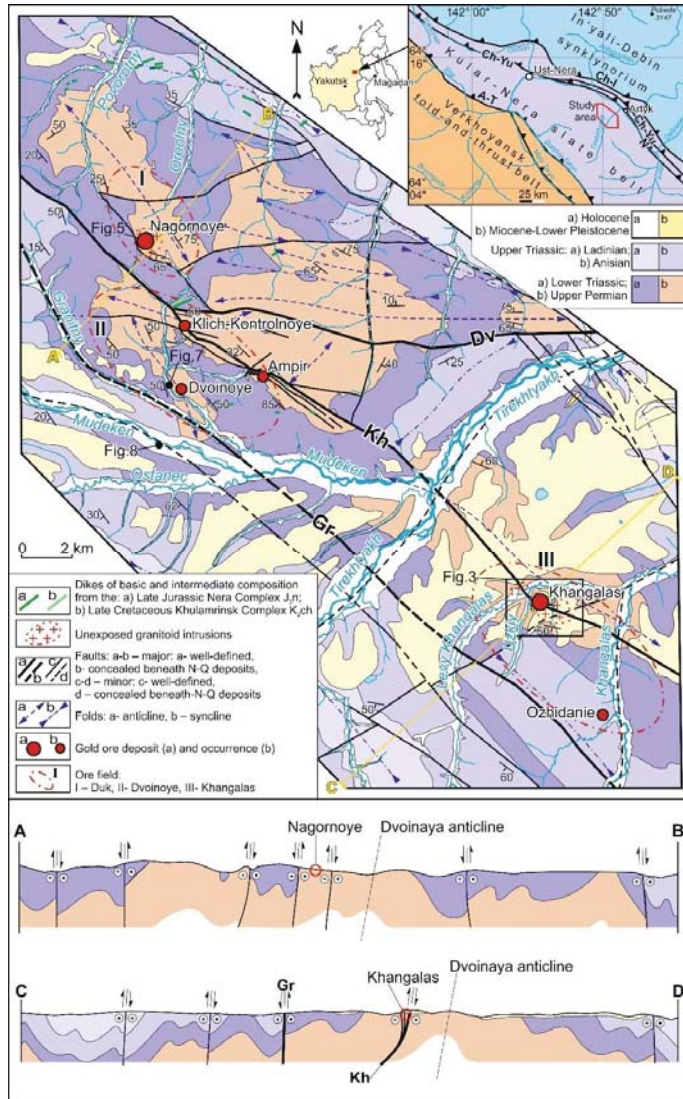


**Figure 1.** Geological sketch map, sections and location of gold deposits and occurrences of the Khangalas ore cluster, modified and supplemented from [2]. The inset map shows the position of the Khangalas ore cluster. Faults: Ch-I, Charky-Indigirka; Ch-Yu, Chai-Yureye; N, Nera; A-T, Adycha-Taryn.

Microthermometric studies of the fluid were conducted at the laboratory of the M.K. Ammosov North-Eastern Federal University on an optical microscope AxioScope.A1 fitted with a motorized heating stage (up to 600 °C) and a liquid nitrogen sample cooling system (down to −196 °C) (LNP95). Analyses were made on milk-white quartz samples from the ore veins. The results of thermo-

and cryo-metric studies showed that ore-forming fluids of the KOC originated at temperatures of 310–330 °C and a pressure of 0.9 kbar. The data obtained suggest that gold mineralization was formed at a depth of about 3.5 km.

Age determinations are scarce for the KOC mineralization. The K-Ar sericite age of the Nagornoye deposit is  $130.0 \pm 4.0$  Ma [23]. The authors of the given paper conducted Re-Os dating of gold (Sample Number X-45-14) from a quartz vein from the Yuzhnaya ore zone of the Khangalas deposit at the Center of Isotope Research of the Karpinsky All-Russian Scientific-Research Geological Institute (St. Petersburg, Russia). The isochron Re-Os age of gold was  $137.0 \pm 7.6$  Ma. This indicates that productive orogenic gold-quartz mineralization of the region was formed in Valanginian-Hauterivian times.

The mineralized brittle fault zones consist of breccias and blocks of quartzose sandstones and siltstones and are often accompanied by concordant (a few cm to 1–2 m thick, in swells up to 5 m) and cross-cutting quartz veins and veinlets and disseminated sulfide mineralization (Figure 2). They are mainly localized in sandstones and at their contacts with siltstones and have conformable and crossing relations with the host rocks. The ore zones underwent strong supergene alteration as indicated by the presence of Fe oxides, sulfates, clay minerals, etc. Nesterov N.V. [26] has reported on a secondary gold enrichment at the Khangalas deposit. The quartz veins are often deformed in the mineralized fault zones, which is indicative of post-ore deformation. The host siltstones and sandstones contain disseminated sulfide mineralization (Figure 2D) represented by fine to coarse crystalline arsenopyrite and pyrite occurring as crystals, nests and veinlets.

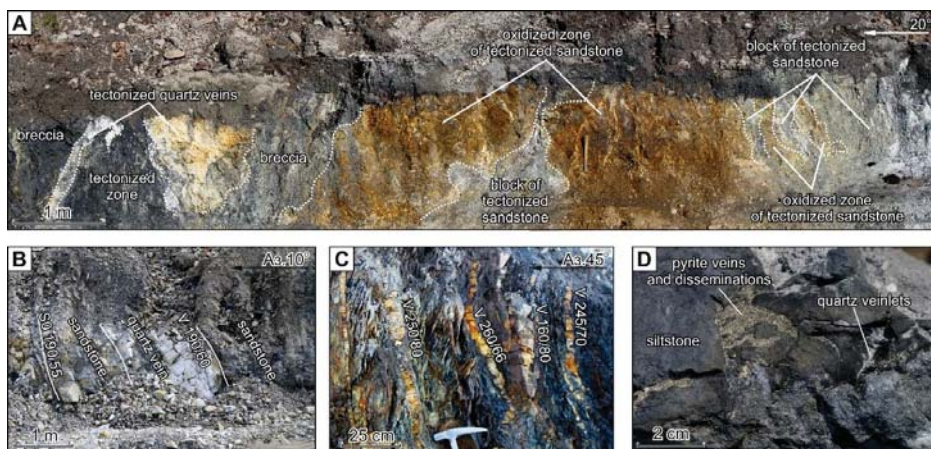


**Figure 2.** Khangalas Fault (A) and types of mineralization in the Khangalas ore cluster (KOC): (B) concordant veins, Centralnaya zone of the Khangalas deposit; (C) vein-veinlet mineralization; (D) veinlet-disseminated mineralization.

#### 4. Deformation Structures of Key Deposits and Localities of the Khangalas Ore Cluster

This section presents the results of the analysis of the deformation structures of accretionary-collisional and post-accretionary stages in the formation history of the Khangalas and Nagornoye deposits, Dvoinoye occurrence and Mudeken locality.

##### 4.1. Khangalas Deposit

The deposit occurs in the southeastern part of the KOC, on the right bank of Levy Khangalas Creek, in the area between its Uzkiy and Zimniy tributaries (Figure 1). The host rocks are represented by Upper Permian sandstones and, more rarely, siltstones. Mineralization is localized in five fault zones

(Severnaya, Promezhutochnaya, Centralnaya, Yuzhnaya and Zimnyaya, length up to 1400 m) with concordant and cross quartz veins 0.1–5 m thick in the crest of the Dvoynaya anticline (Figures 3 and 4). Ore zones with a thickness of up to 32 m dip S-W, S and S-E at 30–50° to 70–80°. The reserves exceed 11 tons of gold with an average grade of 11.2 g/t Au [27].

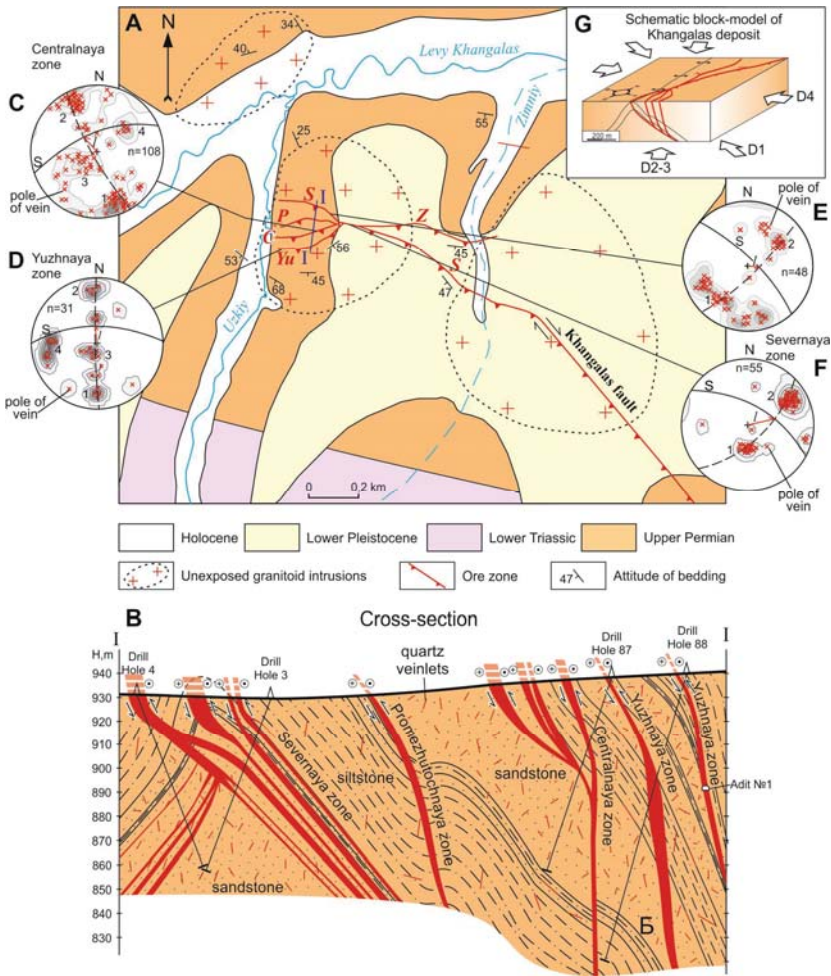


**Figure 3.** Geological sketch map (A), cross-section (B) and stereograms of the quartz veins poles (C–F), Khangalas deposit, (G) Schematic block-model of Khangalas deposit. In (A), the I–I line shows the position of the cross-section (B). Mineralized fault zones: S, Severnaya; P, Promezhutochnaya; C, Centralnaya; Yu, Yuzhnaya; Z, Zimnyaya. Symbols in stereograms and figures hereafter are: S, position of fault or ore zone; *l*, calculated direction of rock motion; *n*, number of measurements; dashed line, belt of vein poles. Contours of poles to planes (per 2% area).

Various deformation structures are manifested at the Khangalas deposit (Figures 3 and 4). Early isoclinal and tight concentric folds (F) with N–W strike and subhorizontal hinges (b) occur in narrow (up to a few tens of meters) zones (Figure 4D). In the study area, such folds were first mapped on the northeast limb of the Nera anticlinorium, in the zone influenced by the Chay–Yureye

Fault [8]. Early folds are draped during progressive deformation into late folds, so that crests of late folds can often be seen on the limbs of early folds (Figure 4C). F1 folds are the most widespread in the KOC area; they have NW-SE strike and gentle hinges (b1) (Figure 4A). These are for the most part open folds that pass into tight ones nearby the fault zones. On the right side of Uzkiy Creek, folds and ore zones have E-W and, less frequently, N-E strike due to superimposed strike-slip deformation. F1 folds are accompanied by *C1* cleavage (Figure 4). It is platy, rarely shelly-platy, and its intensity depends on the rock composition. The most intense cleavage is observed in siltstones, whereas in sandstones, it becomes coarse-platy. Its regional NW strike changes to NE-SW and E-W in areas of superposed strike-slip deformation.

The Severnaya mineralized zone is the most extensive one. On the western side of the Khangalas deposit, the Promezhutochnaya, Centralnaya and Yuzhnaya zones branch off from the Severnaya zone forming a horse tail termination structure, and on the eastern side, the Zimnyaya zone diverges from it in the E-W direction. The ore-controlling structures are confined to the core of the Dvoynaya anticlinal fold. The strike of the ore zones varies from NW-SE to S-W and, locally, to NE-SW.

Analysis of the attitude of quartz veins and veinlets revealed five variously-oriented systems (Figures 2 and 3). Veins of the first system have persistent parameters; they are conformable with the host rocks (Figures 2B,C and 3). Quartz veins of the second system follow the orientation of the bedding plane and ore zones, but they dip in the opposite direction. Low-angle veins of the third system localized in tension fractures in sandstones are rather common. The orientation of the fourth vein system is normal to the strike of mineralized faults. In some areas, all five systems of veins and veinlets are present, which form stockworks. Such systems of quartz vein mineralization, which are related to the reverse and thrust fault stress field, are also found at other gold deposits in the central part of the Kular-Nera slate belt (Bazovskoye, Malo-Tarynskoye, Levoberezhnoye and Sana) [7,28–32].



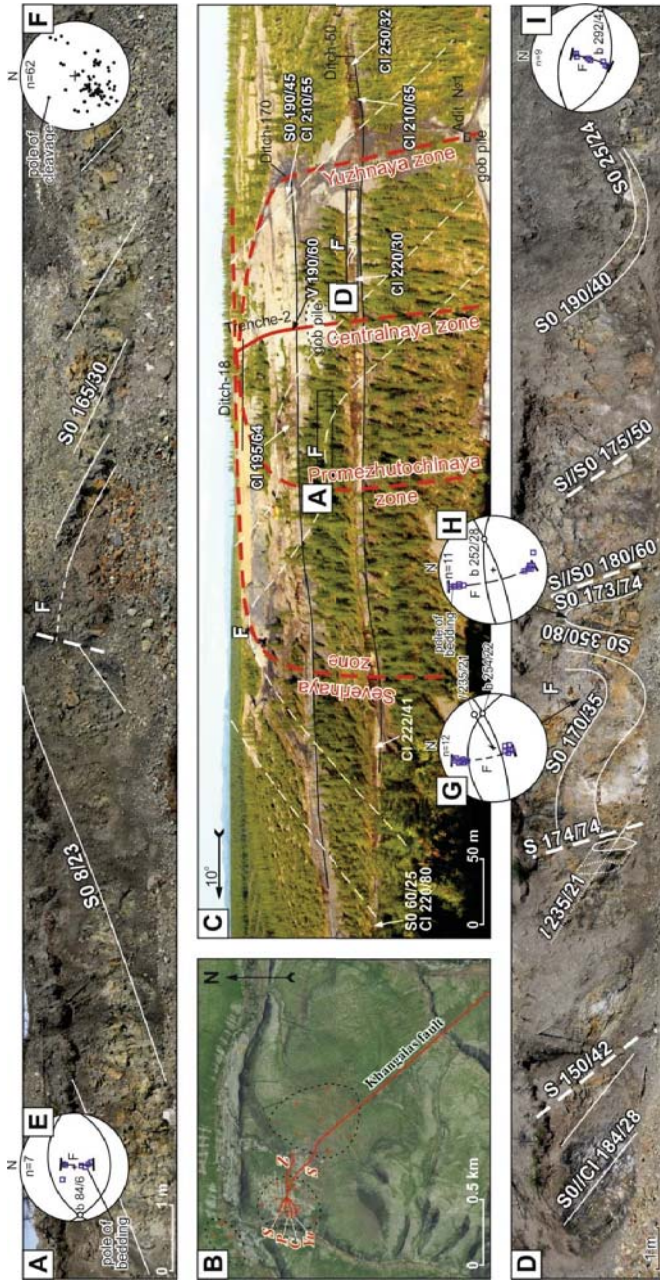


**Figure 4.** Bing Maps-satellite image (B), panoramic photo (A,D) of the Khangalas deposit. (E–I) Stereograms of bedding poles; (E–I) Stereograms of bedding poles; (E–I) Stereograms of bedding poles; (E–I) Stereograms of bedding poles; (E–I) Stereograms of bedding poles. Mineralized fault zones: S, Severnaya; P, Promezhutochnaya; C, Centralnaya; Yu, Yuzhnaya; Z, Zimnyaya.

4.2. Nagornoye Deposit

The deposit is located in the northwestern part of the KOC within the Duk ore field (Figure 5). Ore bodies are between bedding planes within faults of an ESE-WNW trend. In some places, the fault zones are accompanied by concordant (up to 100 m in extent) and feathering quartz veins and veinlets (Figure 5E,F). The faults have reverse fault and strike-slip kinematics. The thickness of ore zones on the Nagornoye deposit varies from 0.6 to 3–4 m (average 1.0 m). Ore minerals include native gold, pyrite, arsenopyrite, Fe-gersdorffite, galena, sphalerite, chalcopyrite, tetrahedrite, bournonite and the rutile-group minerals [33]. They constitute up to 3% of the veins' volume. The host rocks are mostly represented by Upper Permian sandstones with siltstone interbeds. They have an ESE-WNW strike and a steep (70–75°) to vertical, sometimes overturned bedding. They are deformed into ESE-WNW F folds with horizontal b hinges in which limbs with NNE-striking open folds with steep hinges have developed (Figure 5C,D).

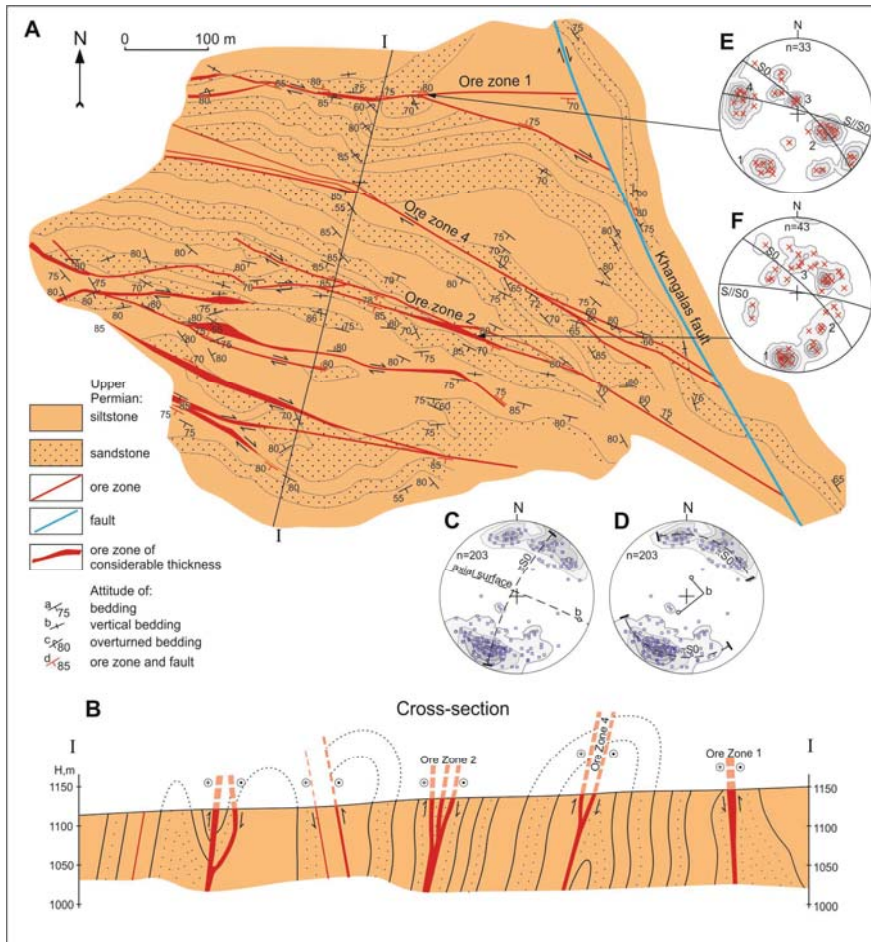


**Figure 5.** Geological sketch map and section of the Nagornoye occurrence. In (A), the I-I line shows the position of the cross-section (B). The diagrams show: (C,D) bedding poles; (E) quartz vein poles in Ore Zone 1; (F) quartz vein poles in Ore Zone 2. Contours of poles to planes (per 2% area).

The most extensively studied is Ore Zone 2 (Figures 5 and 6A). It is exposed over much of its length in a mining trench, where it parallels a subvertical sequence of quartz sandstones interlayered with siltstones (Figure 6A). Statistical analysis of the attitude of quartz veins showed that on the diagrams, fields of poles of veins are grouped, in spite of their significant scatter, along the great circle arcs corresponding to the projection of mineralized ore zones (S) (190/85) conformable with the rock bedding (S0) (Figure 5E,F). This indicates that feathering veins are mainly localized in extension fractures oriented at an obtuse angle to ore-bearing structures. Concordant veins of the first system are common (Figure 5E,F).

Variably-oriented slickenlines are established (Figure 6B). One can observe subvertical slickenlines (l-178/81) of the early thrust-faulting stage of deformation on E-W fault planes (Figure 6B). Strike slip accretionary slickenlines are manifested at the contacts of ore bodies (Figure 6C). These structural elements are associated with low-amplitude zones of warping observed on the northern wall of a trench that exposed Ore Zone 1. The axes of the warping zones plunge to SE (120/59) and are orthogonal to (l-290/30).

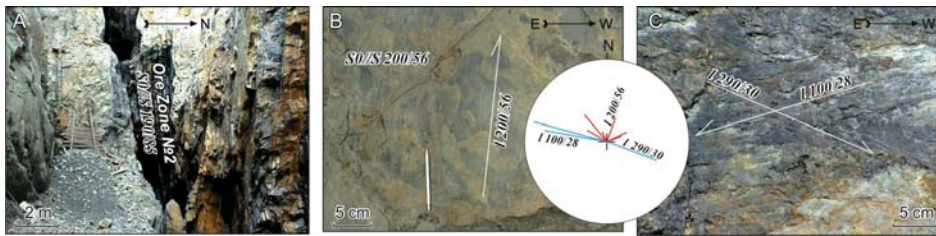


**Figure 6.** Ore Zone 2 (A), reverse-faulting (B) (red lines on the diagram) and strike-slip faulting (C) (blue lines on the diagram) slickenlines, Nagornoye deposit. Arrows show the direction of displacement of the faults' hanging walls.

#### 4.3. Dvoynoye Occurrence

The occurrence is located on the left side of the valley of Dvoynoy Creek (Figure 1). The host rocks are dominantly Late Permian sandstones with lesser siltstones. The ore bodies are represented by mineralized fault zones with quartz veins and veinlets ranging from 0.3–1.8 m (average 1.0 m) in thickness. The gold grade varies from 0.5–30.7 g/t Au.

At Dvoynoye, one can observe two systems of boudinage-structures on the limbs of folds (Figure 7). The first system is characterized by a subhorizontal long axis (Figure 7B), and the second system plunges to SE (120/54) (Figure 7C).

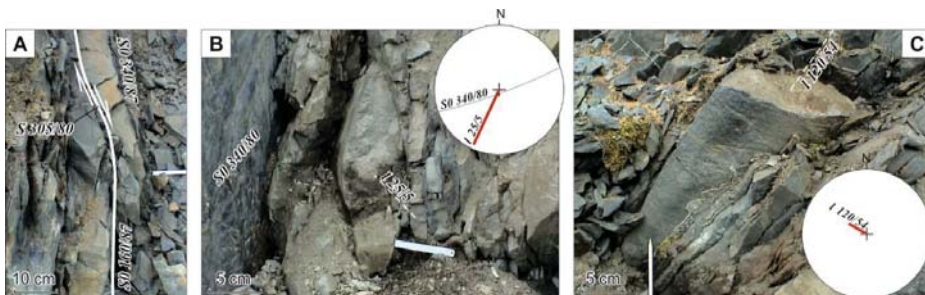


**Figure 7.** Dextral strike-slip fault (A) and boudinage-structures (B,C), Dvoynoy Creek.

#### 4.4. Mudeken Locality

Mudeken is located on the right side of the same name creek, ~6 km upstream from the Dvoynoy Creek mouth (Figure 1). Two faults and several folds are seen in an exposure of interlayered sandstones and siltstones along the creek bank (Figure 8). Fault S (77/60) is made of brecciated siltstones and sandstones with quartz veinlets. Two shelly-platy cleavages are manifested in its walls. The first *Cl* cleavage dips to W (265/80) and is subconformable with *S0* (278/50). The second *Cl* cleavage dips gently to SE (130/35–49) following the strike of fault S (160/40), which is traced by an 8 cm thick quartz-carbonate vein of banded structure. In the lying and hanging walls of the fault are observed several en echelon systems of quartz-carbonate veins: V-SE (220–260/55), V-NE (75/80) and V-SE (136/42). Kinematic reconstructions of the vein systems revealed their relation to dextral strike-slip motions (Figure 8H).

To the east, in the footwall of S fault, one can observe widely developed folds with the axial planes conformable with the fault plane. The folds are asymmetric, with gentle and extensive SE limbs and steeper SW limbs; commonly, they are overturned due to dextral strike-slip motions along the bedding plane (Z-shaped folds) (Figure 8D). Bedding poles measured on the fold limbs form a belt along the great circle arc, which is characteristic of cylindrical folds (Figure 8F). Fold hinges (b) mostly dip S-SE at 35–60°. Early cleavage (*Cl*) is deformed in folds (Figure 8G). The cleavage poles presented in Figure 8G show that early cleavage was deformed during dextral strike-slip motions.

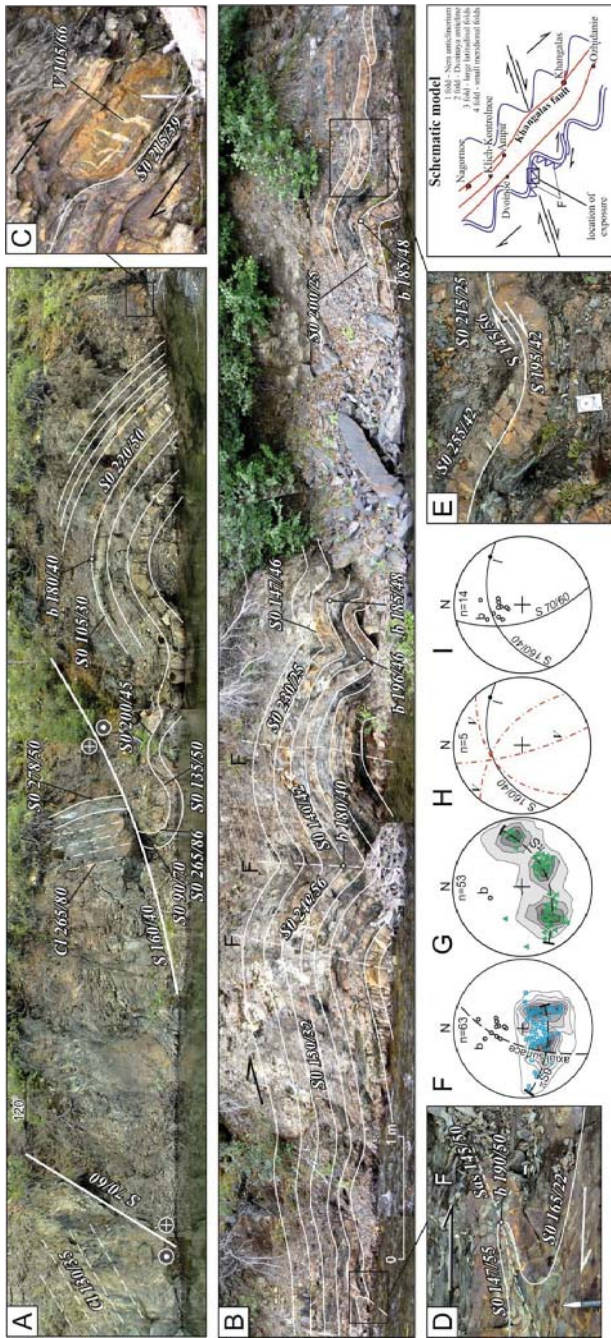


**Figure 8.** Dextral strike-slip deformations in Upper Triassic sandy siltstones, Mudeken Creek. (A,B) Fold and fault structures; (C) ladder veins in sandstone beds (plan view); (D) shaped overturned fold (plan view); (E) dextral strike-slip fault (plan view); (F–I) diagrams: (F) bedding poles, (G) cleavage poles, (H) projection of quartz-carbonate veins shown in (C,I) projections of faults and hinges of folds; I, direction of tectonic transportation. Contours of poles to planes (per 2% area).

5. Discussion

Structural-kinematic analysis of deformation elements within the KOC revealed specific structures of deposits and occurrences. Figure 9 shows stereograms of major structural elements of the KOC (bedding, cleavage, quartz veins and veinlets, as well as mineralized fault zones). Fold structures of the Khangalass deposit have NW-SE to E-W strike. Fold hinges (b1) dip to WSW at angles varying from 4–28°. Steep dip angles are due to superposed strike-slip deformations. Hinges of the third order F1 folds smoothly undulate in the direction of NW regional folding within the Nera anticlinorium. C11 cleavage at the Khangalass deposit has a NW-SE strike. In the fault zones, cleavage is deformed by late strike-slip faulting, as well as bedding. In stereographic projections, poles of quartz veins and veinlets are arranged along subvertical belts. From the aforesaid, it appears that the formation of auriferous quartz veins and veinlets is related to major fold and thrust deformations of D1 stage (J<sub>3</sub>-Knc). Faults and ore zones at the Khangalass deposit have sublatitudinal and, more rarely, northeast and northwest strike. The majority of them dip S at 30–60°.

F1 compressed folds of sublatitudinal strike are deformed, like C11 cleavage at the Nagornoye deposit, by late strike-slip faults. This led to the formation on the limbs of F1 folds of F4 open folds with steep (b4) hinges plunging to NNE and SSW. On the stereogram, vein bodies form a steeply-dipping belt of poles. Faults and ore zones are, for the most part, interstratal and have latitudinal to NE-SW, rarely NW-SE orientation.

Bedding of rocks in the Dvoynoy ore field is characterized by NW-SE and NE-SW strike related to two different deformation stages: D1 and D4, respectively. Cleavages of NW-SE and E-W orientation are recognized. The first cleavage C11 is associated with the D1 stage. It was formed in relation to early fold-and-thrust dislocations. Cleavage C14 is related to the right-lateral strike-slip stage (D4). Fault zones within the Dvoynoy ore field have mostly WNW-ESE strike.

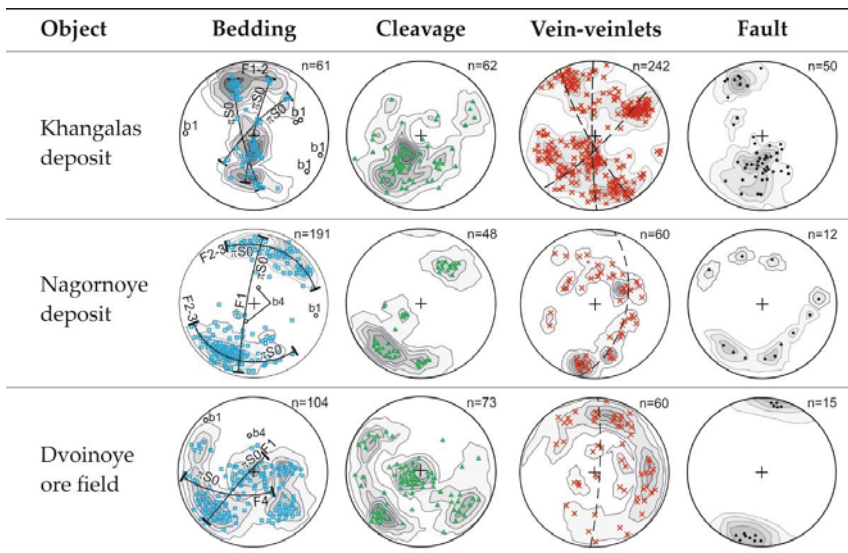






Figure 9. Stereograms of poles of bedding, cleavage, veins and faults, Khangalass ore cluster. Dashed line, belt of vein poles. Contours of poles to planes (per 2% area).

The results of studying other deposits within the Kular-Nera slate belt [22,31–36] in combination with the available information on the general tectonic and metallogenic evolution of the Verkhoyansk-Kolyma folded region [6,7,9,37] and the data on the relationships between the mapped

structural elements obtained in this study indicate that deformation occurred in four stages: D1, D2, D3 and D4 (Table 1).

**Table 1.** Evolution of tectonic events and associated mineralization in the southwestern part of the Kular-Nera slate belt.

Characteristic	Deformation Event			
	D1	D2	D3	D4
Geodynamic setting	Frontal accretion	Oblique accretion	Post-accretionary	Post-accretionary
Kinematics of NW faults	Thrust	Sinistral strike-slip	Sinistral strike-slip	Dextral strike-slip
Structural paragenesis	Interstratal detachment thrust, interstratal ramps, thrusts, cross and oblique ramps, NW tight and isoclinal folds, NW-SE open and tight folds (F1) with horizontal hinges (b1), boudinage, fault cleavage, downdip slickenlines	Sinistral strike-slip, NE-SW and NW-SE folds (F2), horizontal slickenlines	Sinistral strike-slip, NE-SW and NW-SE folds (F3), horizontal slickenlines	Dextral strike-slip, W-E and NW-SE fold (F4), sublatitudinal cleavage horizontal slickenlines
Veins	V1	-	V3	V4
Mineralization	Au	-	Sb	Ag
Attitude of $\sigma_1$	Subhorizontal, NE-SW	Subhorizontal, E-W	Subhorizontal, E-W	Subhorizontal, N-S
Graphic model				

D1 and D2 deformations occurred in the Late Jurassic-Early Cretaceous in response to frontal (D1) and then oblique (D2) accretion of the Kolyma-Omolon microcontinent to the North Asian craton margin, as well as subsynchronous subduction-related processes within the Uda-Murgal active margin. The first Late Jurassic deformation event (D1) is characterized by development of NW-trending tight and isoclinal folds (F1), interstratal detachment thrusts at the contacts of rocks with contrasting physical-mechanical properties and ramps. The sense of tectonic transportation is SW. Mineralization consists of rare non-auriferous quartz-chlorite or quartz-chlorite-calcite veins occurring throughout the area. The thickness of the veins does not exceed a few tens of centimeters. Often, the veins are concordant with the host rock bedding.

During subsequent progressive deformation, the early interstratal detachment thrusts are deformed into reverse faults. Thrust deformations are associated with linear open and tight folds (F1) of the concentric type with prevailing NW-SE strike and platy cleavage. Within the ore zones, F1 folds form bands of intense deformation up to a few hundreds of meters wide. On the limbs of F2 folds, one can observe rootless intrafolio fold hinges of the early F1 folds [8] and slickenlines oriented in the direction of dip. This stage was marked by the origination of orogenic ore-magmatic systems and intrusion of granitoids and mafic and intermediate dikes of the Late Jurassic Nera complex, which produced vein, vein-veinlet and veinlet-disseminated gold-quartz (gold-sulfide-quartz) mineralization. According to the mineralogical data, mineralization was formed at a depth of about 3.5 km. The ore bodies are localized in mineralized fault zones, in the crests of folds (saddle veins) and sandstone strata (vein-veinlet bodies).

D2: The Late Neocomian is the period when the direction of motion of the Kolyma-Omolon microcontinent and of subduction in the Uda-Murgal arc began changing [6]. Within the Kular-Nera slate belt, the second stage of accretion (Aptian, Lower-Cretaceous) is characterized by the first left-lateral strike-slip motions (D2) on NW-striking faults, which occurred under prevailing W-E compression. At that time, intrusions of subvolcanic granite-porphphy were formed [24]. Strike-slip

deformations reworked hydrothermal-metamorphogenic and gold-quartz (gold-sulfide-quartz) mineralizations causing their corrosion and remobilization, as well as the dynamic metamorphism of ore bodies. In association with strike-slip faults, F2 open folds were formed. The width of the mapped folds ranges up to a few hundred meters, but wider folds are likely, as well. Fold hinges plunge to N-E and N. At the contacts of mineralized fault zones, one can see variously-oriented subhorizontal slickenlines superposed on vertical ones.

D3: Post-accretionary tectonic events are associated with Late Cretaceous subduction in the Okhotsk-Chukotka arc [6,24]. This stage is marked by the formation of N-S and NE-SW folds (F3) with steep hinges and by activation of earlier structures, including ore-controlling ones. Note the similar kinematics of D2 and D3 deformations. F3 folds have various morphologies: from open symmetric to tight overturned ones. Characteristic are sinistral motions most widely manifested along the axial part of the Adycha-Taryn Fault [36].

At that stage, gold mineralization was superposed by Late Mesozoic antimony mineralization [24]. As shown in [36], a strong influence of Sb-bearing fluid caused significant reworking of the mineral complex of gold mineralization in the Adycha-Taryn zone. Formation of Sb mineralization was related to leaching and replacement processes that led to the formation of new mineral parageneses. Quartz-sericite metasomatites of the gold ore stage are characterized by the superposed late carbonate-paragonite-pyrophyllite-dickite paragenesis. Pyrite and arsenopyrite metacrysts are replaced by a mixture of antimonite and pyrophyllite. In the ore zones, late ore deposition is manifested by berthierite and antimonite. They form numerous streaks in milk-white quartz cementing its fragments and forming brecciated zones. The broken down milk-white quartz is freed from impurities along the fluid conductors. Solution occurs along the quartz grain boundaries. Transparent regenerated quartz forms streaks and aggregates of small (up to 1–2 mm) prismatic crystals, with pyramidal terminations. The early sulfides and sulfosalts also underwent intensive corrosion, leaching and redeposition, which led to the formation of an association of regenerated minerals. Microcrystals of the regenerated high-fineness (900–1000%) gold are often surrounded by reaction rims of aurostibite and antimony gold (Sb up to 8%) [36].

D4: The latest and fourth deformation event (D4) is characterized by dextral strike-slip faulting, refolding of rocks, reactivation of the earlier ore-controlling structures, as well as the formation of E-W folds and cleavage. Maastrichtian-Early Eocene strike-slip deformation is inferred to be related to oblique subduction of the Pacific Ocean plates beneath the eastern margin of north Asia [6] and/or to the formation of a transform margin in northeast Asia [38].

## 6. Conclusions

Studies of deformation structures of the Khangalas gold-ore cluster showed that they were forming over a long time during the course of the Late Jurassic-Neocomian accretionary and Late Cretaceous-Early Paleocene post-accretionary events in the Verkhojansk-Kolyma folded region.

The first deformation event (D1) was characterized by the development of NW-striking tight to isoclinal folds of the first generation (F1) and interstratal detachment thrusts. Major folds, extensive thrusts, boudinage, cleavage, Au-bearing mineralized fault zones and quartz-vein mineralization were formed in the conditions of the tectonic stress field characteristic of reverse and thrust faulting, with the horizontal  $\sigma_1$  and vertical  $\sigma_3$ . The D1 stage was progressive deformation under a contractional regime. In the zones of regional faults, where deformations are most intensely manifested, inter- and intra-stratal reverse and thrust faults developed in sandstones and at their contacts with siltstones, which were accompanied by intense, small-scale folding. These were favorable structural conditions for localization of mineralized fault zones with concordant and cross Au-quartz veins.

Post-ore deformations are widely manifested within the KOC. The D2 and D3 structures are co-axial. Sinistral strike-slip motions (D2–3) occurred along NW-striking faults. Associated with them were submeridional and NE-trending folds (F2–3) with steep hinges, as well as warping of the earlier, including ore-controlling, structures. The sinistral strike-slip stage is poorly manifested within the



KOC, but its presence is established from the analysis of fractures, slickenlines and fault-line folds. Faults of NE strike can also be assigned to this structural paragenesis. It is likely that sinistral strike-slip deformations changed to dextral ones that are strongly manifested within the KOC.

The fourth event (D4) is represented by normal-dextral strike-slip motions, refolding of rocks, earlier structural elements and ore bodies. At this stage, latitudinal structures (F4 folds, C14 cleavage and S4 faults) were formed, which are more widespread here than in other metallogenic zones of the Upper Indigirka district (Adycha-Taryn, Mugurdakh-Selerikan). It is assumed that large-scale dextral strike-slip faults modified the structure of deposits and occurrences in the KOC. In the most strongly-deformed areas, the strike of the structures changed to sublatitudinal and, more rarely, to NE (Khangalas deposit). Ore zones of the Khangalas deposit were previously considered as “horse tail” structures [2], but detailed analysis of the relationships between auriferous quartz veins, ore zones and rock bedding permitted assigning them to the first-stage paragenesis (D1). The large scale and long duration of post-ore strike-slip motions can be inferred from the observation that early Au-bearing quartz veins are ground to “quartz flour” in the zones of later strike-slip faults. Also observed are quartz breccias in which early milk-white quartz is cemented by later chalcedony-like grey quartz typical for Ag-Sb mineralization known from the Verkhoyansk-Kolyma folded region [39,40].

Thus, it can be concluded that tectogenesis within the Verkhoyansk-Kolyma folded region followed a regular change from the Late Jurassic-Neocomian frontal accretionary regime to the Aptian-Early Eocene strike-slip regime and that gold mineralization was related to orogenic processes, as is exemplified by the Khangalas ore cluster described in this article.

**Author Contributions:** Idea of the study conceived by V.Y.F. Collection of field materials by V.Y.F., M.V.K. and L.I.P. Treatment of data and writing the text of the paper by V.Y.F. and M.V.K. Figure drawing by M.V.K.

**Funding:** This research was funded by Diamond and Precious Metal Geology Institute, Siberian Branch of the Russian Academy of Sciences, project number [No. 381-2016-004] and by Russian Foundation for Basic Research, grant number [No. 18-35-00336].

**Conflicts of Interest:** The authors declare no conflicts of interest.

## References

1. Rozhkov, I.S.; Grinberg, G.A.; Gamyarin, G.N.; Kukhtinskiy, Y.G.; Solovyev, V.I. *Late Mesozoic Magmatism and Gold Mineralization of the Upper Indigirka District*; Nauka: Moscow, Russia, 1971; p. 238. (In Russian)
2. Oxman, V.S.; Suzdalova, N.I.; Kraev, A.A. *Deformation Structures and Dynamic Conditions for the Formation of Rocks in Upper Indigirka District*; Yakut Scientific Center Siberian Branch of the Russian Academy of Sciences: Yakutsk, Russia, 2005; p. 200, ISBN 5-463-00128-6. (In Russian)
3. Fridovsky, V.Y.; Kudrin, M.V. Deformation structures of the Khangalas ore cluster. In Proceedings of the All-Russian Scientific-Practical Conference Geology and Mineral Resources of Northeast Russia, Yakutsk, Russia, 31 March–2 April 2015; pp. 537–540. (In Russian)
4. Voroshin, S.V.; Tyukova, E.E.; Newberry, R.J.; Layer, P.W. Orogenic gold and rare metal deposits of the Upper Kolyma District, Northeastern Russia: Relation to igneous rocks, timing, and metal assemblages. *Ore Geol. Rev.* **2014**, *62*, 1–24. [[CrossRef](#)]
5. Petrov, O.V.; Morozov, A.F.; Mikhailov, B.K.; Orlov, V.P.; Militenko, N.V.; Mezhelovsky, N.V.; Feoktistov, V.P.; Shatov, V.V.; Molchanov, A.V.; Migachev, I.F.; et al. *Mineral Potential of the Russian Federation*; Petrov, O.V., Ed.; FSBI A.P. Karpinsky Russian Geological Research Institute: St. Petersburg, Russia, 2009; p. 223, ISBN 978-5-93761-156-7. (In Russian)
6. *Tectonics, Geodynamics, and Metallogeny of the Sakha Republic (Yakutia) Territory*; Parfenov, L.M.; Kuzmin, M.I. (Eds.) MAIK Nauka/Interperiodika: Moscow, Russia, 2001; p. 571, ISBN 5-7846-0046-X. (In Russian)
7. Fridovsky, V.Y.; Prokopiev, A.B. Tectonics, geodynamics and gold mineralization of the eastern margin of the North Asia Craton. In *The Timing and Location of Major Ore Deposits in an Evolving Orogen*; Blundel, D.J., Neuber, F., von Quadt, A., Eds.; Geological Society: London, UK, 2002; Volume 204, pp. 299–317.

8. Fridovsky, V.Y.; Polufuntikova, L.I.; Solovyev, E.E. Dynamics of the formation and structures of the southeastern sector of the Adycha-Nera metallogenic zone (northeast Yakutia). *Russ. J. Domest. Geol.* **2003**, *3*, 16–21. (In Russian)
9. Fridovsky, V.Y. Structural control of orogenic gold deposits of the Verkhoyansk-Kolyma folded region, northeast Russia. *Ore Geol. Rev.* **2017**, in press. [CrossRef]
10. Goryachev, N.A.; Pirajno, F. Gold deposits and gold metallogeny of Far East Russia. *Ore Geol. Rev.* **2014**, *59*, 123–151. [CrossRef]
11. Groves, D.I.; Goldfarb, R.J.; Gebre-Mariam, M.; Hagemann, S.G.; Robert, F. Orogenic gold deposits: A proposed classification in the context of their crustal distribution and relationship to other gold deposit types. *Ore Geol. Rev.* **1998**, *13*, 7–27. [CrossRef]
12. Groves, D.I.; Condie, K.C.; Goldfarb, R.J.; Hronsky, J.M.A.; Vielreicher, R.M. Secular changes in global tectonic processes and their influence on the temporal distribution of gold-bearing mineral deposits. *Econ. Geol.* **2005**, *100*, 203–224. [CrossRef]
13. Ramsay, J.G.; Huber, M.I. *The Techniques of Modern Structural Geology*; Academic press: London, UK, 1987; Volume 2, p. 704, ISBN 0-12-576922-9.
14. Fossen, H. *Structural Geology*; Cambridge University Press: Cambridge, UK, 2010; p. 463, ISBN 978-0-521-51664-8.
15. Prokopiev, A.V.; Fridovsky, V.Y.; Gaiduk, V.V. *Faults (Morphology, Geometry, Kinematics)*; Parfenov, L.M., Ed.; Yakut Scientific Center Siberian Branch of the Russian Academy of Sciences: Yakutsk, Russia, 2004; p. 148, ISBN 5-463-00016-6. (In Russian)
16. Price, N.J.; Cosgrove, J.W. *Analysis of Geological Structures*; Cambridge University Press: Cambridge, UK, 2005; p. 502, ISBN 0521319587.
17. Fossen, H.; Cavalcante, G.C.G.; Pinheiro, R.V.L.; Archanjo, C.J. Deformation—Progressive or multiphase. *J. Struct. Geol.* **2018**, in press. [CrossRef]
18. Sherman, S.I.; Dneprovsky, Y.I. *Stress Fields of the Earth's Crust and Geological Structural Methods of Their Study*; Nauka: Novosibirsk, Russia, 1989; p. 158. (In Russian)
19. Spencer, E.W. *Introduction to the Structure of the Earth*; McGraw-Hill Book Company: New York, NY, USA, 1977.
20. Gusev, G.S. *Folded Structures and Faults of the Verkhoyansk-Kolyma System of the Mesozoic*; Nauka: Moscow, Russia, 1979; p. 208. (In Russian)
21. Bakharev, A.G.; Zaitsev, A.I. The Tas-Kystabyt magmatic belt. In *Tectonics, Geodynamics and Metallogeny of the Republic of Sakha (Yakutia)*; Parfenov, L.M., Kuzmin, M.I., Eds.; MAIK Nauka/Interperiodika: Moscow, Russia, 2001; pp. 263–269, ISBN 5-7846-0046-X. (In Russian)
22. Fridovsky, V.Y. Structures of gold ore fields and deposits of the Yana-Kolyma ore belt. In *Metallogeny of Collisional Geodynamic Settings*; Mezhelovskiy, N.V., Gusev, G.S., Eds.; GEOS: Moscow, Russia, 2002; Volume 1, pp. 6–241. (In Russian)
23. Sokolov, S.D. Tectonics of northeast Asia: An overview. *Geotectonics* **2010**, *44*, 493–509. (In Russian) [CrossRef]
24. Bortnikov, N.S.; Gamynin, G.N.; Vikent'eva, O.V.; Prokof'ev, V.Y.; Prokop'ev, A.V. The Sarylakh and Sentachan gold-antimony deposits, Sakha-Yakutia: A case of combined mesothermal gold-quartz and epithermal stibnite ores. *Geol. Ore Depos.* **2010**, *52*, 339–372. (In Russian) [CrossRef]
25. Akimov, G.Y. New data on the age of Au-quartz mineralization in the Upper-Indigirka district. *Dokl. Acad. Nauk.* **2004**, *398*, 80–83. (In Russian)
26. Nesterov, N.V. Secondary zonation of gold ore deposits in Yakutia. *Izvestiya Tomsk Polytech. Univ.* **1970**, *239*, 242–247. (In Russian)
27. GeoInfoComLLC. Available online: <http://mestor.geoinfocom.ru/publ/1-1-0-55> (accessed on 5 April 2017).
28. Fridovsky, V.Y. Collisional metallogeny of gold deposits of the Verkhoyansk-Kolyma orogenic region. *Izvestiya VUZOV Geol. Explor.* **2000**, *4*, 53–67. (In Russian)
29. Fridovsky, V.Y.; Gamyranin, G.N.; Polufuntikova, L.I. Dora-Pil ore field: Structure, mineralogy, and geochemistry of the ore-formation environment. *Ores Met.* **2012**, *5*, 7–21. (In Russian)
30. Fridovsky, V.Y.; Gamyranin, G.N.; Polufuntikova, L.I. The Sana Au-quartz deposit within the Taryn ore cluster. *Raz. I Okhrana Nedr.* **2013**, *2*, 3–7. (In Russian)
31. Fridovsky, V.Y.; Gamyranin, G.N.; Polufuntikova, L.I. The structure, mineralogy, and fluid regime of ore formation in the polygenic Malo-Taryn gold field, northeast Russia. *Russ. J. Pac. Geol.* **2015**, *9*, 274–286. [CrossRef]

32. Fridovsky, V.Y.; Polufuntikova, L.I.; Goryachev, N.A.; Kudrin, M.V. Ore-controlling thrusts of the Bazovskoe gold deposit (East Yakutia). *Dokl. Earth Sci.* **2017**, *474*, 617–619. [[CrossRef](#)]
33. Akimov, G.Y. Lithological-structural control of Au-quartz ores of the Nagornoye deposit, East Yakutia. *Ores Met.* **2000**, *4*, 42–46. (In Russian)
34. Fridovsky, V.Y. Strike-slip duplexes on the Badran deposit. *Izvestiya VUZOV Geol. Explor.* **1999**, *1*, 60–65. (In Russian)
35. Fridovsky, V.Y. Analysis of deformational structures of the El'gi ore cluster (East Yakutia). *Russ. J. Domest. Geol.* **2010**, *4*, 39–45. (In Russian)
36. Fridovsky, V.Y.; Gamyarin, G.N.; Polufuntikova, L.I. Gold quartz and antimony mineralization in the Maltan deposit in northeast Russia. *Russ. J. Pac. Geol.* **2014**, *8*, 276–287. [[CrossRef](#)]
37. Prokopiev, A.V.; Tronin, A.V. Structural and sedimentation characteristics of the zone of junction of the Kular-Nera slate belt and Inyali-Debin synclinorium. *Russ. J. Domest. Geol.* **2004**, *5*, 44–48. (In Russian)
38. Khanchuk, A.I.; Ivanov, V.V. Meso-Cenozoic geodynamic settings and gold mineralization of the Russian Far East. *Russ. Geol. Geophys C/C Geol. Geofiz.* **1999**, *40*, 1607–1617.
39. Gamyarin, G.N.; Goryachev, N.A. Subsurface mineralization of eastern Yakutia. *Tikhook. Geol.* **1988**, *2*, 82–89. (In Russian)
40. Goryachev, N.A.; Gamyarin, G.N.; Prokofiev, V.Y.; Velivetskaya, A.V.; Ignatiev, A.V.; Leskova, N.V. Silver-antimony mineralization of the Yana-Kolyma belt (Northeast Russian). *Tikhook. Geol.* **2011**, *30*, 12–26. (In Russian)



© 2018 by the authors. Licensee MDPI, Basel, Switzerland. This article is an open access article distributed under the terms and conditions of the Creative Commons Attribution (CC BY) license (<http://creativecommons.org/licenses/by/4.0/>).

Article

# Tectonic Control, Reconstruction and Preservation of the Tiegelongnan Porphyry and Epithermal Overprinting Cu (Au) Deposit, Central Tibet, China

Yang Song <sup>1,\*</sup>, Chao Yang <sup>2</sup>, Shaogang Wei <sup>3</sup>, Huanhuan Yang <sup>1,4</sup>, Xiang Fang <sup>1,2</sup> and Hongtao Lu <sup>1</sup>

<sup>1</sup> Key Laboratory of Metallogeny and Mineral Assessment, Institute of Mineral Resources, Chinese Academy of Geological Sciences, Beijing 100037, China; zggyhh@163.com (H.Y.); francisfx@126.com (X.F.); hai5987@163.com (H.L.)

<sup>2</sup> Department of Geology and Geological Engineering, University Laval, QC G1V 0A6, Canada; yangchao2012cags@126.com

<sup>3</sup> First Crust Monitoring and Application Center, China Earthquake Administration, Tianjin 300180, China; shaogang\_wei@yahoo.com

<sup>4</sup> College of Earth, Ocean, and Atmospheric Sciences, Oregon State University, Corvallis, OR 97331, USA

\* Correspondence: songyang@mail.cgs.gov.cn; Tel.: +86-010-6899-9087

Received: 9 May 2018; Accepted: 6 September 2018; Published: 10 September 2018

**Abstract:** The newly discovered Tiegelongnan Cu (Au) deposit is a giant porphyry deposit overprinted by a high-sulfidation epithermal deposit in the western part of the Bangong–Nujiang metallogenic belt, Duolong district, central Tibet. It is mainly controlled by the tectonic movement of the Bangong–Nujiang Oceanic Plate (post-subduction extension). After the closure of the Bangong–Nujiang Ocean, porphyry intrusions emplaced at around 121 Ma in the Tiegelongnan area, which might be the result of continental crust thickening and the collision of Qiangtang and Lhasa terranes, based on the crustal radiogenic isotopic signature. Epithermal overprinting on porphyry alteration and mineralization is characterized by veins and fracture filling, and replacement textures between two episodes of alteration and sulfide minerals. Alunite and kaolinite replaced sericite, accompanied with covellite, digenite, enargite, and tennantite replacing chalcopyrite and bornite. This may result from extension after the Qiangtang–Lhasa collision from 116 to 112 Ma, according to the reopened quartz veins filled with later epithermal alteration minerals and sulfides. The Tiegelongnan deposit was preserved by the volcanism at ~110 Ma with volcanic rocks covering on the top before the orebody being fully weathered and eroded. The Tiegelongnan deposit was then probably partly dislocated to further west and deeper level by later structures. The widespread post-mineral volcanic rocks may conceal and preserve some unexposed deposits in this area. Thus, there is a great potential to explore porphyry and epithermal deposit in the Duolong district, and also in the entire Bangong–Nujiang metallogenic belt.

**Keywords:** tectonic control; overprinting; preservation; vein-filling; replacement; porphyry; epithermal; Tiegelongnan; Tibet

## 1. Introduction

In the past two decades, some large porphyry deposits have been found in Tibet, China, such as Yulong deposit (6.22 Mt at 0.99% Cu) [1], Qulong deposit (7.1 Mt at 0.5% Cu) [2], Jiama deposit (7.4 Mt at 0.5% Cu) [3], Duobuza deposit (2.9 Mt at 0.46% Cu) [4], and Bolong deposit (3.8 Mt at 0.5% Cu) [5]. This indicates that Tibet can be considered one of the most significant potential porphyry Cu systems in the world. Recently, epithermal deposits have also been discovered and reported in Tibet. Epithermal deposits are genetically associated with porphyry Cu deposits, especially high and intermediate sulfidation epithermal ones, which could be discovered at upper or lateral locations of

porphyry deposits in some cases [6]. However, the epithermal deposits do not always occur close to porphyry deposits, because epithermal deposits are normally at shallow crustal levels (surface to 1–2 km depth), therefore they could be easily eroded by later orogenesis [6].

The Duolong porphyry Cu–Au district is located in the Bangong–Nujiang metallogenic belt (BNMB), central Tibetan Plateau, which was discovered in 2007 and hosts several large porphyry and epithermal deposits and ore prospects (Figure 1). The Tiegelongnan deposit was discovered in 2013, containing the largest scale Cu resource within this district, and it was documented as a porphyry Cu (Au) deposit overprinted by high-sulfidation mineralization [7]. The total Cu content persevered in the Tiegelongnan deposit is around 1600 Mt at 0.51% Cu. The Au content is small at about 280 Mt with a low grade of 0.13g/t Au on average.

Despite numerous studies on the metallogeny of the Tiegelongnan deposit, the tectonic control of this type deposit has rarely been demonstrated. Formation of the porphyry and epithermal deposits in the Duolong district was indicated to be associated with the magma arising from the closure of the Bangong–Nujiang Ocean (BNO) in the Early Cretaceous [8,9]. However, how the tectonic activities control the formation of the porphyry Cu system is controversial. The Tiegelongnan deposit is the first high-sulfidation epithermal deposit being discovered in the Tibetan Plateau. Previous studies suggested that the limited number of epithermal deposits found in the Tibetan Plateau is due to the dramatic uplift and deep level erosion. The Tiegelongnan deposit is an example to study the tectonic control, reconstruction and preservation process of porphyry Cu systems in the Tibetan Plateau. In this study, we reviewed history of the tectonic setting, magma emplacement, multiple episodes' mineralization, exhumation, and preservation of the Tiegelongnan deposit, based on published literatures and the detailed drill core logging and deposit 1:500 scale mapping. Besides, we discussed the implications of this study on exploration of porphyry and epithermal deposits in the Duolong district and other places in Tibet.

## 2. The Duolong District

The Duolong ore district is located approximately at 100 km northwest of Gerze county, on the western BNMB (Figure 1). This belt is supposed to be a suture zone as the remnants of the Bangong–Nujiang Ocean (BNO) which records the evolution of the BNO during the period of Permian to Cretaceous. This belt is over 2000 km-long striking to the east, and it is dominated by Jurassic–Cretaceous flysch, mélangé, and ophiolitic fragments [10,11]. The Bangong–Nujiang suture zone extends across the central Tibetan Plateau, which separates the Qiangtang and Lhasa terranes (Figure 1a) [12,13].

There are several porphyry deposits, epithermal deposits, and porphyry and epithermal ore prospects in the Duolong district (Figure 1). The Duobuza [4], the Bolong [5], and the Naruo [14] are porphyry Cu (Au) deposits. Whereas, the Tiegelongnan deposit is a porphyry deposit overprinted by epithermal deposit [7,15]. In the Dibao, Nadun, Sena, Saijiao, and the Ga'erqin areas, there are porphyry or epithermal ore prospects (Figure 1b). Li et al., (2011) and Lin et al., (2017) suggested these deposits are related to granodiorite and quartz diorite porphyry intrusions being emplaced during 123–116 Ma, and their mineralization timing is between 120 Ma and 118 Ma [16,17].

The intrusions in the Duolong district are dominated by intermediate to felsic rocks with minor gabbro. The granodiorite porphyry and quartz-diorite porphyry are more widespread than other rock types—including diorite, granodiorite, and gabbro. The porphyry and epithermal deposits in the Duolong district are hosted by the granodiorite and quartz diorite porphyries, and also by the contact zone between these intrusions and the Jurassic quartz-feldspar sandstones. Volcanic rocks like basalt, andesite, and basaltic andesite are also widespread in the Duolong district. These volcanic rocks in this district all belong to the Meiriqiecuo Formation ( $K_1m$ ) unconformably overlying on the sedimentary rocks.

The sedimentary sequences in the Duolong ore district are dominated by Mesozoic pelagic sediments and Cenozoic continental sediments including conglomerates and sandstones.

These sequences are composed of the Upper Triassic Riganpeicuo Formation ( $T_{3r}$ ), the Lower Jurassic Quse Formation ( $J_{1q}$ ), the Lower to Middle Jurassic Sewa Formation ( $J_{1-2s}$ ), the Upper Cretaceous Abushan Formation ( $K_2a$ ), and the Upper Oligocene Kangtuo Formation ( $E_3k$ ). The Riganpeicuo Formation dominated by limestone is unconformably overlain by the Quse and Sewa formations. The Quse Formation mainly occurred in the center and southwestern part of the ore district as the main host formation of the Duobuza and Bolong porphyry deposits. It conformably contacts with the overlying Sewa Formation, which is the predominant host formation of the Tiegelongnan deposit. These two Jurassic formations are thought to be part of the metamorphosed accretionary complex formed by north-dipping subduction of the BNO plate under the Qiangtang terrane [18]. They were also interpreted to be bathyal to abyssal flysch succession, implying a stable shallow-marine continental-shelf sedimentary environment along the southern continental margin of the South Qiangtang terrane [10]. Furthermore, Wei et al. (2017) [9] proposed that a continental margin arc setting in the southern Qiangtang terrane during the Early Cretaceous.

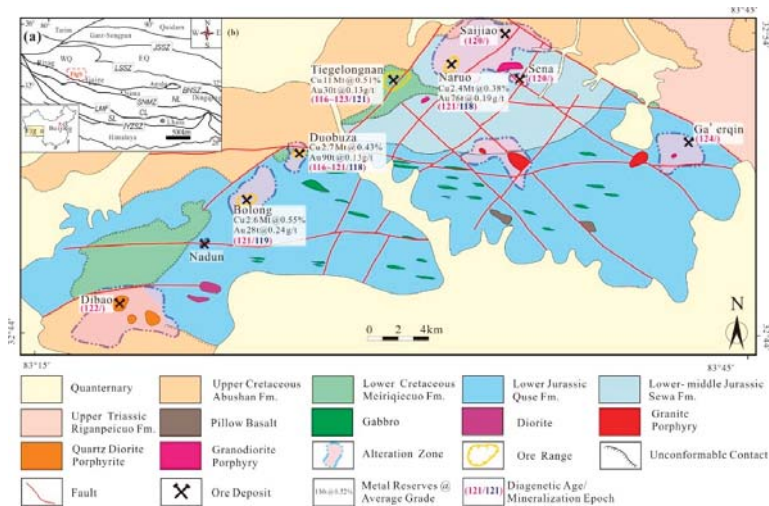


Figure 1. Regional geological map of the Duolong ore cluster, modified after [8], ages are from [17].

There are three main faults in the Duolong district striking at NE–SW, E–W, and NW–SE, respectively (Figure 1). The NE–SW fault is a major ore-controlling structure. A number of ore-bearing granodioritic porphyry intrusions emplaced along this fault, and therefore, many large porphyry copper deposits such as the Bolong, Duobuza, Tiegelongnan, and Naruo deposits occurred.

Most E–W thrust faults are large scale and traverse across the entire Duolong district, dipping to the south with an angle between  $49^\circ$  and  $16^\circ$  [19]. There are some granodiorite porphyries (125–120 Ma, unpublished data) beaded along this NE–SW fault. A mylonite sample obtained from the fault zone was well constrained with a  $^{40}\text{Ar}/^{39}\text{Ar}$  plateau age at  $127.8 \pm 1.1$  Ma [19], which represents an early period of thrusting. The NW–SE faults are normal slip faults dipping to the south, which might be related to the neo-tectonic movements. These faults are characterized by sunken landform and valleys with fault breccia exposed.

### 3. Tiegelongnan Alteration and Mineralization

The Tiegelongnan deposit is hosted by the Sewa Formation quartz-feldspar sandstones and some intermediate and felsic porphyry intrusions. These rocks were mostly concealed by the andesite of the Meiriqiecuo Formation which is currently well exposed (Figure 2a). The earliest diorite porphyry within this deposit was intruded at 123 Ma before the mineralization, which is mainly distributed

at the eastern and southern margins of this area [8]. Several phases of granodiorite porphyries are syn-mineral intrusions with ages ranging from 121 Ma to 116 Ma [8,20,21]. They are indistinguishable from petrology and crosscutting relationships, because subsequent strong alteration weakened their differences and boundaries. Therefore, the geochemistry data, especially the mobile elements, could not be used to discriminate their geochemical features.

3.1. Alteration

Drill core logging reveals concealed features of the Tiegelongnan deposit (Figure 2b). Five phases of hydrothermal alteration were identified in the Tiegelongnan deposit, according to the dominant alteration mineral assemblage, including: biotite alteration, sericite-pyrite-quartz (phyllitic) alteration, chlorite alteration, alunite alteration, and kaolinite-dickite alteration [22]. Alunite-kaolinite-dickite assemblages are also named as advanced argillic alteration in high-sulfidation epithermal deposits [23].

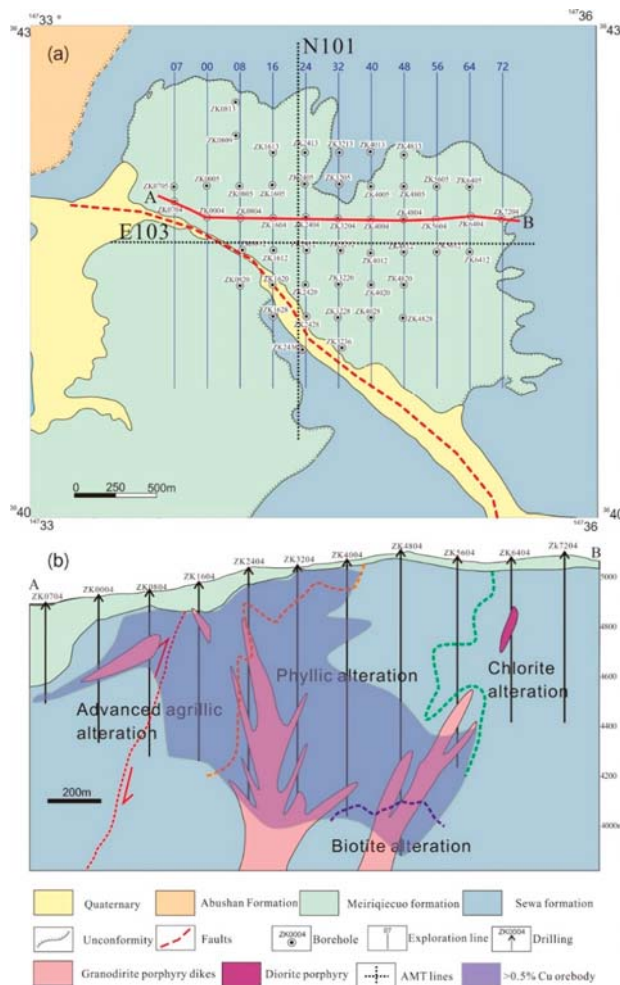
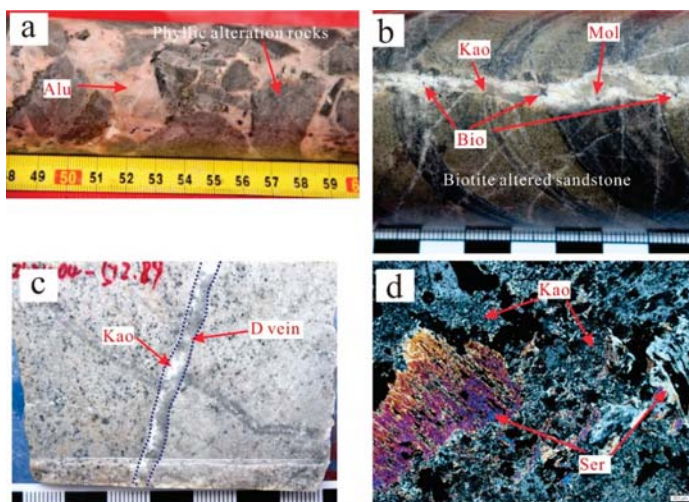


Figure 2. Ground surface and cross-section map of the Tiegelongnan porphyry Cu (Au) deposit.

Hydrothermal biotite occurs in wall-rock sandstones beneath an elevation of ~4100 m as disseminated fine grains and less commonly as vein biotite-quartz. It is not typical potassic alteration with no K-feldspar, and rare magnetite, rutile, and anhydrite. Sericite-pyrite-quartz (phyllic) alteration is widespread in the Tiegelongnan deposit, hosting most of the ore minerals. These granodiorite porphyries and their surrounding sandstones are mostly altered to sericite and quartz. Some fluorite, rutile, anhydrite, and magnetite can be identified under the microscope. There are some quartz-chalcopyrite-pyrite and quartz-molybdenite veins occurring in the phyllic alteration zone, not intensely. Chlorite alteration is in the southern and eastern part of the deposit, which scattered in the sandstone and diorite and pyrite-chlorite veins. Alunite mostly occurs in the alunite-sulfides veins, locally with kaolinite and dickite, distributed in a narrow and shallow place at a height ranging from 4500 m to 4950 m. Kaolinite-dickite alteration occurs as more widespread kao-dic veins than the alunite veins, which is featured with kaolinite replacing sericite (fine grained muscovite) grains. Except for those minerals, some pyrophyllite occurs in the sericite-pyrite-quartz alteration zone, and the rutile is widespread from the biotite alteration to alunite alteration zones. Biotite, sericite, and chlorite are typical porphyry stage alteration minerals [24]. It is typical that these porphyry alteration stage minerals are overprinted by epithermal alteration minerals in the Tiegelongnan deposit, and these minerals formed in different occurrences, such as breccia, vein-filling, or as replacement, which corresponds with the multiple dating results on the altered minerals. Biotite and sericite display a  $^{40}\text{Ar}$ - $^{39}\text{Ar}$  age at ~121 Ma, whereas alunite indicates the age ranging from 117 to 100 Ma [21]. Alunite-kaolinite-dickite breccia is late epithermal stage products, breaking earlier phyllic altered rocks (Figure 3a). Kaolinite-dickite veins cut the early phyllic and biotite alteration stages' quartz-sulfide veins. However, they are most commonly shown as kaolinite filling in biotite veins (Figure 3b), and kaolinite fills the barren quartz-pyrite veins in phyllic alteration zone (Figure 3c). Kaolinite also replaces fine muscovite grains in the phyllic alteration zone (Figure 3d). In some cases, a mineral sequence is shown as a single vein, firstly with quartz crystalizing, followed by alunite alteration, and ending up with kaolinite crystalized in the center of the vein. This alunite, kaolinite, and dickite assemblage was documented as acidic minerals and epithermal products in condition of low temperature and low pH value [25].



**Figure 3.** The epithermal alteration overprinted on the porphyry alteration. (a) Alunite breccia break phyllic altered and mineralized host rocks, (b) kaolinite vein crosscutting biotite altered host rocks and filling in biotite-molybdenite vein, (c) kaolinite filling in cavity of quartz-pyrite vein, (d) sericite replaced by kaolinite grains. Alu: alunite, Bio: biotite, Ser: sericite, Kao: kaolinite, Mol: molybdenite.



### 3.2. Mineralization

Chalcopyrite, bornite, and pyrite are sulfide assemblage precipitating in biotite and phyllic alteration zone with minor molybdenite, whereas the Cu (Fe)-As-S minerals enargite, tennantite, and Cu-S covellite, digenite are the dominant sulfides in advanced argillic alteration zone [26,27]. Chalcopyrite and bornite in the biotite and phyllic alteration zone are the main Cu mineralization of the porphyry stage, including quartz-chalcopyrite ± bornite veins and disseminated chalcopyrite and bornite. This is the main porphyry Cu orebody, hosted as quartz-sulfides veins, and disseminated sulfides in wall rocks. The enargite-tennantite-covellite-digenite assemblage mostly occurs in the alunite and kaolinite alteration zone, which are the products of the high-sulfidation epithermal Cu orebody [8]. Epithermal stage Cu sulfides are mainly presented as alunite-kaolinite-sulfides veins.

These two stages of sulfide mineral assemblages display a complicated overprinting and cross-cutting relationship. Kaolinite-sulfide veins crosscut quartz veins (Figure 4a), those sulfides are mostly Cu (Fe)-(As)-S minerals, also some chalcopyrite and bornite were reported as result of solid solution from those minerals [25]. Under the microscope, we find some enargite filling in the fractures of quartz veins along with kaolinite. The pyrite occurs as early phyllic alteration product, because it is the most easily being replaced by the enargite. Replacement textures of chalcopyrite, bornite, and pyrite affected by Cu (Fe)-As-S and Cu-S minerals are common in the Tiegelongnan deposit. The pyrite is replaced from the edge firstly by bornite, and then the bornite is replaced by digenite and covellite (Figure 4b). Enargite and tennantite replace chalcopyrite (Figure 4c). There are some arguments that replacement relationship between sulfides is supergene replacement textures, because covellite and digenite are typical supergene sulfides also. However,  $\delta^{65}\text{Cu}$  of covellite and digenite in the Tiegelongnan are averaging at 0.25‰ [28], which is similar to the hypogene copper sulfides  $\delta^{65}\text{Cu}$  value [29]. In some cases, the Cu (Fe)-As-S and Cu-S minerals are filled in the fractures instead of replacing Fe-bearing minerals (Figure 4d), which might indicate a brittle force condition before the epithermal mineralization. This corresponds with the alunite and kaolinite breccia in Figure 3a. The Cu (Fe)-As-S and Cu-S sulfides even cut through post-mineral porphyry and breccia rocks. Generally, overprinting of the Cu (Fe)-As-S and Cu-S on chalcopyrite-bornite-pyrite assemblage is common in the Tiegelongnan deposit, and it was demonstrated in different occurrences, including the former replacing the latter minerals, the former filling in fractures of the latter sulfides, and the former cutting the chalcopyrite-bornite mineralized rocks or veins.

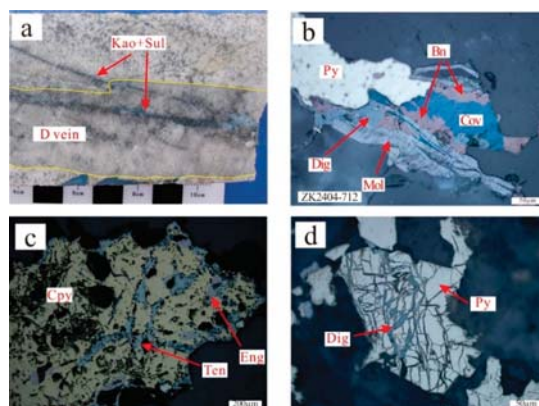


**Figure 4.** Textures of epithermal sulfides overprinting porphyry sulfides. (a) Kaolinite-sulfide veinlets cross-cut quartz-pyrite veins, (b) later covellite and digenite replacing bornite and pyrite, (c) tennantite and enargite replacing chalcopyrite, (d) pyrite fractures filled with digenite. Bn: bornite; Cpy: chalcopyrite, Cov: covellite, Dig: digenite, Eng: enargite, Mol: molybdenite; Kao: kaolinite, Py: pyrite, Sul: sulfides, Ten: tennantite.

#### 4. Structures

The Tiegelongnan deposit and most of other deposits in the Duolong district are along the NE–SW faults. It is widely accepted that these faults mainly controlled the emplacement of magma and hydrothermal fluids in the Duolong district [30]. However, there were few convincing studies clarifying the overlying volcanic rocks which conceal the whole porphyry and epithermal ore bodies. The NW–SE faults, named as Rongna Fault, are characterized by geomorphologically linear sunken terrain, valleys, with fault springs seen at the ground level. In the deposits area, the fault occurred as a river valley, which is called the Rongna Valley (Figure 5). The fault divides the Meiriqiecuo Formation andesite into two parts, suggesting the structural movement took place after andesite eruption, which is dated at ~110 Ma [8].

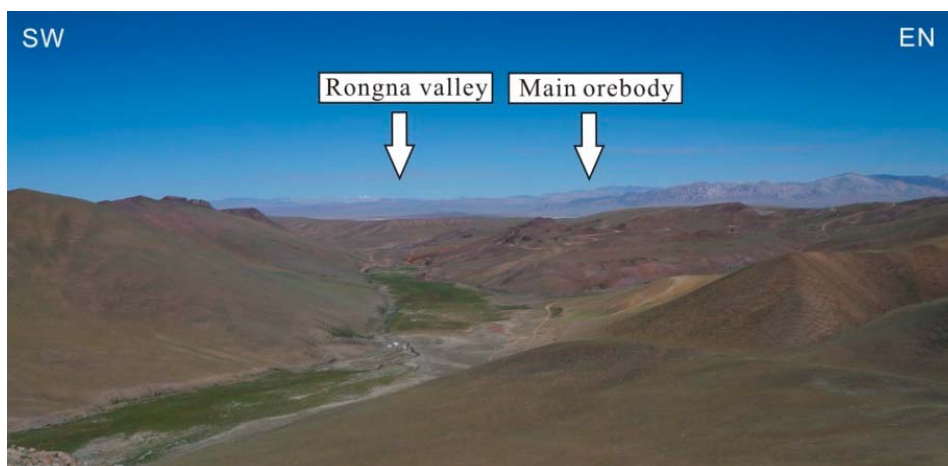


**Figure 5.** Rongna Valley, topography of the Rongna fault in the Tiegelongnan deposit.

The audio-frequency magneto-telluric method (AMT) was applied to understand the fault features, and further to predict the occurrences of the orebody in a deep level on the south side. From the ATM tests, electrical properties of different rocks obviously vary from each other in the Tiegelongnan deposit. The Cretaceous volcanic cap-rocks have low polarizability, whereas extremely high resistivity is shown in the paleo-weathering crust. The Jurassic sandstone showed low resistivity and high polarization, while the advanced argillic altered sandstone has high resistivity. We found the >0.5% grade Cu whole porphyry and epithermal orebodies correspondent with the low resistivity zone (Figure 6). There are two low-resistivity anomalies (C1 and C2) in the E103 AMT cross-section and the C1 anomaly coincides with the explored orebody. Therefore, the C2 low-resistivity anomaly could be another part of the whole orebody. The fault plane shown in the AMT cross-section is dipping to the south with an angle of 70° to 80° (Figure 6).

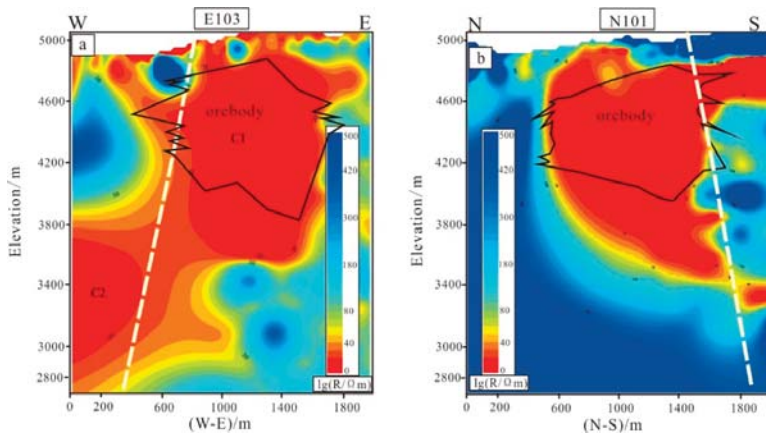


**Figure 6.** 2D inversion resistivity section of the audio-frequency magneto-telluric method (AMT) test (a) north-south cross-section; (b) east-west cross-section.

**5. Post-Mineral Weathering and Erosion**

The epithermal Cu (Au) mineralization orebody found by diamond drilling is covered by the Meiriqiecuo Formation volcanic rocks (Figure 7a). The dome-shaped and gently dipping andesite layer was discovered by drilling at an elevation of 5110–4930 m above sea level at the ground surface and 5080–4620 m at the bottom. The average thickness of the andesite is 90 m, thinning from southwest to northeast (Figure 7b).

A layer of weathered paleosol is observed between the andesite and the underlying porphyry and epithermal Cu (Au) orebodies, which suggests that prominent weathering occurred after mineralization before the overlying andesite. Three types of erosional surfaces are recognized (Figure 8). The first type is a weakly weathered eluvium without movement, containing detrital sandstone, with some malachite and azurite. The second type of erosional surface is residual ancient soil, defined as a complex of clay soil and illuvial soil with a small amount of debris, which is generally formed in the watershed or on slope landforms. The third type is slope washes, which is weakly weathered eluvial material transported by water, accumulated on a slope, and incorporated rounded fragments of the basement. Slope washes form in the transitional area between erosional and depositional zones in this area.

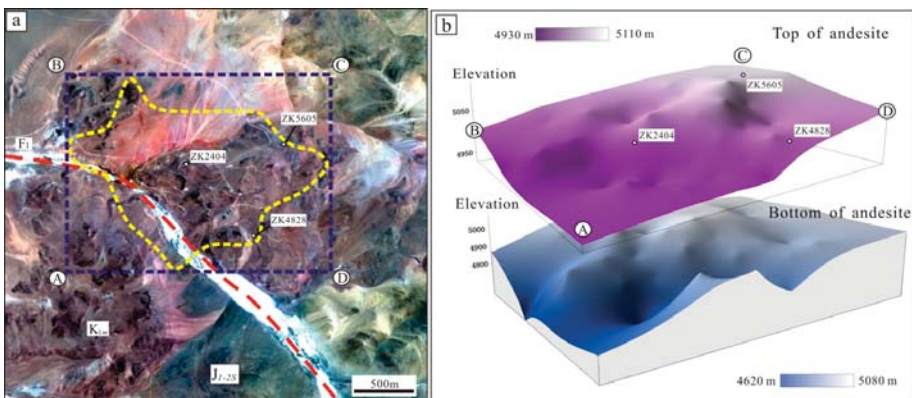


**Figure 7.** (a) High-resolution remote sensing image, and (b) a 3-D map of the Meiriqiecuo Formation andesite [31]. Red dotted lines: faults; the yellow dotted line: the boundary of the mineralized body.

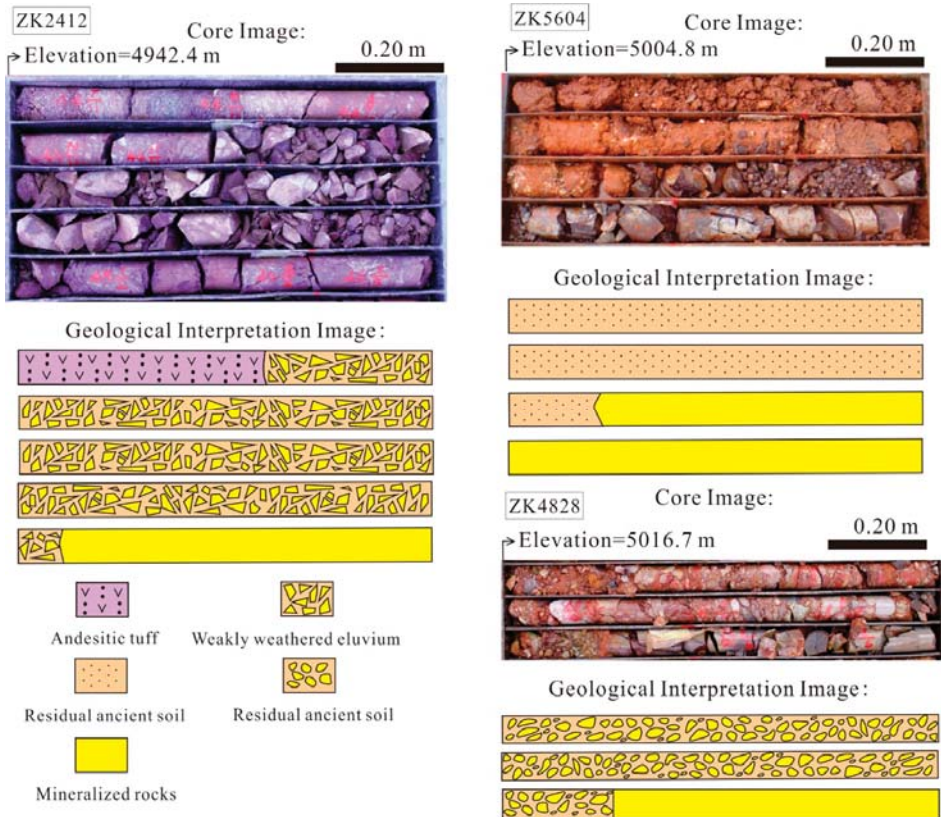


**Figure 8.** Photographs of typical weathering paleo-crusts in the Tiegelongnan deposit. ZK2412—The first type weathering weakly weathered eluvium. ZK5604—The second type weathering residual ancient soil. ZK4828—The third type weathering slope washes.

## 6. Discussion

### 6.1. Magmatism Indication of Tectonic Setting in the Duolong District

The Bangong–Nujiang ocean crust has started subducting northwards beneath the southern Qiangtang terrane since the Middle Jurassic. This leads to the formation of the large intermediate to felsic magmatic arc that emplaced inboard of the southern continental margin of the south Qiangtang terrane in the Middle to Late Jurassic (170–145 Ma) [32–36]. Some authors argued that the Bangong–Nujiang oceanic crust may subduct in two directions, both northward beneath southern Qiangtang Terrane and southward beneath northern Lhasa Terrane, respectively [36,37]. From 145 to 130 Ma, however, there is a noticeable magmatic gap in the southern Qiangtang terrane. Similar magmatic gaps occur in the Andes [38] and southern Gangdese areas [39] in response to the low-angle or flat-slab subduction of the oceanic crust. After that, the Bangong–Nujiang oceanic basin was closed. Although the closure time is controversial, it is generally as accepted as the period from Middle Jurassic to Late Cretaceous [12,40–43]. Recent research narrowed the closure time within 10 Ma from 140 Ma to 130Ma [37]. Based on the time constraints, it suggests that the collision between the Qiangtang and Lhasa terranes occurred through an arc–arc ‘soft’ collision from the east to the west after the BNO closure [32,40,41]. The Jurassic to Lower Cretaceous (<125 Ma) marine sedimentary rocks were

transposed, intruded by granitoids, and were uplifted above sea level before around 118 Ma [40]. The extensive magmatism in the Duolong district is associated with the Qiangtang–Lhasa collision event [9,37].

Numerous igneous rocks such as gabbro, basalt, basaltic andesite, andesites, rhyolite, and intermediate to felsic porphyries are widely distributed in vicinity of the Tiegelongnan deposit. Zircon U–Pb ages of the porphyry intrusions in the Tiegelongnan deposit range from 115.9 Ma to 123.1 Ma, which is consistent with the mineralization (molybdenite Re–Os) ages ( $119.0 \pm 1.4$  Ma [20];  $121.2 \pm 1.2$  Ma [8]). This is also consistent with porphyry intrusions and mineralization ages of other deposits in the Duolong district, such as Bolong and Duobuza deposits [17]. They are temporally associated with this younger generation of magmatic emplacement which is related with the Qiangtang–Lhasa collision. Intrusion rocks geochemistry and isotope studies have been conducted to understand the genetic association between those porphyry deposits and tectonic settings. Geochemistry data mostly obtained from the ore-bearing porphyritic intrusions in the Duolong district indicate they are magmatic rocks and adakite-like rocks [11,14,44,45]. They have relatively high oxygen fugacity ( $f_{O_2}$ ) and high H<sub>2</sub>O contents that are critical to the formation of porphyry and epithermal deposits [46]. During the process of magma upwelling, adakite-like melts might get mixed with large amount of copper and other metals and sulfur from either interaction with hot peridotite in the mantle wedge region [47] or mixing with mantle-derived melts [48]. It eventually resulted in mantle-derived juvenile materials, which are thought to bring heat and materials to generate juvenile mafic lower crust. The magmas experience various degrees of fractional crystallization and crustal contamination during its emplacement, when it is derived from the remelting of the juvenile mafic lower crust as a result of previous arc magmatism. Some of these hybrid magmas formed calc-alkaline ore bearing porphyries via the shallow magma emplacement, leading to the formation of giant porphyry and epithermal Cu (Au) deposits [49–52].

The Jurassic (170–145 Ma) intermediate–felsic intrusive rocks of the southern Qiangtang terrane primarily exhibit negative whole-rock  $\epsilon_{Nd}(t)$  and zircon  $\epsilon_{Hf}(t)$  and old Hf isotope crustal model ages, indicating that those Jurassic rocks were largely derived from mature or recycled continental crust materials [35,36,53]. This is compatible with what been observed in the Early Cretaceous Fuye pluton, Caima pluton and Qingcaoshan pluton in the Qiangtang Terrane [53]. In contrast,  $\epsilon_{Nd}(t)$  and  $\epsilon_{Hf}(t)$  value and Hf isotope model ages of the Early Cretaceous (~126–116 Ma) magmatic rocks from the Duolong district indicate they were probably derived from magma as a mixture of the juvenile lower crust and mature crustal materials [9]. In addition, previous studies on Pb isotopic compositions of the porphyry intrusions, sulfides, and sulfate in the Tiegelongnan deposit suggest that the Pb of this deposit is mainly derived from a crust–mantle mixed subduction zone [26,54,55].

Although there is no specific research on the geochemistry of the porphyry intrusions in the Tiegelongnan deposit, owing to their strong alteration and leaching erasing its geochemical signature, the features of the intrusions in the Duolong district could represent that in the Tiegelongnan deposit. Thus, it suggests that plenty of juvenile crust materials are involved in the intrusions in the Tiegelongnan porphyry Cu (Au) deposit. The juvenile crust materials have been becoming gradually dominated during the Late Mesozoic since the vertical growth and thickening of the continental crust of the southern Qiangtang terrane during the Early Cretaceous [9,56]. It is commonly accepted that variable sources conjunctly contributed to the formation of magma in this district [53]. The dominant crust signature from radiogenic isotopes is reported as features of the post-subduction products, which is well explained by Richards (2009) [57]. All of these suggest that magmatism and mineralization of the Tiegelongnan porphyry Cu (Au) deposit probably occurred in an active continental margin environment after the subduction of BNO plate, as result of continental crust thickening and terranes collision (Figure 9).

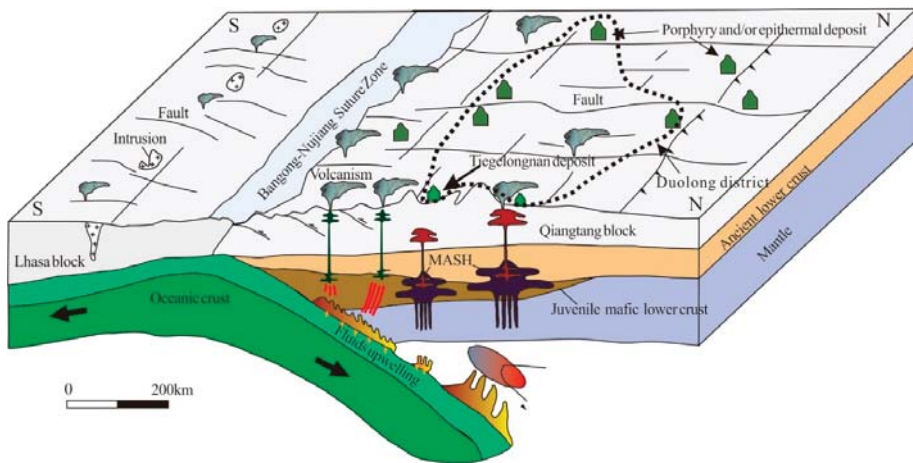


**Figure 9.** Tectonic setting model for the formation of the Duolong deposit, Tibet.

### 6.2. Tectonic Reconstruction of Epithermal Overprinting Porphyry

The continental crust thickening resulted from the Qiangtang–Lhasa collision might be the reason for the emplacement of magma and formation of porphyry deposits in the Duolong district. An extensional condition is common during the post-subduction stage of two plates or terranes [57], thus Sillitoe and Hedenquist (2003) explained that some arcs are subjected to neutral stress condition or mild extension where high-sulfidation epithermal deposits formed [23]. This might be one of the reasons that porphyry mineralization is overprinted by epithermal mineralization in the Tiegelongnan deposit. Besides, water table decline is another possible reason for epithermal mineralization formed at deep level where porphyry mineralization formed earlier at depth [58]. The paleosol occurred between the whole mineralization Cu orebody and the overlying andesite in the Tiegelongnan deposit indicates weathering and erosion took place before andesite covering at 110 Ma, which is possible to decrease the water table. Furthermore, fluid inclusion pressure evidence suggests that rapid mountains lifting and erosion took place between two stages of porphyry intrusions at 121 and at 116 Ma respectively in the Tiegelongnan deposit [22]. The occurrences of overprinting of epithermal on porphyry alteration and mineralization in the Tiegelongnan deposit are mainly characterized by veins and fracture filling, and the replacement between the typical minerals of two episodes. From the absolute geochronology data, alunite was formed between 117 and 100 Ma, which postdates the ages of biotite and sercite at 121 Ma [21]. Early formed veins were reopened under an extensional situation, giving channels for later epithermal fluids. Reopening of early formed textures can improve rock permeability. It enables magmatic-hydrothermal fluid to cool with low temperature isotherm dropping. When the isotherm line decline to deep level of earlier formed porphyry deposit, epithermal minerals formed and replaced porphyry minerals. Specifically, the low temperature minerals alunite and kaolinite and high sulfidation state sulfides (tennantite, enargite, digenite, covellite, etc.) precipitated and replaced porphyries stage alteration and sulfide minerals at a higher temperature and in a deeper level. Although most porphyry deposits are formed in convergent and compressive settings [49], high sulfidation epithermal can be generated in calc-alkaline andesitic-dacitic arcs under neutral stress or mild extension conditions [23]. During the formation of this porphyry and epithermal deposit, the extensional strain in the Duolong district might be related with the Bangong–Nujiang subduction zone retreating after the BNO closure [9,10,44].

During the epithermal stage, some breccia formed, and straight veins break phyllic altered rocks, indicate that epithermal events overprinting on the porphyry events. Plenty of breccia implies that rocks are brittle in the epithermal stage. Hydrothermal processes in ductile and brittle rocks in a

magmatic–epithermal environment study suggest that the ductile–brittle transition commonly occurs about 370–400 °C [59]. This is higher than epithermal hydrothermal fluid temperature 160–270 °C [6]. Therefore, before epithermal events taking place, the wall rocks of the Tiegelongnan deposit is brittle and could be easily broken by the accumulation of hydrothermal fluid or by fault events in the Duolong district. This gives access to epithermal fluid arriving at shallow sites, and overprints porphyry system along those faults, fractures, and other opened space.

### 6.3. Post-Mineral Erosion and Preservation

The crust thickening and terranes collision in the Bangong–Nujiang suture zone, combining with later coming India–Asia plate collisions, resulted in rapid uplifting and erosion of the deposits in the Duolong district. It also affects the uplifting and erosion of most parts of the Tibetan Plateau [33,41]. The large-scale uplift was activated by the Lhasa–Qiangtang collision [60,61], that resulted in the angular unconformity contact between the continental Abushan Formation and the underlying marine sediments [33]. The erosion of the Tiegelongnan deposit happened right after its formation, which is observed from the weathered rocks under the andesite. The fluid inclusion study suggested the eroded layers may reach a thickness of 600–1200 m before cover of the andesite at 110 Ma [27]. In the following exhumation rate calculations, the youngest formation age of the Tiegelongnan deposit was used at ~118 Ma dated from the molybdenite. The exhumation rate of ground surface increased with the elevation [62] and it has functional relationship with elevation. The smallest exhumation thickness and interval of the protection can be used to calculate the smallest exhumation rate. Thus the Tiegelongnan deposit has experienced exhumation for 6 to 7 m.y. and the exhumation rate is 0.1–0.2 mm/y.a, averagely at 0.15 mm/y.a. This is consistent with the common exhumation rate of the epithermal deposit at ~0.167 mm/y.a, and the porphyry deposit at 0.158 mm/y.a [63].

Northern Tibet has been elevated more than 5000 m, and it is continuously affected by the India–Asia collision system, thus leading to a more intensive exhumation than other parts of Tibet, while the southern Tibetan Plateau attained a 3–4 km elevation at ~99 Ma [64]. The Tiegelognan deposit was overlain by the andesite after small interval of exhumation which protected the Tiegelongnan deposit from totally erosion. The erosion after andesite settle is still non-negligible. The apatite HeFTy program [65] was used to model the prolonged thermal history of the Tiegelongnan deposit [66]. It suggested that the Tiegelongnan deposit has experienced four cooling stages: (i) relatively slow cooling from Early Cretaceous to Late Cretaceous (120–75 Ma); (ii) fast cooling in Late Cretaceous (75–60 Ma); (iii) moderately fast cooling from Eocene to Oligocene (45–30 Ma); (iv) very fast cooling since Late Miocene (<7.8 Ma). The exhumation thickness is at least 3600 m since Late Cretaceous in the Duolong district. Yin et al., (2000) and Kapp et al., (2007) reported the subsequent India–Asia collision led to 1400 km of shortening within recent 70 m.y. [40,41]. The andesite has a thickness of ~500 m [67], which is not thick enough to withstand that intensive exhumation. Therefore, the andesite is not the solely protective cover for the Tiegelongnan deposits. Post-mineral sediments, such as the Upper Cretaceous Abushan Formation ( $K_2a$ ) and the Upper Oligocene Kangtuo Formation ( $E_3k$ ), might also act as significant caps for protecting orebodies.

Along with the thickening of the continental arc, collapse of the crust may destruct the whole porphyry and epithermal Cu (Au) orebodies. The Rongna Fault might be the result of the collapse of the accumulated crust rocks. The inversion resistivity cross-section in Figure 6a showed that a normal high angle fault breaks the high resistivity zone into two separated C1 and C2 zones. It also cuts through the andesite from the Rongna Valley, and may dislocate and conceal the western part of the Cu (Au) orebody to deeper places.

A simplified model (Figure 10) was applied to describe the porphyry Cu system in the Tiegelongnan deposit. Epithermal Cu (Au) mineralization veins are mostly retained in the advanced argillic alteration zone, which overprints phyllic alteration zone on top of porphyry Cu orebody (Figure 10a). This is a transitional zone between the disseminated high-sulfidation epithermal precious metal deposit and the porphyry Cu (Au) orebody (Figure 10b). There might have been disseminated

epithermal precious metal deposit existing in theory. The reason of not being detected on the deposit is that it either was not well preserved because of severe erosion or has not been found yet. Deep in the porphyry Cu (Au) system, the bottom of the porphyry Cu orebody has not been detected yet. We suggest there could be economic potential at depth, because biotite alteration is shown at depth, if it could represent the typical potassic alteration, which usually is the core of mineralization orebody in the porphyry Cu system [68]. Obviously, we did not reveal the whole biotite alteration, which might be concealed at a deeper level.

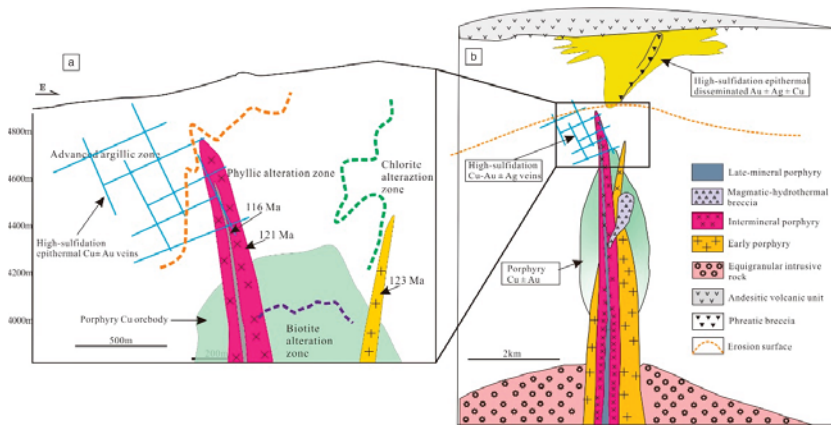


**Figure 10.** (a) Simplified geology map of the A-B sections in Tiegelongnan [31]. (b) Anatomy of a condensed porphyry Cu system showing the spatial interrelationships of porphyry Cu orebody, high-sulfidation epithermal Cu ± Au orebody, and late-mineralization andesitic volcanic rocks [31].

## 7. Implications and Conclusions

The geological history of the Tiegelongnan deposit is as follows: (i) Early Jurassic active continental margin sandstone (pre-mineral stage); (ii) emplacement of multiple porphyry intrusions and formation of the porphyry ore system (first mineral stage); (iii) overprinting of epithermal alteration and mineralization (second mineral stage); (iv) weathering and erosion ( $\geq 600$  m) and volcanic extrusion (preservation); (v) continuous lifting and erosion/movement of the Rongna fault (dislocation). This process is associated with the movement of the Bangong–Nujiang oceanic plate, following Qiangtang–Lhasa terranes collision and the effect of the India–Lhasa terranes subduction and collision. Marine sandstone was deposited before or during subduction of the oceanic plate in Jurassic. Igneous rocks emplacement and eruption are the results of the subduction of oceanic plate during 170–145 Ma, and the Qiangtang–Lhasa terrane collision between 126 and 116 Ma. Hydrothermal fluid is induced by those porphyry intrusions, and it contributes to porphyry mineralization. Shortly after that, younger stage of epithermal fluid overprinted the porphyry mineralization because of erosion of the system due to the extensional structures at around 116 Ma. With continuous collision of Qiangtang and Lhasa terranes, rapid lifting and strong exhumation partly eroded the ore deposit. Volcanic andesite (~110 Ma) covered on the top of the orebody protects it from entire erosion. Subsequent India and Lhasa plates subduction and collision uplifted the plateau and caused the erosion of those deposits in the Duolong district again. Post-mineral structure such as the Rongna Fault possibly dislocated the main orebody of the Tiegelongnan deposit (Figure 6a).

This review of the Tiegelongnan deposit is significant for the future exploration programs, even for exploration of porphyry and epithermal deposits in the Duolong district or even the Bangong–Nujiang suture zone. The Rongna Fault dislocated the Tiegelongnan deposit in its western part. Another part of the orebody on the hanging wall of the fault might slip southwestward and be concealed



to a deeper domain. The nearly 11 Mt of Cu resource currently being explored might be part of the entire Tiegelongnan porphyry and epithermal Cu (Au) orebody, which is similar to the San Manuel-Kalamazoo porphyry copper deposit in South America [69]. Comparably, we are confident on the great potential of the Tiegelongnan deposit. Further understanding of the dislocation of the Rongna Fault should be conducted later, which would contribute to increasing the ore reserves of the deposit at depth.

The volcanic rocks unconformably overlie on the whole porphyry and epithermal Cu (Au) orebody, which prevents the orebody from being subject to further erosion. This might be the reason for only epithermal copper orebody being found at the top the Tiegelongnan deposit so far, but not anywhere else. There might be epithermal mineralization on the Duobuza and Bolong deposits, but they might be fully eroded away due to the lack of overlying protection. Furthermore, due to the large range of volcanic rocks in the Duolong district, more porphyry and epithermal copper and gold deposits are of great potential to be preserved, and that could be the future exploration direction in the Duolong district.

**Author Contributions:** Y.S. carried out the project and coordinated this study. All authors took part in the field work, analyzed the results and wrote the manuscript; Y.S. and C.Y. mainly revised and edited the paper.

**Funding:** This research was partly funded by the National Key R & D Program of China (No. 2018YFC0604106), the National Natural Science Foundation of China (No. 41402178), and the Chinese Geological Survey Program (DD20160026).

**Acknowledgments:** We thank three anonymous reviewers, the Editor Shi, and the academic editor of *Minerals* Alain Chauvet for their positive and constructive comments that are helpful to improve the manuscript significantly. Qing Zhang from the University of Wollongong provided major contributions to the English editing of the paper.

**Conflicts of Interest:** The authors declare no conflict of interest.

## References and Notes

- Hou, Z.; Xie, Y.; Xu, W.; Li, Y.; Zhu, X.; Khin, Z.; Beaudoin, G.; Rui, Z.; Huang, W.; Luo, C. Yulong deposit, eastern Tibet: A high-sulfidation Cu-Au porphyry copper deposit in the eastern Indo-Asian collision zone. *Int. Geol. Rev.* **2007**, *49*, 235–258.
- Yang, A.; Hou, Z.; White, C.N.; Chang, Z.; Li, Z.; Song, Y. Geology of the post-collisional porphyry copper-molybdenum deposit at Qulong, Tibet. *Ore Geol. Rev.* **2009**, *36*, 133–159. [[CrossRef](#)]
- Zheng, W.; Tang, J.; Zhong, K.; Ying, L.; Leng, Q.; Ding, S.; Lin, B. Geology of the Jiama porphyry copper-polymetallic system, Lhasa Region, China. *Ore Geol. Rev.* **2016**, *74*, 151–169. [[CrossRef](#)]
- Zhu, X.; Li, G.; Chen, H.; Ma, D.; Zhang, H.; Zhang, H.; Liu, C.; Wei, L. Petrogenesis and metallogenic setting of porphyries of the Duobuza porphyry Cu–Au deposit, central Tibet, China. *Ore Geol. Rev.* **2017**, *89*, 858–875. [[CrossRef](#)]
- Zhu, X.; Li, G.; Chen, H.; Ma, D.; Huang, H. Zircon U–Pb, Molybdenite Re–Os and K-feldspar <sup>40</sup>Ar/<sup>39</sup>Ar Dating of the Bolong Porphyry Cu–Au Deposit, Tibet, China. *Resour. Geol.* **2015**, *65*, 122–135. [[CrossRef](#)]
- Hedenquist, J.W.; Arribas, A.; Gonzalez-Urien, E. Exploration for epithermal gold deposits. *Rev. Econ. Geol.* **2000**, *13*, 245–277.
- Tang, J.; Sun, X.; Ding, S.; Wang, Q.; Wang, Y.; Yang, C.; Chen, H.; Li, Y.; Li, Y.; Wei, L.; et al. Discovery of the epithermal deposit of Cu (Au–Ag) in the Duolong ore concentrating area, Tibet. *Acta Geosci. Sin.* **2014**, *35*, 6–10. (In Chinese) [[CrossRef](#)]
- Lin, B.; Tang, J.-X.; Chen, Y.-C.; Song, Y.; Hall, G.; Wang, Q.; Yang, C.; Fang, X.; Duan, J.-L.; Yang, H.-H. Geochronology and Genesis of the Tiegelongnan Porphyry Cu (Au) Deposit in Tibet: Evidence from U–Pb, Re–Os Dating and Hf, S, and H–O Isotopes. *Resour. Geol.* **2017**, *67*, 1–21. [[CrossRef](#)]
- Wei, S.-G.; Tang, J.-X.; Song, Y.; Liu, Z.-B.; Feng, J.; Li, Y.-B. Early Cretaceous bimodal volcanism in the Duolong Cu mining district, western Tibet: Record of slab breakoff that triggered ca. 108–113 Ma magmatism in the western Qiangtang terrane. *J. Asian Earth Sci.* **2017**, *138*, 588–607. [[CrossRef](#)]
- Geng, Q.; Zhang, Z.; Peng, Z.; Guan, J.; Zhu, X.; Mao, X. Jurassic–Cretaceous granitoids and related tectono-metallogenesis in the Zapug–Duobuza arc, western Tibet. *Ore Geol. Rev.* **2016**, *77*, 163–175. [[CrossRef](#)]

11. Li, J.X.; Qin, K.; Li, G.; Xiao, B.; Zhao, J.; Chen, L. Petrogenesis of Cretaceous igneous rocks from the Duolong porphyry Cu–Au deposit, central Tibet: Evidence from zircon U–Pb geochronology, petrochemistry and Sr–Nd–Pb–Hf isotope characteristics. *Geol. J.* **2016**, *51*, 285–307. [[CrossRef](#)]
12. Pan, G.; Wang, L.; Li, R.; Yuan, S.; Ji, W.; Yin, F.; Zhang, W.; Wang, B. Tectonic evolution of the Qinghai-Tibet plateau. *J. Asian Earth Sci.* **2012**, *53*, 3–14. [[CrossRef](#)]
13. Zhu, D.; Zhao, Z.; Niu, Y.; Dilek, Y.; Hou, Z.; Mo, X. The origin and pre-Cenozoic evolution of the Tibetan Plateau. *Gondwana Res.* **2013**, *23*, 1429–1454. [[CrossRef](#)]
14. Ding, S.; Chen, Y.; Tang, J.; Zheng, W.; Lin, B.; Yang, C. Petrogenesis and Tectonics of the Naruo Porphyry Cu (Au) Deposit Related Intrusion in the Duolong Area, Central Tibet. *Acta Geol. Sin.* **2017**, *91*, 581–601. [[CrossRef](#)]
15. Li, J.; Qin, K.; Li, G.; Noreen, J.; Zhao, J.; Cao, M.; Huang, F. The Nadun Cu–Au mineralization, central Tibet: Root of a high sulfidation epithermal deposit. *Ore Geol. Rev.* **2016**, *78*, 371–387. [[CrossRef](#)]
16. Li, G.; Li, J.; Qin, K.; Duo, J.; Zhang, T.; Xiao, B.; Zhao, J. Geology and Hydrothermal Alteration of the Duobuza Gold-Rich Porphyry Copper District in the Bangongco Metallogenic Belt, Northwestern Tibet. *Resour. Geol.* **2012**, *62*, 99–118. [[CrossRef](#)]
17. Lin, B.; Chen, Y.; Tang, J.; Wang, Q.; Song, Y.; Yang, C.; Wang, L.; He, W.; Zhang, L. <sup>40</sup>Ar/<sup>39</sup>Ar and Rb–Sr Ages of the Tiegelongnan Porphyry Cu–(Au) Deposit in the Bangong Co–Nujiang Metallogenic Belt of Tibet, China: Implication for Generation of Super-Large Deposit. *Acta Geol. Sin.* **2017**, *91*, 602–616. [[CrossRef](#)]
18. Li, G.; Duan, Z.; Liu, B.; Zhang, H.; Dong, S.; Zhang, L. The discovery of Jurassic accretionary complexes in Duolong area, northern Bangong Co–Nujiang suture zone, Tibet, and its geologic significance. *Geol. Bull. China* **2011**, *30*, 1256–1260. (In Chinese)
19. Liu, Y.; Wang, M.; Li, C.; Xie, C.; Chen, H.; Li, Y.; Fan, J.; Li, X.; Xu, W.; Sun, Z. Cretaceous structures in the Duolong region of central Tibet: Evidence for an accretionary wedge and closure of the Bangong–Nujiang Neo-Tethys Ocean. *Gondwana Res.* **2017**, *48*, 110–123. [[CrossRef](#)]
20. Fang, X.; Tang, J.; Song, Y.; Yang, C.; Ding, S.; Wang, Y.; Wang, Q.; Sun, X.; Li, Y.; Wei, L.; et al. Formation epoch of the South Tiegelong superlarge epithermal Cu (Au–Ag) deposit in Tibet and its geological implications. *Acta Geosci. Sin.* **2015**, *36*, 168–176. (In Chinese)
21. Yang, C.; Beaudoin, G.; Tang, J.; Song, Y. An extreme long life span of porphyry and epithermal Cu deposit: The Tiegelongnan deposit, Tibet, China. 2018; in preparation.
22. Yang, C.; Beaudoin, G.; Tang, J.; Song, Y. Geology and genesis of Tiegelongnan porphyry and epithermal base metal deposit in Duolong district, Tibet, China: From stable isotope and fluid inclusions constrains. 2018; in preparation.
23. Sillitoe, R.H.; Hedenquist, J.W. Linkages between volcanotectonic settings, ore-fluid compositions, and epithermal precious metal deposits. *Spec. Publ. Soc. Econ. Geol.* **2003**, *10*, 315–343.
24. Seedorff, E. Porphyry deposits: Characteristics and origin of hypogene features. *Econ. Geol.* **2005**, *29*, 251–298.
25. Stoffregen, R. Genesis of Acid-Sulfate Alteration and Au–Cu–Ag Mineralization at Summitville, Colorado. *Econ. Geol.* **1987**, *82*, 1575–1591. [[CrossRef](#)]
26. Wang, Y.; Tang, J. The First Discovery of Colusite in the Tiegelongnan Super-large Cu (Au, Ag) Deposit and Significance for the Genesis of the Deposit. *Acta Geol. Sin.* **2018**, *92*, 400–401. [[CrossRef](#)]
27. Yang, C.; Tang, J.; Wang, Y.; Yang, H.; Wang, Q.; Sun, X.; Feng, J.; Yin, X.; Ding, S.; Fang, X.; et al. Fluid and geological characteristics researches of Southern Tiegelong epithermal porphyry Cu–Au deposit in Tibet. *Miner. Depos.* **2014**, *33*, 1287–1305. (In Chinese)
28. Duan, J.; Tang, J.; Li, Y.; Liu, S.; Wang, Q.; Yang, C.; Wang, Y. Copper isotopic signature of the Tiegelongnan high-sulfidation copper deposit, Tibet: Implications for its origin and mineral exploration. *Miner. Depos.* **2016**, *51*, 591–602. [[CrossRef](#)]
29. Mathur, R.; Munk, L.; Nguyen, M.; Gregory, M.; Ansell, H.; Lang, J. Modern and paleofluid pathways revealed by Cu isotope compositions in surface waters and ores of the Pebble porphyry Cu–Au–Mo deposit, Alaska. *Econ. Geol.* **2013**, *108*, 529–541. [[CrossRef](#)]
30. Chen, H.Q.; Qu, X.M.; Fan, S.F. Geological characteristics and metallogenic prospecting model of Duolong porphyry copper gold ore concentration area in Gerze County, Tibet. *Miner. Depos.* **2015**, *34*, 321–332.

31. Song, Y.; Yang, H.H.; Lin, B.; Liu, Z.B.; Qin, W.; Ke, G.; Chao, Y.; Xiang, F. The Preservation System of Epithermal Deposits in South Qiangtang Terrane of Central Tibetan Plateau and Its Significance: A Case Study of the Tiegelongnan Superlarge Deposit. *Acta Geosci. Sin.* **2017**, *38*, 659–669. (In Chinese)
32. Kapp, P.; Yin, A.; Manning, C.; Harrison, T.; Taylor, M.; Ding, L. Tectonic evolution of the early Mesozoic blueschist-bearing Qiangtang metamorphic belt, central Tibet. *Tectonics* **2003**, *22*. [[CrossRef](#)]
33. Kapp, P.; Yin, A.; Harrison, T.; Ding, L. Cretaceous–Tertiary shortening, basin development, and volcanism in central Tibet. *Geol. Soc. Am. Bull.* **2005**, *117*, 865–878. [[CrossRef](#)]
34. Pullen, A.; Kapp, P.; Gehrels, G.; Ding, L.; Zhang, Q. Metamorphic rocks in central Tibet: Lateral variations and implications for crustal structure. *Geol. Soc. Am. Bull.* **2011**, *123*, 585–600. [[CrossRef](#)]
35. Liu, D.; Huang, Q.; Fan, S.; Zhang, L.; Shi, R.; Ding, L. Subduction of the Bangong–Nujiang Ocean: Constraints from granites in the Bangong Co area, Tibet. *Geol. J.* **2014**, *49*, 188–206. [[CrossRef](#)]
36. Hao, L.; Wang, Q.; Wyman, D.A.; Ou, Q.; Dan, W.; Jiang, Z.; Wu, F.; Yang, J.; Long, X.; Li, J. Underplating of basaltic magmas and crustal growth in a continental arc: Evidence from Late Mesozoic intermediate–felsic intrusive rocks in southern Qiangtang, central Tibet. *Lithos* **2016**, *245*, 223–242. [[CrossRef](#)]
37. Zhu, D.; Li, S.; Cawood, P.; Wang, Q.; Zhao, Z.; Liu, S.; Wang, L. Assembly of the Lhasa and Qiangtang terranes in central Tibet by divergent double subduction. *Lithos* **2016**, *245*, 7–17. [[CrossRef](#)]
38. Allmendinger, R.; Jordan, T.; And, S.; Isacks, B. The evolution of the Altiplano-Puna plateau of the Central Andes. *Annu. Rev. Earth Planet. Sci.* **1997**, *25*, 139–174. [[CrossRef](#)]
39. Zhu, D.; Pan, G.; Wang, L.; Mo, X.; Zhao, Z.; Zhou, C.; Liao, Z.; Dong, G.; Yuan, S. Tempo-spatial variations of Mesozoic magmatic rocks in the Gangdese belt, Tibet, China, with a discussion of geodynamic setting-related issues. *Geol. Bull. China* **2008**, *27*, 1535–1550. (In Chinese)
40. Kapp, P.; Decelles, P.; Gehrels, G.; Heizler, M.; Lin, D. Geological records of the Lhasa–Qiangtang and Indo-Asian collisions in the Nima area of central Tibet. *Geol. Soc. Am. Bull.* **2007**, *119*, 917–933. [[CrossRef](#)]
41. Yin, A.; Harrison, T.M. Geologic evolution of the Himalayan–Tibetan orogen. *Annu. Rev. Earth Planet. Sci.* **2000**, *28*, 211–280. [[CrossRef](#)]
42. Qu, X.-M.; Wang, R.; Xin, H.; Jiang, J.; Chen, H. Age and petrogenesis of A-type granites in the middle segment of the Bangonghu–Nujiang suture, Tibetan plateau. *Lithos* **2012**, *146*, 264–275. [[CrossRef](#)]
43. Li, J.-X.; Qin, K.; Li, G.; Xiao, B.; Zhao, J.; Cao, M.; Chen, L. Petrogenesis of ore-bearing porphyries from the Duolong porphyry Cu–Au deposit, central Tibet: Evidence from U–Pb geochronology, petrochemistry and Sr–Nd–Hf–O isotope characteristics. *Lithos* **2013**, *160*, 216–227. [[CrossRef](#)]
44. Li, X.; Li, C.; Sun, Z.; Wang, M. Origin and tectonic setting of the giant Duolong Cu–Au deposit, South Qiangtang Terrane, Tibet: Evidence from geochronology and geochemistry of Early Cretaceous intrusive rocks. *Ore Geol. Rev.* **2017**, *80*, 61–78. [[CrossRef](#)]
45. Li, G.; Qin, K.; Li, J.; Evans, N.; Zhao, J.; Cao, M.; Zhang, X. Cretaceous magmatism and metallogeny in the Bangong–Nujiang metallogenic belt, central Tibet: Evidence from petrogeochemistry, zircon U–Pb ages, and Hf–O isotopic compositions. *Gondwana Res.* **2017**, *41*, 110–127. [[CrossRef](#)]
46. Hou, Z.; Mo, X.; Gao, Y.; Qu, X.; Meng, X. Adakite, a possible host rock for porphyry copper deposits: Case studies of porphyry copper belts in Tibetan Plateau and in Northern Chile. *Miner. Depos.* **2003**, *22*, 1–12. (In Chinese)
47. Defant, M.J.; Drummond, M.S. Derivation of some modern arc magmas by melting of young subducted lithosphere. *Nature* **1990**, *347*, 662. [[CrossRef](#)]
48. Sillitoe, R. Epochs of intrusion-related copper mineralization in the Andes. *J. S. Am. Earth Sci.* **1988**, *1*, 89–108. [[CrossRef](#)]
49. Sillitoe, R.H. A plate tectonic model for the origin of porphyry copper deposits. *Econ. Geol.* **1972**, *67*, 184–197. [[CrossRef](#)]
50. Hou, Z.; Gao, Y.; Qu, X.; Rui, Z.; Mo, X. Origin of adakitic intrusives generated during mid-Miocene east–west extension in southern Tibet. *Earth Planet. Sci. Lett.* **2004**, *220*, 139–155. [[CrossRef](#)]
51. Hou, Z.; Yang, Z.; Lu, Y.; Kemp, A.; Zheng, Y.; Li, Q.; Tang, J.; Yang, Z.; Duan, L. A genetic linkage between subduction-and collision-related porphyry Cu deposits in continental collision zones. *Geology* **2015**, *43*, 247–250. [[CrossRef](#)]


52. Oyarzun, R.; Márquez, A.; Lillo, J.; López, I.; Rivera, S. Reply to Discussion on “Giant versus small porphyry copper deposits of Cenozoic age in northern Chile: Adakitic versus normal calc-alkaline magmatism” by Oyarzun R, Márquez A, Lillo J, López I, Rivera S (Mineralium Deposita 36: 794–798, 2001). *Miner. Depos.* **2002**, *37*, 795–799. [[CrossRef](#)]
53. Li, J.; Qin, K.; Li, G.; Richards, J.; Zhao, J.; Cao, M. Geochronology, geochemistry, and zircon Hf isotopic compositions of Mesozoic intermediate–felsic intrusions in central Tibet: Petrogenetic and tectonic implications. *Lithos* **2014**, *198–199*, 77–91. [[CrossRef](#)]
54. Lv, L.; Zhao, Y.; Song, L.; Tian, Y.; Xin, H. Characteristics of C, Si, O, S and Pb isotopes of the Fe-rich and Cu (Au) deposits in the western Bangong–Nujiang metallogenic belt, Tibet, and their geological significance. *Acta Geol. Sin.* **2011**, *85*, 1291–1304. (In Chinese)
55. Xin, H.; Qu, X.; Wang, R.; Liu, H.; Zhao, Y.; Wei, H. Geochemistry and Pb, Sr, Nd isotopic features of ore-bearing porphyries in Bangong Lake porphyry copper belt, western Tibet. *Miner. Depos.* **2009**, *28*, 785–792. (In Chinese)
56. Hawkesworth, C. The generation and evolution of the continental crust. *J. Geol. Soc.* **2010**, *167*, 229–248. [[CrossRef](#)]
57. Richards, J.P. Postsubduction porphyry Cu-Au and epithermal Au deposits: Products of remelting of subduction-modified lithosphere. *Geology* **2009**, *37*, 247–250. [[CrossRef](#)]
58. Sillitoe, R. Styles of high-sulphidation gold, silver and copper mineralisation in porphyry and epithermal environments. In Proceedings of the Australasian Institute of Mining and Metallurgy, Melbourne, Australia, 11–13 September 2000; Volume 305, pp. 19–34.
59. Fournier, R.O. Hydrothermal processes related to movement of fluid from plastic into brittle rock in the magmatic-epithermal environment. *Econ. Geol.* **1999**, *94*, 1193–1211. [[CrossRef](#)]
60. Zhang, K.; Zhang, Y.; Tang, X.; Xia, B. Late Mesozoic tectonic evolution and growth of the Tibetan plateau prior to the Indo-Asian collision. *Earth Sci. Rev.* **2012**, *114*, 236–249. [[CrossRef](#)]
61. Li, Y.; Wang, C.; Li, Y.; Ma, C.; Wang, L.; Peng, S. The Cretaceous tectonic event in the Qiangtang Basin and its implications for hydrocarbon accumulation. *Pet. Sci.* **2010**, *7*, 466–471. [[CrossRef](#)]
62. Yang, K.; Ma, C. Some advances in the rates of continental erosion and mountain uplift. *Geol. Sci. Technol. Inf.* **1996**, *15*, 89–96.
63. Kesler, S.E.; Wilkinson, B.H. The role of exhumation in the temporal distribution of ore deposits. *Econ. Geol.* **2006**, *101*, 919–922. [[CrossRef](#)]
64. Murphy, M.; Yin, A.; Harrison, T.; Dürr, S.; Chen, Z.; Ryerson, J.; Kidd, F.; Wang, X.; Zhou, X. Did the Indo-Asian collision alone create the Tibetan plateau? *Geology* **1997**, *25*, 719–722. [[CrossRef](#)]
65. Ketcham, R.A. Forward and inverse modeling of low-temperature thermochronometry data. *Rev. Mineral. Geochem.* **2005**, *58*, 275–314. [[CrossRef](#)]
66. Yang, H.H.; Tang, J.; Dilles, J.; Song, Y. Temperature Study of the Duolong Porphyry Cu-Au District and its implications for the Evolution of the Qiangtang Terrane in Tibet, China. *Int. Geol. Rev.* **2018**. submitted.
67. Li, G. High temperature, salinity and strong oxidation ore-forming fluid at Duobuza gold-rich porphyry copper in the Bangonghu tectonic belt, Tibet: Evidence from fluid inclusions study. *Acta Petrol. Sin.* **2007**, *23*, 935–952.
68. Sillitoe, R.H. Porphyry Copper Systems. *Econ. Geol.* **2010**, *105*, 3–41. [[CrossRef](#)]
69. Lowell, J.D.; Guilbert, J.M. Lateral and vertical alteration-mineralization zoning in porphyry ore deposits. *Econ. Geol.* **1970**, *65*, 373–408. [[CrossRef](#)]



© 2018 by the authors. Licensee MDPI, Basel, Switzerland. This article is an open access article distributed under the terms and conditions of the Creative Commons Attribution (CC BY) license (<http://creativecommons.org/licenses/by/4.0/>).

Review

# The Jbel Saghro Au(–Ag, Cu) and Ag–Hg Metallogenic Province: Product of a Long-Lived Ediacaran Tectono-Magmatic Evolution in the Moroccan Anti-Atlas

Johann Tuduri <sup>1,2,\*</sup>, Alain Chauvet <sup>3</sup> , Luc Barbanson <sup>2</sup>, Jean-Louis Bourdier <sup>2</sup>, Mohamed Labriki <sup>4</sup>, Aomar Ennaciri <sup>4</sup>, Lakhlifi Badra <sup>5</sup>, Michel Dubois <sup>6</sup>, Christelle Ennaciri-Leloix <sup>4</sup>, Stanislas Sizaret <sup>2</sup> and Lhou Maacha <sup>4</sup>

<sup>1</sup> BRGM, F-45060 Orléans, France

<sup>2</sup> ISTO, UMR7327, Université d’Orléans, CNRS, BRGM, F-45071 Orléans, France; luc.barbanson@univ-orleans.fr (L.B.); jean-louis.bourdier@univ-orleans.fr (J.-L.B.); stanislas.sizaret@univ-orleans.fr (S.S.)

<sup>3</sup> Géosciences Montpellier, cc. 060, Université de Montpellier 2, CEDEX 5, 34095 Montpellier, France; alain.chauvet@univ-montp2.fr

<sup>4</sup> MANAGEM, Twin Center, BP 5199, Casablanca 20100, Morocco; m.labriki@managemgroup.com (M.L.); a.ennaciri@managemgroup.com (A.E.); cleloix@yahoo.fr (C.E.-L.); l.maacha@managemgroup.com (L.M.)

<sup>5</sup> Faculté des Sciences, Université Moulay Ismaïl, BP 11201 Zitoune, Meknes 50 000, Morocco; badra\_lakhlifi@yahoo.fr

<sup>6</sup> Laboratoire de Génie Civil et géo-Environnement–Lille Nord de France, EA 4515, Département des Sciences de la Terre, Université de Lille, Bât. SN5, 59655 Villeneuve d’Ascq, France; michel.dubois@univ-lille1.fr

\* Correspondence: j.tuduri@brgm.fr; Tel.: +33-238-644-790

Received: 31 August 2018; Accepted: 10 December 2018; Published: 13 December 2018

**Abstract:** The Jbel Saghro is interpreted as part of a long-lived silicic large igneous province. The area comprises two lithostructural complexes. The Lower Complex consists of folded metagreywackes and N070–090°E dextral shear zones, which roughly results from a NW–SE to NNW–SSE shortening direction related to a D<sub>1</sub> transpressive tectonic stage. D<sub>1</sub> is also combined with syntectonic plutons emplaced between ca. 615 and 575 Ma. The Upper Complex is defined by ash-flow caldera emplacements, thick and widespread ignimbrites, lavas and volcanoclastic sedimentary rocks with related intrusives that were emplaced in three main magmatic flare ups at ca. 575, 565 and 555 Ma. It lies unconformably on the Lower Complex units and was affected by a D<sub>2</sub> trantensive tectonic stage. Between 550 and 540 Ma, the magmatic activity became slightly alkaline and of lower extent. Ore deposits show specific features, but remain controlled by the same structural setting: a NNW–SSE shortening direction related to both D<sub>1</sub> and D<sub>2</sub> stages. Porphyry Au(–Cu–Mo) and intrusion-related gold deposits were emplaced in an earlier stage between 580 and 565 Ma. Intermediate sulfidation epithermal deposits may have been emplaced during lull periods after the second and (or) the third flare-ups (560–550 Ma). Low sulfidation epithermal deposits were emplaced late during the felsic alkaline magmatic stage (550–520 Ma). The D<sub>2</sub> stage, therefore, provided extensional structures that enabled fluid circulations and magmatic-hydrothermal ore forming processes.

**Keywords:** structural control; silicic large igneous province; ignimbrite flare-ups; ash-flow caldera; epithermal; porphyry; IRGD; Anti-Atlas

## 1. Introduction

In northwest Africa, the Anti-Atlas, Ougarta and Hoggar domains consist of pericratonic terranes located at the margin of the West African Craton (WAC, Figure 1a) and that were mostly amalgamated

from Palaeoproterozoic to Phanerozoic times [1–5]. These terranes were the site of recurring tectonic activity and periods of intense magmatic activity. The most important magmatic pulses occurred during the Mesoproterozoic [6–8] and at the end of Triassic when the Central Atlantic Magmatic Province (CAMP) was emplaced [9–11]. According to Ernst [12] and Ernst and Bleeker [13], both events have been related to large igneous provinces (LIPs). Indeed LIPs consist of large volumes of mainly mafic magma ( $>0.1 \text{ Mkm}^3$ ) in provinces whose areal extent might exceed  $0.1 \text{ Mkm}^2$ . LIPs are thought to emplace in a short duration pulse or multiple pulses (less than 1–10 Myr each) with a whole maximum duration of ca. 50 Myr. Intense felsic magmatism may also occur as silicic large igneous provinces (SLIPs) [12,14]. Dacite–rhyolite pyroclastic rocks (ignimbrites), along with transitional calc-alkaline I-type [15] to A-type granites, mainly characterise these SLIPs [16]. Further, LIPs are commonly related to a wide variety of metal deposits [17] including world-class deposits such as magmatic sulfide ore deposits associated with mafic and ultramafic magmatism (Ni, Cu, PGE, Cr, Ti, Fe [18,19]), with carbonatite and peralkaline complexes (Nb, Ti, REE, Zr [20,21]), or with diamondiferous kimberlites [22]. Iron oxide copper gold (IOCG) deposit types [23] and epithermal deposits of mostly low and intermediate sulfidation gold-based metal types [24–26] may be also related to more silicic LIPs. Another magmatic event described in peri-Gondwanan terranes of, e.g., Avalonian and Cadomian types, is mostly characterised by huge volumes of pyroclastic flows and was emplaced at the end of the Neoproterozoic era [27–30]. Conditions and geodynamical environment at the origin of such a silicic province remain insufficiently understood, although Moume et al. [31] recently proposed that this event might be related to the Central Iapetus Magmatic Province event (CIMP) of Ediacaran-Cambrian age [13,32]. In the Moroccan Anti Atlas, world-class deposits occur in an area mostly dominated by rhyolitic ignimbrites such as the giant Ag–Hg Imiter deposit, the Ag–Hg Zgounder deposit and the Co–Ni–Fe–As(–Au–Ag) Bou Azzer district (Figure 1b).

In fact, the Moroccan Anti-Atlas hosts several precious and base-metal deposits affected by at least four major tectonic phases: i.e., the Palaeoproterozoic, the Neoproterozoic, the Variscan and the Alpine cycles [29,33–35]. Until recently, most of the ore deposits from the Anti-Atlas were considered as Neoproterozoic in age due to their occurrence within Proterozoic inliers. One exception was the vein and stratabound copper deposits hosted within the early Palaeozoic cover, which were assumed to be syn-sedimentary or epigenetic and Variscan in age [36,37]. However, recent studies have reassessed the age and origin of numerous metal deposits, assigning younger ages than previously admitted. The arguments are essentially two-fold: (i) absolute dating and (ii) fluid chemistry by isotopic and fluid inclusion study methods. Indeed geochronological methods (e.g., Re/Os, Ar/Ar) frequently give younger ages than expected though possible resetting of dating materials and (or) ore remobilisation are rarely discussed. For instance, the Imiter deposit would coincide with the Permo-Triassic boundary [38]. Similarly, a late Carboniferous age has been proposed for ore enrichment at BouAzzer with a possible earlier pre-mineralising stage [39]. The strong association of mineral deposits with fluids of moderate to high salinities, suggests interpretations favouring the influence of basinal brines in the ore-forming processes [40,41]. Indeed, processes involving basin-related and(or) surface-related brines resulting from evaporation of seawater in Triassic basins in the formation of ore deposits, up to now interpreted as, deposits related to the late Neoproterozoic felsic magmatic event [42–48] have been defended by several recent works [40,41,49] although the debate is still open [50]. This controversy mainly concerns the Bou Azzer (Co–Ni–), Imiter (Ag–Hg) and Zgounder (Ag–Hg) mines that represent the main three world-class ore deposits of the Moroccan Anti-Atlas after the Akka gold mine was closed few years ago. The Imiter concentration has been proposed to be associated with the  $550 \pm 3 \text{ Ma}$  rhyolitic magmatism [51], a hypothesis recently controverted by Ar–Ar geochronology [38] and palaeo-fluid geochemistry investigations [41]. The Zgounder deposit is supposed to be emplaced around  $564 \pm 5 \text{ Ma}$  at the same time as rhyolitic intrusions [46,52] although fluid geochemistry would suggest a Triassic fluid contribution [41,49] sedimentary. The Bou Azzer Co–Ni–Fe–As(–Au–Ag) district hosts the only mine in the world where Co is produced as a primary commodity directly from Co- and As-bearing

arsenide minerals [53]. It is interpreted as having experienced many ore remobilisations from Late Neoproterozoic, Variscan to Triassic magmatic-hydrothermal stages [39,40,44,54,55].

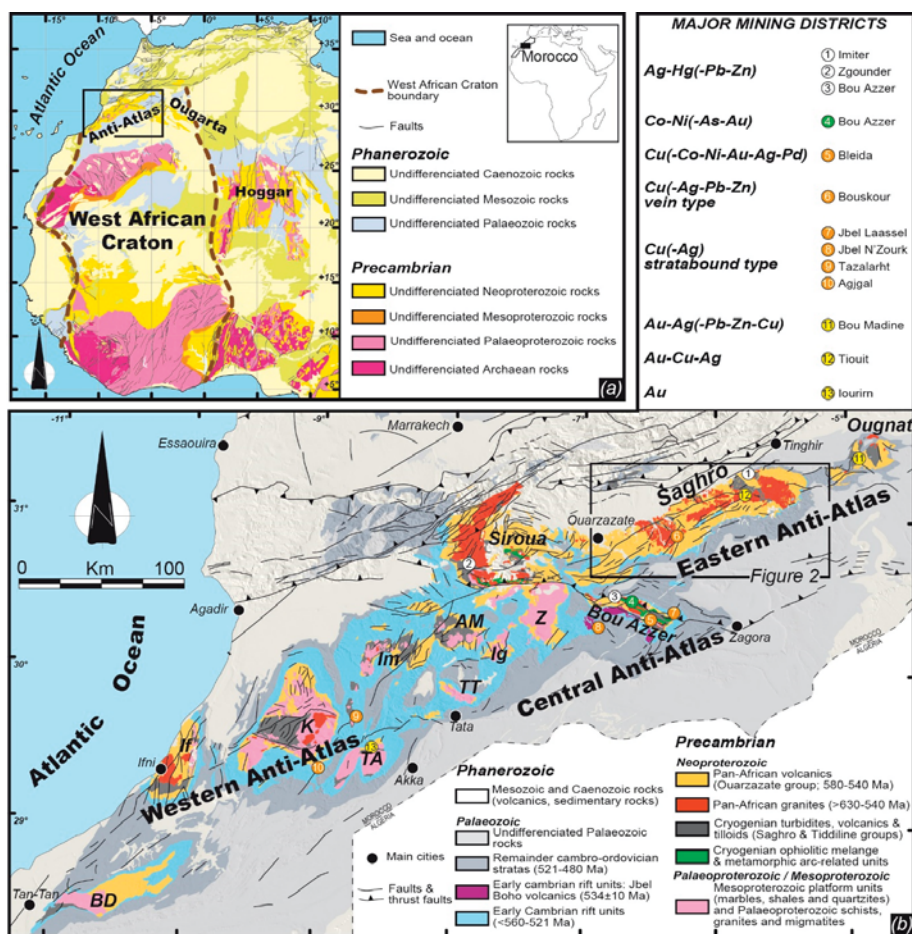


**Figure 1.** (a) Location of the Anti-Atlas belt at the northern limit of the West African Craton, after Thiéblemont et al. [56]. (b) Main geological units and major mining districts of the Moroccan Anti-Atlas [5,7,29,48,57–59]. Inliers—BD: Bas Drâa; If: Ifni; K: Kerdous; TA: Tagragra d’Akka; Im: Igherm; TT: Tagragra de Tata; Ig: Iguerda; AM: Agadir-Melloul; Z: Zenaga.

The debate as to whether the Anti-Atlas ore deposits are mostly Neoproterozoic in age and magmatic-related, or Phanerozoic and disconnected from any magmatic input, is similar to the one that exists between the orogenic and intrusion-related gold deposit models [60–65]. For instance, as applied to the Variscan gold ore deposits in the French Massif Central and beyond, this debate is focused on the involvement of magmatic fluids in the formation of mineralised systems. Arguments supporting the orogenic model are mostly based on fluid inclusion studies and isotopic data on quartz-bearing veins and highlight the meteoric and/or metamorphic signatures of the fluids [66,67]. In such cases, heat production from possible synchronous granitoids is supposed to generate only thermal convection cells. Arguments in favour of an intrusion-related model highlight the systematic spatial association between granite and hydrothermal systems, while fluid compositions and metal source are interpreted as showing a magmatic signature [68–70].

Therefore, it may be relevant to clarify whether most of the ore deposits of the Moroccan Anti-Atlas are linked to a Neoproterozoic magmatic input (the magmatic-related alternative), or to a more recent stage related to the penetration and circulation of sedimentary brines and (or) metamorphic fluids into the basement (the orogenic alternative). Indeed, as the Anti-Atlas domain may be considered as an important Neoproterozoic magmatic province with respect to the abundance of plutonic and volcanic rocks, evidences for a major Neoproterozoic metallogenetic province need to be deciphered. In this work, we present a review of the global geology and metallogeny of the Jbel Saghro in the Eastern Anti-Atlas with a specific emphasis on the formation, styles and tectonic controls of different ore deposit occurrences in order to assess and discuss a tectono-magmatic evolution of the studied area and a metallogenetic and geodynamic model. The world-class Bou Azzer deposit is not concerned in this study because of its location far from the Jbel Saghro. Its characterisation will be the subject of work currently in progress.

## 2. Geological Overview of the Anti-Atlas Mountains

The Moroccan Anti-Atlas belt, located in the northern part of the WAC (Figure 1a), constitutes an important segment of the Pan-African orogeny, also known as the Cadomian orogeny, that occurred from the Middle Neoproterozoic to Early Cambrian. This area is currently elevated at altitudes exceeding 1000 m in large areas due to a Cenozoic uplift [35,71,72] although they basically represent a Variscan intra-cratonic, thick-skinned basement inversion belt [34]. Consequently, the Anti-Atlas mountains present significant exposures of WSW–ENE trending inliers, (aka *boutonnieres*), which consist of Proterozoic rocks in core of Phanerozoic, mainly Palaeozoic, sedimentary sequences (Figure 1b).

During Precambrian times, the Anti-Atlas domain has recorded two major orogenic cycles: the Eburnean, a Palaeoproterozoic cycle from about 2.1 to 2.0 Ga and the Pan-African/Cadomian cycle from about 885 to 540 Ma [5,33,73–75]. The Pan-African orogeny is characterised by three main tectono-magmatic events [29,73,75–77]. (i) The first event corresponds to an oceanic basin closure, oceanic subduction and arc-craton accretion, coeval with calc-alkaline magmatism and ophiolite obduction. This event is supposed to have occurred between 770 and 630 Ma and related formations are mainly observable in the Central Anti-Atlas [29,59,78–80]. (ii) Then, the development of an active margin along the amalgamated West African Craton was responsible for an intense high-K calc-alkaline magmatism and transpressive tectonics between ca. 615 and ca. 560 Ma [29,48,59,74,75,77,81,82]. (iii) Finally, late to post-orogenic granites with cogenetic volcanic and volcanoclastic cover are emplaced between ca. 560 and 550 Ma together with subsequent transtensional tectonics [5,29,47,74]. The transition from transpressive to transtensive tectonics remains the subject of debate but it likely occurred between 580 and 560 Ma [29,48,74]. There is still also an ongoing debate on the origin of the two late magmatic events, which are either described as arc-related [29] or as post-orogenic related to an asthenospheric rise beneath the West African Craton, without any active subduction [74,83]. Then, the Ediacaran–Cambrian transition is recognised as a carbonate-dominated succession (the Adoudou formation) that unconformably overlies the late Ediacaran plutonic and volcanoclastic rocks [84–86]. This sedimentation period shows dramatic and rapid thickness changes, consistent with an active extensional faulting related to incipient continental rifting [86,87]. Intercalated alkaline volcanic ash and flows dated between 550 and 520 Ma confirm that deposition of the Adoudou formation took place during the Early Cambrian and is in tectono-magmatic continuity with the Ediacaran volcano-tectonism [74,88–90].

In the Eastern Anti-Atlas of interest here, Jbel Saghro, Palaeoproterozoic terranes are not exposed (Figures 1b and 2), so, the oldest rocks outcropping consist of Middle Neoproterozoic (Cryogenian) metasedimentary rocks [91,92]. These are slightly deformed and unconformably overlain by a thick and widespread upper Neoproterozoic (Ediacaran) volcanic and volcanoclastic sequence (Figure 2). Both Cryogenian and Ediacaran units are intruded by Pan-African plutons (Figure 2).

Prior to the Variscan compression, the Palaeozoic sedimentary cover reaches an overall thickness of 8–10 km in the western Anti-Atlas and only 4 km in the eastern part of the Anti-Atlas, being



mainly characterised by shallow marine sedimentary rocks [34,86,93–95]. Subsidence is assumed to be regular and characterised by two main steps [34,96]. The first step occurs during the Cambrian, from the Terreneuvian to the Miaolingian. It corresponds to a rifting episode [84,86,97,98]. The Adoudou formation and related alkaline volcanic rocks mentioned above belong to this step. The second step occurs during the Upper Devonian and is characterised by a multi-directional extension mainly controlled by NNW–SSE and ENE–WNW faults inherited from the Pan-African basement [93]. Fission track dating on zircon [99] yields a peak temperature affecting the basement around  $328 \pm 30$  Ma (Carboniferous, Upper Mississippian). It is interpreted as the age of maximum burial. The subsequent uplift is attributed to the Variscan compression [34,100] during the Upper Carboniferous (early Pennsylvanian). It results in the inversion tectonics of these palaeofaults as thrusts and strike-slip–reverse faults. The main shortening directions are assumed to be NW–SE to N–S in the Western Anti-Atlas [34,100], and NE–SW in the Eastern Anti-Atlas [93]. The Precambrian basement is actually uplifted and folded into huge antiformal culminations probably at the origin of the present days inliers which characterise the Anti-Atlas fold belt. Thus, many authors e.g., [34,86,93,100] suggest that brittle deformations related to the Variscan compression occur in the whole Anti-Atlas and reactive structures from the Precambrian basement. Ductile deformation related to the Variscan tectonics has not yet been described in the Anti-Atlas. It might be suggested in the Western Anti-Atlas because the overall Palaeozoic rock thickness reaches 10 km making it possible a ductile–brittle transition. However, with a maximum thickness of only 4 km such ductile deformations seem precluded in the Eastern Anti-Atlas. Consequently, how and to what extent the Palaeozoic tectono-hydrothermal events may have an influence on the main ore deposits of the Eastern Anti-Atlas remains an important topic. For this reason, we focus our work below on the re-examination of the model of formation and structural control of different ore-bearing deposits of the Jbel Saghro. We highlight the relevance of a pluri-disciplinary approach involving analyses of regional tectonics, vein geometry, internal texture and mineralogy of ore deposits in order to decipher the mode of formation for each deposits. The ore-forming processes are specifically addressed with the view of their possible relationships with the Precambrian magmatism, in order to better assess whether they could have been mainly formed during the Neoproterozoic times, or mostly formed and remobilised during the Phanerozoic. We also stress that conventional approaches of ore deposits involving kinematic criteria on slip surfaces of faults and palaeostress reconstructions in the brittle regime are here excluded, since the whole Anti-Atlas is still an active seismic area [94]. So, the Precambrian or Palaeozoic features should be erased by recent tectonic reactivations.

The Jbel Saghro hosts numerous precious and base metal deposits (Figure 2). The most famous are: the giant Ag Imiter mine (8.5 Mt @ 700 g/t Ag; [41,45,51,101,102]) and the Cu Bouskour mine (21 Mt @ 1.3% Cu; [103]) and also the now closed Cu–Ag Tizi Mouddou (1.5 Mt @ 2% Cu, 250 g/t Ag; [43]) and Cu–Au–Ag Tiwit (1.06 Mt @ 8 g/t Au, 65 g/t Ag, ~0.4% Cu; [43]) mines. Mining activity in the Jbel Saghro area dates back a very long time as suggested for the Imiter and Bouskour mining sites [101,103]. Although no precise dating is available, some historical texts suggest that workings occurred since the beginning of medieval times. These sites were subsequently abandoned and forgotten and were rediscovered under the French Protectorate between 1912 to 1956, leading to subsequent intensive exploration and mining. Since the mid 1990s and after reinterpreting the regional geology of the Anti-Atlas area, the BRPM (Bureau de Recherches et de Participation Minière, currently ONHYM: Office National des HYdrocarbures et des Mines) and Reminex (a subsidiary of the Managem Group) conducted several exploration campaigns. Indeed, before the 1990s, the Anti-Atlas was mainly interpreted as a collisional belt and the formation of ore deposits was related to orogenic processes, e.g., [43,73,76]. Then, the geology and the ore forming processes were related to the complex evolution of active margin(s) in a subduction and accretion setting, e.g., [29,45,47,48,51,77,82]. This led to the discovery of new Au–Ag occurrences such as those of the Issarfane (0.5 Mt @ 1.8 g/t Au), Qal’at Mgouna and Thaghassa (Figure 2).

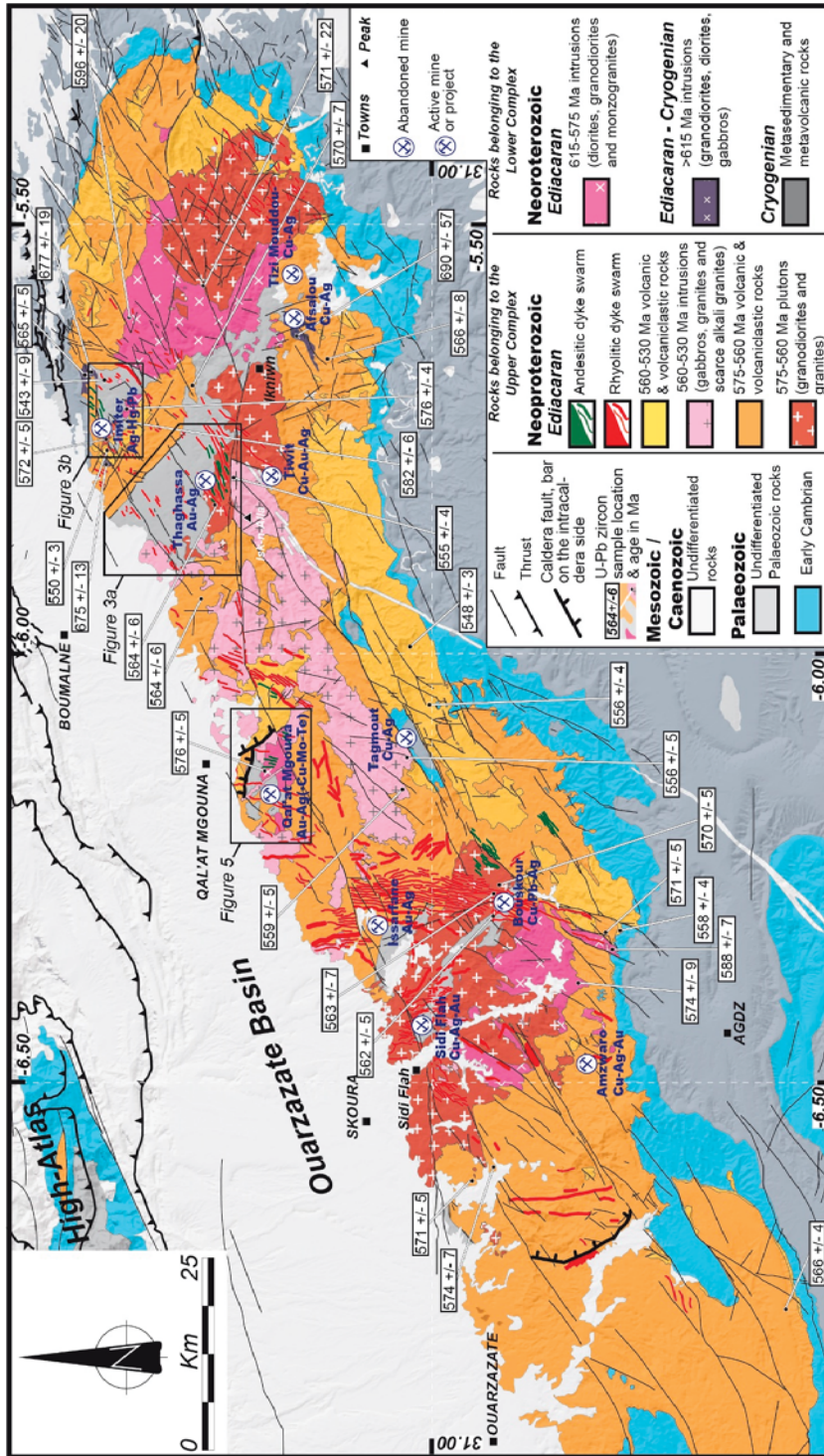


Figure 2. Simplified geologic map of the Ibel Saghro, after Hindermeyer et al. [104], Tuduri et al. [48], Tuduri et al. [47] and Tuduri et al. [48]. U-Pb radiometric ages obtained on zircon [29,48,51,78,105–108].

### 3. Tectono-Magmatic Evolution of the Jbel Saghro

Until the early 2000s, the Precambrian terranes in Morocco were traditionally subdivided into 3 main epochs: the PI for the Palaeoproterozoic era or Archaean aeon; PII for the Tonian and Cryogenian; and PIII for the Ediacaran periods [73,109–112]. These periods have been further subdivided into various units (e.g., P.II<sup>1</sup>, P.II-III, P.II<sup>sup</sup>, P.III3m-1a . . . ) in order to take into account the extraordinary complexity of the different areas [77,109,113]. Geologists then used a lithostratigraphic approach in which rocks were correlated based on their lithological characteristics and grouped in Supergroups, Groups, Subgroups, Formations and Members for layered sedimentary and volcanic sequences, and in Suites for plutonic and metamorphic rocks [5,29,59,107]. However, these lithostratigraphic schemes confuse the geological and tectonic messages and the resulting legends on geological maps. Indeed, showing the cogenetic relationships in a volcano-plutonic setting where plutonic, hypabyssal and volcanic rocks coexist as in the Anti-Atlas, remains a challenge, especially when tectonic controls are combined. For the seek of consistency, we propose below a tectono-lithostratigraphic framework that groups the sedimentary, plutonic and volcanic rocks of the Saghro area in Lower and Upper Complexes with regard to the tectono-magmatic evolution of the eastern Anti-Atlas. Such a complex corresponds to the definition of the ICS (International Commission on Stratigraphy), that is, a lithostratigraphic unit composed of diverse types of any classes of rocks (sedimentary, igneous and metamorphic) and characterised by irregularly mixed lithology or by complicated structural relationships. The definition of the two complexes and rationale behind are given below.

#### 3.1. The Lower Complex and the D<sub>1</sub> Transpressive Tectonics

The Lower Complex is composed of a thick succession of slightly deformed volcano-sedimentary rocks intruded by broadly coeval high-K calc-alkaline plutons (Figure 2). Volcano-sedimentary rocks are deformed and tightly upright folded (Figure 3a,b). They are also affected by a metamorphism below the amphibolite facies with hornfels around plutons [48,91,111]. Elsewhere, cleavage is well expressed in the vicinity of the large-scale, regional, strike-slip faults that mainly trend N070°E (Figure 2). The general structure is characterised by steeply dipping bedding (Figure 3a–c), large-scale folds (Figure 3a,b) and intense fracturing (see below).

##### 3.1.1. The Earlier Arc-Related Metagreywackes and Metavolcanic Rocks

These oldest formations belong to the Anti-Atlas supergroup, Saghro Group or MGouna Group of Thomas et al. [5] or Habab Group of O'Connor et al. [107] and consist of metaturbidites with intercalated thin mafic metavolcanic layers, exposed, from west to east, near the cities of Sidi Flah, Qal'at Mgouna, Boumalne and Imiter (Figure 2). The metasedimentary sequences, hereafter, called metagreywackes, are dominated by sandstones and silty mudstone [91,92,114–118]. Although slightly deformed (Figures 3 and 4), they consist of 2000 to 6000 m of flysh-like turbiditic rocks [83,91,118] that locally alternate with basaltic flows, volcanic breccias, hyaloclastite and pillow structures (Figure 3a,b). Based on geochemical analyses, the interbedded mafic lava rocks may have a transitional character between tholeiites and alkali basalts and may be related to a back-arc environment formed in an extensional setting or correspond to the remnants of a passive-margin [91,115,118,119]. These rocks have a mean Nd depleted mantle model age (T<sub>DM</sub>) of 650 ± 30 Ma, the ε<sub>Nd</sub> range from +7.63 to +8.08, and the initial <sup>87</sup>Sr/<sup>86</sup>Sr from 0.704 to 0.706 that have been interpreted as indicating a mantle origin without any old crust contribution [83,119]. These sedimentary sequences are considered to be Cryogenian [91,115,116]. However, Liégeois et al. [120] in Gasquet et al. [83], using U/Pb geochronology on detrital zircons from similar metagreywacke sequences in the Qal'at Mgouna area, have shown that zircon grains become younger towards the top of the metasedimentary sequences. They suggest that basins infilling were active until more recently than previously suspected, i.e., until 630–610 Ma. This corresponds to the onset of the Ediacaran Period and Pan-African magmatism that culminated during the next stages (see below).

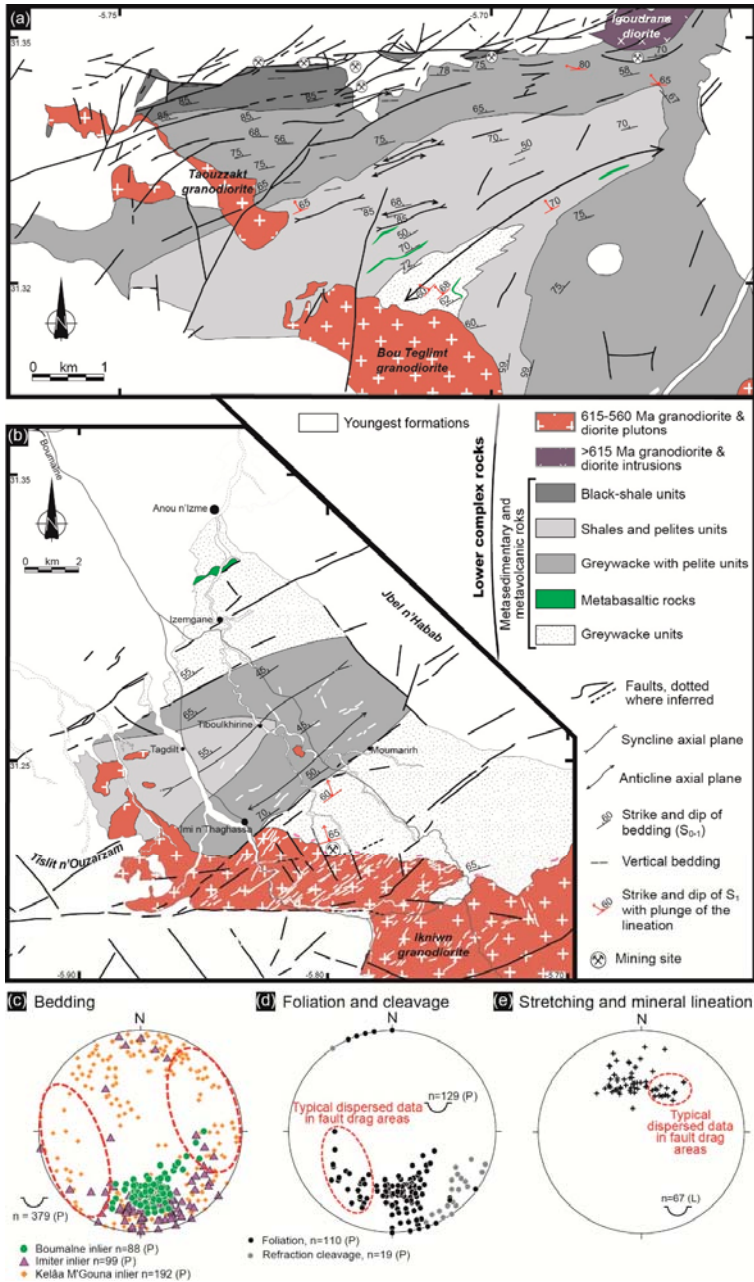


**Figure 3.** Structural maps of the (a) Imiter inlier modified from SMI (Société Métallurgique d’Imiter) data and Ighid et al. [121] and (b) Boumalne inlier (from Tuduri et al. [48]). Note that metabasaltic rocks with pilloid structures have never been observed in the Imiter inlier. Sills have been described and discussed as possibly syn-sedimentary in origin [100]. Stereoplots of structural orientation data: (c) bedding, (d) foliation and refraction cleavage, and (e) lineation. Bedding data are from the Qal’at

MGouna, Boumalne and Imiter Lower Complex inliers whereas foliation, refraction cleavage and lineation data are mainly from the Boumalne and Imiter Lower Complex inliers [47,48]. The dotted red lines in the bedding stereoplot highlight zones where data are locally reoriented because of drag fault zones and disturbance upon pluton emplacement.

### 3.1.2. The Intrusive Rocks

Diorites, granodiorites with minor gabbros and monzogranites [29,47,48,105,122–124], intrude these metaturbiditic and metavolcanic sequences (Figures 2 and 3a,b). The most representative are granodiorite and diorite intrusions that belong to the Ouarzazate Supergroup “precursor rocks” and Bardouz suite of Thomas et al. [5]. They are composed of plagioclase (An<sub>20–56</sub>), biotite, amphibole (Mg-hornblende to Fe-tschermakite and pargasite to Fe-edenite), rare pyroxene and accessory minerals such as titanite, zircon, apatite and magnetite [47,119,123]. K-feldspar and quartz abundances vary depending on pluton compositions. At the contact with the country rocks, cordierite, andalusite and biotite related to contact metamorphism are observed [47,48,121,125].

Rock geochemistry shows that most plutons have moderate to high-K calc-alkaline affinities with trends that are consistent with formation in an active continental margin [29,119]. Available ages range from  $677 \pm 19$  and  $576 \pm 4$  Ma for this event, although most of the data are bracketed between 615 and 575 Ma in the Jbel Saghro [29,51,59,78,81,105–108]. With regard to the oldest intrusions, their age and emplacement conditions remain unclear and debated in the Jbel Saghro [48] and are only evidenced by poorly defined U-Pb zircon geochronology (i.e., >615 Ma) on calc-alkaline tonalite, diorite and granodiorite intrusions [107,108,126]. However, in the Central Anti-Atlas, similar plutons are widespread and were emplaced continuously between 660 and 615 Ma in a supra-subduction setting [29,78]. One can therefore question on a possible diachronism of magmatic activity between the Central Anti-Atlas and the Eastern Anti-Atlas during this period especially if we consider that some rare ages reported in the Eastern Anti-Atlas are inherited ( $677 \pm 19$ ,  $675 \pm 13$ ,  $645 \pm 12$  Ma, [108,126]). However, the following magmatic period spanning from 615 to 575 Ma is well expressed in both the Central and Eastern Anti-Atlas. This is mostly plutonic in the Eastern Anti-Atlas and both volcanic and plutonic in the Central Anti-Atlas.

### 3.1.3. The Main Pan-African D<sub>1</sub> Deformation Event

At map-scale (Figure 3a,b), the overall style of the deformation suggests that steep bedding and folds are the most conspicuous features of the metaturbiditic terranes [47,48,77,125–129]. Two types of folds are observed. (i) At the regional scale, first-order folds are easily discernible such as in the Imiter and Boumalne areas (Figure 3a,b). They are tight (Figure 3c) and the majority of the ENE–WSW axial surfaces are moderately to steeply inclined (50–60°), with a predominance of dips to the NNW suggesting that folds roughly verges toward the SE [125,127,128]. Their hinge lines gently plunge toward the ENE. (ii) At local scale, higher-order folds are metric and open to tight (Figure 4a). They are asymmetric and probably unrelated to lower-order folds as they always show a right-verging (dextral wrenching, [47]). Indeed, they are observed in shear zones where cleavage is well developed. These folds are interpreted as drag folds below. Their axial surfaces are upright (NE–SW to ENE–WSW) with a hinge line that steeply plunges toward the ENE or WSW [47]. In Figure 3c, most of the poles to bedding falling in the NNW and SSE quadrants are related to the regional scale, first-order folds. Gentle poles falling in the SW and NE quadrants are related to drag folds. However, these plots and more generally the ones comprised within the dotted red lines (Figure 3c) highlight areas where data are locally reoriented because of drag fault zones and plutonic interferences. Such interferences are abundant in the Qal’at MGouna area where folds may be also interpreted as open and upright (Figure 3c, [47]).

In detail, metaturbiditic rocks show finite strain markers including foliation and stretching and mineral lineation [47,48,77,81,128–130]. Foliation that usually consists in a slaty cleavage is evident throughout the entire inlier. It is noteworthy that both metamorphic planar fabrics and lineations have

been only observed in the eastern part of the Jbel Saghro, in the Boumalne and Imiter areas. Indeed, these fabrics (Figures 3 and 4b) remain difficult to observe except in the hornfels zone surrounding the diorite and granodiorite intrusions described above (Figure 4b). Foliations show a constant ENE strike and dip toward the NW (N075°E 60°N, Figure 3d), except when reoriented in fault drag areas (i.e., NW–SE strikes) or when refracted (NE–SW strikes). Such foliation is axial planar and, thus, is generally parallel to the bedding of the metaturbiditic rocks when localised along the limbs of the first-order tight folds. It is called herein  $S_{0-1}$ . A  $S_2$  cleavage refraction (Figure 4c) may also occur in specific areas, that define an obliquity with respect to the  $S_{0-1}$ . It is caused by localised shear developed in incompetent layers usually associated with the drag fold structures. Stretching and mineral lineations ( $L_1$ ) are always carried by the  $S_{0-1}$  foliation. They are discrete and their orientation (Figure 3e) also appear fairly constant with a rather low dispersion from NW–SE to N–S trending directions (average: N170°E 55°N). According to mineralogic and micro-structural evidences, at least 2 distinct metamorphic assemblages are observed but appear to be related to the same tectonic event defined as a hornfels assemblage and a regional chlorite to amphibole assemblage. (i) The hornfels zone is observed in the contact metamorphic aureoles caused by the diorite and granodiorite intrusions within the Cryogenian greywackes [48,121,130]. It consists of a spotted phyllite zone in which foliation (phyllitic cleavage to gneissic foliation) and lineation are easily discernable. Rocks are mostly characterised by K-feldspar, muscovite, biotite and small spots of retrogressed andalusite and/or cordierite (Figure 4b). The latter frequently highlights the lineation and, therefore, suggests a probable relationship between pluton emplacement and the  $D_1$  tectonics. Garnet-amphibole assemblage and spessartine occurrences are associated with skarns and skarnoids as reported by Benziane [130] and Tuduri [47]. (ii) When observable far from intrusions, foliation (slaty to phyllitic cleavage) is defined by a planar-linear fabric mainly formed by phyllosilicates such as chlorite, sericite to biotite [48]. In both assemblages, rolling structures and S-C fabrics (Figure 4d) define unambiguous south- to southeast-verging noncoaxial shear criteria, parallel to the average lineation trending direction. These structures indicate reverse sense top-to-the-south deformation in the Boumalne and Imiter areas [47,48,77,82,121,123].

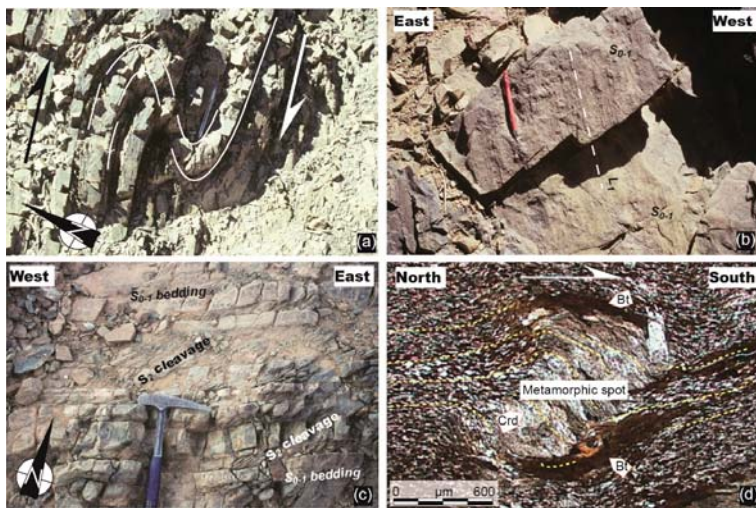


**Figure 4.** (a) Drag fold from the Qal’at Mgouna metagreywacke inlier. (b) Regional  $S_{0-1}$  metamorphic foliation and related lineation marked by elongate contact metamorphic minerals that affect the metagreywacke sequence. (c)  $S_2$  cleavage refraction, from the Imiter metagreywacke inlier, consistent with a dextral shearing. (d) Microphotograph showing syn- to late kinematic metamorphic mineral, a probable cordierite (Crd) showing rolling structure consistent with a top-to-the-south shearing sense. Note the asymmetric tails composed of biotite (Bt), plane polar light.

The D<sub>1</sub> deformation is also well-expressed along the large-scale N070–090°E trending strike slip faults, about 100 to 150 km long that occur in the northern and central part of the Jbel Saghro (Figures 2 and 3a,b). On both sides of these shear zones, deformation appears more intense especially in the slaty to phyllitic cleavage domains where the S<sub>2</sub> refraction cleavage oriented N040–050°E 80°N is formed (Figure 4c) synchronously with drag-folds (Figure 4a). These structures are consistent with a dextral sense of shearing [47]. Where plutons are emplaced within shear zones, they develop both magmatic foliation and lineation (e.g., the Igoudrane pluton). There, the foliation is parallel to the fault (N075–090°E 80°N) and the lineation roughly horizontal. All structures linked with the D<sub>1</sub> events and the geometry of the associated intrusions indicate that this first Pan-African event developed in response to a NW–SE to WNW–ESE trending shortening.

### 3.2. The Upper Complex or the Inception of a Silicic Large Igneous Province

#### 3.2.1. Generalities

Rocks of the Upper Complex cover nearly 80% of the surface of the Jbel Saghro (Figure 2). This complex, only affected by very low-grade metamorphism and weak deformation, consists of thick and regionally extensive felsic volcanoclastic sequences that are non-conformably above the more deformed and metamorphosed rocks of the Lower Complex [29,30,47,112,131–133]. Related dykes and plutons intrude both the rocks of the Lower and Upper Complexes. These rocks belong to the Ouarzazate Supergroup that includes the lower Mançour Group and the upper Imlas Group [5,107]. Plutonic suites are attributed to the Tanghourt Suite. These plutonic and volcanic rocks were emplaced between ca. 575 and 540 Ma [29,51,74,78,106–108,112,134,135]. Most of the volcanic rocks are ash-flow tuffs, felsic lavas, resedimented volcanoclastic deposits with some andesitic lavas and rare mafic intrusions [29,30,47,112,133] that cover an area of approximately 2000 km<sup>2</sup> and reach a maximum thickness of 1000–1500 m.

#### 3.2.2. The Qal’at Mgouna Ash-Flow Caldera

In the vicinity of Qal’at Mgouna (Figures 2 and 5), the association of lava flows (rhyodacites, rhyolites and andesites), pyroclastic rocks (ash-flow tuffs and ash falls), re-deposited volcanoclastics and reworked volcanic rocks is consistent with an ash-flow caldera environment [47]. The pre-caldera formations mostly consist of metagreywacke basement rocks and diorite and granodiorite intrusion dated at  $576 \pm 5$  Ma [29], all belonging to the Lower Complex. Related to the caldera formation stage, plutonic rocks are mostly represented by monzogranites and coeval porphyries (Figure 5). Volcanoclastic rocks are not deformed, but only tilted when localised inside the caldera (Figure 5). The structural limit of the proposed Qal’at Mgouna caldera can be traced over 5–6 km. Tuduri [47] interprets the near vertical arcuate lineament located at the margin of the caldera as a potential ring-fault that trends E–W to NW–SE (Figures 5 and 6a). Evidence is given because this boundary separates the near vertical Cryogenian metagreywacke bedding to the South from the NNW dipping (50° to 80°) monocline intra-caldera sequences, to the North (Figures 5 and 6b). Numerous rhyolite dykes, 10 to 20 meters wide are located along this lineament (Figures 5 and 6a,b). Dykes are vertical or near-vertical and intrude the Lower Complex rocks as well as the plutonic and volcanoclastic rocks of the Upper Complex. Because these rhyolitic dykes are emplaced along the proposed structural limit and generally present an arcuate shape, they are interpreted as ring dykes.

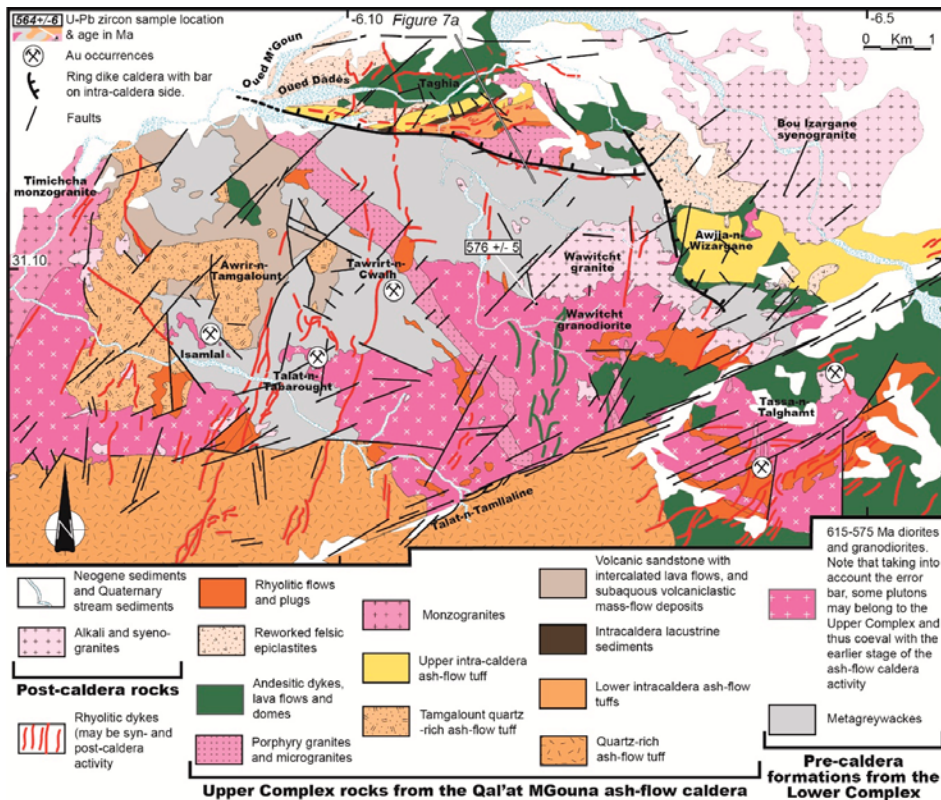


**Figure 5.** Detailed geologic map of the Qal'at MGouna district showing the extra- and intra-caldera rock units (from Benharref [132], Derré and Lécolle [113] and Tuduri [47]).

All the data presented above argue for the existence of a collapse caldera structure as shown on Figure 5 [136–139]. The peripheral structure of the ash-flow caldera where ring dykes occur is herein interpreted as having accommodated both subsidence (caldera collapse and intra-caldera sequences deposition) as well as subsequent uplift and tilting (magmatic resurgence and ring dykes injections). The geometry given by the NW–SE trending structural limit favours an elliptic shape rather than a sub-circular one for the caldera [41,140,141]. The consequence of such a shape will be discussed further. From bottom to top and according to Tuduri [47], the intra-caldera volcanoclastic sequence is detailed below (Figures 5–7):

- (i). A lowermost pyroclastic layer consists of a 400–500 m thick, unwelded to slightly welded, moderately crystal-rich dacitic lapilli tuff (Figure 6c,d and Figure 7a,b) interpreted as an ash-flow deposit [142,143]. Internal stratification of the ash-flow tuff is crude, oriented N060–080°E 80°NW, as highlighted by discrete layers which are either pumice-richer, lithic-richer or entirely devitrified with spherulites. In a specific layer 40 m thick, greenish fibrous pumices displaying silicified tubular micro-vesicles and a silky/fibrous fabric can reach up to 5 cm long. Lithic clasts up to 20 cm in size are common throughout and consist mainly of basement greywackes, lavas and quartz-rich ignimbrite fragments. Phenocrysts are mostly broken plagioclase and K-feldspar, in various ratios with minor amounts of chloritised ferro-magnesian crystals (biotite and probable amphibole) and very scarce quartz.



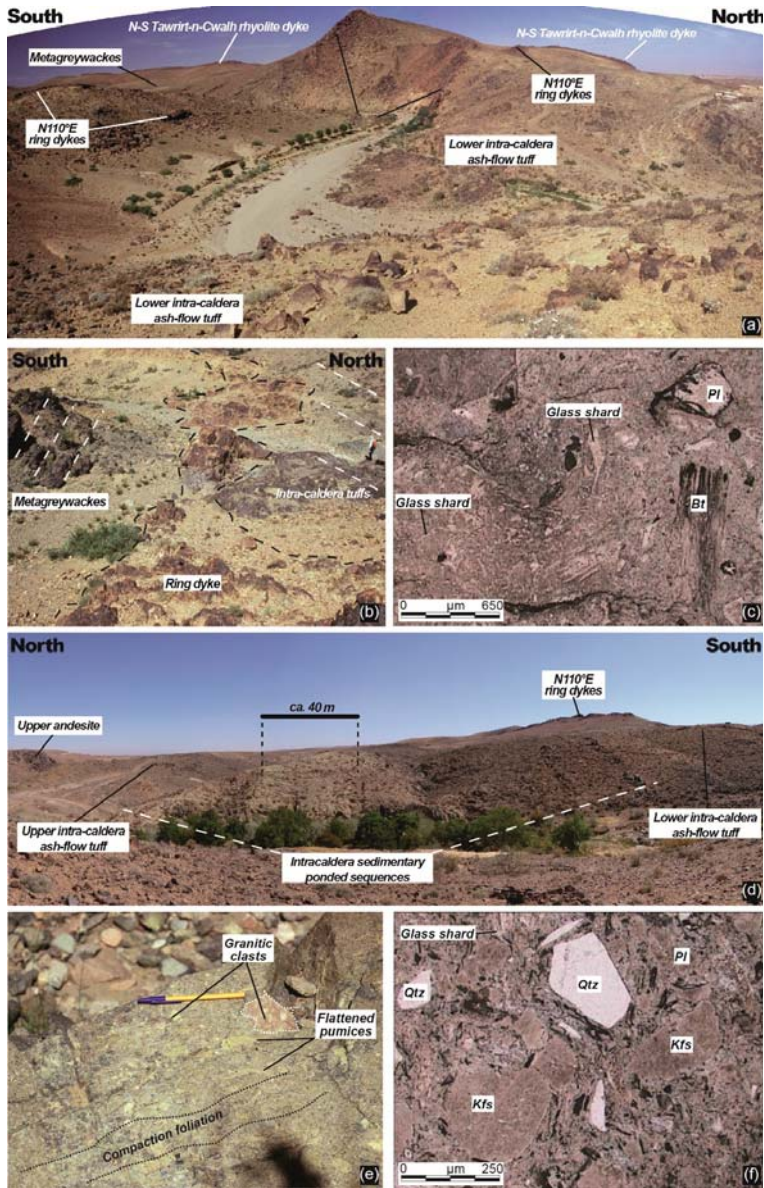


**Figure 6.** (a) View of the structural limit of the caldera showing the contact between the intra-caldera sequence, rhyolite ring dykes and basement, Taghia area (see location on Figure 5). (b) Detailed view of the structural limit showing the ring dykes and the unconformity between the basement to the south and the intra-caldera sequences to the north. (c) Microphotograph of the lower intra-caldera ash-flow tuff. Slight compaction and welding of shards are characteristics of this tuff, Plane Polar Light. (d) View towards the east showing the relationships between the lower and upper intra-caldera tuffs and interbedded sedimentary ponded rock sequences Taghia area (see location on Figure 5). (e) Close-up view of the upper intra-caldera tuff characterised by compacted fiammes (flattened pumices) and lithic fragments of K-feldspar-rich granite. (f) In thin section, the upper ignimbrite shows strong compaction and welding of shards, Plane Polar Light. Bt: biotite, Kfs: K-feldspar, Pl: plagioclase, Qtz: quartz.

- (ii). Above the ash-flow unit lies a ca. 200 m thick volcano-sedimentary (epiclastic) unit with very thin bedding (Figures 6d and 7a,b). The lower part (100 m thick) is made of layered tuffaceous breccias containing ignimbrites fragments. The upper part consists of laminated reddish and greenish mudstones and sandstone oriented N070°E 70°NW. When preserved from important silicification, the identifiable components are microscopic broken crystals and lithic fragments. Beds are broadly continuous laterally, being only sometimes disrupted by syn-sedimentary normal faults and slump-like structures. Faults are roughly oriented NW–SE. Fluid escape textures are common and allow assessment of the polarity of the intra-caldera sequence. All sedimentological features argue for a subaqueous emplacement, at least for the upper part of the epiclastic unit. In our model, and as no marine sediments have been hitherto recognised in the entire Jbel Saghro in the Ediacaran formations, such subaqueous environment may be reasonably related to a caldera lake.
- (iii). Above the volcano-sedimentary unit lies a ca. 200–300 m thick crystal-rich rhyolitic ash-and-lapilli tuff (Figures 6d and 7a–c). Plastic deformation due to significant compaction is evidenced by reddish flattened pumices (Figure 6e). Glass shards and broken phenocrysts are visible under the microscope (Figure 6f). Phenocrysts are quartz, plagioclase, K-feldspar, and scarce amounts of chloritised Fe–Mg minerals (biotite and amphibole). Up to 2 m-sized lithic clasts are abundant, especially in the basal part, and consist of metagreywacke, ash-flow tuff fragments, jasperoids and monzogranite (Figure 6e). This voluminous quartz- and pumice-rich unit is readily interpreted here as a welded ignimbrite.
- (iv). The top of the sequence is dominated by massive andesite lava flows and epiclastic poly lithologic breccias (Figures 5, 6d and 7a,b). The bottom of this whole sequence is intruded by a monzogranite porphyry (Figures 5 and 7a,b). Plugs of similar porphyry facies also locally intrude the upper parts of the sequence. Such porphyry is here interpreted as a resurgent pluton [137,144] that tilted the intra-caldera sequence upon emplacement [47]. Because of the tilting, the thickness of the intra-caldera sequence is exposed over 1500–2000 m, of which 800–1000 m consists of ash-flow tuffs and epiclastic rocks. To the north, the intra-caldera sequence disappears beneath the young sedimentary rocks of the Dadès valley (Figure 5).

Volcanic and pyroclastic rocks also occur outside the caldera structure to the south and west. They form a broadly stratified pile up to 500 m thick with moderate dips toward the W–NW (Figure 5). In the vicinity of the Awrir-n-Tamgalount (Figure 5), the extra-caldera sequences are made up of two units overlain by the Tamgalount tuff (Figure 7d,e). The lower unit is dominated by hundreds of meters of well bedded, normally graded crystal-rich sandstones and siltstones (Figure 7e). Under the microscope some of the silt-sized layers are formed of formerly vitric, now devitrified, material and might be primary ash fall deposit. The stratified lower unit dips towards the west at variable angles (Figure 5), perhaps due to palaeo-topography effects and/or syn-tectonic deposition. The upper unit is dominated by rhyo-dacitic lavas that display distinctive spherulitic devitrification microtexture and pillow texture in the field that suggests emplacement under water. The Tamgalount tuff (Figures 5 and 7d,e) is a porphyritic rhyo-dacitic ash-flow tuff (ca. 25% phenocryst) with eutaxitic texture. Broken phenocrysts consist of quartz, plagioclase, K-feldspar and chloritised Fe–Mg minerals. Lithic fragments are abundant and composed of greywackes, ash-flow tuff fragments and jasperoids. All extra-caldera units lie unconformably on the Lower Complex and are pervasively affected to various degrees by hydrothermal alteration and/or silicification. The importance of this unconformity will be discussed later.

Numerous intrusions are related to the Upper Complex (Figures 2 and 5). They have been mapped according to their mineralogy, texture and geochemical features. Two types are distinguished: (i) gabbros and biotite- and amphibole-rich, pink-coloured coarse-grained granites (monzo- to syenogranites), which are calc-alkaline to highly potassic, and coeval porphyries emplaced at shallower levels (e.g., the intra-caldera resurgent granite and its apophyses); and (ii) Si-rich alkali (K-rich, i.e., shoshonitic in composition) granites and related aplitic bodies (sills, dykes), which frequently appear as late magmatic events in the Upper Complex history. The pink monzogranites contain

quartz, albite-oligoclase, Fe-edenite, annite, K-feldspar and accessory minerals such as thorite, zircon, allanite, apatite, magnetite, sulphides and W and Mo-rich minerals. By analogy with the Isk-n-Alla monzogranite in the central part of the Jbel Saghro (Figure 2), they may have been emplaced around 555 Ma [29,106]. The alkali granites are mainly composed of quartz, albite and K-feldspar displaying granophyric intergrowths. Accessory minerals include tourmaline (fluor-schorl) and metamict zircon [47]. They are associated with late N-S rhyolitic dykes that also display shoshonitic compositions (Figure 5). We assume they may have emplaced later, between 550 and 530–520 Ma [74,107,108].

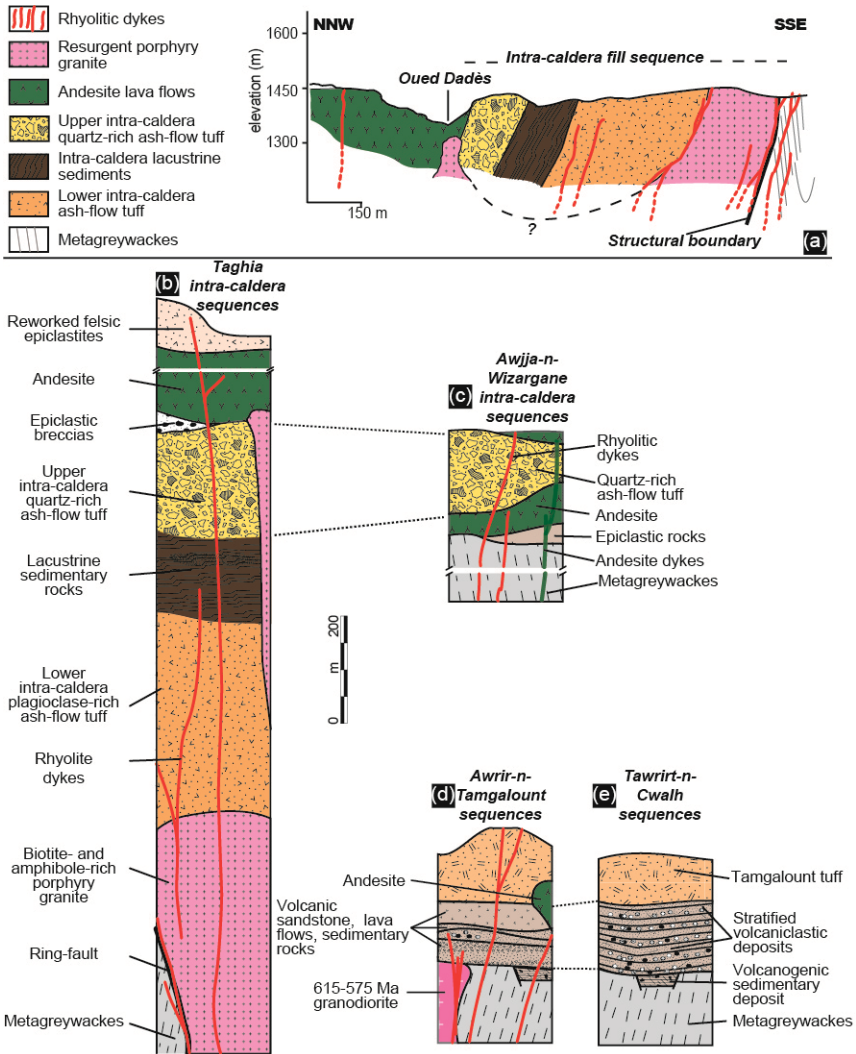


**Figure 7.** Simplified cross section and graphic logs of the Qal'at Mgouna volcanic sequences according to Tuduri [47]. (a) Schematic N-S cross section across the Qal'at Mgouna ash-flow caldera. Summary stratigraphic sections for the (b) Taghia and (c) Awjja-n-Wizargane intra-caldera sequences, and extra-caldera sequences from (d) Awrir-n-Tamgalount and (e) Tawrirt-n-Cwalh (See location on Figure 5).

According to the relative and absolute chronology of both volcanic and plutonic rocks in both the Jbel Saghro and in the Qal'at Mgouna area, three main ignimbrites flare-ups are herein evidenced. The earliest flare-up corresponds to the lower intra-caldera ash-flow tuff emplacement. It is mostly dacitic and may coeval with granodiorite plutons emplaced around 575 Ma [29,74]. Ignimbrites from the Oued Dar'a caldera described by Walsh et al. [29] are herein interpreted as belonging to this earliest flare-up. Then, the emplacement of the Tamgalount ash-flow tuff with rhyo-dacitic affinities, may correspond to a second high-volume magmatic event emplaced around 565 Ma [78,107]. Such an event would have produced similar tuffs that are coeval with the huge rhyo-dacitic dyke swarm [29] observed in the western and southern parts of the Jbel Saghro (Figure 2). The later ignimbrite flare-up corresponds to the upper intra-caldera rhyolitic ash-flow tuff and to the numerous rhyolitic lava flows and domes reported in the literature [29,74,106], coeval with pink monzogranite plutons around 555 Ma.

### 3.2.3. The D<sub>2</sub> Deformation Event

D<sub>2</sub> is interpreted as a strike-slip faulting event [29,47] that is also controlled by a WNW–ESE direction of shortening [47]. Tectonic features are faint, belong to the brittle regime, and affect both the Lower and Upper Complex units. Indeed, large-scale structures (except faults) and intense folding as observed in the Lower Complex are absent. It may be noted that some authors [29,78] described gentle folds that only affect the lower ignimbritic sequences (i.e., the 575 and 565 Ma ones) mainly in the western part of the Jbel Saghro and the Central and Western Anti-Atlas. Field works document: (i) ca. NNW–SSE normal faulting emplaced perpendicular to the extensional direction (i.e., NNE–SSW); and (ii) N070°E strike slip fault systems and associated veining. In the Qal'at Mgouna area, D<sub>2</sub>-related normal faults control the emplacement and development of extra-caldera basins filled by the volcanoclastic rocks (Figures 5 and 7d,e). In contrast to the D<sub>1</sub>-related ones, structures related to the D<sub>2</sub> event are characterised by dominant opening and extensional features [47]. Some specific locations (see below) demonstrate the re-activation of previously formed faults (i.e., the regional strike-slip faults trending N070°E) and fractures under the state of stress link with D<sub>2</sub>. Others structures were formed, mainly in the Upper Complex. As fractures are favourable sites for fluid circulations and fluid trapping, intense veining occur within domains where intense fracturing is coeval of significant magmatic activity and related hydrothermal events. All these factors lead to the establishment of a general D<sub>2</sub>-related extensional/transensional setting that is particularly favourable for the emplacement of fluid-filled structures and, consequently, to the formation of the numerous ore deposits concerned by this study.

In the Qal'at Mgouna area, the structural map of the volcanic complex points to a control by a combination between E–W to NW–SE faults and NNE–SSW normal faults (Figure 5). Both structural directions controlled block-faulting, collapse and caldera formation. Because E–W to NW–SE faults are more developed and have a longer extent, they are assumed to represent the structural limit of the Qal'at Mgouna caldera (Figure 5). The orientation of these faults is consistent with a caldera formed under the control of a transensional regime with a WNW–ESE shortening direction and a NNE–SSW extensional direction. Similar tectonic features have been described in the Oued Dar'a caldera which is localised 60 km to the WSW [29]. Few examples of ash-flow calderas developed in strike-slip and/or extensional tectonic regimes have been documented [145–150].

## 4. Characteristics of Ore Deposits

Au–Ag showings and/or mines occur in several areas of the studied area (Figure 2). Four zones were selected. These showings are hosted in rocks of the Lower Complex (i.e., Thaghassa), the Upper Complex (i.e., Zone des Dykes area), or both (i.e., Imiter and Qal'at Mgouna) depending upon the depth of their formation. Mineralisation formed during the D<sub>2</sub> tectonic event within the four localities herein described in detail.

#### 4.1. The Thaghassa Intrusion-Related Gold Deposit

The Thaghassa intrusion-related gold deposit (IRGD) is an exploration project with drill core data showing the presence of several intersects of 1–2 m at 5 g/t Au, and up to 400 g/t Ag. It is hosted in hornfelsed metagreywacke rocks (Figure 8a) that are adjacent to a large granodioritic pluton [47,48,151], while the metagreywackes belong to the Lower Complex, the intrusion may correspond to the earlier development of the Upper Complex. Two main tectono-magmatic stages control the formation of the deposit. (i) The first stage corresponds to the top-to-the-south asymmetry and the syn-kinematic Iknwiw pluton emplacement controlled by a transpressional strain regime. Zircon U-Pb dating yields a Concordia age of  $564 \pm 6$  Ma for the intrusion [48]. (ii) The second stage (Figure 8b) is characterised, from older to younger and further away from the intrusion, by: metatexite with leucocratic stromatic bands, aplo-pegmatite sills (Figure 8c), intermediate veinlets composed of quartz, K-feldspar and muscovite (Figure 8d), and then gold-bearing striped foliation-veins (Figure 8e). All these are assumed to have been emplaced under large-scale ENE–WSW dextral shearing that results from an ESE–WNW shortening during transtensive tectonics (Figure 8b). Tuduri et al. [48] suggested that the progressive and continuous shearing was initiated at the aplo-pegmatite stage and achieved during the hydrothermal phase (Figure 8b–f). The existence of intermediate veins characterised by quartz-rich core and apatite-muscovite-feldspar-rich rims demonstrates a progressive evolution from a magmatic to a hydrothermal stage and the persistence of the magmatic character, at least until the onset of the hydrothermal process. The main Au-mineralization was concentrated at the end of such a magmatic-hydrothermal evolution. The ore paragenesis is characterised by arsenian pyrite with refractory gold ( $<5 \mu\text{m}$ ) arsenopyrite, sphalerite and scarce grains of chalcopyrite, loellingite, pyrrhotite, tetraedrite, freibergite, argentite and cassiterite. Galena is abundant but always in the form of microscopic inclusions within pyrite. Fluid inclusion characterisation, based on the concept of fluid inclusion assemblages (FIA, [152]) as in all the cited references, combined with mineral geothermometry [48] suggests that the system evolved from hot fluids ( $\sim 550$  °C) dominated by  $\text{N}_2$  and  $\text{CH}_4$  to intermediate temperature ( $\sim 300$ – $450$  °C) and low salinity aquo-carbonic fluids in the system ( $\text{H}_2\text{O}$ - $\text{NaCl}$ - $\text{CO}_2$ ) +  $\text{CH}_4$ . Salinities are low to intermediate, being lower than 11.5 wt. % NaCl equiv. Gold precipitation is related to intermediate temperature mineralising fluids that have strongly interacted with the hornfelsed country rocks. According to Tuduri et al. [48], such a metallogenetic system is assumed to have developed due to migmatization and partial melting of metagreywackes country rocks in response to heat transfer from the underlying Iknwiw intrusion. Fluid and metal sources may originate from magmatic processes (i.e., magmatic exsolution of incompatible elements from newly formed peraluminous melts and perhaps from the Iknwiw intrusion) and from the devolatilisation of the metamorphic host rocks. (iii) A third, later tectono-magmatic stage in the area developed a large volcanic dyke swarm and brittle faulting and is assumed to belong to the Upper Complex.

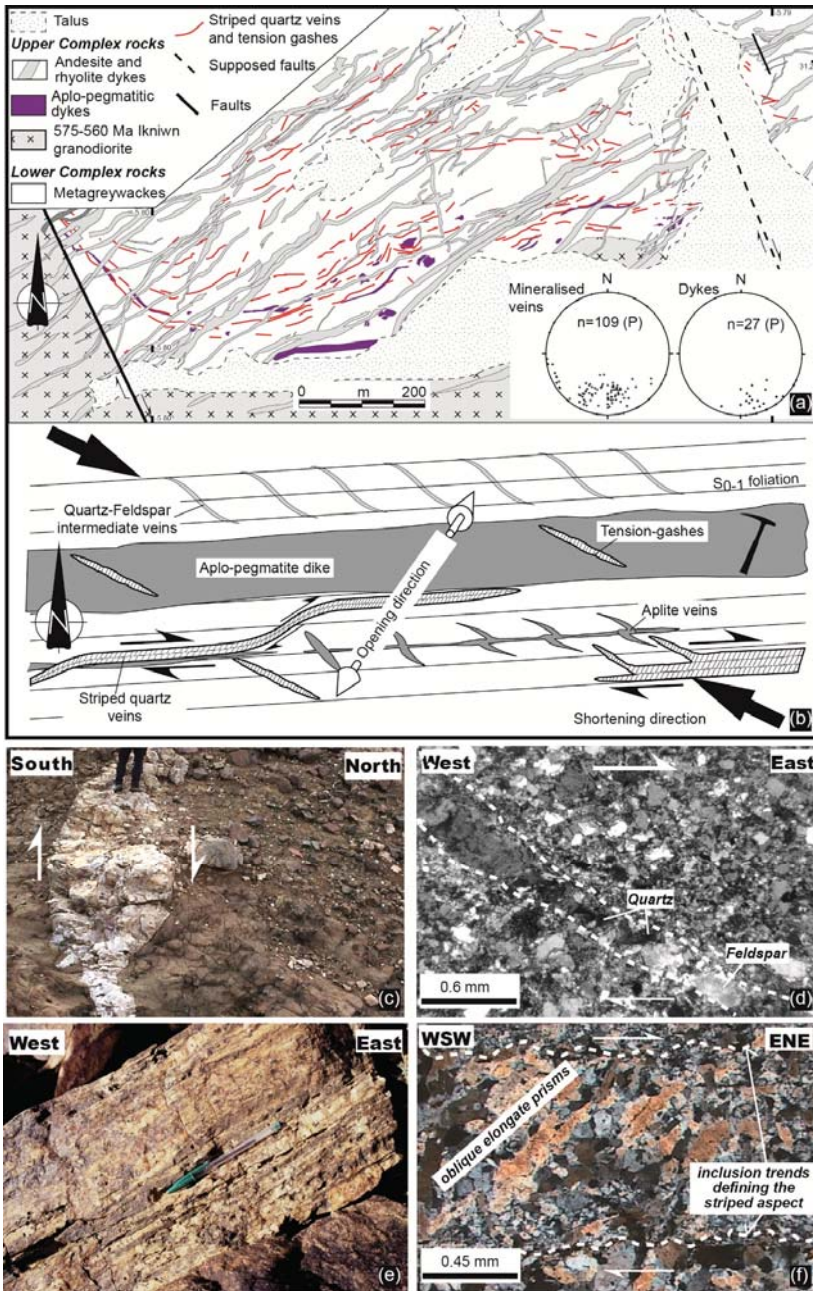


**Figure 8.** Main features of the Taghassa intrusion-related gold deposit (IRG) [47,48]. (a) General map and stereoplots of structural orientation data of the Au–Ag Taghassa intrusion-related gold deposit. These reveal the high density of veins developed north of the 575–560 Ma Iknwv granodiorite. (b) Interpretative sketch illustrating the magmatic-hydrothermal model that involved a progressive and continuous tectonic event including the aplo-pegmatitic dykes and sills emplacement, then the intermediate veins and the hydrothermal and gold-rich striped quartz veins. (c) Pegmatite dike

showing a dextral pull-apart geometry. (d) N120°E trending intermediate veins filled by quartz, muscovite and feldspar assemblage, cross polar light. (e) Macrostructure illustrating the gold-bearing quartz vein stage. The layering texture defined the striped aspect of veins. (f) Microtextural characteristics of gold-bearing quartz veins. The internal texture shows elongate quartz grains with obliquity with respect to vein walls suggesting a dextral shearing, cross polar light.

#### 4.2. The Qal'at Mgouna Au–Ag (Cu, Mo, Bi, Te) District

The Qal'at Mgouna district is composed of three main exploration projects: the Isamlal, Talat-n-Tabarought and Tawrirt-n-Cwalh districts, all of which located outside of the caldera structure (Figures 5 and 9). Based on mineralogical, chemical, textural and structural constraints, two distinct ore deposit types have been identified: an older porphyry ore deposit on which a younger epithermal system is superimposed [47,113,153,154].

##### 4.2.1. The Isamlal Porphyry Au–(Cu–Mo) Deposit

The porphyry Au–(Cu–Mo) deposit type is related to high-temperature hydrothermal system observed in the Isamlal and Talat-n-Tabarought areas (Figure 9a–e). The Isamlal project appears as being the most promising [47,154–157]. Ore emplacement is assumed to be synchronous to slightly late with respect to the emplacement of diorite and granodiorite stocks [158]. Most of these intrusive stocks, that display porphyritic textures in drill cores (Figure 9e), present a preferential NW–SE orientation in map (Figure 9a,b). Their age of emplacement is still unknown. However, a large pluton, the Wawitcht granodiorite, displaying similar mineralogy and located ca. 4 km east of the Isamlal deposit, has been dated at  $576 \pm 5$  Ma (U–Pb radiometric ages on zircon, [29]). Alterations are mostly observed within the Lower Complex and affect both the metagreywackes and diorite–granodiorite intrusions. The deposit is characterised by a Au mineralisation hosted by the metagreywackes that is also elongated along a ca. NW–SE trending direction (Figure 9b). Cu and Mo occurrences are additionally associated. In paragenetic order, the mineralisation includes magnetite, K-feldspar and late forming and less pervasive quartz veins that form a well developed stockwork. The stockwork occurs along a ca. N120°E preferred orientation, highlighting a strong structural control (Figure 9c). It is localised in the vicinity of the granodiorite intrusion or related apophyses but seems more developed within the metagreywackes at the hanging-wall (Figure 9d). Veins range in size from 0.5 to 30 cm in width and are  $\leq 10$  m in length except for the largest veins which are more than 30 m long. Such an important structural control on the stockwork may suggest that the main opening direction (i.e., NE–SW) is controlled by an ESE–WNW shortening direction. In drill cores, the central part of the mineralised zone is characterised by potassic-altered rocks. K-feldspar mostly occurs in highly reactive igneous rocks (Figure 9e). Biotite may coexist with K-feldspar but also occurs around the central zone whereas the propylitic alteration is more distal [158]. In the Isamlal area, the quartz-rich stockwork is characterised by K-feldspar, magnetite, F–Cl-rich amphibole, Cl–F-rich biotite with scarce F-rich tourmaline, brannerite and rutile in the central part of the deposit, and muscovite with scarce iron oxides more externally. Note that such a stockwork has never been reported in rocks belonging to the Upper Complex [47]. Sulfides mostly occur in the central zone and mainly consist of pyrite, chalcopyrite, with scarce molybdenite, pyrrotite, electrum, galena and tetradymite [47,155,157,158]. Fluid inclusions from the quartz-rich stockwork veinlets were used to constrain the palaeohydrothermal conditions [154,155,159]. Primary multiphase fluid inclusions are composed of liquid, vapour and halite cubes, as well as other salts such as sylvite, and  $\text{CaCl}_2$ . In addition, uncommon mineral inclusions that may be abundant have been identified, such as calcite, brookite–titanite, haematite, magnetite, and a solid phase with a very high refringence identified as andradite.

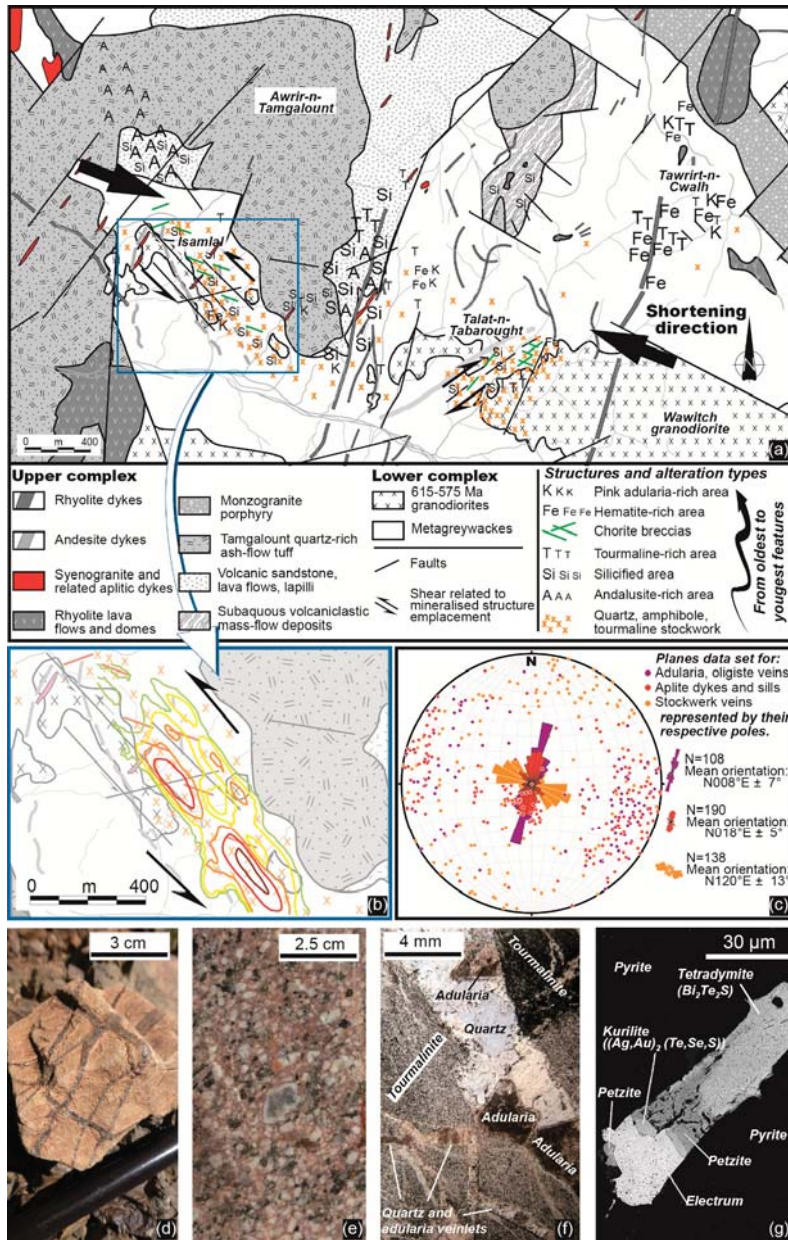


**Figure 9.** Main features of the Qal' at Mgouna deposit types [47,158]. (a) Detailed map of the Au(-Cu-Mo-Ag-Te-Bi) Qal' at Mgouna district (from Tuduri [47]). Note that the kinematics shown by shear zones are consistent with a WNW-ESE direction of shortening. (b) Kriging interpolation revealed that gold anomalies are correlated with both the quartz stockwork and the NW-SE faulted corridor in the Isamal porphyry deposit. The red colour is indicative of the highest Au grades [158]. (c) Stereoplots of structural orientations data for: the quartz stockwork related to the porphyry stage (mean orientation N120°E); the aplitic dykes and sills related to the alkali-syeno-granite stocks (mean



orientation N018°E); and the adularia-specularite-quartz veins from the epithermal stage (mean orientation N008°E). (d) Quartz stockwork from the Isamlal porphyry Au(-Cu-Mo) system. (e) Typical potassic alteration (pink coloured zones) of a porphyritic granodiorite (the Isamlal porphyry Au(-Cu-Mo) system). (f) Typical alteration and vein development of the epithermal stage: pervasive tourmalinites are cut by quartz and adularia-rich veins in the vicinity of the Tawrirt-n-Cwalh deposit, plane polar light. (g) Economic paragenesis of the epithermal stage characterised by Au-Ag tellurides, electrum and Bi-telluride veinlets within pyrite; Tawrirt-n-Cwalh deposit, SEM back scattered picture.

Chalcopyrite and gold were also observed in multiphase inclusions. Multiphase inclusions have a high though variable salinity (30 to 45 wt. % NaCl equiv.) and are characterised through homogenization by halite-disappearance. The large range of homogenization temperatures (160–460 °C) combined with a zoned potassic to propylitic alteration, stockwork structures and with an Au(-Cu-Mo) paragenesis is interpreted as characteristic of Au(-Cu-Mo) porphyry environments. This porphyry Au(-Cu-Mo) system is herein described as a vein-dominated deposit (stockwork) that is consistent with the emplacement of a porphyry stock, then exsolution and cooling of a magmatic-derived hydrothermal fluid. The overall system appears as mostly controlled by a ca. WNW-ESE trending direction. Indeed, this pattern suggests that the stockwork structure both reflects the magmatic stress associated with the porphyry emplacement and fluid exsolution, and also, a ca. NNE-SSW-oriented minimum principal stress (i.e., extensional direction) associated with a regional deformation that may be consistent with a WNW-ESE shortening direction although no clear tectonic regime has been proposed for the hydrothermal stage.

#### 4.2.2. The Qal'at Mgouna Au-Ag(-Bi-Te) Epithermal System

In contrast to the porphyry deposit type, this low sulfidation epithermal deposit type appears more atypical (Figure 9a,c,f,g). From west (Timicha) to east (Isamlal then Tawrirt-n-Cwalh), the Qal'at Mgouna area (Figure 5) displays a progressive and continuous tectono-magmatic activity initiated as the plutonic stage (mostly observed to the west) and ending with a volcanic and hydrothermal stage observed from west to east [47]. The magmatic stage produced small pink-coloured Si-rich alkali granites, and sill and dyke intrusions with a typical fine-grained aplitic texture. Rhyolitic K-feldspar-phyrhic dykes are also assumed to belong to this stage. Such intrusive bodies may intrude rock units from both the Lower and Upper Complexes. The transition to hydrothermal stage is characterised by fluid exsolutions from the alkali granites and the formation of (i) quartz, Fe- and F-rich tourmaline with scarce F-rich muscovite miarolitic cavities; (ii) quartz, K-feldspar with scarce tourmaline stockscheider; (iii) tourmaline-rich quartz veins and NW-SE chlorite-rich transtensive cataclases; and (iv) quartz, adularia, specularite veins with magnetite, fluorite, sulphides and gold (Figure 9f,g; [47,158–160]). The magmatic-hydrothermal processes strongly affected rocks especially the highly reactive volcanoclastic ones from the Upper Complex. These alterations correspond to a strong pervasive silicification. In addition to quartz, andalusite, diaspore pyrophyllite, Mg- F-rich tourmaline, F-rich phlogopite, F-rich muscovite, Cl-F-rich apatite occur along with rutile, haematite, monazite, xenotime, thorite and uranothorite as well as pyrite with inclusions of galena, coloradoite, hessite and altaite [47,113,153]. In some locations close to the Isamlal porphyry, the association of andalusite, pyrophyllite and diaspore with phlogopite and muscovite may be associated with the late epithermal or earlier porphyry stages [47,113,153]. Tourmalinisation is noteworthy and well developed along pervasive axes. Chlorite appears later in the paragenesis and mostly occurs in fault breccias. Ore concentration occurs during the hydrothermal stage with the quartz-adularia veins by crystallisation of As- and Co-rich pyrite, minor chalcopyrite and precious metal (Au-Ag telluride, electrum, Ag-telluride and Bi-telluride, Figure 9f) in the core of previously formed quartz-adularia-chlorite veins. Except for the chloritic breccias, which are strongly oriented along the NW-SE trending direction, all sills, dykes and veins related to the hydrothermal stage are roughly N-S with a maximum of 20° of dispersion toward the NNW and NNE (Figure 9c). The structural control of this event remains poorly evidenced as both extensional and transtensional features have been reported [47]. Paragenetic and

microthermometric studies show the mineralising system is characterised by decreasing temperature of formation [154,160]. Indeed quartz from the miarolitic and stockscheider stages are characterised by high temperature of formation (400–600 °C), multiphase highly saline fluid inclusions (22–32 wt. % NaCl + CaCl<sub>2</sub> equiv.), while the intermediate stages related to massive tourmalinisation show temperatures of homogenization of 200–250 °C. The system then evolves toward lower salinity fluids probably belonging to the H<sub>2</sub>O–NaCl–CaCl<sub>2</sub> (11–27 wt. % NaCl equiv.) system, with the absence of multiphase inclusions, and temperature around 180 ± 20 °C for the quartz-adularia veins. This hydrothermal stage corresponds to the formation of Au–Ag(–Te–Bi) epithermal showings in this part of the Jbel Saghro [47]. The issue whether this system belongs to an alkaline, low sulfidation or intermediate epithermal deposit remains open. The age of formation is unclear, although it may be coeval with the slightly alkaline N–S rhyolitic dykes dated between 550 and 530–520 Ma in the eastern Saghro [74,107,108].

#### 4.3. The Zone des Dykes Intermediate Sulfidation Epithermal Au-Base Metal Deposit

The Zone des Dykes, also known as the Issarfane area, is located in the western part of the Jbel Saghro inlier (Figure 2) in the vicinity of a huge N–S rhyolitic dyke swarm emplaced around 565 Ma [29]. The Zone des Dykes ore district consists of quartz veins systems hosted by two ash-flow tuff units belonging to the Upper Complex (Figure 10). Therein, three mineralised systems, called the F1, F5 and Bou Issarfane structures, respectively (Figure 10a), are identified [47]. The F1 structure consists of a 2 km long and 2 m width vein system that trends N180–160°E and dips about 50–60° to the east. The vein system shows several step-over zones showing a left lateral pull-apart geometry (Figure 10b) with a faint vertical component. The F5 structure also consists of a vein system, 1 km long and 2 m width, that is roughly oriented N080°E 60–70°S and is characterised by right-lateral shear structures (Figure 10c). The F1 and F5 structures are both interpreted as developed as conjugate pairs (Figure 10d). Because cross-cutting relationships are observed, we interpret the N080°E direction trend (i.e., F5) as the dominant direction. The F1 shear structures is herein interpreted as emplaced along a pre-existing NNW–SSE fracture analogous to the ones occurring between the Bouskour and Issarfane areas (Figure 2). The F5 structure is also emplaced along an important pre-existing fracture set that corresponds to a main ENE–WSW regional fault. This may explain why the F1 and F5 shear fractures are almost orthogonal yet conjugated, but also why the F1 pull-apart structures are always brecciated. The Bou Issarfane structure has a ca. N–S orientation like the F1 system, but unlikely lies at dip angles of 20–40° to the east. It consists of a 1.5 km long and 5 to 10 m thick silicified breccia system hosted by ignimbrites and rhyolitic tuff that is affected by E–W brittle faults (Figure 10a). While an unsilicified rhyodacitic lava flow occurs at the hanging wall, the footwall is made up of a 5–10 m thick anastomosed quartz stockwork. All veins are mostly filled in by quartz (Figure 10e,g–i) with scarce amount of adularia, sericite, chlorite, calcite and rare fluorite [47]. Sulphides are also common and mainly consist of arsenian pyrite (Figure 10f). Chalcopyrite, sphalerite, Pb–Cu–Bi assemblages (aikinite group) and electrum are accessory minerals and appear as inclusions within the As-rich pyrites (Figure 10f). Chlorite has a pycnochlorite composition and a Fe/Fe + Mg ratio close to 0.48 which is consistent with temperature of crystallisation bracketed between 210 and 280 °C [47]. All veins are characterised by internal textures typical of epithermal deposits according to Dong et al. [161]. The most representative quartz textures are those showing a partial replacement of a silica gel precursor characterised by colloform and moss texture (Figure 10g). Such textures are specific of siliceous sinters in active geothermal systems [161]. Ghost-bladed calcite textures [162] are also observed (Figure 10h,i). The occurrence of platy calcite (ghost-bladed calcite) demonstrates that boiling processes were active during vein formation [163–165]. Veins also show complex texture reflecting several stages of crystallisation, replacement and re-crystallisation occur. Within this complex process of vein formation, Tuduri [47] suggests that sulphides crystallised after the second stage of quartz replacement while electrum is mostly located within fissures of the pyrite. While the structural control of the F1 and F5 structures is clearly evidenced, the emplacement of the Bou Issarfane breccia remains

unclear and needs to be discussed. Fragments from the Bou Issarfane breccia are silicified, sub-angular and of dimensions lower than 1 cm. Their probable volcanic origin suggest minor distance of transport. The matrix is highly silicified and seems composed by detritus of rock fragments (host rocks), and (or) by comminuted gangue minerals.

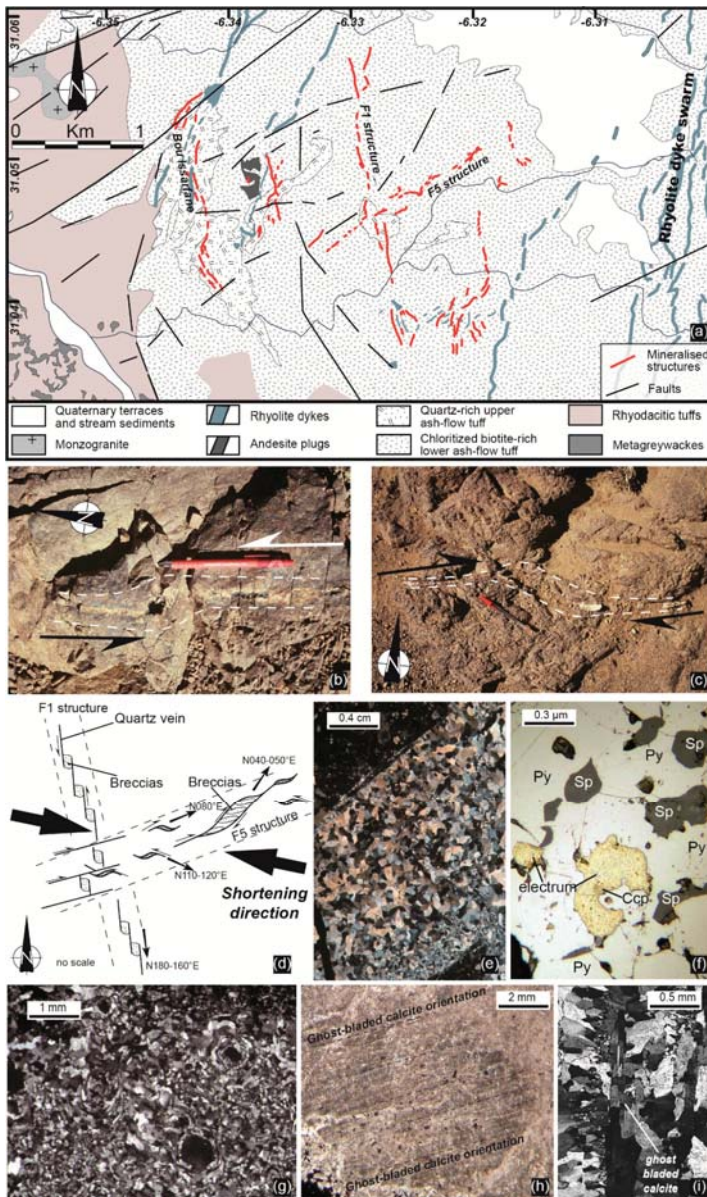


**Figure 10.** Main features of the Zone des Dykes deposits [47]. (a) General map of the Zone des Dykes Au-Ag deposit at the crossing between the F1 and F5 vein systems and Bou Issarfane area (after Tuduri [47]). (b) Pull-apart texture indicative of a left-lateral shearing movement along the F1 structure.

The filling is composed by quartz. (c) Pull-apart geometry of the F5 structure mainly filled by quartz and formed by dextral kinematics. (d) Global kinematic interpretation for the F1 and F5 structures integrating all the structural features observed in the field. (e) Microphotograph showing internal microtexture of the F1 structure characterized by a saccharoidal layout of quartz grains, cross polar light. (f) Typical gold-rich paragenesis of the F5 structure. Py: pyrite, Sp: sphalerite, Ccp: chalcopyrite. (g) Microphotograph of silica spheroid aggregates displaying moss texture, cross polar light. (h) Microphotograph of parallel ghost bladed calcites replaced by quartz, cross planar light and (i) plane polarized light microscopy.

The origin of this breccia may be therefore compared with phreatic or phreatomagmatic breccia pipes, although we cannot exclude a tectonic origin corresponding to a silicified cataclasite. According to salinity and homogenization temperatures, two type of fluids are assumed to be at the origin of the mineralised system [166]. The Bou Issarfane stockwork is characterised by primary multiphase fluid inclusions composed of liquid, vapour and halite cubes. Values obtained using the FIA concept indicate homogenization temperatures between 210 and 230 °C and moderate salinities (14–17 wt. % eq. NaCl). Secondary inclusions have lower homogenization temperatures between 130 and 180 °C. The F1–F5 veins consist of primary multiphase inclusions composed of liquid, vapour and halite cube with CaCl<sub>2</sub> assemblages.

Homogenization temperatures are bracketed between 160 and 180°C. Salinities are variable from 6% to 29% (wt. % NaCl + CaCl<sub>2</sub> equiv.) and may reflect the effects of boiling processes. Such textural, mineralogical and fluid characteristics suggest this hydrothermal Au–Ag(–Cu–Zn–Pb–Bi) system is comparable with intermediate sulfidation epithermal deposits as the ones reported in the Sierra Madre Occidental in Mexico [25,26,167]. The age of this ore deposit is still unknown. Considering the N–S trending direction of the F1 and Bou Issarfane structures, and the N–S trending direction of the rhyolitic dyke swarm, the mineralisation may have been formed coevally with this volcanic pulse around 565 Ma, i.e., after the emplacement of the ash-flow tuffs, that host the mineralisation dated, at 574 ± 7 and 571 ± 5, respectively [29]. However, we cannot exclude that the mineralisation is related to a later magmatic-hydrothermal period (e.g., the 550 or 530–520 Ma event) whilst no study has so far evidenced such later activity in the Bou Issarfane area.

#### 4.4. The Giant Ag–Hg Imiter Deposit

The world-class Ag–Hg mining district of Imiter (Figures 2 and 11a) with 8.5 Mt of ore at a concentration of 700 g/t Ag consists of mineralised quartz–carbonate veins hosted by metagreywackes and more seldomly by the lower volcanoclastic units of the Upper Complex. The ore is located along a major E–W faulted corridor (Figure 11a) and results from a two-stage model of formation [47,102]. The main economic stage 1 developed within a N070–090°E 75–90°N trending dextral vein system filled by grey quartz, adularia and minor pink dolomite (Figure 11b,c, [102]). Satellite veins are common (e.g., F0 South, F0 North, R7 and R6, Figure 11b) and were formed synchronously with the main ones (e.g., F0 and B3, Figure 11b) within a global model of formation that involves double restraining bends along a strike-slip system. Indeed, such a push-up geometry results from irregular trends and stepovers developed along the N070–090°E dextral regional-scale faults (Figures 2 and 11a,b). The system also includes steeply-dipping, listric reverse faults and veins that flatten with depth (N065°E 50°SE, Figure 11b,d,e) and therefore that become flat-lying faults/veins in deeper parts of mine (N065°E 20–30°SE, Figure 11b). Reverse motions are clearly observed along all these structures (Figure 11d,e) and are assumed to have been formed during transpression. They serve as receptacles for the late emplacement of the high-grade silver deposit defined by Ag–Hg and Ag-rich minerals (Figure 11f, [102]). The main economic paragenesis is characterised by massive deposition of Ag–Hg amalgam (luanheite, eugenite), polybasite–pearceite, acanthite, stephanite, pyrargyrite–proustite and imiterite [47,168–170]. Sphalerite and galena are abundant while no silver was detected. Arsenopyrite is well represented but always as small euhedral crystals of a few hundred micrometers [47].

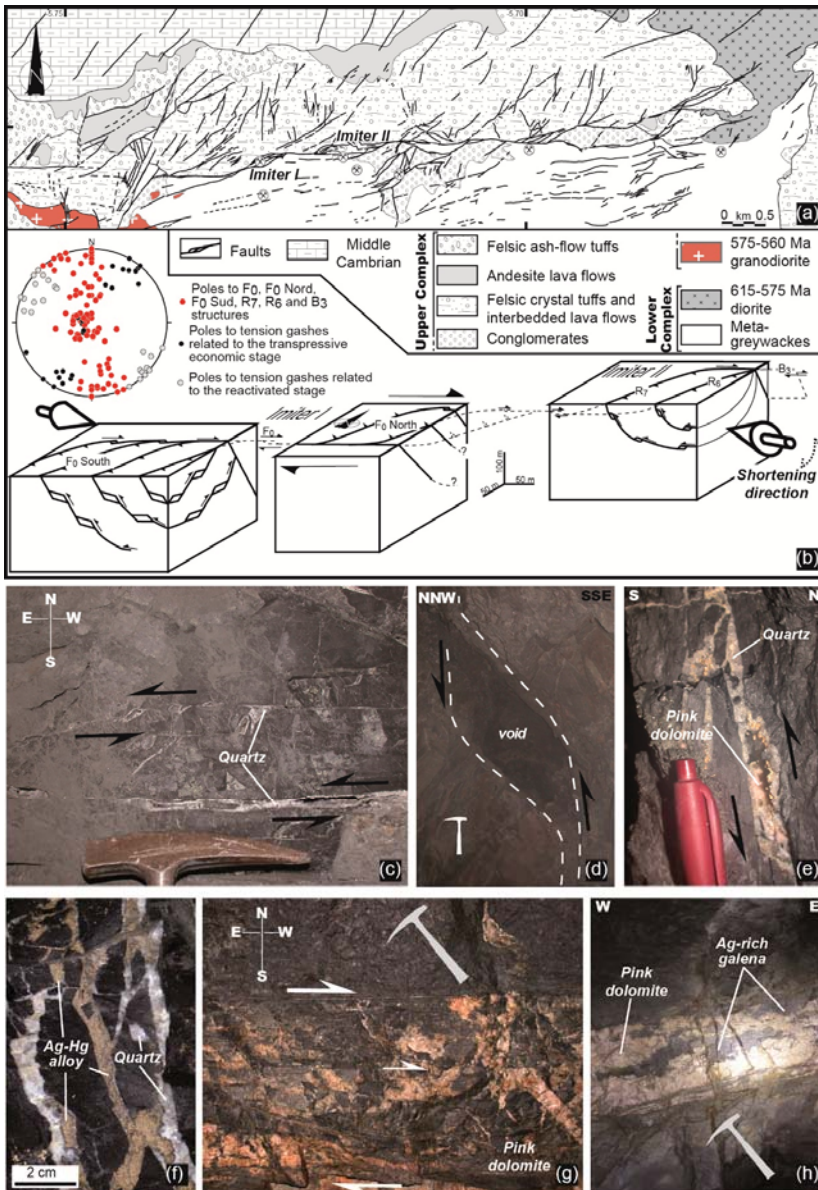


**Figure 11.** Main features of the world-class Ag–Hg Imiter mining district [47,102]. (a) General map of the giant Ag–Hg Imiter mine (after Leistel and Qadrouci [127] and Tuduri [47]) and (b) stereoplots of structural orientations and interpretative block diagram explaining the formation of the main ore-bearing vein system. Thrusts are formed in core of transpressive push-up structures. Note that the mineralised structures were everywhere controlled by a ESE–WNW direction of shortening. (c) Pull-apart and tension-gashes structures of the economic stage filled by geodic quartz and formed

during dextral kinematics,  $F_0$  North vein systems, view realised towards the top of the mining gallery, Imiter I. (d) Pull-apart geometry of the economic stage indicative of a reverse shearing towards the north and showing void formations,  $R_6$  structure, Imiter II. (e) Pull-apart texture of the  $F_0$  South vein systems, thrusting towards the NW–NNW. The filling is composed by quartz (economic stage) and scarce pink dolomite in core of pull-apart texture. (f) Typical paragenesis of the economic stage 1 composed by quartz veins and huge concentration of Ag–Hg alloys, Imiter I,  $F_0$  south. (g) Tension gashes and left lateral pull-apart structures filled with pink dolomite of the stage 2,  $F_0$  structure, Imiter I. (h) Typical features of the stage 2 pink dolomite stage with large patches of Ag-rich galena,  $F_0$  structure, Imiter I. Since photographs c and h were taken towards the top of exploration galleries, kinematics interpretation must be inverted.

Tuduri et al. [102] further demonstrated that a stage 2 reactivated the transpression-related structures in the opposite sense, and developed normal left-lateral motions associated with massive pink dolomite crystallisation, as well as prismatic quartz and variable amounts of Ag-rich galena and sphalerite, pyrite, chalcocopyrite, arsenopyrite and freibergite (Figure 11g,h). Note that these two economic stages were preceded by a barren quartz vein network stage associated with sericite, illite-chlorite and base-metal sulphide minerals such as pyrite, galena, sphalerite with chalcocopyrite exsolutions [45,47,51,127,169–171].

The main driving mechanism for silver ore deposition is assumed to be the dilution of ore-bearing fluids that were  $\text{CaCl}_2$ -dominated. Values obtained using the FIA concept [172,173] point to a general temperature decrease from stage 1 (280–100 °C) to stage 2 (110–60 °C). Note that the deepest levels of the mine workings (–220 m below the surface) record temperature in excess of 60 °C (i.e., lowest temperatures >160 °C) with respect to the shallow levels (–100 m) where the lowest temperatures are around 100 °C. During stage 1, fluid salinities are moderate to high (8.4 to 26.1 wt. %  $\text{NaCl} + \text{CaCl}_2$  equiv.), whereas they are very high when stage 2 dolomite precipitates (24.6 to 30 wt. %  $\text{NaCl} + \text{CaCl}_2$  equiv.). Such value ranges are in agreement with data published by previous authors whether or not they used the FIA concept [41,45,101,171]. At shallower levels, additional supergene enrichment has been responsible for massive formation of native silver (1500 g/t Ag) associated with cerussite and mimetite [164].

Work in progress shows that Ag–Hg sulfosalts could also be related to the supergene processes [174]. Two opposing ore-forming models are strongly debated at Imiter. Some authors taking into account halogen composition of fluid inclusions, stable (C, O, S) and radiogenic (Pb, Re/O) isotope data together with noble gas (He) isotope compositions, suggest that the deposit is consistent with an epithermal model related to the felsic volcanic event at the Precambrian–Cambrian transition [45,47,51,101,127,170,175]. In that way, the huge Ag–Hg deposit would be comparable with the ones from the Mexican Sierra Madre Occidental Ag–Pb–Zn–Au belt, and should be considered as an intermediate sulfidation epithermal deposit [167,175]. On the other hand, a lithogene model [176] has been alternatively proposed in which fluids, according to laser ablation inductively coupled plasma-mass spectrometry (LA-ICP-MS) data on fluid inclusions, halogen signatures, and stable isotopes (H, C, O), are the products of diagenetic brine–evaporite interactions within a sedimentary basin [41]. The ore deposit might also be the result of basin inversion that expelled deep Ag-rich brines during, or at the end, of the Palaeozoic orogeny [41,175]. Recent  $^{40}\text{Ar}/^{39}\text{Ar}$  age measured at  $255 \pm 3$  Ma on adularia from stage 1 quartz vein supports the late Palaeozoic brine model [38].

## 5. Discussion

### 5.1. A Simplified Tectono-Magmatic Evolution Model of the Eastern Anti-Atlas

The evolution and transition between two main tectono-magmatic events is of importance in the Eastern Anti-Atlas and deserves to be discussed extensively and integrated with metallogenetic issues.

5.1.1. The Lower Complex and the D<sub>1</sub> Deformation

The D<sub>1</sub> deformation affects metagreywackes and metavolcanics and is associated with the syntectonic emplacement of calc-alkaline diorite and granodiorite plutons (Figure 12a). It is consistent with a NW–SE to WNW–ESE trending horizontal shortening. Structural studies have highlighted several important deformation structures related to that D<sub>1</sub> stage, i.e., upright tight folds with large-scale anticline and syncline, development of an axial planar S<sub>0–1</sub> foliation, regional-scale N070–090°E trending dextral wrenching shear-zones, contact metamorphic minerals defining a stretching lineation (L<sub>1</sub>) and rare S–SE-verging thrusts; Figures 2–4. Some plutons are inferred to be coeval with the D<sub>1</sub> deformation. Indeed, some of them are emplaced within the N070–090°E dextral shear-zones where they develop penetrative magmatic foliation and lineation. Elsewhere, other plutons seem to be emplaced in the core of folded sequences [47,121]. Furthermore, a tectonically-controlled fabric is best expressed in the thermal metamorphic aureoles developed around such plutons. There, foliations, lineations and related shear sense indicators show top-to-the-SSE–SE thrusting (Figure 4b,d) and dextral shearing depending on the distance from major shear-zones [47,121]. For those reasons, such diorite and granodiorite intrusions are herein interpreted as syntectonic and emplaced under the control of a NW–SE to WNW–ESE trending shortening [47,48,121]. This is consistent with the model of Saquaque et al. [77] who proposed that the main regional deformation results in top-to-the-SE thrusting, right-lateral wrenching along ca. E–W to ENE–WSW shear zones and syn-tectonic plutons. Since we herein combine strike-slip and shortening that is roughly perpendicular to the shear-zones, we infer a global transpressive tectonic regime as dominant in the D<sub>1</sub> stage. The characteristics of this tectonic stage that associates transpressive tectonics, pluton emplacement, strike-slip and rare thrusts explain the heterogeneity of the deformation observed within the entire Jbel Saghro.

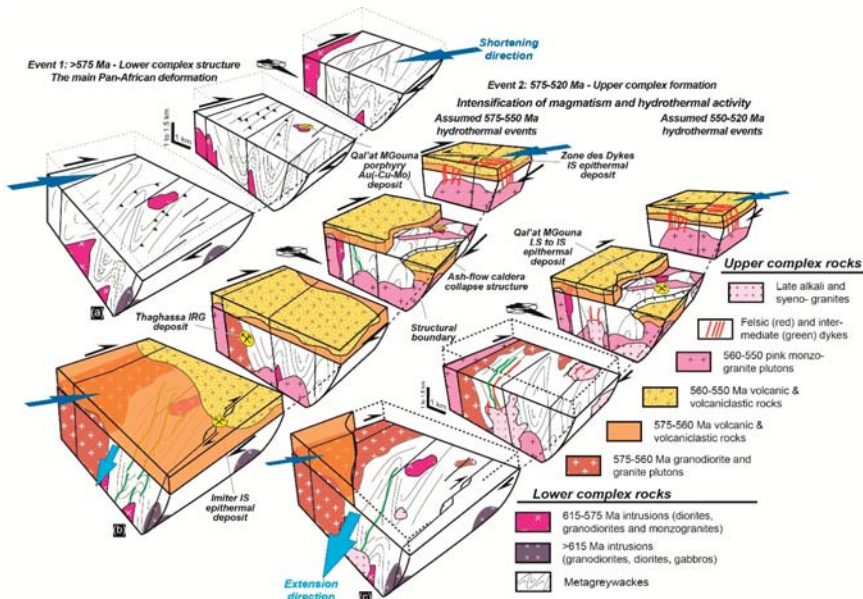


**Figure 12.** Interpretative three-phase model (a–c) explaining the tectono-magmatic evolution as well as the Lower and Upper Complexes definition of the Jbel Saghro and the formation of the ore-bearing vein systems of the Zone des Dykes, Qal’at MGouna, Thaghassa and Imiter districts. The size of the blue arrow relates with the inferred intensity of regional stress. See text for explanation. Note that the Qal’at MGouna porphyry deposit may belong to either the late stage of event 1 or the earlier stage of event 2 as the related porphyry stock emplaced at the transition between the two at 576 ± 5 Ma [29].

Previous interpretations tried to link each type of structures or pluton emplacement to one distinct tectonic event, increasing the complexity. From this study, it appears more appropriate to interpret all these features by the occurrence of a single and unique  $D_1$  tectono-magmatic event. According to Gasquet et al. [83], as basins infilling with greywacke sequences was active until the onset of the Ediacaran period between 630 and 610 Ma; we suggest that the  $D_1$  deformation probably occurred coevally with the syn-tectonic calc-alkaline magmatic occurrences, those being dated from ca. 615 Ma until ca. 575–565 Ma. This upper 575–565 Ma limit for the  $D_1$  age is an important issue and will be further discussed below.

### 5.1.2. The Upper Complex and the $D_2$ Deformation

The Upper Complex is dominated by ash-flow tuffs emplaced in three main flare-ups and exposed inside or outside caldera structures, and by plutonic intrusions, mostly granitic, that were coeval with this  $D_2$ -related deformation (Figure 12b). Deformation was very weak and characterised by a brittle regime mainly represented by fault zones and vein formation throughout the Jbel Saghro area. Faults are mostly characterised by ca.  $N070\text{--}090^\circ\text{E}$  orientations for the dextral strike-slip ones [47] whereas the ca. NW–SE trending direction may correspond to conjugate strike slip faults. However and according to Soulaimani et al. [86,87] and Azizi Samir et al. [177], the ca. NW–SE trending direction also corresponds to normal faulting yielding tilted blocks with syn-sedimentation processes. Such sedimentary deposits are volcanoclastic. The huge volumes of ash-flow tuffs associated with lava flows and related intrusions is considered as evidence for ash-flow caldera such as in the Qal'at Mgouna or Oued Dar'a areas (Figures 2 and 12b). We cannot exclude the presence of other caldera structures elsewhere in the Eastern Anti-Atlas. Because the structural limits of these caldera structures preferentially trend WNW–ESE to NW–SE [29,47], i.e., perpendicular to the direction of extension, the caldera yields an elliptic shape and is interpreted to be structurally controlled [141].

Three main ignimbrite flare-ups have been defined in the Upper Complex formation. The first one may have been emplaced at ca. 575 Ma and consists of dacitic ash-flow tuffs with related granodiorite and monzogranites [29]. The second flare-up occurred probably around 565 Ma and is related to monzogranite and granodiorite intrusions as well as the huge rhyo-dacitic dyke swarm in the western part of the Saghro [29,48,78,107]. The third ignimbrite flare-up is related to rhyolitic ash-flow tuff and cogenetic monzo-to-syenogranite emplaced around 555 Ma [29,51,74,106,107]. Finally, a late magmatic stage is composed of the alkali-syenogranite plutons and related rhyolite dykes (Figure 12c). Such late alkali magmas highlight the persistence of the magmatism even after the emplacement of caldera-related rocks although they are less abundant. No radiometric ages are currently available on the alkali granites but related dykes provide ages bracketed between 550 and 520 Ma at the transition between the Proterozoic and Phanerozoic aeon [51,74,107,108]. Note that most of the intrusives such as aplitic and rhyolite dykes display a change in their orientation (i.e.,  $\sim N020^\circ\text{E}$ , Figure 9c). Also, most of the hydrothermal veins related to those dykes and alkali plutons have the same direction pattern (Figure 9c). As no clear direction of shearing is evidenced in the horizontal plane, it is herein suggested that an external tectonic setting may control and assist the emplacement of both magmatic and hydrothermal structures in the ca. 550–520 Ma interval. The  $D_2$  event is controlled by a ca. NW–SE to WNW–ESE direction of shortening and a ca. NE–SW to NNE–SSW direction of extension. Such control may evolve later toward a ca. N–S shortening direction and a ca. E–W extensional direction during the early Cambrian stage. This would be consistent with what is observed during the Adoudouian rifting period [86,87,106].

### 5.1.3. About the Transition between the Two Complexes and the $D_1$ and $D_2$ Tectonics

In the Eastern Anti-Atlas, the transition between the Lower and Upper Complexes is characterised by a significant increase of the magmatic addition rate [178] mostly evidenced by the Ediacaran volcanic flare-ups and by a change in the tectonic regime. However, such a transition appears as diachronous whether we consider the start of the volcanic activity or the change in tectonic regime.



The key evidence highlighting such a transition is the existence of an angular unconformity between the Lower and Upper Complex units [29,47,74,78]. However, the age of the transition remains elusive and debated. If we consider the available ages earlier volcanics of the Upper Complex that lie above the unconformity, the transition might occur between 580 and 570 Ma taking into account the error bars of the radiometric ages. This has been well described in the Western Anti-Atlas on the Tizgui geological map [29,179]. In the Central Anti-Atlas, Blein et al. [78] also suggest that most of the regional deformation observed there was completed by ca. 580 Ma and followed by an important erosional phase prior to the deposition of the Upper Complex volcanoclastic sequences. The 575 Ma age, therefore, represents a mean value.

Dating the deformations and thus the change in the tectonic regime from  $D_1$  to  $D_2$  is matter of more confusion. Indeed, the transition between the two complexes is estimated at ca. 575 Ma with the incipient volcanic activity and the occurrence of a strong angular unconformity. By contrast, the transition between the two deformation events would be a little more recent and would have occurred around 565 Ma. The age assigned to the  $D_1$  deformation appears thus mostly dependent on the radiometric ages obtained on the syntectonic plutons, and the issue of what plutons are syntectonic or not in the Eastern Anti-Atlas is clearly to be better assessed from field data. Currently, numerous plutons emplaced between ca. 575 and 565 Ma have been interpreted as syntectonic as they develop a coherent and homogenous ductile deformation in contact aureoles [48,105,106,121,123]. Given the error bars on the ages, we can actually question on their belonging to the earlier Upper Complex structuration, or to the later stage of the Lower Complex and  $D_1$  deformation. As a matter of fact, discussions do exist about the possible intrusive character of some of these plutons in the lower part of the Upper Complex (e.g., The Igoudrane, Taouzzakt and Iknwn plutons, Figures 2 and 3), while they may display an erosive roof on which lies Upper Complex volcanoclastics (at least the upper part of the Upper Complex). In addition, we have shown above that magmatic mushes at the origin of plutons emplaced around 575 and 565 Ma may be at the origin of the former ignimbritic flare-ups.

In any case, we assume that between 575 and 565 Ma, syn- $D_1$  plutons have developed in the Lower Complex metagreywackes, both contact metamorphism and ductile deformation that we interpret as the ongoing tectono-magmatic evolution between the Lower and Upper Complex structuration as suggested by Tuduri et al. [48]. Possibly, the  $S_2$  cleavage refraction that developed after the main first-order folding event may be related to this transitional stage. It also remains difficult to assess whether some plutons were intruded within folds (e.g., the Bou Teglimt granodiorite in core of the Imiter inlier anticline, Figure 3a) and thus after the folding event (i.e., plutons would belong to the earlier stage of the Upper Complex) or if their emplacement played a part in the anticline structuring (i.e., plutons would belong to the Lower Complex tectono-magmatic history). Consequently, taking the important dioritic and granodioritic plutonism as systematically belonging to the Lower Complex might be misleading. As well, it is not straightforward to math the change in the tectonic regime ( $D_1$ - $D_2$  transition) with the transition between the Lower and Upper Complexes.

Therefore, we herein suggest that the reported tectonic transition must have been an ongoing process through the Lower-Upper Complex transition, given the deformation features (cleavage, weak upright folding) observed in the volcanoclastic rocks of the lower part of the Upper Complex in the western Saghro and Central Anti-Atlas [29,78]. Indeed, Blein et al. [78] recall that rapid variations in thickness of the volcanic and volcanoclastic rocks of the Upper Complex suggest they were deposited during active tectonics and on highly variable basement (i.e., Lower Complex units) topography. Such variations in the topography may be due to the earlier transpressive stage but also to later extensional-transensional tectonics. In the rest of the Jbel Saghro no clear evidence of deformation (except cleavage) has been described affecting the lower part of the Upper Complex rocks. Note that the “Série molassique du Dadès” described by Walsh et al. [29] in the northern Qal’at Mgouna area, as being bedded, deformed and weakly metamorphosed in lower greenschist facies corresponds to the tilted intra-caldera volcanic sequence which underwent prophylic hydrothermal alteration. This formation herein belongs to the Upper Complex.

The preservation of the same shortening direction and tectonic style (i.e., strike slip dominated) further suggests that D<sub>2</sub> is a continuation of D<sub>1</sub> even though D<sub>1</sub> was associated with transpressive tectonics and D<sub>2</sub> linked with transtension to extension. Eventually, the transition between the D<sub>1</sub> and the D<sub>2</sub> deformation regimes occurred, while the shortening direction (parallel to Z strain axis) remained roughly constant (i.e., NWSE to WNW–ESE). However, one can note a shift in the two other strain directions showing a decrease of the vertical extension that becomes horizontal. This explains the numerous extensional features developed during the D<sub>2</sub> stage (i.e., calderas formation and multiple ore concentrations within open structures). We note that the transition from D<sub>1</sub> to D<sub>2</sub> must be achieved prior the emplacement of the Thaghassa IRGD around 565 Ma [48]. This transition is supposed to be progressive and the earliest mineralisation stages, such as the ones emplaced in the Thaghassa area, are the witnesses of this transition.

Therefore, we assume that the D<sub>1</sub> deformation might affect the lower units of the Upper Complex. Future works may focus on testing this assumption. The contrasting structural levels that exist between the Lower Complex and Upper Complex units may argue against such a continuum. However, the combination of exhumation processes along strike-slip fault systems and of denudation history, integrating erosion processes [180–182] provides the first elements of an answer. Moreover, ignimbrite flare-ups and caldera formation are assumed to have been occurred rapidly as catastrophic events, contributing unconformities between the volcanoclastic rocks of the Upper Complex and the Lower Complex units.

### *5.2. The Mineralising Model*

This study demonstrates the strong spatial link that exists between ore deposits and magmatism in the Eastern Anti-Atlas. A common hypothesis for the source of the mineralisation is to involve fluid exsolutions from intrusions. Even though we cannot demonstrate this assumption for all the ore deposits, a progressive and continuous vein formation model that began in the magmatic stage, developed an intermediate stage and finally ended under hydrothermal conditions is well constrained at Thaghassa and Qal'at Mgouna. Such a model of ore formation thus involves a three-stage model as stated in Table 1. About the economic stages, even though they were formed late during the veining stage, they benefited from the existence of previously formed veins. This model again highlights the significant role of the magmatism and related structures for ore deposition and concentration [183].

Table 1. Synthetic table summarizing the magmatic-hydrothermal features of main ore deposits of the Saghro area.

	The Zone des Dykes Deposit	The Qal'at MGouna District	The Thaghassa Deposit	The Imiter Deposit
Stage I (strong magmatic affinities)	Not expressed	Alkali-granite emplacement with quartz, K-feldspar, F-tourmaline, F-muscovite in miarolitic cavities and stockschneider (400 < T °C < 600) <sup>1</sup>	Aplite dyke emplacement (500 < T °C < 600 °C) <sup>1</sup>	Not expressed
Stage II (intermediate stage between magmatic and hydrothermal conditions)	Not expressed	Strong alteration with quartz, F-tourmaline, F-Cl-micas, andalusite, F-Cl apatite, monazite (250 < T °C < 400) <sup>1</sup>	Quartz, K-feldspar, muscovite, apatite, tourmaline and apatite (T °C < 500) <sup>1</sup>	Not expressed
Stage III (hydrothermal)	Quartz, adularia veins with calcite, chlorite, sulfides and gold (210 < T °C < 280) <sup>1</sup>	Quartz stockwork with Cl-biotite, Cl-amphibole, muscovite, sulfides (Cu-Mo) and gold (160 < T °C < 460) <sup>1</sup>	Striped quartz veins filled by quartz, sericite, sulfides and gold (300 < T °C < 450) <sup>1</sup>	Firstly, quartz-adularia veins with silver-rich sulfides and alloys (100 < T °C < 280) <sup>1</sup> and then dolomite-quartz veins with Ag-rich galena and sphalerite (60 < T °C < 110) <sup>1</sup>

<sup>1</sup> Temperatures have been estimated using selected geothermometers applied on micas [184], chlorites [185,186], arsenopyrites [187,188], activity diagrams generated for tourmaline, albite, andalusite, paragonite and kaolinite [189] and microthermometric data results [41,45,48,155,159,160,166,170–173]. See Tuduiri [47] for details.

- The first stage shows strong magmatic influence. It is characterised by emplacement of porphyry stocks, aplite dykes and sills at high temperatures from 400 °C up to 600 °C. At Thaghassa, this stage was responsible for the partial melting of the metagreywackes in response to the Iknawn granodiorite thermal effect and for the related genesis of leucocratic S-type haplogranitic sills. In the Qal'at Mgouna district, this stage was responsible for the formation of stockscheider and miarolitic cavities within sills and dykes.
- The second intermediate stage consists of magmatic-hydrothermal vein emplacement and associated pervasive alteration. The persistence of the magmatic character is shown by the occurrence of high-temperature alteration phases such as tourmaline, micas, andalusite, apatite, K-feldspar with quartz. In the Qal'at Mgouna district, at Isamlal, this stage can be compared with the classical potassic and magnetite alteration in some porphyry type systems [190]. It is also marked by the wide pervasive development of Al-silicate–Al-hydroxide–phosphate–muscovite–F-rich phlogopite and F-rich tourmaline alteration, related to the late Si-rich alkali granites. K-feldspar, apatite, white mica along vein rims are observed at the beginning of vein aperture at Thaghassa. Temperatures of formation are bracketed between 250 and 500 °C.
- The third stage is hydrothermal and formed at lower temperature ( $60 < T (^{\circ}\text{C}) < 300$ ) producing gangue minerals except for the Thaghassa and Isamlal deposits where high-temperature minerals were also formed (350–450 °C). This stage end with the emplacement of economic ore.

The conditions of vein formation vary depending on their location in the Lower or Upper Complex and are reflected by variations in mineralogy and internal texture. Such variations are basically due to different structural levels of formation. Indeed, the geometry of the mineralised structures is controlled by tectonics, hydrostatic pressure, effective vertical stress and volcano-related effects. The Thaghassa prospect, hosted by the Lower Complex metagreywakes, exhibits texture and mineralogy indicative of high-temperature conditions of formation. The Zone des Dykes vein system, entirely developed in Upper Complex ash-flow tuffs, shows internal textures consistent with low-temperature epithermal deposits. The Qal'at Mgouna deposits are developed at an intermediate structural level. Veins hosted by the Lower Complex rocks are related to high-temperature formation (i.e., the Isamlal porphyry Au(–Cu\_Mo) deposit) whereas those formed at shallower levels reflect low-temperature conditions (Talat-n-Tabarought and Tawirt-n-Cwalh districts). Tuduri et al. [154] suggest that high temperature systems emplaced at ca. 150–200 MPa, whereas the lower temperature systems were formed at a lower depth (20–50 MPa). The regional variations clearly document the transition from magmatic to hydrothermal conditions, i.e., from somewhat high temperature fluids (350 °C and higher) at Thaghassa and Isamlal, to lower temperature hydrothermal fluids (below 300 °C) at the Zone des Dykes and Imiter.

For all ore deposits described in this study, the Ag and Au economic concentrations (with Cu, Zn, Pb) correlate with ore-forming fluids with moderate to high salinity. This is consistent with transport by chloro-complexes and confirms the importance of brines in such ore formation. If brines are frequent in the formation of porphyry copper deposit [183,191] and probably IRGDs [64,68], their role in intermediate sulfidation epithermal systems remains a matter of debate. In large Mexican epithermal silver deposits of intermediate sulfidation state, Wilkinson et al. [26] suggested that the ore forming fluids, were injected into a geothermal circulation system in response to the ascent of a magmatic intrusion. Such hydrothermal diapirs would be sourced from a stratified hyper-saline brine reservoir, formed in response to incremental exsolution of magmatic fluid, and intense brine condensation at depth, with halite precipitation, being stored above the source magma reservoirs [26, 192,193]. By contrast, Essarraj et al. [40,41,49] suggested that the ore-forming fluids were related to deep-basinal sedimentary brines and that metals had no genetic relationship with Neoproterozoic magmatism, on the basis of numerous deposits they investigated in the Eastern and Central Anti-Atlas. They suggested that ore brines resulted from evaporatively concentrated seawater in Triassic basins producing hot basinal brines, comparable with conditions for Mississippi Valley-Type (MVT) deposits.

We here suggest that all ore deposits described above are related to the Ediacaran magmatic-hydrothermal complex emplaced from 575 to 530–520 Ma. The concept of stored hypersaline brines is emphasised following Scott et al. [193]. Nevertheless, while a magmatic origin of such stored brines is obvious, the origin for Ca-rich brines has yet to be defined. Though such Ca-rich brines may derive from magmatic processes, they are also widespread in the deeper parts of many sedimentary basins and involved in ore forming processes [194,195]. This is, pro parte, the reason why Essarraj et al. [40,41,49] support a deep-basinal sedimentary brine model in the Anti-Atlas. Surprisingly, they do not support an Ediacaran model for such a model but a more recent one that is Permo-Triassic in age. Nevertheless, prior and during the early stage of development of the SLIP that characterise the Upper Complex and the related ore deposits, periods that roughly belong to the Ediacaran Gaskiers glaciation on the West African Craton and around [196,197], would have occurred between 595 and 565 Ma in the Anti-Atlas [198]. Such evidence may also point to a possible contribution of natural cryogenic brines in the ore forming processes. Indeed, according to the Starinsky model of evolution of a marine-cryogenic basin [199], these brines usually are seawater-derived and also enriched in Mg, K, Na, Ca, Cl, SO<sub>4</sub> and Br, even if they may have been heavily modified by fluid–rock interactions and(or) dilution [200]. Future studies would have to address the possible role of Ediacaran glaciations on the ore-forming processes in the Anti-Atlas.

The age of the mineralisations in the Jbel Saghro remains poorly constrained due to the lack of absolute dating. Nevertheless, we can assume that the transtensional regime characteristic of the Upper Complex provided extensional structures for melt and fluid circulations that are favourable for magmatic-hydrothermal ore forming processes. This period of time (575–550 Ma and 550–520 Ma) was suitable for ore emplacement as suggested above. We thus assume that most of the mineralised systems may have been emplaced between ca. 575 and 520 Ma. Indeed, these ore deposits seem to have been emplaced when tectonic regime changes at the transition between the Lower and Upper Complexes and when the typical medium-K calc-alkaline arc magmatism became more abundant in between 580 and 570 Ma. Some porphyry Au(–Cu–Mo) deposit may have been emplaced earlier around 575 Ma. In the Sirwa mountains belonging to the Central Anti-Atlas, Cu–Mo ± Au mineralisations associated with high-K calc-alkaline intrusions are also assumed to have been formed between 575 and 560 Ma [59,201]. Similar ages are also suggested in the vicinity of Bouskour where Re/Os analyses on molybdenite related to a Cu-rich mineralised stage, yield a weighted average age of  $574.9 \pm 2.4$  Ma [103]. Further, the Thaghasa deposit displays strong similarities with the earlier base metal assemblage observed at Imiter and Tiouit [43,45,47,48,51]. Indeed, in the Tiouit gold deposit, the ore body is closely associated with the Iknawn granodiorite dated at  $564 \pm 6$  [48]. At Imiter, <sup>40</sup>Ar/<sup>39</sup>Ar dating on sericites related to the earlier base metal sulphide veins range from  $577 \pm 4$  to  $563 \pm 5$  Ma, in good agreement with the synchronous Taouzzakt granodiorite dated at  $572 \pm 5$  Ma and the Thaghasa model of emplacement (U–Pb radiometric ages on zircon, [48,51]). The intermediate sulfidation epithermal Au(–Ag–Cu–Pb–Zn) deposit of the Zone des Dykes may have been emplaced during lull periods soon after the emplacement of the second ignimbrite flare-up and related huge dyke swarm in the western Saghro (around 560 Ma). Similarly, the huge intermediate sulfidation epithermal Ag(–Hg–Pb–Zn) deposit at Imiter may have been emplaced following the third ignimbrite flare-up around 550 Ma. This assumption adopts the age already proposed for the Imiter mineralisation on the basis of absolute dating of felsic volcanism at 550 Ma [45,51,101]. Lastly, we suggest that the intermediate to low sulfidation epithermal Au–Ag–Te deposits were emplaced later when magmatism became less abundant, more silicic and alkaline between 550 and 530–520 Ma [74,107,108]. This is supported by the fact that some late rhyolitic dykes do not cross the Cambrian boundary while they cut across mineralised structures, at Qal’at Mgouna for example (Figure 9a)

5.3. Implication of the Tectonic Regime Changes for the Late Neoproterozoic—Early Cambrian Geodynamic Evolution and Ore Deposit Emplacement

In the light of our results, a geodynamic evolution model is proposed (Figure 13), showing the spatial and temporal distribution of metal deposits in the Eastern Anti-Atlas that may be reasonably extended to the whole Anti-Atlas. Considering the tectonic and metallogenetic framework at the scale of the Anti-Atlas regional scale, we suggest a first-order influence of subduction dynamics on the shift with time of metal concentrations and ore deposit types in the Anti-Atlas. In our scenario (Figure 13a,b) and according to Walsh et al. [29], the 615–575 Ma period is characterised by an Andean-type subduction of a wide continuous slab along the northern Gondwana margin (i.e., the currently northern side of South America and Africa). This long period of subduction (ca. 40 Myr) probably occurs because the large slab width (>2000 km) increases the viscous resistance of the mantle on the slab [202]. In that model, oceanic lithosphere *subducts* beneath the continental lithosphere that progressively becomes thicker due to the presence of the West African Craton. Suction between ocean and continent increases, favouring slab flattening and mantle wedge closure [203].

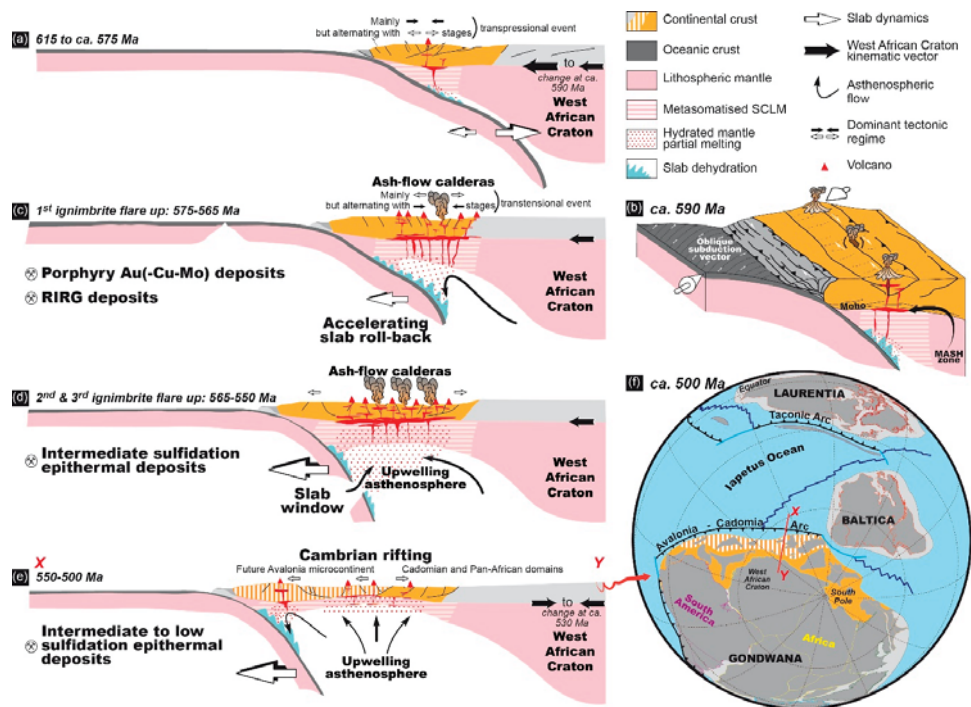


Figure 13. Compiled lithospheric-scale reconstructions (a–e) of the Pan-African/Cadomian belt systems from the West African Craton foreland to the Iapetus oceanic domain showing the possible progressive slab retreat since ca. 575 Ma to 500 Ma as suggested in text. Zones of partial melting in both the subcontinental lithospheric mantle (SCLM) and the lower crust, as well as the zones of storage and transfer of melts are shown in red. Kinematic vectors related to the West African Craton drifting are from Merdith et al. [204] using the GPlates software [205]. The palaeotectonic map reconstruction of Gondwana (f) has been realised using the GPlates software and the global plate models with kinematic continuity of Domeier [206].

Both slab flattening and probably relatively high convergence rate control the D<sub>1</sub> deformation in the overriding plate. A subduction vector (Figure 13b) oblique to the continental margin may explain

the overall transpression regime that characterises the Lower Complex. Indeed, the lack of nappes, fold nappes, mylonitic fabrics and metamorphic gradient preclude a continental collision setting in that period. Possibly, a volcanic arc accretion event may locally emphasize this deformation. Melt generation remains limited given the restricted size of the mantle wedge while their ascent may occur when regional or local extensional regime occurred (Figure 13a,b). Ore forming processes are limited in this setting as they depend on the generation and ascent of fertile melts. However, melts produced and stored at depth in the MASH (melting, assimilation, storage and homogenization) zone may become more fertile in the following stages.

From 575 Ma, the ongoing evolution of the flattened subduction of oceanic beneath cratonic lithospheres causes a dynamic push on the slab surface [203]. This occurs as the rate of wedge closure increases, pushing the slab backward and initiating slab roll-back and high-volume magmatic production (Figure 13c), ultimately leading to the first ignimbrite flare-up. Ongoing slab roll-back along with tectonic regimes becoming more extensional initiate the second, and then the third ignimbrite flare-ups (Figure 13d). Slab tearing and (or) breakoff provide important asthenospheric flow that probably catalyse partial melting of both the asthenospheric mantle wedge and subcontinental lithosphere mantle (SCLM). The latest alkali magmas are assumed to have been emplaced at an extensional stage related to the Adoudounian rift in the Western Anti-Atlas [87,106] that corresponds to a back-arc setting. Such ongoing extensional tectonics [206,207] will ultimately result in the opening of the future Rheic Ocean (Figure 13e,f).

A collision then post-collision scenario cannot be applied to the Anti-Atlas region between 615 and 520 Ma, since subduction do not cease in our model but progressively migrate towards lower latitudes (Figure 13). Eventually, such subduction dynamics determine the dominant stress regime in the overriding plate, which influences the metals mobilization in the MASH zone and, their ascent through the crust, and thus controls the distribution of resulting metal occurrences [208–212].

According to Tosdal and Richards [211], most of the mineralised structures are suggested to have formed during the D<sub>2</sub>-related transtensive regime caused by shortening in a WNW–ESE direction and extension along the NNE–SSW direction (Figures 12c and 13c–e). In our interpretation, porphyry Au(–Cu–Mo) and intrusion-related gold deposits are emplaced earlier than the first and(or) second ignimbrite flare-ups (i.e., 575 and(or) 565 Ma). Intermediate sulfidation epithermal Au, Ag deposits may be emplaced during lull periods after the second and (or) the third flare-ups (i.e., 560 and(or) 550 Ma). Compressive structures are indicated in the Zone des Dykes and Imiter districts, as the result of likely a specific structures geometry with respect to the shortening direction. Intermediate to low sulfidation epithermal Au–Ag–Te deposits are emplaced late and in relation with the felsic alkaline magmatic stage (550–520 Ma).

We have stressed here the existence of a long period of magmatism, i.e., over a 95 Myr duration, which is characterised by an increase in produced magmatic volumes, probably in response to geodynamical controls, marked by a late magmatic paroxysm in the form of several ignimbrite flare-ups over a shorter duration of ca. 25 Myr. Such long-lived magmatic activity is paralleled by a tectonic progressive evolution from beginning within transpression conditions to transtension then extension, allowing the mineralisations to take place.

At the regional scale, we may question a possible diachronism of the magmatic activity between the western Bou Azzer and Siroua and the eastern Saghro inliers (Figure 2). Indeed, the main volcanic event occurred between 580 and 560 Ma in Bou Azzer, Siroua and western Saghro inliers. In the central and eastern Jbel Saghro area, volcanic rocks as reported are somewhat younger and mostly dated between 570 and 550 Ma from west to east [51,74]. This suggests that the main volcanic stage progresses toward the east along with the D<sub>2</sub> tectonic regime. If we compare with the Sierra Madre Occidental as a model of large silicic volcanic province [14,147,148,213], the widespread ash-flow tuff deposits of the Anti-Atlas domain should be emplaced as ignimbrite flare-ups and are correlated with progressive and diachronic formation toward the east of caldera collapse structures, broadly oriented E–W to NW–SE. This volcano-structural framework developed coevally with a transtensive tectonic

regime characterised by both NNE–SSW extension and WNW–ESE shortening. In terms of melting processes, the main controlling factor in the generation of such a SLIP is a crustal setting located along a long-lived active subduction zone that evolves into a post-subduction domain via slab-roll back processes. According to Bryan and Ferrari [14] and Ernst [12], a huge thermal pulse is at the origin of a large-scale crustal anataxis of fertile and hydrous lower-crustal materials as well as metasomatised subcontinental lithospheric mantle. Flare-up models are in part inherited from the late evolution of arc settings that underwent slab-roll back, slab-breakoff and slab-window [14,147,148,214], as propoded here and correlated with the D<sub>1</sub> and D<sub>2</sub> tectonic model (Figure 13). Because they represent transient events of high magmatic fluxes from the mantle [215], volcanic flare ups are considered here as highly potential for Ag(–Au) economic deposits emplacement.

## 6. Conclusions

We document in this paper a long-lived tectono-magmatic event that produced two main litho-structural units we refer to as the Lower and Uper Complexes, respectively. The Lower Complex is coeval with the main Pan-African D<sub>1</sub> deformation consisting of a transpressive regime responsible for folding, faulting and pluton emplacement under the effects of a NW–SE to WNW–ESE direction of shortening from 615 to 575 Ma. The Upper Complex is characterised by the emplacement of large volumes of ash-flow tuffs and volcanoclastic rocks and related intrusions. These were linked with the formation of ash-flow caldera structures which are uncommon examples of preserved Precambrian ash-flow calderas.

Ore deposits (porphyry, intermediate and low sulfidation epithermal deposit types, and IRGD) show strong spatial and temporal relationships with the emplacement of the widespread magmatic units belonging to the Upper Complex. For each ore deposit, fluid circulations associated with plutonic and/or volcanic systems can be invoked to be at the origin of the genesis of economic paragenesis. We suggest that magmatism of the Upper Complex and ore concentrations were both coeval with a D<sub>2</sub> deformation stage (575–540 Ma) and were controlled by the same transtensive tectonic regime under the effect of a nearly WNW–ESE shortening direction.

Despite an incomplete record by absolute datations, we infer that the Jbel Saghro was affected over a long period of time (i.e., 95 Myr) by successively magmatic, magmato-hydrothermal and hydrothermal events which formed a large mineralised province with substantial economic potential. Previous authors have already envisioned such a long period of magmatism and hydrothermalism in the area [29,47,74]. We further defend such a view and contend the Jbel Saghro province compares in this respect to numerous examples of large magmatic-related mineralised systems documented elsewhere during the Archaean to Cenozoic times. It may be questioned whether the particular longevity of the magmatic activity in areas dominated by transpressive and transtensive tectonics could be related to the specific behaviour of ancient continental domains in which tectonics are dominated by vertical forces and are linked with especially huge magmatism [216–218]. This debate is currently open and our results illustrate one additional example of long-lived tectono-magmatic event that characterises the late Precambrian in this part of the African continent. Considering the large volume of ash-flow tuffs that crop out in the Western, Central and Eastern Anti-Atlas and their long-lived magmatic activity (575–550 Ma), we infer that the whole Anti-Atlas area (i.e., 700 km long) belongs to a continental silicic large igneous province as defined by Bryan and Ferrari [14], and Ernst [12], and emplaced in a subduction to post-subduction setting and that may be linked to a wide area including the Cadomian segments [28,206,207,219]. Anyway, our results offer further evidence that the majority of metal deposits in the Moroccan Anti-Atlas could be formed during the Neoproterozoic times coevally with the tectonic and magmatic evolutions in this period. They also demonstrate that structural geology can provide relevant constraints for debating the age and mode of formation of ore deposits, specifically in the context of a large silicic magmatic provinces.

**Author Contributions:** J.T., A.C., L.B. (Luc Barbanson), J.-L.B., M.L., A.E., L.B. (Lakhlifi Badra), C.E.-L., M.D. and S.S. took part in the field investigation; M.L., A.E. and L.M. supported the field investigation; J.T., A.C., L.B.



(Luc Barbanson), J.-L.B., C.E.-L., S.S., and M.D. interpreted the data and took part in the discussion; J.T., A.C., J.-L.B. and M.D. wrote the original draft; J.T. and A.C. reviewed and edited the paper.

**Funding:** This work has been undertaken with the help of the French-Moroccan programs “Action Intégrée No 222/STU/00”.

**Acknowledgments:** The REMINEX exploration team and SMI mining company provided funds and logistics for field and laboratory studies. We particularly acknowledge El Hajj Bouiroukouten and the intern geologists of MANAGEM for their constant help and support. We are grateful to the Masters students from the BRGM Campus, University of Orléans, University of Lille and LaSalle Beauvais who were involved in the field for geological mapping exercises. Olivier Rouer and Gilles Drouet are warmly thanked for assistance and help with electronic microprobe analyses. The manuscript benefitted considerably from constructive reviews by four anonymous referees.

**Conflicts of Interest:** The authors declare no conflict of interest.

## References

1. Dostal, J.; Caby, R.; Keppie, J.D.; Maza, M. Neoproterozoic magmatism in Southwestern Algeria (Sebkh el Melah inlier): A northerly extension of the Trans-Saharan orogen. *J. Afr. Earth Sci.* **2002**, *35*, 213–225. [[CrossRef](#)]
2. Ennih, N.; Liegeois, J.-P. The boundaries of the West African craton, with special reference to the basement of the Moroccan metacratonic Anti-Atlas belt. *Geol. Soc. Lond. Spec. Publ.* **2008**, *297*, 1–17. [[CrossRef](#)]
3. Liégeois, J.P.; Latouche, L.; Boughrara, M.; Navez, J.; Guiraud, M. The LATEA metacraton (Central Hoggar, Tuareg shield, Algeria): Behaviour of an old passive margin during the Pan-African orogeny. *J. Afr. Earth Sci.* **2003**, *37*, 161–190. [[CrossRef](#)]
4. Ouzegane, K.; Kienast, J.-R.; Bendaoud, A.; Drareni, A. A review of Archaean and Paleoproterozoic evolution of the In Ouzzal granulitic terrane (Western Hoggar, Algeria). *J. Afr. Earth Sci.* **2003**, *37*, 207–227. [[CrossRef](#)]
5. Thomas, R.J.; Fekkak, A.; Ennih, N.; Errami, E.; Loughlin, S.C.; Gresse, P.G.; Chevallier, L.P.; Liegeois, J.-P. A new lithostratigraphic framework for the Anti-Atlas Orogen, Morocco. *J. Afr. Earth Sci.* **2004**, *39*, 217–226. [[CrossRef](#)]
6. El Bahat, A.; Ikenne, M.; Söderlund, U.; Cousens, B.; Youbi, N.; Ernst, R.; Soulaïmani, A.; El Janati, M.H.; Hafid, A. U–Pb baddeleyite ages and geochemistry of dolerite dykes in the Bas Drâa Inlier of the Anti-Atlas of Morocco: Newly identified 1380Ma event in the West African Craton. *Lithos* **2013**, *174*, 85–98. [[CrossRef](#)]
7. Ikenne, M.; Söderlund, U.; Ernst, R.E.; Pin, C.; Youbi, N.; El Aouli, E.H.; Hafid, A. A c. 1710 Ma mafic sill emplaced into a quartzite and calcareous series from Ighrem, Anti-Atlas—Morocco: Evidence that the Taghdout passive margin sedimentary group is nearly 1 Ga older than previously thought. *J. Afr. Earth Sci.* **2017**, *127*, 62–76. [[CrossRef](#)]
8. Youbi, N.; Kouyaté, D.; Söderlund, U.; Ernst, R.E.; Soulaïmani, A.; Hafid, A.; Ikenne, M.; El Bahat, A.; Bertrand, H.; Rkha Chaham, K.; et al. The 1750Ma Magmatic Event of the West African Craton (Anti-Atlas, Morocco). *Precambrian Res.* **2013**, *236*, 106–123. [[CrossRef](#)]
9. Davies, J.H.F.L.; Marzoli, A.; Bertrand, H.; Youbi, N.; Ernesto, M.; Schaltegger, U. End-Triassic mass extinction started by intrusive CAMP activity. *Nat. Commun.* **2017**, *8*, 15596. [[CrossRef](#)]
10. Knight, K.B.; Nomade, S.; Renne, P.R.; Marzoli, A.; Bertrand, H.; Youbi, N. The Central Atlantic Magmatic Province at the Triassic–Jurassic boundary: Paleomagnetic and  $^{40}\text{Ar}/^{39}\text{Ar}$  evidence from Morocco for brief, episodic volcanism. *Earth Planet. Sci. Lett.* **2004**, *228*, 143–160. [[CrossRef](#)]
11. Marzoli, A.; Callegaro, S.; Dal Corso, J.; Davies, J.H.F.L.; Chiaradia, M.; Youbi, N.; Bertrand, H.; Reisberg, L.; Merle, R.; Jourdan, F. The Central Atlantic Magmatic Province (CAMP): A Review. In *The Late Triassic World: Earth in a Time of Transition*; Tanner, L.H., Ed.; Springer International Publishing: Cham, Switzerland, 2018; pp. 91–125.
12. Ernst, R.E. *Large Igneous Provinces*; Cambridge University Press: Cambridge, UK, 2014.
13. Ernst, R.; Bleeker, W. Large igneous provinces (LIPs), giant dyke swarms, and mantle plumes: Significance for breakup events within Canada and adjacent regions from 2.5 Ga to the Present. *Can. J. Earth Sci.* **2010**, *47*, 695–739. [[CrossRef](#)]
14. Bryan, S.E.; Ferrari, L. Large igneous provinces and silicic large igneous provinces: Progress in our understanding over the last 25 years. *GSA Bull.* **2013**, *125*, 1053–1078. [[CrossRef](#)]

15. Chappell, B.W.; White, A.J.R. Two contrasting granite types: 25 years later. *Aust. J. Earth Sci.* **2001**, *48*, 489–499. [[CrossRef](#)]
16. Bonin, B. A-type granites and related rocks: Evolution of a concept, problems and prospects. *Lithos* **2007**, *97*, 1–29. [[CrossRef](#)]
17. Ernst, R.E.; Jowitt, S.M. Large Igneous Provinces (LIPs) and Metallogeny. In *Tectonics, Metallogeny, and Discovery: The North American Cordillera and Similar Accretionary Settings*; Colpron, M., Bissig, T., Rusk, B.G., Thompson, J.F.H., Eds.; Society of Economic Geologists: Littleton, CO, USA, 2013; Volume 17, pp. 17–51.
18. Arndt, N.T.; Leshner, C.M.; Czamanske, G.K. Mantle-derived magmas and magmatic Ni-Cu-(PGE) deposits. In *Economic Geology 100th Anniversary Volume*; Hedenquist, J.W., Thompson, J.F.H., Goldfarb, R.J., Richard, J.P., Eds.; Society of Economic Geologists: Littleton, CO, USA, 2005; pp. 5–23.
19. Barnes, S.J.; Holwell, D.A.; Le Vaillant, M. Magmatic Sulfide Ore Deposits. *Elements* **2017**, *13*, 89–95. [[CrossRef](#)]
20. Goodenough, K.M.; Schilling, J.; Jonsson, E.; Kalvig, P.; Charles, N.; Tuduri, J.; Deady, E.A.; Sadeghi, M.; Schiellerup, H.; Müller, A.; et al. Europe's rare earth element resource potential: An overview of REE metallogenetic provinces and their geodynamic setting. *Ore Geol. Rev.* **2016**, *72*, 838–856. [[CrossRef](#)]
21. Ernst, R.E.; Bell, K. Large igneous provinces (LIPs) and carbonatites. *Mineral. Petrol.* **2010**, *98*, 55–76. [[CrossRef](#)]
22. Rao, N.V.C.; Lehmann, B. Kimberlites, flood basalts and mantle plumes: New insights from the Deccan Large Igneous Province. *Earth-Sci. Rev.* **2011**, *107*, 315–324. [[CrossRef](#)]
23. Barton, M.D. 13.20—Iron Oxide-(Cu-Au-REE-P-Ag-U-Co) Systems A2—Holland, Heinrich, D. In *Treatise on Geochemistry (Second Edition)*; Turekian, K.K., Ed.; Elsevier: Oxford, UK, 2014; pp. 515–541.
24. Camprubí, A. Tectonic and Metallogenetic History of Mexico. In *Tectonics, Metallogeny, and Discovery: The North American Cordillera and Similar Accretionary Settings*; Colpron, M., Bissig, T., Rusk, B.G., Thompson, J.F.H., Eds.; Society of Economic Geologists: Littleton, CO, USA, 2013; Volume 17, pp. 201–243.
25. Camprubí, A.; Albinson, T. Epithermal deposits in México—Update of current knowledge, and an empirical reclassification. *Geol. Soc. Am. Spec. Pap.* **2007**, *422*, 377–415.
26. Wilkinson, J.J.; Simmons, S.F.; Stoffell, B. How metalliferous brines line Mexican epithermal veins with silver. *Sci. Rep.* **2013**, *3*, 2057. [[CrossRef](#)]
27. Ballèvre, M.; Le Goff, E.; Hébert, R. The tectonothermal evolution of the Cadomian belt of northern Brittany, France: A Neoproterozoic volcanic arc. *Tectonophysics* **2001**, *331*, 19–43. [[CrossRef](#)]
28. Linnemann, U.; Pereira, F.; Jeffries, T.E.; Drost, K.; Gerdes, A. The Cadomian Orogeny and the opening of the Rheic Ocean: The diachrony of geotectonic processes constrained by LA-ICP-MS U–Pb zircon dating (Ossa-Morena and Saxo-Thuringian Zones, Iberian and Bohemian Massifs). *Tectonophysics* **2008**, *461*, 21–43. [[CrossRef](#)]
29. Walsh, G.J.; Benziane, F.; Aleinikoff, J.N.; Harrison, R.W.; Yazidi, A.; Burton, W.C.; Quick, J.E.; Saadane, A. Neoproterozoic tectonic evolution of the Jebel Saghro and Bou Azzer—El Graara inliers, eastern and central Anti-Atlas, Morocco. *Precambrian Res.* **2012**, *216–219*, 23–62. [[CrossRef](#)]
30. Boyer, C.; Leblanc, M. Les appareils émissifs de la formation volcanique infracambriennes de Ouarzazate, Anti-Atlas (Maroc). *Comptes rendus hebdomadaires des séances de l'Académie des sciences* **1977**, *285*, 641–644.
31. Moume, W.; Youbi, N.; Marzoli, A.; Bertrand, H.; Gärtner, A.; Linnemann, U.; Gerdes, A.; Ernst, R.; Söderlund, U.; Hachimi Hind, E.; et al. The distribution of the Central Iapetus Magmatic Province (CIMP) into West African craton: U-Pb dating, geochemistry and petrology of Douar Eç-cour and Imiter mafic Dyke Swarms (High and Anti-Atlas, Morocco). In Proceedings of the 2nd Colloquium of the International Geoscience Programme (IGCP638), Casablanca, Morocco, 7–12 November 2017.
32. Puffer, J.H. A late Neoproterozoic eastern Laurentian superplume: Location, size, chemical composition, and environmental impact. *Am. J. Sci.* **2002**, *302*, 1–27. [[CrossRef](#)]
33. Barbey, P.; Oberli, F.; Burg, J.P.; Nachit, H.; Pons, J.; Meier, M. The Palaeoproterozoic in western Anti-Atlas (Morocco): A clarification. *J. Afr. Earth Sci.* **2004**, *39*, 239–245. [[CrossRef](#)]
34. Burkhard, M.; Caritg, S.; Helg, U.; Robert-Charrue, C.; Soulimani, A. Tectonics of the Anti-Atlas of Morocco. *Comptes Rendus Geosci.* **2006**, *338*, 11–24. [[CrossRef](#)]
35. Missenard, Y.; Zeyen, H.; Frizon de Lamotte, D.; Leturmy, P.; Petit, C.; Sébrier, M.; Saddiqi, O. Crustal versus asthenospheric origin of relief of the Atlas Mountains of Morocco. *J. Geophys. Res. Solid Earth* **2006**, *111*, B03401. [[CrossRef](#)]

36. Bourque, H.; Barbanson, L.; Sizaret, S.; Branquet, Y.; Ramboz, C.; Ennaciri, A.; El Ghorfi, M.; Badra, L. A contribution to the synsedimentary versus epigenetic origin of the Cu mineralizations hosted by terminal Neoproterozoic to Cambrian formations of the Bou Azzer–El Graara inlier: New insights from the Jbel Laassel deposit (Anti Atlas, Morocco). *J. Afr. Earth Sci.* **2015**, *107*, 108–118. [[CrossRef](#)]
37. Pouit, G. Paléogéographie et répartition des minéralisations stratiformes de cuivre dans l’Anti-Atlas occidental (Maroc). *Chronique de la Recherche Minière* **1966**, *34*, 279–289.
38. Borisenko, A.S.; Lebedev, V.I.; Borovikov, A.A.; Pavlova, G.G.; Kalinin, Y.A.; Nevol’ko, P.A.; Maacha, L.; Kostin, A.V. Forming conditions and age of native silver deposits in Anti-Atlas (Morocco). *Dokl. Earth Sci.* **2014**, *456*, 663–666. [[CrossRef](#)]
39. Oberthur, T.; Melcher, F.; Henjes-Kunst, F.; Gerdes, A.; Stein, H.; Zimmerman, A.; El Ghorfi, M. Hercynian age of the cobalt-nickel-arsenide-(gold) ores, Bou Azzer, Anti-Atlas, Morocco: Re-Os, Sm-Nd, and U-Pb age determinations. *Econ. Geol.* **2009**, *104*, 1065–1079. [[CrossRef](#)]
40. Essarraj, S.; Boiron, M.-C.; Cathelineau, M.; Banks, D.A.; Benharref, M. Penetration of surface-evaporated brines into the Proterozoic basement and deposition of Co and Ag at Bou Azzer (Morocco): Evidence from fluid inclusions. *J. Afr. Earth Sci.* **2005**, *41*, 25–39. [[CrossRef](#)]
41. Essarraj, S.; Boiron, M.-C.; Cathelineau, M.; Tarantola, A.; Leisen, M.; Boulvais, P.; Maacha, L. Basinal Brines at the Origin of the Imiter Ag-Hg Deposit (Anti-Atlas, Morocco): Evidence from LA-ICP-MS Data on Fluid Inclusions, Halogen Signatures, and Stable Isotopes (H, C, O). *Econ. Geol.* **2016**, *111*, 1753–1781. [[CrossRef](#)]
42. Abia, E.H.; Nachit, H.; Marignac, C.; Ibhi, A.; Saadi, S.A. The polymetallic Au-Ag-bearing veins of Bou Madine (Jbel Ougnat, eastern Anti-Atlas, Morocco): Tectonic control and evolution of a Neoproterozoic epithermal deposit. *J. Afr. Earth Sci.* **2003**, *36*, 251–271. [[CrossRef](#)]
43. Al Ansari, A.E.; Sagon, J.P. Le gisement d’or de Tiout (Jbel Saghro, Anti-Atlas, Maroc). Un système mésothermal polyphasé à sulfures-or et hématite-or dans une granodiorite potassique d’âge Protérozoïque supérieur. *Chronique de la Recherche Minière* **1997**, *527*, 3–25.
44. Leblanc, M.; Lbouabi, M. Native silver mineralization along a rodingite tectonic contact between serpentinite and quartz diorite (Bou Azzer, Morocco). *Econ. Geol.* **1988**, *83*, 1379–1391. [[CrossRef](#)]
45. Levresse, G.; Cheillett, A.; Gasquet, D.; Reisberg, L.; Deloule, E.; Marty, B.; Kyser, K. Osmium, sulphur, and helium isotopic results from the giant Neoproterozoic epithermal Imiter silver deposit, Morocco: Evidence for a mantle source. *Chem. Geol.* **2004**, *207*, 59–79. [[CrossRef](#)]
46. Marcoux, E.; Wadjiny, A. Le gisement Ag–Hg de Zgounder (Jebel Siroua, Anti-Atlas, Maroc): Un épithermal néoproterozoïque de type Imiter. *Comptes Rendus Geosci.* **2005**, *337*, 1439–1446. [[CrossRef](#)]
47. Tuduri, J. Processus de formation et relations spatio-temporelles des minéralisations à or et argent en contexte volcanique Précambrien (Jbel Saghro, Anti-Atlas, Maroc). Implications sur les relations déformation-magmatisme-volcanisme-hydrothermalisme. Ph.D. Thesis, University of Orléans, Orléans, France, 2005.
48. Tuduri, J.; Chauvet, A.; Barbanson, L.; Labriki, M.; Dubois, M.; Trapy, P.-H.; Lahfid, A.; Poujol, M.; Melleton, J.; Badra, L.; et al. Structural control, magmatic-hydrothermal evolution and formation of hornfels-hosted, intrusion-related gold deposits: Insight from the Thaghassa deposit in Eastern Anti-Atlas, Morocco. *Ore Geol. Rev.* **2018**, *97*, 171–198. [[CrossRef](#)]
49. Essarraj, S.; Boiron, M.-C.; Cathelineau, M.; Banks, D.A.; El Boukhari, A.; Chouhaidi, M.Y. Brines related to Ag deposition in the Zgounder silver deposit (Anti-Atlas, Morocco). *Eur. J. Mineral.* **1998**, *10*, 1201–1214. [[CrossRef](#)]
50. Levresse, G.; Bouabdellah, M.; Gasquet, D.; Cheillett, A. Basinal Brines at the Origin of the Imiter Ag-Hg Deposit (Anti-Atlas, Morocco): Evidence from LA-ICP-MS Data on Fluid Inclusions, Halogen Signatures, and Stable Isotopes (H, C, O)—A Discussion. *Econ. Geol.* **2017**, *112*, 1269–1272. [[CrossRef](#)]
51. Cheillett, A.; Levresse, G.; Gasquet, D.; Azizi-Samir, M.R.; Zyadi, R.; Archibald, A.D.; Farrar, E. The giant Imiter silver deposit: Neoproterozoic epithermal mineralization in the Anti-Atlas, Morocco. *Miner. Depos.* **2002**, *37*, 772–781. [[CrossRef](#)]
52. Pelleter, E.; Cheillett, A.; Gasquet, D.; Mouttaqi, A.; Annich, M.; Camus, Q.; Deloule, E.; Ouazzani, L.; Bounajma, H.; Ouchtouban, L. U/Pb Ages of Magmatism in the Zgounder Epithermal Ag–Hg Deposit, Sirwa Window, Anti-Atlas, Morocco. In *Mineral Deposits of North Africa*; Bouabdellah, M., Slack, J.F., Eds.; Springer International Publishing: Cham, Switzerland, 2016; pp. 143–165.

53. Ahmed, A.H.; Arai, S.; Ikenne, M. Mineralogy and Paragenesis of the Co-Ni Arsenide Ores of Bou Azzer, Anti-Atlas, Morocco. *Econ. Geol.* **2009**, *104*, 249–266. [[CrossRef](#)]
54. Ennaciri, A.; Barbanson, L.; Touray, J.C. Mineralized hydrothermal solution cavities in the Co-As Ait Ahmane mine (Bou Azzer, Morocco). *Miner. Depos.* **1995**, *30*, 75–77. [[CrossRef](#)]
55. Leblanc, M. Co-Ni arsenide deposits, with accessory gold, in ultramafic rocks from:Morocco. *Can. J. Earth Sci.* **1986**, *23*, 1592–1602. [[CrossRef](#)]
56. Thiéblemont, D.; Chêne, F.; Liégeois, J.-P.; Ouabadi, A.; Le Gall, B.; Maury, R.C.; Jalludin, M.; Ouattara Gbéle, C.; Tchaméni, R.; Fernandez-Alonso, M. *Geological Map of Africa at 1:10 Million Scale*, 35th International Geology Congress ed; CCGM-BRGM: Orléans, France, 2016.
57. Hollard, H.; Choubert, G.; Bronner, G.; Marchand, J.; Sougy, J. Carte géologique du Maroc, échelle: 1/1.000.000. *Notes et Mémoires du Service Géologique du Maroc* **1985**, 260.
58. Mouttaqi, A.; Rjimati, E.; Maacha, A.; Michard, A.; Soulaïmani, A.; Ibouh, H. Les principales mines du Maroc. *Notes et Mémoires du Service Géologique du Maroc* **2011**, 564, 375.
59. Thomas, R.J.; Chevallier, L.P.; Gresse, P.G.; Harmer, R.E.; Eglington, B.M.; Armstrong, R.A.; de Beer, C.H.; Martini, J.E.J.; de Kock, G.S.; Macey, P.H.; et al. Precambrian evolution of the Sirwa Window, Anti-Atlas Orogen, Morocco. *Precambrian Res.* **2002**, *118*, 1–57. [[CrossRef](#)]
60. Goldfarb, R.J.; Groves, D.I. Orogenic gold: Common or evolving fluid and metal sources through time. *Lithos* **2015**, *233*, 2–26. [[CrossRef](#)]
61. Groves, D.I.; Santosh, M.; Goldfarb, R.J.; Zhang, L. Structural geometry of orogenic gold deposits: Implications for exploration of world-class and giant deposits. *Geosci. Front.* **2018**, *9*, 1163–1177. [[CrossRef](#)]
62. Hart, C.J. Reduced intrusion-related gold systems. In *Mineral Deposits of Canada: A Synthesis of Major Deposit Types, District Metallogeny, the Evolution of Geological Provinces, and Exploration Methods*; Special Publication; Geological Association of Canada, Mineral Deposits Division: St. John’s, NL, Canada, 2007; pp. 95–112.
63. Kontak, D.; O’Reilly, G.; MacDonald, M.; Horne, R.; Smith, P. Gold in the Meguma Terrane, Southern Nova Scotia: Is There a Continuum between Mesothermal Lode Gold and Intrusion-related Gold Systems? In Proceedings of the 49th Annual Meeting of the GAC-MAC, St. Catharines, ON, Canada, 12–14 May2004; p. 128.
64. Lang, J.R.; Baker, T. Intrusion-related gold systems: The present level of understanding. *Miner. Depos.* **2001**, *36*, 477–489. [[CrossRef](#)]
65. Walshe, J.; Neumayr, P.; Cooke, D. Two boxes we don’t need: Orogenic and intrusion-related gold systems. In Proceedings of the STOMP 2005: Structure, Tectonics and Ore Mineralisation Processes, Townsville, Australia, 29 August–2 September 2005; EGRU: Townsville, Australia, 2005; p. 143.
66. Boiron, M.-C.; Cathelineau, M.; Banks, D.A.; Fourcade, S.; Vallance, J. Mixing of metamorphic and surficial fluids during the uplift of the Hercynian upper crust: Consequences for gold deposition. *Chem. Geol.* **2003**, *194*, 119–141. [[CrossRef](#)]
67. Vallance, J.; Cathelineau, M.; Boiron, M.C.; Fourcade, S.; Shepherd, T.J.; Naden, J. Fluid-rock interactions and the role of late Hercynian aplite intrusion in the genesis of the Castromil gold deposit, northern Portugal. *Chem. Geol.* **2003**, *194*, 201–224. [[CrossRef](#)]
68. Baker, T.; Lang, J.R. Fluid inclusion characteristics of intrusion-related gold mineralization, Tombstone–Tungsten magmatic belt, Yukon Territory, Canada. *Mineral. Depos.* **2001**, *36*, 563–582. [[CrossRef](#)]
69. Chauvet, A.; Volland-Tuduri, N.; Lerouge, C.; Bouchot, V.; Monié, P.; Charonnat, X.; Faure, M. Geochronological and geochemical characterization of magmatic-hydrothermal events within the Southern Variscan external domain (Cévennes area, France). *Int. J. Earth Sci.* **2012**, *101*, 69–86. [[CrossRef](#)]
70. Mustard, R.; Ulrich, T.; Kamenetsky, V.S.; Mernagh, T. Gold and metal enrichment in natural granitic melts during fractional crystallization. *Geology* **2006**, *34*, 85–88. [[CrossRef](#)]
71. Gouiza, M.; Charton, R.; Bertotti, G.; Andriessen, P.; Storms, J.E.A. Post-Variscan evolution of the Anti-Atlas belt of Morocco constrained from low-temperature geochronology. *Int. J. Earth Sci.* **2017**, *106*, 593–616. [[CrossRef](#)]
72. Teixell, A.; Ayarza, P.; Zeyen, H.; Fernández, M.; Arboleya, M.-L. Effects of mantle upwelling in a compressional setting: The Atlas Mountains of Morocco. *Terra Nova* **2005**, *17*, 456–461. [[CrossRef](#)]
73. Choubert, G. Histoire géologique du Précambrien de l’Anti-Atlas de l’Archéen à l’aurore des temps primaires. *Notes et Mémoires du Service Géologique du Maroc* **1963**, 162, 352.

74. Gasquet, D.; Levresse, G.; Cheilletz, A.; Azizi-Samir, M.R.; Mouttaqi, A. Contribution to a geodynamic reconstruction of the Anti-Atlas (Morocco) during Pan-African times with the emphasis on inversion tectonics and metallogenic activity at the Precambrian–Cambrian transition. *Precambrian Res.* **2005**, *140*, 157–182. [[CrossRef](#)]
75. Hefferan, K.; Soulaïmani, A.; Samson, S.D.; Admou, H.; Inglis, J.; Saquaque, A.; Latifa, C.; Heywood, N. A reconsideration of Pan African orogenic cycle in the Anti-Atlas Mountains, Morocco. *J. Afr. Earth Sci.* **2014**, *98*, 34–46. [[CrossRef](#)]
76. Leblanc, M.; Lancelot, J.R. Interprétation géodynamique du domaine panafricain (Précambrien terminal) de l’Anti-Atlas (Maroc) à partir de données géologiques et géochronologiques. *Can. J. Earth Sci.* **1980**, *17*, 142–155. [[CrossRef](#)]
77. Saquaque, A.; Benharref, M.; Abia, H.; Mrini, Z.; Reuber, I.; Karson, J.A. Evidence for a Panafrican volcanic arc and wrench fault tectonics in Jbel Saghro, Morocco. *Geol. Rundsch.* **1992**, *81*, 1–13. [[CrossRef](#)]
78. Blein, O.; Baudin, T.; Chèvremont, P.; Soulaïmani, A.; Admou, H.; Gasquet, P.; Cocherie, A.; Egal, E.; Youbi, N.; Razin, P.; et al. Geochronological constraints on the polycyclic magmatism in the Bou Azzer-El Graara inlier (Central Anti-Atlas Morocco). *J. Afr. Earth Sci.* **2014**, *99*, 287–306. [[CrossRef](#)]
79. El Hadi, H.; Simancas, J.F.; Martínez-Poyatos, D.; Azor, A.; Tahiri, A.; Montero, P.; Fanning, C.M.; Bea, F.; González-Lodeiro, F. Structural and geochronological constraints on the evolution of the Bou Azzer Neoproterozoic ophiolite (Anti-Atlas, Morocco). *Precambrian Res.* **2010**, *182*, 1–14. [[CrossRef](#)]
80. Inglis, J.D.; D’Lemos, R.S.; Samson, S.D.; Admou, H. Geochronological constraints on late Precambrian intrusions, metamorphism, and tectonism in the Anti-Atlas mountains. *J. Geol.* **2005**, *113*, 439–450. [[CrossRef](#)]
81. Inglis, J.D.; MacLean, J.S.; Samson, S.D.; D’Lemos, R.S.; Admou, H.; Hefferan, K. A precise U-Pb zircon age for the Blelda granodiorite, Anti-Atlas, Morocco: Implications for the timing of deformation and terrane assembly in the eastern Anti-Atlas. *J. Afr. Earth Sci.* **2004**, *39*, 277. [[CrossRef](#)]
82. Saquaque, A.; Admou, H.; Karson, J.; Hefferan, K.; Reuber, I. Precambrian accretionary tectonics in the Bou Azzer-El Graara region, Anti-Atlas, Morocco. *Geology* **1989**, *17*, 1107–1110. [[CrossRef](#)]
83. Gasquet, D.; Ennih, N.; Liégeois, J.-P.; Soulaïmani, A.; Michard, A. The Pan-African Belt. In *Continental Evolution: The Geology of Morocco*; Michard, A., Saddiqi, O., Chalouan, A., Frizon de Lamotte, D., Eds.; Springer-Verlag: Berlin/Heidelberg, Germany, 2008; pp. 33–64.
84. Álvaro, J.J.; Benziane, F.; Thomas, R.; Walsh, G.J.; Yazidi, A. Neoproterozoic–Cambrian stratigraphic framework of the Anti-Atlas and Ouzellagh promontory (High Atlas), Morocco. *J. Afr. Earth Sci.* **2014**, *98*, 19–33. [[CrossRef](#)]
85. Choubert, G. In *Essai d’application de la notion d’Infracambrien aux formations anciennes de l’Anti-Atlas (Maroc)*. In Proceedings of the 19th International Geological Congress, Alger, Algeria, 8–15 September 1952; pp. 33–71.
86. Soulaïmani, A.; Michard, A.; Ouanaïmi, H.; Baïdder, L.; Raddi, Y.; Saddiqi, O.; Rjimat, E.C. Late Ediacaran–Cambrian structures and their reactivation during the Variscan and Alpine cycles in the Anti-Atlas (Morocco). *J. Afr. Earth Sci.* **2014**, *98*, 94–112. [[CrossRef](#)]
87. Soulaïmani, A.; Bouabdelli, M.; Piqué, A. The Upper Neoproterozoic–Lower Cambrian continental extension in the Anti-Atlas (Morocco). *Bulletin de la Société Géologique de France* **2003**, *174*, 83–92. [[CrossRef](#)]
88. Chèvremont, P.; Blein, O.; Razin, P.; Baudin, T.; Barbanson, L.; Gasquet, D.; Soulaïmani, A.; Admou, H.; Youbi, N.; Bouabdelli, M.; et al. Carte géologique du Maroc (1/50 000), feuille de Bou Azer. *Notes et Mémoires du Service Géologique du Maroc* **2013**, *535bis*, 153.
89. Ducrot, J.; Lancelot, J.R. Problème de la limite Précambrien–Cambrien: Étude radiochronologique par la méthode U–Pb sur zircons du volcan du Jbel Boho (Anti-Atlas marocain). *Can. J. Earth Sci.* **1977**, *14*, 2771–2777. [[CrossRef](#)]
90. Maloof, A.C.; Schrag, D.P.; Crowley, J.L.; Bowring, S.A. An expanded record of Early Cambrian carbon cycling from the Anti-Atlas Margin, Morocco. *Can. J. Earth Sci.* **2005**, *42*, 2195–2216. [[CrossRef](#)]
91. Fekkak, A.; Pouclet, A.; Ouguir, H.; Ouazzani, H.; Badra, L.; Gasquet, D. Géochimie et signification géotectonique des volcanites du Cryogénien inférieur du Saghro (Anti-Atlas oriental, Maroc). *Geodin. Acta* **2001**, *13*, 1–13.
92. Ouguir, H.; Macaudière, J.; Dagallier, G. Le Protérozoïque supérieur d’Imiter, Saghro oriental, Maroc: Un contexte géodynamique d’arrière arc. *J. Afr. Earth Sci.* **1996**, *22*, 173–189. [[CrossRef](#)]

93. Baïdder, L.; Raddi, Y.; Tahiri, M.; Michard, A. Devonian extension of the Pan-African crust north of the West African craton, and its bearing on the Variscan foreland deformation: Evidence from eastern Anti-Atlas (Morocco). *Geol. Soc. Lond. Spec. Publ.* **2008**, *297*, 453–465. [[CrossRef](#)]
94. Malusà, M.G.; Polino, R.; Feroni, A.C.; Ellero, A.; Ottria, G.; Baïdder, L.; Musumeci, G. Post-Variscan tectonics in eastern Anti-Atlas (Morocco). *Terra Nova* **2007**, *19*, 481–489. [[CrossRef](#)]
95. Michard, A.; Soulaïmani, A.; Hoepffner, C.; Ouanaimi, H.; Baïdder, L.; Rjïmati, E.C.; Saddiqi, O. The South-Western Branch of the Variscan Belt: Evidence from Morocco. *Tectonophysics* **2010**, *492*, 1–24. [[CrossRef](#)]
96. Frizon de Lamotte, D.; Tavakoli-Shirazi, S.; Leturmy, P.; Averbuch, O.; Mouchot, N.; Raulin, C.; Leparmentier, F.; Blanpied, C.; Ringenbach, J.-C. Evidence for Late Devonian vertical movements and extensional deformation in northern Africa and Arabia: Integration in the geodynamics of the Devonian world. *Tectonics* **2013**, *32*, 107–122. [[CrossRef](#)]
97. Alvaro, J.J.; Macouin, M.; Ezzouhairi, H.; Charif, A.; Ayad, N.A.; Ribeiro, M.L.; Ader, M. Late Neoproterozoic carbonate productivity in a rifting context: The Adoudou Formation and its associated bimodal volcanism onlapping the western Saghro inlier, Morocco. *Geol. Soc. Lond. Spec. Publ.* **2008**, *297*, 285–302. [[CrossRef](#)]
98. Álvaro, J.J. Late Ediacaran syn-rift/post-rift transition and related fault-driven hydrothermal systems in the Anti-Atlas Mountains, Morocco. *Basin Res.* **2013**, *25*, 348–360. [[CrossRef](#)]
99. Sebti, S.; Saddiqi, O.; El Haimer, F.Z.; Michard, A.; Ruiz, G.; Bousquet, R.; Baïdder, L.; Frizon de Lamotte, D. Vertical movements at the fringe of the West African Craton: First zircon fission track datings from the Anti-Atlas Precambrian basement, Morocco. *Comptes Rendus Geosci.* **2009**, *341*, 71–77. [[CrossRef](#)]
100. Caritg, S.; Burkhard, M.; Ducommun, R.; Helg, U.; Kopp, L.; Sue, C. Fold interference patterns in the Late Palaeozoic Anti-Atlas belt of Morocco. *Terra Nova* **2004**, *16*, 27–37.
101. Levresse, G.; Bouabdellah, M.; Cheilletz, A.; Gasquet, D.; Maacha, L.; Tritlla, J.; Banks, D.; Moulay Rachid, A.S. Degassing as the Main Ore-Forming Process at the Giant Imiter Ag–Hg Vein Deposit in the Anti-Atlas Mountains, Morocco. In *Mineral Deposits of North Africa*; Bouabdellah, M., Slack, J.F., Eds.; Springer International Publishing: Cham, Switzerland, 2016; pp. 85–106.
102. Tuduri, J.; Chauvet, A.; Ennaciri, A.; Barbanson, L. Modèle de formation du gisement d’argent d’Imiter (Anti-Atlas oriental, Maroc). Nouveaux apports de l’analyse structurale et minéralogique. *Comptes Rendus Geosci.* **2006**, *338*, 253–261. [[CrossRef](#)]
103. Bouabdellah, M.; Maacha, L.; Jébrak, M.; Zouhair, M. Re/Os Age Determination, Lead and Sulphur Isotope Constraints on the Origin of the Bouskour Cu–Pb–Zn Vein-Type Deposit (Eastern Anti-Atlas, Morocco) and Its Relationship to Neoproterozoic Granitic Magmatism. In *Mineral Deposits of North Africa*; Bouabdellah, M., Slack, J.F., Eds.; Springer International Publishing: Cham, Switzerland, 2016; pp. 277–290.
104. Hindermeyer, J.; Choubert, G.; Destombes, J.; Gauthier, H. Carte géologique de l’Anti-Atlas oriental: Feuille Dadès et Jbel Saghro 1/200 000. *Notes et Mémoires du Service Géologique du Maroc* **1977**, *161*.
105. Baidada, B.; Ikenne, M.; Barbey, P.; Soulaïmani, A.; Cousens, B.; Haïssen, F.; Ilmen, S.; Alansari, A. SHRIMP U–Pb zircon geochronology of the granitoids of the Imiter Inlier: Constraints on the Pan-African events in the Saghro massif, Anti-Atlas (Morocco). *J. Afr. Earth Sci.* **2018**. [[CrossRef](#)]
106. De Wall, H.; Kober, B.; Errami, E.; Ennih, N.; Greiling, R.O. Age de mise en place et contexte géologique des granitoïdes de la boutonnière d’Imiter (Saghro oriental, Anti-Atlas, Maroc). In Proceedings of the 2ème Colloque International 3MA (Magmatisme, Métamorphisme & Minéralisations Associées), Marrakech, Maroc, 10–12 May 2001; p. 19.
107. O’Connor, E.; Barnes, R.; Beddoe-Stephens, B.; Fletcher, T.; Gillespie, M.; Hawkins, M.; Loughlin, S.; Smith, M.; Smith, R.; Waters, C. *Geology of the Drâa, Kerdous, and Boumalne districts, Anti-Atlas, Morocco*; British Geological Survey: Nottingham, UK, 2010; p. 310.
108. Schiavo, A.; Taj Eddine, K.; Algouti, A.; Benvenuti, M.; Dal Piaz, G.V.; Eddebi, A.; El Boukhari, A.; Laftouhi, N.; Massironi, M.; Ounaimi, H.; et al. Carte géologique du Maroc au 1/50000, feuille Imtir. *Notes et Mémoires du Service Géologique du Maroc* **2007**, *518*.
109. Charlot, R.; Choubert, G.; Faure-Muret, A.; Tisserant, D. Etude géochronologique du Précambrien de l’Anti-Atlas (Maroc). *Notes et Mémoires du Service Géologique du Maroc* **1970**, *30*, 99–134.
110. Choubert, G. Sur le Précambrien marocain. *Comptes rendus hebdomadaires des séances de l’Académie des sciences* **1945**, *221*, 249–251.

111. Hindermeier, J. Le Précambrien I et le Précambrien II du Saghro. *Comptes rendus hebdomadaires des séances de l'Académie des sciences* **1953**, 237, 921–923.
112. Hindermeier, J. Le Précambrien III du Saghro. *Comptes rendus hebdomadaires des séances de l'Académie des sciences* **1953**, 237, 1024–1026.
113. Derré, C.; Lécôle, M. Altérations hydrothermales dans le Protérozoïque supérieur du Saghro (Anti-Atlas oriental). Relations avec les minéralisations. *Chronique de la Recherche Minière* **1999**, 536–537, 39–61.
114. Fekkak, A.; Boualoul, M.; Badra, L.; Amenzou, M.; Saquaque, A.; El-Amrani, I.E. Origine et contexte géotectonique des dépôts détritiques du Groupe Néoprotérozoïque inférieur de Kelaat Mgouna (Anti-Atlas Oriental, Maroc). *J. Afr. Earth Sci.* **2000**, 30, 295–311. [[CrossRef](#)]
115. Fekkak, A.; Pouclet, A.; Badra, L. The Pre-Panafrican rifting of Saghro (Anti-Atlas, Morocco): Exemple of the middle Neoproterozoic Basin of Boumalne. *Bulletin de la Société Géologique de France* **2002**, 173, 25–35. [[CrossRef](#)]
116. Fekkak, A.; Pouclet, A.; Benharref, M. The Middle Neoproterozoic Sidi Flah Group (Anti-Atlas, Morocco): Synrift deposition in a Pan-African continent/ocean transition zone. *J. Afr. Earth Sci.* **2003**, 37, 73–87. [[CrossRef](#)]
117. Fekkak, A.; Pouclet, A.; Ouguir, H.; Badra, L.; Gasquet, D. The Kelaat Mgouna early Neoproterozoic Group (Saghro, Anti-Atlas, Morocco): Witness of an initial stage of the pre-Pan-African extension. *Bulletin de la Société Géologique de France* **1999**, 170, 789–797.
118. Marini, F.; Ouguir, H. Un nouveau jalon dans l'histoire de la distension pré-panafricaine au Maroc: Le Précambrien II des boutonnières du Jbel Saghro nord-oriental (Anti-Atlas, Maroc). *Comptes Rendus de l'Académie des Sciences Série II Mécanique-physique Chimie, Sciences de l'univers, Sciences de la Terre* **1990**, 310, 577–582.
119. Errami, E.; Bonin, B.; Laduron, D.; Lasri, L. Petrology and geodynamic significance of the post-collisional Pan-African magmatism in the Eastern Saghro area (Anti-Atlas, Morocco). *J. Afr. Earth Sci.* **2009**, 55, 105–124. [[CrossRef](#)]
120. Liégeois, J.-P.; Fekkak, A.; Bruguier, O.; Errami, E.; Ernih, N. The Lower Ediacaran (630–610 Ma) Saghro group: An orogenic transpressive basin development during the early metacratonic evolution of the Anti-Atlas (Morocco). In Proceedings of the IGCP485 4th Meeting, Algiers, Algeria, 2 September 2006; p. 57.
121. Ighid, L.; Saquaque, A.; Reuber, I. Plutons syn-cinématiques et la déformation panafricaine majeure dans le Saghro oriental (boutonnière d'Imiter, Anti-Atlas, Maroc). *Comptes Rendus de l'Académie des Sciences Série II Mécanique-physique Chimie, Sciences de l'univers Sciences de la Terre* **1989**, 309, 615–620.
122. El Baghdadi, M.; El Boukhari, A.; Jouider, A.; Benyoucef, A.; Nadem, S. Calc-alkaline arc I-type granitoid associated with S-type granite in the Pan-African belt of eastern Anti-Atlas (Saghro and Ougnat, South Morocco). *Gondwana Res.* **2003**, 6, 557–572. [[CrossRef](#)]
123. Errami, E.; Olivier, P. The Iknouen granodiorite, tectonic marker of Ediacaran SE-directed tangential movements in the Eastern Anti-Atlas, Morocco. *J. Afr. Earth Sci.* **2012**, 69, 1–12. [[CrossRef](#)]
124. Karl, A.; de Wall, H.; Rieger, M.; Schmitt, T.; Errami, E.; Kober, B.; Greiling, R.O. Petrography and geochemistry of the Bou Teglmit, Taouzzakt and Igoudrane intrusions in the Eastern Saghro (Anti Atlas, Morocco). In *Magmatic evolution of a Neoproterozoic island-arc: Syn- to post-orogenic igneous activity in the Anti-Atlas (Morocco)*; de Wall, H., Greiling, R.O., Eds.; Forschungszentrum Jülich, International Cooperation, Scientific Series: Jülich, Germany, 2001; Volume 45, pp. 243–253.
125. Ouguir, H.; Macaudière, J.; Dagallier, G.; Qadrouci, A.; Leistel, J.-M. Cadre structural du gîte Ag-Hg d'Imiter (Anti-Atlas, Maroc); implication métallogénique. *Bulletin de la Société Géologique de France* **1994**, 165, 233–248.
126. Massironi, M.; Moratti, G.; Algouti, A.; Benvenuti, M.; Dal Piaz, G.V.; Eddebi, A.; El Boukhari, A.; Laftouhi, N.; Ounaimi, H.; Schiavo, A.; et al. Carte géologique du Maroc au 1/50000, feuille Boumalne. *Notes et Mémoires du Service Géologique du Maroc* **2007**, 521.
127. Leistel, J.-M.; Qadrouci, A. Le gisement argentifère d'Imiter (Protérozoïque supérieur de l'Anti-Atlas, Maroc). Contrôles des minéralisations, hypothèses génétiques et perspectives pour l'exploration. *Chronique de la Recherche Minière* **1991**, 502, 5–22.
128. Benkirane, Y. Les minéralisations à W (Sn, Mo, Au, Bi, Ag, Cu, Pb, Zn) du granite de Taourirt-Tamellalt dans leur cadre géologique, la boutonnière protérozoïque du SE de Boumalne du Dadès (Saghro oriental, Anti-Atlas, Maroc). In *3<sup>ème</sup> Cycle*; Université de Paris VI: Paris, France, 1987.

129. Lécalle, M.; Derré, C.; Nerci, K. The Proterozoic sulphide alteration pipe of Sidi Flah and its host series. New data for the geotectonic evolution of the Pan-African Belt in the eastern Anti-Atlas (Morocco). *Ore Geol. Rev.* **1991**, *6*, 501–536. [[CrossRef](#)]
130. Benziane, F. Lithostratigraphie et évolution géodynamique de l'anti-Atlas (Maroc) du paléoprotérozoïque au néoprotérozoïque: Exemples de la boutonnière de Tagragra Tata et du Jebel Saghro. In *3<sup>ème</sup> Cycle*; Université de Chambéry: Chambéry, France, 2007.
131. Bajja, A. Volcanisme syn à post orogénique du Néoprotérozoïque de l'Anti-Atlas: Implications pétrogénétiques et géodynamiques. Ph.D. Thesis, Université Chouaib Doukkali, El Jadida, Maroc, 1998.
132. Benharref, M. Le Précambrien de la boutonnière d'El Kelaa des M'Gouna (Saghro, Anti-Atlas, Maroc). Pétrographie et structures de l'ensemble. Implications lithostratigraphiques et géodynamiques. In *3<sup>ème</sup> Cycle*; Université Cadi Ayyad: Marrakech, Maroc, 1991.
133. Bouladon, J.; Jouravsky, G. Les ignimbrites du Précambrien III de Tiouine et du sud marocain. *Notes et Mémoires du Service Géologique du Maroc* **1954**, *120*, 37–59.
134. Fauvelet, E.; Hindermeyer, J. Note préliminaire sur les granites associés à des coulées rhyolitiques au Sud de Ouarzazate (Anti-Atlas central) et dans le Sarho. *C. R. Hebd. Seances Acad. Sci.* **1952**, *234*, 2626–2628.
135. Mifidal, A.; Peucat, J. Datation U-Pb et Rb-Sr du volcanisme acide de l'Anti-Atlas marocain et du socle sous-jacent dans la région de Ouarzazate. Apport au problème de la limite Précambrien-Cambrien. *Sci. Géol. Bull.* **1985**, *38*, 185–200.
136. Acocella, V. Understanding caldera structure and development: An overview of analogue models compared to natural calderas. *Earth-Sci. Rev.* **2007**, *85*, 125–160. [[CrossRef](#)]
137. Lipman, P.W. The roots of ash flow calderas in western north america: Windows into the tops of granitic batholiths. *J. Geophys. Res. Solid Earth* **1984**, *89*, 8801–8841. [[CrossRef](#)]
138. Lipman, P.W. Subsidence of ash-flow calderas: Relation to caldera size and magma-chamber geometry. *Bull. Volcanol.* **1997**, *59*, 198–218. [[CrossRef](#)]
139. Williams, H. Calderas and their origin. University of California publications. *Bull. Dep. Geol. Sci.* **1941**, *25*, 239–346.
140. Acocella, V.; Korme, T.; Salvini, F.; Funicello, R. Elliptical calderas in the Ethiopian Rift: Control of pre-existing structures. *J. Volcanol. Geotherm. Res.* **2003**, *119*, 189–203. [[CrossRef](#)]
141. Holohan, E.P.; Troll, V.R.; Walter, T.R.; Münn, S.; McDonnell, S.; Shipton, Z.K. Elliptical calderas in active tectonic settings: An experimental approach. *J. Volcanol. Geotherm. Res.* **2005**, *144*, 119–136. [[CrossRef](#)]
142. Ross, C.S.; Smith, R.L. Ash-flow tuffs: Their origin, geologic relations and identification. *Geol. Surv. Prof. Pap.* **1961**, *366*, 81.
143. Smith, R.L. Ash flows. *Geol. Soc. Am. Bull.* **1960**, *71*, 795–842. [[CrossRef](#)]
144. Smith, R.L.; Bailey, R.A. Resurgent cauldrons. *Geol. Soc. Am. Mem.* **1968**, *116*, 613–662.
145. Bellier, O.; Sébrier, M. Relationship between tectonism and volcanism along the Great Sumatran Fault Zone deduced by image analyses. *Tectonophysics* **1994**, *233*, 215–231. [[CrossRef](#)]
146. Chesner, C.A.; Rose, W.I. Stratigraphy of the Toba Tuffs and the evolution of the Toba Caldera Complex, Sumatra, Indonesia. *Bull. Volcanol.* **1991**, *53*, 343–356. [[CrossRef](#)]
147. Ferrari, L.; Valencia-Moreno, M.; Bryan, S. Magmatism and tectonics of the Sierra Madre Occidental and its relation with the evolution of the western margin of North America. *Geol. Soc. Am. Spec. Pap.* **2007**, *422*, 1–39.
148. Ferrari, L.; Lopez-Martinez, M.; Rosas-Elguera, J. Ignimbrite flare-up and deformation in the southern Sierra Madre Occidental, western Mexico: Implications for the late subduction history of the Farallon plate. *Tectonics* **2002**, *21*. [[CrossRef](#)]
149. Lécuyer, F.; Bellier, O.; Gourgaud, A.; Vincent, P.M. Tectonique active du Nord-Est de Sulawesi (Indonésie) et contrôle structural de la caldeira de Tondano. *Comptes Rendus de l'Académie des Sciences Ser. IIA Earth Planet. Sci.* **1997**, *325*, 607–613. [[CrossRef](#)]
150. Van Wyk de Vries, B.; Merle, O. Extension induced by volcanic loading in regional strike-slip zones. *Geology* **1998**, *26*, 983–986. [[CrossRef](#)]



151. Tuduri, J.; Chauvet, A.; Barbanson, L.; Labriki, M.; Badra, L. In Atypical gold mineralization within the Neoproterozoic of Morocco. Structural and mineralogical constraints from the Thaghassa prospect (Boumalne inlier, Jbel Saghro, Eastern Anti-Atlas). In Proceedings of the Mineral Exploration and Sustainable Development, Athens, Greece, 24–28 August 2003; Eliopoulos, D.G., Ed.; Millpress: Athens, Greece; pp. 537–540.
152. Goldstein, R.H.; Reynolds, T.J. *Systematics of Fluid Inclusions in Diagenetic Minerals*; Society for Sedimentary Geology: Broken Arrow, OK, USA, 1994; Volume 31, p. 199.
153. Lécalle, M.; Derré, C.; Rjimati, E.C.; Fonteilles, M.; Azza, A.; Benanni, A. Une altération hydrothermale peralumineuse à silicates, phosphates et rutile dans le Protérozoïque supérieur du Saghro (Anti-Atlas, Maroc). Genèse et implications des métallogéniques. *Comptes Rendus de l'Académie des Sciences Série II Mécanique-physique Chimie Sciences de l'univers Sciences de la Terre* **1993**, *316*, 123–130.
154. Tuduri, J.; Dubois, M.; Try, E.; Chauvet, A.; Barbanson, L.; Ennaciri, A. The porphyry to epithermal transition in atypical late Neoproterozoic REE-Au-Ag-Te occurrences. *Acta Mineral.-Petrogr. Abstr. Ser.* **2010**, *6*, 288.
155. Delapierre, A. Etude de la minéralisation aurifère d'Isamlal (Jbel Saghro, Anti-Atlas, Maroc). In *Mem. Diplôme*; Université de Lausanne: Lausanne, Switzerland, 2000; p. 128.
156. Leloix, C. Etude des minéralisations aurifères épithermales d'Isamlal. District de Kelaat M'Gouna (Anti-Atlas, Maroc). In *Rapport Reminex*; Université d'Orléans: Orléans, France, 1999; p. 44.
157. Sizaret, S. Etude des minéralisations aurifères d'Isamlal (district de Kelâa M'Gouna, Anti-Atlas, Maroc). Master's Thesis, Université d'Orléans, Orléans, France, 1999.
158. Gaspard, E. Etude du prospect d'Isamlal (Anti-Atlas Oriental- Maroc): Caractérisation d'un porphyre à Au-Cu-Mo. Master's Thesis, Université d'Orléans—ENAG, Orléans, France, 2014.
159. Try, E.; Dubois, M.; Tuduri, J.; Ventalon, S.; Potdevin, J.-L.; Chauvet, A.; Barbanson, L. The transition between porphyric and epithermal styles: Insights from F.I. of the Kelâa M'Gouna prospect, Morocco. In Proceedings of the ECROFI-XX 20th Biennial Conferences, Granada, Spain, 21–27 September 2009; Volume 20, pp. 261–262.
160. Tomczyk, C. Âge de mise en place et modèle génétique du stockwerk du prospect à Au-Ag-Te de Kelâa M'Gouna (Maroc). Master's Thesis, University of Lille, Lille, France, 2010.
161. Dong, G.; Morrison, G.; Jaireth, S. Quartz textures in epithermal veins, Queensland; classification, origin and implication. *Econ. Geol.* **1995**, *90*, 1841–1856. [[CrossRef](#)]
162. Etoh, J.; Izawa, E.; Watanabe, K.; Taguchi, S.; Sekine, R. Bladed quartz and its relationship to gold mineralization in the Hishikari low-sulfidation epithermal gold deposit, Japan. *Econ. Geol.* **2002**, *97*, 1841–1851. [[CrossRef](#)]
163. André-Mayer, A.-S.; Leroy, J.L.; Bailly, L.; Chauvet, A.; Marcoux, E.; Grancea, L.; Llosa, F.; Rosas, J. Boiling and vertical mineralization zoning: A case study from the Apacheta low-sulfidation epithermal gold-silver deposit, southern Peru. *Mineral. Depos.* **2002**, *37*, 452–464. [[CrossRef](#)]
164. Chauvet, A.; Bailly, L.; André, A.-S.; Monié, P.; Cassard, D.; Tajada, F.; Vargas, J.; Tuduri, J. Internal vein texture and vein evolution of the epithermal Shila-Paula district, southern Peru. *Mineral. Depos.* **2006**, *41*, 387–410. [[CrossRef](#)]
165. Simmons, S.F.; Christenson, B.W. Origins of calcite in a boiling geothermal system. *Am. J. Sci.* **1994**, *294*, 361–400. [[CrossRef](#)]
166. Saule, A. La Zones des Dykes, Anti-Atlas Marocain: Caractérisation des fluides minéralisateurs et du gisement. Master's Thesis, Institut National Polytechnique de Lorraine, Nancy, France, 2012.
167. Albinson, T.; Norman, D.I.; Cole, D.; Chomiak, B. Controls on Formation of Low-Sulfidation Epithermal Deposits in Mexico: Constraints from Fluid Inclusion and Stable Isotope Data. In *New Mines and Discoveries in Mexico and Central America*; Society of Economic Geologists: Littleton, CO, USA, 2001; Volume 8, pp. 1–32.
168. Guillou, J.-J.; Monthel, J.; Picot, P.; Pillard, F.; Protas, J.; Samana, J.-C. L'imitérite, Ag<sub>2</sub>HgS<sub>2</sub>, nouvelle espèce minérale; propriétés et structure cristalline. *Bull. Mineral.* **1985**, *108*, 457–464.
169. Guillou, J.-J.; Monthel, J.; Samana, J.-C.; Tijani, A. Morphologie et chronologie relative des associations minérales du gisement mercuro-argentifère d'Imiter (Anti-Atlas—Maroc). *Notes et Mémoires du Service Géologique du Maroc* **1988**, *44*, 215–228.
170. Levresse, G. Contribution à l'établissement d'un modèle génétique des gisements d'Imiter (Ag-Hg), Bou Madine (Pb-Zn-Cu-Ag-Au), Bou Azzer (Co, Ni, As, Au, Ag) dans l'Anti-Atlas marocain. In *3<sup>ème</sup> Cycle*; Institut National Polytechnique de Lorraine: Nancy, France, 2001.

171. Baroudi, Z.; Beraaouz, E.H.; Rahimi, A.; Chouhaidi, M.Y. Minéralisations polymétalliques argentifères d’Imiter (Jbel Saghro, Maroc): Minéralogie, évolution des fluides minéralisateurs et mécanismes de dépôt. *Chronique de la Recherche Minière* **1999**, 536–537, 91–111.
172. Hulin, C.; Dubois, M.; Tuduri, J.; Chauvet, A.; Boulvais, P.; Gaouzi, A.; Mouhajir, M.; Essalhi, M.; Outhounjite, S. New fluid inclusions and oxygen isotope data to constrain a formation model for the Imiter Ag world class deposit (Anti-Atlas, Morocco). In Proceedings of the ECROFI XXII 22nd Biennial Conferences, Antalya, Turkey, 4–9 June 2013; pp. 78–79.
173. Hulin, C.; Dubois, M.; Tuduri, J.; Chauvet, A.; Boulvais, P.; Gaouzi, A.; Mouhajir, M.; Essalhi, M.; Outhounjite, S. A fluid inclusion and stable isotope study of the world class Imiter silver deposit (Morocco). In Proceedings of the 24ème Réunion des Sciences de la Terre, Pau, France, 27–31 October 2014; p. 373.
174. Tuduri, J.; Pourret, O.; Chauvet, A.; Barbanson, L.; Gaouzi, A.; Ennaciri, A. Rare earth elements as proxies of supergene alteration processes from the giant Imiter silver deposit (Morocco). In *Let’s Talk Ore Deposits, Proceeding of the Eleventh Biennial SGA Meeting*; Barra, F., Reich, M., Campos, E., Tornos, F., Eds.; Ediciones Universidad Católica del Norte: Antofagasta, Chile, 2011; Volume 2, pp. 826–828.
175. Tuduri, J.; Pourret, O.; Boulvais, P.; Chauvet, A.; Barbanson, L.; Gaouzi, A.; Hulin, C.; Dubois, M. A reassessment of fluid-mineral relations in the world-class Imiter silver deposit (Anti-Atlas, Morocco). In Proceedings of the SEG 2012 Conference, Lima, Peru, 23–26 September 2012; Society of Economic Geologists: Lima, Peru, 2012.
176. Graybeal, F.T.; Vikre, P. A review of silver-rich mineral deposits and their metallogeny. In *SEG Special Publication: The Challenge of Finding New Mineral Resources: Global Metallogeny, Innovative Exploration, and New Discoveries*; Goldfarb, R.J., Marsh, E.E., Monecke, T., Eds.; Society of Economic Geologists: Littleton, CO, USA, 2010; Volume 15, pp. 85–117.
177. Azizi Samir, M.R.; Ferrandini, J.; Tane, J.L. Tectonique et volcanisme tardi-Pan Africains (580-560 M.a.) dans l’Anti-Atlas Central (Maroc): Interpretation géodynamique à l’échelle du NW de l’Afrique. *J. Afr. Earth Sci.* **1990**, 10, 549–563. [[CrossRef](#)]
178. Ducea, M.N.; Paterson, S.R.; DeCelles, P.G. High-Volume Magmatic Events in Subduction Systems. *Elements* **2015**, 11, 99–104. [[CrossRef](#)]
179. Harrison, R.W.; Yazidi, A.; Benziane, F.; Quick, J.E.; El Fahssi, A.; Stone, B.D.; Yazidi, M.; Saadane, A.; Walsh, G.J.; Aleinikoff, J.N.; et al. Carte géologique au 1/50 000, Feuille Tizgui. *Notes et Mémoires du Service Géologique du Maroc* **2008**, 470, 131.
180. McQuarrie, N.; Barnes, J.B.; Ehlers, T.A. Geometric, kinematic, and erosional history of the central Andean Plateau, Bolivia (15–17° S). *Tectonics* **2008**, 27, TC3007. [[CrossRef](#)]
181. Till, A.B.; Roeske, S.; Sample, J.C.; Foster, D.A. *Exhumation Associated with Continental Strike-Slip Fault Systems*; The Geological Society of America: Boulder, CO, USA, 2007; Volume 434, p. 264.
182. Willett, S.D.; Brandon, M.T. On steady states in mountain belts. *Geology* **2002**, 30, 175–178. [[CrossRef](#)]
183. Hedenquist, J.W.; Lowenstern, J.B. The role of magmas in the formation of hydrothermal ore deposits. *Nature* **1994**, 370, 519–527. [[CrossRef](#)]
184. Monier, G.; Robert, J.L. Muscovite solid solutions in the system K<sub>2</sub>O, MgO, FeO, Al<sub>2</sub>O<sub>3</sub>, SiO<sub>2</sub>, H<sub>2</sub>O: An experimental study at 2 kbar P<sub>H<sub>2</sub>O</sub> and comparison with natural Li-free white micas. *Mineral. Mag.* **1986**, 50, 257–266. [[CrossRef](#)]
185. Cathelineau, M.; Nieva, D. A chlorite solid solution geothermometer: The Los Azufres (Mexico) geothermal system. *Contrib. Mineral. Petrol.* **1985**, 91, 235–244. [[CrossRef](#)]
186. Kranidiotis, P.; MacLean, W.H. Systematics of chlorite alteration at the Phelps Dodge massive sulfide deposit, Matagami, Quebec. *Econ. Geol.* **1987**, 82, 1898–1911. [[CrossRef](#)]
187. Kretschmar, U.; Scott, S.D. Phase relations involving arsenopyrite in the system Fe-As-S and their application. *Can. Mineral.* **1976**, 14, 364–386.
188. Sundblad, K.; Zachrisson, E.; Smeds, S.A.; Berglund, S.; Aalinder, C. Sphalerite geobarometry and arsenopyrite geothermometry applied to metamorphosed sulfide ores in the Swedish Caledonides. *Econ. Geol.* **1984**, 79, 1660–1668. [[CrossRef](#)]
189. Lynch, G.; Ortega, J. Hydrothermal alteration and tourmaline-albite equilibria at the Coxheat porphyry Cu-Mo-Au deposit, Nova Scotia. *Can. Mineral.* **1997**, 35, 79–94.
190. Sillitoe, R.H. Porphyry Copper Systems. *Econ. Geol.* **2010**, 105, 3–41. [[CrossRef](#)]

191. Kouzmanov, K.; Pokrovski, G.S. Hydrothermal controls on metal distribution in porphyry Cu (-Mo-Au) systems. In *Geology and Genesis of Major Copper Deposits and Districts of the World: A Tribute to Richard H. Sillitoe*; Hedenquist, J.W., Harris, M., Camus, F., Eds.; Special Publications of the Society of Economic Geologists: Littleton, CO, USA, 2012; Volume 16, pp. 573–618.
192. Rottier, B.; Kouzmanov, K.; Casanova, V.; Wälle, M.; Fontboté, L. Cyclic Dilution of Magmatic Metal-Rich Hypersaline Fluids by Magmatic Low-Salinity Fluid: A Major Process Generating the Giant Epithermal Polymetallic Deposit of Cerro de Pasco, Peru. *Econ. Geol.* **2018**, *113*, 825–856. [[CrossRef](#)]
193. Scott, S.; Driesner, T.; Weis, P. Boiling and condensation of saline geothermal fluids above magmatic intrusions. *Geophys. Res. Lett.* **2017**, *44*, 1696–1705. [[CrossRef](#)]
194. Letsch, D.; Large, S.J.E.; Buechi, M.W.; Winkler, W.; von Quadt, A. Ediacaran glaciations of the west African Craton—Evidence from Morocco. *Precambrian Res.* **2018**, *310*, 17–38. [[CrossRef](#)]
195. Pinneker, Y.V.; Lomonosov, I.S. Concentrated brines of Siberian Platform and their counterparts in Asia, Europe, Africa and America. *Int. Geol. Rev.* **1968**, *10*, 431–442. [[CrossRef](#)]
196. Richard, A.; Pettke, T.; Cathelineau, M.; Boiron, M.-C.; Mercadier, J.; Cuney, M.; Derome, D. Brine–rock interaction in the Athabasca basement (McArthur River U deposit, Canada): Consequences for fluid chemistry and uranium uptake. *Terra Nova* **2010**, *22*, 303–308. [[CrossRef](#)]
197. Linnemann, U.; Pidal, A.P.; Hofmann, M.; Drost, K.; Quesada, C.; Gerdes, A.; Marko, L.; Gärtner, A.; Zieger, J.; Ulrich, J.; et al. A ~565 Ma old glaciation in the Ediacaran of peri-Gondwanan West Africa. *Int. J. Earth Sci.* **2018**, *107*, 885–911. [[CrossRef](#)]
198. Vernhet, E.; Youbi, N.; Chellai, E.H.; Villeneuve, M.; El Archi, A. The Bou-Azzer glaciation: Evidence for an Ediacaran glaciation on the West African Craton (Anti-Atlas, Morocco). *Precambrian Res.* **2012**, *196*–197. [[CrossRef](#)]
199. Starinsky, A.; Katz, A. The formation of natural cryogenic brines. *Geochim. Cosmochim. Acta* **2003**, *67*, 1475–1484. [[CrossRef](#)]
200. Toner, J.D.; Catling, D.C.; Sletten, R.S. The geochemistry of Don Juan Pond: Evidence for a deep groundwater flow system in Wright Valley, Antarctica. *Earth Planet. Sci. Lett.* **2017**, *474*, 190–197. [[CrossRef](#)]
201. Belkacim, S.; Ikenne, M.; Souhassou, M.; Elbasbas, A.; Toummite, A. The Cu-Mo±Au mineralizations associated to the High-K calc-alkaline granitoids from Tifnoute valley (Siroua massif, anti-atlas, Morocco): An arc-Type porphyry in the late neoproterozoic series. *J. Environ. Earth Sci.* **2014**, *4*, 90–106.
202. Loiselet, C.; Husson, L.; Braun, J. From longitudinal slab curvature to slab rheology. *Geology* **2009**, *37*, 747–750. [[CrossRef](#)]
203. Manea, V.C.; Pérez-Gussinyé, M.; Manea, M. Chilean flat slab subduction controlled by overriding plate thickness and trench rollback. *Geology* **2012**, *40*, 35–38. [[CrossRef](#)]
204. Merdith, A.S.; Collins, A.S.; Williams, S.E.; Pisarevsky, S.; Foden, J.D.; Archibald, D.B.; Blades, M.L.; Alessio, B.L.; Armistead, S.; Plavska, D.; et al. A full-plate global reconstruction of the Neoproterozoic. *Gondwana Res.* **2017**, *50*, 84–134. [[CrossRef](#)]
205. Boyden, J.A.; Müller, R.D.; Gurnis, M.; Torsvik, T.H.; Clark, J.A.; Turner, M.; Ivey-Law, H.; Watson, R.J.; Cannon, J.S. Next-generation plate-tectonic reconstructions using GPlates. In *Geoinformatics: Cyberinfrastructure for the Solid Earth Sciences*; Keller, G.R., Baru, C., Eds.; Cambridge University Press: Cambridge, UK, 2011; pp. 95–113.
206. Domeier, M. A plate tectonic scenario for the Iapetus and Rheic oceans. *Gondwana Res.* **2016**, *36*, 275–295. [[CrossRef](#)]
207. Torsvik, T.H.; Cocks, L.R.M. Gondwana from top to base in space and time. *Gondwana Res.* **2013**, *24*, 999–1030. [[CrossRef](#)]
208. Richards, J.P. Postsubduction porphyry Cu-Au and epithermal Au deposits: Products of remelting of subduction-modified lithosphere. *Geology* **2009**, *37*, 247–250. [[CrossRef](#)]
209. Richards, J.P. Magmatic to hydrothermal metal fluxes in convergent and collided margins. *Ore Geol. Rev.* **2011**, *40*, 1–26. [[CrossRef](#)]
210. Sillitoe, R.H.; Hedenquist, J.W. Linkages between volcanotectonic settings, ore-fluid compositions and epithermal precious metal deposits. In *Volcanic, Geothermal and Ore-Forming Fluids; Rulers and Witnesses of Processes within the Earth*; Simmons, S.F., Graham, I., Eds.; Society of Economic Geologist Special Publication: Littleton, CO, USA, 2003; Volume 10, pp. 315–343.


211. Tosdal, R.; Richards, J. Magmatic and structural controls on the development of porphyry Cu±Mo±Au deposits. *Rev. Econ. Geol.* **2001**, *14*, 157–181.
212. Menant, A.; Jolivet, L.; Tuduri, J.; Loiselet, C.; Bertrand, G.; Guillou-Frottier, L. 3D subduction dynamics: A first-order parameter of the transition from copper- to gold-rich deposits in the eastern Mediterranean region. *Ore Geol. Rev.* **2018**, *94*, 118–135. [[CrossRef](#)]
213. Bryan, S.E.; Orozco-Esquivel, T.; Ferrari, L.; López-Martínez, M. Pulling apart the Mid to Late Cenozoic magmatic record of the Gulf of California: Is there a Comondú Arc? *Geol. Soc. Lond. Spec. Publ.* **2013**, *385*. [[CrossRef](#)]
214. Thorkelson, D.J.; Breitsprecher, K. Partial melting of slab window margins: Genesis of adakitic and non-adakitic magmas. *Lithos* **2005**, *79*, 25–41. [[CrossRef](#)]
215. de Silva, S. Arc magmatism, calderas, and supervolcanoes. *Geology* **2008**, *36*, 671–672. [[CrossRef](#)]
216. Chauvet, A.; Alves Da Silva, F.C.; Faure, M.; Guerrot, C. Structural evolution of the Paleoproterozoic Rio Itapicuru granite-greenstone belt (Bahia, Brazil): The role of synkinematic plutons in the regional tectonics. *Precambrian Res.* **1997**, *84*, 139–162. [[CrossRef](#)]
217. Hickman, A.H. Two contrasting granite-greenstone terranes in the Pilbara Craton, Australia: Evidence for vertical and horizontal tectonic regimes prior to 2900 Ma. *Precambrian Res.* **2004**, *131*, 153–172. [[CrossRef](#)]
218. Van Kranendonk, M.J.; Collins, W.J.; Hickman, A.; Pawley, M.J. Critical tests of vertical vs. horizontal tectonic models for the Archaean East Pilbara Granite-Greenstone Terrane, Pilbara Craton, Western Australia. *Precambrian Res.* **2004**, *131*, 173–211. [[CrossRef](#)]
219. Nance, R.D.; Murphy, J.B.; Strachan, R.A.; Keppie, J.D.; Gutiérrez-Alonso, G.; Fernández-Suárez, J.; Quesada, C.; Linnemann, U.; D'lemos, R.; Pisarevsky, S.A. Neoproterozoic-early Palaeozoic tectonostratigraphy and palaeogeography of the peri-Gondwanan terranes: Amazonian v. West African connections. *Geol. Soc. Lond. Spec. Publ.* **2008**, *297*, 345–383. [[CrossRef](#)]



© 2018 by the authors. Licensee MDPI, Basel, Switzerland. This article is an open access article distributed under the terms and conditions of the Creative Commons Attribution (CC BY) license (<http://creativecommons.org/licenses/by/4.0/>).

Article

# Fault Zone Evolution and Development of a Structural and Hydrological Barrier: The Quartz Breccia in the Kiggavik Area (Nunavut, Canada) and Its Control on Uranium Mineralization

Alexis Grare <sup>1,\*</sup>, Olivier Lacombe <sup>1</sup>, Julien Mercadier <sup>2</sup>, Antonio Benedicto <sup>3</sup>, Marie Guilcher <sup>2</sup>, Anna Trave <sup>4</sup> , Patrick Ledru <sup>5</sup> and John Robbins <sup>5</sup>

<sup>1</sup> Sorbonne Université, CNRS-INSU, Institut des Sciences de la Terre de Paris, ISTeP UMR 7193, F-75005 Paris, France; olivier.lacombe@sorbonne-universite.fr

<sup>2</sup> Université de Lorraine, CNRS, CREGU, GeoRessources lab, 54506 Vandoeuvre-lès-Nancy, France; julien.mercadier@univ-lorraine.fr (J.M.); marie.guilcher1@gmail.com (M.G.)

<sup>3</sup> UMR Geops, Université Paris Sud, 91405 Orsay, France; antonio.benedicto@u-psud.fr

<sup>4</sup> Departament de Mineralogia, Universitat de Barcelona (UB), Petrologia i Geologia Aplicada, Facultat de Ciències de la Terra, 08028 Barcelona, Spain; atrave@ub.edu

<sup>5</sup> Orano Canada Inc., 817 45th Street, West Saskatoon, SK S7L 5X2, Canada; patrick.ledru@orano.group (P.L.); john.robbins@orano.group (J.R.)

\* Correspondence: alexisgrare@gmail.com

Received: 25 May 2018; Accepted: 24 July 2018; Published: 27 July 2018

**Abstract:** In the Kiggavik area (Nunavut, Canada), major fault zones along, or close to, where uranium deposits are found are often associated with occurrence of thick quartz breccia (QB) bodies. These bodies formed in an early stage (~1750 Ma) of the long-lasting tectonic history of the Archean basement, and of the Proterozoic Thelon basin. The main characteristics of the QB are addressed in this study; through field work, macro and microscopic observations, cathodoluminescence microscopy, trace elements, and oxygen isotopic signatures of the quartz forming the QB. Faults formed earlier during syn- to post-orogenic rifting (1850–1750 Ma) were subsequently reactivated, and underwent cycles of cataclasis, pervasive silicification, hydraulic brecciation, and quartz recrystallization. This was synchronous with the circulation of meteoric fluids mixing with Si-rich magmatic-derived fluids at depth, and were coeval with the emplacement of the Kivalliq igneous suite at 1750 Ma. These processes led to the emplacement of up to 30 m thick QB, which behaved as a mechanically strong, transverse hydraulic barrier that localized later fracturing, and compartmentalized/channelized vertical flow of uranium-bearing fluids after the deposition of the Thelon Basin (post 1750 Ma). The development and locations of QB control the location of uranium mineralization in the Kiggavik area.

**Keywords:** hydrothermal breccia; hydraulic breccia; uranium deposits; structural control; silicification; Kiggavik

## 1. Introduction

Fault zones are often associated with enhanced, focused, repeated fluid circulations in the earth's crust [1–7]. These fluids may have different origins: Meteoric, magmatic, metamorphic or basinal, and possibly transport metals to a favorable area of deposition [8,9]; that will ultimately allow for the formation of potential economic ore deposits. In many conceptual models of the formation of ore deposits, fault zones are important structural features acting as pathways [2,10] and/or as traps for fluids, and related metals [11]. In the uppermost crust, deformation is dominantly

brittle and breccias are commonly observed in fault zones [12–15]. Among the different families of breccias, hydrothermal breccias are one sub-class that would develop early, in response to fracture propagation processes [13], through interaction between brecciated rocks and hydrothermal solutions. Hydrothermal breccias can be of various types depending on several parameters, such as pressure, temperature, depth of emplacement, and elements in the fluids [14]. Among them, quartz-cemented breccias can have an economic interest, being possibly associated with ore deposits such as epithermal (Au-Ag-Cu-Pb-Zn-Sb, [16,17]), orogenic gold (Au, [18]), and porphyritic (Cu-Mo-Au-Ag, [19,20]). They display thickness from meter to several meters, thicker hydrothermal breccias being relatively rarely described. Quartz breccias in fault zones form progressively during several cycles of fluid pressure growth, seismogenic fault slip and quartz precipitation [21,22]. Unaltered, quartz-rich bodies have a lowered porosity and thus have an impact on later fluid circulation within the fault zone. Such silicification would be comparable to fluid-flow being constrained by horizontal barriers, such as sedimentary layers indurated through diagenesis (aquitards, [23,24]), or impermeable (clay-rich) layers in roll-front uranium deposits [25]. In addition, the likely hardening of the fault rocks in response to multiple cycles of quartz brecciation and healing may cause a significant rheological contrast between the “strong” fault zone and the expectedly “weaker” hosting terranes, possibly controlling localization of subsequent deformation.

In this contribution, we focus on one structural feature encountered in many fault zones within the Uranium (U)-rich district of the Kiggavik area (Nunavut, Canada): The so-called hydrothermal Quartz Breccia (QB). The importance of this breccia, only briefly described by previous authors [26–30] was recently highlighted by Grare et al. [31] who documented the control exerted by this breccia on later fracturing events, hydrothermal alterations and uranium mineralization at the Contact uranium prospect. However, despite observations in several locations of the Kiggavik area and its seemingly strong control on the current distribution of the uranium mineralization, the genetic model of the QB remains poorly characterized and explained to date. Grare et al. [31] showed that the QB emplaced along faults of inferred Archean age, and that this emplacement was a key event within a long-lasting (~1000 Ma) complex brittle tectonic history that led to uranium mineralization within or in the vicinity of the quartz breccia (Figure 1C). In order to better constrain the nature, emplacement, significance and role of the QB, we carried out a structural analysis combined with vein cement petrography using optical and cathodoluminescence observations, trace elements, and oxygen stable isotope analysis of quartz. Our study addresses the structural, mineralogical and geochemical characteristics of the QB. Combined with the reconstructed geochemical signature of the fluids, a model of formation of the QB is proposed and its role in controlling uranium mineralization in the Kiggavik area is highlighted.

## 2. Geological Setting

### 2.1. Regional Geological Setting

The Kiggavik area is located on the eastern border of the Proterozoic intracratonic Thelon Basin (ca. 1670–1540 Ma, [32,33]) in Nunavut, Canada, within the Churchill province. The Churchill province is known to host the Athabasca Basin (1740–1540 Ma, [34]); another Proterozoic basin, which itself hold the world-class Cigar Lake and McArthur River uranium deposits. The Thelon Basin is one analogue of the Athabasca Basin and the Kiggavik area displays several economically significant uranium orebodies: Four of the deposits yield calculated resources of 48,953 t of uranium at a grade of 0.47% U [35]. Exploration began in the 1980s by Urangesellschaft, and the property is now held by Orano Canada (formerly known as AREVA Resources Canada) in joint venture with JCU (Canada) Exploration Company Ltd. (Vancouver, BC, Canada).

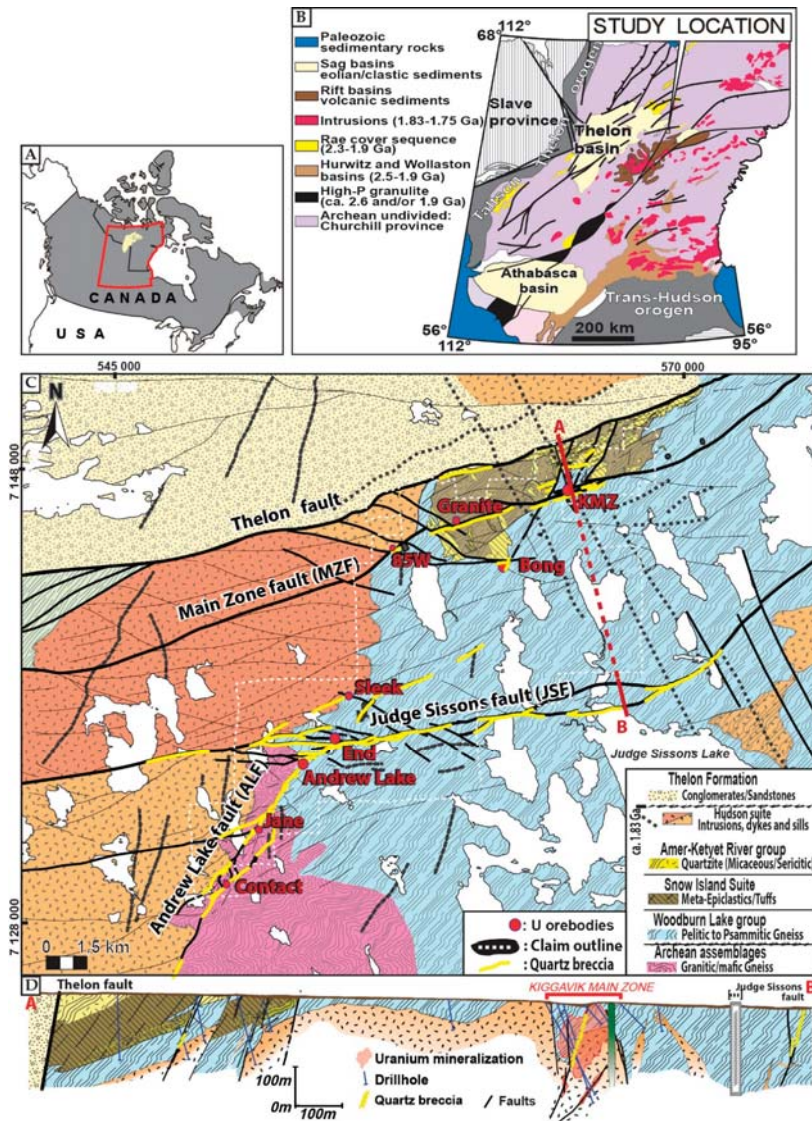


**Figure 1.** (A) Outline of Canada and location of the Thelon basin in yellow; (B) geological map of the Churchill-Wyoming craton showing the location of the Thelon basins and the Kiggavik area on its Eastern border; (C) simplified geological map of the Kiggavik area (Orano internal document) highlighting the occurrence of the QB (yellow) along the major faults; and (D) cross-section from the Thelon fault to the Judge Sisson fault. Deposits and prospects are indicated with red circles.

The Churchill province (Figure 1B) is bordered to the NW by the Thelon-Taltson (ca. 2020–1900 Ma), and to the SE by the Trans-Hudson orogenic belts (ca. 2070–1800 Ma). At the end of the Trans-Hudsonian orogeny, the Baker Lake Basin developed as a result of (retro-arc) extensional to transtensional rifting tectonics [36], and was filled with sedimentary and bi-modal volcanic-sedimentary rocks (Baker Lake and Wharton Grps, ca. 1850–1750 Ma, [37,38]). It was

followed by uplift, extensive erosional peneplanation and regolith formation, over which deposited the eolian sandstones and conglomeratic red-beds of the Thelon formation (ca. 1670–1540 Ma [32,33]), linked to thermal subsidence in the sag, fault-controlled intracratonic Thelon basin [36,38,39]. This volcano-sedimentary pile unconformably overlies a metamorphosed basement consisting of Archean rocks that include Mesoarchean (ca. 2870 Ma) granitic gneisses, 2730–2680 Ma, supracrustal rocks of the Woodburn Lake Group [40], and a distinctive package of 2620–2580 Ma felsic volcanic and related hypabyssal rocks known as the Snow Island Suite [41–47].

Before emplacement of the Thelon formation, the Archean to Paleoproterozoic rocks of the Churchill province were intruded by three magmatic suites: (i) The late syn-orogenic (ca. 1830 Ma) Hudson Suite [48], (ii) the Dubawnt Minette Suite (contemporaneous of the Hudson Suite), with ultrapotassic intrusions, minette dikes and lamprophyres, and (iii) the anorogenic (ca. 1750 Ma) Kivalliq Igneous Suite (KIS) [46,49–51].

## 2.2. Local Geological Setting

A simplified geological map of the Kiggavik area is presented in Figure 1C. The local litho-structural pile consists of Mesoarchean granitic, granodioritic, and augen gneisses ( $2866 \pm 6$  Ma; [52]) tectonically overlain by a Neoarchean metavolcano-sedimentary package retro-morphosed to greenschist facies: The Woodburn Lake Group. This package consists of quartzo-feldspathic wackes and minor quartzite with thin, interbedded banded iron formation layers, rare black shales, and locally komatiite and rhyolite ( $2710 \pm 2.1$  Ma). These rocks, together with overlying Paleoproterozoic (2300–2150 Ma) rocks of the Ketyet River Group [53], include a prominent unit of orthoquartzite [52]. These rocks are intruded by the Schultz Lake Intrusive Complex (SLIC, [51]). The SLIC comprises rocks from the two intrusive suites previously described [51]: (i) The “Hudson granite” consists of non-foliated granitoid sills, syenites and lamprophyre dikes of the late syn-orogenic Hudson Suite; and (ii) the “Nueltin granite” comprises anorogenic granite to rhyolite of the KIS [46].

The diabase dikes of the Mackenzie diabase swarm form prominent linear aeromagnetic features trending NNW-SSE [44,45] and cut across all previous lithologies. This intrusive event is dated at  $1267 \pm 2$  Ma [54,55], and represents the last magmatic-tectonic event in the region.

The main structural features in the Kiggavik area are the ENE-trending Thelon fault (TF) and the Main Zone fault (MZF) in the northern part of the property, the ENE-trending Judge Sisson fault (JSF) in the central part, and the NE-trending Andrew Lake Fault (ALF) in the southwestern part of the study area (Figure 2). These faults date back to at least ~1920 Ma [56] and had a subsequent complex structural and kinematic evolution with several episodes of reactivation and fluid circulation during Proterozoic time [31,56]. These faults host several uranium orebodies; prospects and deposits, the main uranium mineralizing events being bracketed between 1540 and 1270 Ma [28,29,31]. The MZF hosts various deposits and prospects: 85 W, Granite Grid and Kiggavik (Main, Central and East Zones, Figure 1C). End is hosted by the JSF, while Andrew Lake, Jane and Contact occur along the ALF (Figure 1C).



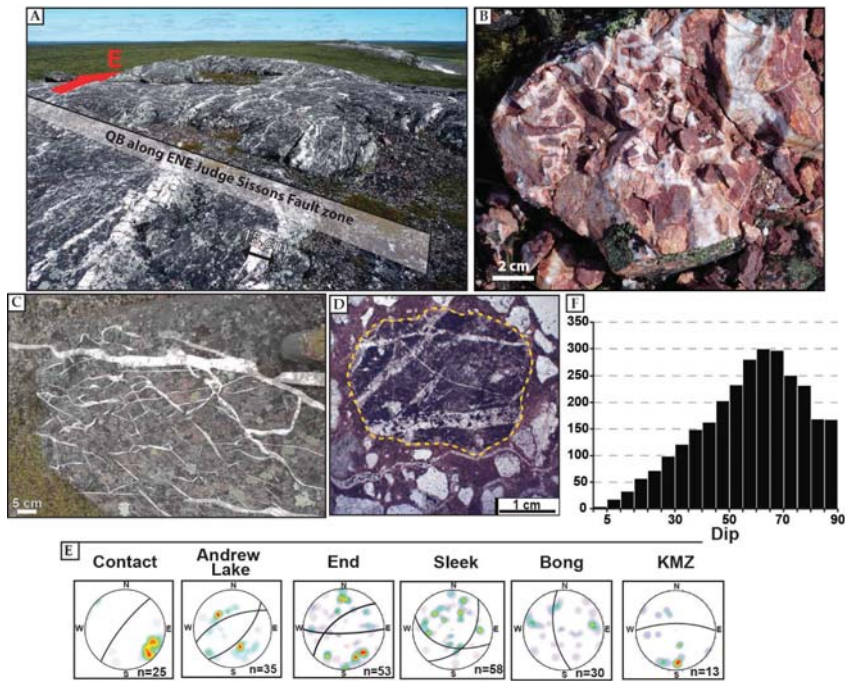


**Figure 2.** (A) Outcrop view looking east on the N80-trending steeply dipping to the north Judge Sisson fault (JSF) underlain by at least 10 m of white quartz veins; (B) heterogeneous size, pervasively hematized clasts cemented by a white quartz matrix; (C) right lateral relay step, N80 trending main veins (outcrop on the JSF); (D) optical microphotograph picture (OM): Clasts bearing quartz veins in the Thelon sandstones; (E) oriented data of thick quartz veins for deposits and prospects; and (F) histogram of all measured quartz vein dips in the Kiggavik area.

### 3. Sampling and Methods

#### 3.1. Drillhole Observations, Sampling Strategy and Collection of Oriented Data

The QB has been observed in the field but the scarcity of outcrops in the area is the reason why most observations and oriented measurements were taken from drill holes within the deposits and prospects in the Kiggavik area (location in Figure 1C). Porosity was measured systematically in the field following the fluid resaturation method. A clean and dried sample is weighted, saturated with a liquid of known density, and then reweighed. The weight change divided by the density of the fluid results in the pore volume. Many of the observations and samples come from the recently drilled Contact prospect (2014 and 2015 Orano exploration campaigns). More than 5000 m of drill core were reviewed, with several hundreds of meters dedicated to the characterization and study of the QB. Recent drilling (2014–2015) in the Kiggavik area was done with NQ™ coring providing a 47.6 mm diameter sample. Oriented data measured on drill core were restored in their original position and plotted with Dips 6.0 software (Rocscience, Toronto, ON, Canada). Uncertainty on fault/fracture orientation measurements is estimated to be  $\pm 10^\circ$ .

#### 3.2. Quartz Microscopic Characterisation by Optical and Cathodoluminescence Microscopy

Quartz Fifty-five drill core samples (10 to 20 cm in length) displaying veins or breccias linked to the QB were collected, mainly from the Contact prospect, but also from End, Andrew Lake and Bong

deposits. All samples were studied from the macro- to the micro-scale in order to characterize the macroscopic texture of the quartz breccia and its relationships with predating and postdating fracturing and faulting events. Thirty-five thin sections were prepared for petrographic and microstructural studies. Thin sections were observed through optical microscopy (plane polarized transmitted and reflected light microscope Motic BA310 POL Trinocular, equipped with a 5 M pixel Moticam camera) (Motic Instruments Inc., Richmond, BC, Canada), and cathodoluminescence microscopy (CITL Cold Cathodoluminescence device Model MK5-1, made at University of Barcelona (Barcelona, Spain), for deciphering quartz generations.

### 3.3. Fluid Characterization by Trace Elements and Oxygen Isotopes Analyses

Laser ablation ICP-MS analyses of quartz were conducted at GeoRessources, Université de Lorraine (Vandoeuvre-lès-Nancy, France), using a 7500e quadrupole ICP-MS (Agilent, Santa Clara, CA, USA) coupled with a nanosecond excimer laser (GEOLAS Pro; 193 nm wavelength). Zones free of fluid inclusions (FIs) were selected for analyses. Analyses were performed using a laser beam diameter of 60 (first session of analyses) and 90 (second session)  $\mu\text{m}$ , with a fluence of  $\sim 10 \text{ J/cm}^2$  and a repetition rate of 5 Hz. The laser beam was focused onto the sample with a Schwarzschild reflective objective (magnification  $\times 25$ ; numerical aperture = 0.4). Each analysis consisted of 20 s of background measurement during laser warm-up, 20 to 40 s of ablation (depending on the thickness of the quartz) and 15 s of washout before repeating the process on a nearby location. The external standards were NIST SRM610 and NIST SRM 612 [57], the external standards being analysed twice at the beginning and at the end of each set of samples, following a bracketing standardization procedure. LA-ICP-MS calibration was optimized for highest sensibility for the whole mass/charge range, while maintaining Th/U  $\sim 1$  and ThO/Th  $< 0.5\%$  as determined on NIST SRM 610 or 612. The following isotopes were measured:  $^7\text{Li}$ ,  $^{11}\text{B}$ ,  $^{23}\text{Na}$ ,  $^{24}\text{Mg}$ ,  $^{27}\text{Al}$ ,  $^{28}\text{Si}$ ,  $^{39}\text{K}$ ,  $^{44}\text{Ca}$ ,  $^{48}\text{Ti}$ ,  $^{57}\text{Fe}$ ,  $^{74}\text{Ge}$ ,  $^{85}\text{Rb}$ ,  $^{88}\text{Sr}$ ,  $^{89}\text{Y}$ ,  $^{90}\text{Zr}$ ,  $^{133}\text{Cs}$ ,  $^{138}\text{Ba}$  and  $^{153}\text{Eu}$  for the first session, and  $^7\text{Li}$ ,  $^{11}\text{B}$ ,  $^{23}\text{Na}$ ,  $^{27}\text{Al}$ ,  $^{29}\text{Si}$ ,  $^{45}\text{Sc}$ ,  $^{47}\text{Ti}$ ,  $^{51}\text{V}$ ,  $^{53}\text{Cr}$ ,  $^{55}\text{Mn}$ ,  $^{59}\text{Co}$ ,  $^{60}\text{Ni}$ ,  $^{63}\text{Cu}$ ,  $^{66}\text{Zn}$ ,  $^{69}\text{Ga}$ ,  $^{72}\text{Ge}$ ,  $^{75}\text{As}$ ,  $^{85}\text{Rb}$ ,  $^{88}\text{Sr}$ ,  $^{90}\text{Zr}$ ,  $^{93}\text{Nb}$ ,  $^{95}\text{Mo}$ ,  $^{115}\text{In}$ ,  $^{118}\text{Sn}$ ,  $^{121}\text{Sb}$ ,  $^{133}\text{Cs}$ ,  $^{137}\text{Ba}$ ,  $^{181}\text{Ta}$ ,  $^{182}\text{W}$ ,  $^{197}\text{Au}$ ,  $^{208}\text{Pb}$ , and  $^{209}\text{Bi}$  for the second session.  $^{28}\text{Si}$  or  $^{29}\text{Si}$  were used as internal standard, using a  $\text{SiO}_2$  concentration of 100%. Data reduction was done using Iolite software [58].

In situ oxygen isotope analysis of the main quartz generations was performed by secondary ion mass spectrometry (SIMS, CAMECA, Gennevillier, France) using the Cameca IMS1270 at CRPG/CNRS in Vandoeuvre-les-Nancy, France, following the approach of Hervig et al. [59]. The isotopes  $^{16}\text{O}$  and  $^{18}\text{O}$  were measured, based on standard polished sections coated with gold. A  $\sim 4 \text{ nA}$  defocused primary ion beam of Cs impact energy 10 keV was used, producing sub-circular ablation craters of  $\sim 10\text{--}20 \mu\text{m}$  diameter. A mass resolution ( $\Delta M/M$ ) of 5000 was used, to resolve potential interference of  $^{17}\text{O}$  on  $^{16}\text{O}$ . Two in-house standards were used (Brésil ( $\delta^{18}\text{O} = 9.6\text{‰}$ ) and Brésil-2 ( $\delta^{18}\text{O} = 19.6\text{‰}$ )) to set-up the instrument and correct for drifts and fractionations using a standard bracketing approach. The internal precision for  $\delta^{18}\text{O}$  was between 0.06 and 0.1‰ (measurements on the standards Brésil and Brésil-2 and on the different quartz generations of Kiggavik).  $\delta^{18}\text{O}$  values are reported relative to the V-SMOW standard.

## 4. Results

### 4.1. Spatial Organisation and Macroscopic Characteristics of the QB

Occurrence of QB has been recognized along various segments of the major faults within the Kiggavik area (e.g., ALF, JSF, Figure 1C,D and Figure 2A). The QB consists of a up to 30 m thick complex network of mosaic quartz-sealed breccia and veins (Figure 2A–C), typically displaying angular fragments and jigsaw pattern (Figure 2B), and associated with a pervasive iron-oxidation of the host rock (Figure 2B). This kind of observation is common in drill holes. Lithologies within and around the QB display a pervasive red-purple hematization, as documented at the Contact prospect [31]. Clasts bearing veins of the QB are observed in the sandstones of the Thelon formation

(Figure 2D), indicating that QB predates formation of the Thelon Basin, as already suggested by several authors [29,31] and crosscuts, thus postdates, Hudsonian intrusions (ca. 1.83 Ga). Fault zones outlined by the QB are presumably better preserved in the field due to the silicification process that increases their resistance to erosion.

The outcrop shown in Figure 2B illustrates the complexity of the identification of the main structural trends on limited exposures. We considered that the most regionally significant structural trend of the breccia bodies is given by the thicker (>10 cm) veins and breccias, because where they are visible, minor quartz veins are more randomly oriented or give a mean statistical value that is different between two (2) nearby drill holes. By plotting the orientations of thick veins we infer the true orientation of the quartz breccia (Figure 2E), which was revealed to be consistent with the major fault trends in map view (Figure 1D). The QB usually displays a consistent high angle dip, reflecting the orientation of the main fault trend: N30, dip to the NW at Contact, N175, dip to the W at Bong, N50 and N90, dip to the NW and to the S, respectively, at End (Figure 2E). Even though the majority of minor quartz veins display throughout the Kiggavik area a steep dip (60–90°), a significant amount of veins (Figure 2F) shows relatively shallow dip angles (<30°).

Figure 3 summarizes the data collected on drill holes at the Contact prospect (Figure 3A). The QB bodies usually display two main distinct zones, an outer zone and an inner (core) zone. The outer zone (blue in Figure 3B) is represented by a dense to scarce network of millimeter to centimeter-thick quartz veins, while the inner (core) zone (red in Figure 3B) is represented by thick (>10 cm thick) quartz veins and a dense quartz vein network, where angular clasts of the fragmented host rock are barely observable. Several QB core zones were crosscut by drill holes (Cont-24, Cont-16, Cont-06). These core zones are discontinuous from the SW to the NE. They are tapering toward their ends (Figure 3C) both laterally (for example, between Cont-26 and Cont-25, Figure 3B), and vertically (for example, between Cont-10 and Cont-11, Figure 3B). This supports that they have elliptical shapes, connected by quartz vein networks. This observation explains the important changes in thickness of the QB between two nearby drill holes (e.g., Cont-06 and Cont-13).

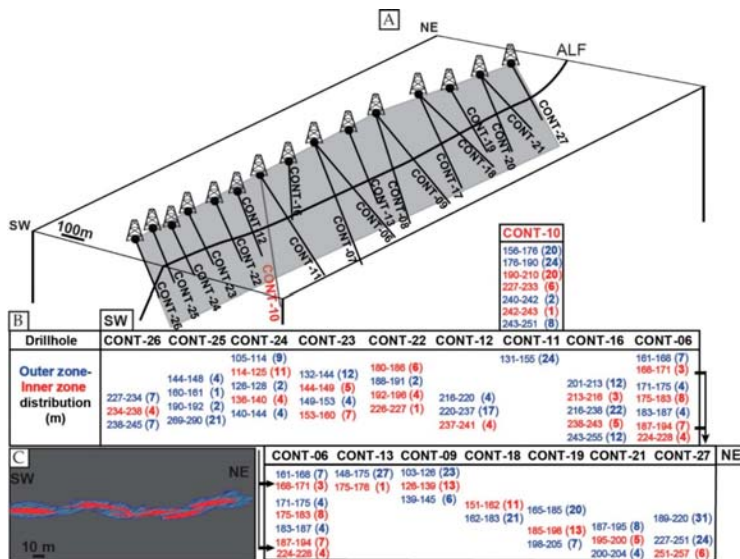


Figure 3. Organisation of inner (core) and outer zones of the quartz breccia (QB) crosscut in drillholes at Contact. (A) Plan view of the drill holes; (B) lateral variation in thickness of QB inner (core) and outer zones; and (C) simplified interpretative drawing of the QB intersected in drill holes (grey plane).

One observation not highlighted by previous studies in the Kiggavik area is the presence of a large (20–100 m) brittle fault zone predating emplacement of the QB but systematically spatially associated with it. Macroscopically, the QB consists of thin to massive quartz veins as described in Figure 2; however, our detailed observations document numerous quartz healing events crosscutting clay-altered cataclastic to ultra-cataclastic fault rocks that are now silicified and “preserved”. Clasts are monomictic, sub-rounded, millimetric to centimetric in size and clay altered, embedded in a light red to brown matrix (Figure 4A,B).



**Figure 4.** (A) Pervasively silicified cataclastic fault rock; (B) same as (A), crosscut by a white quartz vein of the QB; (C) pervasively silicified fault zone crosscut by late fracturing and clay alteration event (End deposit); and (D) typical intersection of the QB displaying deep purple hematized rock, massive and minor white quartz veins. Jigsaw textures are locally observable (e.g., at 189 m, yellow arrow; Contact prospect).

The quartz veins of the QB were observed in several locations as cutting across the cataclasites (Figure 4B). These early cataclastic fault rocks therefore predate the QB; they could be related to extensional to trans-tensional faulting during formation of the Baker Lake Basin [31]. This early,

now silicified fault zones and the QB are spatially associated, indicating that the pervasive silicification likely occurred at the onset of emplacement of the QB. However, even though the pervasive silicification of the fault zone is spatially and likely roughly temporally associated with the QB, we differentiate hereafter these two features: The silicified fault zone on one hand and the QB that results from brecciation sealed by quartz on the other hand.

Both features display different thicknesses: In Figure 4C, the pervasively silicified fault zone with its light reddish color is observable along 40 m of drill core and is cut by numerous small quartz veins and a 4 m thick core zone of the QB. A late faulting and white clay alteration pattern is observed at depth 389–395 m (Figure 4C, post ore faulting f7). In Figure 4D, the silicified fault zone is observed along 5 m of drill core and is cut by 23 m of QB.

The pre-QB silicified fault zone displays evidence of multiple events of tectonic brecciation and comminution. In the sample observed at micro-scale under transmitted light (Figure 5A), three generations of cataclastic fault rocks are observed, with each generation of cataclasis consuming the previous one. They are crosscut by at least three generations of quartz veins, building a complex pattern (Figure 5B,C). Minerals from the original host rock (psammo-pelitic gneiss with quartz, apatite, illite, muscovite, pyrite) are preserved in the first generation of clasts (pink, Figure 5B). A closer look at the cataclastic fault rocks reveals that the different cements are made of micro-crystalline quartz and white micas (Figure 5D,E). The superimposition of multiple generations of cataclasites indicates that the localized zone of deformation was repeatedly reactivated during progressive deformation.

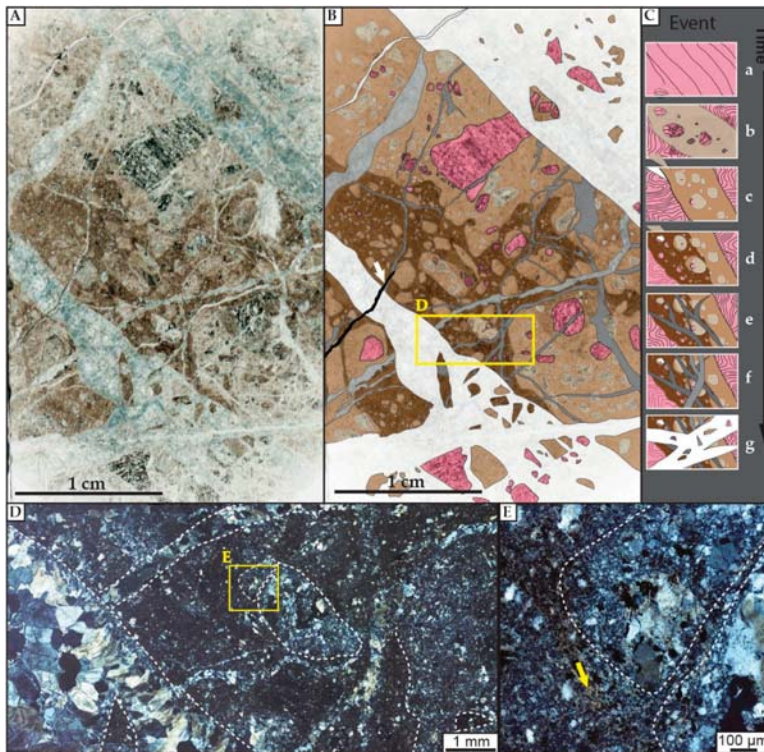


**Figure 5.** (A,B) Thin section of a polyphase cataclastic fault rock crosscut by several generations of quartz veins of the QB. White arrow indicates a late microcrystalline quartz veinlet; (C) simplified chronology of the events; (D) zoom on the different generations of clasts; and (E) matrix of the latest cataclastic event displaying white micas and micro-crystalline quartz.

In order to better understand and characterize the influence of silicification on fluid circulation, we selected porosity data measured in the field for four types of rocks: Fresh host rock (granitic gneiss, before fracturing and alteration), silicified type 1 (pervasively silicified fault zone), silicified type 2 (typical white QB), and clay-altered/fractured samples. Results are presented in Figure 6. Fresh granitic gneiss yields the lowest porosity values, <2%. Fault rock and samples displaying quartz brecciation and pervasive silicification yield values slightly higher but <5%. Fractured and clay altered fault rock display much higher values, up to 40%. Cataclastic fault rocks formed before the QB should have displayed a high porosity, but after pervasive silicification they have a porosity comparable to fresh rock (Figure 6), unlike strongly clay altered and fractured samples (Figure 6).

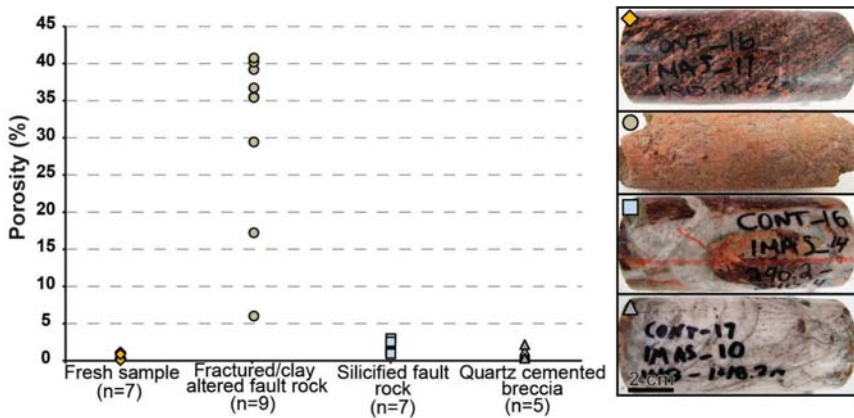


**Figure 6.** Porosity measured for fresh samples (granitic gneiss from the Contact prospect), pervasively silicified cataclastic fault rock, thick quartz veins within granitic gneiss, and clay-altered, fractured host rock (examples for each category are displayed on the right of the chart).

#### 4.2. Microscopic-Scale Characteristics of the QB

Microscopic observations indicate that the pervasive hematization spatially associated with the QB is defined by disseminated micro-grains of hematite (aggregates of micrometric grains) and specular hematite (Figure 7A; specular hematite being less common in samples compared to hematite); possibly observed in banded veins synchronous with microcrystalline quartz (Figure 7B). Subhedral specular hematite (~100–200 μm) is observed filling quartz vugs and disseminated in the host rock. Where present, the specular hematite is responsible for the dark-red to purplish color of the oxidized host rock. Anhedronal magnetite (50–100 μm) was locally observed as being mixed with (likely replaced by) hematite (Figure 7B) in banded quartz veins and likely represents changes in the oxidation state of the fluid. These observations, along with the spatial association of iron oxidation and quartz brecciation, support the overall synchronicity of the two phenomena. However, the precise timing of the oxidation, within the several episodes of silicification, remains unconstrained.

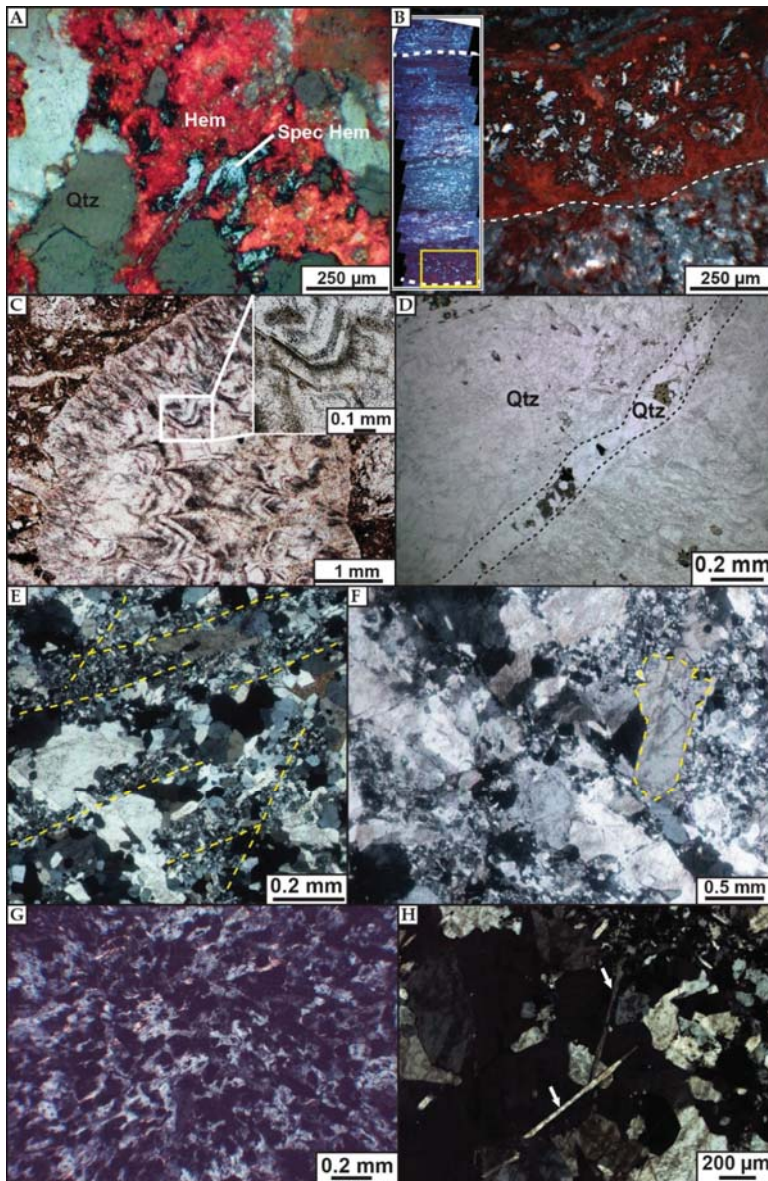


**Figure 7.** Optical microscope microphotograph (OM): (A) Disseminated hematite (Hem) and specular hematite (Spec Hem). Qtz: Quartz; (B) banded microcrystalline quartz (Qtz) with synchronous anhedral hematite and magnetite; (C) euhedral quartz crystals and arrays of dense monophasic fluid inclusions (vapor rich); (D) euhedral clear quartz cement a fracture that crosscuts previous quartz generations; (E) trends of microcrystalline quartz (yellow); (F) comb quartz grains (example in yellow) engulfed in a fine-grained quartz matrix; (G) moss quartz texture; and (H) bladed lattice calcite (white arrow) replaced by quartz.

Microscopic observations also document a variety of quartz textures (Figure 7C–F for example), mutually crosscutting each other, and defining different conditions of quartz precipitation. The two most common types of quartz are: Euhedral quartz (comb quartz, ~200  $\mu\text{m}$  in size) and microcrystalline quartz (~<50  $\mu\text{m}$ ). Two generations of euhedral white quartz can be distinguished: One (millimetric quartz) being characterized by dense arrays of monophase fluid inclusions (vapor rich), usually at the tip of the quartz crystal (Figure 7C); and the second, clearer, nearly fluid inclusions-free, usually observed as a late quartz generation (~100  $\mu\text{m}$ , Figure 7D). In addition to the banded microcrystalline quartz-hematite texture, microcrystalline quartz is also observed filling vugs, and as conjugate “trends” (Figure 7E) in subhedral quartz veins. In other samples, subhedral quartz can be found as clasts in a microcrystalline quartz mass (Figure 7F). In term of quartz texture, comb quartz, microcrystalline quartz and “moss” textures were observed (Figure 7G). Additionally, rare recrystallized bladed calcite were found (Figure 7H).

Quartz observed under cathodoluminescence display weak luminescence intensity, with a 20 s exposure time required in order to get enough signal for imaging. The most recurrent color observed under cathodoluminescence is a deep blue observed for microcrystalline quartz veins, sometimes synchronous with hematite (Figure 8A), and quartz cementing microbreccias. The fluid inclusion (FI)-rich euhedral quartz crystals exhibit alternating growth zones of brown and blue luminescence (oscillatory growth-zoning, Figure 8B). Clasts of euhedral quartz crystals are found within a blue luminescent quartz matrix (Figure 8C). The brown luminescence is also observed in breccias where the quartz has likely completely recrystallized, leaving the breccia texture only observable under cathodoluminescence; the “cement” of the breccia displays a brown luminescence (Figure 8D). These colors characterize the main generations of quartz in the QB.

The luminescence of the latest generation of quartz (i.e., euhedral quartz filling vugs and open fractures), is dark blue with rare concentric zoning. It also displays greenish luminescence associated with primary to pseudo-secondary fluid inclusions (Figure 8E). In terms of spatial occurrence of this quartz generation, it is more frequently observed in the vicinity of the QB than in its inner zone.

Quartz which was formerly in contact with uranium minerals displays a characteristic luminescence: Red/pink close to uranium-bearing minerals and yellow/greenish further from the uranium-bearing mineral (Figure 8F). This is especially well observed in quartz veins that were later microfractured as described by Grare et al. [31] and in quartz of the host rock (when not dissolved by circulation of the uranium-bearing fluid). This peculiar luminescence is brighter than the original luminescence of the quartz and displays a nearly uniform circular shape of 35–45  $\mu\text{m}$  width (Figure 8F). The latest quartz generation, which fills vugs and open fractures, is characterized by dark blue luminescence with rare concentric zoning. This generation is observed more in the vicinity of the QB.



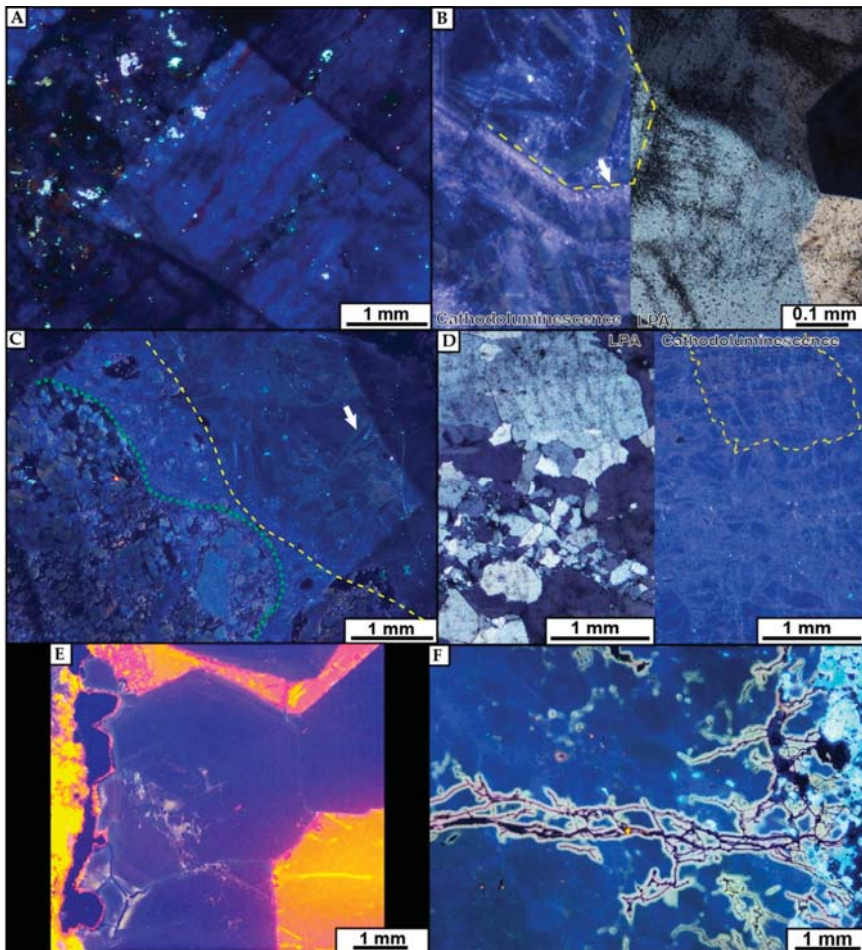


**Figure 8.** Cathodoluminescence microphotograph (CM): (A) Deep blue luminescent microcrystalline quartz and red luminescent hematite in banded vein; (B) fracture cemented with euhedral quartz (blue-brown luminescence in concentric zoning, yellow dotted line) and arrays of purplish FIs (white arrow); (C) quartz breccia (green) cemented by subhedral, sub-millimetric blue-purple quartz, crosscut by dark blue luminescent subhedral millimetric quartz vein (yellow), the white arrow highlight brown-luminescent overgrowth; (D) OM and CM of the same zone: Subhedral and microcrystalline quartz (blue luminescence) displaying microbrecciation/recrystallization (brown luminescence). Yellow dashed line outlines a quartz crystal; (E) dark blue luminescent euhedral syntaxial quartz. The boundary of the fracture on the left is lined with U-oxides (black) and calcite (orange); and (F) quartz vein orthogonally crosscut by a microfracture and cemented with pitchblende. The boundaries of the microfractures display a “buffer area” where the luminescence of the quartz is modified, from pink to yellow.

### 4.3. Geochemical Signature of Quartz

#### 4.3.1. Trace Element Concentrations

Concentrations of selected elements were measured with LA-ICP-MS for the three main quartz generations (identified through microscopic texture and luminescence color): Deep blue microcrystalline quartz, blue euhedral quartz with brown concentric zoning, late dark blue euhedral vuggy quartz. Results are presented in Figure 9A for Li, K, and Ba; in Figure 9B for Zr, Ti, and B; in Figure 9C for Mg, Na, Al, Fe, and Ca. Several elements we tried to measure show values below the limit of detection and thus are not displayed here.

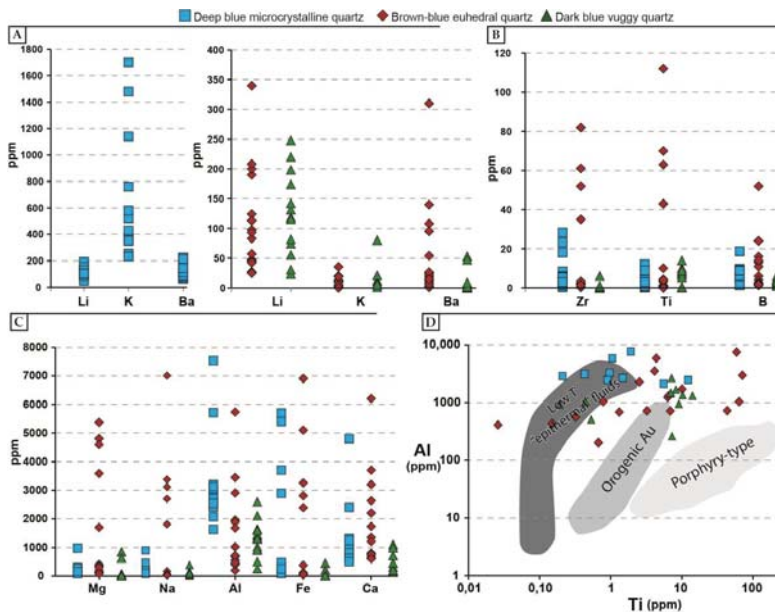


**Figure 9.** Concentration of trace elements measured in quartz through LA-ICP-MS, for main quartz generations: (A) Li, K, and Ba; (B) Zr, Ti, and B; (C) Mg, Na, Al, Fe, and Ca; and (D) Al vs. Ti concentrations of main quartz generation. Zones correspond to values of hydrothermal quartz from low T °C, orogenic Au, and porphyry-type deposits [60].

In some analyses, trace elements display extreme values above 10,000 ppm (e.g., Al or Mg, Figure 9) which likely represent analysis of undetected solid inclusions, hence are not displayed in Figure 9. The high Fe content in both the deep blue microcrystalline and brown-blue euhedral quartz could reflect the analysis of micro-inclusions of iron oxides, related to the pervasive hematization synchronous with the QB event. Microcrystalline quartz in banded veins associated with iron oxides shows a small range of values for all elements except for K and Fe. Brown-blue euhedral quartz displays bimodal concentrations for most of the elements consistent with observed concentric zoning. For all quartz generations, Li, K, and Na are positively correlated with Al. Dark blue vuggy quartz usually display a small range of values for most elements compared to other quartz generation, except for Li (23–248 ppm) and Al (255–2593 ppm).

Li contents are homogeneous between the three quartz generations and are below 250 ppm. Such values correlate positively with Al concentrations, Li balancing the replacement of Si by Al [61]. K is enriched in deep blue microcrystalline quartz with values up to 1700 ppm, compared to

concentrations below 100 ppm in the case of the two other quartz generations. Fe yields high values (up to 7000 ppm) in the case of the two quartz generations of the QB (deep blue microcrystalline and brown-blue euhedral quartz). B displays concentrations below 20 ppm except for 2 analysis. Concentrations in B are lower in the case of post-QB dark blue vuggy quartz.

Deep blue microcrystalline and dark blue vuggy quartz yield low values of Ti (<20 ppm for most measurements). Bi-modal concentrations of Ti were measured for brown-blue euhedral quartz, with one group of values below 20 ppm and the other above 40 ppm.

#### 4.3.2. Oxygen Isotope Values

Oxygen isotopes were measured in the main quartz generations while paying attention to variations in luminescence, for instance for quartz displaying concentric zoning. Results are shown in Table 1.  $\delta^{18}\text{O}_{\text{quartz}}$  values are relatively homogeneous within one quartz generation (maximum variation of 5‰) and are independent of Cathodoluminescence (CL) color variations except for dark blue vuggy quartz: Zones of this quartz close to fluid inclusions display a green luminescence with higher  $\delta^{18}\text{O}_{\text{quartz}}$ .

The different quartz generation display different ranges of  $\delta^{18}\text{O}_{\text{quartz}}$ , with values ranging between +12‰ and +14‰ for microcrystalline quartz with hematite, between +7.5‰ and +9.3‰ for brown blue quartz and between +14.4‰ and +15.5‰ for druzy/vug-filling quartz. These ranges show two exceptions: Vug-filling euhedral quartz displaying green luminescence with higher isotopic values (from +16.2‰ to +21.9‰) in zones close to fluid inclusions (Figure 7C), and a microcrystalline quartz vein crosscutting the one cemented with microcrystalline quartz and iron-oxides exhibiting much higher isotopic values (from +18.8‰ to +23.9‰).

$\delta^{18}\text{O}_{\text{quartz}}$  values between the two main generations of quartz in the QB are different with an average of +12.9‰ for banded microcrystalline quartz and +8.4‰ for zoned euhedral quartz.

**Table 1.**  $\delta^{18}\text{O}_{\text{quartz}}$  measured in main quartz generations and calculated values of  $\delta^{18}\text{O}_{\text{fluid}}$ . To calculate  $\delta^{18}\text{O}_{\text{fluid}}$ , an average temperature of 250 °C was used for quartz generations of the QB (lines 1–3 of the table), while an average temperature of 150 °C was used for late druzy quartz (lines 4–5).

Quartz Type	CL Luminescence Color	$\delta^{18}\text{O}_{\text{quartz}}$	Avg.	n	$\delta^{18}\text{O}_{\text{fluid}}$	Avg.
Banded microcrystalline quartz (alternated with iron oxides)	Deep blue	12.0–14.0	12.9	14	2.4–5.3	3.9
Euhedral quartz with concentric zoning	Alternating blue and brown luminescence	7.5–9.3	8.4	18	−1.6–0.3	−0.6
“Late” microcrystalline quartz	Deep blue	18.8–23.9	22.1	10	11.5–14.8	12.4
Vuggy quartz	Dark blue	14.4–15.5	14.9	29	−5.3–2.5	−3.3
Quartz alteration associated with fluid inclusions	Green	16.2–22.0	17.8	5	−2.5–3.8	−0.3

$\delta^{18}\text{O}_{\text{quartz}}$  and temperatures measured by fluid inclusion microthermometry in quartz veins in the area [26,29,62] were used to calculate the  $\delta^{18}\text{O}_{\text{fluid}}$  following the equation of Clayton et al. [63], set for measuring oxygen isotope exchange between quartz and water (assuming that the fluid was in equilibrium with the quartz at the temperature of mineralisation). We considered homogenisation temperatures in the range of 200–300 °C, avg. 250 °C (i.e., the range of temperatures revealed by low salinity fluid inclusions), to be representative for the quartz generations of the QB and of 100–200 °C, avg. 150 °C (i.e., the range of temperature revealed by high salinity fluid inclusions), to be representative for late druzy quartz probably precipitating from basinal brines [29]. However, a microthermometric study on primary fluid inclusions for each quartz generation is missing actually and would give a more accurate calculation of fluid isotopic values. Results are displayed in Table 1. The  $\delta^{18}\text{O}_{\text{fluid}}$  value range from 2.4‰ to 5.3‰ (+3.9‰ on average) for microcrystalline quartz associated with hematite. In contrast, late veinlets of micro-crystalline quartz display a much higher  $\delta^{18}\text{O}_{\text{fluid}}$  value: Between +11.5‰ and +14.8‰ (+12.4‰ on average). Brown-blue quartz precipitated from a fluid with a lighter  $\delta^{18}\text{O}_{\text{fluid}}$  value comprised between −1.6‰ and +0.3‰ (−0.6‰

on average). Late vug-filling euhedral quartz yield lighter isotopic values from  $-5.3\text{‰}$  to  $-3.3\text{‰}$  ( $-3.3\text{‰}$  on average).

## 5. Interpretation of Results and Discussion

### 5.1. Origin and Nature of Silicifying Fluids

Although relations between most quartz trace elements and the conditions of quartz formation are not direct, recent studies suggest that the quartz trace element composition may be influenced by the rate of crystallization [64], pressure, temperature [65], and fluid composition [66,67]. Nevertheless, it has been shown that—like CL textures, colors and intensity—the concentrations of trace elements vary systematically among ore deposit types [67], and thus can be used to fingerprint the type of ore deposits. Combined with oxygen isotope signature, trace elements of quartz generations can be used to constrain the origin and nature of the fluids responsible for the formation of the QB.

Quartz analyses yield low but detectable ( $<20$  ppm) values of Ti except for quartz with concentric zoning ( $>40$  ppm). Additionally, all the quartz observed under cathodoluminescence display a weak luminescence. Several authors showed that Ti content in quartz is positively correlated with the fluid temperature and also with CL intensities [67–69], while Al is anti-correlated with CL intensity in most of low temperature deposits (e.g., [70]). Such Ti-T °C relationship can be used to directly estimate the temperature of the fluid in some specific case (i.e., the TitaniQ thermobarometer [71]).

Ti values for the QB indicate an overall temperature of formation below  $350$  °C [67], a value consistent with temperatures obtained from fluid inclusion microthermometric studies at the End and Andrew Lake deposit [26–29]. Concentric zoning with low and high Ti values ( $>40$  ppm, characterizing higher temperature) could reflect cyclic episodes of circulation of  $>350$  °C fluids, which would agree with concentric zoning and with the occurrence of dense trends of monophasic vapor rich FIs at the tip of some growth zones (Figure 7B). Associated with the bi-modal concentration of Al [67], these observations support precipitation of quartz from a low temperature ( $<\sim 350$  °C) fluids, mixing cyclically with high temperature ( $>\sim 350$  °C) fluids.

The  $\delta^{18}\text{O}_{\text{fluid}}$  value of  $+3.9\text{‰}$  in average for microcrystalline quartz associated with hematite points toward a magmatic origin ( $+5.5$  to  $+10\text{‰}$ , although this may vary for a particular intrusion) for the high temperature fluids [72,73]. This is consistent with the presence of the KIS at the presumable time of emplacement of the QB (ca. 1750 Ma [46]). Moreover, oxygen isotopic values for the main quartz generations of the QB are comparable to those obtained for quartz veins at the nearby Mallery lake epithermal (low-sulfidation) deposit by Turner et al. [62]. The Mallery lake deposit displays similar quartz brecciation formed at the time of emplacement of the KIS (ca. 1.75 Ga). In contrast, brown-blue quartz precipitated from a fluid with a lighter  $\delta^{18}\text{O}_{\text{fluid}}$  value of  $-0.62\text{‰}$  in average, which could represent mixing between the magmatic derived fluids and a meteoric fluid: The  $\delta^{18}\text{O}_{\text{fluid}}$  value of meteoric fluids at the latitude of the Kiggavik area at this time would have been  $\sim -13\text{‰}$  [74]. Such interpretation is consistent with the bi-modal distribution of Ti concentrations for this quartz generation but also with the differences in concentrations for different trace elements between the two quartz within the QB. This phenomenon is more easily explained by a fluid mixing rather by changes in temperature for a same fluid (which could explained only the difference in  $\delta^{18}\text{O}$  values). The two quartz generations have clearly different  $\delta^{18}\text{O}$  values as the internal precision of the SIMS measurements is  $<0.1\text{‰}$ . The observation of hematite surrounding magnetite in some microcrystalline banded vein further supports an input of fluids with different redox signatures in the system.

Higher values of  $\delta^{18}\text{O}_{\text{fluid}}$  ( $\sim 12.9\text{‰}$ ) for microcrystalline quartz (another generation within the same sample) could suggest a stronger input of magmatic fluids, which is however unsupported by Ti values for this quartz generation. This apparent discrepancy could be explained by cooling of the fluid before quartz precipitation. Contrasting  $\delta^{18}\text{O}_{\text{fluid}}$  values between similar quartz generation in the same samples (2 generations of microcrystalline quartz, deciphered on the basis of  $\delta^{18}\text{O}_{\text{fluid}}$ ) could

be explained by a local effect of rock buffering within breccia cavity. As a result, veinlets would have formed from an isotopically isolated fluid reservoir, thus yielding higher  $\delta^{18}\text{O}_{\text{quartz}}$  values.

Cathodoluminescence observations support the above interpretations, as blue-purple quartz luminescence is commonly found in quartz precipitated in magmatic/hydrothermal environments [75] while brown luminescence is rather observed in sedimentary-diagenetic (i.e., lower temperature) environments [76]).

The very low B content of the post-QB dark blue vuggy quartz could be explained by co-crystallization of other minerals enriched in B in the uranium deposits of the Kiggavik area; such as magnesiofoitite (dravite), which is commonly observed in environments seeing brine circulations [77]. Accordingly, the isotopic values for vug-filling euhedral quartz (post-QB) are consistent with those obtained for quartz precipitated from relatively low temperature ( $\sim 150\text{ }^{\circ}\text{C}$ ) brines in the Proterozoic Athabasca [78] and Komolgie basins [79,80] and linked to the formation of U deposits. Considering that the QB predates the formation of the Thelon Basin, from which brines are likely derived, this supports that brines circulated after the emplacement of the QB, in agreement with the findings of Grare et al. [31]. In the Kiggavik area, the fluid inclusion studies by Pagel [26] on the hydrothermal quartz, at Andrew Lake, and by Chi et al. [29] on the hydrothermal quartz, at End, are in agreement with our observations. Indeed, these authors documented low temperature ( $100\text{--}200\text{ }^{\circ}\text{C}$ )-high salinity (25–38 wt % NaCl) fluids, low temperature ( $150\text{--}200\text{ }^{\circ}\text{C}$ )-low salinity ( $<9$  wt % NaCl) fluids, and high temperature ( $200\text{--}300\text{ }^{\circ}\text{C}$ )-low salinity ( $<9$  wt % NaCl) fluids within the QB. Our study indicates that low-T  $^{\circ}\text{C}$ /high salinity fluids (brines) circulated after formation of the QB, while the high-T  $^{\circ}\text{C}$ /low salinity fluids are more characteristic of the QB that formed earlier in the history of the Kiggavik area.

Using data from several deposits type, it has been shown that deposits linked to low (Mississippi Valley type, Carlin, Epithermal) and high (porphyry Cu-Au) fluid temperatures can be distinguished one from another based on Al and Ti concentrations in quartz associated with orebodies [60]. Figure 9D plots Al-Ti concentrations for the main quartz generations in our study. The epithermal domain of Figure 9D was built after data from low temperature ( $\sim 100\text{--}350\text{ }^{\circ}\text{C}$ ) hydrothermal fluids. The distribution is scattered even within one quartz generation (e.g., deep blue microcrystalline). Primary (comb quartz) and secondary (“moss” quartz) textures [81,82] indicate primary quartz deposition and recrystallization. Bobis [83] also attributed the rounded shapes of the moss texture to recrystallisation of silica gel, which preserved the original structure and impurities of the silicate phase. These quartz textures, along with recrystallized bladed calcite, also characterize phases of silica precipitation by boiling and non-boiling hydrothermal fluids in a geothermal/epithermal system [84]. Some textures observed within the QB are typical of epithermal deposits, but they are rare. Commonly encountered precious metals (e.g., Au, Ag) are lacking within the breccia even though they were observed at the nearby Mallery Lake deposit [62]. However, such environment of formation is consistent with the geochemical signature of quartz in the QB and is much more plausible for the formation of the QB than orogenic Au and porphyric deposits.

To sum up, even though it is difficult to be truly conclusive with the measured trace elements concentrations only, the combination of these data with oxygen isotope values and quartz textures points toward a scenario in which high (magmatic-derived) and low (meteoric-derived) temperature fluids interacted and mixed during silicification of the fault zone that led to the formation of the QB. The important volumes of Si would have been provided by intrusive bodies of the KIS emplaced at depth and related to the rift-related extensional tectonics that occurred at ca. 1750 Ma (Figure 10).

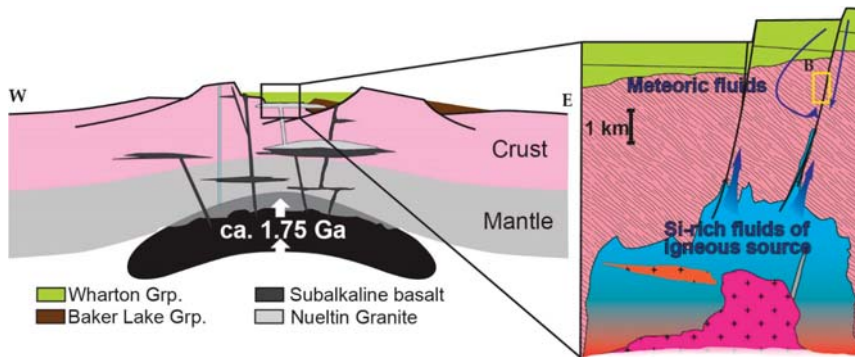


Figure 10. Cross-section after Peterson et al. [46] and zoom in the zone of formation of the QB.

### 5.2. Fault Zone Processes Leading to the Formation of the QB: Cataclasis, Silicification and Hydraulic Brecciation

Macroscopic observations of the QB and petrographic and textural observations on quartz, although lacking a simple and clear chronology of events, provide additional constraints on the processes behind its formation. Before emplacement of quartz cemented veins and breccias, the superimposition of multiple generations of cataclasites indicates that a localized zone of deformation was repeatedly reactivated during progressive deformation. The presence of microcrystalline quartz in clasts generated before emplacement of quartz veins show that the pervasive silicification of the fault zone was a syn-tectonic process. Regarding quartz-cemented fractures, the common macroscopic textural observation of quartz cemented breccia with angular fragments and jigsaw pattern indicates hydraulic brecciation [14] of the host rock. The pervasive silicification of the fault zone was a first step (Figure 11A,B) before emplacement of the quartz veins and breccias of the QB: It likely triggered fluid pressure build up in the fault zone leading to hydraulic brecciation of the host rock, hence to the “building” of the so-called QB.

The complex patchwork of quartz textures observed under optical microscope shows a still more complex pattern under cathodoluminescence, but highlights several events of quartz fracturing (reworked quartz clasts) and recrystallization. The white quartz mass which displays fine-grained subhedral quartz crystals also shows in some locations numerous fragments of earlier aggregates. The conjugate trends of microcrystalline quartz likely reflect shearing in the quartz mass and synchronous quartz recrystallization. A better evidence for such fracturing and synchronous quartz crystallization is provided by white quartz veins in which euhedral quartz grains are surrounded by microcrystalline quartz and other quartz of heterogeneous sizes (Figure 7F). We interpret this as cataclasis and tectonic comminution (i.e., fracture propagation and wear abrasion) of previously formed quartz mass and recrystallization of quartz (i.e., syn-tectonic). This process differs from the formation of sub-horizontal quartz veins and hydraulic breccias related to transient fluid overpressurization followed by fluid pressure drop and quartz precipitation [21].

To summarize, textures and crosscutting relationships of quartz cements reveal the following sequence of events: (1) Episodes of brittle faulting and cataclasis, before silicification and quartz-brecciation; (2) pervasive silicification of the fault zones (beginning of the QB event); and (3) episodes of brittle fracturing synchronous with the circulation of silica-rich fluids (QB event). During this last event, there were stages of hydrothermal hydraulic brecciation with slow and rapid silica precipitation in relation to boiling of magmatic and/or meteoric fluids (trace elements and  $\delta^{18}\text{O}$  data inconclusive). This boiling process is supported by the monophasic fluid inclusions within the quartz generations of the QB. The presence of 100% of monophasic vapor inclusions can be only explained by a boiling process, affecting either magmatic fluids (with a spatial separation between

vapor and brines) or meteoric fluids heated due to emplacement of a magmatic intrusion at low depth at ca. 1750 Ma. Boiling process can be marked in other geological environments by the presence of monophasic vapor fluid inclusions spatially associated with multiphase and of relatively high-salinity brines due to demixion of the magmatic fluids. The absence of two-phase fluid inclusion in the observed samples of the QB could indicate that the vapor migrated farther than the magmatic brines. The hydraulic brecciation alternated with stages of fluid-assisted cataclasis and quartz recrystallization (Figure 11A). Arrays of monophasic fluid inclusions (vapor-rich) also indicate abrupt pressure drops following rupture of the “seal” of the system [78]. The so-called QB therefore appears to be a composite structural feature much more complex than previously thought, which consists of a mass of quartz emplaced by alternating quartz healed hydraulic brecciation and tectonic-induced cataclasis with synchronous quartz recrystallization during fault zone reactivation.

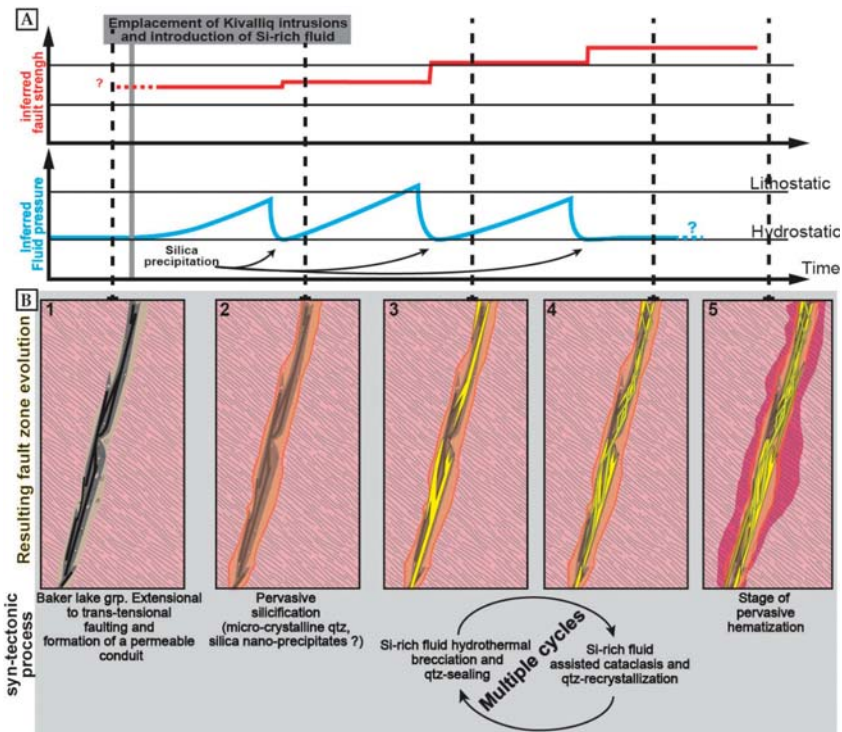


**Figure 11.** (A) Evolution of inferred fault strength (frictional shear resistance) and fluid pressure in the fault zone as a response of fluid pulse, fracturing and silica-precipitation. (B) Scheme depicting the succession of events that produced the QB.

Intense multi-episodic hydraulic brecciation of the early fault zone at the time of QB formation would have occurred during the interaction of two isotopically distinct fluids: Meteoric water, mixed with a magmatic-derived fluid. The processes of faulting/fracturing discussed in this section, that led to the formation of the QB, likely occurred at shallow depth (~2 km, [29]) and, looking at relative chronology and geochemical constraints, were likely initiated by the emplacement of the KIS (Figure 10). To a first glance, the fluid temperature of ~350 °C is not easy to reconcile with this shallow depth even if considering an abnormal thermal gradient related to the emplacement of the Kivalliq intrusions. We infer that hydrothermal fluids originated at a greater depth (about 5 km,

which may indicate a 70°/km geothermal gradient), and flowed upward sufficiently fast to prevent any significant cooling before they mixed with downward-moving meteoric fluids and precipitated the quartz generations of the QB in thermal disequilibrium with the hosting basement rocks. Interestingly, such a quartz cemented breccia and its complex spatial organization are similar to the meter-thick hydrothermal quartz breccia related to the emplacement of an igneous intrusion described by Tanner et al. [85] in Scotland.

We therefore propose a conceptual tectono-hydrological model for the QB formation involving mixing of deep silica-rich fluids of igneous origin with downward-moving meteoric fluids. The possible mechanisms allowing for such meteoric fluid downward flow in fault zones are either active seismic pumping or passive meteoric infiltration throughout a permeable fault zone. We favor a mechanism of syn-tectonic seismic pumping because beside the formation of quartz-filled fractures, the intrinsic low permeability of the unaltered basement rock surrounding the fault zone and the impermeabilization of the fault zone—including its damage zone—through multiple silicification events presumably make a simple, gravity-driven downflow of meteoric fluids difficult, hence unlikely. Fluid pressure built up at depth through the input of meteoric fluids and magmatic-derived fluids together with likely pore cementation of basement rocks (that decreased porosity). Fluid mixed and flowed upward to higher crustal levels along the fault zones which served as conduits (Figures 10 and 11). This upward flow likely occurred cyclically as the fluid pressure evolved between hydrostatic and supralithostatic (Figure 11A), depending, among other factors, on the sealing effectivity of the reactivated fault zone by quartz precipitation [86]. In turn, fluid pressure increased during the QB event also likely favored multiple reactivations of the high angle fault zone under the regional stress field.

### *5.3. Evolution of the Fault Zone Properties through Time and Structural Control on Later Uranium Mineralization*

The QB is found along many segments of the main fault (Figure 1C) trends, and uranium orebodies are systematically spatially associated with more or less thick bodies of QB along these fault zones. Even though a systematic study of QB thickness could not be undertaken throughout the area, the QB was observed as being usually thinner where it is not associated with uranium mineralization, which implies a possible control on later uranium mineralization by the thickness of the QB in fault zones.

Cataclastic fault rocks formed before the QB should have displayed an initial high porosity, but after pervasive silicification they likely ended with a low porosity comparable to that of the fresh basement rocks, unlike strongly clay altered and fractured samples (Figure 6). Since the evolution of the porosity can be to some extent directly linked to the evolution of permeability since it is controlled by fracturing and mineralogical destabilization/dissolution, we can safely infer that these multiple events of pervasive silicification, faulting/fracturing and quartz cementation caused the destruction of the porosity (hence of the permeability) and thus directly impacted the fluid circulation within the conduit.

At all deposits and prospects in Kiggavik, three main fracturing events postdate emplacement of the QB (two stages of faulting/fracturing and uranium mineralization and one stage of faulting and strong clay alteration [31]). The distribution of fractures and mineralization in some drill holes intersecting uranium orebodies in the vicinity of the QB is shown in Figure 12A for Contact, End, Bong and Andrew Lake. Post-QB fracturing and uranium mineralization are clearly restricted to the hanging wall of the QB in Contact, where the thickness of the breccia is far greater compared to the earlier silicified fault zone. At End, Andrew Lake and Bong, post-QB fracturing and uranium mineralization are observed in both the hanging wall and the footwall, but still not within the QB (inner zone). In the case of End, the QB displays lateral variations in thickness comparable—even less important—to what is observed at Contact. This distribution indicates that post-QB fracturing was preferentially localized in the hanging-wall and/or in the footwall of the QB, along its contact with the host rocks, while most of the QB (core zone) remained poorly fractured.



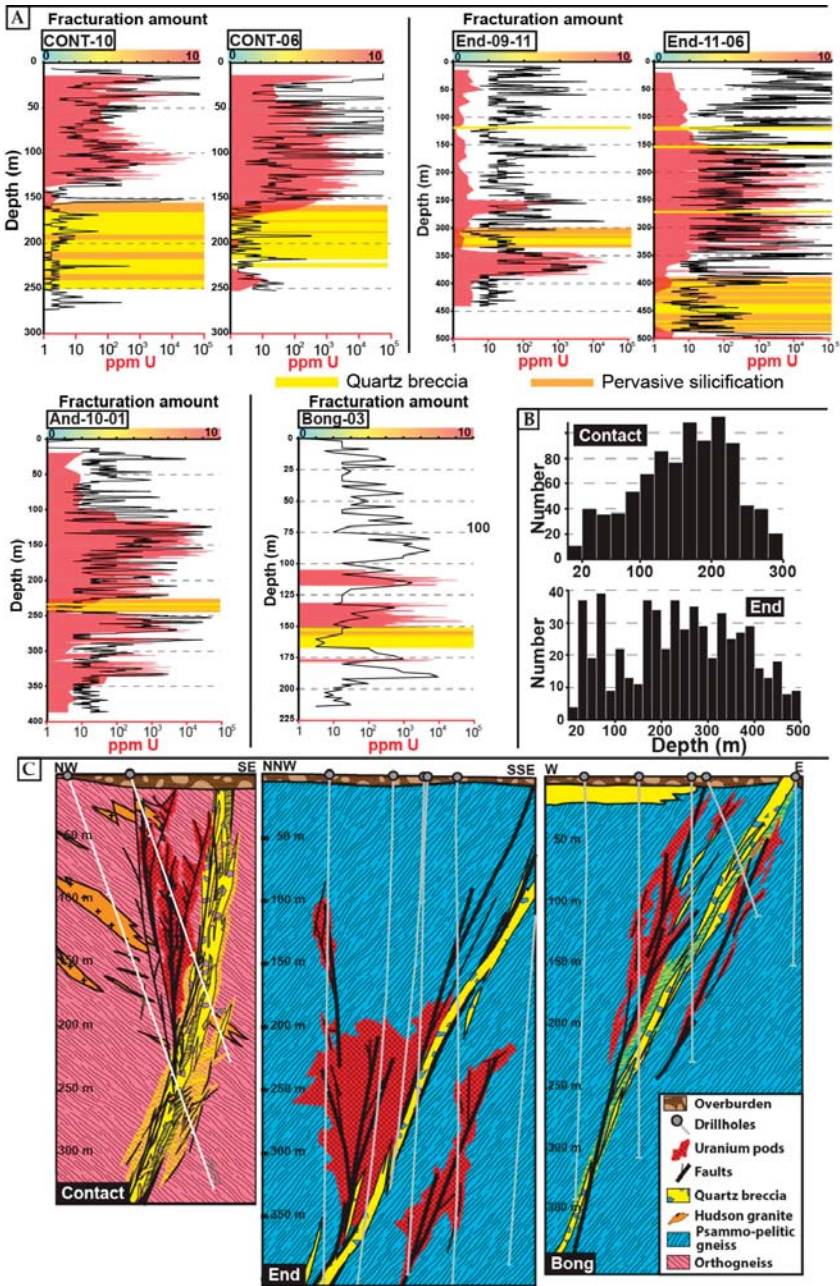


**Figure 12.** (A) Distribution of fracture density and uranium mineralization as a function of depth, for selected drillholes from Contact (Cont), End, Andrew Lake (And) and Bong. Fracture density as black lines; 0: Non-fractured drill-core, 10: Intensely fractured drill-core. Uranium mineralization in red: U in ppm measured by assays, logarithmic scale. (B) Number of quartz veins as a function of depth for Contact and End. (C) Simplified cross sections.

A significant amount of quartz veins (Figure 12B) were observed up to the top of drill holes, i.e., in the transition from the outer zone of the QB to the host rock. Such quartz veins are typically re-opened and were also used as pathways for uranium bearing fluids at the first stage of uranium mineralization [31]. Ore minerals are observed along the vein boundaries (Figure 13A) and cementing orthogonal microfractures (Figure 13B,C; see also Chi et al. [29]). Quartz with uranium-oxides in their vicinity display specific luminescence which has been described in many places worldwide [87–90]; it has been explained by the destabilization of the crystal lattice by radiation damages (due to liberation of alpha particles through  $U^{238}$  decay series).

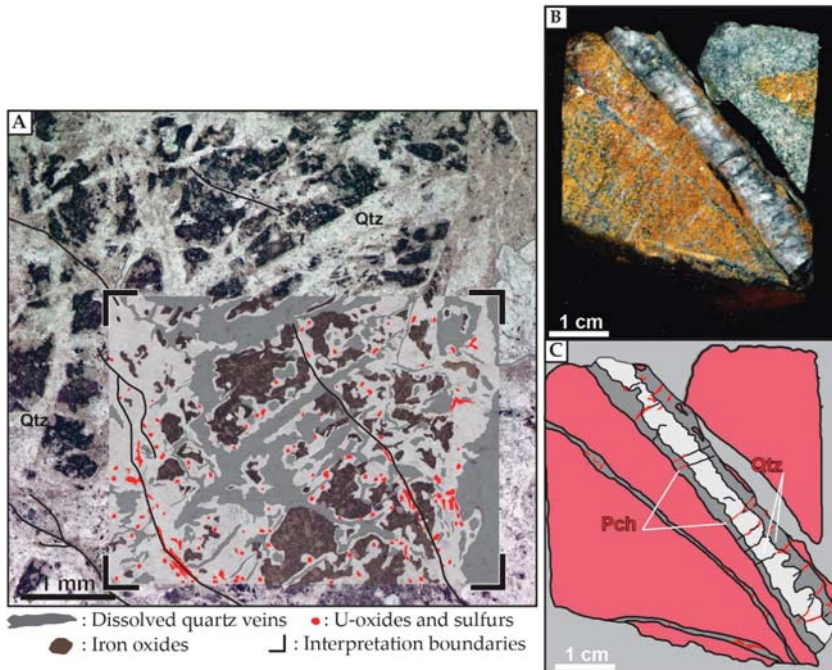


**Figure 13.** (A) Plane polarized light picture and interpretation drawing of a quartz vein network guiding the mineralizing fluid along its boundaries. Quartz and iron oxides display evidence for dissolution; (B,C) macroscopic drill core sample scan and interpretation drawing: Examples of a QB related quartz vein bearing pitchblende (Pch) along edges or in orthogonal microfractures.

This change of the luminescence, together with the fact that the micro-fractures cemented with uranium minerals crosscut several generations of quartz, show that formation of the QB and deposition of uranium bearing minerals are two distinctive events, supporting isotope data on dark blue vuggy quartz. Uranium minerals and associated specific luminescence are only observed in the vicinity of the QB. Vuggy quartz precipitated from basinal brines (potentially U-bearing; [29]) are observed mainly in the outer zone and in the vicinity of the QB and further demonstrate the barrier role played by the QB in fluid flow partitioning. These observations suggest that the QB behaved as a rigid and hard body compared to the weaker host rocks, so that later deformation preferentially localized in the host rocks along the contact with the strong QB body.

Quartz veins in the outer zone of the QB form a network that, when microfractured, helped focusing mineralizing fluid flow—thus creating local traps for uranium deposition. Post QB fractures located in its vicinity acted as preferential pathways parallel to the QB for later, uranium-rich brines, leading to deposition of uranium ore bodies at ca. 1500–1300 Ma for main stages [28–30]. To conclude,

the silicification processes ultimately led to the building of a complex quartz-cemented breccia body, up to tens of meters thick, acting as a transverse hydraulic barrier depending on the vertical and lateral variations in thickness and the degree of quartz cementation. As a result, the distribution of mineralization in the Kiggavik area was heavily controlled—at different scales—by the mechanical and hydraulic properties of the reactivated pre-existing fault zones where the QB was emplaced. The QB behaved as a mechanically strong, transverse hydraulic barrier, that localized later fracturing and compartmentalized/channelized vertical flow of uranium-bearing fluids, hence orebodies (Figure 12C) in its hanging-wall and/or footwall during fault zone reactivation.

Even if the 3D architecture is not perfectly constrained, and would deserve proper 3D geometrical and kinematic modelling, we could expect that relays within the QB, vertical and horizontal variations in thickness, and overlap between QB bodies would likely influence fluid flow properties (e.g., fluid velocity)—hence would impact uranium deposition rate [91]. The quartz breccia in the Kiggavik area seems to be a good example of the “physical seal” developed by McCuaig and Hronsky [92] in their mineral system concept, in conjunction with other factors to generate ore in a considered area.

## 6. Conclusions

Based on a structural analysis combined with vein cement petrography, trace elements, and oxygen stable isotope analysis of quartz, we constrain the nature, emplacement and significance of the QB which strongly controlled the location of uranium deposits in the Kiggavik area (Nunavut, Canada). The formation of the breccia bodies appears to be linked to fluctuations in pressure, temperature and compositions of fluids during tectonic reactivation of the fault zones along which the QB was emplaced. Faults formed during syn- to post-orogenic rifting processes and formation of the Baker Lake basin (ca. 1850–1750 Ma) were subsequently reactivated, and cycles of underwent pervasive silicification, hydraulic brecciation, and quartz recrystallization linked to cataclasis. This was associated with the circulation of meteoric-derived fluids mixing with Si-rich magmatic-derived fluids at depth. This is interpreted to be linked to the emplacement of the KIS at ca. 1750 Ma.

Post-QB fracturing at 1500–1300 Ma was constrained in the hanging wall and footwall of the QB, with flow of basin-derived brines being channeled along the fault zones where QB emplaced. The network of quartz veins in the vicinity of the QB was a favorable pathway for circulation of these uranium-rich fluids and related uranium precipitation, as they were re-opened and micro-fractured. Thus, the QB bodies likely exerted a major structural and hydrological control on the formation of significant uranium orebodies in the Kiggavik area. Beyond regional implications, this study demonstrates how an unconventional trap was built in impermeable Archean basement rocks. It also emphasizes the importance of the spatial organization, and long-term evolution of fault zones in the location of uranium orebodies of economic interest.

**Author Contributions:** A.G. and O.L. conceptualized both the study and the final model and wrote the original draft. J.M., A.B., A.T., P.L., J.R. reviewed and edited the draft. A.G. performed macro to micro-scale petrographic and microstructural characterization; A.G. and A.T. performed cathodoluminescence microscopy; A.G. and J.M. performed trace elements and isotopes analyses and their interpretation. P.L. and J.R. gave their validation. Funding acquisition and project administration were performed by A.B. and P.L., and geochemical analyses were funded by O.L. and J.M.

**Funding:** This research was funded by Orano Canada and the laboratory ISTEf.

**Acknowledgments:** The authors thank ORANO and ORANO Canada for the full financial support and access to the Kiggavik camp and exploration data. Special thanks to geologists R. Zerff, R. Hutchinson, K. Martin, and D. Hrabok for their help and enriching discussions during field work. The authors also want to acknowledge the first exploration geologists (Cogema and/or Orano) that worked on, and developed preliminary concepts on the quartz breccia in the Kiggavik area: D. Baudemont, N. Flotte, J.-L. Feybesse, J.-L. Lescuyer. The authors thank The SIMS team of the CRPG (Vandoeuvre-lès-Nancy, France) for their assistance in measuring the O isotopic composition of the quartz by SIMS. Special thanks to A. Pêtre for his thoughtful comments.

**Conflicts of Interest:** The authors declare no conflict of interest. The founding sponsors had no role in the design of the study; in the collection, analyses, or interpretation of data; in the writing of the manuscript, and in the decision to publish the results“.

## References

1. Sibson, R.H.; Robert, F.; Poulsen, K.H. High-angle reverse faults, fluid-pressure cycling, and mesothermal gold-quartz deposits. *Geology* **1988**, *16*, 551–555. [[CrossRef](#)]
2. Blundell, D.J.; Karnkowski, P.H.; Alderton, D.H.M.; Oszczepalski, S.; Kucha, H. Copper mineralization of the polish Kupferschiefer: A proposed basement fault-fracture system of fluid flow. *Econ. Geol.* **2003**, *98*, 1487–1495. [[CrossRef](#)]
3. Micklethwaite, S.; Cox, S.F. Fault-segment rupture, aftershock-zone fluid flow, and mineralization. *Geology* **2004**, *32*, 813–816. [[CrossRef](#)]
4. Cox, S.F. Coupling between deformation, fluid pressures, and fluid flow in ore-producing hydrothermal systems at depth in the crust. *Econ. Geol.* **2005**, *100th Anniv. Vol.*, 39–75. [[CrossRef](#)]
5. Muchez, P.; Heijlen, W.; Banks, D.; Blundell, D.; Boni, M.; Grandia, F. 7: Extensional tectonics and the timing and formation of basin-hosted deposits in Europe. *Ore Geol. Rev.* **2005**, *27*, 241–267. [[CrossRef](#)]
6. Micklethwaite, S.; Sheldon, H.A.; Baker, T. Active fault and shear processes and their implications for mineral deposit formation and discovery. *J. Struct. Geol.* **2010**, *32*, 151–165. [[CrossRef](#)]
7. Caine, J.S.; Evans, J.P.; Forster, C.B. Fault zone architecture and permeability structure. *Geology* **1996**, *24*, 1025–1028. [[CrossRef](#)]
8. McCuaig, T.; Kerrich, R. P-T-t-deformation-fluid characteristics of lode gold deposits: Evidence from alteration systematics. *Ore Geol. Rev.* **1998**, *12*, 381–453. [[CrossRef](#)]
9. Ridley, J.R.; Diamond, L. Fluid chemistry of orogenic lode gold deposits and implications for genetic models. *Rev. Econ. Geol.* **2000**, *13*, 141–162.
10. Kolb, J.; Rogers, A.; Meyer, F.M.; Vennemann, T.W. Development of fluid conduits in the auriferous shear zones of the Hutti Gold Mine, India: Evidence for spatially and temporally heterogeneous fluid flow. *Tectonophysics* **2004**, *378*, 65–84. [[CrossRef](#)]
11. Sibson, R. Earthquake rupturing as a mineralizing agent in hydrothermal systems. *Geology* **1987**, *15*, 701–704. [[CrossRef](#)]
12. Sibson, R.H. Fault rocks and fault mechanisms. *J. Geol. Soc. Lond.* **1977**, *133*, 191–213. [[CrossRef](#)]
13. Phillips, W.J. Hydraulic fracturing and mineralization. *J. Geol. Soc. Lond.* **1972**, *128*, 337–359. [[CrossRef](#)]
14. Jébrak, M. Hydrothermal breccias in vein-type ore deposits: A review of mechanisms, morphology and size distribution. *Ore Geol. Rev.* **1997**, *12*, 111–134. [[CrossRef](#)]
15. Laznicka, P. *Breccias and Coarse Fragmentites: Petrology, Environments, Associations, Ores*; Developments in Economic Geology Series; Elsevier Science & Technology Books: New York, NY, USA, 1988; ISBN 9780444412508.
16. Simmons, S.F.; White, N.C.; John, D. Geological characteristics of epithermal precious and base metal deposits. *Econ. Geol.* **2005**, *100*, 485–522.
17. Zhong, J.; Pirajno, F.; Chen, Y.-J. Epithermal deposits in South China: Geology, geochemistry, geochronology and tectonic setting. *Gondwana Res.* **2017**, *42*, 193–219. [[CrossRef](#)]
18. Goldfarb, R.; Christie, A.; Bierlein, F. The orogenic gold deposit model and New Zealand: Consistencies and anomalies. In Proceedings of the 2005 New Zealand Minerals Conference: Realising New Zealand’s Mineral Potential, Auckland, New Zealand, 13–16 November 2005; pp. 105–114.
19. Cannell, J.; Cooke, D.R.; Walshe, J.L.; Stein, H. Geology, mineralization, alteration, and structural evolution of the El Teniente Porphyry Cu-Mo Deposit. *Econ. Geol.* **2005**, *100*, 979–1003. [[CrossRef](#)]
20. Landtwing, M.R.; Furrer, C.; Redmond, P.B.; Pettke, T.; Guillong, M.; Heinrich, C.A. The Bingham Canyon Porphyry Cu-Mo-Au deposit. III. Zoned copper-gold ore deposition by magmatic vapor expansion. *Econ. Geol.* **2010**, *105*, 91–118. [[CrossRef](#)]
21. Henderson, I.H.C.; McCaig, A.M. Fluid pressure and salinity variations in shear zone-related veins, central Pyrenees, France: Implications for the fault-valve model. *Tectonophysics* **1996**, *262*, 321–348. [[CrossRef](#)]

22. Rusk, B.; Reed, M. Scanning electron microscope-cathodoluminescence analysis of quartz reveals complex growth histories in veins from the Butte porphyry copper deposit, Montana. *Geology* **2002**, *30*, 727–730. [CrossRef]
23. Tóth, J.; Corbet, T. Post-Palaeocene evolution of regional groundwater flow systems and their relation to petroleum accumulations, Taber Area, southern Alberta, Canada. *Geol. Soc. Lond. Spec. Publ.* **1987**, *34*, 45–77. [CrossRef]
24. Hiatt, E.E.; Palmer, S.E.; Kyser, K.; O'Connor, E.; Terrence, K.H. Basin evolution, diagenesis and uranium mineralization in the Paleoproterozoic Thelon Basin, Nunavut, Canada. *Basin Res.* **2010**, *22*, 302–323. [CrossRef]
25. Reynolds, R.L.; Goldhaber, M.B. Origin of a South Texas roll-type uranium deposit; I, Alteration of iron-titanium oxide minerals. *Econ. Geol.* **1978**, *73*, 1677–1689. [CrossRef]
26. Pagel, M.; Ahamdach, N. *Etude des Inclusions Fluides dans les Quartz des Gisements U de l'Athabasca et du Thelon*; Internal Report of Centre de Recherches sur la Géologie des Matières Premières Minérales et Energétiques (CREGU): Nancy, France, 1995.
27. Riegler, T.; Lescuyer, J.-L.; Wollenberg, P.; Quirt, D.; Beaufort, D. Alteration related to uranium deposits in the kiggavik-andrew lake structural trend, Nunavut, Canada: New insights from petrography and clay mineralogy. *Can. Mineral.* **2014**, *52*, 27–45. [CrossRef]
28. Sharpe, R.; Fayek, M.; Quirt, D.; Jefferson, C.W. Geochronology and genesis of the Bong Uranium deposit, Thelon Basin, Nunavut, Canada. *Econ. Geol.* **2015**, *110*, 1759–1777. [CrossRef]
29. Chi, G.; Haid, T.; Quirt, D.; Fayek, M.; Blamey, N.; Chu, H. Petrography, fluid inclusion analysis, and geochronology of the End uranium deposit, Kiggavik, Nunavut, Canada. *Miner. Depos.* **2017**, *52*, 211–232. [CrossRef]
30. Shabaga, B.M.; Fayek, M.; Quirt, D.; Jefferson, C.W.; Camacho, A. Mineralogy, geochronology, and genesis of the Andrew Lake uranium deposit, Thelon Basin, Nunavut, Canada. *Can. J. Earth Sci.* **2017**, *54*, 850–868. [CrossRef]
31. Grare, A.; Benedicto, A.; Lacombe, O.; Trave, A.; Ledru, P.; Blain, M.; Robbins, J. The Contact uranium prospect, Kiggavik project, Nunavut (Canada): Tectonic history, structural constraints and timing of mineralization. *Ore Geol. Rev.* **2018**, *93*, 141–167. [CrossRef]
32. Hiatt, E.E.; Kyser, K.; Dalrymple, R.W. Relationships among sedimentology, stratigraphy, and diagenesis in the Proterozoic Thelon Basin, Nunavut, Canada: Implications for paleoaquifers and sedimentary-hosted mineral deposits. *J. Geochem. Explor.* **2003**, *80*, 221–240. [CrossRef]
33. Davis, W.J.; Gall, Q.; Jefferson, C.W.; Rainbird, R.H. Fluorapatite in the Paleoproterozoic Thelon Basin: Structural-stratigraphic context, in situ ion microprobe U-Pb ages, and fluid-flow history. *GSA Bull.* **2011**, *123*, 1056–1073. [CrossRef]
34. Jefferson, C.; Thomas, D.J.; Gandhi, S.; Ramaekers, P.; Delauney, G.; Brisbin, D.; Cutts, C.; Portella, P.; Olson, R. Unconformity-associated uranium deposits of the Athabasca Basin, Saskatchewan and Alberta. *Bull. Geol. Surv. Can.* **2007**, *588*, 23–67.
35. AREVA (Areva, Paris, France). Internal Reference Document 2015. Available online: <http://www.sa.areva.com/EN/finance-1176/regulated-financial-information.html> (accessed on 24 July 2018).
36. Hadlari, T.; Rainbird, R.H. Retro-arc extension and continental rifting: A model for the Paleoproterozoic Baker Lake Basin, Nunavut. Geological Survey of Canada Contribution 2010 04 36. *Can. J. Earth Sci.* **2011**, *48*, 1232–1258. [CrossRef]
37. Rainbird, R.H.; Davis, W.J.; Stern, R.A.; Peterson, T.D.; Smith, S.R.; Parrish, R.R.; Hadlari, T. Ar-Ar and U-Pb geochronology of a Late Paleoproterozoic Rift Basin: Support for a Genetic Link with Hudsonian Orogenesis, Western Churchill Province, Nunavut, Canada. *J. Geol.* **2006**, *114*, 1–17. [CrossRef]
38. Rainbird, R.H.; Davis, W.J. U-Pb detrital zircon geochronology and provenance of the late Paleoproterozoic Dubawnt Supergroup: Linking sedimentation with tectonic reworking of the western Churchill Province, Canada. *GSA Bull.* **2007**, *119*, 314. [CrossRef]
39. Rainbird, R.H.; Hadlari, T.; Aspler, L.B.; Donaldson, J.A.; LeCheminant, A.N.; Peterson, T.D. Sequence stratigraphy and evolution of the paleoproterozoic intracontinental Baker Lake and Thelon basins, western Churchill Province, Nunavut, Canada. *Precambrian Res.* **2003**, *125*, 21–53. [CrossRef]
40. Pehrsson, S.J.; Berman, R.G.; Eglington, B.; Rainbird, R. Two Neoproterozoic supercontinents revisited: The case for a Rae family of cratons. *Precambrian Res.* **2013**, *232*, 27–43. [CrossRef]

41. Peterson, T.D. Geological setting and geochemistry of the ca. 2.6 Ga Snow island Suite in the central Rae Domain of the Western Churchill Province, Nunavut. *Geol. Surv. Can. Open File* **2015**, 7841. [[CrossRef](#)]
42. Jefferson, C.; Pehrsson, S.; Peterson, T.; Chorlton, L.; Davis, B.; Keating, P.; Gandhi, S.; Fortin, R.; Buckle, J.; Miles, W.; et al. Northeast Thelon region geoscience framework—new maps and data for uranium in Nunavut. *Geol. Surv. Can.* **2011**, 288791. [[CrossRef](#)]
43. McEwan, B. Structural style and regional comparison of the Paleoproterozoic Ketyet River group in the region North-Northwest of Baker Lake, Nunavut. Master's Thesis, University of Regina, Regina, SK, Canada, 2012; p. 155.
44. Tschirhart, V.; Morris, W.A.; Jefferson, C.W. Framework geophysical modelling of granitoid vs. supracrustal basement to the northeast Thelon Basin around the Kiggavik uranium camp, Nunavut. *Can. J. Earth* **2013**, *50*, 667–677. [[CrossRef](#)]
45. Tschirhart, V.; Jefferson, C.W.; Morris, W.A. Basement geology beneath the northeast Thelon Basin, Nunavut: Insights from integrating new gravity, magnetic and geological data. *Geophys. Prospect.* **2017**, *65*, 617–636. [[CrossRef](#)]
46. Peterson, T.D.; Scott, J.M.J.; LeCheminant, A.N.; Jefferson, C.W.; Pehrsson, S.J. The Kivalliq Igneous Suite: Anorogenic bimodal magmatism at 1.75 Ga in the western Churchill Province, Canada. *Precambrian Res.* **2015**, *262*, 101–119. [[CrossRef](#)]
47. Johnstone, D.; Bethune, K.M.; Quirt, D. Lithostratigraphic and structural controls of uranium mineralization in the Kiggavik East, Centre and Main Zone deposits, Nunavut. In Proceedings of the Geological Association of Canada-Mineralogical Association of Canada, Joint Annual Meeting, WhiteHorse, YT, Canada, 1–3 June 2016.
48. Peterson, T.D.; Van Breemen, O.; Sandeman, H.; Cousens, B. Proterozoic (1.85–1.75 Ga) igneous suites of the Western Churchill Province: Granitoid and ultrapotassic magmatism in a reworked Archean hinterland. *Precambrian Res.* **2002**, *119*, 73–100. [[CrossRef](#)]
49. Hoffman, P.F. United Plates of America, The Birth of a Craton: Early Proterozoic Assembly and Growth of Laurentia. *Annu. Rev. Earth Planet. Sci.* **1988**, *16*, 543–603. [[CrossRef](#)]
50. Van Breemen, O.; Peterson, T.D.; Sandeman, H.A. U-Pb zircon geochronology and Nd isotope geochemistry of Proterozoic granitoids in the western Churchill Province: Intrusive age pattern and Archean source domains. *Can. J. Earth Sci.* **2005**, *42*, 339–377. [[CrossRef](#)]
51. Scott, J.M.J.; Peterson, T.D.; Davis, W.J.; Jefferson, C.W.; Cousens, B.L. Petrology and geochronology of Paleoproterozoic intrusive rocks, Kiggavik uranium camp, Nunavut. *Can. J. Earth Sci.* **2015**, *52*, 495–518. [[CrossRef](#)]
52. Zaleski, E.; Pehrsson, N.D.; Davis, W.J.; L'Heureux, R.; Greiner, E.; Kerswill, J.A. *Quartzite Sequences and Their Relationships, Woodburn Lake Group, Western Churchill Province, Nunavut*; West. Churchill NATMAP Project; Geological Survey of Canada: Ottawa, ON, Canada, 2000; pp. 1–10.
53. Rainbird, R.H.; Davis, W.J.; Pehrsson, S.J.; Wodicka, N.; Rayner, N.; Skulski, T. Early Paleoproterozoic supracrustal assemblages of the Rae domain, Nunavut, Canada: Intracratonic basin development during supercontinent break-up and assembly. *Precambrian Res.* **2010**, *181*, 167–186. [[CrossRef](#)]
54. LeCheminant, A.N.; Heaman, L.M. Mackenzie igneous events, Canada: Middle Proterozoic hotspot magmatism associated with ocean opening. *Earth Planet. Sci. Lett.* **1989**, *96*, 38–48. [[CrossRef](#)]
55. Heaman, L.M.; LeCheminant, A.N. Paragenesis and U-Pb systematics of baddeleyite (ZrO<sub>2</sub>). *Chem. Geol.* **1993**, *110*, 95–126. [[CrossRef](#)]
56. Anand, A.; Jefferson, C.W. Reactivated fault systems and their effects on outcrop patterns of thin-skinned early thrust imbrications in the Kiggavik uranium camp, Nunavut. *Geol. Surv. Can.* **2017**. [[CrossRef](#)]
57. Peter, J.K.; Ulrike, W.; Brigitte, S.; Dmitry, K.; Qichao, Y.; Ingrid, R.; Andreas, S.; Karin, B.; Detlef, G.; Jacinta, E. Determination of Reference Values for NIST SRM 610–617 Glasses Following ISO Guidelines. *Geostand. Geoanal. Res.* **2010**, *35*, 397–429. [[CrossRef](#)]
58. Paton, C.; Hellstrom, J.; Paul, B.; Woodhead, J.; Hergt, J. Iolite: Freeware for the visualisation and processing of mass spectrometric data. *J. Anal. At. Spectrom.* **2011**, *26*, 2508–2518. [[CrossRef](#)]
59. Hervig, R.L.; Williams, L.B.; Kirkland, I.K.; Longstaffe, F.J. Oxygen isotope microanalyses of diagenetic quartz: Possible low temperature occlusion of pores. *Geochim. Cosmochim. Acta* **1995**, *59*, 2537–2543. [[CrossRef](#)]
60. Kempe, U.; Götze, J.; Dombon, E.; Monecke, T.; Poutitvsev, M. *Quartz: Deposits, Mineralogy and Analytics*; Springer: Berlin, Germany, 2012; pp. 331–355.

61. Dennen, W.H. Stoichiometric substitution in natural quartz. *Geochim. Cosmochim. Acta* **1966**, *30*, 1235–1241. [[CrossRef](#)]
62. Turner, W.; Richards, J.; Nesbitt, B.; Muehlenbachs, K.; Biczok, J. Proterozoic low-sulfidation epithermal Au-Ag mineralization in the Mallery Lake area, Nunavut, Canada. *Miner. Depos.* **2001**, *36*, 442–457. [[CrossRef](#)]
63. Clayton, R. Oxygen isotope exchange between quartz and water. *J. Geophys. Res.* **1972**, *77*, 3057–3067. [[CrossRef](#)]
64. Lowenstern, J.B.; Sinclair, W.D. Exsolved magmatic fluid and its role in the formation of comb-layered quartz at the Cretaceous Logtung W-Mo deposit, Yukon Territory, Canada. *Trans. R. Soc. Edinb. Earth Sci.* **1996**, *87*, 291–303. [[CrossRef](#)]
65. Thomas, J.B.; Bruce Watson, E.; Spear, F.S.; Shemella, P.T.; Nayak, S.K.; Lanzirrotti, A. TitaniQ under pressure: The effect of pressure and temperature on the solubility of Ti in quartz. *Contrib. Mineral. Petrol.* **2010**, *160*, 743–759. [[CrossRef](#)]
66. Perny, B.; Eberhardt, P.; Ramseyer, K.; Pankrath, R. Microdistribution of Al, Li, and Na in  $\alpha$  quartz: Possible causes and correlation with short-lived cathodoluminescence. *Am. Mineral.* **1992**, *77*, 534–544.
67. Rusk, B.G.; Lowers, H.A.; Reed, M.H. Trace elements in hydrothermal quartz: Relationships to cathodoluminescent textures and insights into vein formation. *Geology* **2008**, *36*, 547–550. [[CrossRef](#)]
68. Spear, F.; Wark, D. Cathodoluminescence imaging and titanium thermometry in metamorphic quartz. *J. Metamorph. Geol.* **2009**, *27*, 187–205. [[CrossRef](#)]
69. Leeman, W.P.; MacRae, C.M.; Wilson, N.C.; Torpy, A.; Lee, C.-T.; Student, J.J.; Thomas, J.B.; Vicenzi, E.P. A Study of cathodoluminescence and trace element compositional zoning in natural quartz from volcanic rocks: Mapping titanium content in quartz. *Microsc. Microanal.* **2012**, *18*, 1322–1341. [[CrossRef](#)] [[PubMed](#)]
70. Rusk, B.; Koenig, A.; Lowers, H. Visualizing trace element distribution in quartz using cathodoluminescence, electron microprobe, and laser ablation-inductively coupled plasma-mass spectrometry. *Am. Mineral.* **2011**, *96*, 703–708. [[CrossRef](#)]
71. Huang, R.; Audétat, A. The titanium-in-quartz (TitaniQ) thermobarometer: A critical examination and re-calibration. *Geochim. Cosmochim. Acta* **2012**, *84*, 75–89. [[CrossRef](#)]
72. Taylor, H.P. The Application of oxygen and hydrogen isotope studies to problems of hydrothermal alteration and ore deposition. *Econ. Geol.* **1974**, *69*, 843–883. [[CrossRef](#)]
73. Bettencourt, J.S.; Leite, W.B.; Goraieb, C.L.; Sparrenberger, I.; Bello, R.M.S.; Payolla, B.L. Sn-polymetallic greisen-type deposits associated with late-stage rapakivi granites, Brazil: Fluid inclusion and stable isotope characteristics. *Lithos* **2005**, *80*, 363–386. [[CrossRef](#)]
74. Bowen, G.J. Statistical and Geostatistical Mapping of Precipitation Water Isotope Ratios. In *Isoscapes: Understanding Movement, Pattern, and Process on Earth through Isotope Mapping*; West, J.B., Bowen, G.J., Dawson, T.E., Tu, K.P., Eds.; Springer: Dordrecht, The Netherlands, 2010; pp. 139–160, ISBN 978-90-481-3354-3.
75. Vollbrecht, A.; Oberthür, T.; Ruedrich, J.; Weber, K. Microfabric analyses applied to the Witwatersrand gold- and uranium-bearing conglomerates: Constraints on the provenance and post-depositional modification of rock and ore components. *Miner. Depos.* **2002**, *37*, 433–451. [[CrossRef](#)]
76. Kraishan, G.; Rezaee, R.; Worden, R. Significance of trace element composition of quartz cement as a key to reveal the origin of silica in sandstones: An example from the cretaceous of the Barrow Sub-Basin, Western Australia. *Quartz Cementation Sandstones* **2009**, *29*, 317–331.
77. Rosenberg, P.E.; Foit, F.F. Magnesianite from the uranium deposits of the Athabasca Basin, Saskatchewan, Canada. *Can. Mineral.* **2006**, *44*, 959–965. [[CrossRef](#)]
78. Richard, A.; Boulvais, P.; Mercadier, J.; Boiron, M.-C.; Cathelineau, M.; Cuney, M.; France-Lanord, C. From evaporated seawater to uranium-mineralizing brines: Isotopic and trace element study of quartz–dolomite veins in the Athabasca system. *Geochim. Cosmochim. Acta* **2013**, *113*, 38–59. [[CrossRef](#)]
79. Polito, P.A.; Kyser, T.K.; Thomas, D.; Marlatt, J.; Drever, G. Re-evaluation of the petrogenesis of the Proterozoic Jabiluka unconformity-related uranium deposit, Northern Territory, Australia. *Miner. Depos.* **2005**, *40*, 257–288. [[CrossRef](#)]
80. Derome, D.; Cathelineau, M.; Fabre, C.; Boiron, M.-C.; Banks, D.; Lhomme, T.; Cuney, M. Reconstitution of paleo-fluid composition by Raman LIBS and crush-leach techniques: Application to mid-Proterozoic evaporitic brines (Kombolgie Formation basin, Northern Territory, Australia). *Chem. Geol.* **2007**, *237*, 240–254.

81. Bodnar, R.J.; Reynolds, T.J.; Kuehn, C.A. Fluid-Inclusion Systematics in Epithermal Systems. In *Geology and Geochemistry of Epithermal Systems*; Berger, B.R., Bethke, P.M., Eds.; Society of Economic Geologists: Littleton, CO, USA, 1985.
82. Dong, G.; Morrison, G.; Jaireth, S. Quartz textures in epithermal veins, Queensland; classification, origin and implication. *Econ. Geol.* **1995**, *90*, 1841–1856. [[CrossRef](#)]
83. Bobis, E.R. A review of the description, classification, and origin of quartz textures in low-sulphidation epithermal veins. *J. Geol. Soc. Philipp.* **1994**, *99*, 15–39.
84. Moncada, D.; Mutchler, S.; Nieto, A.; Reynolds, T.J.; Rimstidt, J.D.; Bodnar, R.J. Mineral textures and fluid inclusion petrography of the epithermal Ag–Au deposits at Guanajuato, Mexico: Application to exploration. *J. Geochem. Explor.* **2012**, *114*, 20–35. [[CrossRef](#)]
85. Tanner, P.W. The giant quartz-breccia veins of the Tyndrum-Dalmally area, Grampian Highlands, Scotland: Their geometry, origin and relationship to the Cononish gold-silver deposit. *Earth Environ. Sci. Trans. R. Soc. Edinb.* **2012**, *103*, 51–76. [[CrossRef](#)]
86. Sibson, R.H. Implications of fault-valve behaviour for rupture nucleation and recurrence. *Tectonophysics* **1992**, *211*, 283–293. [[CrossRef](#)]
87. Meunier, J.D.; Sellier, E.; Pagel, M. Radiation-damage rims in quartz from uranium-bearing sandstones. *J. Sediment. Res.* **1990**, *60*, 53–58. [[CrossRef](#)]
88. Hu, B.; Pan, Y.; Botis, S.; Rogers, B.; Kotzer, T.; Yeo, G. Radiation-induced defects in drusy quartz, Athabasca basin, Canada: A new aid to exploration of uranium deposits. *Econ. Geol.* **2008**, *103*, 1571–1580. [[CrossRef](#)]
89. MacRae, C.M.; Wilson, N.C.; Torpy, A. Hyperspectral cathodoluminescence. *Mineral. Petrol.* **2013**, *107*, 429–440. [[CrossRef](#)]
90. Cerin, D.; Götze, J.; Pan, Y. Radiation-Induced Damage In Quartz At the Arrow Uranium Deposit, Southwestern Athabasca Basin, Saskatchewan. *Can. Mineral.* **2017**, *55*, 457–472. [[CrossRef](#)]
91. Zhang, Y.; Robinson, J.; Schaubs, P.M. Numerical modelling of structural controls on fluid flow and mineralization. *Geosci. Front.* **2011**, *2*, 449–461. [[CrossRef](#)]
92. McCuaig, T.C.; Hronsky, J.M.A. The Mineral System Concept: The Key to Exploration Targeting. In *Building Exploration Capability for the 21st Century*; Kelley, K.D., Golden, H.C., Eds.; Society of Economic Geologists: Littleton, CO, USA, 2014; ISBN 9781629491424.





© 2018 by the authors. Licensee MDPI, Basel, Switzerland. This article is an open access article distributed under the terms and conditions of the Creative Commons Attribution (CC BY) license (<http://creativecommons.org/licenses/by/4.0/>).



Article

# Structural Control on Clay Mineral Authigenesis in Faulted Arkosic Sandstone of the Rio do Peixe Basin, Brazil

Ingrid B. Maciel <sup>1</sup>, Angela Dettori <sup>2</sup>, Fabrizio Balsamo <sup>2,\*</sup> , Francisco H.R. Bezerra <sup>1,3</sup>,  
Marcela M. Vieira <sup>3</sup>, Francisco C.C. Nogueira <sup>4</sup>, Emma Salvioli-Mariani <sup>2</sup> , and  
Jorge André B. Sousa <sup>5</sup>

<sup>1</sup> Post-Graduation Program on Geodynamics and Geophysics, Universidade Federal do Rio Grande do Norte, Natal, RN 59078-970, Brazil; ingridbmaciel@gmail.com (I.B.M.); bezerrafh@geologia.ufrn.br (F.H.R.B.)

<sup>2</sup> Department of Chemistry, Life Sciences and Environmental Sustainability, University of Parma, I-43124 Parma, Italy; angela.dettori@studenti.unipr.it (A.D.); emma.salviolimariani@unipr.it (E.S.-M.)

<sup>3</sup> Department of Geology, Federal University of Rio Grande do Norte, Natal, RN 59078-970, Brazil; marcela@geologia.ufrn.br

<sup>4</sup> Department of Petroleum Engineering, Federal University of Campina Grande, Campina Grande, PB 58100-000, Brazil; aulacezar@gmail.com

<sup>5</sup> Petrobras Research Center—CENPES, Rio de Janeiro, RJ 21941-915, Brazil; jorgeabs@petrobras.com.br

\* Correspondence: fabrizio.balsamo@unipr.it; Tel.: +39-0521-905365

Received: 3 July 2018; Accepted: 13 September 2018; Published: 14 September 2018

**Abstract:** Clay minerals in structurally complex settings influence fault zone behavior and characteristics such as permeability and frictional properties. This work aims to understand the role of fault zones on clay authigenesis in arkosic, high-porosity sandstones of the Cretaceous Rio do Peixe basin, northeast Brazil. We integrated field, petrographic and scanning electron microscopy (SEM) observations with X-ray diffraction data (bulk and clay-size fractions). Fault zones in the field are characterized by low-porosity deformation bands, typical secondary structures developed in high-porosity sandstones. Laboratory results indicate that in the host rock far from faults, smectite, illite and subordinately kaolinite, are present within the pores of the Rio do Peixe sandstones. Such clay minerals formed after sediment deposition, most likely during shallow diagenetic processes (feldspar dissolution) associated with meteoric water circulation. Surprisingly, within fault zones the same clay minerals are absent or are present in amounts which are significantly lower than those in the undeformed sandstone. This occurs because fault activity obliterates porosity and reduces permeability by cataclasis, thus: (1) destroying the space in which clay minerals can form; and (2) providing a generally impermeable tight fabric in which external meteoric fluid flow is inhibited. We conclude that the development of fault zones in high-porosity arkosic sandstones, contrary to other low-porosity lithologies, inhibits clay mineral authigenesis.

**Keywords:** fault zones; deformation bands; clay authigenesis; shallow diagenesis

## 1. Introduction

Clay minerals have important economic applications in industry—e.g., [1]. Additionally, in most geological settings clay minerals can occur in faults, thus influencing their permeability, frictional properties [2–8] and subsurface fluid flow [4,9–14]. Therefore, the understanding of the feedback between faulting and clay mineral authigenesis has important implications for seismicity, the migration and accumulation of oil and gas in the subsurface, and contaminant transport in aquifers.

Faults in high-porosity sandstones are generally considered as barriers to fluid flow, due to the combined effect of grain size and porosity reduction within fault cores and associated deformation

bands in damage zones [15–22]. In this context, clay minerals are commonly described as mechanically weak minerals, and because of this weakness their presence in faults commonly contributes to stable sliding failures [23,24]. Furthermore, the origin and distribution of clays in sandstone are also important in oil industry, because these minerals contribute to increases in the sealing potential of faults and can determine reservoir compartmentalization [3,6,8].

Several studies have described the clay mineralogy of fault zones [24–26], however little attention has been paid to the role of faults in determining the type and amount of clay mineral transformation in faulted, arkosic sandstones. The goal of this study is to investigate how fault zones in arkosic sandstones (composed of a fault core surrounded by deformation bands) modify grain-scale fabric and control clay mineral authigenesis at shallow burial depths. We selected the Cretaceous Rio do Peixe basin in northeast Brazil (Figure 1) as a case study, due to its excellent exposures of undeformed sandstones and well-preserved fault zones. By integrating field analysis with laboratory data, we conclude that deformation-band faulting in arkosic, high-porosity sandstones inhibits clay mineral authigenesis, rather than promoting alteration and clay mineral formation.

## 2. Geological Background of the Rio do Peixe Basin

The Rio do Peixe basin (RPB) is a pull-apart Early Cretaceous basin situated in northeastern Brazil. The basin was generated during the reactivation of Precambrian basement shear zones during the opening of the South Atlantic Ocean [27–30]. The basin's deeper depocenters were established based on gravity data, and reach depths of ~2420 m [30]. These depocenters are filled by continental siliciclastic sedimentary units which were deposited in fluvial and lacustrine depositional systems. These deposits are divided into three main stratigraphic units, namely, from the base to the top: (1) the Antenor Navarro Formation, represented by conglomerates and mudstones; (2) the Sousa Formation, composed of mudstones; and (3) the Rio Piranhas Formation, composed of conglomerates and coarse sandstones [31–33].

The Antenor Navarro Formation is the basal unit. It represents the main fill of the basin and contains typical syn-rift deposits. The formation consists of siliciclastic fluvial deposits that are exposed in large and continuous outcrops in different sectors of the basin (Figure 1). The sandstones and conglomerates are composed of quartz, feldspars, rock fragments and biotite. Their matrix consists of silt and dark brown clay (approximately 1–1.5%) [34]. The Souza Formation is the intermediate unit and consists mostly of mudstones and a few occurrences of sandstones and marls. These units were deposited in floodplains or shallow lakes on meandering rivers. The Rio Piranhas Formation is the top unit and consists of conglomerates and coarse sandstones interfingering with sandy mudstones [32].

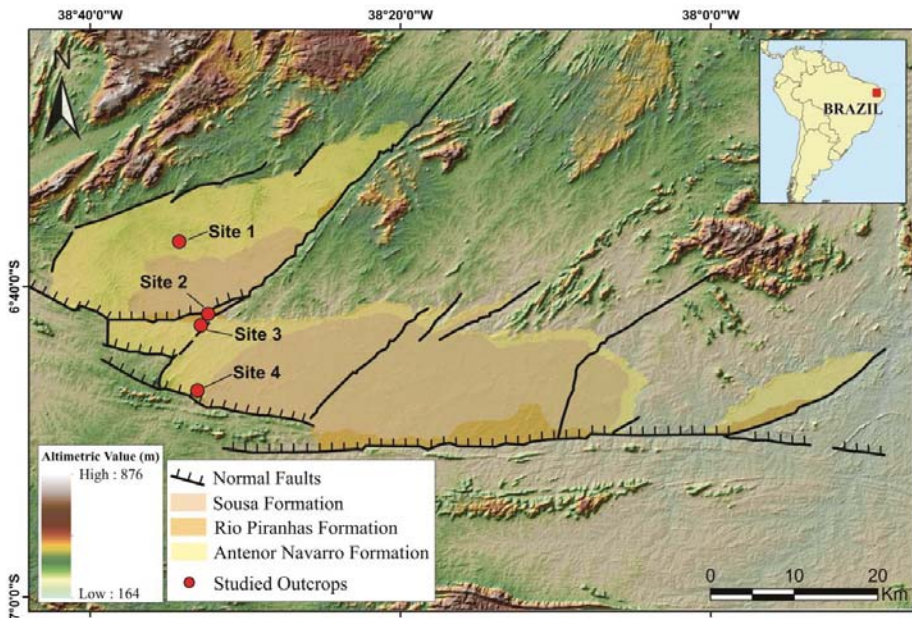


**Figure 1.** Simplified geological map of the Rio do Peixe Basin, showing major faults and the lithostratigraphic units. The location of the four selected outcrops is indicated. Modified from [27,29,35].

The sedimentary rocks of the Rio do Peixe basin were affected by two main tectonic phases: an Early to Late Cretaceous NW–SE oriented extension [29] followed by a basin inversion in a strike–slip regime from the Late Cretaceous to Cenozoic [35]. The extensional faults that developed during the first phase are dominated by deformation bands, often associated with slickensided surfaces [34]. The deformation bands occur as cm-thick tabular structures developed in the fault damage zone, and are arranged as single elements or in clusters. Within deformation bands, a cataclastic foliation was formed by preferential grain alignment and the selective fragmentation of feldspar grains [34].

### 3. Methods and Materials

This study focused on the western side of the Rio do Peixe basin, both in its central part far from major faults and in the proximity of the basin-boundary faults (Figure 1). Field analysis and sampling were performed at four main outcrops: one represents undeformed host rocks (Site 1) and the other three are deformed sites near major faults (Sites 2, 3 and 4). Site 1 is located in the undeformed part of the basin, where the basal Antenor Navarro sandstones are not affected by faults and fractures. In this site, we constructed a vertical sedimentary log to characterize the undeformed rocks. Sites 2 and 3 are located along the major intra-basinal fault zones in the Rio Piranhas sandstones and conglomerates, and are characterized by abundant fault zones with meter-scale offsets. Site 4 is located in the hanging wall block of the major basin-boundary fault in the Antenor Navarro sandstones, and has a displacement of ~170 m [36].

In the studied field sites, we collected a total of 95 samples of undeformed and faulted rocks, from which we made 34 thin sections. In the lab, we examined the following materials: (1) undeformed sandstones and conglomerates (i.e., host rocks); (2) deformed rocks collected within the fault zones, consisting of both deformation bands (single or clustered) and foliated cataclasites (see Section 4.1 for a description of fault zone structure). Thin section analysis was performed using an optical microscope, and scanning electron microscopy (SEM) combined with energy dispersive spectroscopy (EDS). The thin sections were impregnated with stained blue epoxy to highlight porosity. For observations

using the light petrographic microscope, we focused on grain size and roundness, sorting, packing, porosity, mineral composition and amount of clay. We also described depositional and diagenetic features in undeformed and faulted samples. Small representative samples were analyzed using a scanning electron microscope (SUPERSCAN SSX-550, Shimadzu Corporation, Kyoto, Japan) to improve clay mineral identification and textural analysis. EDS was used to identify the main chemical elements and mineral composition of the samples. X-ray diffraction (XRD) analyses were performed using a Bruker (Billerica, MA, USA) D2 Phaser powder diffractometer (CuK $\alpha$  radiation, voltage of 30 kV, current of 10 mA, step size of 0.018, interval of 1 s per step) on powdered bulk samples ( $n = 10$ ) and fraction samples  $<2 \mu\text{m}$  in size ( $n = 6$ ) for clay mineral identification in undeformed and faulted rocks. The oriented samples of the clay fractions were analyzed under three different conditions: air dried; ethylene glycol saturated; and heated to a temperature of 550 °C. The powdered bulk samples were measured in the range 2–80° 2 $\theta$ , and the clay fraction samples were measured in the range 2–20° 2 $\theta$ . Mineral phase identification and semi-quantitative estimations were performed using the DIFFRAC.EVA suite software provided by Bruker Corporation (Billerica, MA, USA). The results of the XRD analyses, together with sample description and location, are listed in Table 1.

## 4. Results

### 4.1. Fault Zone Structure

The studied fault zones exhibit three major structural domains (Figure 2): (1) the host rock, i.e., the undeformed sandstone and conglomerates without any significant deformational features; (2) the fault core, where most of the fault slip is accommodated; and (3) the surrounding footwall and hanging wall damage zones, interposed between the host rock and fault core, and composed of deformation bands.

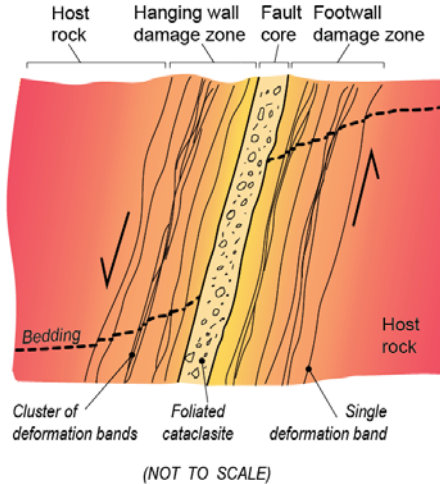


**Figure 2.** Conceptual sketch showing the typical architecture of fault zones in the Rio do Peixe basin. The host rock represents the sandstones and conglomerates with pristine textures and sedimentary structures not affected by faults. The fault core is the most deformed part of the fault zone, where slip surfaces were frequently developed and where several movements (different slicken lines) are observed. The damage zone is the deformed rock volume next to the fault core that has single or clusters of deformation bands (Sites 2, 3 and 4 in this study). Colors are indicative of the amount of weathering observed in the field.

Concerning the host rock, the original undeformed fluvial facies of the Rio do Peixe basin exhibit a massive laminated structure with trough–festoon crossbedding stratification (Figure 3). These units vary from silty sandstones to fine conglomerates. In a few cases, thin silt lenses are also observed (Figure 3). The sandstones are generally clast-supported with a granular texture, and grains are locally fractured. The grain sizes vary between silt and gravel.

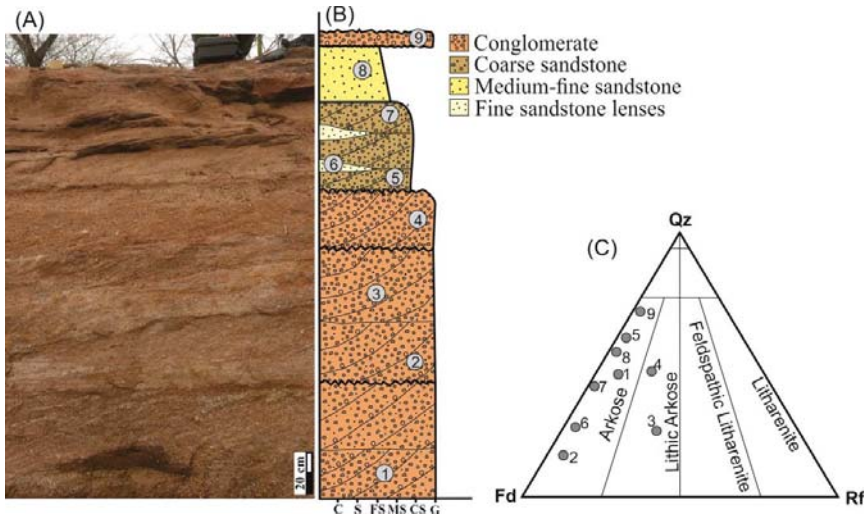


**Figure 3.** Schematic profile and compositional classification of the host rock (Antenor Navarro Formation) in the Rio do Peixe basin, Site 1. (A) Outcrop photograph showing fluvial sedimentary structures with tabular and lenticular shapes of fine sandstones and trough–festoon conglomerates. Note the intense red-orange coloration of undeformed rocks. (B) Vertical sedimentary log showing sampling position (Samples 1 to 9) in the fluvial succession. (C) Compositional classification of analyzed Samples 1 to 9, based on [37]. Key: c—clay; s—sand; fs—fine sand; ms—medium sand; cs—coarse sand; g—gravel; Qz—quartz; Fd—feldspar; Rf—rock fragments.

The fault cores range from 0.1 m to 0.3 m in thickness, whereas the width of the damage zones broadly range from ~5 m to 10 m (in small faults of Sites 2 and 3) up to ~200 m (in the hanging wall damage zone of Site 4). The fault cores and the inner damage zone generally form topographic relief up to 1 m in height with respect to the surrounding undeformed rock (Figure 4A). The sandstones in the fault core show a strong decrease in grain size and a preferential grain alignment, which forms a tectonic foliation visible at the hand scale (Figure 4B). Most offsets are extensional or slightly oblique. The footwall and hanging wall damage zones consist of clusters of anastomosing deformation bands (Figure 4C) and isolated single deformation bands (Figure 4D). Deformation bands also form a small positive relief. The fault cores and deformation bands exhibit lighter colors than surrounding host rocks (Figure 4B–D) and in some cases an orange to red coloration is also observed.

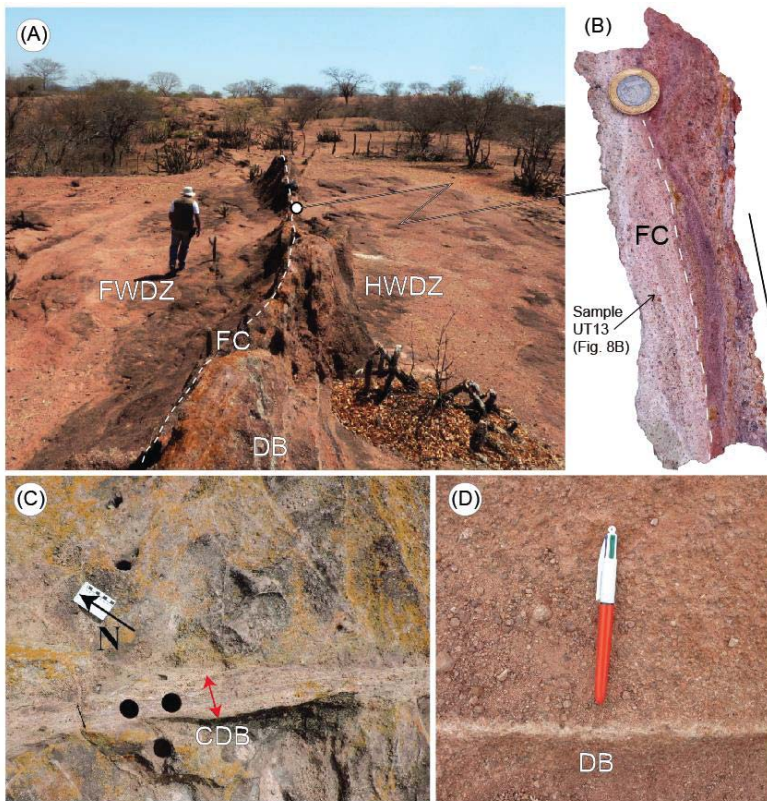


**Figure 4.** Field photographs showing the main structural features of studied fault zones in the Rio do Peixe basin. (A) Example of an extensional fault zone with m-scale offset showing positive relief with respect to the host sandstone, Site 2. The dotted line indicates the approximate position of the fault core. (B) Foliated fault core rock (sample UT13 in Table 1) showing light grey to red colors, Site 2. The diameter of the coin is ~2.5 cm. (C) Example of a 12.0 cm-thick cluster of deformation bands, in positive relief, developed in the fault damage zone, Site 4. The length of the white scale is ~8.0 cm. (D) Whitish single deformation band in positive relief developed in the damage zone, Site 2. The length of the pen is ~14.0 cm. Key: FWDZ—footwall damage zone; HWDZ—hanging wall damage zone; FC—fault core; DB—deformation band; CDB—cluster of deformation bands.

#### 4.2. Petrography

##### 4.2.1. Host Rock

The host rock comprises: (1) fine-grained sandstones with moderate sorting and angular grains (Figure 5A); and (2) coarse-grained, generally poorly sorted sandstones with sub-rounded grains (Figure 5B,C). Point, line and concave-convex grain contacts predominate, while floating and sutured grains are rare. These grain contacts indicate that the sandstones have moderate packing and shallow burial conditions. The sandstones are composed of feldspar, quartz, chert, metamorphic lithoclasts and opaque minerals, although the percentage of these minerals varies in each sample. In thin sections, feldspar is usually the most abundant constituent (~60%), followed by quartz (~40%), lithoclasts (up to 10%) and opaque minerals (~1%). Feldspar grains generally show microfractures and are often partially to completely dissolved, while quartz grains are generally intact. The sandstones vary from arkose to lithic arkose according to the Folk (1968) classification (Figure 3C). All analyzed samples commonly

exhibit primary intergranular porosity and, subordinately, secondary moldic porosity associated with the selective dissolution of feldspar grains (Figure 5E,F). Fracture porosity is also observed (Figure 5C), although fractures are mostly filled by clay minerals. In thin sections, visual porosity was observed to be 17% and 28% in fine and coarse sandstones, respectively. Generally, grains are coated by thin layers of clay minerals; these are even more abundant within intergranular pores and microfractures. In some samples, pores show shrinkage (Figure 5B,C). In rare cases, the porosity is almost entirely filled by clay minerals (Figure 5A).

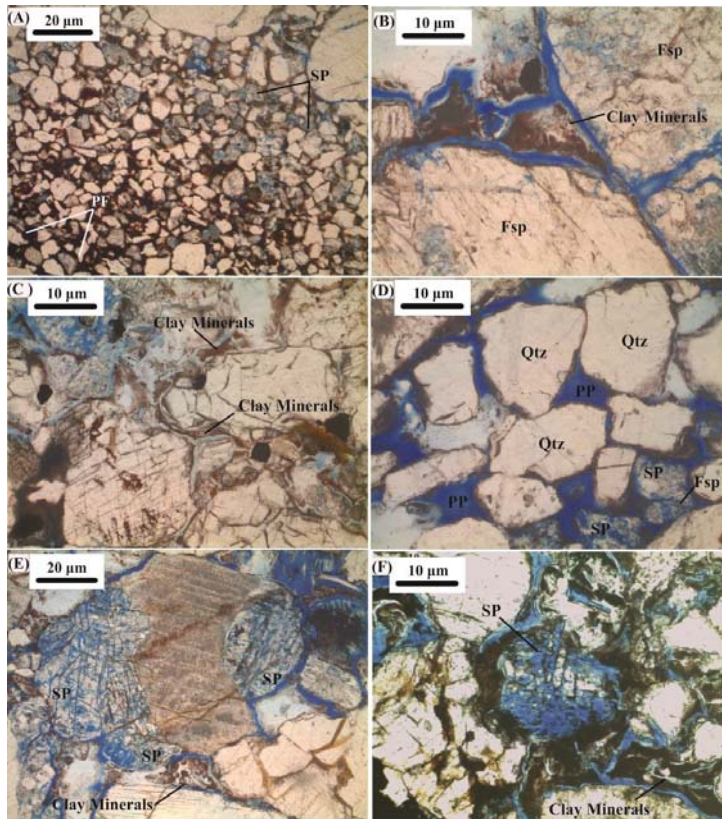


**Figure 5.** Optical microscopic images of the undeformed Rio do Peixe basin sandstones at Site 1. (A) Host rock, with very fine grains and abundant small pores which are frequently filled by clay minerals (pore filling, PF). The porosity is mainly secondary porosity (SP). (B) Coarse-grained sandstone showing sub-rounded grains and primary porosity, partially filled by smectite and illite. (C) Example of a feldspar clast dissolved and replaced by abundant clays. (D–F) show intergranular primary porosity (PP) between quartz grains (Qtz) and SP resulting from the dissolution of feldspar grains (Fsp).

#### 4.2.2. Fault Rocks

The deformed sandstones show different degrees of deformation, most likely due to the amount of offset accommodated within the fault zones (Figure 6). The samples from single deformation bands exhibit a tight fabric and limited intergranular and secondary moldic (feldspar dissolution) porosity compared to the host rock (Figure 6A,B). The visual porosity inside the deformation bands is around 11%, i.e., lower than host rock samples. Intragranular fractures are common in quartz and feldspar

grains within the deformation bands (Figure 6C). In places, fractures are open and filled by fine-grained angular cataclastic material (Figure 6D).

Samples from fault cores exhibit a strong reduction in grain size with abundant fractions ranging from fine sand to silt (Figure 6E,F). In strong contrast to the undeformed host rock, fault core samples are clearly matrix-supported and very poorly sorted (Figure 6E,F). The brown colored, fine-grained matrix consists of crushed feldspar grains, in agreement with recent observations [34]. In the fault cores, the visual porosity determined using the optical microscope is practically zero due to the presence of the cataclastic matrix (Figure 6F).

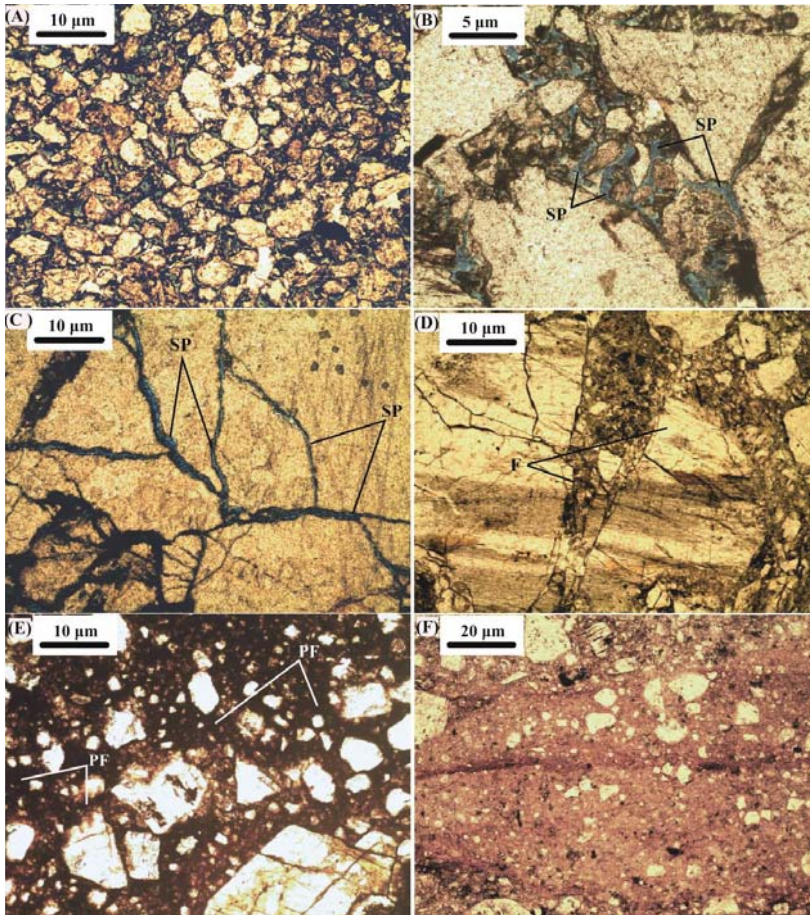


**Figure 6.** Fault rocks viewed under optical microscope. (A) Example of tight fabric in a deformation band within the damage zone, Site 2. (B) Detail of primary porosity filled by small angular clasts generated by the cataclasis process in a deformation band, Site 2. Note that feldspar grain dissolution is limited. (C) Secondary porosity (SP) developed by intragranular microfractures in a deformation band. (D) Detail of intragranular fractures filled by fine-grained angular cataclastic material in a small fault core. (E) Fine-grained matrix in the fault core resulting from high grain comminution, in which the pore space was completely destroyed, Site 3. (F) A high degree of cataclasis within the fault core, showing a dramatic reduction in grain size and porosity, Site 4. The brown crushed material in (E) and (F) mostly consist of very small feldspar grains developed during a cataclastic process cf. [34].



#### 4.3. Clay Minerals

The clay minerals observed in the undeformed host rock are smectite, illite and subordinately kaolinite (Figure 7). These generally form a coating around clasts. The feldspars have a pore lining with an arrangement similar to the surrounding clay minerals, indicating growth into an open void (Figure 7A). The smectite and kaolinite exhibit a pore-filling texture (Figure 7B), while the illite shows a pore-lining geometry on quartz (Figure 7C). The smectite is marked by contraction fractures, likely due to sample drying (Figure 7D).

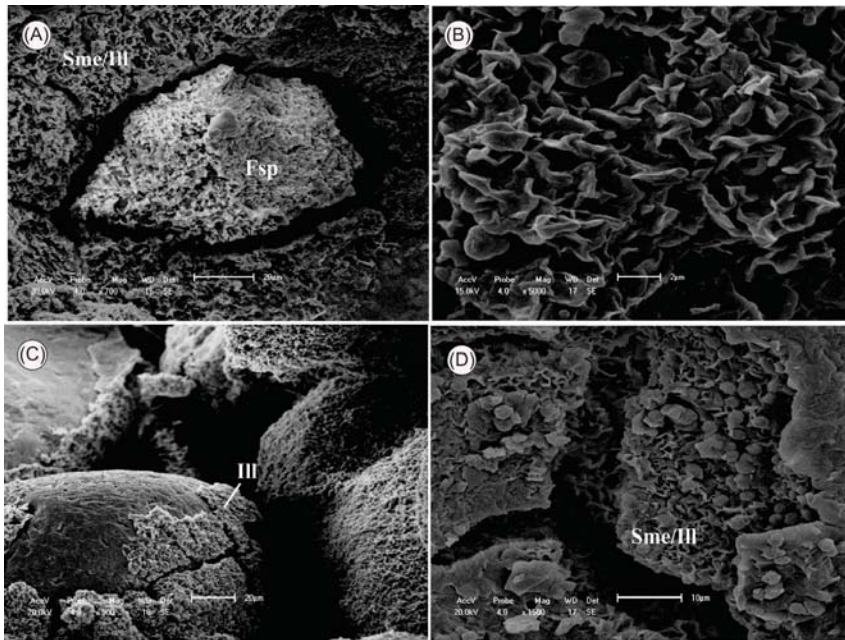


**Figure 7.** SEM images of clay minerals in undeformed sandstones. (A) Feldspar grain surrounded by fractured smectite. (B) Well developed smectite flakes inside a pore. (C) Pore-line illite coatings capping quartz grains. (D) Mixed layers of smectite and illite. Key: Sme—smectite; Fsp—feldspar; Ill—illite.

#### 4.4. XRD Data

XRD bulk analysis was carried out on 10 samples as listed in Table 1. The results show that the main mineral phases identified in both undeformed and faulted sandstones are very similar (Figure 8A–C). Undeformed and faulted sandstones contain mostly quartz and feldspar (orthoclase, microcline and albite) and subordinately micas (Table 1). Hematite was only detected in three out of five undeformed sandstones, and was not detected in faulted samples. At low  $2\theta$  values, when clay minerals can be identified, undeformed sandstones show small spectral peaks (see enlargement in Figure 8A) which have a very low intensity (or are absent) in faulted sandstones (see enlargements in Figure 8B,C). Overall, semi-quantitative estimates based on XRD peak intensity, combined with thin section observations, indicate that the amount of clay minerals is systematically <1–2%. In three faulted samples (one of fault core rock and two of deformation bands), either no clay minerals were detected or insufficient material was available for clay fraction analysis (Table 1).

**Table 1.** Results of XRD analyses (bulk and clay fractions) performed in undeformed and faulted rocks from Sites 1, 2 and 4. (I-S: illite-smectite; DB: deformation bands). Sample labels are the same as Figures 8 and 9.

Sample #	Site	Formation	Structural Domain	Bulk Mineralogy	Clay Mineralogy
SCP01	Site 1	Antenor Navarro	Host rock (fine conglomerate)	Quartz, feldspars, muscovite, hematite	Illite, smectite
SCP05	Site 1	Antenor Navarro	Host rock (fine sandstone)	Quartz, feldspars, muscovite, hematite	Illite, smectite
UT01	Site 2	Rio Piranhas	Host rock (fine sand)	Quartz, feldspars, muscovite	Illite, smectite, I-S mixed layers
UT11	Site 2	Rio Piranhas	Host rock (Fine sand)	Quartz, feldspars, muscovite	Illite, smectite, I-S mixed layers
UT13	Site 2	Rio Piranhas	Fault core (foliated cataclasite)	Quartz, feldspars, muscovite	Not analyzed (no enough clay)
UT14	Site 2	Rio Piranhas	Fault core (foliated cataclasite)	Quartz, feldspars	Illite, chlorite
SVEM1	Site 4	Antenor Navarro	Host rock (fine sandstone)	Quartz, feldspars, muscovite, hematite	Illite, smectite, I-S mixed layers
SVEF3	Site 4	Antenor Navarro	Damage zone (deformation band)	Quartz, feldspars, muscovite	No clay phase
SVEA1	Site 4	Antenor Navarro	Damage zone (cluster of DB)	Quartz, feldspars	Illite, smectite
SVEB2	Site 4	Antenor Navarro	Damage zone (cluster of DB)	Quartz, feldspars	No clay phase

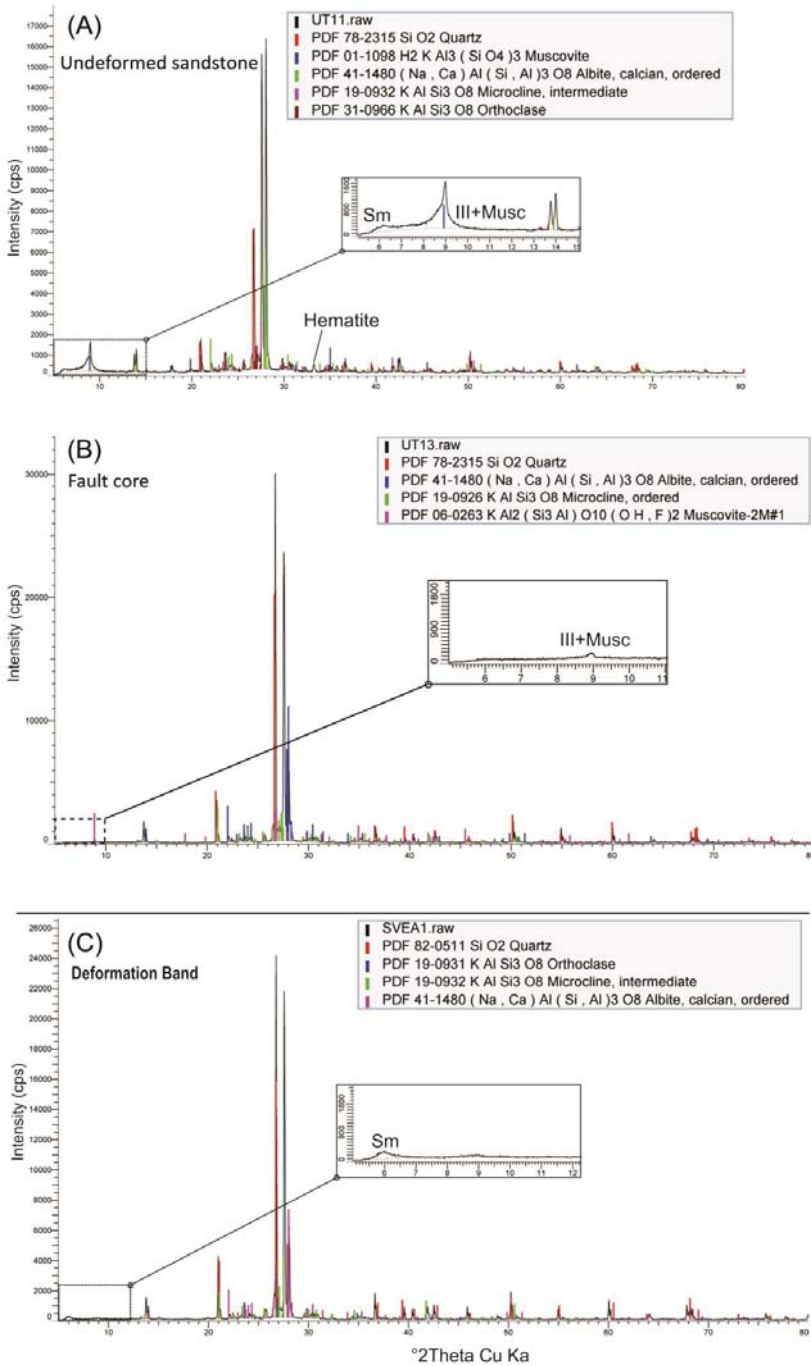


**Figure 8.** Examples of XRD analyses on bulk samples representative of undeformed sandstone (A), foliated cataclasis in fault core rock (B) and deformation band (C).

XRD analyses of clay fractions, performed on the six samples which had sufficient clay minerals in bulk analyses, indicate that the main types of clay minerals in both undeformed and faulted sandstones are smectite and subordinately illite (Figure 9), as indicated by the comparison between the XRD spectra of air-dried, glycolated and heated samples. Based on spectral peak intensities, in all the spectra the amount of illite was found to be less than that of smectite. Both illite and smectite occur as both distinct phases and mixed layers (Figure 9). In undeformed samples (Figure 9A–D) the spectral peaks of illite and smectite have greater intensities than in faulted samples (Figure 9E,F). Smectite is absent in the foliated fault-core rock (Figure 9E), which also shows the lowest amount of illite of all the analyzed samples; this is consistent with the non-weathered, whitish foliated cataclastics that are often observed in the field (e.g., Figure 4B) and the observed lack of clay minerals in thin sections (Figure 7E,F). A very small amount of chlorite is also observed in the fault core rock sample (Figure 9E).

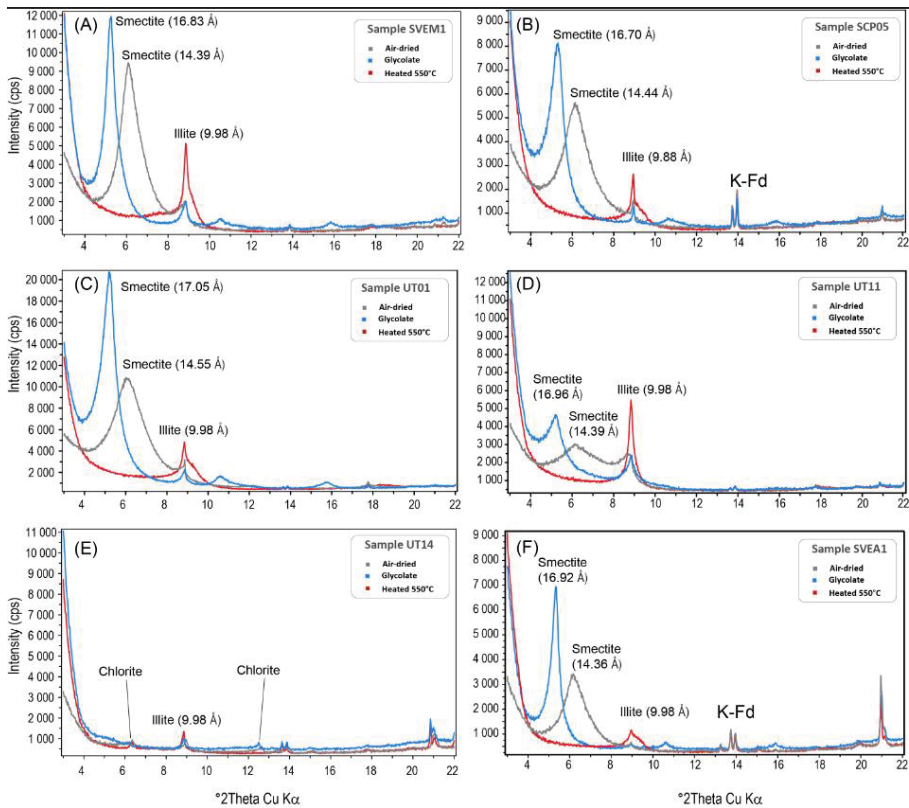


**Figure 9.** XRD diffractograms of aggregates of clay-size fractions of undeformed (A–D) and fault core (E) rocks, and a deformation band in a fault damage zone (F). Air-dried (in grey), heated at 550 °C (in red), and treated with ethylene glycol (in blue) conditions are shown.

### 5. Discussion

It is well known that the development of fault zones in sandstones can significantly modify fluid circulation pathways e.g., [12], thus influencing a variety of shallow diagenetic processes [21,24,38]. In this study, fault zones that developed in high-porosity arkosic sandstones are found to have the typical architecture described in other settings [9,24,38], being organized in a foliated fault-core surrounded by a damage zone hosting cataclastic deformation bands [34].

### 5.1. Origin of Clay Minerals

In the analyzed samples, illite and smectite were found to be the most abundant clay minerals (Figures 9 and 10) that typically occupy the spaces of the intergranular porosity of undeformed sandstones (Figures 5 and 7B). These phases are not easily distinguishable from one another under optical and electronic microscopy, however the results of XRD analysis on clay fractions indicate that illite and smectite occur both in mixed layers and as independent phases (Figure 9). Illite and smectite are among the most common clay minerals in sedimentary rocks. These minerals may form under diagenetic conditions at low pressure and temperature at near-surface conditions [5,8,24], typical of the shallow crust of the studied Rio do Peixe basin. The shallow burial depth during faulting (<1–2 km) is attested by the following conditions: (1) the syn-rift nature of extensional faults; (2) poorly lithified lithology; (3) the high-porosity framework in thin sections of undeformed sandstones; (4) the absence of high temperature mineral phases; and (5) the absence of quartz overgrowth in thin sections. Therefore, we interpret the occurrence of illite and smectite as the result of the partial weathering of K-feldspar and plagioclase grains during shallow early diagenesis under meteoric conditions [14]. This interpretation is strongly supported by the intense and selective dissolution of feldspar grains observed in thin sections (Figure 5). A detrital origin of the clay minerals in the studied samples is excluded since such clays are much more abundant in undeformed (porous) sandstones than in their faulted (non-porous) counterparts (Figure 10A–C), as discussed below.

### 5.2. Timing Between Clay Authigenesis and Faulting

The greater presence of clay minerals in the host rocks, and their scarcity or absence in the fault zone domains (both in thin sections and in X-ray diffractograms) indicates that, in the Rio do Peixe basin, clay authigenesis mostly occurred after the formation of faults. This interpretation implies that the studied fault zones acted as barriers to weathering meteoric fluids rather than preferential conduits, which is consistent with previously published data in similar lithologies. This hydraulic behavior is in agreement with pervasive grain fragmentation and cataclasis, as documented in thin sections (Figure 6), which provides a more compact, tight and impermeable fabric within the fault zones cf. [34]. Accordingly, when the studied extensional faults and deformation bands were formed at shallow burial depth, the rock volume incorporated into the fault zones could not provide an effective pathway for meteoric influx, thus compromising the process of clay authigenesis and limiting the development of clay phases. This is also consistent with: (1) the presence of Fe-oxides in the host rocks, and not in their faulted counterparts (Table 1); and (2) the intense reddish coloration of host rocks and the orange to whitish coloration of faulted rocks observed in the field (as shown schematically in Figure 3).

Therefore, we believe that no significant amount of detrital clays was present in the sandstone before deformation, due to their absence in faulted samples. If clay minerals were present in the host sandstones at the time of faulting, they would have certainly been incorporated into the fault zones, probably reducing the friction between grains and preventing (or at least hindering) both cataclasis [23,24] and the development of deformation bands. In summary, we suggest that when the diagenetic process of clay authigenesis occurred in the high-porosity undeformed sandstones, there was no significant porosity and sufficient permeability within the fault zones for meteoric fluid circulation and intense alteration of feldspars.

### 5.3. Evolutionary Model

Based on field observations and laboratory results, we propose the following evolutionary model for the generation of clay minerals after sediment deposition in the following sequence: (1) the syn- to post-sedimentary formation of extensional faults and deformation bands in poorly lithified sandstones, inducing localized grain compaction and early comminution within the fault zones; (2) the further evolution of failure and the generation of low-permeability cataclastic fault zones; (3) the beginning of the weathering process during shallow diagenesis and meteoric fluid circulation; (4) the selective

weathering and dissolution of feldspar grains in a semi-arid environment (as shown by moldic porosity in thin sections) and clay mineral authigenesis in the high-porosity undeformed sandstones and conglomerates; (5) the exhumation of faults during regional basin inversion and the formation of positive reliefs of fault zones (due to differential surface erosion) caused by a tight cataclastic fabric.

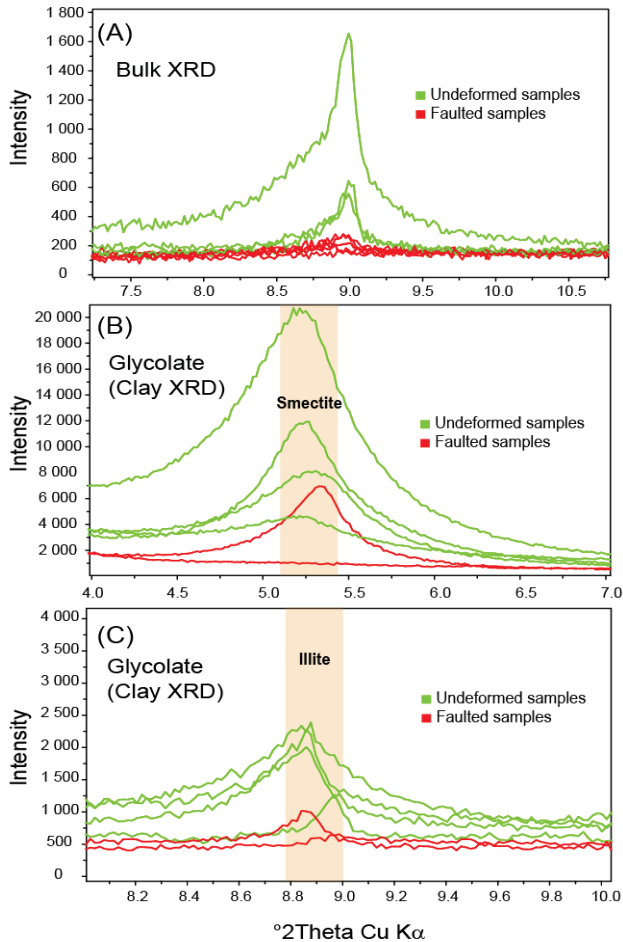


**Figure 10.** Summary diagrams showing a comparison between diffractograms of undeformed host rocks (green lines) and faulted rocks (red lines). (A) Bulk XRD analysis indicating that the amount of clay minerals in the undeformed samples is higher than that in faulted samples. (B) The relative abundance of smectite in undeformed and faulted samples. (C) The relative abundance of illite in undeformed and faulted samples.

## 6. Conclusions

We studied clay mineral assemblages in faulted, high-porosity arkosic sandstone of the Rio do Peixe basin (northeast Brazil) to understand the role of faults in clay mineral authigenesis. We integrated field observations with analysis of microstructures, optical and scanning electron microscopy and XRD (bulk and clay-fraction) mineralogy. The results obtained in this study indicate the following conclusions:

- (1) The bulk mineralogy of the Rio do Peixe sandstone does not change significantly between the undeformed and faulted domains, consisting of lithic arkose with feldspar grains generally comprising >50%.
- (2) In both undeformed and faulted domains, clay minerals are <1–2% and consist of smectite and illite, and subordinately illite–smectite mixed layers. Despite the similar mineralogy, the amount of clay is systematically less in the faulted domain than in pristine rocks and in some cases is not observed at all.
- (3) Clay minerals in the studied arkosic sandstones most likely developed during feldspar weathering processes in a shallow meteoric environment. A detrital origin of clay is excluded in the analyzed sandstones and conglomerates.
- (4) Contrary to the results of other fault rock studies in similar lithologies, clay is found to be less abundant in the faulted domains (fault core and damage zone) than in the host rocks. We conclude that this is due to the tight fabric that developed in the faulted porous sandstone, which inhibited meteoric fluid circulation and clay mineral authigenesis.

We conclude that, contrary to several other faulted settings which have a high abundance of authigenic clays, the development of fault zones in high-porosity arkosic sandstone in semi-arid regions prevents the authigenesis of clay minerals. Consequently, clay authigenesis is more efficient in undeformed sandstones than faulted domains, which has important implications for oil and water reservoir quality in siliciclastic rocks and fault behavior in structurally complex settings.

**Author Contributions:** I.B.M. participated to the fieldwork and sampling, performed petrographic and SEM analysis, contributed to manuscript writing. A.D. participated to the fieldwork, performed XRD analyses and thin section observations. F.B. conceived the research, participated to the fieldwork and sampling, contributed to manuscript writing; F.H.R.B. participated to fieldwork, contributed to manuscript writing; M.M.V. supervised SEM and petrographic analyses; F.C.C.N. organized the overall fieldwork and participated to sampling; E.S.-M. supervised and interpreted the XRD analysis; J.A.B.S. participated to the fieldwork and supported the project.

**Funding:** This research was funded by Petrobras/Federal University of Campina Grande project (TC 0050.0096065.15.9 grant to Francisco C. C. Nogueira); Fieldwork of Angela Dettori and Fabrizio Balsamo was funded by University of Parma, Italy (Overworld program 2016–2017 grant to Fabrizio Balsamo); Ingrid Maciel was supported by a Brazilian CAPES grant.

**Acknowledgments:** We kindly thank two anonymous reviewers which significantly improve the original early version of this manuscript. We thank Luca Aldega and Luciana Mantovani for helpful discussion on XRD data. We also thank the Brazilian Agency of Oil, Gas, and Biofuels (*Agência Nacional do Petróleo, ANP*) for sharing data on the Rio do Peixe basin. Fabrizio Balsamo wishes to dedicate this work in faulted sandstones to his mother Isabella Bellina, died in Albano Laziale (Rome, Italy) the 14 June 2018.

**Conflicts of Interest:** The authors declare no conflicts of interest.

## References

1. Xi, K.; Cao, Y.; Liu, K.; Jähren, J.; Zhu, R.; Yuan, G.; Hellevang, H. Authigenic minerals related to wettability and their impacts on oil accumulation in tight sandstone reservoirs: An example from the Lower Cretaceous Quantou Formation in the southern Songliao Basin, China. *J. Asian Earth Sci.* **2018**. [[CrossRef](#)]
2. Rice, J.R. Fault stress states, pore pressure distributions, and the weakness of the San Andreas Fault. In *International Geophysics*; Academic Press: Cambridge, MA, USA, 1992; pp. 475–503.
3. Fisher, Q.J.; Knipe, R.J. Fault sealing processes in siliciclastic sediments. In *Faulting, Fault Sealing and Fluid Flow in Hydrocarbon Reservoirs. Geol. Soc. Spec. Publ.* **1998**, *147*, 117–134. [[CrossRef](#)]
4. Haines, S.H.; Van der Pluijm, B.A.; Ikari, M.J.; Saffer, D.M.; Marone, C. Clay fabric intensity in natural and artificial fault gouges: Implications for brittle fault zone processes and sedimentary basin clay fabric evolution. *J. Geophys. Res.* **2009**, *114*, B05406. [[CrossRef](#)]
5. Lander, R.H.; Bonnell, L.M. A model for fibrous illite nucleation and growth in sandstones. *AAPG Bull.* **2010**, *94*, 1161–1187. [[CrossRef](#)]
6. Faulkner, D.R.; Jackson, C.A.L.; Lunn, R.J.; Schlische, R.W.; Shipton, Z.K.; Wibberley, C.A.J.; Withjack, M.O. A review of recent developments concerning the structure, mechanics and fluid flow properties of fault zones. *J. Struct. Geol.* **2010**, *32*, 1557–1575. [[CrossRef](#)]

7. Balsamo, F.; Aldega, L.; De Paola, N.; Faoro, I.; Storti, F. The signature and mechanics of earthquake ruptures along shallow creeping faults in sediments. *Geology* **2014**, *42*, 435–438. [[CrossRef](#)]
8. Buatier, M.D.; Cavaiilhes, T.; Charpentier, D.; Lerat, J.; Sizun, J.P.; Labaume, P.; Gout, C. Evidence of multi-stage faulting by clay mineral analysis: Example in a normal fault zone affecting arkosic sandstones (Annot sandstones). *J. Struct. Geol.* **2015**, *75*, 101–117. [[CrossRef](#)]
9. Antonellini, M.; Aydin, A. Effect of Faulting on Fluid Flow in Porous Sandstones: Petrophysical Properties. *AAPG Bull.* **1994**, *78*, 355–377.
10. Rawling, G.C.; Goodwin, L.B.; Wilson, J.L. Internal architecture, permeability structure, and hydrologic significance of contrasting fault-zone types. *Geology* **2001**, *29*, 43–46. [[CrossRef](#)]
11. Eichhubl, P.; Taylor, W.L.; Pollard, D.D.; Aydin, A. Paleo-fluid flow and deformation in the Aztec Sandstone at the Valley of Fire, Nevada—Evidence for the coupling of hidrogeologic, diagenetic, and tectonic process. *GSA Bull.* **2004**, *116*, 1120–1136. [[CrossRef](#)]
12. Fossen, H.; Schultz, R.A.; Shipton, Z.K.; Mair, K. Deformation bands in sandstone: A review. *J. Geol. Soc.* **2007**, *164*, 755–769. [[CrossRef](#)]
13. Caine, J.S.; Minor, S.A. Structural and geochemical characteristics of faulted sediments and inferences on the role of water in deformation, Rio Grande Rift, New Mexico. *GSA Bull.* **2009**, *121*, 1325–1340. [[CrossRef](#)]
14. Vrolijk, P.; Van der Pluijm, B. Clay gouge. *J. Struct. Geol.* **1999**, *21*, 1039–1048. [[CrossRef](#)]
15. Gibson, R. Physical character and fluid-flow properties of sandstone-derived fault gouge, in Structural Geology in Reservoir Characterization. *Geol. Soc. Spec. Publ.* **1998**, *127*, 87–93. [[CrossRef](#)]
16. Fisher, Q.; Knipe, R.J. The permeability of faults within siliclastic petroleum reservoirs of the North Sea and Norwegian Continental Shelf. *Mar. Pet. Geol.* **2001**, *18*, 1063–1081. [[CrossRef](#)]
17. Fossen, H.; Bale, A. Deformation bands and their influence on fluid flow. *AAPG Bull.* **2007**, *91*, 1685–1700. [[CrossRef](#)]
18. Rotevatn, A.; Torabi, A.; Fossen, H.; Braathen, A. Slipped deformation bands: A new type of cataclastic deformation bands in Western Sinai, Suez rift, Egypt. *J. Struct. Geol.* **2008**, *30*, 1317–1331. [[CrossRef](#)]
19. Eichhubl, P.; Davatzes, N.C.; Becker, S.P. Structural and diagenetic control of fluid migration and cementation along the Moab Fault, Utah. *AAPG Bull.* **2009**, *93*, 653–681. [[CrossRef](#)]
20. Balsamo, F.; Storti, F.; Salvini, F.; Lima, C.C. Structural and petrophysical evolution of extensional fault zones in low-porosity, poorly lithified sandstones of the Barreiras Formation NE Brazil. *J. Struct. Geol.* **2010**, *32*, 1806–1826. [[CrossRef](#)]
21. Balsamo, F.; Bezerra, F.H.; Vieira, M.; Storti, F. Structural control on the formation of iron oxide concretions and Liesegang bands in faulted, poorly lithified Cenozoic sandstones of the Paraiba basin, Brazil. *Bulletin* **2013**, *125*, 913–931. [[CrossRef](#)]
22. Williams, J.N.; Toy, V.G.; Massiot, C.; McNamara, D.D.; Wang, T. Damaged beyond repair? Characterising the damage zone of a fault late in its interseismic cycle, the Alpine Fault, New Zealand. *J. Struct. Geol.* **2016**, *90*, 76–94. [[CrossRef](#)]
23. Hoffman, U.; Endell, K.; Wilm, M.D. Kristallstruktur und Quellung von Montmorillonit. *Z. Kristallogr. Cryst. Mater.* **1933**, *86*, 340–348. [[CrossRef](#)]
24. Solum, J.G.; Davatzes, N.C.; Lockner, D.A. Fault-related clay authigenesis along the Moab Fault: Implications for calculations of fault rock composition and mechanical and hydrologic fault zone properties. *J. Struct. Geol.* **2010**, *32*, 1899–1911. [[CrossRef](#)]
25. Van der Pluijm, R. Out-of-Plane Bending of Masonry: Behaviour and Strength Eindhoven. Ph.D. Thesis, Technische Universiteit Eindhoven, Eindhoven, The Neitherlands, 1999.
26. Solum, J.G.; Van der Pluijm, B.A.; Peacor, D.R. Neocrystallization, fabrics and age of clay minerals from an exposure of the Moab Fault, Utah. *J. Struct. Geol.* **2005**, *27*, 1563–1576. [[CrossRef](#)]
27. Sénant, J.; Popoff, M. Early Cretaceous extension in northeast Brazil related to the South Atlantic opening. *Tectonophysics* **1991**, *198*, 35–46. [[CrossRef](#)]
28. Matos, R.M.D. The Northeast Brazilian Rift System. *Tectonics* **1992**, *11*, 766–791. [[CrossRef](#)]
29. Françolin, J.B.L.; Cobbold, P.R.; Sztamari, P. Faulting in the early Cretaceous Rio do Peixe basin (NE Brazil) and its significance for the opening of the Atlantic. *J. Struct. Geol.* **1994**, *16*, 647–661. [[CrossRef](#)]
30. De Castro, D.L.; De Oliveira, D.C.; Gomes Castelo Branco, R.M. On the tectonics of the Neocomian Rio do Peixe Rift Basin, NE Brazil: Lessons from gravity, magnetics, and radiometric data. *J. South. Am. Earth Sci.* **2007**, *24*, 184–202. [[CrossRef](#)]



31. Albuquerque, J.P.T. *Inventário Hidrogeológico do Nordeste*; Folha 15; Sudene, Divisão de Documentação: Recife, Brazil, 1970; p. 187.
32. Lima, M.R.; Coelho, M.P.C.A. Estudo palinológico da sondagem de Lagoa do Forno Bacia do Rio do Peixe Cretáceo do Nordeste do Brasil. São Paulo. *Bol. IG-USP Sci.* **1987**, *18*, 67–83.
33. Córdoba, V.C.; Antunes, A.F.; Jardim de Sá, E.F.; Nunes da Silva, A.; Sousa, D.C.; Lins, F.A.P.L. Análise estratigráfica e estrutural da Bacia do Rio do Peixe Nordeste do Brasil: Integração de dados a partir do levantamento sísmico pioneiro 0295\_rio\_do\_peixe\_2d. *Bol. Geoci. Petrobras* **2008**, *16*, 53–68.
34. Nicchio, M.A.; Nogueira, F.C.C.; Balsamo, F.; Souza, J.A.B.; Carvalho, B.R.B.; Bezerra, F.H.R. Development of cataclastic foliation in deformation bands in feldspar-rich conglomerates of the Rio do Peixe Basin, NE Brazil. *J. Struct. Geol.* **2018**, *107*, 132–141. [[CrossRef](#)]
35. Nogueira, F.C.C.; Marques, F.O.; Bezerra, F.H.R.; de Castro, D.L.; Fuck, R.A. Cretaceous intracontinental rifting and post-rift inversion in NE Brazil: Insights from the Rio do Peixe Basin. *Tectonophysics* **2015**, *644*, 92–107. [[CrossRef](#)]
36. Araujo, R.E.B.; Bezerra, F.H.R.; Nogueira, F.C.C.; Balsamo, F.; Carvalho, B.R.B.M.; Souza, J.A.B.; Sanglard, J.C.D.; de Castro, D.L.; Melo, A.C.C. Basement control on fault formation and deformation band damage zone evolution in the Rio do Peixe Basin, Brazil. *Tectonophysics* **2018**, *745*, 117–131. [[CrossRef](#)]
37. Folk, R.L. *Petrology of Sedimentary Rocks*; Hemphill Publishing Company: Austin, TX, USA, 1968; p. 182.
38. Balsamo, F.; Storti, F.; Grocke, D. Fault-related fluid flow history in shallow marine sediments from carbonate concretions, Croton Basin, south Italy. *J. Geol. Soc.* **2012**, *169*, 613–626. [[CrossRef](#)]



© 2018 by the authors. Licensee MDPI, Basel, Switzerland. This article is an open access article distributed under the terms and conditions of the Creative Commons Attribution (CC BY) license (<http://creativecommons.org/licenses/by/4.0/>).

Article

# Structural Controls on Copper Mineralization in the Tongling Ore District, Eastern China: Evidence from Spatial Analysis

Tao Sun <sup>1,2,\*</sup> , Ying Xu <sup>3</sup>, Xuhui Yu <sup>4</sup>, Weiming Liu <sup>1</sup>, Ruixue Li <sup>1</sup>, Zijuan Hu <sup>1</sup> and Yun Wang <sup>5</sup>

<sup>1</sup> School of Resources and Environmental Engineering, Jiangxi University of Science and Technology, Ganzhou 341000, China; wm\_liu@sina.com (W.L.); liruihue0911@163.com (R.L.); m18370956200@163.com (Z.H.)

<sup>2</sup> Jiangxi Key Laboratory of Mining Engineering, Jiangxi University of Science and Technology, Ganzhou 341000, China

<sup>3</sup> Institute of Multipurpose Utilization of Mineral Resources, CAGS, Chengdu 610041, China; yingxuhui@foxmail.com

<sup>4</sup> College of Earth Sciences, Chengdu University of Technology, Chengdu 61005, China; yuxuhui@foxmail.com

<sup>5</sup> School of Water Resource and Environment, China University of Geosciences, Beijing 341515, China; yunwang\_1123@163.com

\* Correspondence: suntao@jxust.edu.cn; Tel.: +86-0797-831-2751

Received: 4 May 2018; Accepted: 14 June 2018; Published: 15 June 2018

**Abstract:** Structures exert significant controls on hydrothermal mineralization, although such controls commonly have cryptic expression in geological datasets dominated by 2D maps. Analysis of spatial patterns of mineral deposits and quantification of their correlation with detailed structural features are beneficial to understand the plausible structural controls on mineralization. In this paper, a series of GIS-based spatial methods, including fractal, Fry, distance distribution and weights-of-evidence analyses, were employed to reveal structural controls on copper mineralization in the Tongling ore district, eastern China. The results indicate that Yanshanian intrusions exert the most significant control on copper mineralization, followed by EW-trending faults, intersections of basement faults and folds. The scale-variable distribution patterns of copper occurrences are attributed to the different structural controls operating in the basement and sedimentary cover. In the basement, EW-trending faults serve as pathways for channeling Yanshanian magma from a deep magma chamber to structurally controlled trap zones in the caprocks, imposing an important regional control on the spatial distribution of Cretaceous magmatic-hydrothermal system genetically related to copper mineralization. In the sedimentary cover, bedding-parallel shear zones, formed during the progressive folding and shearing in Indosinian and overprinted by tensional deformation in Yanshanian, act as favorable sites for hosting, focusing and depositing the ore-bearing fluids, playing a vital role in the localization of stratabound deposits at fine scale.

**Keywords:** structural control; spatial analysis; fractal; buffer-based analysis; data-driven model; Tongling

## 1. Introduction

Structural controls on hydrothermal mineralization at various scales have been widely recognized [1–5]. At a global scale, hydrothermal systems usually form in specific tectonic settings, e.g., porphyry systems mostly occur in magmatic arc settings [1–3]. At a regional scale, hydrothermal deposits show close proximity to regional faults system or shear zones, which sever as pathways for transporting ore-forming fluids from deep-seated sources to shallow depositing spots [6,7]. At a deposit scale, hydrothermal replacement disseminations, breccias and veins, which are related to

subsidiary fracture zones of regional structures, serve as favorable sites for focusing and depositing the ore-bearing fluids and are interpreted to be responsible for localization of orebodies [7]. However, such controls may usually have cryptic expression in various sources of geological records, because (i) structures, especially large-scale structures, may have variable expressions from depth to surface (e.g., mylonite zone at depth and fault zone near the surface) [7]; (ii) spatial associations between map-generalized structures and surface-projected deposits in 2D maps may lead to an inaccurate view or even misunderstanding with respect to controls of mineralization; and (iii) structural features together with structurally controlled mineralization may be formed through successive deformation and polyphase tectonics [8]. Thus, it is a challenge to identify ore-related structural features and elucidate structural controls, as well as measure their contributions to the formation of mineral deposits.

GIS-based spatial analysis has been well-established and developed in the last three decades, assisting in identification of inherent patterns of ore-related geological features and delineation of interplay of the processes that constrain the formation of mineral deposits [9–12]. More specifically, with the help of quantitative methods and easy-to-use GIS software, delineating the spatial patterns of known occurrences of mineral deposits and their associations with geological features (e.g., structural, lithological and geochemical features) can, in addition to field observations, geochemical and mineralogical laboratory methods, provide insights into the controlling mechanisms operating at different scales [10,13–15], especially in the brownfield areas where a relatively large number of mineral deposits have been well-explored [15]. Furthermore, recognition of geological features controlling the mineralization is critical for defining exploration criteria in future prospecting [16].

Since mineral occurrences are simplified to be represented as points on large-scale maps in various applications of spatial analyses, methods of spatial analysis for point patterns have been increasingly employed in studying spatial distribution and geological controls of mineral deposits, mostly involving fractal geometry [17,18] and Fry analysis [19,20]. Through statistical calculation, fractal and Fry analyses are able to highlight the distribution pattern of mineral deposits that may be difficult to be recognized by exclusively relying on visual interpretation [5]. Moreover, distance distribution [14,21] and weights-of-evidence (WofE) analyses [22,23] can further quantify the strength of the spatial association between mineral deposits and geological features believed to be favorable in predicting the location of the mineralization. A joint application of these methods is necessary as individual methods only characterizes a particular aspect, such as non-random clustering of deposits or preferential direction of deposits distribution, of complex spatial features of mineralization systems [10,24].

The Tongling ore district (TOD) is one of the most important Cu producers in China, with totally estimated reserves of over 5 Mt copper [25]. Large stratabound copper deposits constitute the majority of the copper reserves in this area, e.g., the Donggushan deposit with 1 Mt Cu @ 1.01% [26] and the Xinqiao deposit with 0.5 Mt Cu @ 0.71% [27], which have attracted many studies focusing on their genesis [28–36]. These stratabound deposits were firstly considered to be of SEDEX origin by many researchers because of their stratiform orebodies and massive sulfide ores, and the major orebodies occurring in the Carboniferous strata were thought to be products of Late Paleozoic (Hercynian) sedimentary exhalative system [28–30]. Some researchers further proposed an exhalative origin overprinted by Yanshanian magmatic-hydrothermal processes, based on the restricted occurrences of the stratabound orebodies in areas where Yanshanian intrusions are particularly extensive [31–33]. In contrast, some authors advocated that the stratabound mineralization is of epigenetic origin and genetically associated with the Jurassic-Cretaceous tectono-thermal events [34–36]. The precise geochronological data derived from recent studies confirmed that the massive sulfide and skarn orebodies were coeval with the Yanshanian intrusions [25,27,37], supporting the magmatic-hydrothermal origin of these stratabound deposits.

Although the genesis of stratabound deposits is still disputable, most of the researchers tend to agree with the epigenetic origin or at least the dominant contribution of Yanshanian magmatic-hydrothermal activities in the superimposed ore-forming processes [38,39]. In the

magmatic-related genetic model, the stratiform orebodies were formed as a result of progressive fluid-rock interaction along the bedding-parallel structurally controlled conduits and were integral but distal parts of a large hydrothermal system that produced the proximal skarn orebodies at the contact zones and porphyry orebodies in the Yanshanian intrusions [35]. Such hydrothermal system and stratabound deposits are similar to their counterparts elsewhere [35], among which the porphyry-skarn polymetallic deposits in the Ertsberg district of Indonesia and manto-type copper deposits in Chile are two representative examples. In the Ertsberg district, the Ertsberg East skarn orebody, one of the largest orebodies, is hosted by a bedding-parallel fault-bounded zone between the limestone of the Faumai Formation and dolomitic carbonate of the Waripi Formation [40]. In the Punta del Cobre district in Chile, the stratabound tabular orebodies occur in the andesite breccia horizons between underlying massive andesite and overlying shale, while the sites of economic copper concentration appear to be controlled by faults [41]. Since structure is an important controlling factor of these stratabound deposits, some relevant studies have been conducted in the TOD, including the spatial patterns [34], deformation model [42] and formative process [43] of ore-controlling structures. However, these studies mostly focus on theoretical deduction and qualitative analysis, and lack quantitative analysis concerning detailed structural features. Hence, this paper attempts to delineate the structural controls by both qualitative and quantitative analytical methods, focusing on the structural controlling mechanisms operating at different scales, which can facilitate the understanding of the formation of copper deposits and provide criteria for future exploration in the TOD.

## 2. Materials and Methods

### 2.1. Study Area

The TOD is situated in the central part of the Middle-Lower Yangtze Cu-Au-Fe metallogenic belt (MLYMB) along the Northern margin of the Yangtze craton, bordered by the Qingling-Dabieshan orogenic belt and the North China craton to the North (Figure 1a).

The Northern Yangtze craton is underlain by tonalitic-trondhemitic-granitic (TTG) gneisses aged from 3.45 to 2.87 Ga [44]. The TTG gneisses and unconformably overlying Archean to Paleoproterozoic metamorphic rocks constituted the basement of the TOD [44]. From Cambrian to Middle Triassic, the TOD represented a stable trough filled with carbonate and clastic rocks of shallow marine facies [36]. Two sedimentary sequences developed in this period, including the Lower Silurian to Upper Devonian regressive bathyal to littoral clastic rocks and overlying Upper Carboniferous to Middle Triassic littoral to neritic carbonates interbedded with bathyal and alternative marine-continental clastic rocks [45]. The sedimentary strata were folded during the Indosinian movement which is initiated at the end of Middle Triassic due to the collision between the Yangtze craton and North China craton [35]. From Jurassic to Cretaceous, this region experienced an event that has long been interpreted as an intracontinental deformation stage with abundant magmatism [35,38,45], and developed thick terrestrial sedimentary and volcanic sequences which unconformably overlie the Silurian to Triassic strata. The detailed lithological description and contact relationship of sedimentary strata in the TOD are listed in Table 1.

The regional structures in the TOD are dominated by several folds with NE-striking axial surfaces and sigmoidal-shaped axes (Figure 1b). Secondary structures include NE-trending thrust faults, NW- and NNW-trending strike-slip faults [46]. The regional gravity anomalies [47] and deep seismic reflection profiles [48] indicate the presence of EW- and NS-trending basement faults. The Yanshanian magmatism resulted in more than 70 intrusions that are mainly composed of granodiorite, quartz monzonite, gabbro monzonite and their hypabyssal equivalents [26,49]. High-precision zircon U-Pb dating results have shown that the intrusions of this region were formed in the Early Cretaceous (mainly 145–129 Ma) [50,51]. The copper-polymetallic deposits discovered in the TOD are dominated by skarn-type, with minor porphyry-type copper deposits occurring in the deeper parts of some skarn deposits [45,50,51]. More than 60 copper-polymetallic skarn deposits and prospects have been

discovered in the TOD, mainly clustering in four ore fields designated as Tongguanshan, Shizishan, Fenghuangshan and Shatanjiao ore field from west to east (Figure 1b).

**Table 1.** Stratigraphy and tectonic events in the Tongling ore district

Epoch	Lithostratigraphic Unit	Code	Lithological Description	Tectonic Activity
Upper Cretaceous	Xuannan Formation	K <sub>2</sub> x	Conglomerate and sandstone	Yanshanian movement (ca. 135 Ma)
Middle Jurassic	Luoling Formation	J <sub>2</sub> l	Feldspar sandstone, siltstone and shale	
Lower Jurassic	Moshan Formation	J <sub>1</sub> m	Feldspar sandstone with interlays of silty shale and coal, conglomerate at bottom	
Middle Triassic	Tongtujian Formation	T <sub>2</sub> t	Siltstone with interlays of sandy shale	Indosinian movement (ca. 195 Ma)
	Yueshan Formation	T <sub>2</sub> y	Limestone, dolomite in upper and siltstone in lower	
Lower Triassic	Nanlinghu Formation	T <sub>1</sub> n	Limestone	
	Helongshan Formation	T <sub>1</sub> h	Limestone	
Upper Permian	Yingkeng Formation	T <sub>1</sub> y	Limestone with interlays of silt shale	
	Dalong Formation	P <sub>2</sub> d	Siliceous shale with interlays of limestone	
Lower Permian	Gongtan Formation	P <sub>2</sub> l	Fine sandstone and silt shale with interlays of coal	
	Gufeng Formation	P <sub>1</sub> g	Siliceous slate and siliceous shale	
	Qixia Formation	P <sub>1</sub> q	Bioclastic limestone in upper and carbonaceous shale in lower	
Upper Carboniferous	Chuanshan Formation	C <sub>2</sub> c	Orbicular limestone and bioclastic limestone	
	Huanglong Formation	C <sub>2</sub> h	Bioclastic limestone and dolomite	
Upper Devonian	Wutong Formation	D <sub>3</sub> w	Quartz sandstone and silty shale	
Middle Silurian	Fentou Formation	S <sub>2</sub> f	Sandstone, siltstone and sandy shale	
Lower Silurian	Gaojiabian Formation	S <sub>1</sub> g	Black shale	
	Wufeng Formation	O <sub>3</sub> w	Black siliceous shale	
Upper Ordovician	Tangtou Formation	O <sub>3</sub> t	Calcareous shale with interlayers of limestone	
Middle Ordovician	Tangshan Formation	O <sub>2</sub> t	Limestone with interlayers of thin slate	
Lower Ordovician	Lunshan Formation	O <sub>1</sub> l	Limestone in upper and dolomite in lower	
Cambrian	Huangjiabang Formation	ε	Limestone	
Precambrian	Dongling Group	Pt <sub>3</sub> d	Biotite quartz schist and gneiss	Jinning movement (ca. 850–800 Ma)

Modified from [26]; dashed line represents disconformity; and double line represents angular unconformity.

The copper occurrences (including known deposits and prospects) and structural features employed in this study were derived from Geological Database of Bureau of Geological and Mineral Resources of Anhui Province based on 1:50,000 geological survey and complemented by the literature available for the study area concerning regional geological settings [26,42,45,49,51]. The raw data were examined before being inputted into a spatial database. Only those copper and copper-dominated polymetallic deposits were included in the analysis, since the other types of copper-related polymetallic deposits may be products of different structurally controlled processes when compared with copper mineralization. The structural features were reclassified into three categories including the basement faults, cover faults and folds. All the examined data were compiled to vector formats and imported into the ArcGIS 10 platform (Environmental Systems Research Institute, Redlands, CA, USA) for the subsequent spatial analyses.

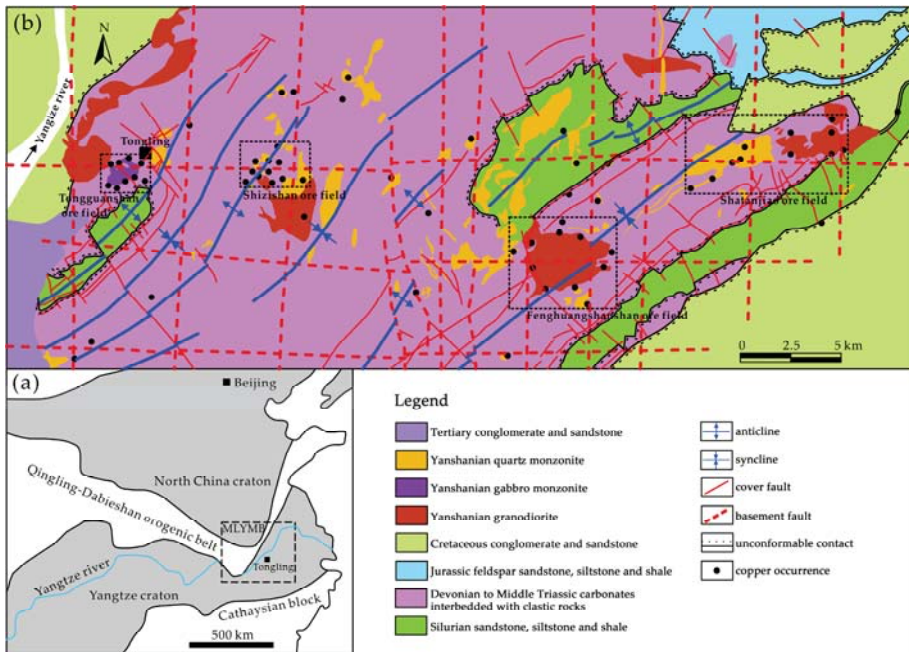


**Figure 1.** Geological map of the study area: (a) simplified tectonic map showing the location of the TOD; and (b) geological map of the TOD showing the locations of copper occurrences, modified from a 1:50,000 scale geological map [52] and [37,42,43,53].

2.2. Fractal Analysis

Fractals are entities that have similar geometrical patterns when observed in ranges of scales [17]. This scale-invariance can be depicted by a power-law proportional relationship between a measurement of the target pattern and its scale [17]. Various methods have been proposed for estimating the fractal dimension of a given pattern, each of which reveals an aspect of geometrical complexity of the target pattern [10,54]. The box-counting and radial-density methods, which are the most commonly used methods in analyzing geological point patterns, were employed to estimate corresponding fractal dimensions in this study. The fractal analysis can reveal the statistical scale-related laws of the distribution of copper occurrences, which may be products of structurally controlled processes.

In the box-counting method, the study area involving geological features of interest (e.g., mineral deposits) is overlain by a grid that comprises square cells or boxes with side length  $\delta$ , and then the number  $N(\delta)$  of those boxes containing parts of target features is counted (Figure 2a). The above process is repeated using different box size  $\delta$  to obtain corresponding box number  $N(\delta)$  (Figure 2b,c). If the pattern under analysis pertains to fractal pattern, the relationship between  $N(\delta)$  and  $\delta$  should follow a power-law function as below [17]:

$$N(\delta) \propto A\delta^{-D_B} \tag{1}$$

where  $D_B$  is the box-counting fractal dimension, and  $A$  is a constant. Practically, a graph of  $\log(N(\delta))$  versus  $\log(\delta)$  is plotted and then a best-fit regression line is drawn by the least square method, while the slope of the regression line represents the box-counting fractal dimension (Figure 2d).

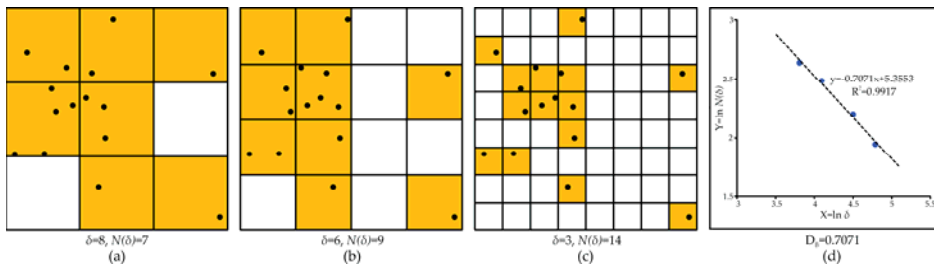


**Figure 2.** Schematic diagram of box-counting analysis: (a) 7 boxes containing target points with box size  $\delta = 8$ ; (b) 9 boxes counted with box size  $\delta = 6$ ; (c) 14 boxes counted with box size  $\delta = 3$ ; and (d) log-log plot revealing the power-law relationship of counted box number  $N(\delta)$  and box size  $\delta$ , obtaining box-counting fractal dimension  $D_B = 0.7071$ .

In the radial-density method, fractal points, also called fractal dusts, have been demonstrated to satisfy a radial-density relationship, which can be described as [55]:

$$d \propto Br^{D_R-2} \tag{2}$$

where,  $d$  is the average point density of the circles with a radius  $r$  that center in every point, and  $B$  is a constant, while  $D_R$  is the radial-density fractal dimension. Likewise,  $D_R$  is usually obtained by calculating the slope of a regression line that presents the linear relationship of  $d$  and  $r$  in a log-log plot.

### 2.3. Fry Analysis

Fry analysis is a geometrical method of spatial autocorrelation for analyzing point patterns [22], which is implemented by the construction of an autocorrelation diagram called Fry plot. Figure 3 shows a basic procedure for creating Fry plot [10,24]: (i) two analogue sheets including an original sheet recording raw points (Figure 3a) and a blank tracing sheet are prepared; (ii) the origin of the original sheet  $O$  is placed on one of the raw points, thus preserving the orientations and distances of all the other points (Figure 3b); (iii) the points in the original sheet are then translated to the tracing sheet with  $O$  coinciding with the origin of the tracing sheet  $O'$  (Figure 3c); (iv) the origin  $O$  moves to another raw point (Figure 3d), and the new distribution pattern of raw points is copied to the tracing sheet following step (iii) (Figure 3f). This procedure is repeated until every point in the original sheet is used as the origin  $O$  (Figure 3e,f), resulting in  $(n^2-n)$  points in the tracing sheet for  $n$  raw points (Figure 3g). The final tracing sheet is termed as Fry plot, and the points in this sheet are called Fry points.

Fry plot records the distances and orientations of each raw point relative to every other point, thus enhancing subtle patterns of target point features [24], based on which rose diagrams are usually constructed to analyze preferential orientations of point pairs within specific distances that reveal the directional controls on mineralization at different map scales.

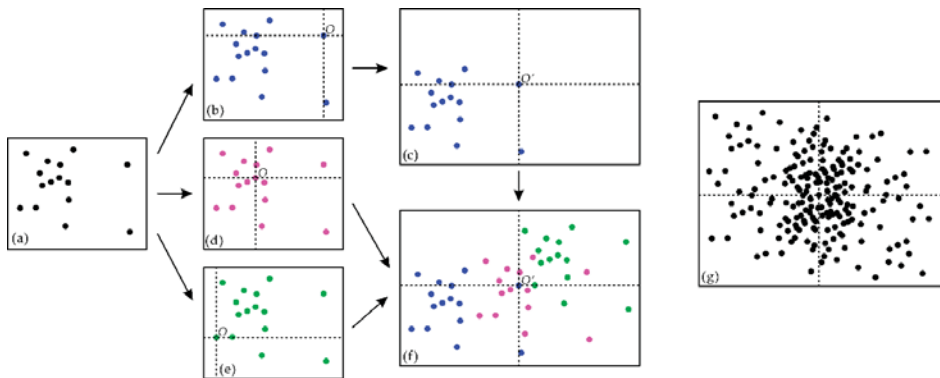


**Figure 3.** Schematic diagram for constructing a Fry plot: (a) the original sheet records raw points; (b) the origin *O* is placed on one of the raw points; (c) distribution pattern of raw points according to the origin *O* is transferred to the tracing sheet; (d,e) the origin *O* is re-placed on every raw point; (f) the tracing sheet records all distribution patterns of raw points with respect to different origins; and (g) Fry plot is constructed.

#### 2.4. Distance Distribution Analysis

Distance distribution analysis is a spatially buffer-based method for quantifying spatial association between a set of points (i.e., mineral occurrences) and another set of spatial features [24,56]. This analysis involves calculating and comparing the cumulative relative frequency according to given distances from a certain set of geological features to (i) mineral occurrence locations (denoted as  $D_M$ ) and (ii) non-occurrence locations (denoted as  $D_N$ ).  $D_N$  indicates naturally random probability density distribution of regular patterns within a given buffer distance, while  $D_M$  presents a non-random probability density distribution of mineralized patterns that is characterized by unevenly clustering of mineral occurrences within the corresponding buffer. The difference  $D$ , which is calculated by  $(D_M - D_N)$ , represents how much the cumulative frequency of mineral occurrences (i.e.,  $D_M$ ) is higher or lower than that expected due to chance (i.e.,  $D_N$ ), measuring the intensity of spatial association between the analyzed geological feature and mineralization.

In order to manifest statistically if  $D_M$  is significantly greater than  $D_N$ , an upper confidence band for the curve of  $D_N$  (denoted as  $uc$ ) can be given by [57]:

$$uc = D_N + \sqrt{9.21(M + N)/4MN} \tag{3}$$

where  $M$  is the number of mineral occurrences that used to estimate  $D_M$ , while  $N$  is the number of non-occurrence locations using for calculating  $D_N$ , and 9.21 is a constant for significance level  $\alpha = 0.01$  [24].

#### 2.5. Weights of Evidence (WofE) Analysis

The WofE analysis is a data-driven Bayesian statistical method that offers a quantitative measurement of spatial association between a set of given geological features and the target occurrences (e.g., mineral deposits, prospects or geological anomalies) [58,59].

A detailed mathematical explanation of the WofE method is available in Bonham-Carter (1994) [9]. In the GIS-based application of a mineral occurrence-related analysis, the WofE analysis is implemented on the basis of several binary predictor maps of geological features [9]. Firstly, the study area is subdivided into  $T$  square cells with an equal size, among which  $D$  cells are occupied by mineral occurrences. The prior probability can be defined as:



$$P_{prior} = P(D) = \frac{D}{T} \quad (4)$$

and the relative importance of spatial association between the geological feature  $B_i$  and mineralization is estimated by a pair of weights, namely positive weight  $W^+$  and negative weight  $W^-$ , which can be given by:

$$W^+ = \ln \left\{ \frac{P(B|D)}{P(B|\bar{D})} \right\}, \quad W^- = \ln \left\{ \frac{P(\bar{B}|D)}{P(\bar{B}|\bar{D})} \right\} \quad (5)$$

where  $P$  denotes the corresponding probability;  $B$  and  $\bar{B}$  are the presence and absence of geological features;  $D$  and  $\bar{D}$  are the presence and absence of mineral occurrences.  $P(B|D)$ , for example, represents the probability of  $B$  occurring given the presence of  $D$ . The contrast  $C$  is defined as an overall measurement of spatial correlation, which is given by:

$$C = W^+ - W^- \quad (6)$$

In order to evaluate the significance of the contrast  $C$ , the confidence of the contrast (denoted as  $C_s$ ), obtained from a Student  $t$ -test, is employed here and defined as:

$$C_s = \frac{C}{S(C)} = \frac{C}{\sqrt{S^2(W^+) + S^2(W^-)}} \quad (7)$$

where  $S$  denotes the standard deviation of the corresponding parameter.

### 3. Results and Discussion

#### 3.1. Spatial Patterns of Copper Occurrences

The box-counting log-log graph shows that the distribution of copper occurrences in the study area exhibits a bifractal pattern, i.e., the log-log plot of box number  $N(\delta)$  versus box size  $\delta$  can be fitted with two regression lines (Figure 4a), resulting in two fractal dimensions of 0.2468 ( $\delta \leq 1.6$  km) and 0.75 ( $\delta > 1.6$  km). In contrast, the radial-density analysis yields a trifractal pattern, as indicated by three regression lines that represent three fractal dimensions varying from 0.796 ( $r \leq 1.4$  km), 1.1722 (between 1.5 and 4.5 km) to 0.8092 ( $r > 4.5$  km) (Figure 4b). A single regression line represents a power-law (fractal) relationship between the measurements and their scales, implying a scale-invariance pattern resulted from a nonlinear process. In this study, the different fractal patterns of copper occurrences indicated by the multi-line fractal model could be ascribed to the different ore-controlling processes operating at different scales. It is noteworthy that the log-log graph, especially for radial-density analysis, seems to be alternatively fitted with one single regression line. However, the two-lines and three-lines fractal models shown in Figure 4 are assumed to be optimum because they reach the maximum regression coefficients ( $R^2$ ) of the fitted lines, meaning that the reduction of any regression line would lower the regression coefficients.

Although apparent differences in the fractal dimensions are noted in the above analyses, there is a general agreement between the result of box-counting method and that of radial-density analysis, such that variations in fractal dimensions, indicated by intersection of the neighbor regressing lines, both occur at around 1.5 km, suggesting that the different fractal structures exist within identical ranges (within 1.5 km and beyond 1.5 km) in both box-counting and radial-density fractal relationship. It is also noted that there is an intersection at 4.5 km in the radial-density fractal plot; however, it is not clear whether there also exists another fractal dimension in the box-counting analysis when taking box size greater than 4.5 km, since box number under such situation is not large enough to be statistically counted.

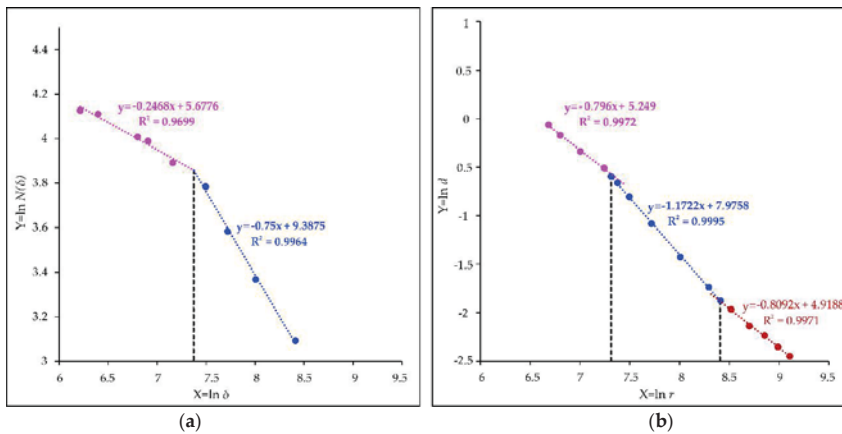


**Figure 4.** Log-log plot defining the fractal dimensions of spatial pattern of copper occurrences in the TOD: (a) box-counting linear relationship; and (b) radial-density linear relationship.

The results of fractal analyses in this study, including the multi-fractal dimension model and fractal structures occurring within identical ranges, are consistent with those of some previous studies [10,15,16,24]. It is considered that discrepancies in fractal dimensions are plausibly linked to different geological controls operating at diverse scales, e.g., regional-, local- and prospect-scale [10]. Nevertheless, such scale-variable geological controls are still cryptic and need to be delineated by further analysis.

Fry analysis has been performed to investigate the orientations of plausible controls on copper mineralization. 3906 Fry points were delivered from 63 copper occurrences in the TOD (Figure 5a), based on which rose diagrams were constructed. The rose diagram for all Fry points illustrates a simply dominant EW trend (Figure 5b), suggesting a fundamental EW-trending control on copper mineralization at regional scale. Since fractal analyses indicate variations in fractal dimensions around 1.5 and 4.5 km, we also analyzed the characteristics of Fry points within these ranges. The rose diagram for Fry points within 4.5 km of each other indicates a preferential NNE trend, with subordinate NE and EW trends (Figure 5c). The rose diagram for Fry points within 1.5 km of each other exhibits a main NE-NEE trend, with subsidiary trends in EW and NS directions (Figure 5d).

The results of Fry analysis infer different directional controls at regional- (>4.5 km) and fine- (<4.5 km) scales, which could be correlated to detailed structural features in the TOD. However, such correlation is not specific. For example, the NE-trending control at fine scale may be related to the NE-trending faults or be linked to the folds with NE-striking axes. Further analysis is necessary so as to delineate the one-to-one correspondence between the scale-variable controls and detailed structural features.

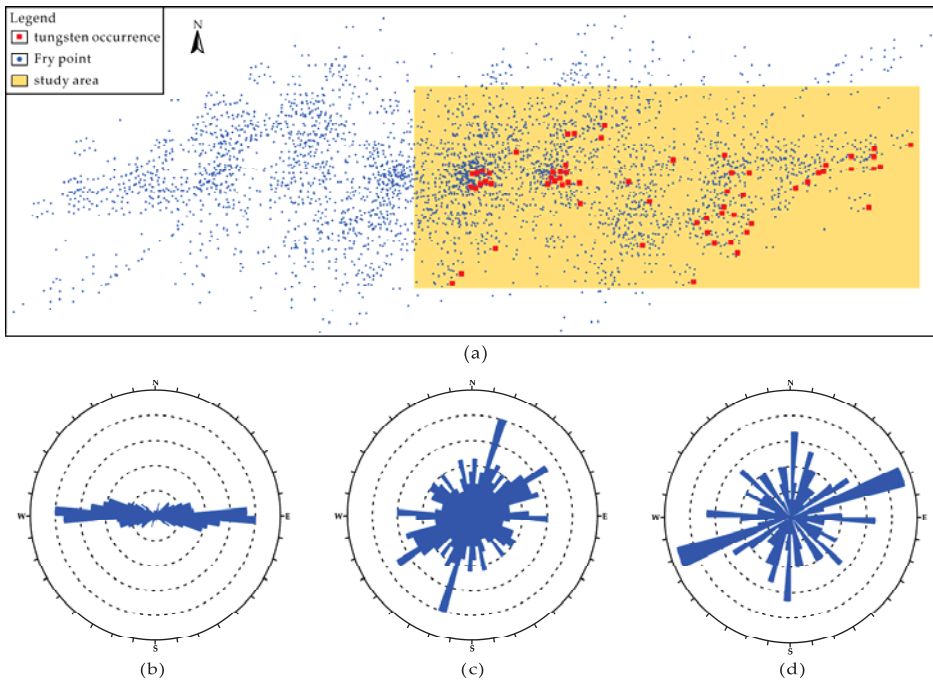


**Figure 5.** (a) Fry plot showing spatial distribution of Fry points derived from 63 copper occurrences; and rose diagram for (b) all Fry points; (c) Fry points within 4.5 km; (d) Fry points within 1.5 km.

### 3.2. Spatial Correlation of Structural Features with Copper Mineralization

Structural features are the outcomes of diverse geological processes, only a few of which are associated with ore-forming processes and sever as structural controls on mineralization [10,24]. In order to reveal the subtle structural controls in the TOD, the structural features were grouped in terms of their orientations, and the spatial associations of these features with copper mineralization were quantitatively assessed by distance distribution analysis. The study area was subdivided into 20,250 square cells with side length of 200 m, among which 63 cells containing copper occurrences represent occurrence samples and the other cells are taken as non-occurrence samples.

The EW-trending basement faults exhibit a positive correlation with copper occurrences according to the curve of  $D$  (Figure 6). Within an optimal buffer distance of 1.5 km, there is at most 21% higher frequency of copper occurrences than what would be expected due to chance. Such correlation is verified to be statistically significant (at  $\alpha = 0.01$ ) since the curve of  $D_M$  is plotted above the upper confidence band of  $D_N$  within a 1.5 km buffer (Figure 6b).

The NS-trending basement faults have a positive but weak association with copper occurrences beyond the buffer distance of 1 km, reaching only 2% higher frequency than what would be expected (Figure 7). However, the curve of  $D_M$  is plotted below the upper confidence band of  $D_N$  in the whole range of buffer analysis (Figure 7b), indicating that the weak association between NS-trending faults and copper mineralization is not of statistical significance.

The intersections of the basements faults have a statistically significantly positive correlation with copper occurrences between the buffer distances of 2 and 3 km (Figure 8). At an optimal buffer distance of 2.5 km, there is 23% higher frequency of copper occurrences than what would be expected (Figure 8b).

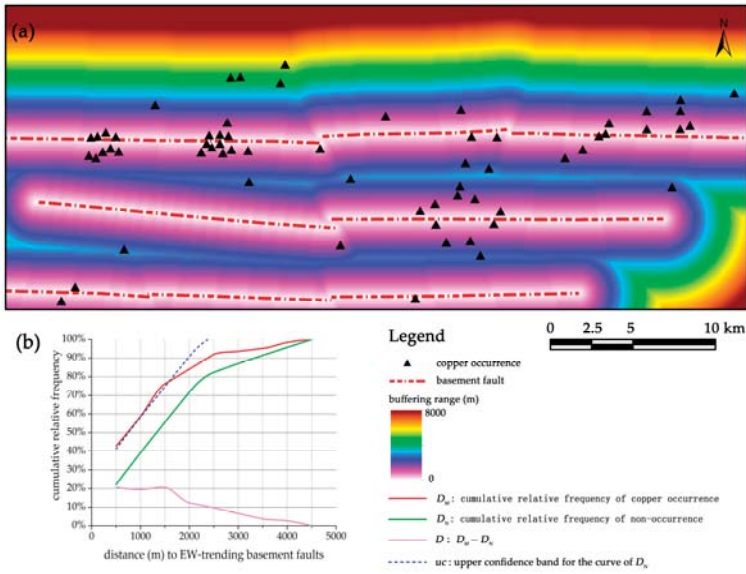


Figure 6. (a) Buffer analysis and (b) graph of cumulative relative frequency concerning distance to EW-trending faults.

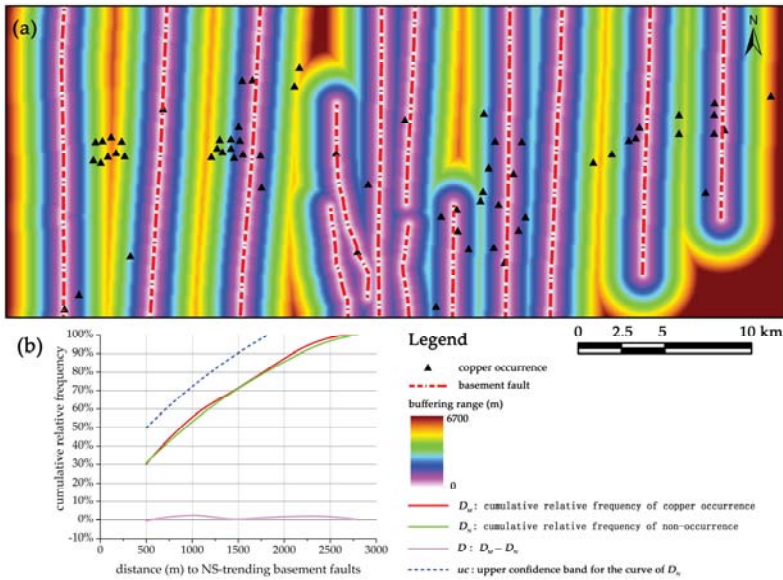


Figure 7. (a) Buffer analysis and (b) graph of cumulative relative frequency concerning distance to NS-trending faults.

The folds exhibit a statistically significantly positive correlation with copper occurrences in the buffers ranging from 1.5 to 3 km (Figure 9). There is 22% higher frequency of copper occurrences than what would be expected at a 2.5 km buffer (Figure 9b).

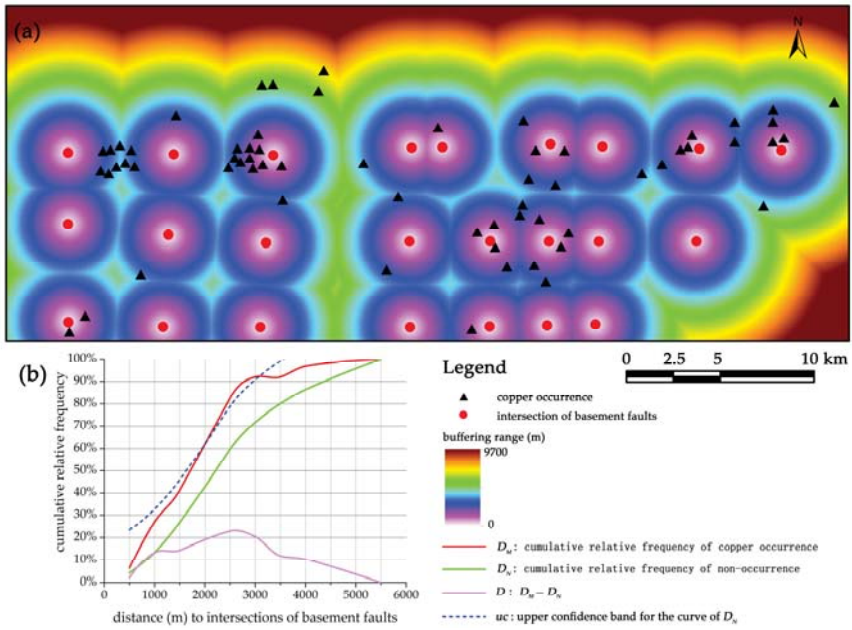


Figure 8. (a) Buffer analysis and (b) graph of cumulative relative frequency concerning distance to intersections of basement faults.

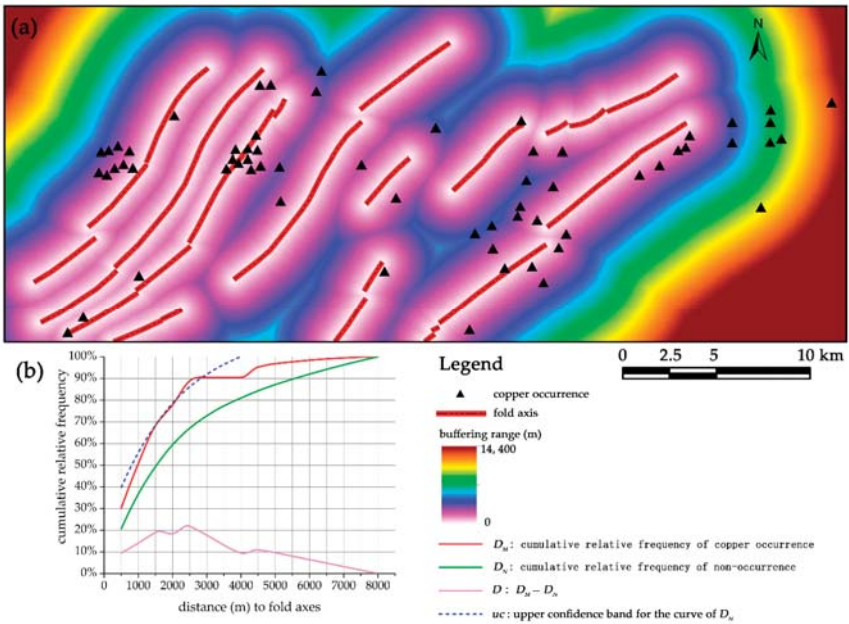


Figure 9. (a) Buffer analysis and (b) graph of cumulative relative frequency concerning distance to folds.

The cover faults consisting of NE- and NW-trending faults as well as the intersections of these faults show positive spatial association with copper occurrences. There are at most 11%, 10% and 9% higher frequencies of occurrences than what would be expected within the optimal buffers of NE-, NW-trending faults and their intersections, respectively (Figures 10–12). Nevertheless, none of these structural features have a statistically significantly associated with copper occurrence at any buffer distance (Figures 10b, 11b and 12b).

WofE analysis was also implemented to investigate the association of structural features with copper occurrences. At corresponding optimal buffer distances, the contrast values and confidences of contrast were calculated. As depicted in Figure 13 and Table 2, the EW-trending faults, intersections of basement faults and folds have top three highest values of both contrast and confidence of contrast, which are remarkably greater than those of the other structural features. The contrasts and confidences of contrast, which can assist in evaluating the intensity of spatial association, show exactly the same variations as the results derived from distance distribution analysis, implying that the EW-trending faults, intersections of basement faults and folds are plausibly major structural controls on copper mineralization in the TOD.

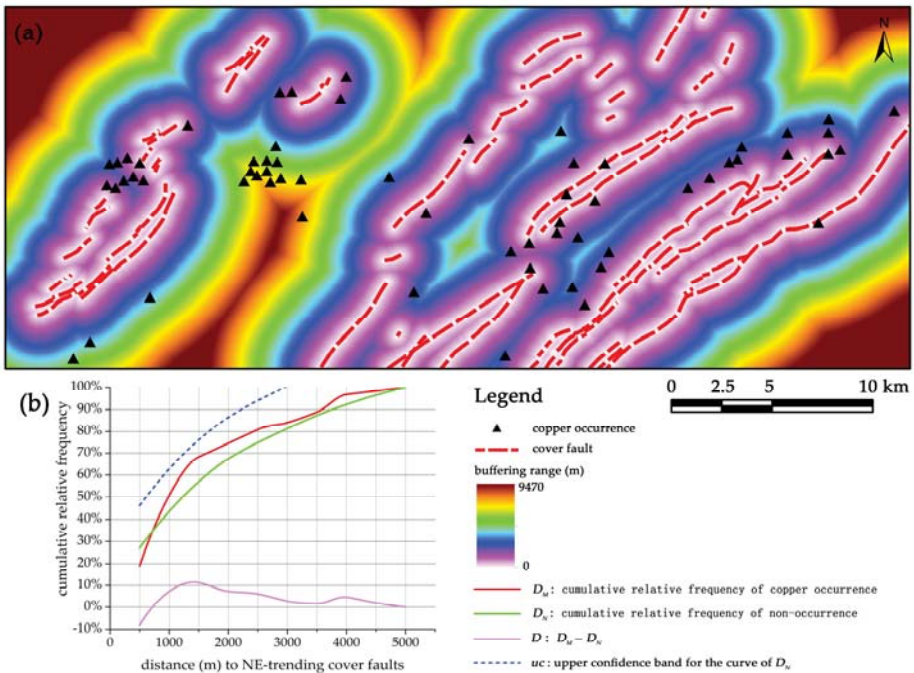


Figure 10. (a) Buffer analysis and (b) graph of cumulative relative frequency concerning distance to NE-trending faults.

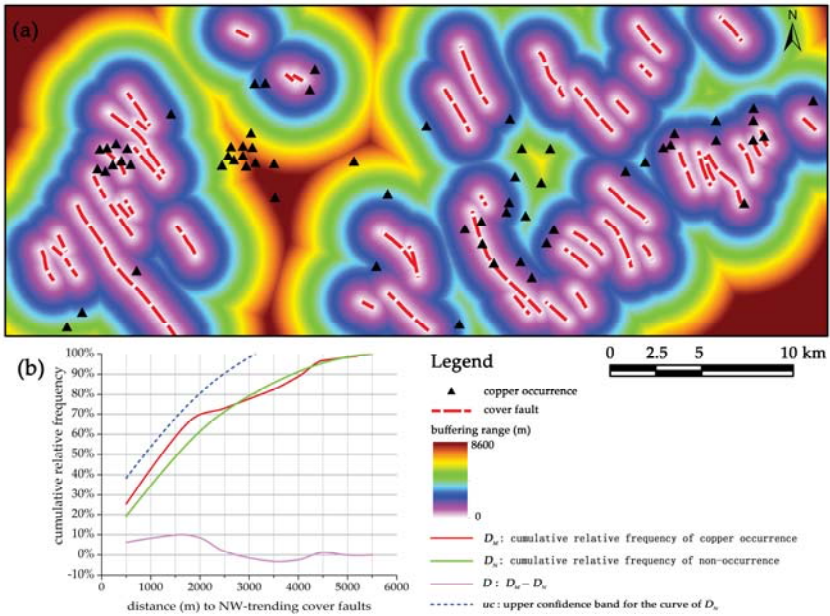


Figure 11. (a) Buffer analysis and (b) graph of cumulative relative frequency concerning distance to NW-trending faults.

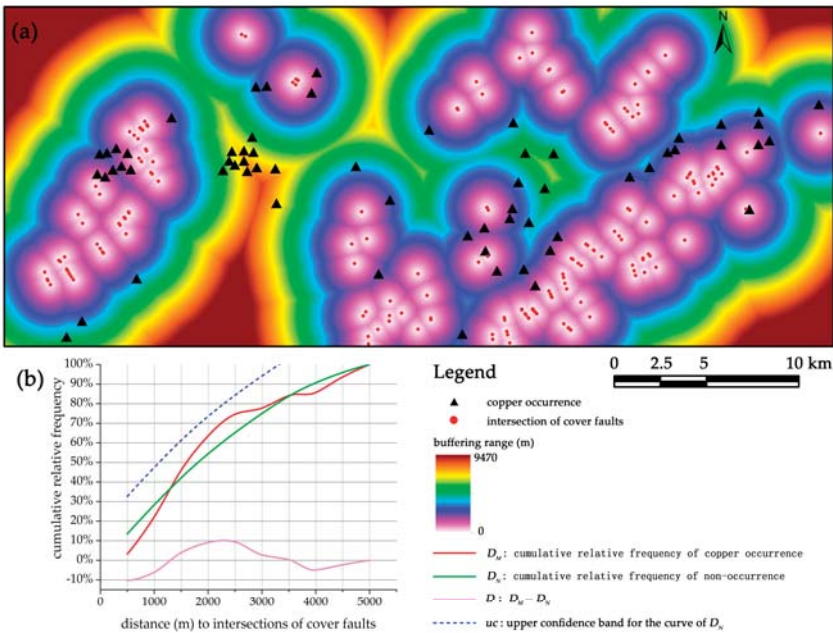


Figure 12. (a) Buffer analysis and (b) graph of cumulative relative frequency concerning distance to intersections of cover faults.

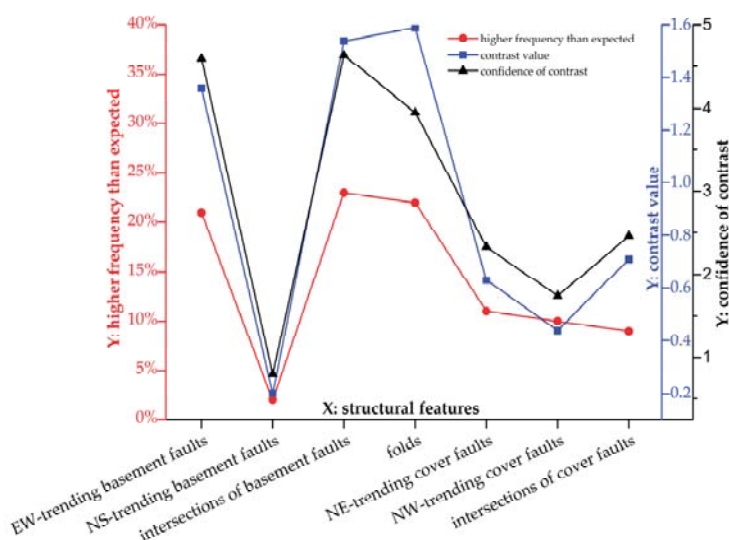


Figure 13. Graph showing variations of higher frequencies than expected, contrasts and confidences of contrast of detailed structural features in the TOD.

Table 2. Results of distance distribution and WofE analyses.

Structural Features	Optimal Buffer Distance (m)	Distance Distribution Analysis				WofE Analysis	
		$D_M$	$D_N$	$D$	$uc$	$C$	$C_s$
EW-trending faults	1500	76%	55%	21%	75%	1.36	4.6
NS-trending faults	1000	55%	53%	2%	72%	0.2	0.8
intersections of basement faults	2500	83%	60%	23%	79%	1.54	4.64
intersections of cover faults	2500	89%	67%	22%	86%	1.59	3.95
NE-trending faults	1500	68%	57%	11%	76%	0.63	2.33
NW-trending faults	1500	59%	49%	10%	68%	0.44	1.74
intersections of cover faults	2500	74%	65%	9%	84%	0.71	2.46
contact of Yanshanian intrusion	350	87%	21%	55%	52%	3.04	8.03

$D_M$ : cumulative relative frequency of copper occurrence;  $D_N$ : cumulative relative frequency of non-occurrence;  $D$ :  $D_N - D_M$ ;  $uc$ : upper confidence band for the curve  $D_N$ ;  $C$ : contrast value; and  $C_s$ : confidence of contrast.

### 3.3. Spatial Correlation of Faults with Intrusions

Considering that copper deposits in the TOD are dominated by skarn-type, Yanshanian intrusion is a key ore-controlling factor and its contact with wall rock can be considered as a special structure. The result of distance distribution analysis shows the strongest association of the contact with copper occurrences. Within a 1.7 km buffer of the contact, there is at most 55% higher frequency of copper occurrences than what would be expected, and such strong association is manifested to be statistically significant (Figure 14). The WofE analysis yields a contrast value of 3.04 and a confidence value of 8.03 which are markedly higher than the corresponding values of the other structural features (Table 2), supporting the most significant association of the contact with copper mineralization.

Since regional faults are considered to control the emplacement of intrusions according to many previous studies [45,48,50], we also performed distance distribution analysis to investigate the correlation of intrusion with the faults of various orientations. The results show that the EW-, NS-trending faults and their intersections have statistically significantly positive correlations with intrusion regions at most of the buffer distances (Figure 15a–c). There are 26% and 17% higher frequencies of intrusion regions than what would be expected at the optimal buffers of the intersections



of basement faults and EW-trending faults, respectively (Figure 15a,c), suggesting strong associations of these structural features with intrusions. The NS-trending basement faults have a moderate correlation with intrusion, delineated by 11% higher frequency of intrusion regions than what would be expected (Figure 15b). In contrast, cover faults and their intersections show negative correlations with intrusion regions within a 1.5 km buffer (Figure 15d–f). Beyond the buffer distance of 1.5 km, they show positive but weak associations with intrusions. There are 6%, 9% and 5% higher frequencies of intrusion regions than what would be expected at the optimal buffers of NE-, NW-trending faults and their intersections, respectively (Figure 15d–f).

It is noteworthy that the EW-trending faults and intersections of basement faults, which show the strongest correlations with intrusions, also exhibit significant associations with copper occurrences in the previous distance distribution analysis. It is necessary to evaluate what extent of these structural controls on intrusion determine their strong correlations with copper mineralization. The EW-trending faults and Yanshanian intrusions were buffered with their optimal distances, and the copper occurrences located within the corresponding buffered zones were counted. It appears that 98% (47 out of 48) of the copper occurrences distributed within the buffers of EW-trending faults are located in the overlapping zones of the buffered EW-trending faults and intrusions which account for 33.58% of total area. Only one occurrence is included in the buffered zones where intrusions are absent (occupying 66.42% of total area) (Figure 16). Likewise, 96% (49 out of 51) of copper occurrences located within the buffers of intersections of basement faults are included in the overlapping zones of buffered intersections of faults and intrusions that occupy 37.11% of total area (Figure 17). It is inferred that the significantly strong associations of EW-trending faults and intersections of basement faults with copper mineralization are attributed to the controls of these structural features on intrusions.

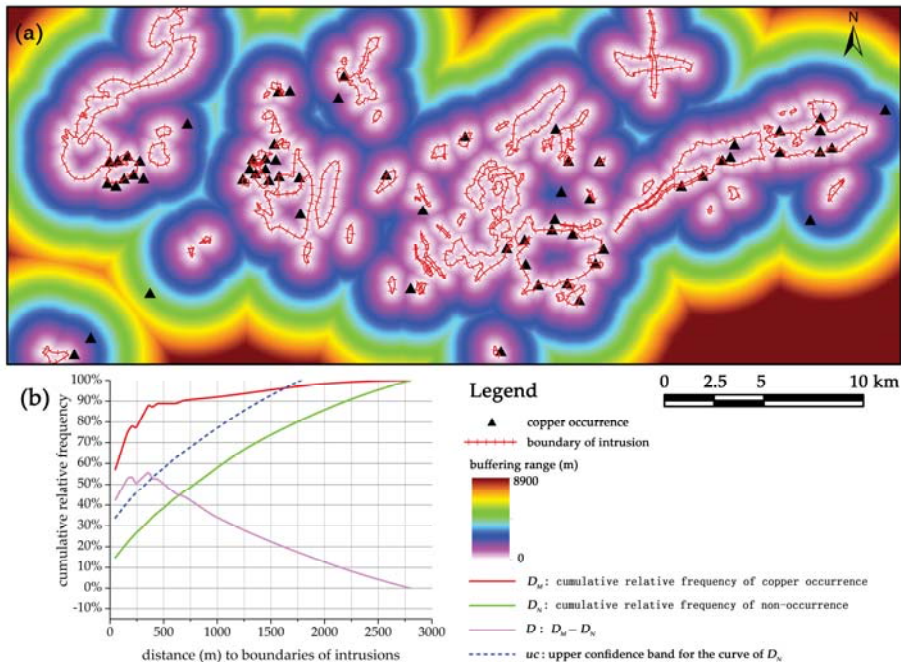


**Figure 14.** (a) Buffer analysis and (b) graph of cumulative relative frequency concerning distance to boundaries of intrusions.

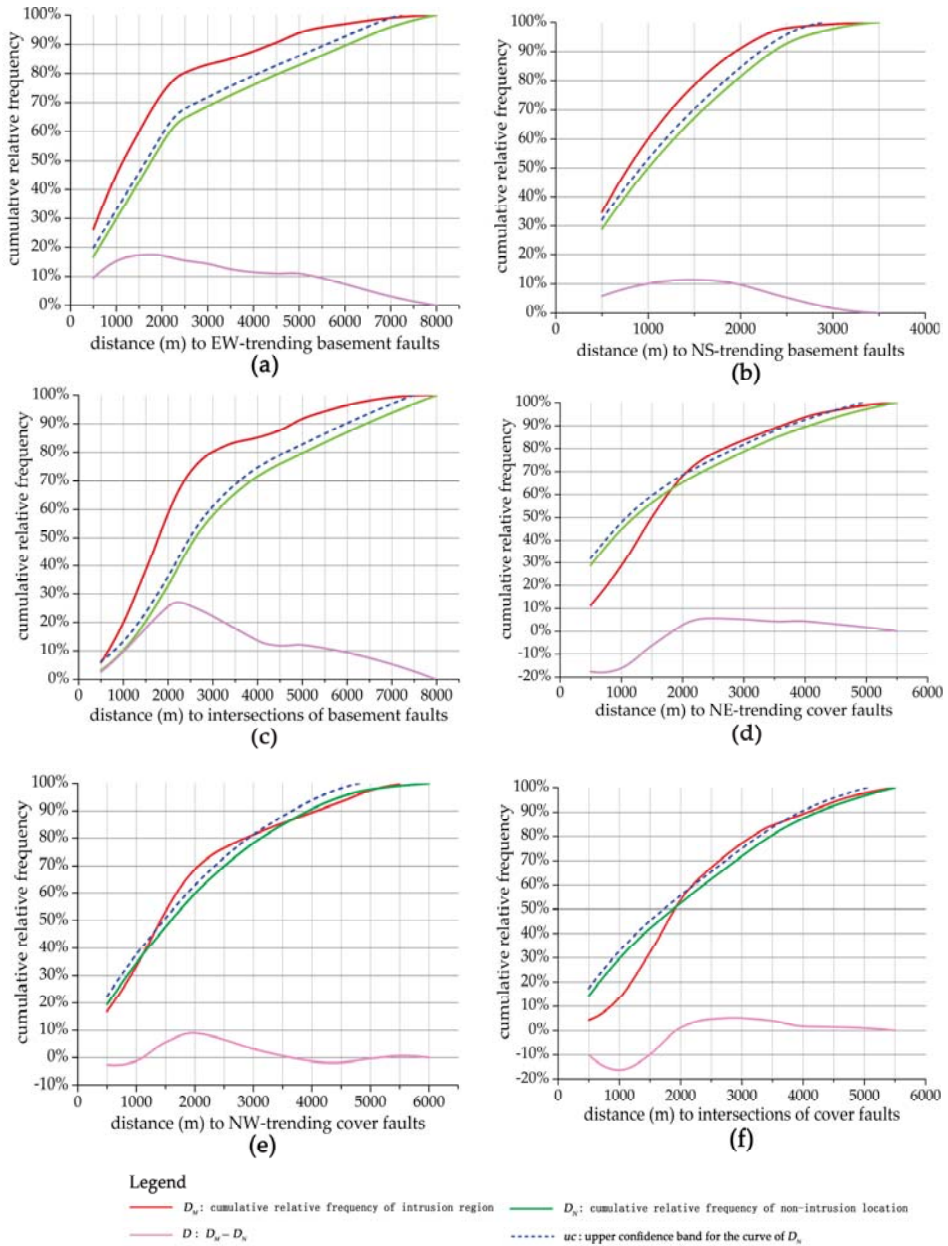
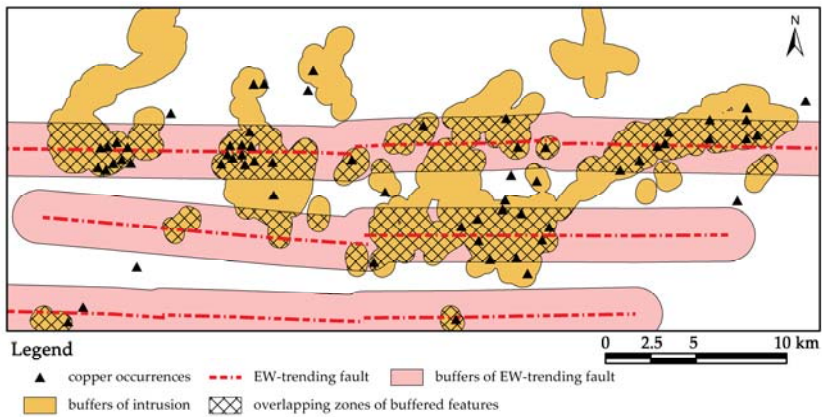
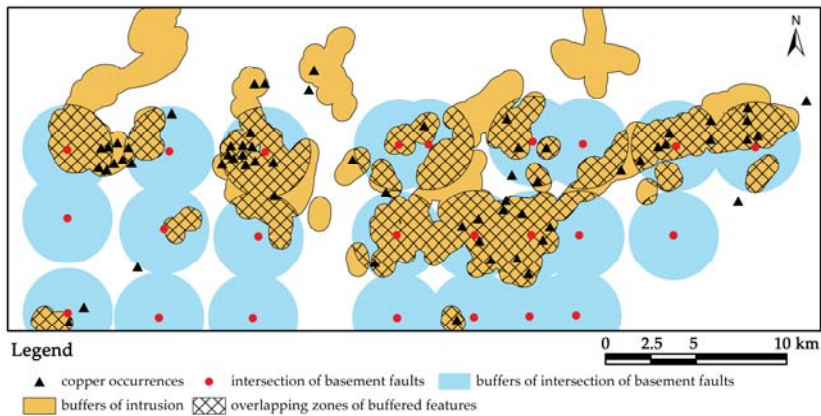


Figure 15. Graph of cumulative relative frequency concerning distance to (a) EW-trending faults; (b) NS-trending faults; (c) intersections of basement faults; (d) NE-trending faults; (e) NW-trending faults and (f) intersections of cover faults.



**Figure 16.** Buffer analysis showing the distribution of copper occurrences in buffered EW-trending faults and intrusions.



**Figure 17.** Buffer analysis showing the distribution of copper occurrences in buffered intersections of basement faults and intrusions.

### 3.4. Interpretation of Structural Controls on Copper Mineralization

The tectonic evolution of the TOD can be divided into four stages. The first stage is the formation and development of the basement of the Lower Yangtze Terrain (LYT) before Jinning movement (ca. 850–800 Ma) when the TOD was still an integral part of the LYT [38]. Secondly, after Jinning movement and before Indosinian movement (ca. 195 Ma), the LYT gradually developed into an archipelagic ocean stage, and the major sedimentary cover in this region formed. Contemporarily, the Cathaysian block and LYT drifted gradually to the North China Craton, leading to several soft collisions [60]. The vertical movement induced by the opening-closing effect related to soft collision was dominated in this stage, resulting in some disconformities (Table 1). Thirdly, the convergence of the Yangtze craton and North China craton (referred to as the Indosinian orogeny) commenced at the end of Triassic, which induced the formation of a series of significant structural features including angular unconformity between the Triassic and Jurassic strata (Table 1), folds and faults [35,60]. It is considered that the Indosinian movement has produced the present structural framework in the TOD, and even in the South China [39]. Eventually, the TOD experienced Yanshanian

movement (ca. 135 Ma) characterized by transformation from contraction to extension since early Cretaceous [35], which induced the formation of widespread intermediate-felsic intrusions and associated mineralization. The multi-stage tectonic evolution is responsible for the structural features in both basement and sedimentary cover that are related to epigenetic copper mineralization.

The basement structures are dominated by EW- and NS-trending faults. These faults, totally overlain by Mesozoic strata, are considered to be formed before Indosinian period and reactivated in the Mesozoic [45], although the detailed geometrical and kinematical characteristics of these faults are still not clear. In previous studies, faults have been proven to act as favorable pathways for transporting ore-related magma and ore-forming fluids from deep sources to shallow trap zones, resulting in a strong association of these faults with hydrothermal mineral deposits [10,16,19]. In the study area, the petrological data and geophysical profiles evidence that a magma chamber was developed in the Mesozoic at about –10 km from the surface [42]. The EW-trending basement faults are interpreted to play a vital role of channeling the magma from the magma chamber to the shallow trap zones during the Yanshanian period. This significant control of the EW-trending faults on Yanshanian intrusions is supported by distance distribution and WofE analyses, which is fully responsible for the strong correlation between the EW-trending faults and copper mineralization. This interpretation can explain the result of Fry analysis that exhibits a predominant EW trend at regional scale.

The known copper deposits are situated in the sedimentary cover where the folds with sigmoidal-shaped axes are the dominant structures, thus delineating the formative process of the folds is crucial for understanding the structural framework and copper mineralization in the cover level. Since the youngest stratum involved in the folds is Middle Triassic, it is deduced that the folds were formed during the Indosinian movement which resulted in the angular unconformity between Middle Triassic and Lower Jurassic (Table 1). A classic model of dextral simple-shear deformation in a strike-slip fault zone is introduced to illustrate the formation of folds and faults under the deformation regime of Indosinian movement dominated by NW-SE compression and dextral shear (Figures 18 and 19). As the fault zone initiates, a structural system forms consisting of (i) conjugate strike-slip faults, (ii) folds, (iii) reverse faults, and (iv) normal faults (Figure 19a) [61,62]. The initially formed folds and reverse faults trend perpendicular to the direction of the greatest shortening, while the normal faults trend parallel to the direction of the greatest shortening. Subsequently, the continued strike-slip shearing can lead to a rotation of the elements in this system [62]. The axes of previously formed folds turn to sigmoidal shape. The earlier formed normal faults accommodate sinistral strike-slip motion, and the reverse faults accommodate dextral strike-slip motion (Figure 19b). The NE-trending thrust faults observed in the field [63] and sinistral strike-slip motion of NW-trending faults identified in the geological map (Figure 1) support the rationality of this model.

In the Mesozoic strata, there existed several interfaces between two adjacent strata which have distinct mechanical properties, some of which also represented the interfaces of unconformity, e.g., the interface between the quartz sandstone of Upper Devonian and limestone of Upper Carboniferous. During the formative process of the folds in Indosinian period, the abovementioned interfaces were subjected to the progressive deformation of folding and shearing, leading to extensive bedding-parallel shear zones [43] (Figures 20 and 21). In particular, the bedding detachments occur in the cores of the folds due to the layer-parallel slippage in the formative process of folds. These shear zones were overprinted by tensional deformation in the Cretaceous when the tectonic regime in this region changed from compression to extension, thus being favorable for trapping and localizing mineralized fluids. This inference is supported by (i) the clearly discordant boundaries between stratiform orebodies and wall rocks which suggest that the ores were deposited in mechanical dilation spaces (Figure 22) [27,35,64], and (ii) the result of a numerical modeling on the Dongguashan deposit which demonstrates that the stratiform high dilation zones induced by extensional stress are favorable for fluids focusing and consistent with those positions where orebodies actually occur [64]. In addition, the bedding-parallel trap zones are located near the contacts of intrusions where sufficient sources of heat and fluid are available, and hosted in a set of carbonate strata suitable for forming skarn (Figure 20).

Therefore, the bedding-parallel structures in the folded strata are favorable for hosting, focusing and depositing ore-bearing fluids, assisting in the formation of the stratabound orebodies in this area. The thickening of orebodies in the cores of folds is attributed to the detachments occurring there (e.g., major orebody within C<sub>2</sub> in Figure 20). This interpretation is supported by distance distribution and WofE analyses, which both exhibit strong spatial association of the folds with copper mineralization. It is also inferred that the dominance of NE, NNE and NEE trends in the rose diagrams of Fry points at fine scales (<4.5 km) is attributed to the control of the folds with NE-striking axes, rather than those of the NE-trending faults which show poor correlation with copper mineralization through spatial analyses. Moreover, neither cover faults of various orientations nor the intersections of these faults show statistically significant correlation with copper mineralization, suggesting that they may only play a role in migrating the ore-bearing fluids towards the favorable host structures (i.e., multi-layered bedding-parallel shear zones) where fluid concentration and mineral deposition actually occurred, therefore leading to a lesser significant association of these cover faults with copper occurrences.

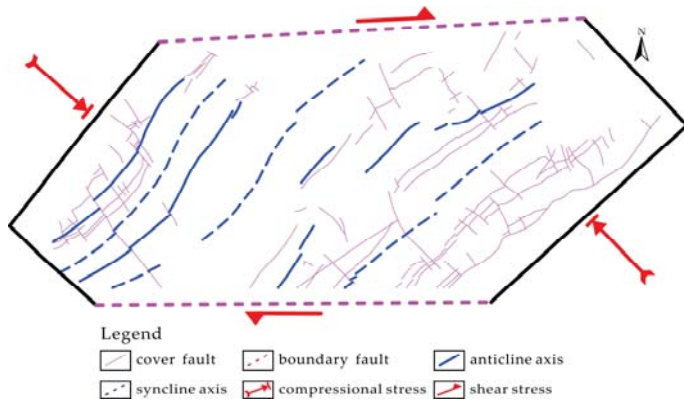


Figure 18. Stress regime during the formative process of the folds with sigmoidal axes, modified from [42].

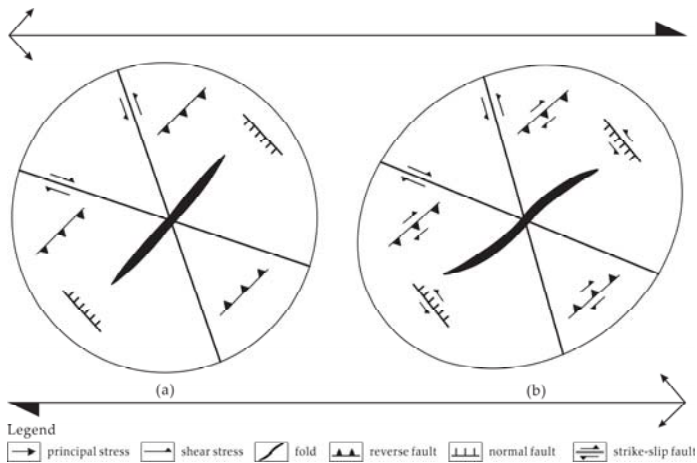


Figure 19. Deformation model of dextral shearing in a strike-slip fault zone, modified from [61]. (a) a structural system formed in initial stage of deformation; and (b) a rotation of structural elements during continued strike-slip shearing.

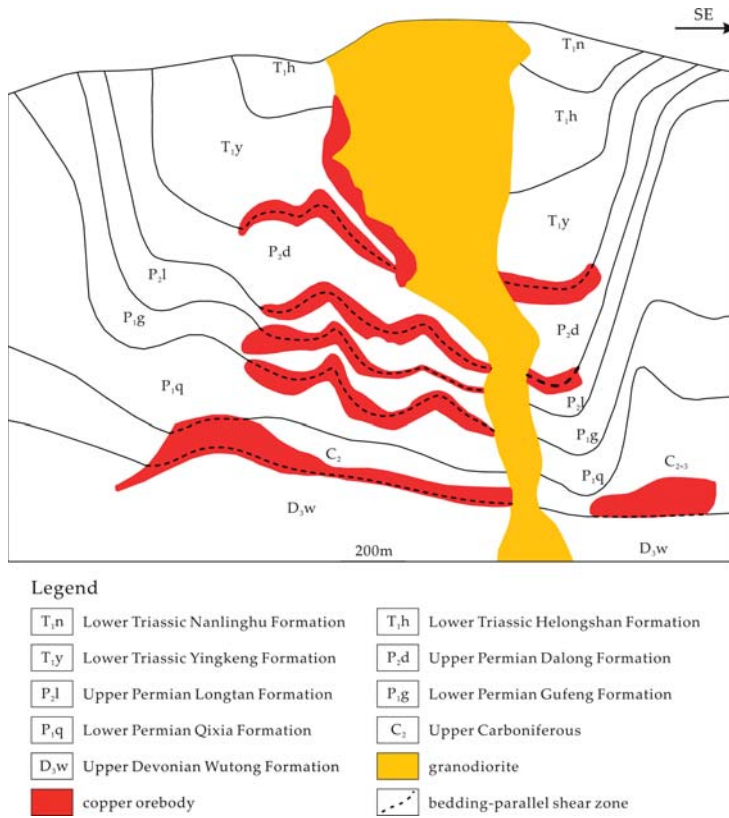


Figure 20. Typical cross-section of Shizishan ore field showing the characteristic stratobound skarn orebodies hosted in the folds, modified from [43].

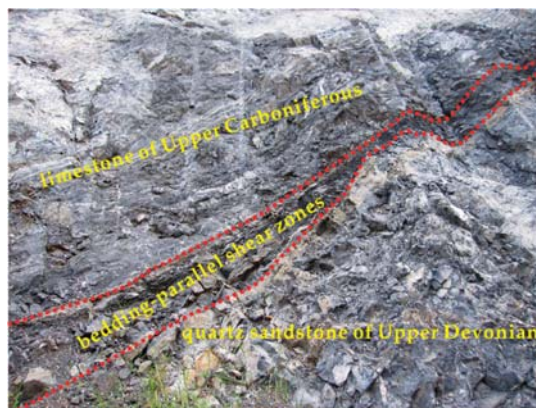
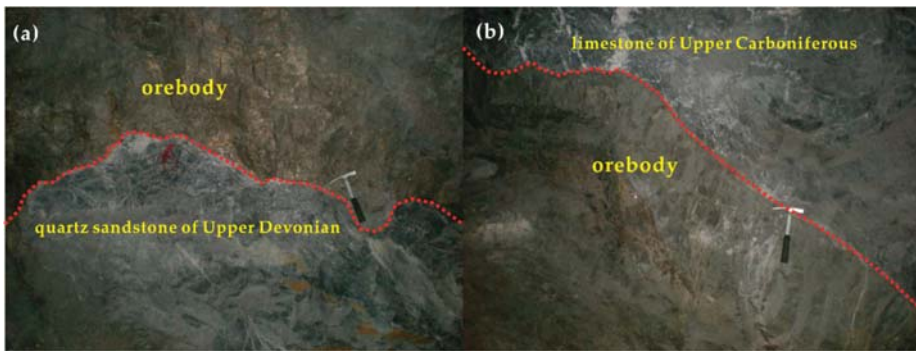


Figure 21. Field photograph of outcropped bedding-parallel shear zone between limestone of Upper Carboniferous and quartz sandstone of Upper Devonian in the Xinqiao deposit.



**Figure 22.** Photographs showing the discordant boundaries between stratiform orebodies and wall rocks in the Xinqiao deposit. (a) the boundary between orebody and underlying Upper Devonian quartz sandstone; and (b) the boundary between orebody and overlying Upper Carboniferous limestone.

#### 4. Conclusions

- (i) Fractal dimensions obtained from box-counting and radial-density analyses suggest that different structural controls operate at diverse scales of <math><1.5\text{ km}</math>, <math>1.5\text{--}4.5\text{ km}</math> and <math>>4.5\text{ km}</math>. This scale-variable controlling behavior is supported and explored by the results of Fry analysis, which illustrates a dominant EW trend at regional scale (>4.5 km) and preferential NE-NNE-NEE trends at fine scale (<4.5 km).
- (ii) The spatial associations of detailed structural features with copper mineralization are further investigated by quantitative spatial analyses. The Yanshanian intrusions, EW-trending faults, intersections of basement faults, and folds have significant associations with copper mineralization, indicated by their high values of quantitative parameters in both distance distribution and WofE analyses.
- (iii) The interpretation of structural controls on copper mineralization is made in combination of foregoing analytical results. The scale-variable patterns of mineral occurrences are attributed to the different structural controls operating in the basement and sedimentary cover. In the basement, the EW-trending faults serve as pathways for channeling magma from a magma chamber into trap zones in the caprocks during Yanshanian period. The significant control of the EW-trending faults on Yanshanian intrusion is fully responsible for the strong correlation between the EW-trending faults and copper mineralization. This inference is supported by the result of Fry analysis which shows a dominant EW trend at regional scale (>4.5 km). In the sedimentary cover, the bedding-parallel shear zones formed during Indosinian folding and shearing and overprinted by tensional deformation in Yanshanian period act as favorable sites for hosting, focusing and depositing the ore-bearing fluids, which is responsible for the dominance of NE-NNE-NEE trends at fine scale (<4.5 m) in the results of Fry analysis. Such bedding-parallel structures, together with the contact zones of intrusion, exert an important control on the formation of characteristic stratabound skarn deposits in the TOD.

**Author Contributions:** T.S. conducted the GIS-based computational experiments, analyzed the results and wrote the draft paper; Y.X. and X.Y. participated in the analysis of experimental results; W.L. and R.L. revised the calculation scheme; Z.H. and Y.W. collected the original data.

**Acknowledgments:** The research leading to this paper was jointly supported by National Natural Science Foundation of China (Grant No. 41602335), Natural Science Foundation of Jiangxi Province (Grant No. 20161BAB213084), Science and Technology Project of Jiangxi Provincial Department of Education (Grants No. GJJ150625 and No. GJJ170537), Program of Qingjiang Excellent Young Talents (Grant No. JXUSTQJYX2017001) and Doctoral Scientific Research Foundation of Jiangxi University of Science and Technology (Grant No. jxxjbs15002).

We would like to express our gratitude to two anonymous *Minerals* reviewers for their constructive comments and suggestions that greatly improved the manuscript. Thanks are also given to Zhongfa Liu from Central South University for assistance with field evidences.

**Conflicts of Interest:** The authors declare no conflict of interest.

## References

1. Sillitoe, R.H. A plate tectonic model for the origin of porphyry copper deposits. *Econ. Geol.* **1972**, *67*, 184–197. [[CrossRef](#)]
2. Tosdal, R.M.; Richards, J.P. Magmatic and structural controls on the developments of porphyry Cu ± Mo ± Au deposits. *Rev. Econ. Geol.* **2001**, *14*, 157–181.
3. Kwelwa, S.D.; Dirks, P.H.G.M.; Sanislav, I.V.; Blenkinsop, T.; Kolling, S.L. Archaean gold mineralization in an extensional setting: The structural history of the Kukuluma and Matandani Deposits, Geita Greenstone Belt, Tanzania. *Minerals* **2018**, *8*, 171. [[CrossRef](#)]
4. Cox, S.F.; Knackstedt, M.A.; Braun, J. Principles of structural control on permeability and fluid flow in hydrothermal systems. *Rev. Econ. Geol.* **2001**, *14*, 1–24.
5. Austin, J.R.; Blenkinsop, T.G. Local to regional scale structural controls on mineralisation and the importance of a major lineament in the eastern Mount Isa Inlier, Australia: Review and analysis with autocorrelation and weights of evidence. *Ore Geol. Rev.* **2009**, *35*, 298–316. [[CrossRef](#)]
6. Sillito, R.H. Iron oxide-copper-gold deposits: An Andean view. *Miner. Deposita* **2003**, *38*, 787–812. [[CrossRef](#)]
7. Zeng, M.; Zhang, D.; Zhang, Z.; Liu, T.; Li, C.; Wei, C. Structural controls on the Lala iron-copper deposit of the Kangdian metallogenic province, Southwestern China: Tectonic and metallogenic implications. *Ore Geol. Rev.* **2018**, *97*, 35–54. [[CrossRef](#)]
8. Chauvet, A.; Piantone, P.; Barbanson, L.; Nehlig, P.; Pedroletti, I. Gold deposit formation during collapse tectonics: Structural, mineralogical, geochronological, and fluid inclusion constraints in the Ouro Preto Gold Mines, Quadrilátero Ferrífero, Brazil. *Econ. Geol.* **2001**, *96*, 25–48. [[CrossRef](#)]
9. Bonham-Carter, G.F. *Geographic Information System for Geoscientists, Modeling with GIS*; Pergamon: Elmsford, NY, USA, 1994; pp. 238–333.
10. Haddad-Martim, P.M.; Filho, C.R.D.S.; Carranza, E.J.M. Spatial analysis of mineral deposit distribution: A review of methods and implications for structural controls on iron oxide-copper-gold mineralization in Carajás, Brazil. *Ore Geol. Rev.* **2017**, *81*, 230–244. [[CrossRef](#)]
11. Schetselaar, E.; Ames, D.; Grunsky, E. Integrated 3D geological modeling to gain insight in the effects of hydrothermal alteration on post-ore deformation style and strain localization in the Flin Flon Volcanogenic Massive Sulfide Ore System. *Minerals* **2018**, *8*, 3. [[CrossRef](#)]
12. Sun, T.; Wu, K.X.; Chen, L.K.; Liu, W.M.; Wang, Y.; Zhang, C.S. Joint application of fractal analysis and weights-of-evidence method for revealing the geological controls on regional-scale tungsten mineralization in Southern Jiangxi Province, China. *Minerals* **2017**, *7*, 243. [[CrossRef](#)]
13. Li, X.H.; Yuan, F.; Zhang, M.M.; Jia, C.; Jowitt, S.M.; Ord, A.; Zheng, T.K.; Hu, X.Y.; Li, Y. Three-dimensional mineral prospectivity modeling for targeting of concealed mineralization within the Zhonggu iron orefield, Ningwu Basin, China. *Ore Geol. Rev.* **2015**, *71*, 633–654. [[CrossRef](#)]
14. Xie, J.Y.; Wang, G.W.; Sha, Y.Z.; Liu, J.J.; Wen, B.T.; Nie, M.; Zhang, S. GIS prospectivity mapping and 3D modeling validation for potential uranium deposit targets in Shangnan district, China. *J. Afr. Earth Sci.* **2017**, *128*, 161–175. [[CrossRef](#)]
15. Carranza, E.J.M. Developments in GIS-based mineral prospectivity mapping: An overview. In Proceedings of the Mineral Prospectivity, Current Approaches and Future Innovations, Orléans, France, 24–26 October 2017.
16. Parsa, M.; Maghsoudi, A.; Yousefi, M. Spatial analyses of exploration evidence data to model skarn-type copper prospectivity in the Varzaghan district, NW Iran. *Ore Geol. Rev.* **2018**, *92*, 97–112. [[CrossRef](#)]
17. Mandelbrot, B.B. *Fractals: Form, Chances and Dimension*; W.H. Freeman: New York, NY, USA, 1977; pp. 1–23.
18. Roberts, S.; Sanderson, D.J.; Gumiel, P. Fractal analysis of Sn-W mineralization from central Iberia; insights into the role of fracture connectivity in the formation of an ore deposit. *Econ. Geol.* **1998**, *93*, 360–365. [[CrossRef](#)]
19. Carranza, E.J.M.; Owusu, E.A.; Hale, M. Mapping of prospectivity and estimation of number of undiscovered prospects for lode gold, Southwestern Ashanti Belt, Ghana. *Miner. Deposita*. **2009**, *44*, 915–938. [[CrossRef](#)]



20. Mehrabi, B.; Ghasemi, S.M.; Tale, F.E. Structural control on epithermal mineralization in the Troude-Chah Shirin belt using point pattern and Fry analyses, North of Iran. *Geotectonics* **2015**, *49*, 320–331. [[CrossRef](#)]
21. Agterberg, F.P.; Bonham-Carter, G.F.; Wrigh, D.F. Statistical pattern integration for mineral exploration. In *Computer Application in Resource Estimation Prediction and Assessment for Metals and Petroleum*; Gaal, G., Merriam, D.F., Eds.; Pergamon: Elmsford, NY, USA, 1990; pp. 1–21.
22. Cheng, Q.M.; Agterberg, F.P. Fuzzy weights of evidence method and its application in mineral potential mapping. *Nat. Resour. Res.* **1999**, *8*, 27–35. [[CrossRef](#)]
23. Yuan, F.; Li, X.H.; Zhang, M.M.; Jowitt, S.M.; Jia, C.; Zheng, T.K.; Zhou, T.F. Three-dimensional weights of evidence-based prospectivity modeling: A case study of the Baixiangshan mining area, Ningwu Basin, Middle and Lower Yangtze Metallogenic Belt, China. *J. Geochem. Explor.* **2014**, *145*, 82–97. [[CrossRef](#)]
24. Carranza, E.J.M. Controls on mineral deposit occurrence inferred from analysis of their spatial pattern and spatial association with geological features. *Ore Geol. Rev.* **2009**, *35*, 383–400. [[CrossRef](#)]
25. Cao, Y.; Zheng, Z.; Du, Y.; Gao, F.; Qin, X.; Yang, H.; Lu, Y.; Du, Y. Ore geology and fluid inclusions of the Hucunna deposit, Tongling, Eastern China: Implications for the separation of copper and molybdenum in skarn deposits. *Ore Geol. Rev.* **2017**, *81*, 925–939. [[CrossRef](#)]
26. Liu, L.M.; Zhao, Y.L.; Zhao, C.B. Coupled geodynamics in the formation of Cu skarn deposits in the Tongling–Anqing district, China: Computational modeling and implications for exploration. *J. Geochem. Explor.* **2010**, *106*, 146–155. [[CrossRef](#)]
27. Zhang, Y.; Shao, Y.J.; Li, H.B.; Liu, Z.F. Genesis of the Xinqiao Cu–S–Fe–Au deposit in the Middle-Lower Yangtze River Valley metallogenic belt, Eastern China: Constraints from U–Pb–Hf, Rb–Sr, S, and Pb isotopes. *Ore Geol. Rev.* **2017**, *86*, 100–116. [[CrossRef](#)]
28. Fu, S.G.; Yan, X.Y.; Yuan, C.X. Geologic feature of submarine volcanic eruption-sedimentary pyrite type deposit in Carboniferous in the Middle-Lower Yangtze River Valley metallogenic belt, Eastern China. *J. Nanjing Univ. Nat. Sci. Ed.* **1977**, *4*, 43–67. (In Chinese)
29. Gu, L.X.; Xu, K.Q. On the carboniferous submarine massive sulfide deposit in the lower reaches of the Yangtze River. *Acta Geol. Sin.* **1986**, *60*, 176–188. (In Chinese)
30. Gu, L.X.; Hu, W.X.; He, J.X. Regional variations in ore composition and fluid features of massive sulfide deposits in South China: Implications for genetic modeling. *Episodes* **2000**, *23*, 110–118.
31. Yang, D.F.; Fu, D.X.; Wu, N.X. Genesis of pyrite type copper in Xinqiao and its neighboring region according to ore composition and structure. *Issue Nanjing Inst. Geol. Miner. Resour. Chin. Acad. Geol. Sci.* **1982**, *3*, 59–68. (In Chinese)
32. Xie, H.G.; Wang, W.B.; Li, W.D. The genesis and metallogenetic of Xinqiao Cu–S–Fe deposit, Anhui Province. *Volcanol. Miner. Resour.* **1995**, *16*, 101–107. (In Chinese)
33. Zhou, T.F.; Zhang, L.J.; Yuan, F.; Fang, Y.; Cooke, D.R. LA-ICP-MS in situ trace element analysis of pyrite from the Xinqiao Cu–Au–S Deposit in Tongling, Anhui, and its constrains on the ore genesis. *Earth Sci. Front.* **2010**, *17*, 306–319. (In Chinese)
34. Chang, Y.F.; Liu, X.G. Layer control type skarn type deposit—Some deposits in the Middle-Lower Yangtze Depression in Anhui Province as an example. *Miner. Depos.* **1983**, *2*, 11–20. (In Chinese)
35. Pan, Y.; Dong, P. The lower Changjiang (Yangtzi/Yangtze River) metallogenic belt, East-center China: Intrusion and wall rock hosted Cu–Fe–Au, Mo, Zn, Pb, Ag deposits. *Ore. Geol. Rev.* **1999**, *15*, 177–242. [[CrossRef](#)]
36. Mao, J.W.; Shao, Y.J.; Xie, G.Q.; Zhang, J.D.; Chen, Y.C. Mineral deposit model for porphyry-skarn polymetallic copper deposits in Tongling ore dense district of Middle-Lower Yangtze Valley metallogenic belt. *Miner. Depos.* **2009**, *28*, 109–119. (In Chinese)
37. Zhang, Y.; Shao, Y.; Zhang, R.; Li, D.; Liu, Z.; Chen, H. Dating ore deposit using garnet U–Pb geochronology: Example from the Xinqiao Cu–S–Fe–Au deposit, Eastern China. *Minerals* **2018**, *8*, 31. [[CrossRef](#)]
38. Zhou, T.; Wang, S.; Fan, Y.; Yuan, F.; Zhang, D.; White, N.C. A review of the intracontinental porphyry deposits in the Middle-Lower Yangtze River Valley metallogenic belt, Eastern China. *Ore Geol. Rev.* **2015**, *65*, 433–456. [[CrossRef](#)]
39. Hu, R.Z.; Chen, W.T.; Xu, D.R.; Zhou, M.F. Reviews and new metallogenetic models of mineral deposits in South China: An introduction. *J. Asian Earth Sci.* **2017**, *137*, 1–8. [[CrossRef](#)]
40. Mertig, H.J.; Rubin, J.N.; Kyle, J.R. Skarn Cu–Au orebodies of the Gunung Bijih (Ertsberg) district, Irian Jaya, Indonesia. *J. Geochem. Explor.* **1994**, *50*, 179–202. [[CrossRef](#)]

41. Sato, T. Manto type copper deposit in Chile—A review. *Bull. Geo. Surv. Japan* **1984**, *35*, 565–582.
42. Wang, Q.F.; Deng, J.; Huang, D.H.; Xiao, C.H.; Yang, L.Q.; Wang, Y.R. Deformation model for the Tongling ore cluster region, East-Central China. *Int. Geol. Rev.* **2011**, *53*, 562–579. [[CrossRef](#)]
43. Wu, G.G.; Zhang, D.; Zang, W.S. Study of tectonic layering motion and layering mineralization in the Tongling metallogenic cluster. *Sci. China Ser. D Earth Sci.* **2003**, *46*, 852–863. [[CrossRef](#)]
44. Li, Y.; Li, J.W.; Li, X.H.; Selby, D.; Huang, G.H.; Chen, L.J.; Zheng, K. A carbonate replacement origin for the Xinqiao stratabound massive sulfide deposit, middle-lower Yangtze Metallogenic Belt, China. *Ore Geol. Rev.* **2017**, *80*, 985–1003. [[CrossRef](#)]
45. Chang, Y.F.; Liu, X.P.; Wu, Y.C. *The Copper–Iron Belt of the Low and Middle Reaches of the Changjiang River*; Geological Publish House: Beijing, China, 1991; pp. 1–359. (In Chinese)
46. Liu, L.M.; Yang, G.Y.; Peng, S.L.; Zhao, C.B. Numerical modeling of coupled geodynamical processes and its role in facilitating predictive ore discovery: An example from Tongling, China. *Resour. Geol.* **2005**, *55*, 21–31. [[CrossRef](#)]
47. Liu, W.C.; Li, D.X.; Gao, D.Z. Analysis on the time sequence of compounding of structural deformation systems and resulting effects in Tongling area. *J. Geomech.* **1996**, *2*, 42–48. (In Chinese)
48. Lü, Q.T.; Hou, Z.Q.; Zhao, J.H.; Shi, D.N.; Wu, X.Z.; Chang, Y.F.; Pei, R.F.; Huang, D.D.; Kuang, C.Y. Complex crustal structure of Tongling ore district: Insights from deep seismic reflection profiling. *Sci. China Ser. D* **2003**, *33*, 442–449. (In Chinese)
49. Liu, Z.F.; Shao, Y.J.; Wei, H.T.; Wang, C. Rock-forming mechanism of Qingshanjiao intrusion in Dongguashan copper (gold) deposit, Tongling area, Anhui province, China. *Trans. Nonferr. Met. Soc. China* **2016**, *26*, 2449–2461. [[CrossRef](#)]
50. Xie, J.C.; Yang, X.Y.; Sun, W.D.; Du, J.G. Early Cretaceous dioritic rocks in the Tongling region, Eastern China: Implications for the tectonic settings. *Lithos* **2012**, *150*, 49–61. [[CrossRef](#)]
51. Liu, L.M.; Peng, S.L. Prediction of hidden ore bodies by synthesis of geological, geophysical and geochemical information based on dynamic model in Fenghuangshan ore field, Tongling district, China. *J. Geochem. Explor.* **2004**, *81*, 81–98. [[CrossRef](#)]
52. 321 Geological Team. *Structural Maps of Tongling Area*; Bureau of Geological and Mineral Resources of Anhui Province: Hefei, China, 1989; pp. 1–33.
53. Du, Y.L. Ore-Controlling Factors and Metallogenic Model of Stratabound Skarn Deposits in Tongling Area, Anhui Province. Ph.D. Thesis, China University of Geosciences, Beijing, China, 2013. (In Chinese)
54. Zuo, R.G.; Wang, J. Fractal/multifractal modeling of geochemical data: A review. *J. Geochem. Explor.* **2016**, *164*, 33–41. [[CrossRef](#)]
55. Mandelbrot, B.B. *The Fractal Geometry of Nature: Updated and Augmented*; W.H. Freeman: New York, NY, USA, 1983; pp. 1–31.
56. Berman, M. Distance distributions associated with poisson processes of geometric figures. *J. Appl. Probab.* **1977**, *14*, 195–199. [[CrossRef](#)]
57. Berman, M. Testing for spatial association between a point process and another stochastic process. *J. R. Stat. Soc. C Appl.* **1986**, *35*, 54–62. [[CrossRef](#)]
58. Allek, K.; Boubaya, D.; Bouguern, A.; Hamoudi, M. Spatial association analysis between hydrocarbon fields and sedimentary residual magnetic anomalies using weights of evidence: An example from the Triassic Province of Algeria. *J. Appl. Geophys.* **2016**, *135*, 100–110. [[CrossRef](#)]
59. Sang, X.J.; Xue, L.F.; Liu, J.W.; Zhan, L. A novel Workflow for geothermal prospectively mapping weights-of-evidence in Liaoning Province, Northeast China. *Energies* **2017**, *10*, 1069. [[CrossRef](#)]
60. Deng, J.; Huang, D.H.; Wang, Q.F.; Hou, Z.Q.; Lü, Q.T.; Yao, L.Q.; Xin, H.B.; Zhang, Q.; Wei, Y.G. Formation mechanism of “drag depressions” and irregular boundaries in intraplate deformation. *Acta Geol. Sin.* **2004**, *78*, 267–272.
61. Waldron, J.W.F. Extensional fault arrays in strike-slip and transtension. *J. Struct. Geol.* **2005**, *27*, 23–34. [[CrossRef](#)]
62. David, G.H.; Reynolds, S.J.; Kluth, C.F. *Structural Geology of Rocks and Regions*, 3rd ed.; JohnWiley & Sons, Inc.: Westwood, MA, USA, 2011; pp. 336–338.

63. Wang, Q.F. Model study of the tectonic-magmatic-metallogenical system in Tongling ore cluster area. Ph.D. Thesis, China University of Geosciences, Beijing, China, 2005. (In Chinese)
64. Liu, L.M.; Sun, T.; Zhou, R.C. Epigenetic genesis and magmatic intrusion's control on the Dongguashan stratabound Cu-Au deposit, Tongling, China: Evidence from field geology and numerical modeling. *J. Geochem. Explor.* **2014**, *144*, 97–114. [[CrossRef](#)]



© 2018 by the authors. Licensee MDPI, Basel, Switzerland. This article is an open access article distributed under the terms and conditions of the Creative Commons Attribution (CC BY) license (<http://creativecommons.org/licenses/by/4.0/>).

Article

# The Hajjar Regional Transpressive Shear Zone (Guemassa Massif, Morocco): Consequences on the Deformation of the Base-Metal Massive Sulfide Ore

Safouane Admou <sup>1,2,\*</sup>, Yannick Branquet <sup>2,3</sup>, Lakhli Badra <sup>1</sup>, Luc Barbanson <sup>2</sup>, Mohamed Outhounjite <sup>4</sup>, Abdelali Khalifa <sup>4</sup>, Mohamed Zouhair <sup>4</sup> and Lhou Maacha <sup>4</sup>

<sup>1</sup> Département des Sciences de la Terre, Faculté des Sciences, Université Moulay Ismaïl de Meknès, B.P. 11201 Zitoune Meknès, Morocco; badra\_lakhli@yahoo.fr (L.B.)

<sup>2</sup> Institut des Sciences de la Terre d'Orléans (ISTO), Université Orléans, CNRS BRGM UMR7327, Campus Géosciences 1A, rue de la Férollerie, 45071 Orléans, CEDEX 2, France; yannick.branquet@univ-orleans.fr (Y.B.); luc.barbanson@univ-orleans.fr (L.B.)

<sup>3</sup> Géosciences Rennes (GR), Université de Rennes 1, CNRS UMR6118, Campus de Beaulieu, CS 74205, 35042 Rennes CEDEX, France

<sup>4</sup> Groupe MANAGEM, Twin center, Tour A, BP 5199, Casablanca, Morocco; M.OUTHOUNJITE@managemgroup.com (M.O.); A.KHALIFA@managemgroup.com (A.K.); M.ZOUHAIR@managemgroup.com (M.Z.); L.MAACHA@managemgroup.com (L.M.)

\* Correspondence: admou.safouane@gmail.com

Received: 30 June 2018; Accepted: 2 October 2018; Published: 7 October 2018

**Abstract:** The genesis of the base-metal massive sulfide deposits hosted within the Moroccan Hercynian Jebilet and Guemassa Massifs is still under debate. No consensus currently exists between the two models that have been proposed to explain the deposits, i.e., (1) syngenetic volcanogenic massive sulfide mineralization, and (2) synmetamorphic tectonic fluid-assisted epigenetic mineralization. Conversely, researchers agree that all Hercynian massive sulfide deposits in Morocco are deformed, even though 3D structural mapping at the deposit scale is still lacking. Therefore, while avoiding the use of a model-driven approach, the main aim of this contribution is to establish a first-order structural pattern and the controls of the Hajjar base metal deposit. We used a classical structural geology toolbox in surface and subsurface mining work to image finite strain at different levels. Our data demonstrate that: i) the Hajjar area is affected by a single foliation plane (not two) which developed during a single tectonic event encompassing a HT metamorphism. This syn-metamorphic deformation is not restricted to the Hajjar area, as it is widespread at the western Meseta scale, and it occurred during Late Carboniferous times; ii) the Hajjar ore deposit is hosted within a regional transpressive right-lateral NE-trending shear zone in which syn- to post-metamorphic ductile to brittle shear planes are responsible for significant inflexion (or virgation) of the foliation yielding an anastomosing pattern within the Hajjar shear zone. Again, this feature is not an exception, as various Late Carboniferous-Permian regional scale wrenching shear zones are recognized throughout the Hercynian Meseta orogenic segment. Finally, we present several lines of evidence emphasizing the role of deformation in terms of mechanical and fluid-assisted ore concentrations.

**Keywords:** Hajjar; shear zone; base metal massive sulfide deposits; structural control; remobilization

## 1. Introduction

Most Volcanogenic Massive Sulfide Deposits (VMSDs) are assumed to form within extensional and subsiding basins during both divergent and convergent plate tectonic settings (e.g., [1]). As a result, in convergent settings leading to continental collision for instance, many VMSDs underwent

deformation, burial, and metamorphism. During these transformations, syngenetic massive sulfide bodies (e.g., stratoid lenses, chimneys and stockwerks) were reworked, and primary metallic bearing mineral assemblages may have been remobilized (e.g., either depleted or enriched). For this reason, the deformation and (re)mobilization of the primary sulfide concentration is a fundamental and economic matter which has been recognized and studied for a long time (e.g., [2–6]).

However, in spite of recent advances in modern textural (e.g., electron backscatter diffraction coupled to chemistry) and opaque mineral strain characterization (e.g., [7–10]), it still remains difficult for economic geologists dealing with deformed VMSD to decipher the respective parts of primary syngenetic vs. epigenetic mineralizing processes. As a result, metallogenic models of very large base metal concentrations all over the world are still ambiguous and under debate.

Currently, the genesis of polymetallic base-metal massive sulfide deposits (MSD) from the western Meseta domain in Morocco are currently under debate. This debate is particularly relevant for MSD from the Central Jebilet unit (Figure 1), e.g., the Kettara, Draa Sfar, Koudiat Aïcha, and Lachach deposits. Many authors consider these MSD as metamorphosed and deformed primary VMS and/or sedimentary exhalative (SEDEX) deposits [11–17]; however, other authors argue for a fluid-assisted syn-metamorphic origin during the major Hercynian deformation event [18–22]. In contrast, the Hajjar MSD located in the Hercynian Guemassa Massif (Figure 1) is considered as a metamorphosed and deformed syngenetic VMS/SEDEX deposit [12,23–25]. Although Hajjar shares many similar geological and mineralogical features (e.g., predominance of pyrrhotite) with the Central Jebilet MSD to the north, the hypothesis of either an epigenetic or a syn-metamorphic origin has not yet been put forward.

Since the pioneering works of Hibti (1993) [23] on the Hajjar MSD, very few studies dealing with the structural controls of this ore deposit have been carried out and published in the international literature. However, on a larger scale, much thermal and geochronological data dealing with the tectono-magmatic evolution of the western segment of the Hercynian Meseta have been published [26–28]. Therefore, using data collected from new outcrops, the aim of this work is to complete the Hajjar MSD structural dataset and to re-evaluate the structural context and controls; this is a prerequisite to being able to have a potential syngenetic vs. syn-metamorphic debate, if required. Our approach is to perform structural mapping at each subsurface exploitation level, yielding a 3D view of the deformation pattern. This pattern is then compared to the structural map of the surface outcrops in the Guemassa Massif.

## 2. The Hajjar Geological and Ore Deposit Framework

The Hajjar MSD is located in the southern part of the Hercynian Occidental Meseta in Morocco, within the Guemassa Massif south of Marrakech (Figure 1). The Guemassa Massif is composed of metasediments, metavolcanites, and intrusions, all of which are Carboniferous in age (see [29–31]) for a detailed description of the volcano-sedimentary series). Massive sulfide lenses (and scarce magnetite bodies) are found and exploited within this volcano-sedimentary sequence [12,23] and references therein). The Hajjar mineralization corresponds to sub-lenticular bodies of various sizes containing 50–75% vol. pyrrhotite, with sphalerite, galena, chalcocopyrite, pyrite, and arsenopyrite as the related major ore minerals. The tonnage is about 20 MT of ore with grades of 8% Zn, 2.3% Pb and 0.4–0.6% Cu [32]. The Hajjar MSD have been classified as an intermediate type between SEDEX and VMS deposits such as the Iberian Pyrite Belt giant deposits, within the “Guemassa-Jebilet” sub-type owing to its high content in pyrrhotite [25]. In the Hajjar MSD, the primary economic massive mineralization is assumed to form in a Viséan basin in which an intense syn-sedimentary volcanism occurred [12,23,25]. Like the other MSD of the Occidental Meseta, the Hajjar MSD is strongly folded, faulted, and metamorphosed, which makes it difficult to recognize syngenetic/diagenetic structures and textures.

Based on the literature, the Guemassa rocks were deformed and metamorphosed during several tectonic/thermal events which affected the Guemassa Massif area [23]: i) a D0 syn-sedimentary event at the Viséan-Namurian with slumps, intraformational breccias attesting to slope instabilities in the basin.

These syn-sedimentary structures are encountered both within host rocks and sulfide mineralized bodies; ii) a D1 event corresponding to the incipient Hercynian deformation and responsible for a steep NW-SE foliation (S1) in the Oriental Guemassa associated with folding under regional greenschist facies metamorphic conditions. It should be noted that S1 cannot be observed clearly within the Hajjar MSD; iii) a D2 Hercynian tectono-thermal event with P2 folds and associated S2 planar cleavage oriented NE-SW under low-grade metamorphism with sericite. S2 is the predominant foliation observable in the Hajjar mine; and iv) finally, a post-kinematic thermal event, likely related to “hidden plutons”, responsible for the crystallization of static biotite porphyroblasts with cordierite and andalousite locally described at Hajjar. In this ore deposit, this thermal event has been dated using “hydrothermal” biotite at ca. 301 Ma [33]. Moreover, for Carboniferous times, the Guemassa Massif is affected by intense multiscale ductile to brittle faulting [34,35], with probable components of Atlasic reactivation during the Tertiary High Atlas orogen (the Guemassa Massif is 15 km to the north of the Atlasic thrusting front, Figure 1B). On a structural map (Figure 1B), these faults and shear zones cross-cut and delineated several blocks within the Guemassa Massif. In the Oriental Guemassa, in which the Hajjar mine is located, the N’Fis block appears to present a peculiar “anarchic” foliation orientation with respect to the bulk NNE-trend of the main Hercynian foliation in the western Meseta domain. These “anarchic” foliation orientations have been explained by deflection or virgations (here defined as a bulk inflexion of foliation plane trajectories) induced by conjugate shear zones during or shortly after a broad E-W-oriented D1 shortening [34,35]: the dominant and earlier shear zones are dextral and trend ENE–WSW (e.g., the Imi-In-Tanout Fault, the eastern branch of the Amizmiz Fault, and the Guemassa Fault, Figure 1B), whereas WNW–ESE-trending shear zones are sinistral, such as the Lalla Takerkoust Fault (Figure 1B). This “virgation model” is compatible with a W–E horizontal shortening, in contrast to Hibti’s hypothesis (1993) [23], which argued for a NE–SW horizontal shortening during the D1 event (cf. supra).

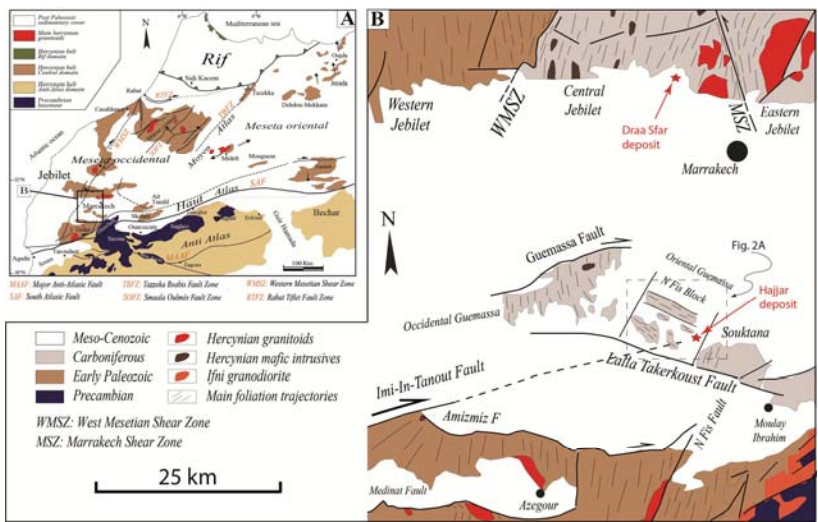


**Figure 1.** (A) Structural map of Morocco showing the major bounding-fault domains. The arrows indicate the sense of shear for the late Variscan structures (modified from Hoepffner et al., 2005 [36]); (B) Geological and structural map of the central domain of the Hercynian belt (from [35,37]). The main foliation trajectories in the Jebilet are reported from Essaifi, 1995 [18]). Within the Guemassa Massif, the Hajjar base metal deposit is located in the N’Fis block which presents an “anarchic” foliation orientation with respect to the bulk N to NNE trend reported in the Jebilet, Occidental Guemassa and western High Atlas Variscan Massifs.

The geology of the Guemassa Massif is similar to the Central Jebilet domain (Figure 1B). Both Massifs host the major MSD of the Occidental Meseta. Thus, recent advances in the tectono-metamorphic and magmatic history of the Jebilet [26,28] may help better constrain the Guemassa Massif evolution. Based on petro-structural data, new absolute dating and thermal investigations, these authors improve the time constraints and the succession of the deformational events as follows: i) from 370 to 325 Ma (D0 of Delchini, 2018 [26]), the Jebilet area was a basin filled with syn- to post-rift sediments (the Sarhlef and Teksmine formations, respectively) intruded by shallow sills and dykes and deeper plutonic laccoliths originating from a tholeiitic bimodal magmatism (e.g., the mafic/ultramafic Kettara and Sarhlef intrusions) and from a calc-alkaline magmatic suite (e.g., the Oulad-Ouaslam granodiorite) respectively; ii) from 325 to around 310 Ma, a first Hercynian event (D1) is marked by the emplacement of shallow thin skinned nappes with syn-sedimentary breccias. The internal strain is very low and no regional foliation/cleavage (S1) is reported; iii) from ca. 310 Ma to 280 Ma, the main Hercynian deformation (D2), which is polyphased and characterized by a first regional metamorphism (M2a), locally reaches the amphibolite facies (Grt-St) and a second HT/BP “contact” metamorphism in the syn- to post tectonic hornfels facies (M2b, biot + Crd + And) is associated with the leucogranite emplacement around 295 Ma. The successive foliations (S2a and S2b), sub-vertical and oriented N0/30, marked a homoaxial progressive and continual strain regime from a coaxial to a non-coaxial transpression with a broad horizontal NW-SE-trending shortening axis. Last, the D2 increments correspond to a right-lateral transpression accommodated and located along the vertical and conjugate ductile shear zones as the sinistral MSZ (Figure 1B). Therefore, the tectonic scenario proposed by Hibti (1993) [23] for the Guemassa which implies strain axis rotation between D1 and D2 and post-tectonic HT/LP metamorphism diverges from the one proposed by Delchini (2018) [26] for the Jebilet domain.

### 3. Surface Structural Data

The surface outcrops of the N’Fis block and Souktana Massif have been mapped and studied in terms of the strain analysis and micro-tectonics (Figures 2 and 3). The lithologies encountered are pelites alternating with sandy- to pure limestones intruded by felsic and basic sills and dykes (Figure 2). Major volcanic rock bodies correspond to rhyolitic domes and plugs.

Many outcrops of the Imarine Massif present soft-sediment deformation as slumps and convolutes (Figure 3A,B), suggesting slope instabilities within syn-rift sediments. These soft sediment structures are cross-cut by a sub-vertical foliation (S1) which is often oblique with respect to the axial plane of isoclinal folds (Figure 3B). This suggests that most isoclinal and disharmonic folds are slumps, and therefore, that they pre-date the development of the planar axial foliation. This S1 foliation is well-developed though the N’Fis block, with a sub-vertical dip and a NW-SE orientation (Figure 2). This widespread S1 planar fabric corresponds to a P1 axial planar cleavage (Figure 3C), and locally transposes the bedding planes (S0//S1, e.g., Figure 3D).

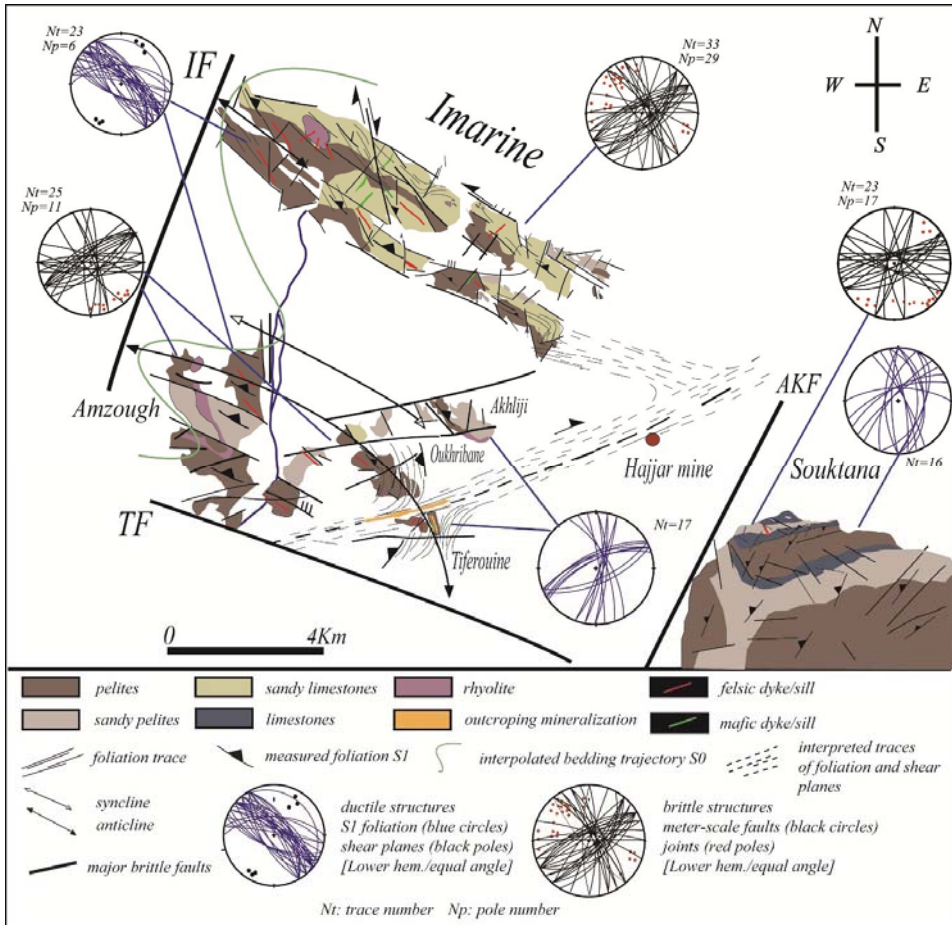


**Figure 2.** Geological map and surface structural data of the N'Fis block and the Souktana Massif. All of the sedimentary formations are Carboniferous in age and are affected by both metamorphism and deformation. IF: Imarine Fault; TF: Lala Takerkoust Fault; AKF: Ait Khaled Fault. The interpolation of the foliation/shear planes is also supported by sub-surface structural data from underground mine works (cf. infra). Note that the S1 trajectories depict a dextral drag fold against the ENE-trending Tiferouine mineralized body.

Locally, the NW-trending S1 is marked by elongated and aligned biotite porphyroblasts, parallel to the stretching of pyrrhotite grains (Figure 3D), suggesting a syn-tectonic growth of biotite. No stretching lineation has been observed in the N'Fis block. Decimeter-scale sinistral WNW to NW-trending vertical ductile shear planes, occurring sparsely and slightly oblique to S1, are responsible for the local deflection of the S1 planes in the Imarine outcrops (six observations plotted on the stereogram, Figure 2). Brittle faults and joints show a predominant NE-trending orientation with a sub-vertical dip (Figure 2). Due to unfavorable rock materials, the precise kinematics of brittle faults are difficult to establish, which enable the reconstruction of the paleo-stress using the right dihedral method, for instance. However, when it can be observed, the apparent map offsets of the NE-trending decimeter-scale faults indicate a dominant dextral sense of shear.



Finally, the Tiferouine outcrop (Figures 2 and 3E) shows a N70-trending gossan which corresponds to the weathered part of a magnetite-bearing body recognized at depth [12]. The supergene alteration appears to overprint an early cataclasite. Along and within the cataclasied mineralized body, the S1 foliation orientation is strongly disturbed (Figure 3E), suggesting drag folding along a right-lateral N70-trending wrench fault (also, see Figure 2 for a map view of the drag folding in the Tiferouine area).

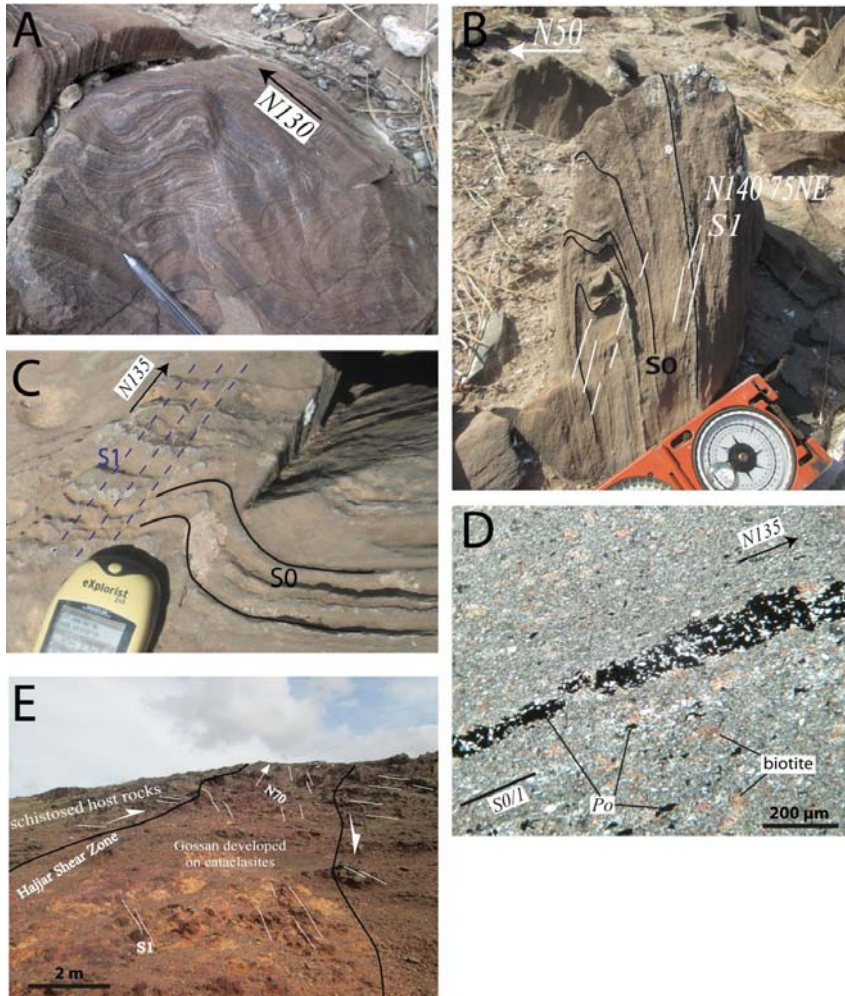


**Figure 3.** Structures observed in the outcrops. (A) syn-sedimentary and soft sediment deformation occurring as slumps and convolutes are widespread in the sandy limestones of the N'Fis block; (B) obliquity between the S1 foliation plane and recumbent fold axial plane suggests that some isoclinal folds are former slumps rather than P1 folds; (C) NW-trending S1 foliation plane developed within the P1 hinge zone; (D) thin sections (cross polars normal to foliation) of metapelite with sulfide ribbons (Po: pyrrhotite) from the N'Fis block. The bedding plane is transposed by the S1 foliation plane, the sulfide ribbon and patches disseminated in the matrix are flattened. Biotite porphyroblasts are elongated broadly parallel to the foliation plane; (E) mineralized Tiferouine body (see location in Figure 2) with an associated gossan inside an ENE-trending dextral shear zone evidenced by cataclasites and the re-orientation of S1.

#### 4. Sub-Surface Structural Data from the Hajjar Deposit

Five mine levels have been mapped in the Hajjar deposit (Figure 4). Moreover, we selected two peculiar cross-sections along the galleries to present the meso-scale structures (Figures 5 and 6). The micro scale structure and texture data are summarized in Figures 7 and 8.

##### 4.1. Strain Pattern and Meso-Scale Structures

Bedding, foliation, and shear planes have been reported at each exploitation level within either host rocks or mineralized bodies (Figure 5). Due to the exploitation, the mineralized bodies are not all accessible yet, and foliation data from Hibti (1993) [23] were used to interpolate the S1 trajectories. The micro petro-structural description of the foliation and shear planes are presented below in the following sections within both host rocks and ore.

The resulting maps show that in the Hajjar MSD, the S1 foliation is near vertical and trends from N0 to N45. With respect to the surface data from the N'Fis block (Figures 2 and 3), NW-oriented foliation has not been measured. The interpolation of the bedding trace emphasizes large-scale tight folding which affects both ore bodies and host rocks. The mineralized bodies have been mapped considering historical grade cut-offs for the exploitation. Geologically, the margins of the ore bodies are much less sharp than those shown on the maps provided in Figure 4. Despite this, the ore body morphologies are distributed among various shapes from a group of lensoid decametric bodies to multi-lobate and "dendritic" shapes (e.g., CP in Figure 4C). It is noteworthy that most of the lensoid decametric bodies, often distributed in clusters, are elongated parallel to the local foliation (e.g., CEWD, CWD, CP in Figure 4D,E).

The brittle deformation marked by fault offsets and joints makes it difficult to locally follow the ductile foliation and shear planes. This brittle deformation is marked by large cataclasite zones (thick lines in Figure 4) with different apparent kinematics that indicate complex and likely diachronous activities. Even though these polyphased cataclasite zones are very important for the continuation, exploration, and production of ore bodies, they require a specific structural study which is outside the scope of this paper which focuses on Variscan ductile strain.

Ductile strain is marked by foliated zones that are heterogeneously distributed, suggesting strain localization in corridors between less deformed areas (Figures 4, 5A and 6A). The strain pattern presents two types of high strain corridors (indicated in Figure 4B): N to NNE-trending and NE to ENE-trending strain corridors.

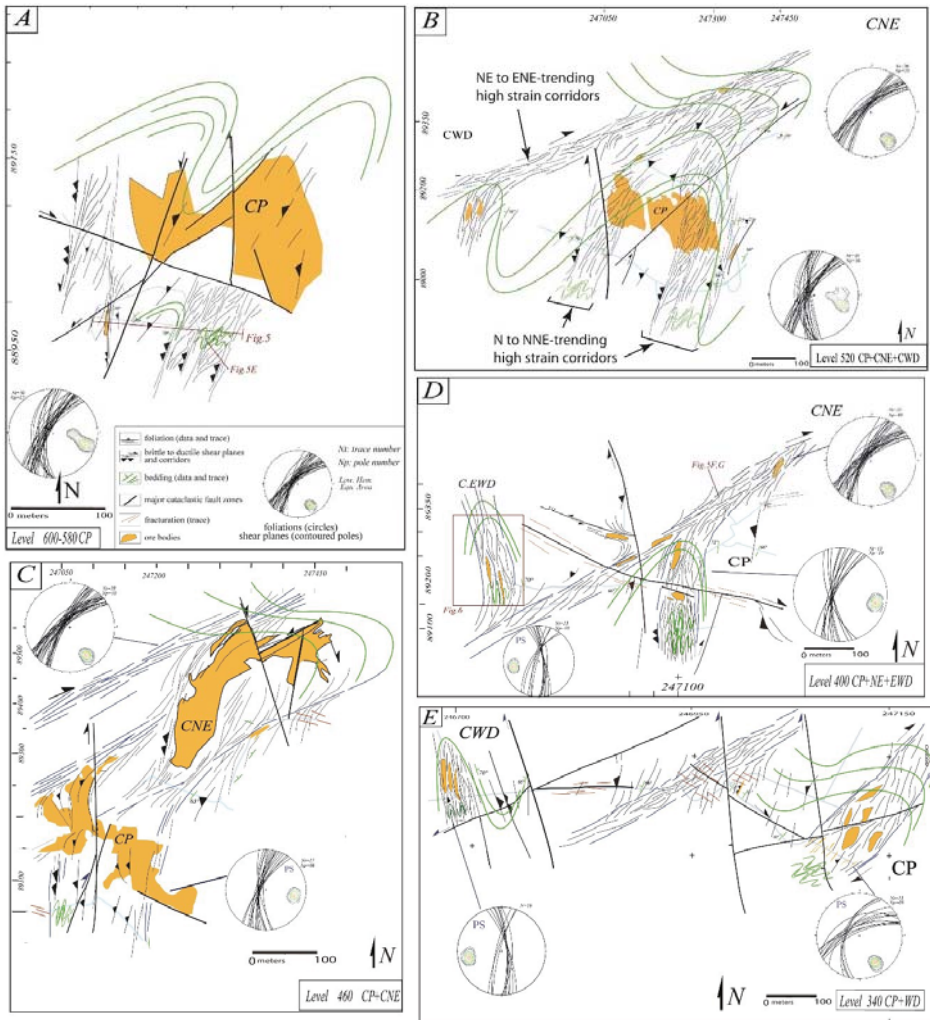


**Figure 4.** Structural maps of the five main exploitation levels (decreasing altitude from A to E) in the Hajjar mine. High strain corridors are marked by the development of dense foliation and shear planes. The light blue traces are galleries. The coordinates are taken from the mine’s own system. Note that the scale is slightly different for each level. The following acronyms are used for the ore bodies (translated from French): CP = main body; CNE = north-eastern body; CWD = western body; CEWD = extreme western body. The CP ore body has been intensively exploited and some zones are no longer accessible, structural data from Hibti (1993) [23] were then added and carefully projected in these areas (see text for explanation).

4.2. The N to NNE-Trending High Strain Corridors

These corridors have been almost fully mapped at all exploitation levels (Figure 4). Two types of strain corridors can be distinguished: the first is characterized by dominant reverse shear planes and folds with an axial planar cleavage S1 (called a “reverse corridor” below, Figure 5A–E), whereas the second corresponds to the development of a strong and penetrative S1 foliation with horizontal

stretching lineation without the occurrence of reverse shear planes (called a “flattening corridor” below, Figure 6).

Within reverse corridors, shear planes present dominant reverse rather than strike-slip kinematics. In the map view (Figure 4), the obliquity between S1 and the shear planes, which seems to indicate a sinistral sense of shear, is an artifact as the strike-slip component which is low and dextral when it is observed. The noticeable meso-scale structures are: i) eastward verging thrusts and decollements, most of time using a weak pyrrhotite-rich layer/body as the sole, which is near-parallel to the bedding in the foot-wall (Figure 5A–C). The associated folds in the hanging-walls developed an axial-planar cleavage S1. Typical meter-scale detachment folds, with thickening of the sulfide-rich decollement level, are frequent (Figure 5C), which might explain the “corrugation” observed along the decollement plane (Figure 5B); ii) the high strain corridors are characterized by the development of an intense foliation associated with similar upright NS-oriented folds (Figure 5A and D) which are frequently in association with reverse shear bands responsible for “pop ups” (Figure 5E). Local evidence of the oblique-slip component is provided by oblique stria, the “pop ups” then corresponding to dextral positive flower structures (Figure 5E).

Within the flattening corridors where thrusting is not observed, bedding marked by sulfide-rich ribbons is fully overprinted by the S1 foliation which bears a horizontal NS stretching lineation (Figure 6A). With increasing strain, the rock color changes to a very dark and black tint. To the west, a massive sulfide body is exploited (CEWD). This body is not continuous as it is instead composed of several distinct massive sulfide lenses aligned parallel to S1. The termination of the sulfide lenses is wavy due to the occurrence of small-scale folds of sulfide ribbons or host rocks. This sulfide lens morphology is frequently observed throughout the mine (e.g., Figure 8D). Near the termination, these lenses integrate clasts of host rocks (Figure 6). Cm- to dm-thick veins are abundant along the high strain corridor (Figure 6A). Locally, tips of massive sulfide lenses present triangular veins (or “saddle reef”) at a “triple junction” position with respect to the foliation (Figure 6).

#### 4.3. The NE to ENE-Trending High Strain Corridors

They are typical dextral shear zones, as indicated by drag folds in map view and obliquity between the near vertical S1 and the ductile shear planes (Figures 4 and 5F). The lineation is horizontal along the shear planes which often presents a graphitic/silvery mirror surface. The angle between S1 and the shear planes may be very low to null thus defining a mylonitic foliation locally (e.g., Figure 4C). These dextral shear planes, steeply dipping and trending NE to ENE (Figure 4), may present brittle characteristics as a gouge zone at the outcrop scale (Figure 5G). In the gallery, this type of high strain corridor is generally responsible for slope/wall instabilities, which makes access, oriented sampling, and structural data collection difficult, particularly where the strain corridors intersect large ore bodies (e.g., northern border of the CNE mineralized body, Figure 4C).

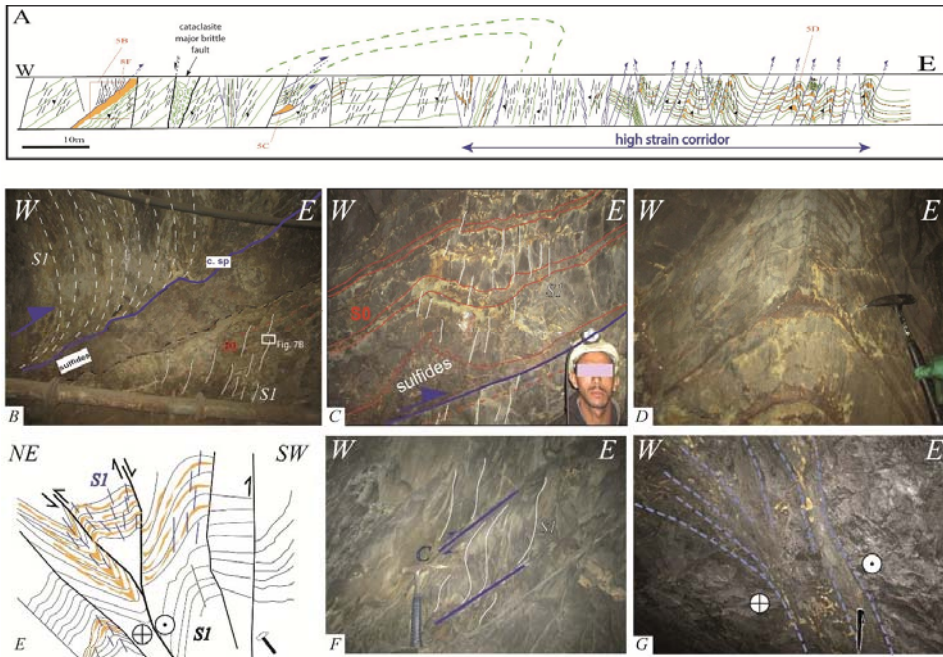


**Figure 5.** Structures and deformation of the Hajjar ore deposit. A to E are from the N to NNE-trending high strain “reverse” corridors; F and G are from the NE to ENE-trending high strain corridors. (A) Cross-section along the gallery from level 600–580 (see location in Figure 4A). S0 is shown in green, S1 is in black, the brittle to ductile shear planes are given in blue, the main massive sulfide bodies are shown in orange. The section is located within the footwall of the CP and is mainly composed of stratified gresio-pelites and tuffs with mm- to cm-thick sulfide ribbons (containing mostly pyrrhotite and pyrite with a small amount of chalcopyrite) with no economic interest. The intensity/spacing of the foliation and high frequency of the shear planes can be used to depict the high strain corridors. Most of the brittle to ductile shear planes have an apparent reverse component: (B) an east-verging thrust developed within a pyrrhotite-rich massive sulfide deposit acting as a decollement layer. In the hanging-wall, the bedding is not observed whereas the S1 cleavage is curved by top-to-the-east drag folding. Both massive sulfide wallrocks are corrugated (c. sp: corrugated shear plane); (C) Detachment fold above a pyrrhotite-rich sulfide layer thickened within the core of a disharmonic fold hinge The S1 axial planar foliation is well-developed in the hanging-wall; (D) Upright similar fold with associated axial planar S1 cleavage. The pyrrhotite-rich red ribbons are extremely thinned in the limbs and thickened within the hinge zone; (E) Positive flower structure associated with similar drag folds and S1 cleavage (line drawing from level 600–580, Figure 4A). Along the N15E-trending faults, high dipping stria show that the reverse component is dominant relatively to the dextral strike-slip one; (F) Ductile dextral NE-trending near the vertical shear planes (C) and associated S1 foliation within a NE-trending right-lateral high strain corridor in meta-siltstones (location CNE area, Figure 4D); (G) ENE-trending steep dextral shear zones marked by foliated gouges and various branches (sense of shear is determined in the gallery roof, location in Figure 4D).

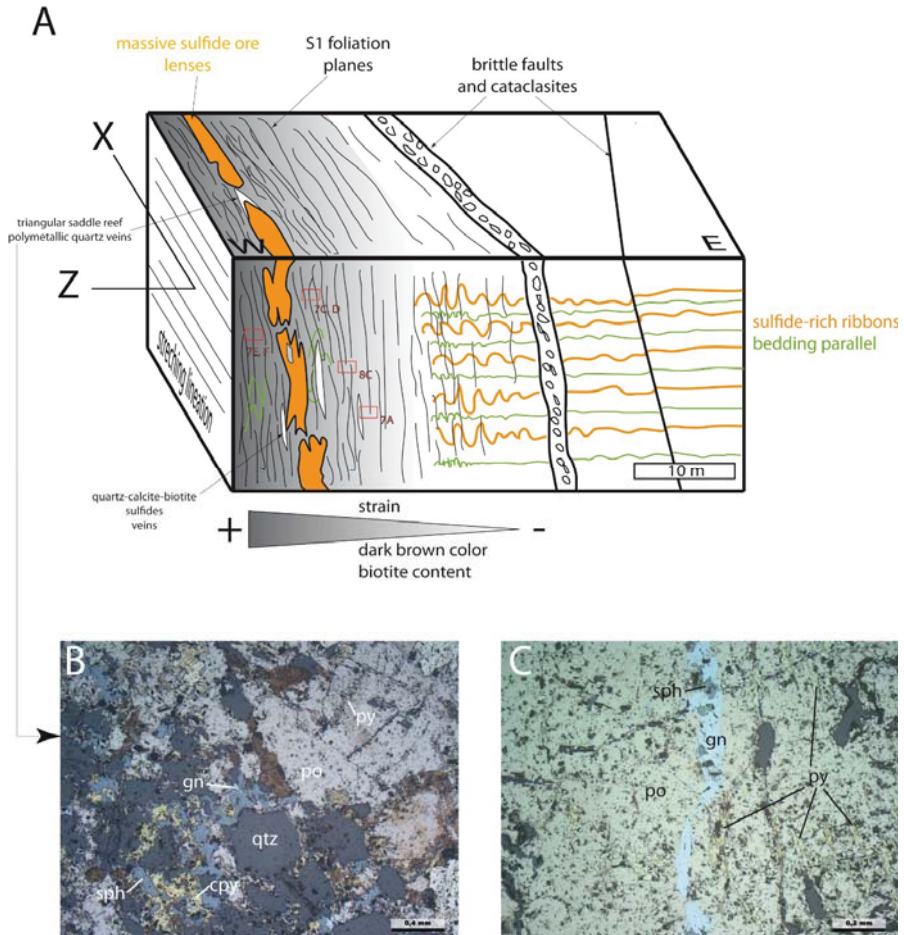


**Figure 6.** Outcrops of the extreme western body (CEWD) gallery, a typical N-trending “flattening” corridor. (A) 3D man-made sketch of the CEWD cross-section located in Figure 6A. The exploited massive ore bodies correspond to meter-scale lenses aligned within a high strain zone marked by an intense foliation in dark host rocks with high biotite and sulfide content. X and Z are the long and short axis of the strain ellipsoid respectively; (B,C) Thin-section photographs of the triangular veins developed at the massive ore lenses termination (RL). The vein is mainly filled with quartz associated with a polymetallic assemblage. Pyrrhotite is replaced by pyrite along cracks (B,C) and sphalerite/galena ( $\pm$  chalcopyrite) veinlets crosscut the former pyrrhotite and arsenopyrite grains (not shown).

#### 4.4. Microstructures and Textures in the Host Rocks

Oriented thin sections were taken from the Hajjar MSD, especially from the N to NNE-trending high strain corridors described above.

The primary lithologies and associated syn- or diagenetic hydrothermal halos have been metamorphosed and/or altered. This metamorphism appears to be better expressed in high strain corridors, i.e., when the S1 foliation planes are densely represented (e.g., Figure 6A). Two metamorphic assemblages can be distinguished in the metapelites. The first one is comprised of quartz + biotite + andalusite ( $\pm$  calcite). (Figure 7A,C,D). Cordierite has not been observed, but the shape of some

porphyroblasts replaced by white mica aggregates indicate the presence of this mineral (e.g., Figure 8E). The second assemblage is made of quartz + chlorite + muscovite ( $\pm$  carbonate). This last assemblage can also be observed in sandy-pelites with sulfide-rich ribbons, where it post-dates and locally replaces the biotites (Figure 7B). Foliation-parallel veinlets are filled with quartz and large biotite crystals associated with calcite in the geodic cavities (Figure 7A).

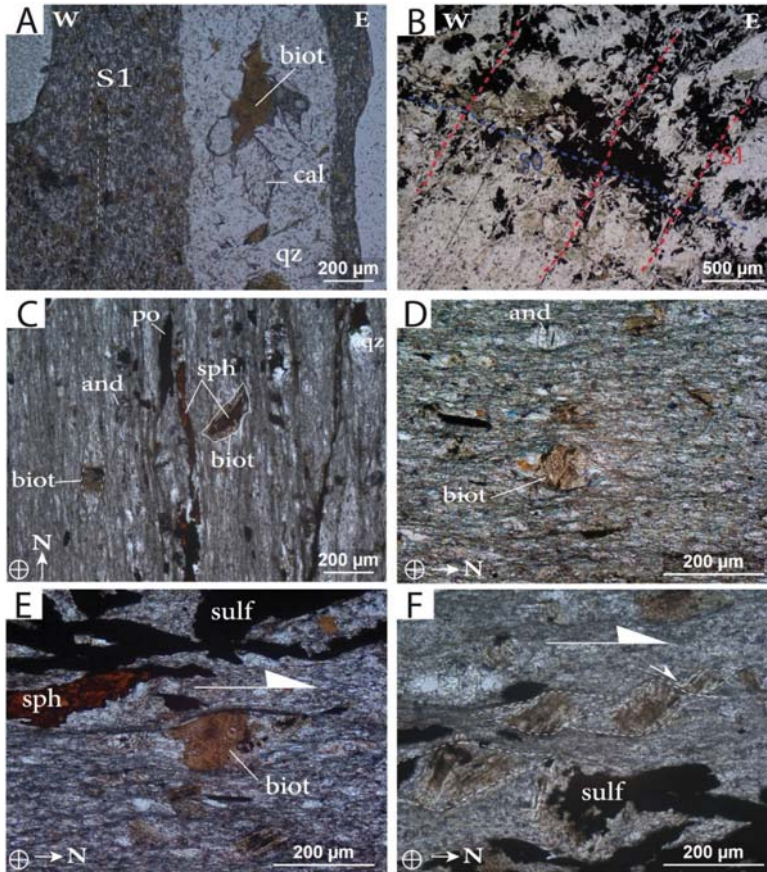


**Figure 7.** Thin section microphotographs of the S1 foliation and associated porphyroblasts within the Hajjar host rocks. A, C, D, E and F are from the flattening corridors; B is from the reverse corridors. (A) Quartz (qz), calcite (cal) and biotite (biot) vein parallel to the incipient S1 foliation, vertical section, see location in Figure 6, NAPL. The host rock presents a fine-grained granoblastic texture composed of biotite and andalousite grains with a local preferred orientation defining an incipient foliation plane; (B) Footwall of the thrust (see location in Figure 5) with the So plane marked by sulfide-rich ribbons (in blue) and discrete S1 planes (in red) characterized by muscovite (white laths) crystallization (NAPL). Please note that the non-oriented biotite (i.e., “static”) porphyroblasts are replaced by chlorite (pale green); (C–F) Horizontal thin sections parallel to the stretching lineation showing the main foliation plane S1 marked by elongated sulfides (sulf) and particularly pyrrhotite (po) and sphalerite (sph); see location in Figure 6. Like the fine-grained foliation, the pressure shadows and caps around the andalousite (and) and biotite (biot) grains are composed of quartz, white micas, chlorite and local carbonates. In the high strain area, asymmetric pressure shadows around the biotite indicate a non-coaxial regime with a dextral sense of shear (E,F).

In areas where the foliation is weakly developed, biotite and andalousite porphyroblasts show a granoblastic “static” texture with a very subtle preferred orientation locally (Figure 7A). With increasing strain, biotite porphyroblasts are generally coarser and present a preferred orientation parallel to the fine-grained S1 foliation, a planar axial surface with micro-folds (Figure 8C). In high strain zones, pressure shadows and strain caps are found around some biotite and andalousite crystals (Figure 7C to F), whereas other biotite crystals remain nearly free of foliation deflection (e.g., a biotite crystal growing around a sphalerite core in Figure 7C). The pressure shadows are generally composed of quartz, muscovite, and chlorite, i.e., the same assemblage constituting the fine-grained foliation (Figure 7D,E). Asymmetric pressure shadows around biotite are common in flattening corridors attesting to a non-coaxial regime, at least locally (e.g., dextral in the CEWD outcrop, Figure 6, Figure 7E,F). Therefore, in high strain and non-coaxial zones, biotite crystals appear as pre-tectonic porphyroblasts, suggesting severe non-coaxial strain increments after the HT/LP metamorphism peak.

#### 4.5. Microstructures and Textures in Sulfides

The internal ductile/plastic strain of the sulfide ribbons and bodies is widespread and high in the Hajjar MSD. This is particularly due to the high content of pyrrhotite within the ore.

Associated with folding, the S1 axial planar cleavage is marked by flattened sulfide ribbons within the XY plane with refractions and hinge thickening (Figure 8A,B). The preferred interpretation is that a refraction mechanism is responsible for this rather than a “bed to bed” flexural slip, because no shear planes have been observed in quartz (Figure 8B). Normal thin sections with XY planes cannot be used to characterize a preferred stretching X direction with respect to the 3D sulfide micro-lens dimensions. Therefore, the strain ellipsoid is mainly oblate and the strain regime is close to pure flattening. In greater detail, different rheological behaviors of the sulfides are expressed along S1, with pyrrhotite behaving much more plastically than chalcopyrite and sphalerite (Figure 8B), which present both a “ductile” and brittle response to the stress. Frequently, the sulfide micro-lenses present an “X-shape” or “chromosome-like” morphology (Figure 8A,C). The elongated sphalerite grains surrounded by pyrrhotite within a foliated silicate matrix (Figure 8C) suggest that the conjugate effects of folding, recrystallization, and rheological contrasts explain this “X” morphology. As mentioned above, this peculiar “X-shape” morphology is also encountered at a larger scale in the edge and tip areas of massive ore bodies (Figures 6 and 8D).

In many places at the Hajjar MSD massive sulfide bodies present an internal planar fabric. Three types of fabrics can be distinguished: i) a planar fabric parallel to the S1 foliation within the host rocks (Figure 8D). In this case, the fabric corresponds to flattened pyrrhotite grains (with various chalcopyrite, sphalerite and galena contents), separated by elongated metamorphic silicate slices/lenses (Figure 8E). The metamorphic assemblage is represented by chlorite and white micas replacing former biotite/andalousite (/cordierite?) blasts (Figure 8E). These silicate slices can be very thin or even absent in the most enriched ore. It is noteworthy that the mechanical twinning of pyrrhotite is regularly distributed in a direction normal to the planar fabric, providing evidence for the tectonic origin of this foliation; ii) mylonitic zones affecting weakly deformed massive sulfides (Figure 8G). These mylonites can be observed where high strain corridors intersect or encompass mineralized bodies. C/S-type structures are common within the sulfide mylonites (Figure 8G). Flattened pyrrhotite grains define the S planes, whereas C planes present finely cataclased sphalerite and chalcopyrite in a foliated silicate gouge; iii) the third planar fabric corresponds to a mineralogical and textural banding marked by alternations of sphalerite-rich and sphalerite-poor ribbons (Figure 8F). For instance, this banding is either parallel to the S1 foliation in the wall rocks or parallel to the bedding planes in the footwall of decollement layers (Figures 5 and 8F). Pyrrhotite grains are elongated with no systematic mechanical twinning. Sphalerite does not show systematic elongation, and the quartz grains are elongated with undulose extinction (Figure 8F). Therefore, the respective part of the syngenetic and diagenetic vs. tectonic processes are still unclear, and cannot be used to explain this banding.



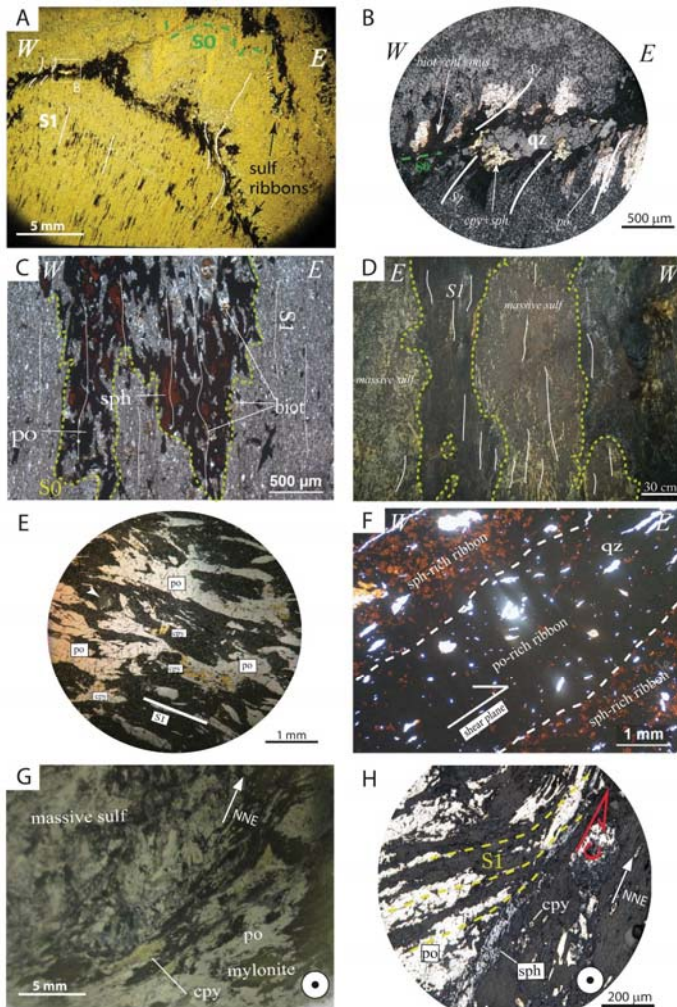


**Figure 8.** Deformation and textures of the sulfides in the Hajjar deposit. (A) The folding and associated S1 foliation of fine-grained sediments containing early sulfide-rich ribbons parallel to the bedding (S0). Note the cleavage refraction and thickening of the hinge zone due to the plastic behavior of pyrrhotite; (B) Details of A with pyrrhotite flowing along the stretching direction whereas the behavior of chalcopyrite and sphalerite is less plastic. A metamorphic assemblage mainly composed of muscovite and chlorite ( $\pm$  biotite) grows parallel to S1; (C) Micro-fold affecting a sphalerite and pyrrhotite-rich thin ribbon (CEWD, location in Figure 6A). The axial planar cleavage S1 is marked by the stretching of sulfides and elongated biotite blasts; (D) Massive sulfide lenses separated by strongly foliated host rock slices (south of CP, altitude 500 m). The ore bodies are internally banded parallel to the S1 foliation; (E) Texture of deformed pyrrhotite-rich massive sulfide (RL) parallel to the S1 foliation. The dark grey areas correspond to a muscovite/chlorite (replacing biotite locally) assemblage. Andalusite or cordierite porphyroblast ghosts are replaced by white micas (arrow); (F) textural and mineralogical banding within a massive sulfide body in the sole thrust (see location Figure 5A,B). Note the elongation of the quartz grains; (G) Massive sulfide sample affected by ductile shearing and mylonitization (SE part of the CP, level 400, the local name is “la bande Sud-Est”); (H) Details of G, thin section, RL. The sulfide mylonites present typical C/S structures. It should be noted that sphalerite appears to be “localized” in the C planes. The sample view from the bottom shows a dextral sense of shear.

## 5. Interpretation

### 5.1. Hajjar Mine and N'Fis Block: One Single Foliation (Not Two)

The rocks of the Hajjar mine are affected by one single flattening XY plane which is near vertical and trends from N0 to N45. The maps of the S1 trajectories (Figure 4) show that the deformation is not homogenous at the mine scale. In the high strain corridors, this XY plane corresponds to a S1 penetrative foliation overprinting the entire rock, whereas in less deformed areas, S1 is a slaty cleavage that is axial planar in similar folds. Host rocks and sulfide bodies present the same silicate metamorphic assemblages (Figures 7 and 8). With respect to this foliation, the qtz + biot and assemblage presents either a “static” granoblastic texture when the strain is low (i.e., weakly developed foliation, Figure 7A) or pre- to syn-tectonic features when the foliation is strongly expressed (Figures 7C to E, 8C). The texture, shapes, and aggregates of the biotite and andalousite ( $\pm$  suspected cordierite) are typical of HT/LP “contact” metamorphism in the hornfels facies. The syn-tectonic assemblage is composed of quartz + chlorite + white micas ( $\pm$  calcite) and partially replaced the former biotite and andalousite blasts (Figures 7B and 8E).

Similarly, surface data from the N'Fis block (Figures 2 and 3) show the occurrence of a single sub-vertical XY plane oriented N130. This flattening plane is a penetrative foliation secant to slumps (Figure 3B) and axial-planar to P1 folds (Figure 3C). Contact metamorphic biotite blasts are elongated parallel to the foliation and appear as flattened sulfide grains (Figure 3D).

Therefore, these data imply that the Hajjar MSD and the N'Fis block are affected by a single foliation which encompasses a HT/LP contact metamorphism. Although a single Variscan foliation was similarly recognized by Dias et al. (2011) [35] at the regional scale, our results disagree with the previously published works on the Hajjar mine/N'Fis area: i) first, two foliations were identified and consequently two successive tectonic events with sub-normal horizontal shortening directions were invoked [12,23]. In particular, the N20-30 dry joints affecting the N'Fis block at the surface (Figure 2) cannot be related to the N0-30 penetrative and ductile foliation observed in the Hajjar mine. Moreover, there has been no direct observation of an early foliation/cleavage in the Hajjar galleries during our study; ii) second, the biotite blasts were interpreted as post-tectonic with respect to the last deformation event [25].

### 5.2. The Hajjar Mine is Located within a Regional-Scale Shear Zone

The direct consequence of the previous result is the occurrence of a large foliation virgation from the Imarine outcrops to the Hajjar MSD (Figure 2). This virgation in the orogeny is typically caused by wrenching along regional shear zones. Our structural data from the surface (e.g., Tiferouine outcrops, Figures 2 and 3E) and from sub-surface structural maps (Figures 4 and 5) in the Hajjar underground mine fully support the occurrence of a major right-lateral ENE-trending transpressive shear zone at Hajjar.

The strain pattern on the maps show that shear planes are heterogeneously distributed as they are clustered within the shear corridors. Along a broad ENE direction, we identified various types of high strain corridors (see the 2D pattern in Figure 9): i) the N to NNE-trending corridors correspond to either reverse corridors characterized by thrusting and associated folding with a low amount of dextral oblique-slip (Figures 4 and 5A–E) or to flattening corridors characterized by a tight and penetrative foliation with horizontal stretching lineation and a local dextral sense of shear (Figures 6 and 7); ii) The NE to ENE-trending corridors correspond to unequivocal vertical dextral shear zones. The orientation of both strain corridors are connected and form an asymmetric 3D anastomosed pattern that is compatible with a bulk dextral sense of shear along a N60-70 direction (Figure 9). Reverse corridors with vertical thickening indicate that the Hajjar shear zone is transpressive. This result is fully in coherence with previous works dealing with the Western Meseta, in which dominant dextral strike-slip tectonics were clearly identified during the Variscan orogen [35]. However,

in the location near the Hajjar mine, a regional scale shear zone of this type has not been previously recognized and constitutes a key structural feature of the Guemassa Hercynian orogenic segment.

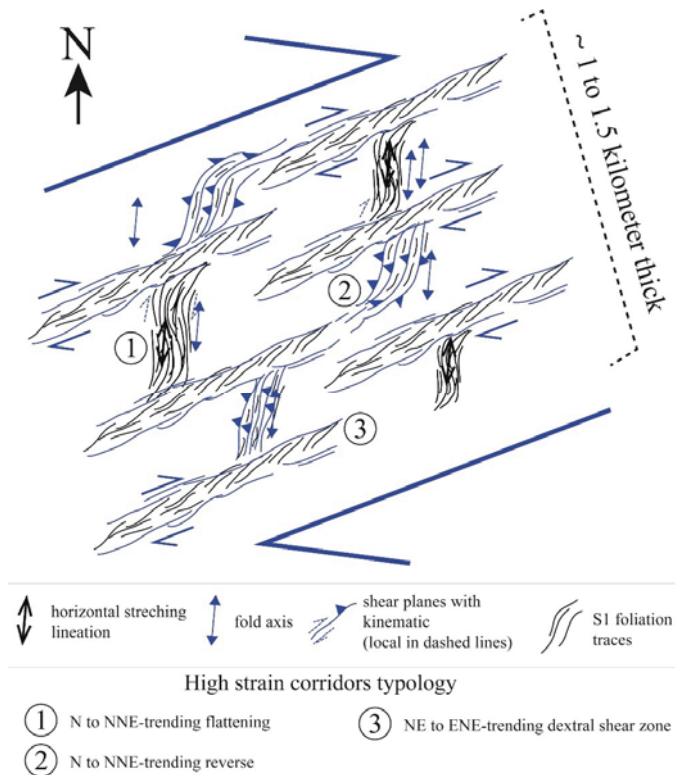


**Figure 9.** Simplified and conceptual map view model of the internal strain pattern within the Hajjar transpressive right-lateral shear zone (see text for explanation).

The shear planes of the Hajjar MSD present both ductile and brittle features (Figures 5 and 8G, H). The last brittle increments cross-cut and offset the former S1 foliation along the gouge zones (Figure 5G). Asymmetric biotite blasts with pressure shadows filled with the chlorite and white mica assemblage (Figure 7E,F) argue for simple shearing after the thermal peak of the HT/LP contact metamorphism. Lower or retrograde metamorphic conditions during simple shearing are also indicated via the cataclasis of sphalerite and chalcopyrite along the shear planes within mylonitic zones affecting massive sulfides (Figure 8H). Therefore, the Hajjar shear zone records simple shearing increments during and after the development of the widespread S1 foliation.

Last, the Atlasic brittle reactivation of this Hercynian shear zone cannot be ruled out, however it is still difficult to precisely depict this.

### 5.3. Ore Deformation and Remobilization

As recognized in previous studies [25], our data indicate that the Hajjar mineralization is strongly deformed and metamorphosed. It is affected by folding, foliation and mylonitic bands within a regional scale shear zone. Structures such as pyrrhotite-rich ribbons clearly pre-date the deformation and the HT/LP contact metamorphism (e.g., Figures 6 and 8A). The primary syn- or diagenetic mineralization is then strongly reworked by deformation. In particular, at the meter scale,

we present clear evidence of tectonic thickening within the fold hinge zone. The wavy termination of the metric-scale massive sulfide lenses parallel to S1 suggests that these lenses were likely thickened by folding before they were flattened within the XY plane of S1 (Figures 6 and 8D). This mechanism is enhanced by the high “plasticity” of pyrrhotite, which is by far the dominant sulfide at Hajjar. The pre-to syntectonic HT/LP metamorphism greatly favor the ductile behavior and recrystallization of sulfides including chalcopyrite and sphalerite. This is observable at the thin section scale, where the tectonic thickening induced the stress-oriented recrystallization of sphalerite, leading to an incipient “banding” of sphalerite-rich/sphalerite-poor slices parallel to S1 (Figure 8C). We suggest that, in Hajjar MSD, this solid-state thickening and remobilization are effective at a larger scale, but further modern textural and mineralogical studies are required in order to be able to investigate this point.

Remobilization of the primary metal stock by fluids (e.g., the fluid state processes and chemical remobilization described by Gilligan and Marshal (1987) [3] is also expressed in the Hajjar MSD. Even though the metal mass balance quantification is outside the scope of this study, the polymetallic veins argue for hydrothermal fluid-assisted remobilization during deformation. In particular, the polymetallic triangular veins at the tips of the massive sulfide lenses indicate such remobilization. This type of vein with a polymetallic assemblage associated with quartz, newly formed sphalerite and galena veinlets, and pyrrhotite replacement by vermicular pyrite (Figure 6B,C), is similar to the so-called “piercement veins” described by authors working on deformed MSD (e.g., [3,38–40]). It has been hypothesized that the metamorphic fluids liberated during the prograde HT/LP contact metamorphism (e.g., quartz veins with biotite in Figure 7A), combined with potential advective hot magmatic fluids exsolved from deeper granitic bodies, are able to chemically rework the primary sulfides and concentrate metals into dilatant sites as triple junction veins during the last increments of deformation [3]. Due to high reactive chemistry, the fluid-assisted chemical reworking of primary VMSD is common in many metamorphic contexts other than HT/LP metamorphic conditions (e.g., [41] and references therein).

## 6. Discussion: Toward an Integrated Tectono-Metamorphic Model for the MSD-Bearing Jebilet and Guemassa Massifs

These interpretations must be discussed in terms of the ages and tectono-metamorphic evolutions established for the Guemassa and Jebilet Massifs; both of these Massifs bear the major MSD in Morocco.

First, syn-sedimentary structures and soft sediment deformation have been identified in the N’Fis block (Figure 3A,B) and in the Hajjar mineralization [23]. These structures are well known within the Visean Sarhlef syn-rift formation in the Jebilet Massif, and correspond to slope instabilities during the opening of the Jebilet basin from 370 to 325 Ma (the D0 transtensive event described by Delchini (2018) [26]). Coeval with this sedimentation, the basin underwent significant bimodal and calc-alkaline magmatism, leading to many intrusions within the sediments and the basement. Consequently, the thermal gradient is very high [26], and primary syn- to diagenetic massive sulfide mineralization occurred within the volcano-sedimentary sequences (Figure 10A). The initial morphology (e.g., normal fault locations and trends, depocenters, etc.) of these basins and sub-basins is not constrained in the Guemassa Massif contrary to the Jebilet Massif where the basins are interpreted as pull-apart systems with NNE-trending normal faults and associated N70E-trending left-lateral strike-slip faults [42]. Therefore, it is likely that the Guemassa Massif and the Hajjar shear zones acted as sinistral strike-slip faults during this Early Carboniferous period (Figure 10A), lateral N to NNE trending normal faults accommodating the formation of local subsiding basins such as the Hajjar one (Figure 10A). However, because it may control the initial MSD distribution, further detailed work is required to specify the Early Carboniferous basin geometries in the Guemassa Massif.

Second, absolute dating of the Hajjar biotites related to thermal aureole metamorphism has been performed by Watanabe (2002) [33] using  $^{40}\text{Ar}/^{39}\text{Ar}$  dating and yields an approximate age of ca. 301 Ma. This age and the associated HT/LP metamorphic assemblage are compatible with the M2b metamorphism reported in the Jebilet Massif [26,28]. In other words, the S1 foliation and HT/LP metamorphism that we document in the Hajjar MSD and in the N’Fis block within the Guemassa

Massifs are structurally and temporally similar to the D2b tectono-metamorphic event described in the Jebilet Massif to the north (see the section on geological settings above and [26]). It is noteworthy that this thermal event is not restricted to the Hajjar mine, as it has been traced by Raman Spectroscopy of Carbonaceous Materials geothermometry method (RSCM) throughout the whole N'Fis block [27]. In the Jebilet as in the Guemassa Massifs, it has been reported that this thermal event is the consequence of hidden plutonic intrusions. Our data suggests the presence of fluid-assisted HT/LP “contact” metamorphism (Figure 7A). Therefore, the vigorous advection of hot fluids exsolved from melts and/or which come from metamorphic devolatilization may also partly explain the large extent of this HP/LP metamorphism observed in the Guemassa and Jebilet Massifs close to 300 Ma. This regional thermal anomaly is represented in Figure 10B. No former foliation/cleavage has been observed in either the N'Fis block or in the Hajjar mine, suggesting that the D2a/M2a event identified by Delchini (2018) [26] in the Jebilet Massif is not expressed in the Guemassa Massif. This is in agreement with the fact that the D2a/M2a event, which reaches the garnet-staurolite amphibolite facies, is poorly represented in the Jebilet Massif, and better expressed northward in the Rehamna Massif. Thus, the S1 foliation/cleavage characterized in this study matches the S2b foliation identified in the Jebilet Massif to the north by Delchini et al. (2016) [28]. Biotites related to the HT/LP metamorphism are not post-kinematic, as proposed by Hibti (1993) [23]. They are pre- to syn-kinematic, which implies that deformation occurred during the peak of the HT/LP “contact” metamorphism (Figure 9B). Based on the biotite blasts vs. strain relationship, we suggest that during the HT peak, the deformation was predominantly coaxial before shifting to a bulk non-coaxial regime.

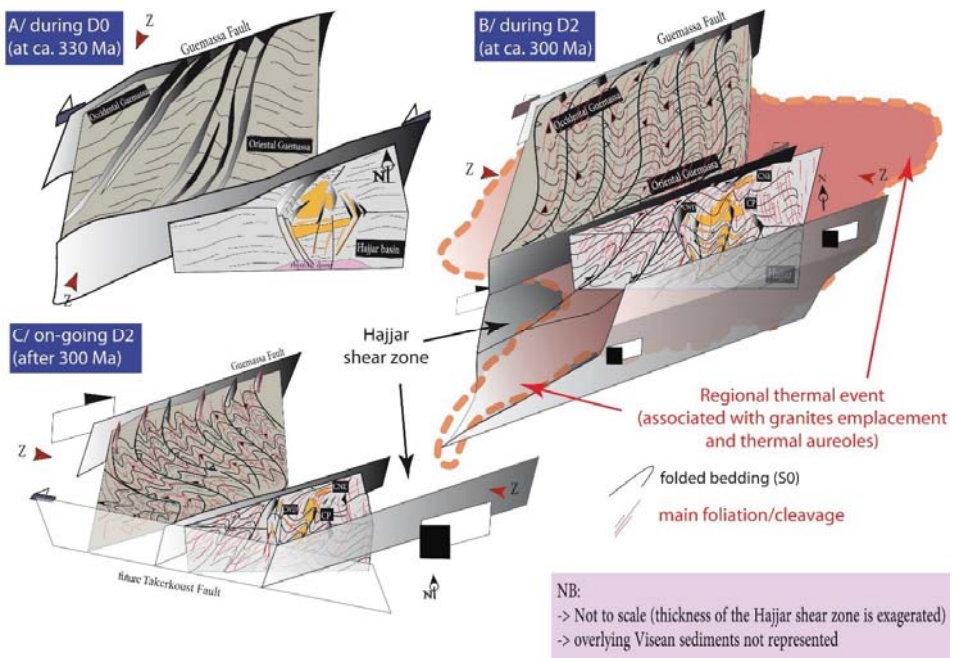


**Figure 10.** Tectono-metamorphic model of the Hajjar shear zone and associated MSD. The name of the tectonic events (D0, D2) corresponds to the tectonic events that have recently been established for the Jebilet Massif by Delchini (2018) [26]. D1 has not been identified in this study. See text for explanations.

Third, during the Early Permian, the D2 event identified in the Jebilet Massif ended with transpressive conjugate regional shear zones, oriented NE/ENE and SE/SSE with a dextral and sinistral (e.g., the MSZ, Figure 1) sense of shear respectively (i.e., the D2c event described by Delchini,

2018) [26]. This led to the development of a regional scale “flower structuration” of the Jebilet Massif. This strain localization along the shear zones appears to post-date the HT/LP contact metamorphism. Our data from the Guemassa Massif are fully compatible with this scenario (Figure 10C): the Hajjar regional shear zone we recognized in this study appears to be one of the dextral shear zones responsible for the large virgation of the main foliation planes. As observed in the Jebilet Massif, this shear zone corresponds to a progressive strain localization during the retrograde metamorphism when the D2 event ended. Last, as proposed by Dias et al. (2011) [35], conjugate WNW-ESE trending sinistral shear zones activated as the Lalla Takerkoust fault (Figure 10 C). This sinistral wrench zone accentuated and is responsible for the virgation of the S1 foliation, resulting in the “anarchic” WNW-orientation of the foliation observed through the N’Fis block.

## 7. Conclusion

The Guemassa Massif and the Hajjar base-metal massive sulfide deposit have been affected by a single foliation during a major Late Carboniferous-Early Permian Hercynian tectonic event. This foliation is strongly affected and deflected by regional scale shear zones such as the Hajjar N70-trending and right-lateral shear zone. Structural mapping in the Hajjar mine demonstrates that the Hajjar shear zone is complex with anastomosing shear plane patterns combined with thrusting and folding. This deformation is partially coeval, with a large thermal anomaly responsible for the HT/LP metamorphism. The tectono-metamorphic evolution of the Oriental Guemassa Hercynian segment is highly compatible with the evolution depicted for the Jebilet Massif. Strain under a high heat flux favored the deformation of the massive sulfides bodies which partly underwent fluid-assisted remobilization in the Hajjar mine. The tectonic thickening of the mineralization is observed at the meter scale, and must be re-examined at a larger scale.

**Author Contributions:** S.A. and Y.B. conceptualized both the study and the final model and wrote the original draft. L.B. (Lakhlifi Badra) and L.B. (Luc Barbanson) reviewed and edited the draft. M.O., A.K., M.Z., L.M. gave their validation, Funding acquisition and project administration.

**Funding:** The PhD thesis of S. Admou has been partly funded by the “Office Méditerranéen de la Jeunesse” through a partnership between Orleans University (France) and Moulay Ismael University (Meknès, Morocco).

**Acknowledgments:** We are grateful to S. Janiec from ISTO and X. Le Coz from Geosciences Rennes who performed high quality thin sections. Our discussion with S. Delchini was greatly appreciated. We thank the reviewers and specially R. Dias for very fruitful and constructive review. The Guest Editor A. Chauvet is also thanked for inviting us to submit our work.

**Conflicts of Interest:** The authors declare no conflict of interest.

## References

1. Cawood, P.A.; Hawkesworth, C.J. Temporal relations between mineral deposits and global tectonic cycles. In *Ore Deposits in an Evolving Earth*; Jenkin, G.R.T., Lusty, P.A.J., McDonald, I., Smith, M.P., Boyce, A.J., Wilkinson, J.J., Eds.; Geological Society of London: London, UK, 2013; pp. 9–21.
2. Graf, J.; Skinner, B. Strength and deformation of pyrite and pyrrotite. *Econ. Geol.* **1970**, *65*, 206–215. [[CrossRef](#)]
3. Marshall, B.; Gilligan, L.B. An introduction to remobilisation: information from ore-body geometry and experimental considerations. *Ore Geol. Rev.* **1987**, *2*, 87–131.
4. Marshall, B.; Spry, P.G. Discriminating between regional metamorphic remobilization and syntectonic emplacement in the genesis of massive sulfide ores. *Rev. Econ. Geol.* **1998**, *11*, 39–80.
5. Marignac, C.; Diagona, B.; Cathelineau, M.; Boiron, M.-C.; Banks, D.; Fourcade, S.; Vallance, J. Remobilisation of base metals and gold by Variscan metamorphic fluids in the south Iberian pyrite belt: evidence from the Tharsis VMS deposit. *Chem. Geol.* **2003**, *194*, 143–165. [[CrossRef](#)]
6. Chauvet, A.; Ouzémine, J.; Charvet, J.; Barbanson, L.; Faure, M. Syn- to late-tectonic stockwork emplacement within the Spanish section of the Iberian pyrite belt: Structural, textural, and mineralogical constraints in the Tharsis and La Zarza areas. *Econ. Geol.* **2004**, *99*, 1781–1792. [[CrossRef](#)]

7. Barrie, C.D.; Boyle, A.P.; Prior, D.J. An analysis of the microstructures developed in experimentally deformed polycrystalline pyrite and minor sulphide phases using electron backscatter diffraction. *J. Struct. Geol.* **2007**, *29*, 1494–1511. [[CrossRef](#)]
8. Barrie, C.D.; Boyle, A.P.; Cook, N.J.; Prior, D.J. Pyrite deformation textures in the massive sulfide ore deposits of the Norwegian Caledonides. *Tectonophysics* **2010**, *483*, 269–286. [[CrossRef](#)]
9. Barrie, C.D.; Peare, M.A.; Boyle, A.P. Reconstructing the pyrite deformation mechanism map. *Ore Geol. Rev.* **2011**, *39*, 265–276. [[CrossRef](#)]
10. Reddy, S.M.; Hough, R.M. Microstructural evolution and trace element mobility in Witwatersrand pyrite. *Contrib. Mineral. Petrol.* **2013**, *166*, 1269–1284. [[CrossRef](#)]
11. Bernard, A.J.; Maier, O.W. Aperçus sur les amas sulfurés Massifs des hercynides Marocaines. *Miner. Depos.* **1988**, *23*, 104–114. [[CrossRef](#)]
12. Hibti, M. Les amas Sulfurés des Guemassa et des Jebilet (Meseta Sud-Occidentale, Maroc): Temoins de L'hydrothermalisme Précoce dans le Bassin Mesetien. Ph.D Thesis, University Cadi Ayyad, Marrakech, Morocco, 2001.
13. Belkabir, A.; Gibson, H.L.; Marcoux, E.; Lentz, D.; Rziki, S. Geology and wall rock alteration at the Hercynian Draa Sfar Zn–Pb–Cu massive sulphide deposit, Morocco. *Ore Geol. Rev.* **2008**, *33*, 280–306. [[CrossRef](#)]
14. Marcoux, E.; Belkabir, A.; Gibson, H.L.; Lentz, D.; Ruffet, G. Draa Sfar, Morocco: A Visean (331 Ma) pyrrhotite-rich, polymetallic volcanogenic massive sulphide deposit in a Hercynian sediment-dominant terrane. *Ore Geol. Rev.* **2008**, *33*, 307–328. [[CrossRef](#)]
15. Moreno, C.; Sáez, R.; González, F.; Almodóvar, G.; Toscano, M.; Playford, G.; Alansari, A.; Rziki, S.; Bajddi, A. Age and depositional environment of the Draa Sfar massive sulfide deposit, Morocco. *Miner. Depos.* **2008**, *43*, 891–911. [[CrossRef](#)]
16. Ben aissi, I. Contribution à L'étude Géologique des Amas Sulfurés Polymétalliques de Draa Sfar et de Koudiat Aïcha: Comparaison avec les Gisements de Ben Slimane et de Kettara (Jebilet Centrales, Maroc Hercynien). Ph.D Thesis, University Cadi Ayyad, Marrakech, Morocco, 2008.
17. Lotfi, F.; Belkabir, A.; Brown, A.C.; Marcoux, E.; Brunet, S.; Maacha, L. Geology and Mineralogy of the Hercynian Koudiat Aïcha Polymetallic (Zn–Pb–Cu) Massive Sulfide Deposit, Central Jebilet, Morocco. *Explor. Min. Geol.* **2008**, *17*, 145–162. [[CrossRef](#)]
18. Essaifi, A. Relations entre Magmatisme-Déformation et al.tération Hydrothermale: L'exemple des Jebilet Centrales (Hercynien, Maroc). Ph.D Thesis, University of RennesI, Rennes, France, 1995.
19. Essaifi, A.; Hibti, M. The hydrothermal system of Central Jebilet (Variscan Belt, Morocco): A genetic association between bimodal plutonism and massive sulphide deposits? *J. Afr. Earth Sci.* **2008**, *50*, 188–203. [[CrossRef](#)]
20. Essaifi, A.; Goodenough, K.M.; Lusty, P.A.J.; Outigua, A. Microstructural and Textural Evidence for Protracted Polymetallic Sulphide Mineralization in the Jebilet Massif (Variscan Belt of Morocco). *Min. Resour. Sustain. World* **2015**, *1–5*, 1603–1606.
21. Lusty, P.A.J.; Goodenough, K.M.; Essaifi, A.; Maacha, L. Developing the lithotectonic framework and model for sulfide mineralization in the Jebilet Massif, Morocco: implications for regional exploration. In *Mineral Resources in a Sustainable World, Proceedings of the 13th Biennial SGA Meeting, Nancy, France, 24–27 August 2015*; André-Mayer, A.S., Cathelineau, M., Muchez, Ph., Pirard, E., Sindern, S., Eds.; Society for Geology Applied to Mineral Deposits (SGA): Genève, Switzerland, 2015; pp. 1635–1638.
22. N'Diaye, I.; Essaifi, A.; Dubois, M.; Lacroix, B.; Goodenough, K.M.; Maacha, L. Fluid flow and polymetallic sulfide mineralization in the Kettara shear zone (Jebilet Massif, Variscan Belt, Morocco). *J. Afr. Earth Sci.* **2016**, *119*, 17–37. [[CrossRef](#)]
23. Hibti, M. L'amas Sulfuré de Hajjar, Contexte Géologique de mie en Place et Déformations Superposées (Haouz de Marrakech, Méseta Sudoccidentale, Maroc). Ph.D Thesis, University Cadi Ayyad, Marrakech, Morocco, 1993.
24. Zouhry, S. Étude Métallogénique D'un amas Sulfuré Viséen à Zn Pb Cu: cas de Hajar, Guemassa, Maroc. Ph.D Thesis, Ecole polytechnique de Montréal, Montréal, Canada, 1999.
25. Hibti, M.; Marignac, C. The Hajjar deposit of Guemassa (SW Meseta, Morocco): A metamorphosed syn-sedimentary massive sulfide ore body of the Iberian type of volcano-sedimentary massive sulfide deposits. In *Mineral Deposits at the Beginning of the 21st Century, Proceedings of the Joint Sixth Biennial SGA-SEG Meeting, Krakov, Poland, 26–29 August 2001*; A.A. Balkema: Lisse, The Netherlands, 2001; pp. 281–284.

26. Delchini, S. Etude Tectono-Thermique D'un Segment Orogénique Varisque à Histoire Géologique Complexe: Analyse Structurale, Géochronologique et Thermique du Massif des Jebilet, de L'extension à la Compression. Ph.D Thesis, University of Orléans, Orléans, France, 2018.
27. Delchini, S.; Lahfid, A.; Ramboz, C.; Branquet, Y.; Maacha, L. New Peak Temperature Constraints using RSCM Geothermometry on the Hajjar Zn-Pb-Cu Mine and its Surroundings (Guemassa Massif, Morocco). In Proceedings of the 13th SGA Biennial Meeting, Nancy, France, 24–27 August 2015.
28. Delchini, S.; Lahfid, A.; Plunder, A.; Michard, A. Applicability of the RSCM geothermometry approach in a complex tectono-metamorphic context: The Jebilet Massif case study (Variscan Belt, Morocco). *Lithos* **2016**, *256*, 1–12. [[CrossRef](#)]
29. Haimmeur, J. Contribution à L'étude de L'environnement Volcano-Sédimentaire et du Minerai de Douar Lahjar (Guemassa, Maroc), Lithologie, Paléo-Volcanisme, Géochimie et Métallogénie. Ph.D Thesis, École Nationale Supérieure de Géologie, Nancy, France, 1988.
30. Raqiq, H. Le bassin Carbonifère des Guemassa (Meseta Sud occidentale, Maroc): Lithostratigraphie, sédimentologie et évolution structurale. Ph.D Thesis, University Cadi Ayyad, Marrakech, Morocco, 1997.
31. Ouadjou, A. Pétrographie, Géochimie et Structure des Roches Magmatiques Antéschisteuses des Massifs Hercyniens des Guemassa et Souktana. Ph.D Thesis, University Cadi Ayyad, Marrakech, Morocco, 1997.
32. Ed Debi, A.; Saquaque, A.; Kersit, M.; Chbiti, A. L'amas sulfuré de Hajar (Guemassa, Maroc). *Chronique de la Recherche Minière* **1998**, *531–532*, 45–54.
33. Watanabe, Y. 40Ar/39Ar geochronologic constraints on the timing of massive sulfide and vein-Type Pb-Zn mineralization in the Western Meseta of Morocco. *Econ. Geol.* **2002**, *97*, 147–157. [[CrossRef](#)]
34. Soulaïmani, A. L'évolution structurale des Massifs hercyniens du Haouz de Marrakech: Guemassa- N'fis (Maroc). Ph.D Thesis, University Cadi Ayyad, Marrakech, Morocco, 1991.
35. Dias, R.; Hadani, M.; Leal Machado, I.; Adnane, N.; Hendaq, Y.; Madih, K.; Matos, C. Variscan structural evolution of the western High Atlas and the Haouz plain (Morocco). *J. Afr. Earth Sci.* **2011**, *61*, 331–342. [[CrossRef](#)]
36. Hoepffner, C.; Soulaïmani, A.; Piqué, A. The Moroccan Hercynides. *J. Afr. Earth Sci.* **2005**, *43*, 144–165. [[CrossRef](#)]
37. Saadi, M.; Hilali, E.A.; Bensaïd, M.; Boudda, A.; Dahmani, M. Carte géologique du Maroc, échelle 1:1 000 000. *Notes Mém. Serv. Géol. Maroc*. 1985. Available online: <https://geodata.mit.edu/catalog/mit-gfcc2renabn5c> (accessed on 6 October 2018).
38. Pedersen, F.D. Remobilization of the massive sulfide ore of the Black Angel Mine, central West Greenland. *Econ. Geol.* **1980**, *75*, 1022–1041. [[CrossRef](#)]
39. Maiden, K.J.; Chimimba, L.R.; Smalley, T.J. Cuspatite ore-wall rock interfaces, piercement structures and the localization of some sulfide ores in deformed sulfide deposits. *Econ. Geol.* **1986**, *81*, 1464–1472. [[CrossRef](#)]
40. Plimer, I.R. Remobilization in high-grade metamorphic environments. *Ore Geol. Rev.* **1987**, *2*, 231–245. [[CrossRef](#)]
41. Gu, L.; Zheng, Y.; Tang, X.; Zaw, K.; Della-Pasque, F.; Wu, C.; Tian, Z.; Lu, J.; Li, X.; Yang, F.; et al. Copper, gold and silver enrichment in ore mylonites within massive sulphide orebodies at Hongtoushan VHMS deposit, NE China. *Ore Geol. Rev.* **2007**, *30*, 1–29. [[CrossRef](#)]
42. Aarab, E.M.; Beauchamp, J. Le magmatisme carbonifère pré-orogénique des Jebilet centrales (Maroc). Précisions pétrographiques et sédimentaires. Implications géodynamiques. *CR Acad. Sci. Paris* **1987**, *304*, 169–174.



© 2018 by the authors. Licensee MDPI, Basel, Switzerland. This article is an open access article distributed under the terms and conditions of the Creative Commons Attribution (CC BY) license (<http://creativecommons.org/licenses/by/4.0/>).



MDPI  
St. Alban-Anlage 66  
4052 Basel  
Switzerland  
Tel. +41 61 683 77 34  
Fax +41 61 302 89 18  
[www.mdpi.com](http://www.mdpi.com)

*Minerals* Editorial Office  
E-mail: [minerals@mdpi.com](mailto:minerals@mdpi.com)  
[www.mdpi.com/journal/minerals](http://www.mdpi.com/journal/minerals)





MDPI  
St. Alban-Anlage 66  
4052 Basel  
Switzerland

Tel: +41 61 683 77 34  
Fax: +41 61 302 89 18

[www.mdpi.com](http://www.mdpi.com)



ISBN 978-3-03897-785-8